Dick, H.J.B., Natland, J.H., Miller, D.J., et al., 1999
Proceedings of the Ocean Drilling Program, Initial Reports Volume 176

3. Site 735[1]

Shipboard Scientific Party[2]

OPERATIONS SUMMARY

Overview and Significant Accomplishments

We began Leg 176 with the first line ashore in Cape Town, South Africa, at 1000 hr on 8 October 1997. Time as reported in this summary is local ship time (Universal Time Coordinated [UTC] + 2 hr). Leg 176 drilling operations were quite different from those of most Ocean Drilling Program (ODP) legs. We conducted all drilling operations at a single site in a single hole. Hole 735B was first established during Leg 118. During that leg, a hard-rock base (HRB; Fig. F1) was set in 731 m of water and a 9⅞-in hole was cored to a depth of 500 meters below seafloor (mbsf). Another 0.7 m of penetration was made on that leg using the 3¾-in Navidrill Core Barrel, establishing a "cored" total depth of 500.7 mbsf. During Leg 176 we set out to reoccupy Hole 735B and deepen it to a depth of at least 1500 mbsf. We were overwhelmingly successful in meeting this objective, deepening Hole 735B from 1235.8 meters below rig floor (mbrf), or 504.8 mbsf, to 2239.0 mbrf, or 1508.0 mbsf. We have not established why our Leg 176 beginning sub-bottom bottom depth was 4.8 m deeper than the total depth documented at the end of Leg 118.

We used the rotary core barrel (RCB) wireline coring system exclusively during the leg. Ten RCB C-7 core bits yielded the recovery of 122 cores. A total of 1003.2 m of new hole was cored, from which 865.99 m of core was recovered, or 86.3% of the section (Table T1). Penetration rates varied from 1.3 to 6.1 m/hr in the gabbro and olivine gabbro. We achieved faster rates in coarser grained olivine gabbros and in fractured rock. Drilling rates were slower in more massive, finer grained, or strongly foliated rocks. Conversely, recovery rates were high, close to 100%, in both massive and fine-grained gabbro, but were much lower in highly fractured rock. The average rate of penetration (ROP) for the

F1. Photomosaic of the hard-rock base, p. 101.

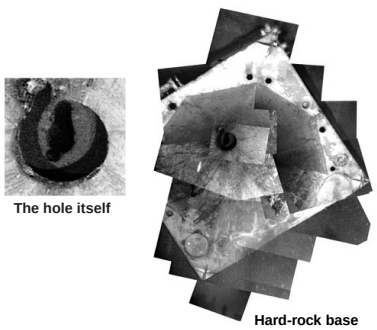

T1. Coring summary for Hole 735B, p. 252.

[1]Examples of how to reference the whole or part of this volume.
[2]Shipboard Scientific Party addresses.

leg was 2.7 m/hr. We took drift measurements at eight stations between 500 and 1400 mbsf. Hole deviation based on the Tensor electronic multishot data was moderate, varying between 4.3° and 4.8°.

Our progress in the hole ended when a 5-in drill pipe connection failed, leaving 131 joints of 5-in drill pipe and a coring bottom-hole assembly (BHA) in the hole, a total of 1403 m of drill string. The failure occurred when the pipe was 97 m off bottom during a routine wiper trip to replace wear-knotted drill pipe with standard 5½-in drill pipe. At the time of the failure, as during most of our operations during this leg, we were experiencing heave of the rig floor in excess of 2 m. On more than one occasion, including this episode, the pipe caught on a ledge in the borehole and lifted out of the elevator at the rig floor. We attempted to fish the severed pipe using a 9½-in overshot dressed with a 6⅞-in basket grapple and mill control. We successfully engaged the pipe and as it was being lifted to its total weight of 130,000 lb the drill string parted again. The new failure point coincided with a point at which the pipe had apparently buckled upon impact with the bottom of the hole. We ultimately recovered a total of 497 m of 5-in drill pipe. The fish remaining in the hole (906 m) consists of 26 stands of 5-in drill pipe (734 m) plus the coring BHA (172 m). We made seven unsuccessful fishing attempts over a period of 7.4 days before abandoning attempts to clear the hole.

Besides the drill string, several historical records were also broken during Leg 176. More hard rock (866 m) was recovered during Leg 176 than during any other leg in the history of ODP or the predecessor Deep Sea Drilling Project (DSDP), nearly doubling the previous record, also made in Hole 735B during Leg 118, of 434 m. We also cored more than twice the hard rock (1003 m) of any other single leg, shattering the previous Leg 118 record of 501 m. Hole 735B is the fifth deepest hole in ODP history. In addition, Leg 176 coring in Hole 735B now qualifies as the third longest single-hole continuously cored interval (mud or rock) in ODP history.

We conducted logging operations in two phases. The first phase (two logging runs to 492 mbsf) was done after the initial reentry into the hole and before commencing coring operations. It included the Triple-Combo (natural gamma sonde [NGS], accelerator porosity sonde [APS], hostile environment lithodensity sonde [HLDS], and the dual laterolog [DLL]) plus temperature log. The second string included the NGS, the dipole shear sonic imager (DSI), and the Formation MicroScanner (FMS). We ended this logging run early, however, because of apparent data acquisition difficulties.

We conducted the second phase of logging and vertical seismic profile (VSP) experiments near the end of the leg, after several attempts to recover the lost drill string. The first tool string consisted of the HLDS, caliper, APS, and the hostile environment spectral natural gamma sonde (HNGS). The second logging run consisted of the natural gamma tool (NGT), DSI, General Purpose Inclinometry Tool (GPIT), and the FMS probes. The third tool string was composed of the NGT, GPIT, and DLL probes.

During the first logging run on phase II, we obtained good density, porosity, and gamma-ray measurements from 49 to 595 mbsf, or 11 m above the hole obstruction (606 mbsf). The second logging run (DSI-FMS) resulted in good data recorded by the DSI. Cross-dipole and *P*- and *S*-wave mode data were recorded during the first pass, and cross-dipole, upper dipole, and Stoneley modes during the second pass. The FMS, however, did not fare as well. After spending some time testing different

gain options to improve the data quality from the FMS, we opted to recover the tool and repeat the logging run with a replacement FMS. Unfortunately, the results of the second tool run were similar to those of the first. Shore processing later showed that the tools could not respond quickly enough to the extreme resistivity contrasts between lithology types. The deployment of the third tool string resulted in very good resistivity data with the DLL.

The fourth and final logging run consisted of the Schlumberger three-component VSP tool. The objectives of the VSP were to acquire data over the section of hole not covered by the Leg 118 VSP and to acquire better VSP data using the new tool. We hoped that new data would resolve sub-bottom reflectors below 1500 mbsf and give better observations of the seismic attenuation at the site. The VSP operation took about 16 hr rig floor to rig floor. We shot both air gun and water gun sources with the sonde clamped at 23 depths in the hole. The tool did not give appreciably better data than were acquired on Leg 118, but we did fill in the coverage between 500 and 600 mbsf.

After concluding the wireline logging and VSP runs we round-tripped the drill string one last time for a final fishing attempt. The fish was contacted ~2 m deeper than before at 1339 mbrf, or 608 mbsf. During subsequent working of the pipe, we contacted the fish at the shallower (606 mbsf) depth; however, all attempts at engagement proved futile. We abandoned our final fishing attempt at 1400 hr on 1 December 1997 and prepared to get under way for Cape Town, South Africa. We departed Hole 735B at 1900 hr on 1 December 1997.

Operations Narrative

Transit to Site 735

At 1300 hr on 15 October 1997, we passed the last line ashore and headed out of Table Bay, Cape Town harbor. At 1346 hr we discharged the pilot and got under way at full speed for Site 735. Rough seas rounding the Cape of Good Hope, strong headwinds, and the effects of the Agulhas Current slowed our transit; however, we ultimately accomplished the 2003-nmi transit to Site 735 in 9.0 days at an average speed of 9.3 kt. Propulsion motor P-17A was taken off-line during the transit due to armature damage when a field coil failed. The engineers rebuilt the assembly while on site, and it was placed back on line before our departure for Cape Town. We were also forced to reduce speed for ~1 hr using manual steering and magnetic compass for heading when an emergency generator test caused a malfunction of the automatic station keeping (ASK) system. This system is linked to the ship's gyrocompass. The problem was ultimately traced to a dead cell in the ASK back-up battery bank. Subsequent system testing was successful once the bad battery was replaced. Besides routine preventive-maintenance system (PMS) tasks, the installation of a rig-floor waste-collection system was completed during the transit and efforts continued on the installation/testing of a new waste-burning incinerator system for future Antarctic expeditions. We arrived on location 24 October 1997, and at 1345 hr the first positioning beacon was dropped using the 10-yr-old Satellite Navigation coordinates (32°43.395′S, 57°15.959′E) for Hole 735B.

Site 735

Locating Hole 735B

We immediately went to work making up an outer core barrel assembly and four stands of 8¼-in drill collars. Three stands were temporarily stored in the derrick because our first pipe trip used only a single stand of drill collars in the BHA for logging the existing 500-m-deep hole. After tripping the drill string to the seafloor, we deployed the vibration-isolated television camera and began searching for Hole 735B. Because this hole was being reoccupied, and the seafloor depth was known to be 731.0 m, we did not require a precision depth recorder reading. In >1 hr, using an expanding-box search pattern, we located the HRB deployed during Leg 118. Final GPS location coordinates for Hole 735B were ultimately determined to be 32°43.3928′S and 57°15.9606′E, or ~5 m away from the original coordinates of 10 yr prior.

Initial Logging of Hole 735B

At 2000 hr on 24 October 97, we reentered Hole 735B; however, resistance was encountered almost immediately at a depth of 736 m (5 mbsf). We pulled clear of the seafloor, picked up the top drive, and using slow rotation reentered for the second time at 2130 hr. This time the end of the drill string was placed at a logging depth of 780 m (49 mbsf) without incident.

Logging operations began with the Triple-Combo consisting of natural gamma, porosity, lithodensity, and temperature tools. We also obtained temperature data using the Lamont-Doherty Earth Observatory temperature tool. The first logging run advanced to 492 mbsf, or just 8 m short of the total depth of 500.7 mbsf. Our second logging run included the NGS, the DSI, and the FMS. We had to end this run early because of data acquisition difficulties. We completed the first phase of logging operations by 1700 hr on 25 October 1997.

Following a pipe trip to change over to a coring BHA, we again reentered Hole 735B and ran to bottom. The top drive was used at several points to rotate past obstructions; however, minimal resistance was encountered on the trip. Because the last core recovered during Leg 118 was taken with the Motor-Driven Core Barrel (MDCB), we expected the lowermost 0.7 m of the hole would be under gauge for RCB operations. The bit tagged bottom at 504.8 mbsf, or 4.8 m below the depth that RCB coring ended on Leg 118, and 4.1 m below the depth of MDCB drilling. The discrepancy between the depth to the bottom of the hole recorded at the end of Leg 118 and the depth at which Leg 176 coring operations began remains unexplained.

Core Bit 1

We began continuous coring operations with Core 176-735B-89R at a total depth of 1235.8 m, or 504.8 mbsf. For BHA configurations, bit type, drill-string configurations, and bit-specific recovery for all bit trips, the interested reader is referred to Table T2.

Partial cores (ranging in length from 3.7 to 8.0 m) were taken beginning with Core 176-735B-92R because of the extremely slow ROP. Core jamming inside the acetate butyrate core liners occurred on three cores in a row, so, beginning with Core 176-735B-96R, we deployed the core barrels without liners. We used bentonite gel mud exclusively during Leg 176, circulating the mud in 20-bbl sweeps every other core to

T2. Operations parameters for Hole 735B, p. 254.

enhance hole cleaning. Upon recovering Core 176-735B-96R, we found that the core catchers and cored material were missing. The threaded connection between the core catcher sub and the 11⅛-in inner barrel sub unscrewed, leaving the core barrel components and core material inside the pipe just above the bit. We decided that attempting to fish the items out of the pipe would be futile; therefore, the bit run was ended at a depth of 556.3 mbsf. The bit cleared the rig floor at 2145 hr, and Core 176-735B-96R was recovered from the pipe. We found the core bit to be in good condition except for the inner (nose) row of carbide buttons.

Core Bit 2

Using the same BHA configuration we deployed the subsea television camera and reentered the HRB in less than 15 min of ship maneuvering. These quick (15 min) reentries proved to be the rule for the remainder of the leg. In this case, the driller again could not induce the bit into the hole, and another reentry had to be made with the top drive picked up. On the second attempt we reentered the HRB at 0300 hr on 28 October 1997 and, using slow top-drive rotation, walked the bit into the off-center hole (Fig. **F1**) without incident. Continuous coring began with Core 176-735B-97R from 556.3 mbsf. Coring on this bit run was affected by large long-period swells, which translated into rig floor heaves of 2.0 to 3.0 m, making it difficult for the driller to maintain optimum weight on bit (WOB). The seas moderated on the third day, but by then it was time to pull the bit for replacement. Our original goal was to obtain a minimum of 40 rotating hours on this bit, but because of the large load fluctuations, we decided to be conservative and terminate coring operations slightly earlier than planned. In addition, the driller noted elevated pump pressure during the final three cores, and we suspected that two of the bit jets may have become plugged. We suspended coring after cutting Core 176-735B-111R to a depth of 642.7 mbsf. The bit cleared the rig floor at 0930 hr on 30 October 1997. The core bit was in good condition except for the inner (nose) row of carbide buttons. The bit did have two jets plugged with a combination of cuttings and Teflon bit-seal material. In addition, a 5-in-long crack extended longitudinally outward from the base of the pocket in the drilling-jar body.

Core Bit 3

After reentry with this bit run, we encountered 8 m of loose fill at the bottom of the hole. We initiated continuous coring with Core 176-735B-112R at 642.7 mbsf. Our goal on this run was to replace the bit after completing Core 176-735B-124R; however, observations of core tapering and some suspicious markings in Core 176-735B-123R persuaded us to halt operations with only 3.4 m of advance on Core 176-735B-124R. The bit cleared the rig floor at 0530 hr on 2 November 1997. Surprisingly, we again found the bit to be generally in good condition with effective bearing seals and no sign of imminent catastrophic failure. The internal cutter wear was more advanced than on the two earlier bits with the inner (nose) row of carbide buttons completely worn back into the matrix material. One of the two opposite cutters with three carbide inserts was also worn back to the matrix material. In addition, there was some wear at the tip of the core guide, indicating that ROP would have soon begun to suffer.

Core Bit 4

As a precaution, because of the earlier cracking incident, we again laid out the drilling jars for nondestructive testing (NDT) inspection and pressure testing prior to running them back in the hole with the fourth core bit. During the NDT inspection, we identified small cracks initiating from the two corners at the base of each pocket in the jar body. We set these jars aside, and because the remaining set of drilling jars had not yet passed pressure testing, this BHA was made up without jars. At 0845 hr on 2 November 1997, we reentered the hole and ran to 742.0 mbsf, or ~10 m off bottom. Using the Tensor electronic multishot tool we conducted a wireline drift survey from 742.0 to 500.0 mbsf. Six measurements made at 50-m increments indicated a hole deviation of 4.5° ± 0.3°. Upon completing the survey, we began continuous coring with Core 176-735B-125R from 752.1 mbsf. While cutting Core 176-735B-136R, circulating pressure dropped by 100 psi, and we assumed that the RCB bit seal had failed. Although the bit continued to recover gauge core and advance at a respectable rate, we decided again to be conservative and pulled the bit after 46.8 hr. We halted coring after recovering Core 176-735B-140R to 889.3 mbsf. The bit arrived at the rig floor by 0500 hr on 5 November 1997. Once again, the bit was in good condition with no sign of imminent catastrophic failure. As expected, the internal cutter wear was slightly more advanced than on previous bits. The inner (nose) row of carbide buttons was completely worn back into the matrix material, and both of the two opposite cutters with three carbide inserts each were also worn back to the matrix material. There was slight wear at the tip of the core guide. The bearing seals were still effective, and the bearing condition was actually slightly better (tighter) than that of the previous bit.

Core Bit 5—First Deployment

During the previous bit run we rebuilt the final remaining set of drilling jars and added packing to the seal chamber. The jars passed a pressure test of 1500 psi for 10 min and were judged acceptable for use. A new C-7 core bit was made up, and after 15 min we made yet another routine reentry at 0800 hr on 5 November 1997. We were tripping the bit to bottom when it encountered a hard bridge at a depth of 123 mbsf. After picking up the top drive we again encountered an obstruction, this time at 117.0 mbsf. We spent close to 1½ hr attempting to clear the bridge with the C-7 core bit to no avail. The top drive repeatedly stalled out with little or no WOB each time it contacted the obstruction. After deliberation, we decided that a better strategy would be to use a more robust tricone drill bit to clear the hole. The drill string was tripped back to the rig floor by 1545 hr that same day.

Tricone Drill Bit

Leaving the BHA configuration unchanged, we exchanged the Rock Bit Industries C-7–style core bit for a Smith F57 tricone drill bit. We reentered the hole at 1915 hr on 5 November 1997 (15-min reentry), and the pipe tagged the obstruction at the same depth as before (117.0 mbsf). Top-drive stalling continued to be a problem during our attempts to clear the bridge. This was aggravated by significant heave resulting from long-period swells generated by a significant low-pressure cell some 50 miles to the south of the drilling location. Ultimately,

by using high rotation speeds (100–130 rpm) coupled with low WOB and some skillful drilling supervised by the Overseas Drilling Limited (ODL) drilling superintendent, we cleared the bridge in the hole. There were, however, top-drive stalling torques of 750 A and overpulls of up to 60,000 lb during the episode. We theorized that an angular piece of material must have sloughed off of the side of the hole, leaving a high angle bridge that caused both core and drill bits to wedge immediately upon contact. We subsequently washed/reamed the hole to bottom to ensure that any other bridges or hard fill on bottom would be broken up by the more rugged tricone drill bit before resuming coring operations. No other bridges were identified, however, and only 2.0 m of soft fill was encountered on bottom. We circulated this out in short order and pumped a 50-bbl bentonite gel mud sweep. We then tripped the pipe back to return the BHA to a coring configuration. The tricone drill bit cleared the rig floor at 0630 hr on 6 November 1997.

Core Bit 5—Second Deployment

As the bit used in our fifth deployment showed no signs of wear, we ran the same bit back into the hole following hole-cleaning operations. The drilling jars failed a routine pressure test. Because they were the only remaining set of jars, we delayed reentry until the packing on the jars could be replaced and pressure tested. We then made up the jars with the remaining BHA and tripped the drill string to bottom. The hole was reentered at 1230 hr on 6 November 97 after another routine 15-min ship maneuver. We encountered no ledges, and the pipe went straight to bottom without incident. No fill was detected at total depth, and we began continuous coring with Core 176-735B-141R from 889.3 mbsf. While we were cutting the second core of this bit run, the drilling torque escalated to 600 A and we experienced 60,000 lb of overpull picking up off bottom. High torque, top-drive stalling, and overpull of 40,000–60,000 lb continued through Core 176-735B-145R, but we encountered no problems after Core 176-735B-146R. We halted coring while cutting Core 176-735B-151R at a depth of 987.5 mbsf when drilling torque escalated to 40–50 or more amps from the normal and ROP dropped off to 1.6 m/hr. The bit cleared the seafloor at 0250 hr and was at the rig floor by 0415 hr on 9 November 1997. As before, we found the bit to be in good condition with no sign of imminent catastrophic failure. The internal cutter was again severely worn, with the inner (nose) row of carbide buttons completely worn back into the matrix material. Both of the two opposite cutters with three carbide inserts were also worn back to the matrix material. Bearing seals were effective, and the bearing condition was good.

Core Bit 6

We made up yet another new C-7 core bit with the BHA. However, drilling jars were not included on this run because the final remaining set also showed evidence of cracking during NDT inspection. After reentry at 0700 hr on 9 November 1997, the drill string was run to the bottom without incident. We initiated continuous RCB coring on Core 176-735B-152R at a depth of 987.5 mbsf and continued coring through Core 176-735B-163R to a depth of 1099.4 mbsf. We terminated coring early while cutting Core 176-735B-163R because the drilling torque abruptly increased 40–50 or more amps and the ROP dropped to 2.5 m/hr from earlier, higher rates. The bit reached the rig floor by 2330 hr on

11 November 1997 and again was in good condition with no sign of imminent catastrophic failure. The internal cutter wear was severe, however, and the inner (nose) row of carbide buttons was completely worn back into the matrix material, as were both of the two opposite cutters with three carbide inserts. One insert had fallen out of the core-gauge row and another had broken off. Bearing seals were effective, and bearing condition was as good as, or better than, on any of the previous bits.

Core Bit 7

We made up the seventh new C-7 core bit and welded closed a crack in the latch sleeve before running in the hole. The BHA was run in the hole as before without drilling jars. We reentered at 0245 hr on 12 November 97 and ran the drill string to bottom without incident. We initiated continuous RCB coring with Core 176-735B-164R at a depth of 1099.4 mbsf and continued to a depth of 1191.1 mbsf. No fill was identified after any of the connections. However, while cutting Core 176-735B-174R, the drilling torque increased dramatically from the normal 360–400 A to 500–600 A. The torque dropped back to normal when we picked the bit up off bottom. We had only 33.3 rotating hours on the bit; nevertheless, we could not rule out the possibility of a pending bit problem. We therefore decided to err on the side of conservatism and brought back the final core after advancing only 3.0 m. Upon clearing the rig floor at 0430 hr on 14 November 1997, we found the bit to be in excellent condition; similar to the bit used during the second core-bit run of 36.0 hr. There was, instead, a high degree of wear and burnishing on the crossover sub between the 5-in and 5½-in drill pipe during the pipe trip. A check of the pipe tally placed the crossover at or near seafloor in the vicinity of the HRB when the bit was on bottom. This may have been the source of the excessive drilling torque.

Core Bit 8

We ran the eighth new C-7 core bit in the hole and replaced the crossover sub between the 5-in and 5½-in drill pipe during the pipe trip. In addition, we added 10 more stands of 5-in drill pipe to the string to remove the crossover from the area of the HRB. The bit went to the bottom of the hole without incident after another routine 15-min reentry (0700 hr on 14 November 97). We began continuous RCB coring with Core 176-735B-175R at a depth of 1191.1 mbsf and continued to a depth of 1360.6 mbsf. Coring was terminated after advancing 5.6 m on Core 176-735B-193R when the drilling torque increased by 50–100 A. The bit had 53.8 rotating hours at that time so we conservatively pulled the bit. The bit reached the rig floor at 1530 hr on 17 November 1997 and was in good condition. One cover plate from the grease reservoir was missing, however, and this may have contributed to the increased torque downhole.

Core Bit 9

On our ninth bit run, we used another new C-7 core bit with an additional five stands of 5-in drill pipe to keep the 5-in × 5½-in crossover sub well above the HRB. After slipping and cutting the drill line for the first time this leg, we reentered the hole at 2045 hr on 17 November 1997 and ran to a depth of 1295.0 mbsf, where the bit met an obstruc-

tion and was unable to pass. We picked up the top drive and were able to ream the remaining 65.6 m without difficulty. We found no indication of any fill on bottom, and the drilling torque was normal. Continuous RCB coring was initiated with Core 176-735B-194R at a depth of 1360.6 mbsf and continued to a depth of 1386.4 mbsf. We stopped coring 3.1 m into Core 176-735B-197R because of worsening weather. In addition to the heave compensator beginning to exceed operating limits, we experienced five 3% and two 5% positioning alarms. We stopped coring after only 8.8 rotating hours on the bit and began to pull out of the hole. After pulling the pipe to a depth of 739.0 m (8.0 mbsf), the drill string was hung off on the elevators while the driller laid out the previously pulled stand of drill pipe. At that time the bit contacted a ledge in the hole, causing the drill string to jump upward in the landing elevators. Using the stand in the string above the rotary, the string was lifted ~2.0 m off the elevators until the bit was free from the ledge. Two attempts were then required before the drill string could be lowered past the ledge to the next tool joint. The bit cleared the seafloor at 2115 hr on 18 November 1997 with marginal weather and sea conditions. Winds were ranging from 33 to 41 kt gusting to 51 kt, and swells were running 8–18 ft at 8- to 9-s periods. The vessel was heaving 10–18 ft. Because of extremely rough seas at the time, we decided to hang off the BHA/transition pipe below the keel and wait for the weather to abate. At 2215 hr on 18 November 1997, the string was hung off on the elevators, and we commenced "waiting on weather." By 0245 hr the following morning, conditions moderated sufficiently to recover and conduct a NDT of the BHA. We found no cracks during the "magnaflux" inspection; however, two drill collars (2 and 3) were bent. This was obviously the result of the incident just described. The recovered bit was in excellent condition although (nose) cutter wear was much higher (50% of the carbide inserts worn away) than expected of a bit with less than 9 rotating hours.

Core Bit 10

By 1500 hr on 19 November 1997 our sea conditions had moderated, and the captain felt confident that the storm system was both weakening and moving away. We made up another new C-7 core bit, ran in the hole, and reentered at 1945 hr on 19 November 1997. When the bit reached a depth of 1295.0 mbsf it was again unable to pass, just as in the eighth bit run. As before, we picked up the top drive and reamed to bottom without incident. We proceeded to rotary core with Core 176-735B-198R at a depth of 1386.4 mbsf and continued to a depth of 1508.0 mbsf. We took drift measurements at 1100 and 1400 mbsf and determined hole deviation at those points to be 4.6° and 4.8°, respectively.

We interrupted coring after Core 176-735B-210R to short trip five stands of wear-knotted drill pipe out of the hole and replace it with standard 5½-in drill pipe. We could have continued coring using knobby drilling joints, but the cores would have been shorter (9.2 m vs. 9.6/9.7 m) and the knobbies would have been more time-consuming to handle, whereas the wear-knotted pipe could be handled using the automated pipe racker. After pulling all but four joints of the wear-knotted pipe from the hole, we suffered a drill-string failure. The pipe was landed in the elevators while the driller placed a double joint of drill pipe into the mousehole with the top drive. During this time the drill string twice came into contact with a ledge in the hole when the vessel

heaved down, causing the string to rise ~0.5 m above the landing elevators. The driller moved as quickly as possible to reinstall the top drive, and the string was lifted off of the landing elevators. However, by that time the damage had been done; the weight indicator showed a loss of 130,000 lb of string weight.

Our calculations indicated that the string parted in the 5-in drill pipe at or near the seafloor. We sent down the subsea camera to inspect the drill string/HRB, confirming that the failed pipe was not above the seafloor, and then recovered the drill string. At 0600 hr on 22 November 1997, we identified the point of failure as the last-engaged thread of a 5-in drill-pipe pin connection located at 739 m (8 mbsf). The fish we left in the hole was 1403 m in length and consisted of a 172-m-long BHA plus 43⅔ stands of 5-in drill pipe (1231 m).

Fishing Attempts

We made a total of eight attempts to fish the drill string from the hole. Interspersed with the fishing attempts were several pipe trips with milling tools and one for logging operations. During the first fishing attempt, we were able to latch onto the severed drill string. We were lifting it to its total weight of 130,000 lb when it parted once again, leaving only 35,000 lb of weight suspended below the overshot tool. We pulled the fishing string to the surface and recovered a total of 497 m of 5-in drill pipe by 1930 hr on 22 November 1997. The drill string had parted in the 5-in drill pipe tube 2 ft below a box tool joint. This was at a point where the tube had buckled when the string impacted the bottom of the hole after the initial failure. The portion of drill string remaining in the hole (906 m) consisted of 26 stands (734 m) of 5-in drill pipe plus the coring BHA of 172 m.

During subsequent fishing/milling trips, we repeatedly encountered difficulties with ledges near the top of the hole. Although we tried several different fishing and milling tools, many fabricated on site by the ODL crew, none of these was successful in engaging the severed drill string (for a complete list of fishing and milling drill string configurations, see Table T2). A common result of milling operations was advancement of the drill pipe beyond the depth where the top of the severed drill string was initially encountered. Subsequent fishing attempts, however, routinely stopped at the original depth of the top of the severed pipe, indicating that the mills were side-tracking along the drill string rather than grinding away the top of it.

On our third milling attempt, we inserted a drill string stabilizer into the BHA to help keep the mill straight and potentially reduce side-tracking. Unfortunately, unacceptably high torque immediately after reentry indicated that the upper part of the hole was too narrow for such a configuration, and the stabilizer was removed from the milling BHA. Our fourth and final milling attempt went much better than previous attempts, with constant torque and a very slow ROP. On recovery of the milling tool, we noted a concentric wear pattern with a 5-in diameter in the center of the mill face. We were encouraged enough by this evidence to plan a final fishing trip, after allowing time for our logging program.

Wireline Logging and VSP Experiment

We used a shortened BHA for logging and installed a landing saver sub with a “special” landing ring two drill collars up from the bit to pro-

vide a landing point for the Kinley Crimper/Cutter assembly, should it be required. The landing ring inside diameter had to be opened up to 3.918 in to accommodate the oversized Schlumberger VSP tool. We reentered the hole at 0745 hr on 29 November 1997, and the pipe was placed at 780 mbrf, or 49 mbsf, with a 30-ft drilling knobby through the guide horn. At 0915 hr we began to rig up the Schlumberger logging sheaves and wireline compensator.

The first tool string consisted of the high-temperature lithodensity tool (HLDT), caliper, APS, and HNGS probes. The second logging run consisted of NGT, DSI, GPIT, and FMS probes. The third tool string was composed of NGT, GPIT, and DLL probes. The fourth and final run consisted of the Schlumberger BGKT three-component VSP tool. During the experiment, a hydrophone that had been hung off the rear port side crane to monitor noise in the water column failed. To avoid tangling the cable in the main screws, we brought the hydrophone back on deck for the remainder of the experiment. We rigged down the VSP tools and logging sheaves by 0415 hr on 1 December 1997 and proceeded to pull the drill string, clearing the seafloor at 0430 hr and reaching the rig floor by 0530 hr.

Final Fishing Attempt

While the logging/VSP efforts were under way, we fabricated another modified fishing assembly. An overshot assembly was shortened as much as possible, bringing the mill control and basket grapple closer to the open end of the overshot. In addition, "Cutrite" hard facing was applied to the lip guide, creating a "milling-capable" overshot assembly. We hoped that the combination of the shorter fishing assembly and the limited milling ability would allow the basket grapple to engage the drill pipe. We encountered the top of the severed drill string ~2 m deeper than before at 1339 mbrf, or 608 mbsf. During subsequent attempts to grasp the pipe, however, we made contact at the shallower (607 mbsf) depth. To our dismay, even after several hours and a herculean effort by the drilling crew, we were not able to extract the drill string from Hole 735B. We abandoned our final fishing attempt at 1400 hr on 1 December 1997 and prepared to get under way for Cape Town, South Africa. When the fishing tool was recovered, it showed obvious indications that something had at some time been inside the overshot as far as the mill control assembly.

Transit to Cape Town, South Africa

We began the return voyage to Cape Town, at 1900 hr on 1 December 1997. During the transit, the rig crews worked on the usual cleanup, painting, report writing, and PMS activities. In addition we held a meeting with rig personnel and the Leg 176 co-chief scientists/staff scientist to discuss approaches and operational options for a possible future deep hole (2500+ mbsf) in the Hole 735B Southwest Indian Ridge operating area.

We arrived at the pilot station at 1030 hr 9 December 1997 after a 1998-nmi voyage that averaged 10.9 kt. The first line was ashore at 1130 hr on 9 December 1997, officially ending Leg 176.

IGNEOUS PETROLOGY

Introduction

The structure and evolution of the lower ocean crust is a significant issue in earth science. The present study, along with Leg 118, provides the first opportunity to examine a stratigraphically coherent section of the lower oceanic crust sampled in situ. In all, 866 m of rock was recovered from 1004 m of drilled section during Leg 176 from Hole 735B on the Southwest Indian Ridge. This section reports on the igneous petrology of the cores and begins the discussion of its relevance to previously established models for the structure of the ocean crust. The details of the descriptive methods used to characterize these rocks are given in the "Explanatory Notes" chapter of this volume.

Lithostratigraphy

The Hole 735B cores between 504 and 1508 mbsf (Leg 176) were divided into 457 intervals numbered 496 through 952, following in numerical succession the 495 intervals identified in Hole 735B from the Leg 118 core (Dick et al., 1991a). Gabbroic rocks constitute more than 99 vol% of the igneous lithologies, and these, together with 0.5 vol% felsic veins, make up the core. Most of these rocks are coarse grained with a granular to intergranular texture. Rhythmic modal and grain size layering is present in 22 intervals (12 vol% of the core; see Fig. F2 and "Igneous Layering," p. 29). Fine-grained "microgabbro" intrudes the coarse-grained gabbros and constitutes 2 vol% of the core. Oxide-rich gabbroic rocks, which make up 7 vol% of the recovered samples, occur throughout the core, but are concentrated between 500 and 700 mbsf. The oxide-rich gabbros form lenses or networks intruding or replacing normal oxide-poor gabbros (see "Rock Types and Geochemistry," p. 21). Gabbronorites and orthopyroxene-bearing gabbros, with or without oxides, are present in the Leg 176 core only between 536 and 714 mbsf and make up ~8 vol% of the total volume.

The lithologic intervals generally have considerable variety in mode and grain size; thus, their reported characteristics are averages. Rock types deduced from thin sections and chemical analyses of small samples are not necessarily representative of the average rock type in the interval.

Major Rock Types

Rock types are defined in "Rock Classification," p. 5, in the "Explanatory Notes" chapter. The main rock types are distinguished by variations in grain size, and variations in the abundance of olivine, oxides, and orthopyroxene. Two relatively rare rock types in the Leg 176 core, pyroxenite and anorthositic gabbro, are characterized by their respective high modal abundances of augite and plagioclase. We use the term augite to cover the entire range of high-Ca clinopyroxene observed in hand specimens and thin sections. We find only orthopyroxene as the low-Ca pyroxene in the Leg 176 rocks, but pigeonite is present in a few Leg 118 cores. The relative abundances, modes, and grain sizes of the main rock types, based on macroscopic study of the core, are presented in Table T3, along with the average chemical composition of each rock type. Chemical compositions were determined by X-ray fluorescence analysis of small samples from the core (see

F2. Lithostratigraphic variations in Hole 735B, p. 102.

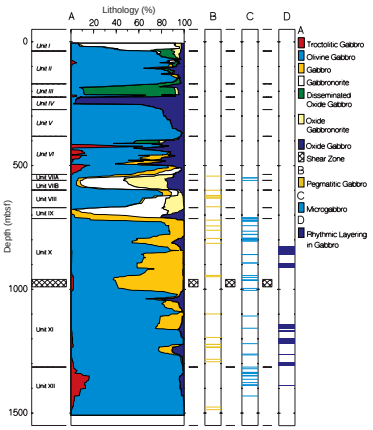

T3. Abundance, mode, chemical composition of major rock types, p. 256.

"Geochemistry," p. 47). Rock names for analyzed samples were determined by point counting of thin sections from adjacent core. The modal compositional variation of the 457 intervals is graphically illustrated in Figures F3 and F4.

In the description below of the lithologic units, no distinction is made between the various oxide-rich rock species except for oxide gabbronorite. Thus oxide gabbro comprises oxide gabbro, oxide olivine gabbro, and troctolitic oxide gabbro.

Only a few nongabbroic intervals were found: four troctolites, three diorites, and four clinopyroxenites (or clinopyroxenitic gabbros); the latter are local augite-rich cumulus layers and probably do not represent separate intrusive units. Many more troctolites occur locally in patches within intervals of varitextured gabbro. Felsic veins constitute approximately 0.5% of the core but were only defined as separate intervals if their width exceeded 5 cm (see "Felsic Veins," p. 28). The majority of veins are leucodiorite; other types are diorite, trondhjemite, tonalite, and granite.

Most of the rocks are intergranular or granular in texture. Although rocks with subophitic textures are not abundant, they are important within several of the major lithologic units (see "Lithologic Units," p. 13). The microgabbros are mainly olivine gabbros, but they have compositions ranging from troctolite through olivine gabbro and gabbro to oxide gabbro; they are presented separately in Table T3. Pegmatitic gabbro constitutes 4 vol% of the core in 29 separate intervals. Photographs of typical rock types are presented in Figures F5, F6, F7, F8, F9, F10, and F11.

Of the major cumulate rock types expected to form in the course of differentiation of a mid-ocean-ridge basalt magma, dunite, troctolite, olivine gabbro, gabbro, gabbronorite, oxide gabbronorite, and oxide gabbro, all are present in the Leg 176 core with the exception of dunite. Given that gabbroic Layer 3 at the SWIR is believed to be only about 2 km thick (Muller et al., 1997), the combined rocks of Legs 118 and 176 may well constitute a fair representation of the gabbroic lower crust generated at a slow-spreading ridge (see also "Rock Types and Geochemistry," p. 21). The overall mode and chemical composition of the Leg 176 core is presented in Table T4.

Lithologic Units

Six new major lithologic units were identified in the core recovered during Leg 176, based on modal mineralogy and the relative abundance of rock types as defined by the 457 reported intervals (see Fig. F2 and below).

Correlations between depth, the distribution of rock types, and unit boundaries are presented in Figure F2. The boundary positions and the characteristics of lithologic Units VI through XII are listed in Table T5. Unit VI continues from 382 mbsf in the Leg 118 core. The bottom of Unit XII was not reached when drilling ended during Leg 176.

Unit VI—Compound Olivine Gabbro (Intervals 304–511)

Unit VI is the compound olivine gabbro recovered during Leg 118 and which continues down into the section drilled during Leg 176. It was defined during Leg 118 on the basis of the occurrence of troctolitic and olivine-rich gabbros with minor oxide-bearing gabbros, orthopyroxene-bearing gabbro, and gabbronorites. The lower part of Unit VI recovered during Leg 176, below 504 mbsf, continues with abundant olivine

F3. Relative abundances of olivine, plagioclase, augite, p. 103.

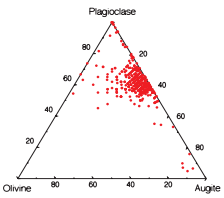

F4. Relative abundances of orthopyroxene, plagioclase, augite, p. 104.

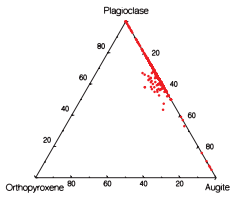

F5. Olivine gabbro with ophitic texture, p. 105.

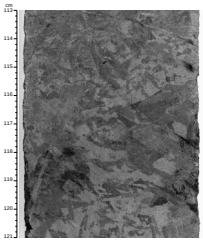

F6. Coarse-grained olivine gabbro, p. 106.

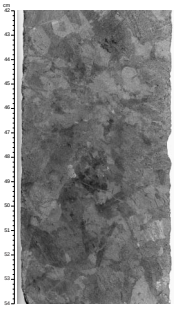

F7. Troctolitic microgabbro, olivine gabbro contact, p. 107.

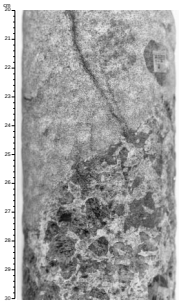

gabbro and troctolitic gabbro intervals and some intervals that are mixtures of the two rock types. The occurrence of Cr-diopside and the high relative abundance of troctolitic rocks with high Mg numbers are evidence of the primitive character of much of Unit VI.

Unit VII—Gabbronorite and Oxide Gabbronorite (Intervals 512–546)

The transition to lithologic Unit VII at 536 mbsf is marked by the occurrence of orthopyroxene-bearing gabbro and gabbronorite, with and without oxides, as well as the disappearance of troctolitic gabbro. Intervals of oxide-bearing rocks are more abundant, and the average grain size decreases relative to the Unit VI rocks recovered during Leg 176. In contrast to the previous unit, the first part of Unit VII has no subophitic intervals. This unit is composed of ~70% orthopyroxene-bearing rocks, which are relatively rare elsewhere in Hole 735B except for Units IX and I in the uppermost part of the Leg 118 core (Unit I extends 0–37 mbsf). The oxide-rich rocks clearly crosscut the gabbros, and some have sheared contacts. Unit VII is divided into two subunits, VIIA (intervals 512–526) and VIIB, at 560 mbsf. The bottom of Subunit VIIA at 560 mbsf coincides with a major fault, the disappearance of olivine gabbro, and the occurrence in Subunit VIIB (intervals 527–546) of intervals with subophitic texture.

Unit VIII—Olivine Gabbro (Intervals 547–568)

The start of Unit VIII at 599 mbsf is marked by a strong increase in grain size and a return to a higher abundance (73%) of olivine gabbro intervals than is present in Unit VI. Some of the intervals in Unit VIII contain subophitic textures, which are rare in Unit VII. Some gabbronorite, oxide-rich gabbronorite, and oxide-rich gabbro intervals are also present in Unit VIII.

Unit IX—Gabbronorite and Gabbro (Intervals 569–600)

Below 670 mbsf, Unit IX is dominated by orthopyroxene-bearing gabbro and gabbronorites (~65%) but contains fewer orthopyroxene-bearing oxide gabbros and oxide gabbronorites than Units VII and VIII. Olivine is not abundant in this unit, there are no subophitic intervals, and the grain size is markedly finer than in Unit VIII. Thus, there are several similarities between Units VII and IX. No pegmatitic gabbro or microgabbro intervals are present in Unit IX. The transition to Unit X is marked by the lowest occurrence of orthopyroxene-bearing rock types.

Unit X—Olivine Gabbro and Gabbro (Intervals 601–716)

Below 714 mbsf, orthopyroxene disappears and the abundance of olivine increases. The upper part of Unit X contains the most intense swarm of microgabbro intervals (Fig. **F2**). Pegmatitic intervals are also common in the upper part of Unit X. Rhythmic igneous layering is present at 827–914 mbsf (see **"Igneous Layering,"** p. 29). Oxide gabbros are extremely rare. In the lower part of Unit X, several intervals (698, 700–702, and 704) have metasomatized patches, which appear to have been generated by late percolating melts. The base of Unit X coincides with a shear zone at 960–990 mbsf (Fig. **F2**).

Unit XI—Olivine Gabbro (Intervals 717–880)

This unit, starting at 960 mbsf, is distinguished by the occurrence of abundant, thin intervals of oxide gabbro, which are most pronounced around 1025 mbsf. The overall abundance of oxide gabbro, however, is much lower than in Units VII and IX. Rhythmic layering (1138–1220

F8. Microgabbro intruding olivine gabbro, **p. 108.**

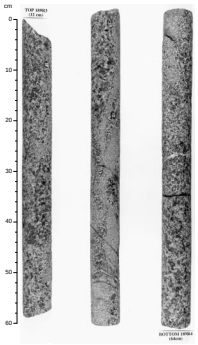

F9. Gabbro with variable texture, **p. 109.**

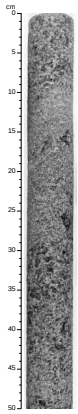

F10. Typical olivine gabbro, **p. 110.**

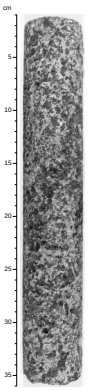

mbsf), very coarse olivine, and rare subophitic textures are present in the unit. The mylonite interval 879 was not chosen as the boundary between Units XI and XII because interval 880 is geochemically more similar to the overlying rocks than to those of Unit XII (see "Geochemistry," p. 47).

Unit XII—Olivine Gabbro and Troctolitic Gabbro (Intervals 881–952)

In Unit XII from 1314 mbsf, olivine gabbro and minor troctolitic gabbro dominate, almost to the total exclusion of other rock types. Only rarely do thin oxide gabbros break this monotonous olivine-rich unit. From the top of the unit to 1390 mbsf, abundant thin microgabbros intrude the main coarse-grained olivine gabbro. This zone resembles the swarm of microgabbro in the upper part of Unit X. Also occurring at this depth in the core are several instances of subvertical, meandering, dikelike pipes of microgabbro. Zones with crosscutting microgabbros (e.g., 880, 882, and 884) were logged as composite intervals. Zones of leucocratic gabbro, often more or less vertically arranged, are present in intervals 930 and 937. Very coarse olivine is present in parts of this unit.

Description of Contacts

Igneous contacts provide important information about the order of intrusion and the degree of crystallinity at the time of arrival of new batches of magma. A total of 457 lithologic intervals were recognized in the Leg 176 core on the basis of abrupt or gradational changes in grain size, modal mineralogy, or texture. Contacts between them were classified as intrusive, sutured, sharp-sheared, tectonic, gradational, not preserved, and not recovered.

Two contact types are thought to be the result of intrusive relationships between one lithology and another; these are "intrusive" and "sutured." These two contact types are illustrated in Figure F12. Intrusive contacts are defined by brittle deformation of the minerals composing the country rock, resulting in a contact that cuts across grain boundaries (Fig. F12A). A much more subtle form of igneous contact is defined as a "sutured" contact. Such a contact follows the outlines of grain boundaries, and grains in the country rock are not broken to make room for the invading magma (Fig. 12B). This is an obvious textural feature of sutured contacts, and thus the "sutured" term is a purely descriptive one, rather than implying a particular genesis of these contacts. Our interpretation of sutured contacts is that a magma intruded a partly consolidated crystal mush, so that grains of the invaded country rock were easily separated from one another during intrusion.

A third type of contact, "sheared," is ambiguously tectonic or intrusive in origin, because its original character is now obscured by shearing. Such contacts are typically quite sharp, and a minor foliation is developed next to the contact in one or both bordering lithologies and is pulled into the contact; this distinguishes them from gradational sheared contacts, where the shearing is distributed over a thicker zone (several centimeters). There are 24 sheared contacts preserved in the Leg 176 section. Tectonic contacts show extensive shearing, foliation in the surrounding lithologies, and in many cases the development of a mylonite along the contact. Where the mylonite is thicker than 5 cm, it is logged as a separate lithology (as in interval 879). Such contacts may imply that a fault zone has juxtaposed differing lithologies that may not have been in contact originally.

F11. Typical gabbro, p. 111.

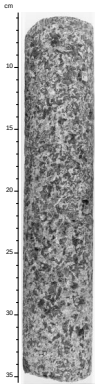

T4. Total mode for Leg 176 core, p. 260.

T5. Lithologic units of Leg 176, p. 261.

F12. Schematic of intrusive contact types, p. 112.

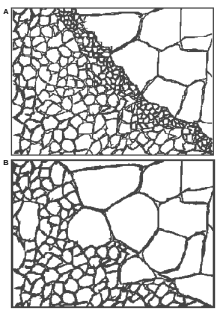

In the case of gradational contacts, one rock type grades into another without a clear, sharp border. Such gradational contacts are interpreted to be intraformational, in that small differences in volatile contents or crystal nucleation and growth rate in the residing magma may have resulted in the formation of the different rock types, rather than the arrival of a new batch of magma. Other gradational contacts may have resulted from the percolation of melt along fractures and grain boundaries beyond the boundaries of the main intruding magma body. This may have been the case for some of the oxide-rich veins and networks present in some parts of the core. Further types include not-preserved contacts, in which case the contact has been completely obscured by metamorphism or low-temperature, brittle deformation, and not-recovered contacts, where the contact occurs between two recovered pieces of the drilled section.

Table T6 lists contacts observed in the Leg 176 section by rock type. Because each contact divides two rock types, each is counted twice in the table, and the total is twice the number of igneous lithologic intervals observed. Some systematics are observable in the data when sorted by rock type. Intrusive contacts are rare in the Leg 176 core (<3% of the total). Sutured contacts were more common (~30% of the total), accounting for 138 contacts (276 in Table T6). Gradational contacts account for 40% to 50% of the contacts for most rock types, with the exception of metagabbros and microgabbros that have mostly sutured and intrusive contacts (~60%), and less abundant gradational contacts (~20%).

Approximately 13% of the contacts (59 of 457) were not recovered. Many of these may be gradational contacts where the recorded contact position was placed between two recovered pieces for convenience in logging. It is unlikely that there is a mechanical reason that gradational contacts may have broken more readily during coring than other contact types. The only rock type with a low percentage of gradational contacts and a high percentage of contacts not recovered is microgabbro, which may be the result of a mechanical weakness associated with intrusive contacts.

T6. Contact types by lithology, p. 264.

Grain-Size Variations

The maximum and minimum grain sizes of each of the major constituent minerals (olivine, plagioclase, augite, and orthopyroxene) in each lithographic interval were measured in hand specimen, and in thin section for selected samples during microscopic descriptions. In both cases measurements were made along the long axis of each mineral. The results for the microscopic measurements and the visual core descriptions are given in Figures F13 and F14, respectively.

The most general feature observed in both hand specimen and thin-section measurements is a positive correlation between the grain sizes of olivine, plagioclase, and augite (Figs. F13, F14). These correlations are independent of rock type. The average grain size of samples recovered during Leg 176 varies from fine grained (<1 mm) to pegmatitic (>30 mm), with average grain sizes generally in the range of coarse (5–15 mm) to very coarse (15–30 mm). In general, the relative grain sizes measured in hand specimen for augite, plagioclase, and olivine are in the order augite > plagioclase > olivine. In thin section, measured grain sizes for plagioclase and augite are approximately the same, with plagioclase generally slightly larger than augite, and both larger than olivine. This difference between hand specimen and thin-section measurements

F13. Grain-size correlation for plagioclase, olivine, and clinopyroxene, p. 113.

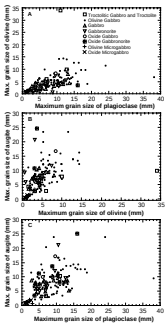

F14. Variations of grain size with depth, p. 114.

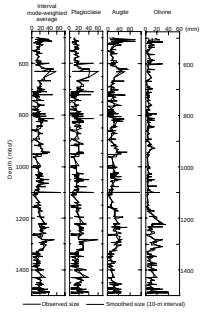

probably reflects the ease with which large poikilitic augite crystals can be seen in hand specimen and the misidentification of augite grain boundaries in thin sections where the augite crystals are slightly distorted, so that isolated parts of the same poikilitic crystal have slightly different orientations and, therefore, different birefringence and angle of extinction.

Peaks in average grain size occur at 510, 635, 825, 940, 1100, 1215, 1300, 1425, and 1480 mbsf (Fig. F14). Although the variation in average grain size is dominated by variations in the plagioclase grain size, the grain size data for augite, plagioclase, and olivine all follow similar trends (Fig. F14), with only a few discrepancies. Plagioclase has only very weak peaks at 510 and 1480 mbsf, where augite and olivine have relatively strong peaks. Augite, on the other hand, has a weak peak at 1425 mbsf, where plagioclase and olivine have relatively strong peaks. Olivine has extra peaks at 590 and 650 mbsf that are only relatively minor or do not appear in the plots of plagioclase and pyroxene. Peaks at 1215 and 1300 mbsf are very pronounced in the olivine plot, whereas in both the pyroxene and plagioclase plot, the whole zone from 1215 to 1300 mbsf is coarse, and the two individual peaks are not as well developed. No overall systematic downcore variation in either plagioclase or pyroxene grain size was observed over the depth range from 500 to 1500 mbsf. Olivine, however, has a slight overall decrease in grain size from 500 to 1200 mbsf, and then an abrupt increase to higher grain sizes over the range of 1200 to 1500 mbsf.

There are a number of thin pegmatitic intervals and thin fine-grained intervals in the core. These intervals generally have abrupt contacts with the surrounding coarse-grained gabbro, and both types tend to occur in clusters. With the exception of the intervals around 710 and 800 mbsf, where both pegmatitic and fine-grained intervals are common, these two rock types appear to be distributed antithetically (see Fig. F2).

Petrography

Modal Variations

Modal abundances of the primary magmatic phases were estimated in thin section using a Swift point counter set up to move in increments of 0.5 mm. Approximately 1500 points were counted for each standard (2.5 cm × 4.5 cm) thin section and 2000 to 2500 points for each oversized (5 cm × 7.5 cm) thin section. In the case of secondary minerals, the original precursor minerals were counted. Common pseudomorphs include smectite, talc, and magnesian amphiboles after olivine, and hornblende after clinopyroxene. Where amphibole occurs together with iron-titanium oxides in intergranular areas, the amphibole was counted as primary. Point counting was done in transmitted light; therefore, opaque minerals (oxides and sulfides) were not differentiated.

The proportions of major silicate phases in different rock types from Leg 176 are summarized in Figure F15 and Table T7. On the basis of Mg numbers (see "Rock Types and Geochemistry," p. 21) and previous work on Hole 735B gabbros (Ozawa et al., 1991; Bloomer et al., 1991), troctolite is the most primitive rock type, followed in turn by olivine gabbro, gabbro, orthopyroxene-bearing gabbro, gabbronorite, oxide gabbronorite, oxide gabbro, and last by oxide olivine gabbro. From troctolite to gabbronorite, the proportion of olivine decreases, whereas

F15. Plot of modal percent of minerals, p. 115.

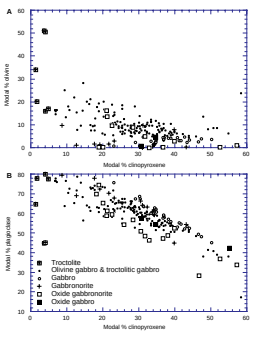

T7. Average primary modal mineralogy, p. 265.

that of orthopyroxene increases. From gabbronorite to oxide olivine gabbro, the trend is reversed with increasing olivine and decreasing orthopyroxene abundance. No pigeonite was recognized in the samples recovered during Leg 176, although some was found in thin sections from Leg 118.

The abundance of opaque minerals in thin section is typically less than 0.5% in troctolite, olivine gabbro, and gabbro; close to 1% in gabbronorite; 8.4% on average in the oxide gabbronorite, with a maximum of 18%; and 2% to 3.5% in the oxide gabbro and oxide olivine gabbro. Ilmenite is the dominant opaque phase in the Fe-Ti oxide-bearing gabbros with lesser amounts of magnetite and sulfide. Amphibole is a common accessory phase in many of the gabbros, averaging between 0% and 0.4% in the primitive gabbros and 0.5% to 1.7% in the evolved Fe-Ti oxide-bearing gabbros. Apatite is common in the Fe-Ti oxide-bearing gabbros, reaching a maximum of 2.5% and averaging 0.4% in the oxide gabbro and oxide gabbronorite.

The average phase proportions in Hole 735B troctolites, troctolite gabbros, and olivine gabbros closely resemble cotectic proportions observed in low-pressure experiments on MORB. The average olivine:plagioclase ratio of 30:67 in the troctolites and troctolitic gabbros is close to the 30:70 cotectic ratio determined experimentally (e.g., Grove and Baker, 1984; Grove et al., 1992; Toplis and Carroll, 1995). The average proportions of olivine, plagioclase, and clinopyroxene in the olivine gabbros (9.8:59.5:29.9; Table T7) are nearly identical to the 11:59:30 proportions observed by Grove et al. (1992) in 2-kbar experiments on MORB. These similarities suggest that the main body of olivine gabbro at Hole 735B crystallized at relatively shallow depths (<6 km) and solidified after efficient expulsion of residual melts. If residual melts had not been expelled, the cotectic proportions would not have been preserved, and the olivine gabbros would contain a higher proportion of accessory phases such as ilmenite and apatite.

The more evolved Fe-Ti oxide-bearing gabbros with an average of 1%–2% olivine, 51% plagioclase, 34%–40% clinopyroxene, 0.2%–3.5% orthopyroxene, and 6%–9% Fe-Ti oxides (Table T7) do not have such experimental cotectic analogs. The closest cotectic assemblages are those of Juster et al. (1989), who found proportions of 46%–51% plagioclase, 18%–35% augite, 13%–30% pigeonite, and 1.5%–4.5% ilmenite + magnetite in crystallization experiments on Fe-Ti basalt from the Galapagos spreading center and those of Toplis and Carroll (1995), who reported proportions of 0%–14% olivine, 37%–48% plagioclase, 38%–48% clinopyroxene, and 4%–22% ilmenite + magnetite in crystallization experiments on a synthetic ferrobasalt. The wide disparity in crystallizing assemblages reflects the reaction relationship between low calcium pyroxene and olivine as well as variations in oxygen fugacity, which control the stability of ilmenite and magnetite. From the modal proportions in Hole 735B gabbros, it appears that some of the oxide gabbros formed by in situ crystallization of pooled residual melt. In contrast, other oxide gabbros with excessive (>20%) oxide abundances must have formed by infiltration of Fe-Ti-rich melts or by concentrating oxides from a much larger volume of magma, which was later expelled.

Rock Textures

Some of the samples recovered during Leg 176 were deformed and, as a result, have porphyroclastic to mylonitic textures (see "Structural Geology," p. 54). In these deformed samples, most of the olivine and

much of the plagioclase have been recrystallized to the point that the original rock textures cannot be determined. Other samples have undergone various percentages of metamorphic alteration such that original textures have been at least partly obscured (see "Metamorphic Petrology," p. 33). Many samples, however, have not been extensively deformed or altered and appear to preserve original igneous textures. These samples are described in detail in thin-section descriptions, and their petrographic features are summarized in this section.

Most of the fine-grained gabbros, and some of the medium-grained and coarse-grained gabbros have granular textures in which subhedral to anhedral crystals form an interlocking matrix. Most of the coarse samples, however, have poikilitic to ophitic textures in which large, anhedral augite, and to a lesser extent olivine, oikocrysts enclose or partly enclose euhedral to subhedral plagioclase crystals, and intergrown subhedral to anhedral plagioclase crystals fill the volume between the large oikocrysts. In a few samples, euhedral to subhedral olivine crystals are enclosed in later subhedral to anhedral plagioclase and anhedral augite oikocrysts. In at least one sample, olivine is enclosed in plagioclase, and both olivine and plagioclase are enclosed in augite. Some of the more plagioclase-rich samples have intergranular textures in which subhedral to anhedral plagioclase laths form an interlocking framework, filled with smaller anhedral augite and olivine crystals in the interstices. A few samples have cumulate textures, in which coarse to pegmatitic euhedral to subhedral cumulus crystals of plagioclase, augite, and olivine form an interlocking framework filled with smaller anhedral crystals in the interstices. A few samples have preferred mineral orientations. In most of these samples, however, the original igneous fabric is overprinted by a later deformation fabric (see "Structural Geology," p. 54).

Mineral Textures

Undeformed plagioclase crystals vary from euhedral to anhedral in form. Euhedral and subhedral crystals typically occur as laths with aspect ratios (width:length) of 1:3 to 1:5. Undeformed olivine occurs as rounded subhedral to anhedral crystals, anhedral amoeboidal crystals, and anhedral ophitic to poikilitic oikocrysts. Subhedral olivine crystals are elongate parallel to extinction directions and typically have aspect ratios of 1:1.5 to 1:2. Augite occurs as tabular subhedral crystals (aspect ratio 1:2 to 1:3), anhedral crystals, and anhedral ophitic to poikilitic oikocrysts. Orthopyroxene is not an abundant phase in the Leg 176 samples. Where present, orthopyroxene is often subhedral with aspect ratios of 1:2 to 1:3. Amphibole is a common, anhedral, interstitial phase in most samples. In some samples amphibole clearly derives from late-stage alteration of original olivine or augite, but in some samples it appears to represent an original igneous phase. In a very few samples, brown amphibole is present as coarse, subhedral to anhedral crystals that enclose smaller, earlier subhedral silicate minerals. Apatite and zircon occur as rare euhedral interstitial crystals or euhedral chadacrysts in opaque oxides and amphibole. Titanite, which ranges from euhedral to anhedral, is an abundant minor constituent in some samples. In most samples, titanite is a replacement of ilmenite or spheroidal euhedra in veins; however, some may have crystallized from late magmatic or deuteric liquids. Quartz and feldspar are present in some of the felsic veins as anhedral crystals or as complex granophyric intergrowths.

Deformation and the development of undulose extinction in plagioclase makes the unambiguous recognition of compositional zoning difficult. In some samples, however, multiple, rectangular zones of changing extinction angle are present, and these roughly parallel the margins of the crystals. Compositional zoning is well developed in plagioclases in some of the felsic veins, and is weakly developed in plagioclase in some of the gabbros. Weakly zoned augite crystals are present in a few samples, and zoned titanite crystals are present in at least one sample.

Exsolution Textures and Mineral Inclusions

Exsolution textures are a common feature in most of the thin sections examined. Augite in most samples has very fine-scale, planar, parallel, exsolution lamellae. In many thin sections, two exsolution textures occur in the augite: fine-scale, planar, exsolution lamellae in very light brown host augite and coarser, bleby exsolution in clear host augite (Fig. F16). In both cases, low-Ca pyroxene is exsolved from augite, indicating that the initial augite crystallized from a magma that was saturated or nearly saturated in low-Ca pyroxene. In a few thin sections, herringbone exsolution patterns with fine-scale, planar exsolution lamellae parallel to 001 and 010 are present. In these sections, 001 exsolution was dominant over 010 exsolution, suggesting that exsolved pigeonite is more common than exsolved orthopyroxene and, hence, that the exsolution occurred at high temperatures. In a few sections, two sets of fine-scale, planar, exsolution lamellae were observed at slight angles to each other (~10°), suggesting two periods of pigeonite exsolution at different temperatures. Orthopyroxene crystals typically contain fine-scale, planar exsolution lamellae of augite. Magnetite in some samples contains lamellae of ilmenite indicating oxidation and exsolution during subsolidus cooling. No exsolution was observed in the associated ilmenite.

F16. Photomicrograph of augite exsolution textures, p. 116.

Many of the silicate minerals in the Hole 735B gabbros contain abundant, small crystals oriented parallel to crystallographic planes or crystallographic directions within the host crystal structure. The origin of these crystals is not clear; they may be inclusions, alteration minerals, or exsolution products. Small brown plates of amphibole are present in many augite crystals, and abundant tiny opaque rods are present in some. Olivine in many thin sections contains abundant transparent brown rods 0.01 to 0.05 mm in diameter and 0.10 to 0.30 mm in length and flattened, opaque dendritic patches up to 0.5 mm across (Fig. F17). In most specimens, the rods are transparent and the dendritic patches are opaque, but in some samples the relationship is reversed, and in a few samples it appears that the two textures may represent different crystal habits of the same mineral phase. In some samples the olivine contains fine needles of sulfide. Plagioclase in many thin sections contains abundant fine opaque rods or needles (as large as 0.001 mm × 0.30 mm; Fig. F18). A few plagioclase crystals contain highly birefringent needles (as large as 0.001 mm × 0.03 mm), or tiny (<0.001 mm) blebs. Orthopyroxene crystals typically contain abundant fine-scale opaque needles.

F17. Photomicrograph of olivine, p. 117.

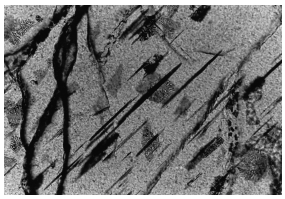

F18. Photomicrograph of plagioclase, p. 118.

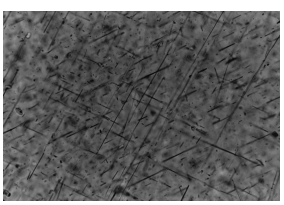

Mineral and melt inclusions are not common within the major rock-forming minerals in the Leg 176 samples. As described above, euhedral to anhedral plagioclase chadacrysts are common within augite oikocrysts. In some oikocrysts, apparently isolated anhedral plagioclase crystals have identical albite-twin patterns, suggesting that they were

once part of a contiguous crystal that was later partly replaced by the augite host. Rounded to subhedral olivine crystals occur as inclusions in augite and plagioclase in some samples, and small, euhedral spinel crystals are present as inclusions in plagioclase in a few samples. Spherical masses of intergrown sulfides are common inclusions in opaque oxides and amphibole and are rare inclusions in augite.

Reaction Textures and Mineral Intergrowths

Olivine in many samples is rimmed by augite, orthopyroxene, or amphibole. Amphibole is also common as rims around augite. Some samples contain wormy plagioclase-augite symplectites, particularly along grain boundaries between large anhedral plagioclase crystals. In a few coarse-grained samples, wormy intergrowths of medium-grained to fine-grained plagioclase and augite are common in interstitial areas and appear to represent initial simultaneous growth from residual magma as is common during the late stages of crystallization in some diabases. Ilmenite-amphibole and ilmenite-augite symplectites are present in a few samples. Granophyric quartz-plagioclase and quartz-microcline intergrowths are common in the felsic veins.

Rock Types and Geochemistry

The geochemical variation of the whole rocks analyzed during Leg 176 is consistent with the modal variations. For example, Figure F19 shows a scattered but significant correlation between CaO/Al_2O_3 and augite/plagioclase ratios (Fig. F19A) and a correlation of TiO_2 (and Fe_2O_3) with modal oxide abundance (Fig. F19B). Some of the scatter in these geochemical plots is undoubtedly due to the small sample size for chemical analysis in relation to the coarse grain size of the rocks.

Ca# and Mg# are well correlated both within rock types and for all rock types as a whole (Fig. F20). This correlation illustrates magmatic evolution from primitive melts that produced high Mg#, Ca# cumulates (troctolitic gabbros and olivine gabbros) to more evolved melts that produced lower Mg#, Ca# rocks (gabbros and gabbronorites), and probably to highly evolved melts that produced oxide-rich gabbros and gabbronorites. However, the Mg# in the oxide-rich rocks partly reflects the accumulation of Fe-Ti oxide. In a plot of TiO_2 vs. Ca# (Fig. F21), it is evident that most of the oxide gabbros and oxide gabbronorites have Ca# (Ca# = 56–73) comparable to the olivine gabbros (Ca# = 61–77, and two at 78 and 92, respectively). As the augite/plagioclase ratios of the oxide-bearing rocks in the majority of cases are similar to the ratios in the olivine gabbros (Fig. F19A), it seems that the oxide gabbros are not generally more evolved than the most evolved olivine gabbros. One possible explanation is that a change in oxygen fugacity or the exsolution of an iron-rich liquid was involved in the crystallization of Fe-Ti-oxides, rather than saturation during the final stages of a liquid line of descent. This would also supply a mechanism for the abnormally high abundance of oxides in some oxide gabbros. Alternatively, the silicates of the oxide gabbros may not have been in equilibrium with the same melt that formed the oxides, but rather are unequilibrated wall-rock minerals. This would be in contrast to the results estimated by electron microprobe on Leg 118 samples (Natland et al., 1991), which indicate that the silicate minerals were in equilibrium with an evolved high-Fe liquid. An additional problem that remains with this alternative, however,

F19. Augite/plagioclase vs. CaO/Al_2O_3, p. 119.

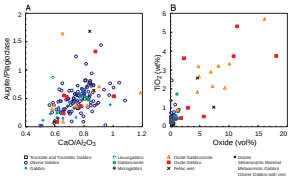

F20. Ca# vs. Mg# for Leg 176 rocks, p. 120.

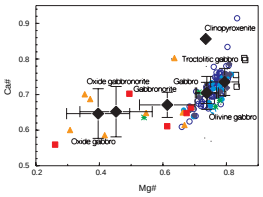

F21. TiO_2 vs. Ca# for Leg 176 rocks, p. 121.

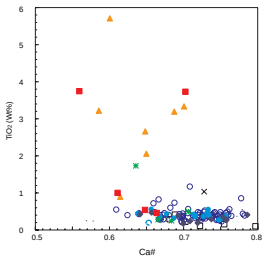

is how an extremely Fe-Ti–rich oxide rock formed, without re-equilibrating the Ca# of the host gabbro.

A remarkable feature of the averages of olivine gabbros and gabbros is their similar Mg# and Ca# (Table T3). Moreover, both major and trace element averages are the same. This implies that the main difference between the two rock types, the abundance of olivine, is not a function of magmatic differentiation of the parent magma. There is also a lack of correlation between the olivine mode and Ni abundance or Mg# of the two rock types, which is evidence that the olivine enrichment in these rock types is probably not related to olivine accumulation by settling. The modal variation present in the samples is probably a function of the same crystallization-related processes that led to the observed igneous layering, and not to a first-order process such as fractional crystallization.

Opaque Minerals

Opaque oxides are very unevenly distributed in the Hole 735B core. Abundances averaged over 1-cm segments of the core range from 0.1% to more than 40% (Fig. F22). In general, the typical rock recovered from Hole 735B has less than 1% opaque oxides evenly distributed as small, interstitial, anhedral crystals. However, within a number of thin segments of the core, 1 to 10 cm in thickness, opaque oxides were concentrated by late-stage processes. Within these oxide-rich segments, oxides commonly form a network or matrix of intergrown anhedral magnetite and ilmenite crystals surrounding the silicate mineral protolith (Figs. F23, F24, F25). Many, but not all, of the oxide-rich zones are also relatively enriched in sulfide minerals.

Although there is considerable scatter in the amount of oxides present in individual samples, there is a general decrease in oxide abundance with depth, and a decrease in oxide abundance with depth within those zones that contain oxides (Fig. F22). Although detailed data are not available for the cores recovered from 0 to 450 mbsf during Leg 118, the trend observed in the Leg 176 core appears to continue upward in the section, reaching a maximum relative abundance in the interval from 224 to 272 mbsf (Natland et al., 1991). In the upper part of the section, the felsic veins are, in general, very poor in oxides. In the lower part of the core, however, there is a strong correlation between felsic veins and oxide concentrations. In this lower section, most of the felsic veins >1 cm in thickness contain coarse subhedral to euhedral oxide crystals along their margins or are associated with high oxide concentrations in the host rock within 5 cm on both sides of the vein. This relationship strongly supports a genetic relationship between at least some of the felsic veins and some of the oxide concentrations.

There is a strong association between the intensity of deformation and the abundance of oxides. In general, oxide-rich segments of the core are concentrated in those sections that have had the most intense deformation (Fig. F26). This relationship accounts for the strong correlation between magnetic susceptibility, which is sensitive to the abundance of coarse-grained magnetite, and deformation intensity (see "Physical Properties," p. 77). The timing of deformation and oxide crystallization is difficult to determine with certainty because of the ease with which oxide minerals texturally re-equilibrate at high temperatures. In most cases, however, it appears that the oxides postdate the major phase of deformation, in that they occur as an undeformed coarse matrix supporting sheared and brecciated silicate porphyroclasts.

F22. Plot of oxide abundance vs. depth, Hole 735B, p. 122.

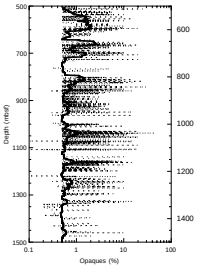

F23. Gabbro with deformed porphyroclasts surrounded by undeformed oxides, p. 123.

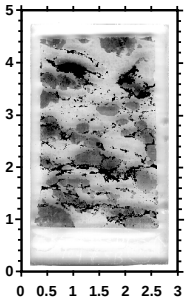

F24. Gabbro with sheared lens of opaques smeared along foliation, p. 124.

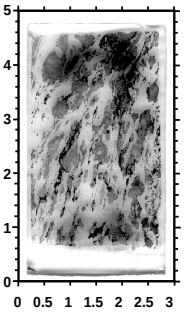

F25. Gabbro with undeformed subhedral to anhedral crystals, p. 125.

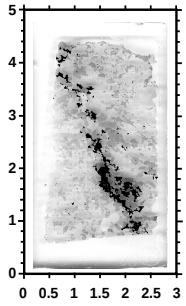

These samples may represent shear zones that were cemented by oxides after the main phase of deformation, or shear zones that have undergone extensive oxide recrystallization after the main phase of deformation. In a few samples, the oxides clearly predate the deformation and are present as fine-grained stringers that parallel the foliation.

The relationship between oxide-rich gabbros and deformation is not consistent throughout the core. Oxide-rich gabbros have at least three distinct textures: (1) in many samples, the crystallization of oxides is concentrated in shear zones and postdates the main episode of deformation, as evidenced by textures in which sheared silicate porphyroclasts are supported by an undeformed oxide matrix (Fig. F23); (2) in some samples, the crystallization of oxides is concentrated along shear zones and clearly predates at least some of the deformation, in that sheared lenses of oxides parallel the deformation-induced foliation (Fig. F24); and (3) in a few samples, the crystallization of oxides appears to be unrelated to deformation, in that coarse oxide segregations are localized along grain boundaries in undeformed rocks (Fig. F25) or are localized along brittle fractures at an angle to the deformation textures in the rocks. In general, oxides are least abundant in the least deformed rocks and most abundant in the most intensely deformed rocks.

F26. Plot of deformation intensity and oxide abundance for Leg 176 core, p. 126.

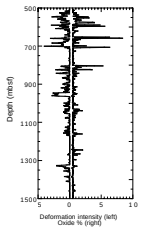

Sulfide and Oxide Minerals in Thin Section

Thin sections were examined in reflected light to identify oxide and sulfide minerals and to establish relationships between them and adjacent silicate minerals. Primary oxides and sulfides, which respectively crystallized and segregated immiscibly from the melt, are present in almost all samples. A few samples, chiefly troctolites, contain Cr-spinel (Fig. F27A). Secondary magnetite is almost universally present, secondary sulfides occur in many samples, and native copper occurs in one.

F27. Photomicrographs of oxide minerals and sulfides, p. 127.

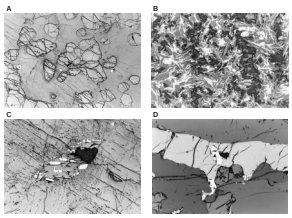

Of these minerals, only the primary oxides, ilmenite and magnetite, are ever present in more than accessory amounts. Rocks with 2%–10% oxide minerals in hand specimen are termed oxide gabbros or oxide-olivine gabbros, and the combined abundances of these "opaque minerals" in thin sections of many of these rocks are recorded as modes in Table T7. Where small amounts (1%–2%) of oxide minerals are observed in hand specimens, the rocks are termed disseminated oxide olivine gabbros, gabbros, or gabbronorites, depending on the silicate mineralogy. However, the gradational aspect of oxide abundances is clearly evident in thin section, as no rock has absolutely no ilmenite, and only a few, all highly altered, have no associated primary magnetite. Similarly, primary sulfides are present in all but a few highly altered rocks.

Nevertheless, in all but the oxide gabbros, abundances of oxide minerals and certainly the sulfides are low enough that it is all but impossible to determine them by point counting. Estimations such as "lots," "some," or "little" might be applied, but in the end, probably only the two estimates, "lots" and "none," have much significance. The most important observations in thin sections have little to do with quantity, but with the simple identification of minerals and the manner in which they occur in the rocks. Accordingly, the petrographic information on oxide minerals and sulfides is recorded under the "Comments" sections of the individual thin-section description forms rather than in a spreadsheet.

As to mineral identifications, there are only a few. The thin sections have abundant and coarse, to rare and vestigial, primary ilmenite-

magnetite intergrowths in which the effects of oxy-exsolution are minimal to nonexistent. In this regard, the mineral name "ilmenite" as used in this report always refers to the solid solution of end-member ilmenite and hematite; "magnetite" refers to the solid solution of end-member magnetite and ulvöspinel. Among the oxides in the thin sections, however, there are few examples of development of exsolution lamellae, reflecting unmixing of these solid solutions, although they are more common in magnetite than in ilmenite. Extended oxy-exsolution, in which mineral phases such as rutile and pseudobrookite form in still other criss-crossing exsolution patterns (e.g., Haggerty, 1991), and which is fairly typical of abyssal gabbros substantially transformed by hydrothermal alteration, does not occur. With only a few exceptions, the oxide minerals reflect the generally fresh condition of the rocks and only minimal influence of hydrothermal alteration.

The grain size of ilmenite and magnetite is roughly in accord with that of the surrounding rock. An exception is the fairly thick (10–15 cm) oxide concentrations that occur in some shear zones and breccias. In such cases, the individual grains in large oxide intergrowths are usually coarser than many of the silicate minerals they surround, particularly the micron-sized neoblasts of clinopyroxene and plagioclase that are present as breccia fragments in some samples. In other examples, subsolidus crystal-fabric deformation and cataclasis have clearly incorporated the pre-existing oxide minerals, as they are strewn along the foliation in such rocks and are substantially divided into subgrains on the order of the size of similarly deformed proximal silicates. Also, in these coarse-grained, deformed rocks, brown amphibole may be particularly abundant, typically forming rims on large patches of oxides. In addition, sulfides can compose up to several percent of the opaque concentration in some samples, several of which contain fairly large euhedral crystals of apatite enclosed within the oxides. This is an indication of the extremely evolved composition of the melts from which the oxide minerals precipitated.

In most samples, the proportion of ilmenite to magnetite in the oxide intergrowths is difficult to estimate. In some samples, magnetite is the more abundant mineral, but in most samples ilmenite is more abundant. Estimates of normative proportions of ilmenite and magnetite using X-ray fluorescence chemical analyses from Leg 118, for which FeO has been determined by titration (Robinson, Von Herzen, et al., 1989), suggest a nominal ratio of ilmenite to magnetite of 4:1, but with proportions as low as 2:1 or as high as 8:1 within individual analyzed samples.

The only other oxide minerals worthy of note are secondary in origin. One of these is magnetite, which is typically found as fine, elongate, dendritic crystals together with a clear amphibole at the altered rims of olivines in almost all rocks. In some more completely replaced olivines, the magnetite crystals are actually fairly large and intricately intergrown (Fig. **F27B**). The fine-grained magnetites may be the source of the stable magnetization component within these rocks. In some samples, primary magnetite is partly to completely replaced by secondary titanite, and the same rocks may contain rhombs of titanite in the rock matrix and in amphibole veins. Details of the replacement of magnetite by titanite, especially the grain-boundary relationships, are best seen in reflected light. In some of the most extensively altered samples, magnetite originally intergrown with ilmenite has been entirely replaced by green amphibole, which retains a trellis of relic ilmenite exsolution lamellae (Fig. **F27C**). In such rocks, there is not even any sec-

ondary magnetite; the rocks are so deficient in magnetite that they have virtually no magnetic susceptibility as measured, for example, using the multisensor track. Although such rocks are present only in rare and narrow intervals, they record such extensive hydrothermal alteration that virtually all the magnetite, primary and secondary, has been wiped out.

This is one of the rare cases in which titanium clearly was not a conservative component in the rocks during alteration, but rather the titanium in these rocks was dissolved and moved around in hydrothermal solutions. The titanium now present in titanite rims clearly came mainly from the ulvöspinel component of the magnetite. The titanite rhombs in amphibole veins, however, contain titanium that was probably derived from both primary magnetite and pyroxene. These textures provide proof of the mobility of titanium in solutions during certain conditions of hydrothermal alteration.

Finally, in one restricted region of the core where oxidative alteration occurred, between about 500 and 600 mbsf, and in which calcite veins are prominent, iron oxyhydroxide and smectites replace olivines, the effect of which is to lend a brownish freckled appearance to host rocks. This is the vicinity of the most prominent fault in the core.

The principal sulfide minerals are pyrite, pyrrhotite, chalcopyrite, and pentlandite, with at least two, and sometimes all four, of these minerals intergrown. These are typically globular to subrounded in shape or otherwise conform to the shapes of adjacent silicate minerals, and they are usually intergrown or associated with primary ilmenite and magnetite together with brown amphibole (Fig. **F27D, F27E, F27F**). All of these sulfide mineral phases in a sense have to be considered as something other than primary, because they crystallized at relatively low temperatures (~700°C) from what were originally immiscible sulfide droplets, containing Fe, Ni, and Cu, which segregated immiscibly from silicate melts at much higher temperature (e.g., Czamanske and Moore, 1977; Barton and Skinner, 1979). Secondary sulfides include rare bornite and chalcocite, found replacing primary chalcopyrite, cubic crystals, veins and vein networks of pyrite, and needles of pyrrhotite, all invariably associated with secondary clear or pale green amphibole and smectite.

The Leg 118 site report for Hole 735B (Robinson, Von Herzen, et al., 1989) notes the prominent occurrence of globular sulfides in the oxide gabbros, which are so abundant in cores from the topmost 500 m of the hole. Not only do the sulfides occur in the same rocks as the oxide minerals, but the two mineral groups are intimately associated texturally. That is, many very large globular sulfides, being aggregates of pyrite, pyrrhotite, and chalcopyrite (Natland et al., 1991), are embedded within large concentrates of ilmenite and magnetite. The two together often are present in shear zones or surround fragments of brecciated silicate minerals. Such rocks have their counterparts in many of the deformed oxide-rich zones cored between 504 and 1508 mbsf during Leg 176. Natland et al. (1991) speculated that the occurrence of oxides and abundant sulfides together was a consequence of extreme high-iron differentiation of abyssal tholeiitic basaltic magma, such that when oxide minerals began to precipitate, extensive sulfide segregation had to follow suit. Natland et al. (1991) also noted that chalcopyrite forms quite a high proportion of the sulfide aggregates and that glass margins to basalts dredged nearby have low concentrations of sulfur. They therefore inferred that basaltic melts in this region initially were not saturated in sulfide, and thus that residual liquids became enriched

rather than depleted in Cu during magmatic differentiation, before sulfide saturation was achieved. Thus, when oxide minerals joined the liquidus, Cu-rich sulfides began to segregate in earnest. Alt and Anderson (1991), however, determined that primary sulfide mineral aggregates in olivine gabbros drilled during Leg 118 include pentlandite as well as chalcopyrite and the iron sulfides. This suggests that sulfide saturation actually occurred much earlier during magmatic differentiation than proposed by Natland et al. (1991).

The resolution of this conundrum is revealed in the thin sections of Leg 176. Ilmenite occurs in every rock, even in troctolites, where, although it is very rare, one or two grains a few microns in diameter are present in every thin section. There are two ways in which a fairly primitive olivine gabbro can reach the point of crystallizing ilmenite. An interstitial oxide mineral can crystallize from a small percentage of trapped intercumulus melt (Wager et al., 1960). If such a melt were basaltic in composition, then adjacent olivines, pyroxenes, and plagioclases might be zoned, and the modal proportion of those zoned minerals, plus the interstitial oxides, could be a measure of the percent of melt trapped in the rock. Usually, however, early formed silicate minerals are not zoned because slow cooling allows intracrystal homogenization by diffusion. In such cases, the amount of trapped melt is best estimated from the concentration of strongly excluded elements, such as P or U (Henderson, 1970). In portions of the core from Hole 735B, however, oxide minerals are concentrated in zones of deformation, suggesting that highly differentiated iron-rich melts flowed through channelized structures that developed in the rocks as a consequence of the deformation and compaction they experienced. This flow may have operated on the scale of individual grains, so that iron-rich melts were able to permeate the existing intergranular porosity structure of adjacent rocks, even olivine gabbros and troctolites, and there precipitate (or segregate) in very tiny proportions the same sorts of minerals that occur more massively in oxide gabbros. The observed oxide minerals and their associated globular sulfides thus might not represent trapped melt, but flowing melt.

In rocks with dispersed rather than massive primary oxide minerals, the oxides and sulfide occur consistently in a single association within which brown amphibole is also a prominent phase. The several minerals, in this association, are always present as intergranular phases (Fig. F28A). In some, troctolites, olivine gabbros, gabbros, and gabbronorites, brown amphibole is quite abundant, forming up to 2% of measured modes, and in such rocks it is more abundant than the oxide minerals and sulfides it contains. Because in many rocks there are both brown and green amphibole, with the latter clearly being secondary in origin, there is some uncertainty as to whether brown amphibole should also be considered a primary mineral, especially where it is intergrown with the green amphibole (Hébert and Constantin, 1991). This issue cannot be resolved using thin sections only, nor is it likely that all brown amphibole should be considered primary (Mével, 1987). However, combined electron-probe and ion-probe analysis can be used to establish the magmatic origin of certain brown amphiboles in abyssal gabbros (Gillis, 1996). In Leg 176 gabbros, however, the brown amphiboles are intimately intergrown with both magmatic oxide minerals and globular sulfides, which are segregations of immiscible sulfide melt. In some cases, ilmenite is intergrown symplectically with olivine (Fig. F28B), orthopyroxene, or amphibole. In the absence of green

F28. Photomicrographs of amphiboles, oxides, and sulfides, p. 129.

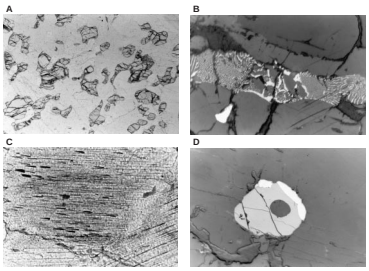

amphibole in many of these rocks, symplectites of ilmenite and brown amphiboles are likely to be magmatic in origin.

In many samples, the minerals of this particular intergranular association extensively penetrated the fabrics of their host rocks. Commonly, elongate ilmenite, blebs of sulfide, and patches of brown amphibole are within individual coarse grains of clinopyroxene, especially along cleavage planes (Fig. F28C). Whereas the amphibole by itself might be construed as a replacement of the pyroxene, most of these inclusions are bounded by faceted pyroxene crystal surfaces, and all of them are present together in the same mineral grains. They have not eaten away at the pyroxene; they have simply filled in spaces within it that were originally the consequences of crystal growth.

Ilmenite is even found along partings and fractures of olivine crystals. In the rare rocks with Cr-spinel, one can find the spinel partly jacketed by ilmenite (Fig. F28D) or ilmenite penetrating into fractures within the spinel (Fig. F28E). All of this is evidence for the ability of a fluid from which oxide minerals, sulfide globules, and brown amphibole were simultaneously forming, to penetrate the very finest-scale interstices of the fabric and mineral structure of primitive rocks. The mineral association suggests a highly evolved penetrating hydrous melt that was simultaneously rich in Ti, Fe, and sulfide.

Pentlandite, the apparently anomalous mineral in this association, can be seen as fine flaring or flamelike structures, somewhat more reflective than enclosing pyrrhotite, in many of the intergranular sulfides, especially in the olivine gabbros. Rarely, the outlines of incipient cubic crystals are present. The pentlandite flares often emanate into the pyrrhotite from the surfaces of intergrown yellowish chalcopyrite. Black-and-white photomicrographs fail to do justice to these features.

These pentlandite-bearing sulfide globules are clearly part of this characteristic intergranular mineral association that also includes ilmenite, intergrown magnetite, and brown amphibole. In rare examples, the pentlandite occurs within intergrowths of iron and copper sulfides and ilmenite, all surrounded by brown amphibole. The nickeliferous sulfide thus appears to be part of a late-crystallizing intergranular mineral assemblage in these rocks. It does not represent any early-segregating sulfide assemblage and is, therefore, not evidence for early saturation of sulfide during crystallization differentiation of parental basaltic magmas.

In part, this interpretation depends on negative evidence, namely that globular sulfides, recrystallized to mineral intergrowths, occur neither as inclusions in the olivines of troctolites and olivine gabbros nor in hypidiomorphic intergrowths of plagioclase with olivine. This is where the descriptor “none” becomes important even though it is difficult to establish. Sulfides at grain boundaries do not count; only those truly enclosed within early-crystallizing minerals provide proof of early sulfide saturation. None was found. The sulfides thus segregated after these minerals crystallized, and the melt was not at sulfide saturation while they did. One can find sulfides in cracks or at grain boundaries, and these are commonly associated especially with ilmenite but sometimes even amphibole, within these grains. There are also globular sulfides in some pyroxenes and plagioclases. However, the crucial question is the stage of differentiation at which sulfide segregated. This was not early during the magmatic evolution of these gabbros.

Highly evolved, very iron-rich basaltic magmas contain almost no nickel. They do not produce nickel-rich immiscible-sulfides. In the Leg 176 samples, however, the Ni evidently came from the olivine, next to

which the intergranular amphibole-oxide-sulfide assemblages commonly occur. Apparently, reaction of the olivines with the throughgoing fluids resulted in dissolution of the Ni, and its later but nearby separation from those fluids in the form of immiscible sulfide droplets. The original interpenetrating melts therefore need not have had much nickel.

One final note concerning overall trends in the core. In the deepest rocks recovered from Hole 735B during Leg 176, between ~1400 and 1500 mbsf, there is very little ilmenite. Intergranular amphibole is also scarce. Sulfides, of the usual multiphase variety, are much more abundant, especially in proportion to the very small quantities of brown amphibole and ilmenite in the same rocks. In the classical cumulate sense, these rocks could be described as almost ideal adcumulates; that is to say, they are rocks that retain only the tiniest fraction of trapped intercumulus melts (Wager et al., 1960), as evidenced by the extremely low proportion of ilmenite and associated magnetite they contain. In the alternative context of the potential for these mineral phases to represent some sort of migrating, iron-rich, hydrous melt phase, it is clear that if such a melt phase was present it was largely expelled from these rocks before much crystallization of amphibole-ilmenite-sulfide intergrowths occurred. Nevertheless, the sulfides are fairly abundant, suggesting that sulfide segregation occurred before crystallization of ilmenite and amphibole from the throughgoing hydrous melts and that the sulfide globules, once formed, were retained in their host rocks while surrounding fluid was expelled. This presumably had to do with the much higher density and viscosity of immiscible sulfide than of hydrous silicate melt.

Details of this process need to be worked out with more care using data from electron and ion microprobe analyses. The general problem of these intergranular mineral assemblages is likely to be tied very closely to the formation and migration through the rocks of iron-rich melts in general and of the formation of massive oxide-sulfide concentrates in other parts of the core.

Felsic Veins

Felsic veins were recovered throughout Hole 735B from 500 to 1500 mbsf during Leg 176. These veins vary in size, geometry, and detailed mineralogical and chemical composition. All such veins, taken together, make up ~0.54% of the total volume of the core. Despite the small volume, their occurrence as an integral part of the gabbroic sequence has important implications for the physical and chemical processes taking place in the context of magma evolution and crustal accretion. Figure F29 shows that despite the scatter, the overall vein abundance recovered during Leg 176 clearly decreases with increasing depth downhole except for the last occurrence at 1430 mbsf.

The felsic veins vary in geometry from regular planar dikes/dikelets to irregularly shaped pockets, and in size/thickness from a few millimeters to several centimeters. Many of the veins are apparently of igneous origin with characteristic primary igneous textures and sharp intrusive contacts (Fig. F30). Some preserve igneous textures, but have clearly undergone subsequent high- and low-temperature alteration and have developed diffusive or reactive boundaries with the host gabbros. Still other veins, particularly some of the thin veinlets/pockets, have uncertain origins. Those associated with late-stage fractures with reaction

F29. Downhole felsic vein intensity averaged over every 10 m of core, p. 131.

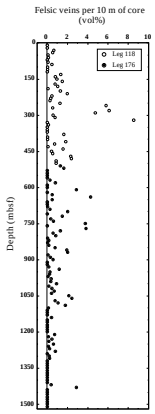

F30. Core photo of a large igneous felsic vein, p. 132.

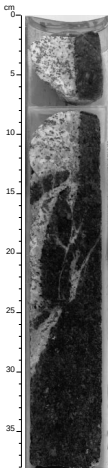

halos may be of hydrothermal origin, but others could be either igneous or metamorphic.

Most of the veins are leucodiorite dominated by plagioclase plus small amounts of green amphibole. Other common lithologies include diorite, trondhjemite, and tonalite with variable amounts of dark-green amphibole, quartz, and biotite. Granitic veins were also recovered (e.g., an X-ray fluorescence chemical analysis from Sample 176-735B-99R-4, 106–108 cm, has ~28% normative quartz and 23.5% normative orthoclase). They often are irregularly shaped and coarse grained; have abundant K-feldspar, plagioclase, quartz, and biotite; and have a well-developed micrographic texture. Less abundant primary minerals associated with these veins include pyroxene, zircon, apatite, and oxides. Superimposed on the primary phases in many of the veins are high-temperature and low-temperature metamorphic mineral assemblages including actinolite, secondary plagioclase, epidote, titanite, chlorite, quartz, clays, sulfides, and oxides. Some of the felsic veins with these assemblages may, in fact, be of hydrothermal origin.

Oxide-mineral concentrations and felsic veins are commonly associated. Oxides occur either as euhedral to subhedral grains or aggregates within veins, or in anhedral aggregates along the margins of the veins and extending into the host lithologies. This association has two possible explanations: (1) the felsic veins may, in fact, have intruded preexisting oxide-rich horizons or veins. (2) The oxides may have been precipitated from a highly evolved, oxide-saturated, magma. This latter process will inevitably result in a more silica-rich residual melt—the vein material.

The origin of the igneous veins is not certain. Most of them likely result from extreme degrees of differentiation. For example, oxide crystallization at late stages of basaltic melt evolution will result in more silica-rich melts. This could also explain the oxide-felsic vein association on local scales (see above). The igneous felsic veins may serve as "conduits" for subsequent fluid migration, which explains why many of these veins are hydrothermally altered. Alternatively, some of the alteration may have resulted from fluid exsolution during the final stages of felsic magma crystallization. Further detailed petrographic, mineralogic, and geochemical studies are required to better understand the genesis of the felsic veins.

Igneous Layering

Layering as used here refers to planar magmatic features that crosscut the core at angles of 0°–40°. The lateral extent of these features is not known and cannot be determined on the basis of a 5- to 6-cm-diameter core. These features are inhomogeneities defined by variations in grain size, modal proportions, and textural appearance. They do not include the fine-grained microgabbros that cut the core with irregular, often sinuous, sutured and intrusive contacts. The types of layering observed are (1) grain-size layering characterized by either sharp breaks in grain size or gradational variations in grain size (graded), (2) modal layering marked by distinct changes in the abundance of plagioclase, olivine, clinopyroxene, and Fe-Ti oxide, (3) magmatic foliation (igneous lamination) defined by the preferred orientation of plagioclase and in some cases olivine and clinopyroxene (see **"Structural Geology,"** p. 54), and (4) layering defined by textural variants such as crescumulate texture.

Grain-size layering is by far the most common type of layering observed and is present in well-developed rhythmic intervals in several

sections of the core (Fig. F2, 827 to 914 mbsf and 1138 to 1220 mbsf). Figure F31 shows rhythmic cycles in grain size between medium and coarse-grained olivine gabbro from Section 176-735B-171R-4 and an isolated coarse-grained layer in a medium-grained olivine gabbro from Section 176-735B-186R-4. In Sections 176-735B-134R-2 to 176-735B-135R-2 (837 to 845 mbsf), grain-size variations are normally graded, coarsening downward, with plagioclase increasing in size from 2–7 mm to 10–20 mm and clinopyroxene increasing in size from 3–5 mm to 10–15 mm within each layer. Figure F32 shows a histogram of layer thickness for 34 layers identified from this part of the core. Layer thickness, which refers to the distance from the coarse base of one layer to the coarse base of the next layer, ranges from 6 to 22 cm with a dominant thickness of 11 cm.

Modal layering often accompanies the grain-size layering. Generally, the coarser parts of a layer are more mafic than the finer parts. In the graded grain-size layers mentioned above (Sections 176-735B-134R-2 to 135R-2), the mode typically varies from 60% plagioclase, 30% clinopyroxene, and 10% olivine in the medium-grained top of a layer to 55% plagioclase, 40% clinopyroxene, and 5% olivine in the coarse-grained base of a layer. A similar variation was observed in layers between 0 and 18 cm in Section 176-735B-138R-7 and was verified by point counting. In this case, the finer grained fraction has a mode of 58% plagioclase, 37% clinopyroxene, 4.5% olivine, 0.2% opaque minerals, and 0.3% amphibole, whereas the coarser grained fraction has a mode of 51.7% plagioclase, 36.8% clinopyroxene, 10.4% olivine, 0.4% opaque minerals, and 0.7% amphibole.

The most striking example of modal layering in the Hole 735B core is the occurrence of Fe-Ti oxide-rich layers (see "Opaque Minerals," p. 22). These layers generally contain 2%–20% Fe-Ti oxide together with 30%–50% plagioclase, 0%–5% olivine, 0%–5% orthopyroxene, and 30%–50% clinopyroxene and in many cases appear to be localized along shear planes. Melanocratic layers rich in clinopyroxene are rare. They occur at 47 to 54 cm and 110 to 118 cm in Section 176-735B-135R-1 (843 mbsf), 131 to 149 cm in Section 176-735B-144R-1 (914 mbsf), and 5 to 12 cm in Section 176-735B-203R-1 (1431 mbsf). Fe-Ti oxide is abundant (3%–10%) in the lower three of these layers.

Pegmatitic layers with an average grain size greater than 30 mm are intermittent throughout the core (Fig. F2). These layers range in thickness from 5 cm to 50 cm and consist mostly of plagioclase and clinopyroxene with lesser, variable amounts of olivine or orthopyroxene, Fe-Ti oxides, and sulfides. In some instances, the large crystals are oriented in a subvertical direction. In Section 176-735B-163R-3 from 11 to 18 cm, for example, single olivine crystals extend vertically for 5 cm or more. These crystals, together with plagioclase crystals, produce a crescumulate texture.

Discussion

Two major paradigms form the backdrop for studies of the lower oceanic crust. First is the concept of layered basic intrusions formed by the cooling and crystallization of large batches of basaltic magma over tens of thousands of years. Layering in such intrusions is derived from a number of processes, including mechanical sorting, variations in cooling and crystal growth rates, crystal-liquid fractionation, and injection of multiple batches of melt (Wager and Brown, 1968; Cawthorn, 1996). A second paradigm that has shaped our ideas about oceanic crustal

F31. Core photo showing grain-size layering, p. 133.

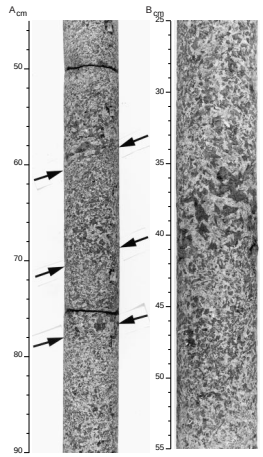

F32. Histogram of layer thickness, p. 134.

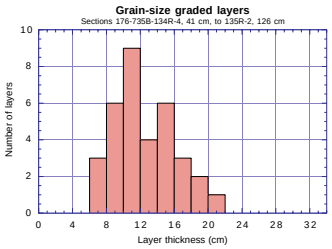

structure is the ophiolite model, characterized by a stratigraphic sequence of pillow lavas, sheeted dikes, isotropic gabbro, layered gabbro, and deformed ultramafic rocks. Recent conceptions of crustal generation at ocean ridges incorporate aspects of both layered intrusions and the ophiolite model. Sinton and Detrick (1992), for example, proposed that eruptions at fast-spreading ocean ridges are fed by a magmatic system consisting of a large crystal mush zone that is overlain by a narrow melt lens. During rifting episodes, melt is transported upward from the lens through dikes and onto the seafloor to form lavas. With time, the solidified mush (gabbro), dikes, and lavas are carried away from the ridge axis by seafloor spreading.

The importance of the present study is that Hole 735B represents the only deep hole (1.5 km) through an in situ section of the lower oceanic crust, providing a unique opportunity to investigate the composition and structure of this crust and to compare these observations with comparable ones on ophiolites and layered intrusions. The lithologies recovered during Legs 118 and 176 represent a generalized evolutionary sequence ranging from primitive troctolitic gabbros to highly evolved oxide gabbronorites. These lithologies, however, do not change systematically through the section but, rather, occur in separated enclaves that in places interpenetrate one another. Although the details of this interpenetration cannot be worked out in a single drill core, it is clear that large batches of magma evolving in situ, such as might be expected by analogy with layered intrusions, were not involved. The main phase of crystallization produced troctolites, olivine gabbros, and gabbronorites. Low abundances of incompatible elements suggest that interstitial melt is largely absent from these rocks.

We subdivided the igneous rocks recovered during Leg 176 from 504 to 1508 mbsf into 458 intervals, grouping them into seven units. The contacts between intervals were chosen to differentiate rock types based on grain size or mode. In some cases, these contacts appear to represent intrusive boundaries; in most cases, however, they separate local variations within a single intrusion. Likewise, the unit boundaries are chosen on the basis of changing proportions of rock types in the section but do not necessarily represent separate magmatic events. The sequence recovered during Leg 176 consists mainly of olivine gabbro (70%), gabbro (15%), and troctolitic gabbro (2%), with similar major and trace element compositions. The section also contains orthopyroxene-bearing gabbro and gabbronorite (6%), oxide gabbro (5%), and orthopyroxene-bearing oxide gabbro and oxide gabbronorite (3%). The bulk composition of the section, calculated from weighted averages of the rock types, is similar to MORB.

Oxide gabbros and orthopyroxene-bearing oxide gabbros and gabbronorites are major lithologies throughout almost 1000 m of Hole 735B and are present in minor proportions throughout. The formation of oxide gabbros clearly follows the main phase of crystallization, in that the oxide gabbros cut previously crystallized rocks. The strong correlation between deformation and oxide-rich gabbros in the Hole 735B section argues that magmatic differentiation was not driven by the filter pressing of residual melts out of cumulates during deformation, with those expelled melts accumulating in undeformed rocks. In such a model, oxide-rich gabbros should be most abundant in rocks with the least evidence for deformation and should be rare in highly deformed samples. The relationships in the Hole 735B core instead require that residual melts are depleted in rocks that show little evidence of deformation or compaction and are concentrated in rocks that are the most

highly deformed. At least three models are supported by the data: (1) lenses of late-stage magma may have acted as zones of weakness along which deformation was concentrated; (2) the late-stage magmas from which the oxides crystallized may have been concentrated in zones that had been previously sheared, because these zones have greater high-temperature permeability; or (3) active shear zones acted as conduits for melt transport through the section. One or more of these processes must have occurred in the Hole 735B section.

The high concentrations of oxides present in some samples require that large volumes of melt were transported through these rocks. A ferrobasaltic liquid migrating through a system of fractures and shear zones would be unlikely to precipitate more than 5% oxides. Some samples contain in excess of 15% oxides, and the shear zones within these samples contain even higher oxide abundances. A ratio of transported melt to fractured rock in excess of 5 to 1 would be necessary to account for these samples. Previous reports of oxide-rich gabbros localized along shear zones in ophiolites are limited to the single instance of the Lizard complex (Hopkinson and Roberts, 1995), and oxide gabbros in layered intrusions are generally present as undeformed, conformable layers or segregations formed during the final stages of crystallization as a result of progressive magma enrichment. The oxide gabbros recovered during Legs 118 and 176 require a differentiation mechanism unlike those previously reported in ophiolites and layered intrusions.

The microgabbros from Hole 735B record relatively late intrusive events. Contact relationships indicate that they were intruded into solid or near-solid-state, coarse-grained, gabbroic host rocks, and as a result, we interpret the microgabbros as a later, separate magmatic cycle. The microgabbros, however, cover a wide range of compositions and rock types and, therefore, they cannot be explained by a single late parental magma. As a result, the microgabbros appear to represent a late episode of intrusion covering approximately the same magma compositions as were responsible for the earlier coarse-grained gabbros. The microgabbros may represent channels through which melt was transported through the earlier coarse-grained, gabbro section. Additional evidence for melt transport through the section is present in the form of monomineralic plagioclase channels that appear to replace the gabbro host rock but preserve only high-temperature igneous minerals, and have fresh igneous textures in thin section. The relative timing of the microgabbros, the plagioclase-rich channels, and the Fe-Ti oxide gabbros is not clear, but all three appear to postdate the main phase of crystallization of the coarse-grained gabbroic rocks.

Felsic to dioritic dikelets and veins with clear crosscutting relationships represent a final intrusive event in the sequence. These commonly intrude fractures or shear planes within the earlier gabbroic sequence. In some cases, the felsic veins are bordered by oxide-rich gabbros, the oxides apparently derived from the late-stage melt. Many of the felsic veins are overprinted by later deuteric or hydrothermal alteration.

Igneous layering is an important feature of both ophiolites and layered basic intrusions where parallel layers can be traced for some distance in weathered outcrops. No well-documented layering, however, has ever been reported in gabbros sampled from the ocean floor except for those recovered during Legs 118 and 176 from Hole 735B. Many styles of layering are present in the Leg 176 sequence, including rhythmic grain-size, modal, and textural layers. Some sections of the core are rhythmically layered, with grain-size or modal layering repeating at reg-

ular intervals of 10 to 20 layers through a 1- to 2-m section. Thick, intensely layered sequences, such as have been reported from layered intrusions and in the lower parts of some ophiolites, are not present, however, in the Leg 118 and Leg 176 cores. Likewise, the systematic cryptic variations in bulk rock chemistry common in some layered intrusions and ophiolite sequences are not found in the Hole 735B section. In addition, the abundance of oxide gabbros localized along shear planes in the Hole 735B sequence, clearly set it apart from gabbroic sequences in typical ophiolites or layered basic intrusions.

METAMORPHIC PETROLOGY

Introduction

Gabbroic samples recovered during Leg 176 preserve a complex record of high-temperature metamorphism, brittle failure, and hydrothermal alteration that began at near-solidus temperatures and continued down to zeolite facies metamorphic conditions. Secondary mineral assemblages in the Leg 176 core are broadly similar to those higher up in the sequence (Dick et al., 1991b; Robinson et al., 1991; Stakes et al., 1991). Rocks deeper in the section, however, are remarkably fresh over large sections of the core, with extensive intervals (>300 m) marked by less than 10% total background alteration. This is in striking contrast to plutonic samples recovered by both drilling and submersible studies of other fracture-zone environments (Gallinati, 1984; Mével et al., 1991; Gillis et al., 1993b; Früh-Green et al., 1996; Kelley, 1996). In Hole 735B, there is a remarkable decrease in the abundance of amphibole veins downsection, and a corresponding decrease in high-temperature background static alteration, reflecting only very localized penetration of high-temperature hydrothermal fluids along the vein networks. Cessation of fluid flow in the plutonic section is marked by the development of late smectite, carbonate, and zeolite ± prehnite veins that are most likely associated with attenuation and uplift of the massif during formation of the transverse ridge. For details of these metamorphic effects, see **"Macroscopic Description of Secondary Mineralogy,"** p. 34 (i.e., background metamorphic variations at the hand specimen and larger scales); **"Microscopic Description,"** p. 38 (thin-section characterization); and "**Magmatic and Hydrothermal Veins,"** p. 41.

Downhole Distribution of Alteration

Rocks recovered during Leg 176 generally vary from fresh to 40% altered, although there are many small intervals of more altered rocks (40%–70% recrystallized), and locally rocks are 80%–90% recrystallized (Figs. **F33, F34**). Several general trends were observed: (1) The most intensely altered portion of the Leg 176 core occurs between 500 and 600 mbsf (Figs. **F34, F35, F36;** Cores 176-735B-89R to 103R), where the core is, on average, 10% to 40% altered. Calcite veins are common in this interval and are associated with low-temperature oxidation of the rocks. (2) A second zone of intense recrystallization occurs between 800 and 1030 mbsf (Cores 176-735B-130R to 156R), where many of the rocks exhibit high-temperature plastic deformation (see **"Structural Geology,"** p. 54) and veins are rare. (3) Two less-altered zones are located in an interval of abundant smectite veins at 700–800 mbsf (Cores 176-735B-119R to 130R), and in relatively uniform olivine gab-

F33. Distribution of dominant secondary metamorphic phases in Hole 735B, **p. 135.**

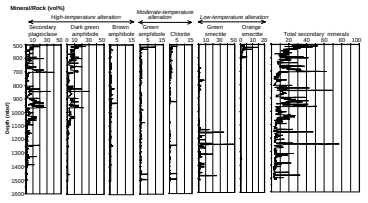

F34. Alteration vs. depth in Hole 735B, **p. 136.**

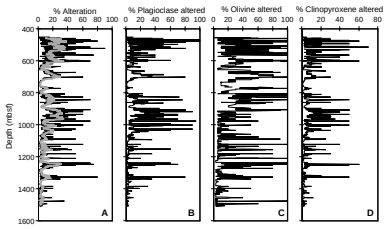

F35. Degree of alteration compared with the total abundance of veins per section, **p. 137.**

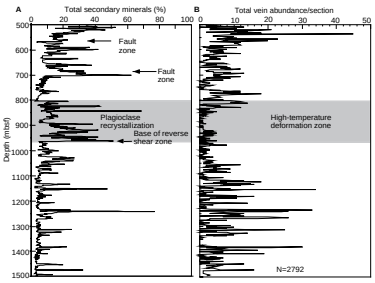

F36. Downhole distribution of secondary phases in Hole 735B, **p. 138.**

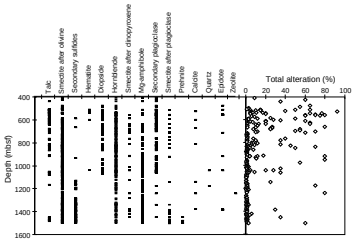

bro with common smectite veins at 1300–1500 mbsf (Cores 176-735B-187R to 210R). At depths greater than 1030 m, the intensity of alteration is typically much less than 10%.

Macroscopic Description of Secondary Mineralogy

In many places, the intensity of alteration in the gabbroic rocks from Hole 735B is strongly related to brittle deformation and the distribution of veins (see "Magmatic and Hydrothermal Veins," p. 41). The upper limit of alteration grade is represented by recrystallized oxide gabbros, which commonly exhibit aggregates of equant grains with 120° grain-boundary triple junctions, and the development of neoblastic olivine and pyroxene that are typical of granulite facies metamorphic conditions (see "Igneous Petrology," p. 12 and "Structural Geology," p. 54). The lower limit of alteration conditions is represented by zones of orange-red smectite and oxyhydroxide minerals that are related to the formation of late carbonate veins in a low-temperature, oxidative environment. The secondary minerals can be divided into three main groups (Fig. F33; Table T8): (1) a high-temperature assemblage that reflects formation under granulite to amphibolite facies conditions, (2) lower temperature mineral assemblages that are typical of formation under greenschist to zeolite facies metamorphic conditions, and (3) a very low-temperature mineral assemblage that is mainly represented by carbonate and clay minerals belonging to the smectite group.

Olivine is more easily altered than the other silicates in Hole 735B gabbros, and, as a result, the alteration profile for olivine roughly correlates with that of total rock (Fig. F34). Olivine, however, exhibits more extreme variations in alteration intensity over small intervals of the core than total rock alteration. Because plagioclase and clinopyroxene are, on average, the dominant primary minerals, variations in rock alteration correlate well with the distribution of secondary plagioclase and altered pyroxene as recorded in the hard rock visual core descriptions (VCDs). Comparison of the thin-section and VCD data confirm that it is difficult to distinguish fine-grained aggregates of pyroxene or olivine neoblasts that rim porphyroclasts in the gabbroic shear zones from high-temperature hydrothermal minerals (Figs. F37, F38, F39).

T8. Summary of alteration minerals and formation conditions, p. 266.

F37. Visual estimate of olivine alteration in thin sections vs. depth, p. 139.

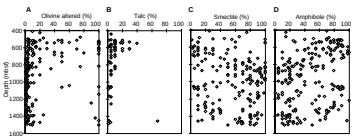

F38. Visual estimate of clinopyroxene alteration in thin sections vs. depth, p. 140.

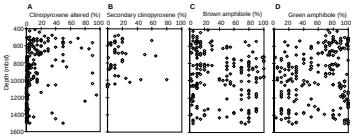

F39. Visual estimation of plagioclase alteration in thin sections vs. depth, p. 141.

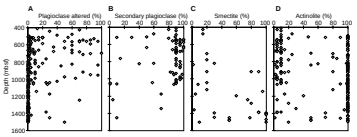

High-Temperature Minerals

Diopside

Secondary diopside is not abundant in the gabbroic rocks, but where it does occur, it is generally associated with veins (see "Magmatic and Hydrothermal Veins," p. 41). It was observed in thin sections between 500 and 1100 mbsf. Diopside commonly replaces augite and is associated with green and brown amphibole and, in some sections, with oxide minerals.

Dark Green Amphibole

Dark green (Ca) amphibole is abundant (up to 20%–25%) and widespread above 700 mbsf (Cores 176-735B-89R to 118R); it is much less common and sparsely distributed below 800 mbsf (Fig. F33). Dark green amphibole forms in the halos of monomineralic amphibole veins and as reaction rims around olivine and pyroxene. In thin section, the amphibole forms coronas that are characterized by fine-grained laths elongated perpendicular to the bounding primary ferromagnesian minerals. Dark green amphibole is also developed in the fine-grained matrix

of highly deformed rocks; however, in these zones it is difficult to distinguish amphibole in hand samples from pyroxene and olivine neoblasts.

Brown Amphibole

Brown amphibole commonly occurs in small amounts (usually <1%) along the cleavage planes of clinopyroxene, as small blebs within pyroxene, and as rims around pyroxene and oxide crystals; less commonly it rims olivine. The modal abundance of brown amphibole generally increases near felsic veins and near some plagioclase + amphibole veins. In these zones it may completely replace clinopyroxene. Where the brown amphibole is igneous or hydrothermal is not yet clearly established (see **"Sulfide and Oxide Minerals in Thin Section,"** p. 23). In deformed rocks, brown amphibole commonly rims clinopyroxene augen and is developed in recrystallized tails together with neoblastic pyroxene.

(Mg-Fe)-Amphibole

(Mg-Fe)-amphibole (e.g., cummingtonite and anthophyllite) was not observed in hand sample, but was observed in thin sections of the gabbroic rocks; modally it is a minor constituent, but it is common as an alteration phase after olivine and orthopyroxene.

Talc

Talc is ubiquitous in all gabbros containing olivine, which represent the most abundant lithology in the core (e.g., Fig. **F40**). The abundance of talc is typically low (<1%), but it increases in olivine-rich gabbros and is particularly high in the upper units (e.g., Sections 176-735B-102R-2 and 102R-3), where the average alteration is highest. The amount of talc is probably underestimated in the VCDs, because it occurs in close association with iron oxide minerals (magnetite) in the cracks of olivine and some pyroxenes (mainly orthopyroxene) and as rims on olivine and orthopyroxene, where it is commonly intergrown with amphibole and more rarely chlorite. The talc abundance decreases with depth (Fig. **F36**). However, in the lowermost units (Cores 176-735B-205R through 209R) olivine has coronas of talc, amphibole, and oxide minerals surrounding fresh cores. In some samples, these cores are replaced by chlorite-smectite.

F40. Coarse-grained highly altered Fe-Ti gabbro, **p. 142.**

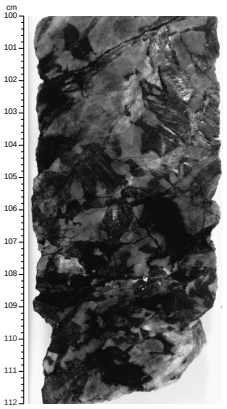

Secondary Plagioclase

Secondary plagioclase, either hydrothermal or as a recrystallized phase, is the most abundant metamorphic mineral (Fig. **F33**). The abundance of milky plagioclase is generally very low in undeformed rocks, and it is sparse away from felsic, amphibole + plagioclase, and amphibole veins; however, it is a common phase in vein halos. Relatively fresh and undeformed rocks, particularly from the lower part of the hole, generally do not exhibit secondary plagioclase in thin section. In these rocks, plagioclase is incipiently altered along cracks and grain boundaries to actinolitic amphibole. Not all the secondary plagioclase is hydrothermal in origin; extensive intervals show evidence of dynamic recrystallization of all the primary phases, and there is a low degree of alteration from 800 to 1100 mbsf.

Secondary Oxide Phases

Magnetite commonly is associated with alteration of ferromagnesian minerals to talc and with amphibole (Fig. **F36**).

Moderate-Temperature Minerals

Green Amphibole

Green amphibole after brown hornblende locally constitutes 5%–10% of both the gabbroic and felsic rocks (Figs. F40, F41). This amphibole is strongly pleochroic in thin section, and it varies from brownish green to greenish blue. It commonly forms monomineralic veinlets between primary crystals. Based on similar descriptions of amphibole in other locales, the green amphibole may contain a significant hornblende component and may reflect formation under amphibolite facies conditions (Robinson et al., 1991; Vanko and Stakes, 1991). These amphiboles are distinct from pale green acicular amphibole that forms halos associated with veins of amphibole and chlorite ± amphibole and patches in alteration areas. The pale green acicular amphibole is likely actinolite and is related to lower temperature conditions of alteration (greenschist or transitional actinolite facies).

F41. Slightly altered Fe-Ti gabbronorite, p. 143.

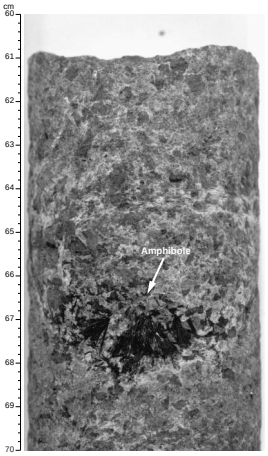

Chlorite

Chlorite is rare and is largely restricted to that part of the core above 750 mbsf (Figs. F33, F36). It generally forms <1 modal% of the rock, but there is a slight increase in abundance (up to 5%) near 512 mbsf (Core 176-735B-90R), and locally at depths near 920, 1242, 1452, and 1493 mbsf. Chlorite is commonly associated with actinolite, chlorite-actinolite, and chlorite veins, and it is present in vein halos. It also forms in patches associated with some amphibole needles and with white secondary minerals that are difficult to identify clearly in hand specimen. In thin section, the white patches are composed of quartz, albite, and zeolite.

Quartz

Quartz appears to be mostly magmatic in origin and occurs in segregation patches and late veins. However, small amounts of secondary quartz (Fig. F36) occur sparsely between 1000 and 1200 mbsf, where it is associated with other greenschist metamorphic minerals, replacing plagioclase.

Sodic Feldspar

Sodic feldspar is difficult to distinguish from more calcic secondary plagioclase and from magmatic plagioclase related to felsic veins. In some sections, milky feldspar is described as albite in the VCDs, and cloudy albite crystals are identified in thin sections of altered gabbroic rocks from the upper cores (Sections 176-735B-90R-3 and 90R-8). Based on its milky white color, some plagioclase in more felsic rocks is probably also replaced by albite. This is particularly evident in some felsic veins in which the cores of the veins appear to be highly altered to albite and chlorite. In some felsic veins, plagioclase is almost completely replaced by white clay.

Titanite

In thin section, titanite occurs sporadically as an alteration product of oxide minerals and is locally related to chlorite patches. Some larger titanite crystals (<1 mm) were identified in hand specimen (Core 176-735B-202R). Rarely, titanite forms after clinopyroxene.

Calc-Silicate Minerals

Prehnite and epidote are the only calc-silicates recognized as vein-forming minerals in hand specimen. Epidote was found in only two veins, but it occurs sporadically as a background alteration phase at various intervals of the core. Prehnite was identified in thin sections of the core recovered from the deepest part of the hole (about 1500 mbsf) and by shipboard X-ray diffraction (XRD) on hand-picked vein fragments from Core 176-735B-188R (Fig. F42). A single peak, possibly corresponding to pumpellyite, appears on the same XRD profile.

Zeolites

Some zeolites were identified in thin sections, but they are rare as background alteration products. The highest occurrence of zeolite in thin section is from Core 176-735B-181R, where it forms veins in association with chlorite-smectite and minor carbonate. Zeolites in Cores 176-735B-188R and 199R are provisionally identified as natrolite or possibly scolecite by shipboard XRD analyses (Fig. F43).

Secondary Sulfide Minerals

Most sulfide minerals form dispersed angular or globular aggregates or crystals in interstitial areas and are probably primary in origin. However, secondary pyrrhotite, pyrite, and, less commonly, chalcopyrite form in association with greenschist facies mineral assemblages (Fig. F36). Pyrrhotite occurs with magnetite, talc, and amphibole in alteration coronas around olivine. Other occurrences of secondary sulfide minerals are related to the formation of late smectite veins and are described in the following section on low-temperature mineralogy.

Low-Temperature Minerals

Smectite Minerals

Smectite is the third most abundant alteration phase after dark green amphibole and secondary plagioclase (Fig. F33). Above 600 mbsf, orange to reddish patches of smectite and Fe-oxyhydroxide minerals partially or completely replace olivine and are related to the presence of carbonate and smectite veins (Cores 176-735B-89R to 94R, and 102R). A second type of smectite (dark green to pale bluish green) is spatially related to smectite veins and appears deeper in the core between 720 and 1500 mbsf. There is a gap in the distribution of green smectite veins between 800 and 1100 mbsf (see "Magmatic and Hydrothermal Veins," p. 41), corresponding to a zone of highly deformed rocks.

In some cores, dark brownish green smectite almost completely replaces olivine and, where alteration intensity is high, pyroxene as well. Olivine is commonly altered to smectite near smectite veins or at some distance if the veins cut felsic material (Fig. F44). This type of smectite is commonly associated with sulfide minerals in olivine pseudomorphs, and it is believed to form under low-temperature, anoxic conditions. Pale green to white smectite after plagioclase occurs mainly close to veins and in or near felsic areas. However, it is not clear if there is any systematic relationship between the presence of felsic material and the development of pale green smectite veins. Green smectite may also replace amphibole in both the felsic material and adjacent gabbroic rocks.

F42. X-ray diffraction profile of smectite, prehnite and pumpellyite(?), p. 144.

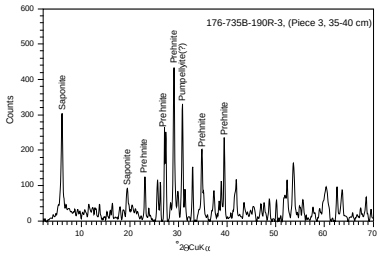

F43. X-ray diffraction profile of zeolite, p. 145.

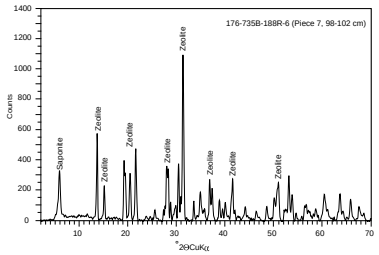

F44. Vein of pale-green smectite with alteration halo, p. 146.

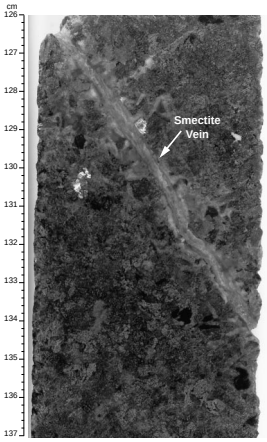

Carbonate Minerals

Carbonates are mainly found as vein-forming minerals, but they also are intergrown with orange smectite in background alteration near veins (Fig. F36). These phases are mainly Ca-carbonate minerals, most probably calcite. Calcite replaces olivine in the oxidative zone (500–600 mbsf) and is found locally deeper in the core near smectite + calcite + pyrite veins. Calcite also forms after plagioclase along some smectite + calcite + pyrite veins (e.g., Sample 176-735B-132R-1 [Piece 11A]). Deeper in the core, calcite locally accompanies zeolite in veins. Fine-grained translucent needles in Section 176-735B-181R-3 may be aragonite.

Low-Temperature Sulfide Minerals

Sulfide never exceeds a few percent of the altered rocks and generally represents less than 1% of the core. Sulfide minerals commonly form after olivine in association with smectite, particularly near smectite veins. In many cases this sulfide appears in hand specimen to be pyrite. However, in Cores 176-735B-205R and 207R a reddish brown sulfide is abundant as an alteration phase in the cores of olivine. This could be marcasite or pyrrhotite, both of which have been identified in thin section.

Oxyhydroxide Minerals

Hematite and orange to brown oxyhydroxide phases are present mainly between 500 and 600 mbsf, in weathered zones related to carbonate veins and in association with orange smectite. In these zones, the minerals form iddingsite-like products after olivine and some pyroxene. Some very limited oxidative alteration occurs further downhole, between 1340 and 1355 mbsf (Cores 176-735B-191R and 192R).

Shear Zones

Narrow zones of crystal-plastic deformation are common in the upper parts of the core. In these zones, plagioclase and, to a lesser extent, pyroxene are granulated and recrystallized (Fig. F45). In many cases, these zones are also impregnated with magnetite and ilmenite. Most of these zones underwent extensive chemical and mineralogical modification. Recrystallized feldspar is typically more sodic than the original plagioclase, recrystallized clinopyroxene is more diopsidic, and orthopyroxene is common. Olivine is rare or absent and, if present, is almost completely altered. Clinopyroxene is typically altered to brown hornblende and green actinolite, particularly in the recrystallized zones. Oxides replace much of the recrystallized feldspar and pyroxene; zircon, titanite, and apatite are abundant.

F45. Highly altered mylonitized and net-veined trondhjemite-gabbro with recrystallized plagioclase, p. 147.

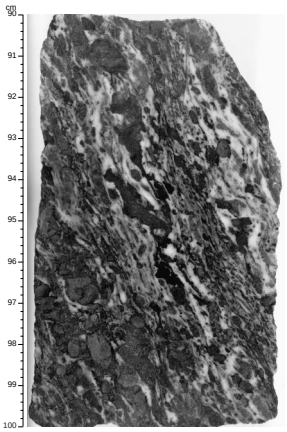

Microscopic Description

During Leg 176, 253 thin sections were prepared from core recovered from Hole 735B; 10 of these were from the lower 100 m of core recovered during Leg 118, and the remainder from new core recovered during Leg 176. The thin sections were all described by a single observer to provide consistency of observation. All secondary minerals were identified optically, and modes are visual estimates.

The average thin-section sample density down the core is about one per 4 m. Thin sections were typically made for all samples analyzed by XRF and for samples from interesting igneous, metamorphic, or struc-

tural intervals. Thus, the amount and character of alteration described in thin section correlates roughly with that determined by visual core description.

In the thin-section descriptions, recrystallized grains, particularly of plagioclase and clinopyroxene, were classified as secondary and included in the estimates of alteration. A study of Leg 118 core showed that recrystallized plagioclase is commonly more sodic than the original igneous grains and that recrystallized pyroxene is more diopsidic (Stakes et al., 1991; Robinson et al., 1991). Sheared and recrystallized zones are commonly impregnated with iron titanium oxide minerals, and they typically have much higher percentages of orthopyroxene than the core as a whole.

Alteration of Olivine

Olivine generally occurs as irregular grains of various size, commonly rimmed with orthopyroxene. Alteration ranges from about 1%–2% to 100% (Fig. F37). Because of the irregular shapes of the grains, completely altered olivine may be difficult to distinguish from altered orthopyroxene. However, secondary minerals after orthopyroxene typically preserve some of the original pyroxene cleavage.

Even the freshest olivine is cut by a network of irregular cracks or fractures lined with dark, opaque material (Fig. F46A, F46C). This material appears to be a mixture of smectite, possibly talc, and very finely divided magnetite, although individual magnetite grains rarely can be identified under the microscope (Fig. F27B). Small irregular grains of sulfide minerals are commonly associated with the smectite. As alteration increases, the rims of the grains are replaced by fine-grained mixtures of talc, magnesian amphibole, and finely divided magnetite or pyrite. Small grains may be completely replaced, whereas larger grains, even in the same sample, exhibit only marginal alteration. Irregular patches of talc, amphibole, and magnetite, mark completely altered olivine grains (Fig. F46B). In a few cases, the cores of olivine grains are replaced by mixtures of deep red to orange hematite and smectite, which in turn are surrounded by rims of talc, amphibole, and magnetite. This late-stage oxidative alteration occurs primarily in a zone from Sections 176-735B-90R-4 to 94R-2 (512 to 539 mbsf), where it is commonly associated with carbonate veinlets.

F46. Photomicrographs of olivine with smectite and oxide; partly altered olivine with talc, Mg-amphibole and oxide; and olivine with clinopyroxene, p. 148.

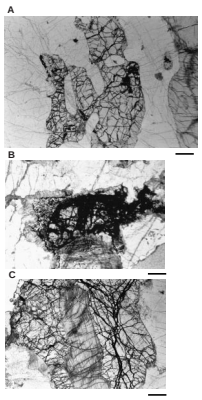

Alteration of Orthopyroxene

Orthopyroxene is relatively rare in samples recovered during Leg 176. In olivine gabbro, it typically occurs as narrow rims or bands on olivine grains, particularly where olivine is in contact with plagioclase. In more evolved, oxide-rich gabbros, orthopyroxene occurs as discrete crystals either as relatively large, subhedral grains or small, anhedral grains. The latter are most common in deformed zones where the primary minerals was granulated and recrystallized and the rock was impregnated with oxide-rich liquids.

Orthopyroxene is typically much less susceptible to alteration than olivine. In some cases where it rims olivine, the olivine shows marginal alteration, whereas the orthopyroxene is completely fresh or only slightly replaced by pale green amphibole. Where alteration is more intense, the orthopyroxene is partly replaced by green amphibole, brown smectite, and disseminated magnetite or pyrite. In a few cases, the cores of orthopyroxene grains are also replaced by mixtures of red-

dish orange hematite and smectite. Again, this type of alteration is most common in the interval between Sections 176-735B-90R-4 and 94R-2 (512 to 539 mbsf).

Alteration of Clinopyroxene

Clinopyroxene is the most abundant ferromagnesian silicate in the rocks from Hole 735B, occurring in every thin section examined. It typically occurs in large, subhedral grains intergrown in complex relationships. It is commonly associated with olivine and, in a few cases, is completely surrounded by it (Fig. F45). Alteration of clinopyroxene is highly variable, ranging from less than 1% to a maximum of 90%, but in any thin section it is always considerably less than that of olivine. Throughout most of the core, it is less than 10% altered, and more intense alteration is almost always adjacent to veins or in narrow shear zones.

Alteration of clinopyroxene is primarily to brown hornblende and green actinolite. The brown hornblende occurs chiefly in oxide gabbros where the rocks have been sheared, recrystallized, and impregnated with fluids, but it occurs elsewhere as well. The hornblende occurs as small blebs within the pyroxene grains, some of which are aligned along cleavage planes. In other cases, brown hornblende occurs along the margins of pyroxene grains, particularly where they are in contact with oxide minerals. Commonly, the brown hornblende is accompanied by small amounts of ilmenite. Only rarely does brown amphibole exceed 2 modal%.

Green actinolite, on the other hand, may compose up to 50 modal% of the rock, depending on the percentage of original clinopyroxene. The actinolite occurs almost exclusively along the margins of pyroxene grains and penetrates short distances into the crystals along cleavage planes. It also extends into adjacent plagioclase grains along narrow cracks. More extensive alteration of clinopyroxene occurs only adjacent to major veins. The actinolite may be accompanied by small amounts of light green to colorless chlorite, and, in rare cases, chlorite is the dominant secondary phase.

Locally, the clinopyroxene is weakly sheared, granulated, and recrystallized. Where this occurs, the recrystallized grains are typically lighter colored and may be more diopsidic than the original grains. These grains are also partly to completely replaced by brown hornblende or light green actinolite, which may or may not be accompanied by minor oxides.

Alteration of Plagioclase

In all specimens examined, plagioclase is the most stable phase. Over large intervals of the core, alteration of plagioclase is limited to 1% or less and consists of minor amounts of actinolite or smectite along cracks and grain boundaries. Where plagioclase grains are in contact with altered clinopyroxene, the actinolite on the margins of pyroxene grains typically extends outward into the plagioclase for short distances. Alteration is commonly more intense adjacent to veins, where chlorite, carbonate, prehnite, or epidote may occur in addition to amphibole or smectite.

The most extensive alteration of plagioclase occurs in narrow shear zones where the original grains are granulated, recrystallized, and partly replaced by more sodic feldspar. Within these zones the plagioclase may

also be replaced by minor epidote and/or chlorite and by more abundant oxides. The plagioclase may be completely recrystallized and replaced, but the zones are typically quite narrow, on the order of a few millimeters to a few centimeters. Elsewhere, alteration of plagioclase rarely exceeds 10% of the amount present.

Magmatic and Hydrothermal Veins

Based on macroscopic description, 21 vein assemblages (Table T9) were recognized in core recovered during Leg 176, and 2792 veins were described and measured. Vein distribution shows wide variation, depending on the mineral paragenesis, but many vein types (e.g., felsic, diopside, and amphibole-bearing veins) show a striking decrease in abundance downsection. Total vein abundance averaged over the core is less than 1%, with felsic veins the dominant vein type by volume; smectite veins are the dominant type by number (Figs. F47, F48). Veins generally were described based on hand samples, as relatively few were observed in thin section. In thin section, most veins are narrow, discrete features with relatively little wall-rock alteration. The common veins in thin section are filled with carbonate, smectite, felsic material, amphibole, diopside ± feldspar, and zeolite in various combinations.

Felsic Veins

The origin of some felsic veins in gabbroic rocks from Leg 176 is equivocal because of a strong hydrothermal overprint (Fig. F49); therefore, the veins were logged by both the igneous and metamorphic working groups. Where there is no strong hydrothermal overprint, mineral assemblages reflect dioritic to trondhjemitic and granitic compositions, with 1 to 2 modal% of accessory minerals (e.g, apatite, zircon, titanite, and magnetite). By number, the felsic veins make up only 4.08% (N = 114) of the veins measured, but volumetrically they are the dominant type, constituting 45% of the total (Fig. F48; Table T9). Their average length and width is 11.69 cm (±10.79) and 8.75 mm (± 8.24), respectively, and they have sharp boundaries with the host rock. The felsic veins do not show a strong preferred orientation within the core (see "Structural Geology," p. 54). The felsic veins are typically, but not always, associated with oxide-bearing gabbros, and they decrease markedly in abundance downsection; below ~1260 mbsf they are rare (Fig. F47B).

Rare felsic veins have cores rich in amphibole ± hydrothermal clinopyroxene (Fig. F50) that are rimmed by plagioclase, but generally mineral phases are irregularly distributed within the veins (Fig. F49). The veins typically contain variable amounts of highly zoned plagioclase, rare potassium feldspar, and myrmekite (Fig. F51C), well-crystallized brown and green amphibole, hydrothermal clinopyroxene, and trace amounts of quartz and biotite (Fig. F51B). The primary vein minerals exhibit negligible to high alteration intensities, and centimeter-wide alteration halos are common.

Commonly, plagioclase forms subhedral to anhedral crystals up to 5 mm across. These typically show strong concentric zoning and patchy or irregular replacement by sodic feldspar and irregular veinlets of secondary plagioclase; in these zones vapor-dominated fluid inclusions are common. In some cases, the plagioclase is extensively replaced by chlorite, which may be accompanied by minor epidote or carbonate. In some veins, plagioclase contains numerous small inclusions of amphib-

T9. Summary of vein types, p. 267.

F47. Distribution of total veins; felsic, plagioclase, and plagioclase + amphibole veins; plagioclase + diopside and diopside veins; amphibole veins; carbonate and smectite veins; and chlorite and zeolite veins, p. 149.

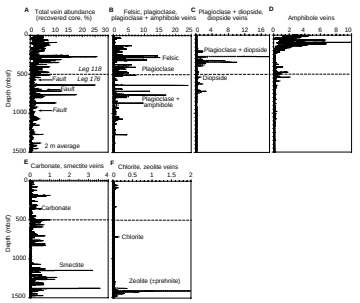

F48. Proportion of veins types relative to the total amount of veins, p. 150.

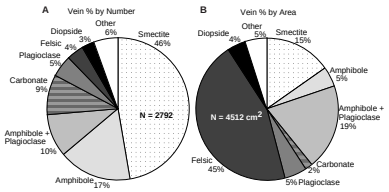

F49. Extensively altered felsic vein, p. 151.

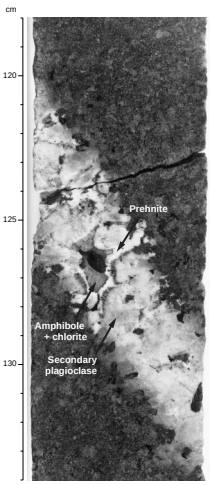

ole, chlorite, and dark, very fine-grained material that give the feldspar a pitted or "dirty" appearance. Microveinlets of actinolite and chlorite cut some samples. In more highly altered zones within the veins, prehnite, calcite, smectite ± zeolite, and rare epidote form irregular pods and patches after plagioclase.

Quartz in these veins commonly is rounded to irregular in habit, and the grains typically contain liquid-dominated inclusions with halite daughter (±opaque) minerals. Quartz in some of these veins is partly replaced by brown smectite. In some veins, there is a high concentration of oxide minerals within the vein margins and in the adjacent host rock. Titanite is also common in some of these veins, and it typically occurs as irregular grains along the vein margins or adjacent to mafic minerals like diopside.

Alteration halos associated with these veins reflect moderate to intense alteration of wall-rock plagioclase to secondary plagioclase, and clinopyroxene to hydrothermal clinopyroxene, amphibole, and oxide minerals. Olivine is replaced by amphibole, traces of chlorite, and oxide minerals. In a few cases, the felsic veins have narrow, late-stage cracks filled with carbonate, zeolite, or smectite.

Plagioclase + Amphibole and Plagioclase Veins

Plagioclase + amphibole and monomineralic plagioclase veins are commonly associated with the felsic veins. In some sections they may represent small veinlets that have splayed off of the larger dioritic to trondhjemitic veins (Fig. F52). Like the felsic veins, they strongly decrease in abundance downsection (Fig. F47B) and only occur sporadically below 1250 mbsf. Numerically they constitute 9.6% and 4.9% of the veins measured, respectively, and 19.3% and 4.9% by volume (Fig. F48). They typically form narrow, 2- to 4-mm-wide veinlets that lack a strong preferred orientation (Fig. F53; see "Structural Geology," p. 54). The plagioclase + amphibole veins contain highly variable amounts of these two mineral phases, although most veins are dominated by plagioclase. Some of these veins are highly zoned with amphibole-rich cores and plagioclase-rich rims (Fig. F54). In areas of intense alteration, the plagioclase is altered to secondary feldspar, prehnite?, zeolite, carbonate, and smectite. Green amphibole is altered to pale-green to colorless amphibole, variable amounts of chlorite, and fine-grained oxide minerals. Typically, these veins do not have strong alteration halos.

Diopside, Diopside + Plagioclase, and Diopside + Amphibole Veins

Clinopyroxene-bearing veins are rare in gabbroic rocks recovered during this leg, occurring predominantly in two intervals at 600–650 mbsf and 700–750 mbsf (Figs. F47C, F55. They comprise only 3% of the veins by number and 4% by volume and occur in zones where gabbros and gabbronorites are common. They do not exhibit a strong preferred orientation, but in some zones they are intensely deformed into mylonites (see "Structural Geology," p. 54). They are typically narrow veins, 2 to 4 mm in width. The plagioclase + diopside veins commonly have diopside-rich cores that are rimmed by plagioclase (Fig. F55). Diopside crystals in the veins are euhedral to subhedral, up to 2 mm across, and commonly zoned. These crystals commonly contain small, dark inclusions and may be rimmed by amphibole. Like the other felsic veins, these commonly contain low-grade minerals, such as prehnite,

F50. Typical zoned felsic vein, p. 152.

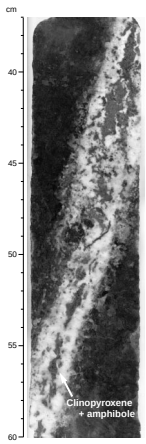

F51. Euhedral titanite in a diopside vein; green amphibole and titanite in a felsic vein; quartz and feldspar in a felsic vein; and a euhedral zircon crystal, p. 153.

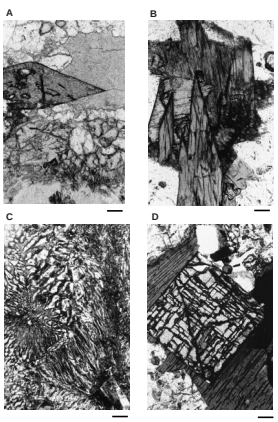

F52. Dioritic vein, p. 154.

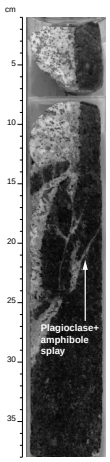

carbonate, zeolite, and smectite in the groundmass. Alteration of these veins is highly variable, and some veins exhibit moderately developed alteration halos (Fig. F55). In more intensely altered zones, plagioclase may be altered to secondary plagioclase, and hydrothermal clinopyroxene is common.

Amphibole Veins

Amphibole veins form the second most abundant vein assemblage, constituting 17% of the veins by number, but they are only 5% of the veins by volume (Figs. F47D, F48; Table T9). They are commonly < 0.5 mm wide, dark green (Fig. F55), and in rare cases they form anastomosing fine vein nets. They are generally subvertical (see "Structural Geology," p. 54), and in places they cut zones of intense deformation (Figs. F56, F57, F58A). Although in the upper 500 m of the core, the amphibole veins are strongy correlated with deformed regions (Dick et al., 1991a), this relationship is not observed in core recovered during Leg 176 (see "Structural Geology," p. 54). Amphibole vein abundance strikingly decreases downsection, and amphibole veins are rare below 1100 mbsf. In rare zones, they are associated with intense, centimeter-wide alteration halos (Fig. F59). In such areas, wall-rock plagioclase is strongly altered to secondary plagioclase, and clinopyroxene is altered to amphibole and less commonly chlorite. Amphibole and chlorite microveinlets cutting plagioclase are common in these zones. Amphibole veins are typically narrow cracks filled with well-crystallized, green amphibole. Where these occur in deformed zones or amphibole gneisses, they typically cut the foliation and, in some samples, they offset bands in the host rock. Most of these veins consist entirely of amphibole, but the largest ones also contain feldspar.

Carbonate Veins

We logged 293 carbonate-bearing veins in the Leg 176 core (Figs. F47F, F48, F60). Carbonate veins compose 9.1% of the total number and 1.8% of the total volume of veins in the core (Fig. F48; Table T9). Carbonate veins are concentrated in the zone between 500 and 600 m, where the rocks exhibit low-temperature oxidation effects and some samples are intensely calcitized. A major fault is present at 560 mbsf within this zone (see "Structural Geology," p. 54), and fracturing related to faulting provided pathways for ingress of seawater solutions to form carbonate veins. Carbonate veins also occur in small amounts locally at greater depths. X-ray diffraction of several samples indicates the presence of calcite (Fig. F61), but prismatic crystals in a 0.2-mm-wide vein at 1245.6 mbsf (Core 176-735B-181R) were tentatively logged as aragonite. Iron oxyhydroxide occurs with calcite in four veins in rocks exhibiting low-temperature oxidation at 522 mbsf, and variable proportions of smectite are present with calcite in 35 veins locally throughout the core at greater depths. Calcite veins range from 0.1 to 11 mm wide and from 3 to 39 cm long but average 0.5 mm wide and 7 cm in length. In thin section, carbonate veins are most common in the intervals where olivine and orthopyroxene are replaced by hematite and smectite.

F53. Plagioclase + amphibole anastomosed vein network, p. 155.

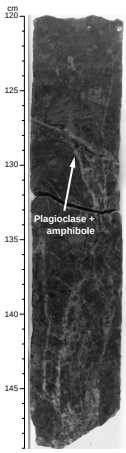

F54. Highly zoned amphibole + plagioclase vein, p. 156.

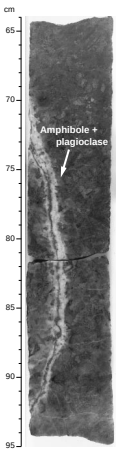

F55. Highly zoned diopside + plagioclase vein, p. 157.

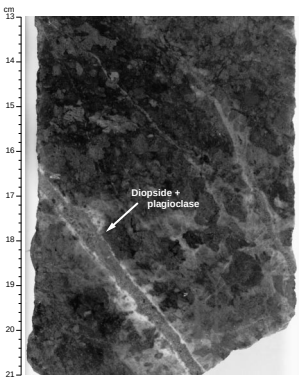

Smectite Veins

We recorded 1016 smectite veins in the Leg 176 section. These veins make up 47% of the total number and 15.2% of the total volume of veins in the core (Figs. F44, F47F, F48; Table T9). Variable proportions of smectite also occur in 35 smectite + calcite veins, 22 smectite + zeolite veins, and 2 smectite + amphibole veins, where later smectite fills former open space in earlier amphibole veins. Smectite commonly forms small (<1 mm) veins at the center of felsic veins throughout the core.

The presence of smectite was confirmed by X-ray diffraction of several air-dried samples (Fig. F61), but observations in thin section suggest that mixed-layer smectite/chlorite may be present in some samples. Dark green smectite veins occur with local small amounts of pyrite in Cores 176-735B-100R through 131R (575 to 813 mbsf), whereas all smectite veins below this depth consist of pale green to white smectite. Smectite veins range from 0.1 to 7 mm wide and 1 to 130 cm long but average 0.6 (+0.6) mm wide and 7 (+5.7) cm long (Fig. F58B).

Smectite veins occur in two general zones where they are by far the dominant vein type, from 575 to 833 mbsf (Cores 176-735B-99R to 134R) and from 1054 to 1500 mbsf (Cores 176-735B-159R to 210R; Fig. F47F). The upper zone of smectite veins overlaps slightly with the interval of abundant calcite veins (Fig. F47F). Fracturing related to the fault at 560 mbsf and another fault marked by cataclasis at 690–700 mbsf (see "Structural Geology," p. 54) may have provided pathways for access of seawater solutions to form smectite within this upper zone. Only very rare smectite veins are present from 833 to 1054 mbsf (Cores 176-735B-135R through 158R; Fig. F47F), corresponding to a zone of high-temperature shearing and intense crystal-plastic deformation (see "Structural Geology," p. 54). Below this interval, smectite veins are abundant from 1054 to 1508 mbsf; they are particularly abundant from 1230 to 1330 mbsf. Local barren zones occur within the lower smectite vein zone, especially from 1340 to 1380 mbsf (Cores 176-735B-192R to 195R). In contrast to the calcite and upper smectite vein zones, the lower smectite vein zone does not correspond to a fault. Fractures in this zone are tensional (see "Structural Geology," p. 54), and they occur within a sequence of relatively uniform and undeformed olivine gabbros (see "Igneous Petrology," p. 12). The host rocks for up to 1–2 cm away from smectite veins are variably altered to smectite: olivine is intensely altered to smectite + magnetite + sulfide (pyrite, pyrrhotite), and plagioclase and pyroxene are slightly altered to smectite.

Zeolite and Prehnite Veins

Zeolite and zeolite + smectite veins occur within the zone of smectite veins near the base of the core, from 1130 to 1490 mbsf (Cores 176-735B-168R to 209R), but are concentrated in the interval 1385–1453 mbsf (Cores 176-735B-197R to 205R; Fig. F47E). These veins range from 0.1 mm to 5 mm wide and from 11.2 cm to 144 cm long, but they average 0.9 mm wide and 11.2 cm long. They typically exhibit a broad range of dips (see "Structural Geology," p. 54), but vertical zeolite + smectite veins occur in Cores 176-735B-201R through 205R (1418–1455 mbsf). A few individual veins extend through more than one section and were thus greater than 144 cm long before curation.

X-ray diffraction of several veins indicates the presence of natrolite, prehnite, and possibly pumpellyite (Fig. F42). Prehnite was confirmed

F56. Subvertical amphibole vein, p. 158.

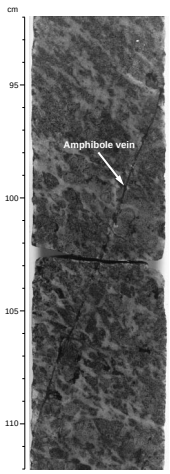

F57. Subvertical anastomosing amphibole vein network, p. 159.

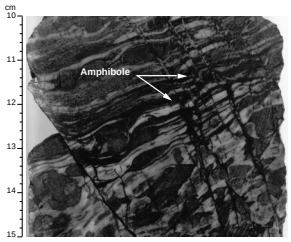

F58. Photomicrograph of amphibole gneiss and smectite vein cutting plagioclase, p. 160.

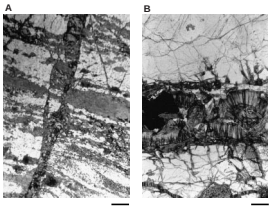

F59. Subvertical amphibole veins with alteration halos, p. 161.

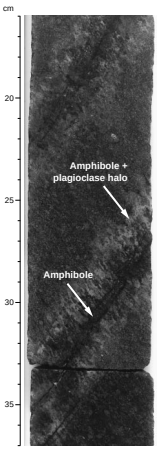

in observations of thin sections, but the tentative identification of pumpellyite is based on the presence of one peak in a single diffractogram, and must be confirmed by further analyses. Prehnite and zeolite were identified in Cores 176-735B-205R to 210R, and their presence was confirmed by X-ray diffraction (Figs. F42, F43). Prehnite veins are commonly zoned with a narrow band of light brown smectite along the outer edge, followed by a band of prehnite. The prehnite in some cases fills the entire central part of the vein, and in other cases occurs with discontinuous patches of carbonate. In a few cases, the prehnite is intimately intermixed with smectite.

Rare Veins

Chlorite

Chlorite veins are present in small amounts locally in the core (Fig. F47E): five veins are present in Core 176-735B-121R at 721 mbsf; one vein each in Cores 176-735B-200R and 202R at 1403 and 1430 mbsf; and 15 subvertical veins of chlorite, chlorite + amphibole, and chlorite + zeolite (natrolite and prehnite) in Cores 176-735B-204R through 209R (1446–1493 mbsf; Fig. F62). The chlorite veins in Cores 176-735B-121R, 200R, and 202R have narrow (millimeter wide) chloritic alteration halos. Along the subvertical chlorite-bearing veins in Cores 176-735B-204R through 209R, plagioclase is altered to a white mineral (zeolite, prehnite, or albite/K-feldspar) in millimeter- to centimeter-wide chloritic alteration halos along the veins (Fig. F62).

Quartz

Quartz veins are rare, with only six identified locally from 1264 to 1505 mbsf (Cores 176-735B-183R through 210R). Amorphous silica was also identified in two veins within this interval. Smectite is present in some of the quartz veins, which are generally less than 2 mm wide.

Epidote

A single large (12 mm wide) epidote vein occurs in Section 176-735B-114R-3 (Fig. F63). Wall rock for as much as 2 cm away from the vein is recrystallized to a chloritic assemblage.

Summary and Discussion

The highest temperature metamorphic effects in the plutonic sequence are transitional from magmatic processes; they most likely overlap both temporally and spatially, and distinguishing the effects of these two processes is difficult in places. High-temperature metamorphism (>800°–1000°C) is clearly marked by localized, narrow zones of crystal-plastic deformation that cut igneous fabrics (see "Structural Geology," p. 54). These intervals are characterized by anastomosing bands of olivine and pyroxene neoblasts that are bounded by plagioclase-rich bands, reflecting formation under granulite-grade metamorphic conditions. In some places the high-temperature shear zones are associated with local impregnation of very iron-rich liquids into the rocks to form oxide gabbros, and in many cases these zones have abundant amphibole. In some of these intervals, porphyroclastic gabbros exhibit a well-developed foliation that is marked by olivine and pyroxene porphyroclasts wrapped by well-crystallized brown hornblende, reflecting formation under granulite to transitional amphibolite facies metamorphic conditions. Also present locally are small (centimeter

F60. Carbonate veinlet and vug, p. 162.

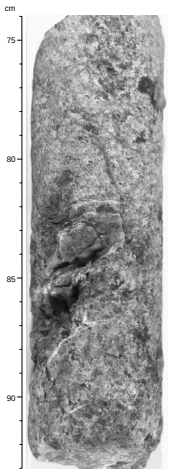

F61. X-ray diffraction profile of vein-forming material, p. 163.

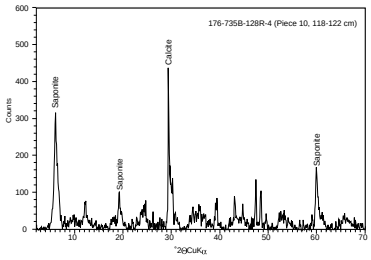

F62. Vertical veins of chlorite and amphibole crosscut by smectite veins, p. 164.

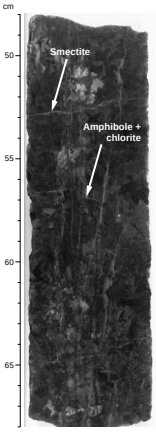

sized) patches of late felsic material that commonly contain high concentrations of amphibole, ilmenite, magnetite, and minor amounts of sulfide, quartz, apatite, and zircon. Many of these rocks, veins, and shear zones may reflect the effects of late magmatic hydrous fluids, but these zones also acted as pathways for later hydrothermal fluids at various temperatures, resulting in the formation of hydrothermal amphiboles and clinopyroxene, chlorite, titanite, smectite, and zeolites. A zone of pervasive deformation and reverse shear from 800 to 1050 mbsf is associated with a high-temperature fault at about 960 mbsf. Brittle veining is rare in this interval. Other high-temperature effects probably resulting from late-stage magmatic activity include the formation of plagioclase + amphibole veins and diopside-rich veins, which in some intervals are progressively transposed into localized zones of high-temperature shear. These veins are most common from 500 to 650 mbsf, and they decrease sharply in abundance below this depth.

High-temperature static background alteration by hydrothermal fluids is patchy throughout the core, and it is commonly most strongly developed in alteration halos associated with felsic veins. This alteration is generally manifested by coronitic alteration halos around olivine grains and the common replacement of clinopyroxene by variable amounts of brown amphibole. In more evolved rocks, magnesian-amphibole ± talc typically replaces orthopyroxene. The secondary minerals most likely formed under low water-to-rock ratios over a range of temperature, from >600°–700°C (talc, amphibole, magnetite, and hydrothermal clinopyroxene) down to much lower temperatures (e.g., where chlorite is present). Mineral paragenesis is commonly marked by disequilibrium textures, and low-temperature mineral phases typically overprint higher temperature assemblages.

Ingress of moderately high temperature fluids (400°–550°C) into the plutonic rocks was facilitated by the development of subvertical amphibole veins that are probably related to cooling and cracking of the rocks in the axial environment. In the upper 500 m of the core, these veins are associated with intense zones of deformation (Dick et al., 1991a; Stakes et al., 1991), but this relationship was not observed at deeper intervals (see **"Structural Geology,"** p. 54). The abundance of amphibole veins decreases markedly with depth in the Leg 176 section, and below 600 mbsf amphibole veins are rare. The absence of intense amphibole veining at depth is reflected in the low degree of background alteration. At a smaller scale, microcracks (<100 µm) filled with talc, magnetite, amphibole, sodic plagioclase, chlorite, and epidote are sporadically present throughout the core and represent smaller scale fracturing and fluid penetration at variable temperatures.

All of these processes reflect a wide temperature range, but temperatures were most likely high enough during this stage to be limited to the spreading axis or to the very near-axis environment. The upper 200 m of the Leg 118 section is more intensely veined and altered, has lost copper and sulfur, and contains fluids with salinities similar to hydrothermal vents; this section is interpreted to be the root zone of an axial hydrothermal system(s) (Alt and Anderson, 1991; Alt, 1995; Kelley, 1996, 1997). In contrast, some intervals of the Leg 176 section are strongly affected by low-temperature fluid penetration, as evidenced by abundant smectite ± carbonate veins. The abundant veins of calcite, smectite, and iron oxyhydroxide minerals and the associated intense alteration localized at 500–600 mbsf reflect low-temperature alteration by circulating seawater solutions. These veins are most likely related to the presence of a fault at 560 mbsf (see **"Structural Geology,"** p. 54).

F63. Rare epidote (+amphibole) vein, **p. 165.**

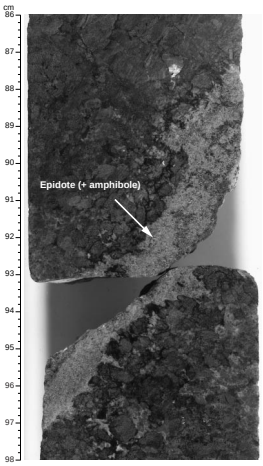

Below this interval, veins of smectite + pyrite + calcite and associated smectitic alteration of surrounding wall rock reflect low-temperature hydrothermal reactions under more reducing conditions. These effects occur throughout much of the core, but the abundant smectite veins at 600–800 mbsf may be related to a second fault at 690 mbsf. The zone of smectite and/or chlorite/smectite, prehnite, and zeolite veins and associated host rock alteration in the lower part of the core (1300–1500 mbsf) requires further work to document and confirm mineral paragenesis, but represents subgreenschist alteration at variable temperatures and fluid compositions. This lower temperature set of veins formed in tensional fractures and is perhaps related to uplift and cooling of the block in an off-axis environment, outside the axial convective cell.

GEOCHEMISTRY

Methods, Sample Selection, and Results

During Leg 176 a set of 188 whole rock samples from Hole 735B was analyzed using XRF for major element composition and for the abundances of the trace elements vanadium, chromium, nickel, copper, zinc, rubidium, strontium, yttrium, zirconium, and niobium. Sample preparation techniques and analytical procedures are outlined in **"Geochemistry,"** p. 11, in the "Explanatory Notes" chapter. Core samples for analysis generally weighed 20 to 30 g. Larger sample slabs were cut from the very coarse-grained intervals. As a rule, a thin section was prepared from a billet from the same or an adjacent core piece. The weight loss on ignition (LOI) was determined on the fraction of powder ignited to prepare the Li-borate beads for major element analysis. The trace element concentrations were determined in pressed powder pellets prepared from dried, not-ignited sample powder.

The main objective of the shipboard analysis was to document the downhole chemical variation of the major lithologies of the cored gabbro section. The majority of the samples are hence olivine gabbro, gabbro, and disseminated oxide gabbro. The sampling density was governed by the lithologic variability within a given part of the hole and by the analytical capacity of the shipboard laboratory. In principle, at least one sample representative of the main lithology was taken from each core (typically 8 to 9 m long), even when an apparently homogeneous unit spanned several cores. Seams of Fe-Ti oxide-rich gabbros and larger felsic veins were occasionally sampled to study the complete range of petrologic differentiation in the gabbro pile. However, in most cases the substantial amount of material required for the routine shipboard procedure precluded the sampling of the felsic veins. A limited number of samples were taken from core intervals that are strongly affected by high- or low-temperature alteration to gain insight into the first-order chemical effects of fluid flow and recrystallization attending alteration.

Of the 458 lithologic intervals identified by the igneous petrology group, about 140 are represented in the set of analyzed samples. Some of the thicker intervals have been sampled two to three times. However, many intervals exhibit significant lithologic variation, and a particular analyzed sample may not necessarily correspond to the dominant lithology. The reader is referred to the thin section descriptions (see the **"Core Descriptions"** contents list) for a complete sample characterization.

During the ship's transit to Hole 735B, the lower 50-m interval of core drilled during Leg 118 was restudied and partially resampled for chemical analysis. Five of the eight new samples from Cores 118-735B-74R through 88N are oxide gabbros. Due to time constraints, these oxide-rich intervals from Unit VI were not sampled and analyzed by the Leg 118 shipboard party. The remaining three samples are two olivine gabbros and one troctolite, the main lithologies from Unit VI. The chemical analyses of these eight samples are included in this volume.

Shipboard data for major elements were supplemented with post-cruise determination of ferrous/ferric iron ratios by a redox-titration method, (see "Geochemistry," p. 11, in the "Explanatory Notes" chapter). The chemical data for major and trace elements are listed in Table T10. The major element data have not been renormalized to sum 100% to correct for systematically high "Totals" of the XRF analyses (see "Metamorphic Petrology," p. 10, in the "Explanatory Notes" chapter). It should be noted that the major element analyses are reported differently from the Leg 118 shipboard data, which consist of reconstituted, renormalized rock compositions.

T10. Major and trace element composition, p. 268.

Concentrations of the trace elements V, Cr, Ni, Cu, Zn, Sr, Y, and Zr are well above the respective determination limits of the technique in virtually all samples. By contrast, the elements Rb and Nb could be detected only in a small number of the analyzed samples. The XRF technique rather serves as a "screening method" to identify samples that show significant enrichment of Rb or Nb with respect to normal concentration levels (less than 1 ppm for both elements) in oceanic gabbros.

LOI values were generally low (less than 1 wt%), as expected given the overall low degree of alteration of the recovered gabbro section. The LOI values provide only a first-order indication of the amount of volatile components (H_2O and/or CO_2) present in the samples, because the loss of mass from expelled volatile components is counterbalanced by uptake of oxygen due to oxidation of ferrous to ferric iron. As a result of this effect, many of the iron-rich rocks actually gained weight upon ignition. To obtain more useful information for all samples exhibiting LOI in excess of 1 wt%, carbon and hydrogen were analyzed using the shipboard Carlo Erba gas analyzer (see "Metamorphic Petrology," p. 10, in the "Explanatory Notes" chapter). The results are shown in Table T11. The combined contents of CO_2 and H_2O are indeed consistently higher than the LOI values. The main volatile component is bound water or hydroxyl in secondary alteration phases. Two samples showing substantial amounts of CO_2 contain secondary carbonates in alteration veins and/or as replacement of olivine (see "Metamorphic Petrology," p. 33, for a systematic discussion of alteration effects).

T11. CO_2 and H_2O content of volatile-rich samples, p. 281.

Overall Geochemical Variation

Figure F64, shows the downhole variation of Mg#, defined as the molar ratio $Mg^{2+}/(Mg^{2+}+Fe^{2+})$. Fe^{2+} was calculated as 85% of total Fe. To avoid needless complication of figures, a straightforward geochemical classification of the samples has been adopted in Figure F64 and all following figures in "Geochemistry," p. 47. Filled diamonds represent the troctolites, troctolitic gabbros, and olivine gabbros containing 0.4 wt% or less TiO_2. Samples having between 0.4 and 1.0 wt% TiO_2 are represented by the half-filled diamonds. This group largely comprises noritic gabbros and disseminated oxide gabbros. Samples represented by open

F64. Downhole variation of Mg#, 500–1508 mbsf, Hole 735B, p. 166.

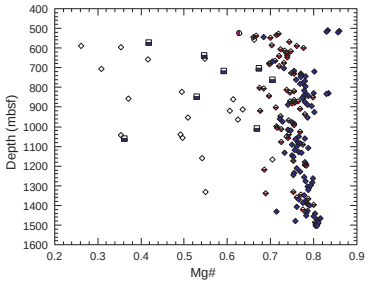

diamonds are oxide gabbros having more than 1.0 wt% TiO_2. The half-filled squares are felsic samples or hybrid samples with a substantial felsic component; their TiO_2 content, and composition in general, is variable. Although this subdivision is one of convenience, it also has some geochemical significance (see discussion of vanadium below).

The dominant rock type from Leg 176 is a moderately fractionated gabbro having Mg#s in the range of 0.70 to 0.80. The least evolved rocks are the troctolites that occur between 500 and 520 mbsf. Ferrous iron makes up 85% to almost 100% of the total iron. Throughout the entire core are numerous thin intervals of oxide gabbros and felsic rocks that are significantly to strongly differentiated and have a lower ferrous to ferric iron ratio. Although the sampling did not aim to be systematic, there are indications, nonetheless, that the abundance of oxide gabbros indeed decreases with depth as suggested by Figure **F64** (see **"Igneous Petrology,"** p. 12).

The Mg# should be used with some caution as a "differentiation index" in the case of the oxide gabbros. Mg#s of these cumulate rocks decrease as a result of the accumulation of Fe-rich minerals, such that the low numbers overestimate the extent of crystallization of ferromagnesian phases from the silicate liquid. As shown in Figure **F65,** the oxide gabbros have intermediate An/(An+Ab) ratios, which are a measure of the chemical/mineralogical evolution of the system (An and Ab are the normative anorthite and albite abundance, respectively). Whereas several of the "felsic" samples indeed have the characteristically low Mg#s and An/(An+Ab) ratios of strongly evolved residual liquids, the oxide gabbros appear to have crystallized from significantly less fractionated liquids. Or, they represent a mixture of evolved Fe-Ti-rich liquids and the normal variety of gabbro. Figures **F64** and **F65** further show that gabbros with TiO_2 between 0.4 and 1.0 wt% tend to have lower Mg#s than gabbros having <0.4 wt% TiO_2, but that both groups largely cover the same range of An/(An+Ab) ratios. This indicates that these gabbros do not make up a simple series of rocks that crystallized from a common, progressively evolving TiO_2-poor parental magma.

The element Ni is strongly enriched in olivine in which it substitutes for Mg. Because the Ni/Mg solid/liquid distribution coefficient is substantially greater than 1, the Ni content of the residual liquid and of gabbros crystallized from it drops exponentially (i.e., almost linearly in a log-log diagram) with decreasing Mg content (Fig. **F66**). This figure also shows that the two groups of gabbros with less than 1% TiO_2 have greatly overlapping MgO and Ni contents. This is another indication that the differences in TiO_2 concentrations cannot be attributed only to simple fractional crystallization processes. Chromium exhibits a more complex variation with Mg content (Fig. **F67**) because the behavior of this element is governed by substitution into clinopyroxene and oxide phases and, possibly, by Cr-spinels included in olivine grains.

The concentration of zinc is strongly correlated with total iron content in all rock types from Hole 735B (Fig. **F68**). The Zn/Fe ratio remains almost constant over 1 order of magnitude variation in Zn and Fe concentrations, which implies that the behavior of Zn is largely controlled by Fe-Ti oxide minerals. Somewhat lower Zn/Fe ratios are observed in felsic veins and some oxide gabbros. It is tempting to ascribe the Zn/Fe fractionation to minor sulfide phases which appear in these rocks. The element Cu is not correlated with any of the analyzed major or minor elements. Judging from the study of Leg 118 samples, the variation of

F65. Variation of TiO_2 content with An/(An+Ab) ratio, **p. 167.**

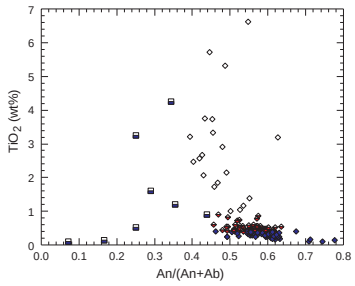

F66. Nickel concentration with MgO content in gabbroic rocks, **p. 168.**

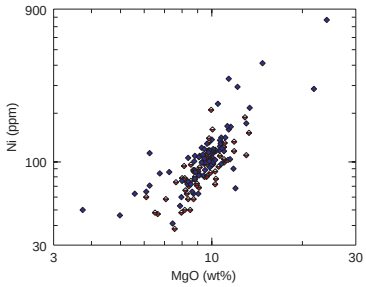

F67. Chromium concentration with MgO content in gabbroic rocks, **p. 169.**

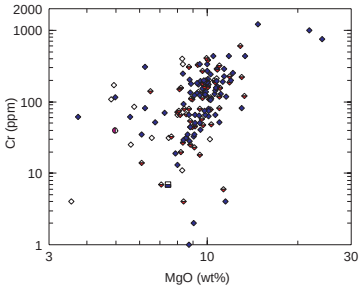

F68. Concentration range of zinc and iron in gabbroic rocks, **p. 170.**

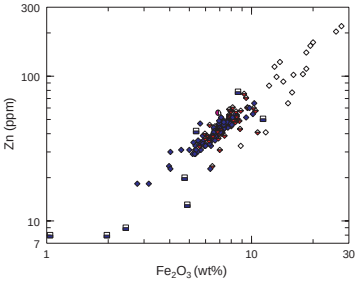

Cu in the gabbro pile appears to be entirely controlled by sulfide phases (Alt and Anderson, 1991).

The trace element vanadium follows titanium in magmatic processes. The vanadium contents are high in the oxide gabbros (Fig. F69), but they are not as high as expected from an extrapolation of the linear V-correlation trend observed in the low-TiO_2 troctolites and olivine gabbros (Fig. F70). An inflection in the V-TiO_2 trend at about 0.4 wt% TiO_2 marks a change in the geochemical processes controlling the abundances of Ti and V. At low Ti-content clinopyroxene is the major host phase of Ti and V. (The nominal abundance of 0.6 wt% TiO_2 and 340 ppm of clinopyroxenes from oceanic gabbros is based on analyses culled from various literature sources.) The steep V-TiO_2 trend of the troctolites and olivine gabbros shown in Figure F70 most likely represents a mixing line between clinopyroxene, olivine, and plagioclase, as the latter minerals have negligible Ti and V contents. The inflection at 0.4 wt% TiO_2 then reflects a higher abundance of intercumulus liquid and/or cumulus Fe-Ti oxide minerals, both of which have lower V/Ti ratios than clinopyroxene. The lower V/Ti ratio of the oxide phases is most likely the result of charge balance difficulties attending substitution of titanium by vanadium. The inferred change of geochemical control of Ti-geochemistry provided a rationale for choosing 0.4 wt% TiO_2 as the criterion for subdividing the gabbros into two groups.

Although the element niobium could be determined in only a limited number of samples, the data indicate that this trace element shows quite complex behavior. It is markedly enriched in some oxide gabbros that also have high vanadium concentrations (Samples 118-735B-78R-1, 114–118 cm; 118-735B-79R-7, 115–118 cm; 118-735B-82R-1, 13–16 cm; 118-735B-85R-3, 47–54 cm; 176-735B-102R-1, 17–23 cm; 176-735B-103R-1, 72–80 cm; 176-735B-114R-5, 23–29 cm; 176-735B-119R-4, 5–11 cm; 176-735B-137R-5, 33–38 cm; 176-735B-157R-4, 66–72 cm; 176-735B-157R-5, 134–140 cm; 176-735B-159R-2, 41–47 cm; 176-735B-171R-2, 56–62 cm; 176-735B-190R-3, 68–77 cm). Such observations are consistent with significant substitution of pentavalent niobium in vanadium-bearing oxide phases. However, niobium also shows strong enrichment in felsic samples having rather low vanadium contents but showing pronounced enrichment of other incompatible trace elements such as yttrium and zirconium (Samples 176-735B-99R-4, 106–108 cm; 176-735B-101R-1, 63–68 cm; 176-735B-110R-4, 0–5 cm; 176-735B-120R-4, 62–67 cm; 176-735B-126R-5, 91–97 cm; 176-735B-135R-3, 98–99 cm; 176-735B-154R-3, 67–72 cm; 176-735B-159R-4, 111–116 cm). This enrichment indicates that the small, highly charged niobium ions are enriched in residual fluids through complexing with minor ligands, such as hydroxyl, fluorine, and chlorine.

Enrichment in residual fluids followed by trapping in accessory minerals such as apatite, titanite, and zircon is the most likely explanation for the occasionally large enrichment of yttrium and zirconium in Ti-rich gabbros, felsic veins, and hybrid samples consisting of oxide-rich and felsic material. The zirconium data reported in Table T10 and Table T1, p. 70, in the "Leg Summary" chapter for troctolites, troctolitic gabbros, and gabbros overestimate the real abundances because of systematic analytical error (see "Metamorphic Petrology," p. 10, in the "Explanatory Notes" chapter). The Leg 118 shipboard data appear to be a more reliable source of Zr data for the rock types recovered from Hole 735B. Further discussion of the enrichment of incompatible elements in Hole 735B is given below.

F69. Correlation of vanadium and TiO_2 in gabbros, p. 171.

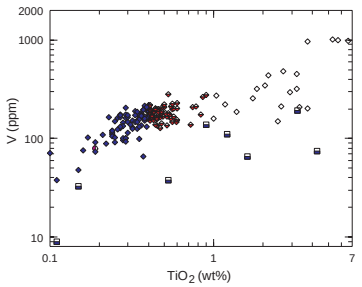

F70. Vanadium and TiO_2 variation, marking change in control of the V and Ti in gabbroic rocks, p. 172.

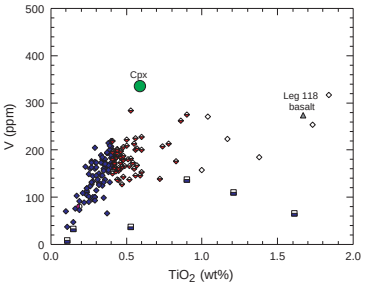

Plagioclase is the major host phase of the trace element strontium. Sr correlates well with the Al_2O_3/MgO ratio, which is a chemical measure of the ratio of plagioclase to ferromagnesian phases (Fig. F71). Several oxide gabbros have lower Sr concentrations probably as a result of accumulation of Sr-poor oxide phases. Plagioclase abundance, however, does not appear to be the sole factor that governs Sr geochemistry in the gabbros. The variation of Sr/Al ratio, which is almost completely determined by plagioclase, with An/(An+Ab) ratio (Fig. F72) indicates that the partitioning of Sr into plagioclase increases with increasing albite content of plagioclase and/or strongly depends on the composition of the liquid from which the plagioclase crystallized. The lower Sr contents of felsic samples can be ascribed to depletion of residual liquids in Sr by protracted plagioclase crystallization.

F71. Strontium content correlated with Al_2O_3/MgO ratio, p. 173.

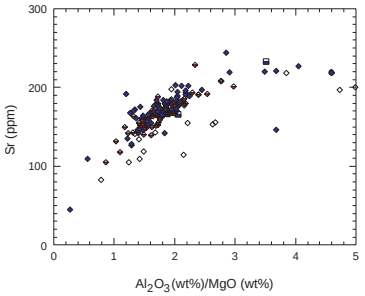

Effects of Alteration

A limited number of samples were analyzed to obtain a first estimate of the extent of chemical change brought about by alteration. The pervasively altered Sample 176-735B-91R-3, 92–100 cm, from the oxidized zone at ~520 mbsf is enriched in Ca-carbonate, bound water, K, and Rb (Tables T10, T11). The MgO content is low due to replacement of olivine by secondary carbonate. Two samples that contain low-temperature secondary smectite (Samples 176-735B-168R-3, 51–56 cm, and 176-735B-181R-2, 83–100 cm) mainly show appreciable enhancement of K and Rb contents and of bound water (see "Metamorphic Petrology," p. 33).

F72. Variation of Sr/Al ratio with An/(An+Ab) ratio, p. 174.

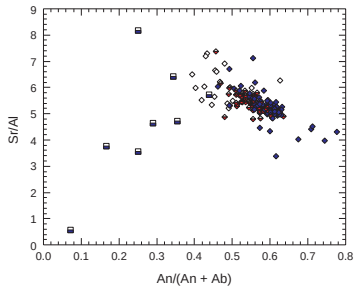

Chemical Stratigraphy

Figure F64 shows that oxide gabbros and felsic material are present throughout the entire section studied during Leg 176, although with decreasing abundance toward the bottom of the hole. Because of the limited sampling and large chemical and mineralogical variability, these two rock types are of little value in establishing a chemical stratigraphy. The downhole stratigraphy will hence be entirely based on the chemistry of the main gabbro types (rocks having less than 1 wt% TiO_2). The "master variable" for present purposes is the Mg# (Fig. F73), because all other chemical variables of the main gabbro types are directly or indirectly correlated with this master variable.

The first 20 m of the Leg 176 core from Hole 735B consists of fairly primitive gabbros and troctolitic rocks. This interval forms the lower part of lithologic Unit VI, as defined by the Leg 118 shipboard party.

Unit VI terminates at about 520 mbsf in a zone of sheared gabbros, colored brown due to extensive oxidative alteration (e.g., Sample 176-735B-91R-3, 92–100 cm). The altered zone is underlain by relatively fractionated gabbros and disseminated oxide gabbros. At approximately 705 mbsf, the chemical composition abruptly changes, as the underlying gabbros have a higher Mg# and lower TiO_2 content. The 705 mbsf depth also marks the onset of a core interval characterized by a very low degree of high-temperature alteration (see "Metamorphic Petrology," p. 33), and by the near absence of crystal-plastic deformation (see "Structural Geology," p. 54). The interval between 520 and 705 mbsf coincides with Units VII, VIII, and IX, as defined by the Leg 176 igneous petrology group (see "Igneous Petrology," p. 12). However, this threefold lithologic subdivision is not clearly expressed in the chemical

F73. Chemical stratigraphy of interval of Hole 735B, p. 175.

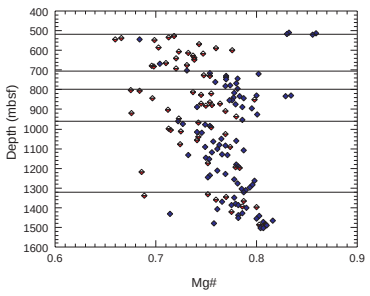

stratigraphy, possibly as a result of the limited number of analyzed samples.

At 800 mbsf, the degree of high-temperature alteration and deformation abruptly changes again. This transition also appears to coincide with a subtle change in rock chemistry because the underlying cores contain a much higher fraction of gabbros with between 0.4 and 1.0 wt% TiO_2. It is highly improbable that the absence of disseminated-oxide gabbros in the 705 to 800 mbsf interval is an artifact due to limited sampling density. As this interval also has distinct alteration and structural characteristics, it is possible that the rocks also have an igneous history different from the overlying and underlying gabbros.

The chemical unit that started at 800 mbsf terminates in a sheared zone at 960 mbsf. The gabbros between 800 and 960 mbsf exhibit considerable variation of Mg# (0.83 down to 0.68) and TiO_2 content. The two chemical units recognized between 705 and 960 mbsf closely coincide with lithologic Unit X (714–960 mbsf).

From 960 to 1320 mbsf, the chemical composition displays a gradual change from moderately fractionated gabbros at the top (Mg# of 0.72) to less fractionated at the bottom (Mg# of 0.80). This section of the core corresponds closely to lithologic Unit XI (960–1314 mbsf).

The trend toward more primitive compositions is interrupted at 1320 mbsf by the appearance of an interval that comprises a large fraction of gabbros that have consistently higher TiO_2 contents (0.40–0.55 wt% vs. 0.25–0.35 wt%). This boundary is marked by a small sheared zone but shows no change of alteration properties. This chemical unit is part of lithologic Unit XII (1314–1508 mbsf).

Downhole Chemical Variation Within Hole 735B

Figure **F74,** shows the downhole variation of Mg# over the whole 1500-m section drilled during Leg 118 and Leg 176. The figure is based on 357 whole-rock analyses. The data for the upper 500 m include the Leg 118 shipboard analyses of 97 samples, the eight additional samples analyzed during Leg 176 (Table **T10**), and 72 unpublished analyses (J. Hertogen and P. Meyer, pers. comm., 1997).

The most striking aspect of the downhole chemical variation is that the gabbro section consists of a stacking of separate units with a thickness varying from 100 to 300 m. The average degree of fractionation of the various units differs. However, almost all units show a trend of increasing degree of fractionation upward within each unit. Most likely these chemical units represent the scale at which individual magmatic events add to the construction of oceanic Layer 3 at slow-spreading centers.

A second salient feature is the ubiquity of oxide-rich gabbro throughout the core (Fig. **F75**). This type of gabbro predominantly occurs in centimeter- to decimeter-thick intervals, and the degree of Fe-Ti enrichment is quite variable. However, the 50-m-thick Unit IV at a depth of 223 to 274 mbsf in the upper part of Hole 735B is almost entirely made up of massive oxide gabbro, which crystallized from differentiated Fe-Ti-rich liquids that undoubtedly migrated from elsewhere. However, the geochemical data offer as yet few clues to the origin of the Fe-Ti-rich liquids from which the oxide seams in other units formed. They all might have migrated from elsewhere, or might have been produced by fractionation within the unit itself.

F74. Downhole variation of Mg# of Hole 735B, **p. 176.**

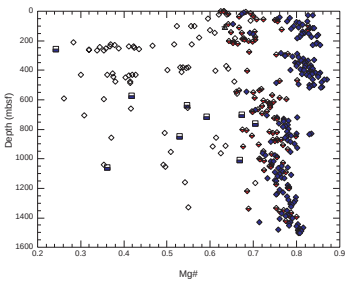

F75. Down variation of TiO_2 of Hole 735B, **p. 177.**

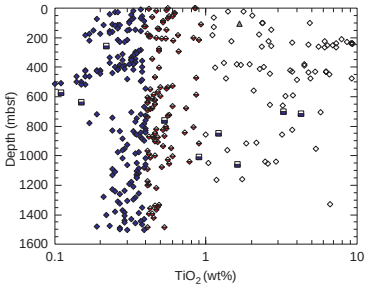

The downhole distribution of TiO_2 (Fig. F75) reflects the downward decrease in abundance of Fe-Ti-rich gabbros with depth in Hole 735B. The reasons are not obvious. It appears, however, that the decrease cannot be ascribed to a decrease of the titanium abundance of the parental liquids. Indeed, gabbros of similar modal composition from the various units have virtually identical average Ti contents. It is important to note that in the upper part of the core where oxide gabbros are more prominent, the units nevertheless have a large fraction of gabbros with low TiO_2 content. A case in point is Unit VI, where one might deduce that the development of oxide gabbros within a given unit might also depend upon emplacement and crystallization conditions that favor protracted crystallization and prevent premature expulsion of evolved residual liquids.

Felsic material present in dispersed form in the section is likely a product of extensive differentiation. The nature of the material is variable; whereas some thicker veins are made up of K-poor trondhjemite, others consist of granodiorite with appreciable potassium feldspar.

The downhole distribution of the trace element yttrium is shown in Figure F76. The concentrations are recast as chondrite-normalized values to facilitate comparison with published abundances of heavy rare earth elements (REEs), for which yttrium is a proxy. From the yttrium data one can conclude that most of the gabbros from Hole 735B have three to five times lower REE abundances than in common mantle magmas, depending upon modal composition and amount of trapped interstitial liquid. The clinopyroxene-poor troctolites and troctolitic gabbros have very low heavy REE abundances, as this mineral is the main mineral host of heavy REE in oceanic gabbros (see Barling et al., 1997, for a discussion of systematics of REE abundances of oceanic gabbros). Hence, a large fraction of the REE (and, by inference, of other incompatible trace elements) either must have been lost from the gabbro pile or is present in strongly concentrated form in minor lithologies. The rather high yttrium content of many oxide gabbros and felsic veins from Hole 735B indicates that the latter is partly the case.

F76. Downhole variation of yttrium of Hole 735B, p. 178.

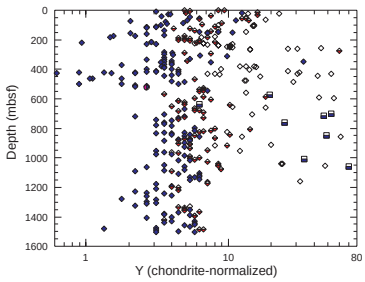

Conclusions

The main conclusions that can be drawn from the shipboard chemical analysis of 180 gabbro samples from the 1000-m-thick section of oceanic Layer 3 drilled during Leg 176 are as follows:

1. The main rock type is a moderately fractionated gabbro having between 0.2 and 1.0 wt% TiO_2. Oxide gabbros containing as much as 7 wt% TiO_2 and up to 20 wt% Fe_2O_3 occur in centimeter- to decimeter-thick intervals throughout the core. The abundance of oxide gabbros decreases with increasing depth, but this is not related to a decrease in TiO_2 abundance of the parental liquids from which the gabbros crystallized. The development of localized concentrations of Fe-Ti-rich gabbro seems to depend on favorable conditions for formation rather than on the TiO_2 content of the starting material.
2. Gabbros with similar Mg#, MgO, and Ni contents but variable TiO_2 content commonly occur together. Hence, the differences in TiO_2 content cannot result from simple fractional crystallization from a common parental magma. Factors other than cotectic crystallization that affect phase proportions and compositions must have been involved. These likely include complex

mixing of early cumulates with more differentiated liquids, assimilation-fractional crystallization processes during melt transport through the mass, and redistribution of crystal phases due to solution channeling of migrating melts.

3. Within the 1000-m-thick section drilled during Leg 176, as many as six distinct chemical units can be identified. With few exceptions the boundaries of these units appear to coincide with changes in lithologic, metamorphic, and structural properties. The thickness of the separate units varies from 100 to 300 m. These chemical units probably represent the scale at which individual magmatic events added to the construction of oceanic Layer 3 at this ultra-slow-spreading ridge.

STRUCTURAL GEOLOGY

Introduction

We present the results of a comprehensive structural analysis of the core recovered from Hole 735B during Leg 176. Five separate categories of observations were recorded: magmatic deformation, crystal-plastic deformation, brittle deformation, microstructural characteristics, and crosscutting relationships. Details of each structural classification scheme are given in **"Structural Geology,"** p. 13, in the "Explanatory Notes" chapter. We discuss the first four of these categories individually, presenting the relevant data with minimal interpretation. We then discuss the relationships, both temporal and spatial, between the categories before presenting initial interpretations in the context of the tectonic setting of Hole 735B. We conclude with a general summary of the structural geology of Hole 735B.

There is a considerable variation in the structures observed throughout Hole 735B, both in style and in position. Many of the characteristic trends observed in the upper 500 m of the hole during Leg 118 were also observed lower in the hole during Leg 176; however, there are a number of different features, notably the occurrence of significant reverse-sense shearing and a general decrease in deformation downhole. Wherever possible, we compare the section logged during Leg 176 with the data collected during Leg 118 to provide a complete structural overview of Hole 735B.

Magmatic Structures

Macroscopic Observations

A majority of the rocks recovered from Hole 735B have coarse- to medium-grained hypidiomorphic-granular, intergranular, and subophitic textures with poikilitic pyroxene crystals and no preferred mineral alignment. Approximately 20% of the recovered material contains a variably developed magmatic foliation defined by the preferred orientation of elongate plagioclase laths and locally of pyroxene crystals. The relative proportions of different magmatic fabric intensities as defined in **"Overview of Macroscopic Core Description,"** p. 13, in the "Explanatory Notes" chapter and the percentage of the total recovery that each intensity value represents are shown in Figure **F77.** Rocks in which no igneous texture is preserved were recorded as magmatic fabric intensity = 0. Weak magmatic foliations predominate, whereas moder-

F77. Histogram of magmatic fabric intensity, **p. 179.**

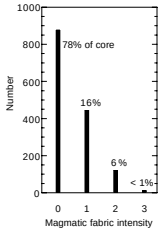

ate to strong fabrics are only sporadically developed (e.g., Sections 176-735B-120R-1 through 120R-3, and 120R-7). Figure F78A displays the variation of fabric intensity as a running average over the entire core. In general, a weak magmatic foliation is variably developed throughout the core, but localized zones of well-developed foliations occur. Two intervals, ~1200 to ~1300 mbsf and ~1400 to ~1500 mbsf, are almost entirely isotropic.

Magmatic foliations vary in both strike and dip with depth. As illustrated in Figure F78B, there is no systematic variation between dips and depth, though the majority have dips between 20° and 50° toward 90° in the core reference frame (Fig. F79B). Marking of the core for splitting into working and archive halves by the Structural Geology Group followed a convention in which the predominant fabric in the rock (magmatic or crystal-plastic foliation, igneous layering, etc.) was dipping toward 90° in the core reference frame. Shipboard paleomagnetic declinations cluster around 250° in the core reference frame throughout the entire interval cored during Leg 176 (see "Paleomagnetism," p. 69). Thus, the clustering of magmatic foliation poles indicates that magmatic fabrics have a preferred orientation. Magmatic lineations, defined by elongate pyroxene crystals in the foliation plane, were noted in Section 176-735B-169R-4, 0–128 cm. A single lineation was measured from this section and is oblique to the dip direction with a trend and plunge in the core reference frame of 143°/33°.

An obliquity between multiple magmatic foliations was only observed in Section 176-735B-191R-3 at 38 cm, where an olivine gabbro with a weak magmatic fabric was intruded by a microgabbro. Eight centimeters away from the contact, the foliation within the olivine gabbro dips toward the contact. In the olivine gabbro immediately adjacent to the microgabbro, plagioclase and pyroxene crystals are subparallel to the margin of the microgabbro, but they do not appear to be deflected into this orientation. One interpretation of this geometry is that intrusion of the microgabbro occurred while the olivine gabbro was partially molten, allowing crystals to be realigned subparallel to the contact. Generally, the microgabbros have a weak magmatic foliation subparallel to the contacts.

Igneous Layers

The orientation of igneous layering was measured wherever continuous and planar contacts separate different layers. Fifty-six contacts separating modal or textural igneous layers were suitable for measurement and dip on average 24° (Fig. F80A). The modal and/or textural differences were often contained within centimeter-scale patches with irregular contacts indicating a lack of continuous layering. The scarcity of igneous layers is illustrated in Figure F80B, which displays the distribution of the 56 measurable layers (i.e., those with planar contacts) per 50-m intervals down the hole.

Layers with subparallel magmatic foliations occur in Sections 118-735B-83R-7, 176-735B-169R-5, 170R-4, 170R-7, 171R-1, 190R-2, and 195R-8. Generally, however, layers in rock cored during Leg 176 contain no magmatic foliation. Obliquities between magmatic foliations and layers were observed twice. In Section 176-735B-169R-5, centimeter-scale anorthositic and pyroxenitic layers dip 10°–20° less than a magmatic foliation of moderate intensity. Magmatic foliations crosscutting layers were not observed.

F78. Variation of magmatic foliation fabric intensity and dip vs. depth, p. 180.

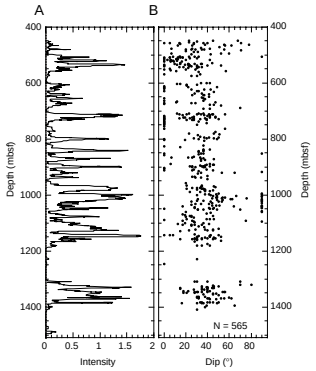

F79. Magmatic and crystal-plastic fabric correlations, p. 181.

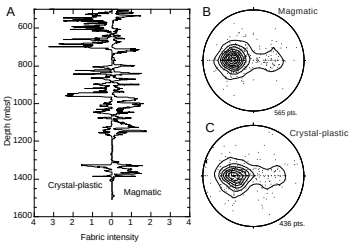

F80. Dip of igneous layers with depth and number of measured igneous layers, p. 182.

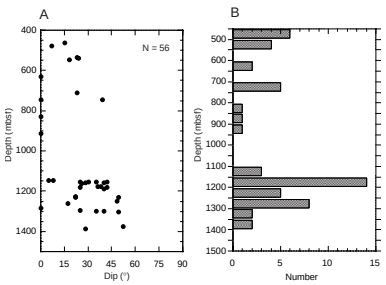

Igneous Contacts

Igneous contacts that correspond to boundaries separating different lithologic intervals are interpreted as intrusive (41% of all contacts), gradational (37%), not recovered/preserved (16%), or tectonic (6%; see "Igneous Petrology," p. 12). The orientations of planar, intrusive, and tectonic contacts were measured; irregular intrusive and gradational contacts were not measured but noted in the Comments section of the MAGMATIC.XLS spreadsheet (see "Appendix," p. 31, in the "Leg 176 Summary" chapter). With the exception of tectonic contacts, dips range from 0° to 90°, average 36°, and display no systematic downhole trends (Fig. F81). Tectonic contacts defined by crystal-plastic shear zones separating different igneous intervals occur from 450 to 590 mbsf (Cores 118-735B-82R through 88R and 176-735B-89R to 102R) and from 950 to 1150 mbsf (Cores 176-735B-148R to 169R). In the second of these intervals, the tectonic contacts shallow with depth from 55° at 950 mbsf to 7° at 1150 mbsf and display reverse-sense displacement (Fig. F81). Near the base of the hole, thin and sinuous microgabbros intrude the coarse-grained olivine gabbro along steeply dipping to vertical intrusive contacts. In contrast, microgabbros higher in the core have contacts with shallow to moderate dips.

F81. Dip of igneous contacts with depth, p. 183.

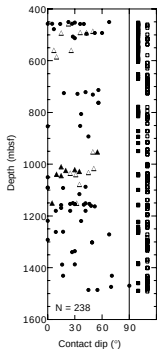

Crystal-Plastic Structures

Structures preserved in the rocks recovered from Hole 735B demonstrate that crystal-plastic deformation occurred over a wide range of conditions during emplacement and cooling of the gabbroic crust at the Southwest Indian Ridge. Fabrics were logged using a semiquantitative deformation intensity scale (Table T2, p. 40, in the "Explanatory Notes" chapter) that ranges from undeformed (fabric intensity = 0) to ultramylonitic (fabric intensity = 5). The orientation of these fabrics was measured in the core reference frame, and where possible we noted the sense of shear of the deformation and whether deformation occurred in association with hydrothermal alteration.

F82. Variations of crystal-plastic deformation, p. 184.

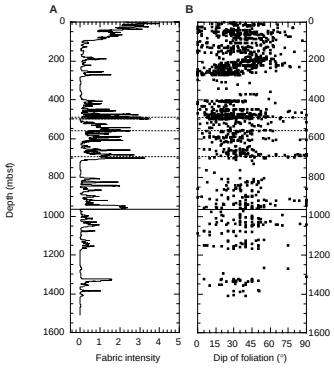

Intensity and Orientation of Crystal-Plastic Fabric

The variation in the intensity of crystal-plastic deformation with depth is illustrated in Figure F82A. Macroscopic observations of deformation intensity from Leg 118 logged using the same intensity scale (Dick et al., 1991a) are also shown in Figure F82A. For comparison, the deformation intensity logged during Leg 176 is plotted beside that measured by Dick et al. (1991a) for the interval between 450 and 500 mbsf (Fig. F83); this series of cores from Hole 735B was relogged during Leg 176 in transit to the site. Data from Leg 176 are 11-cell running averages of the deformation intensity log (see PLASTIC.XLS spreadsheet in "Appendix," p. 31, in the "Leg 176 Summary" chapter), whereas data from Leg 118 are "visual averages" of ~1- to 2-m-long sections (H.J.B. Dick, pers. comm., 1997). Despite the differences in logging techniques, the correlation between data from Legs 118 and 176 is good.

Crystal-plastic deformation in Hole 735B is highly localized with the most intense deformation observed in the intervals 0–50 and 450–600 mbsf (Fig. F82A). Intervals with very little or no crystal-plastic deformation occur at 280–400, 700–800, 1180–1325, and 1400–1500 mbsf. At depths between ~450 and 700 mbsf, the regions with the highest intensity of crystal-plastic deformation were later overprinted by brittle

F83. Crystal-plastic deformation, 450–500 mbsf, Hole 735B, during Legs 118 and 176, p. 185.

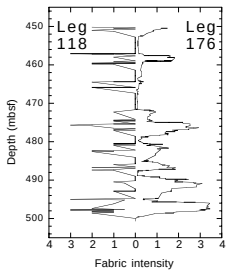

faults. The strongly localized nature of crystal-plastic deformation is further illustrated by calculating the percentage of the core from Leg 176 that displays a particular deformation intensity. As illustrated in Figure F84, 77% of the recovered rocks exhibit no crystal-plastic fabric (fabric intensity = 0) and 16% show only a weakly defined foliation (fabric intensity = 1). Similarly, 71% of rocks recovered during Leg 118 have no crystal-plastic fabric and 15% are weakly foliated (Dick et al., 1991a). However, a significant number of intervals have high intensity deformation. For example, a strong mylonitic fabric (fabric intensity = ≥4) occurs in 127 intervals logged during Leg 176, of which 16 are ultramylonites (fabric intensity = 5). One of the most plastically deformed zones is at the base of a ~20-m-thick shear zone located between 945 and 964 mbsf (Fig. F85); the transition from mylonitic to undeformed rock is just 10 cm below the base of the mylonite.

In general, there are no systematic variations in the dip of the crystal-plastic foliation with depth in the core from 0 to 1500 mbsf (Fig. F82B), with the exception that mylonitic foliations (Pf = ≥4) tend to have a shallow dip at depths below ~1050 mbsf (Fig. F86A; see also Dick et al., 1991a). Although there is no systematic trend in the dip of the foliation with depth, there is a strong concentration of foliations that dip ~30° in the direction of 090° (i.e., poles that plunge to 270°) in the core reference frame (Fig. F80); 090° in the core reference frame is defined in "Structural Measurements," p. 14, in the "Explanatory Notes" chapter. This relationship is primarily a manifestation of the structural team's protocol in orienting the core for splitting. However, the strong preferred orientation of both the deformation fabric and the average declination of the remnant magnetic vector (Fig. F111) indicates that the foliation has a consistent orientation in the hole. The orientations of the foliation can be placed into a geographical reference frame by assuming that the declination of the remnant magnetic vector dips toward the south. In this case, the crystal-plastic foliation would predominantly dip toward the north and, therefore, toward the ridge axis. This hypothesis is supported by initial analysis of FMS data reported in "Downhole Logging," p. 81.

The distribution and orientation of both semi-brittle and retrograde (primarily amphibolite to transitional greenschist grade) shear zones with depth in the hole are illustrated in Figure F86B. The amphibolite to transitional greenschist grade shear zones were identified by the presence of deformed amphibole in hand specimen and confirmed by microscopic observations (Figs. F87, F88F, respectively). We use the term "semi-brittle" to describe rocks in which both brittle and plastic deformation fabrics were observed. A fairly high concentration of amphibole-bearing shear zones occurs at depths between 450 and 600 mbsf. Amphibole veins are also abundant in this interval (e.g., Figs. F47, F87); the correlation between amphibole veins and crystal-plastic deformation is described in detail in "Discussion," p. 30. The highest density of amphibole-bearing shear zones occurs in the strongly deformed region directly above the fault observed at a depth of 490 mbsf (Fig. F86B). Semi-brittle shear zones occur throughout the hole, but these features are most abundant in regions adjacent to faults or major shear zones, especially the fault located at 690 mbsf.

One of the most surprising features of the crystal-plastic deformation fabrics from Hole 735B is the large number of shear zones with reverse sense of shear in the core reference frame. As illustrated in Figure F86C, the reverse shear zones are concentrated within and below the 20-m-wide shear zone located between 945 and 964 mbsf, and also directly

F84. Histogram of different crystal-plastic deformation intensities, p. 186.

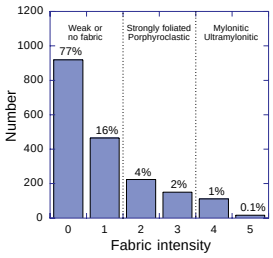

F85. Mylonite at the base of a 20-m shear zone, p. 187.

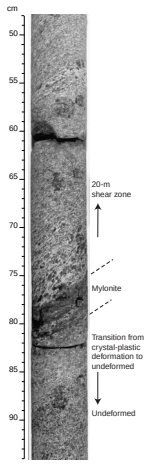

F86. Crystal-plastic foliation variation, p. 188.

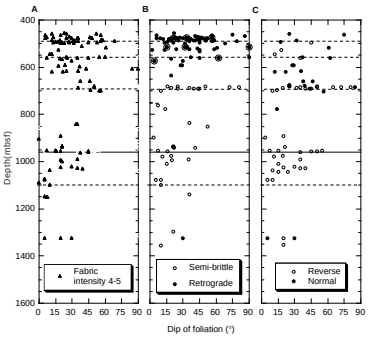

above the fault located at 690 mbsf. Between 450 and ~680 mbsf, most of the shear zones have a normal sense of shear. An example of a reverse shear zone from Section 176-735B-155R-1 is illustrated in Figure F89. We were conservative in our assignment of sense of shear; in many cases, analyses based on asymmetric recrystallization tails were ambiguous. In addition, in many of the mylonitic rocks it was difficult to identify a lineation. The best kinematic indicators in the rocks from Hole 735B were deflected foliations (e.g., Fig. F89) and the orientation of oblique deformation fabrics (i.e., S-C fabrics).

A number of scenarios may be invoked to explain apparent reverse-sense kinematic relations in the higher temperature shear zones, including rotation of normal-fault blocks associated with displacement on low-angle detachments after the Hole 735B massif cools below the Curie temperature. Analysis of paleomagnetic data from Leg 118 indicates a 20° rotation of the tectonic block in which Hole 735B was drilled (Pariso et al., 1991). Assuming that this rotation occurs on a shallowly plunging east-west axis, and therefore that the crystal-plastic foliation predominantly dips toward the north, shear zones with a reverse sense of shear that dip less than ~20° (e.g., Fig. F89) could represent passively rotated normal-sense shear zones. However, a significant proportion of the reverse shear zones have dips in the range of 30°–60° in the core reference frame. These zones generally display macroscopic textures very similar to those exhibited by the gently dipping shear zones and would require block rotations significantly larger than indicated by the paleomagnetic analyses to be normal-sense shear zones. Thus, there is no explanation for all of the reverse shear zones, based on the current structural and magnetic data.

Correlation between Magmatic and Crystal-Plastic Deformation Fabrics

In numerous locations in Hole 735B, a magmatic foliation is overprinted by a crystal-plastic deformation fabric. The variations with depth of the average crystal-plastic fabric and magmatic fabric intensities are directly compared in Figure F79A. In general, there is a good positive correlation between the intensities of the two fabrics; however, there are numerous exceptions to this relationship. Obviously, no magmatic fabric is preserved in regions with a very strong crystal-plastic fabric (e.g., in the intervals 550–700 and 930–960 mbsf). In addition, several portions of the core exhibit a strong magmatic foliation and little or no plastic deformation fabric (e.g., the intervals 710–730, 960–1000, and 1075–1125 mbsf). The strongest correlation between the two fabrics is observed in the intervals 830–920 and 1300–1400 mbsf. Based on the texture in the core, we interpret these zones to show a moderate crystal-plastic overprint of a magmatic fabric; in regions with no crystal-plastic overprint, subhedral and nonrecrystallized plagioclase is observed in addition to sharp "corners" in interstitial pyroxene. In contrast, where a crystal-plastic overprint is observed, the pyroxene is more elongate with "rounded" edges, and the plagioclase is recrystallized (identified by a sugary texture in hand specimen). Microscopic observations discussed later in this section are generally in agreement with the macroscopic observations made on the core.

F87. Amphibole and smectite veined sections, p. 189.

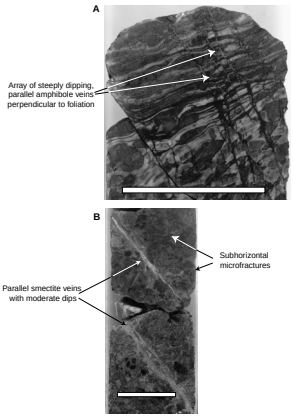

F88. Crystal-plastic and semi-brittle microstructures, p. 190.

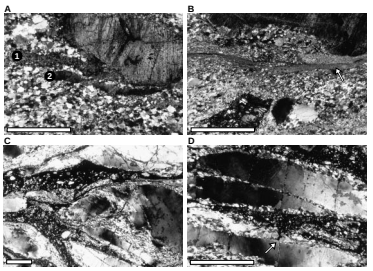

F89. Reverse shear zone, p. 192.

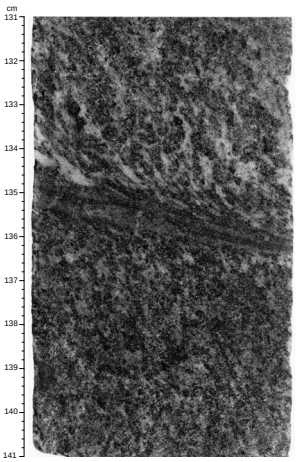

Brittle Deformation

Brittle deformation recorded in the Leg 176 cores is divided into two major types, there being magmatic and lower temperature cataclastic deformation. Brittle magmatic deformation is represented by felsic magmatic or intrusion breccias and veins concentrated in the upper 70% of the hole (to ~1100 mbsf), at a variety of scales from micro- to macroscopic. Brittle features attributed to lower temperature cataclastic deformation at Site 735 include localized microfracturing, discrete faults, zones of cataclasite, veins, and joints. Thick zones of hydrothermal breccia with greenschist-facies mineralization similar to those reported in the lower portions of the Leg 118 section of Hole 735B (Stakes et al., 1991) are absent in the lower 1000 m cored during Leg 176. Direct correlation of lower temperature cataclastic deformation with data gathered during Leg 118 is not possible because occurrences of faults and cataclasites were not recorded during that leg.

Felsic Veins and Magmatic Breccias

Veins and associated breccias of magmatic, or probable magmatic, origin occur throughout the upper 1100 m of Hole 735B, diminishing in significance toward the bottom of the cored interval (Fig. F90A). These felsic veins and magmatic breccias are distinguished from veins of hydrothermal origin by the presence of the following mineral assemblage: plagioclase ± oxide ± clinopyroxene ± amphibole ± biotite ± alkali feldspar ± quartz ± titanite ± apatite ± zircon (see "Igneous Petrology," p. 12, and "Metamorphic Petrology," p. 33).

The felsic material ranges in macroscopic character from narrow 1- to 2-mm-wide veins (Fig. F91A) to centimeter-scale veins and irregular patches. Felsic patches greater than 1–2 cm in width commonly have diffuse, irregular, nonparallel boundaries throughout their length, and they typically host abundant rotated xenoliths of the adjacent wall rock (Fig. F92A, F92B). These breccia contacts have a broad scatter in dip down the core (Fig. F90B), with no significant preferred orientation.

At least two generations of felsic material are recognized in the core. The earliest is characterized by plagioclase (±oxide) that infiltrated and locally brecciated the host gabbro (Sample 176-735B-110R-2, 120–149 cm). On a local scale, there is a correlation between regions rich in plagioclase and areas with moderate to strong crystal-plastic deformation (Samples 176-735B-114R-3, 48–94 cm; 116R-7, 0–12 cm; 117R-2, 8–15 cm; 119R-1, 78–90 cm; 137R-5, 10–14 cm; and 145R-6, 101–113 cm: Fig. F92C). Younger, more evolved felsic material typically intruded after the high-temperature deformation (Samples 176-735B-110R-3, 0–11 and 111–142 cm; 118R-2, 38–41 cm; 118R-6, 120–129 cm; 147R-7, 98–102 cm; 156R-3, 18–20 cm: Fig. F92A, F92B).

Lower Temperature Cataclastic Deformation

Cataclastic features resulting from lower temperature brittle deformation in Hole 735B range in scale from micro- to macroscopic. The predominant cataclastic fabrics are discrete faults and zones of associated cataclasite of variable thickness, fracture intensity, and mineralogy. Based on thickness and fracture intensity of recovered cataclastic rocks, brittle deformation is primarily localized along two faults of unknown displacement (560 and 690–700 mbsf) marked by relatively low core recovery (<60%), and several minor zones of cataclasis (including 1076

F90. Histogram of the number of magmatic breccias per 10-m interval and the orientation of poles to contact of magmatic breccias, p. 193.

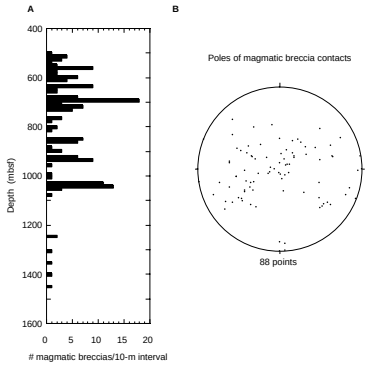

F91. Brittle microstructures in cross-polarized transmitted light, p. 194.

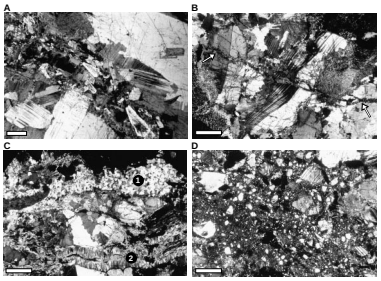

F92. Core photographs of magmatic and tectonic breccias, p. 195.

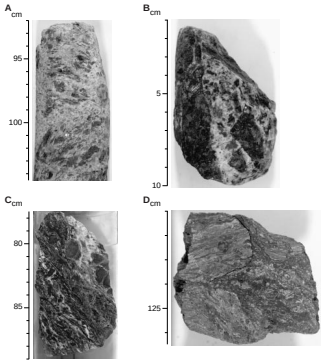

and 1100–1120 mbsf). Both of the lower temperature faults overprint granulite and amphibolite grade shear zones (Fig. F86B) and were active at greenschist grade conditions. The lower 50 m of core obtained during Leg 118 and relogged at the beginning of Leg 176 includes another zone of significant cataclasis and faulting at ~490 mbsf, with several minor zones between ~460 and 495 mbsf. In addition, the fault zone at 560 mbsf is marked by a zone up to 5 m thick of significantly increased porosity and decreased density and resistivity (see "Downhole Logging," p. 81).

Discrete planar faults with associated gouge, breccia, cataclasite, and ultracataclasite, cut all rock types and are associated with brittle and semi-brittle deformation in cores from Leg 176. More than 600 discrete faults and/or zones of cataclasis were logged using the intensity scale outlined in "Deformation Intensities," p. 15, in the "Explanatory Notes" chapter (Fig. F93A, F93B). Faults and associated cataclastic deformation in rocks from Hole 735B are concentrated in the upper 50% of the hole (to ~720 mbsf) and are virtually absent below ~1400 m.

Intense cataclasis is extremely localized downhole into zones of variable thickness that range from less than 1 mm up to 5.5 cm (Samples 176-735B-97R-4, 78–84 cm, and 118R-1, 53–54 cm). Fault rocks of all intensities (see "Deformation Intensities," p. 15, in the "Explanatory Notes" chapter) were recovered, including gouge (Sample 176-735B-97R-4, 127–130 cm), breccia and oxide-rich breccia (Samples 118-735B-87R-1, 98 cm; 176-735B-101R-1, 66–67 cm; 164R-1, 112–113 cm), cataclasite (176-735B-97R-4, 122–127 cm), and ultracataclasite (Sample 118-735B-86R-2, 0–3 cm). The most common brittle tectonic features are, however, small-offset "microfaults" filled with calcite (predominantly above 560 mbsf; Fig. F91C), amphibole (Fig. F88F, F91B), and/or smectite (below ~1050 mbsf). The pale-green smectite veins from the central and lower parts of Hole 735B (Cores 176-735B-127R through 131R, and Cores 176-735B-172R through 180R) often bear slickensided striae of variable orientation. Although these faults are common, they did not accommodate significant displacement, as the delicate smectite veins maintain subparallel margins. Indicators of the existence of faults not recovered include brecciated fragments (i.e., Samples 176-735B-98R-1, 9–30 cm; 100R-2, 0–20 cm; and 103R-4, 0–11 cm) and rubble (i.e., Samples 176-735B-99R-1, 0–5 cm; 131R-1, 76–84 cm; 162R-3, 122–134 cm; and 170R-3, 0–10 cm) with slickensided striae.

Mineral assemblages associated with the brittle tectonic structures range from calcite, amorphous silica, and prehnite to chlorite, epidote, actinolite, and secondary plagioclase, implying a range of conditions associated with cataclastic deformation (see "Metamorphic Petrology," p. 33). The alteration mineral assemblage characteristic of the zone of intense faulting and cataclasis in Section 176-735B-97R-4 (121–126 cm; 560 mbsf; see Fig. F92D) includes fractured clasts of gabbro with talc and amphibole after olivine, hornblende and actinolite after clinopyroxene, and secondary plagioclase. These altered clasts are enclosed in a fine-grained matrix dominated by chlorite and amphibole, indicative of greenschist facies metamorphic conditions during deformation.

Downhole variation in fault dip shows no consistent pattern (Figs. F93C, F94). However, the concentration of poles with a 90° plunge indicates a preferred subhorizontal fault orientation within the lower 1000 m of Hole 735B. Fault displacements observed on the core face were treated as components of dip-slip displacement, either normal or reverse (see "Structural Measurements," p. 14, in the "Explanatory

F93. Downhole variability of cataclasis intensity, p. 196.

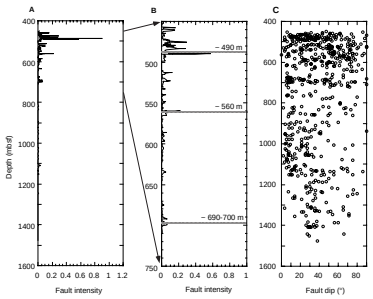

F94. Equal-area plot of poles to all faults with two apparent dips., p. 197.

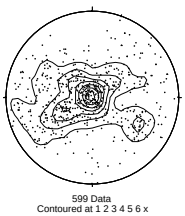

Notes" chapter). Displacement parallel to the trace of the fault was generally measured using displaced planar features, such as grain boundaries, vein walls, and/or igneous contacts. Fracture surfaces with slickenside orientations were used when available to differentiate between strike slip (pitch 0°–10°), oblique slip (pitch 11°–79°), and dip slip (pitch 80°–90°) movement. Of the logged faults, only a small number (7% total) provide information on relative displacement (Fig. F95A). A greater number of the faults were noted on fracture surfaces and vein walls, which allowed the determination of pitch, and therefore relative slip of these minor faults. Of those determined (Fig. F95B), oblique-slip was by far the dominant slip sense (8.8%), followed by nearly pure dip-slip (2.8%), and strike-slip (2.3%). However, the sense and magnitude of displacement associated with the discontinuities at 490, 560, 690, and 1100 mbsf are unknown. The discontinuity at 560 m clearly corresponds with the seismic reflector of Swift et al. (1991; Fig. F96).

F95. Fault displacements: sense of slip and slip direction based on pitch of slickenside striae, p. 198.

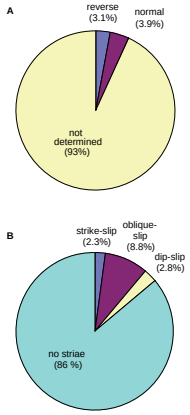

Mixed Brittle and Crystal-Plastic Fabrics (Semi-Brittle)

In cores taken from Hole 735B during Leg 176, localized brittle and crystal-plastic deformation are closely associated spatially at numerous locations. Macroscopic and microstructural textural relations together indicate that in most instances brittle deformation overprints crystal-plastic deformation (Samples 176-735B-117R-2, 62 cm; 137R-3, 134–135 cm; and 146R-5, 139 cm). During visual core description, the term "semi-brittle" was assigned to features where both brittle and crystal-plastic structures coincide and the chronology of deformation could not be determined.

F96. Core recovery plotted against depth, p. 199.

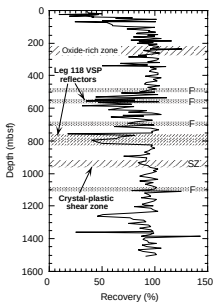

Fracturing and Veining

We measured the intensity and orientation of veins, joints (fractures), and subhorizontal microfractures (SHMs) using the intensity scale outlined in "Structural Geology," p. 13, in the "Explanatory Notes" chapter. The intensity of these planar features is a measure of their average frequency in a 10-cm interval. The majority of joints were found to have minor mineralization along them and, for both structural and metamorphic analyses, these were logged as veins. For this reason the intensity and orientation of jointing is incorporated into the vein data.

F97. Variation in Hole 735B vein intensity with depth and variation in vein dip with depth, p. 200.

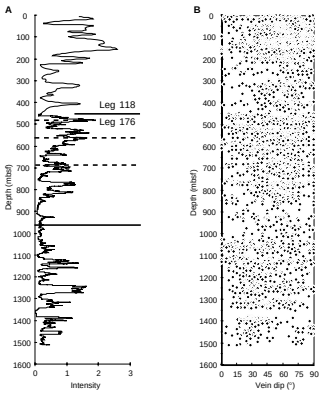

Veins and Joints

The intensity of veining varies considerably throughout the cored interval, as shown in Figure F97A. This figure incorporates data from Leg 118 (H.J.B. Dick, pers. comm., 1997); the interval from 450 to 500 mbsf was logged during both legs, and comparison of the two data sets across this interval allows conversion of the uppermost 450 m data to the Leg 176 intensity scale. In the upper part of the hole, from 0 to 800 mbsf, there is a zone of fluctuating high vein intensity (up to an average of >10 veins per meter) that gradually decreases downhole. This is followed by an interval between 800 and 1100 mbsf of low vein intensity (<2 veins per meter). Below 1100 mbsf, the vein intensity is characterized by short intervals, typically 5–20 m, of high vein intensity separated by similar-sized intervals of little or no veining. This pattern continues down to the bottom of the core to 1508 mbsf. The variation

in vein dip with depth is shown in Figure F94B; the abundance of data makes trends difficult to observe.

There are 17 different types of veins, which can be separated into four broad groups: (1) magmatic veins—compound felsic (plagioclase ± clinopyroxene ± amphibole); (2) amphibole veins; (3) carbonate veins—mostly calcite; and (4) smectite/zeolite veins (see "Metamorphic Petrology," p. 33). Magmatic veins occur throughout the section, but are most abundant in the region between 900 and 1100 mbsf. Both amphibole and carbonate veins are abundant in the interval between 450 and 750 mbsf but rarely occur below 750 mbsf. Smectite veins and, lower in the section, zeolite veins are concentrated into two major intervals (580–850 and 1050–1508 mbsf). These are the most abundant vein types in the entire core; however, the considerable width of magmatic veins makes them more significant in terms of the percentage of the cored interval. A more detailed analysis of vein minerals can be found in "Metamorphic Petrology," p. 33.

In a few places there are crosscutting relationships between different vein types; in general amphibole veins postdate magmatic veins, whereas carbonate and smectite/zeolite veins postdate both the magmatic and amphibole veins.

The dip distribution and dip variation with depth for each of the major vein types is shown in Figure F98. Both the magmatic and the carbonate veins show an approximately normal distribution of dips, with a maximum in the 40°–60° range. As found in the upper 500 m of the hole (Robinson, Von Herzen, et al., 1989), the amphibole veins generally have steeper dips with a maximum between 60° and 80°. A sequence typical of the upper part of the cored interval (450–750 mbsf), illustrated in Figure F87A, shows a number of steeply dipping, parallel amphibole veins orthogonal to the foliation. A more detailed consideration of the relationship between the amphibole veins and the crystal-plastic foliation is given in "Discussion," p. 65. Smectite and zeolite veins generally have a shallower dip, as shown in Figure F98G, with a concentration between 20° and 40°. Typical moderately dipping, parallel smectite veins are shown in Figure F87B. Note that below 1400 mbsf there are a significant number of vertical/subvertical veins, generally of smectite, zeolite, and chlorite; similar orientations only occur in the upper parts of the hole in the form of irregular, subvertical clay-lined fractures (Dick et al., 1991a).

The variation of vein dip with depth, averaged over 50-m intervals is shown in Figure F99. The average vein dip decreases downsection from ~70° at 450 mbsf to <20° at 1508 mbsf. This intriguing trend is accompanied by the shift from amphibole-dominated veining at the top to smectite/zeolite-dominated veining farther down the hole. However, there are several exceptions, notably a cluster of very shallow dips at about 1100 mbsf (due to a number of subhorizontal magmatic veins) and the vertical-dipping chloritic veins below 1400 mbsf mentioned earlier.

The temporal evolution of vein orientations can be traced using the vein mineralogy. A down-temperature sequence of magmatic-amphibole-chlorite-carbonate-smectite/zeolite (from ~900° to <100°C) indicates a general shift from steep vein orientations to shallower vein orientations. It also indicates a temporal shift in fracture location downhole. Although initial inspection of the data suggests a considerable change in the stress conditions with time, closer analysis shows that many of the shallower, later formed smectite/zeolite veins occur in conjugate sets. The orientation of the maximum principal stress direc-

F98. Vein dip distribution and variation with depth for each of the major vein types, p. 201.

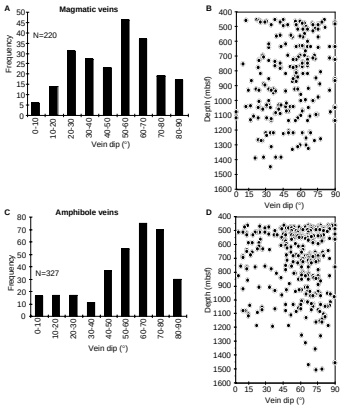

F99. Variation in vein dip with depth, p. 203.

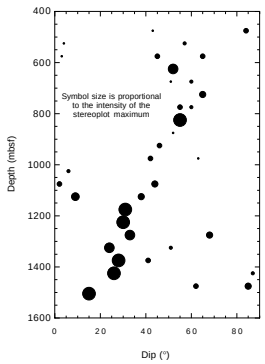

tion (σ_1) calculated from these conjugate sets generally plunges at >65°. The vertical chlorite/smectite/zeolite veins found below 1400 mbsf could have formed in the same stress regime as the shallower dipping smectite/chlorite veins. Therefore, there may have been no substantial shift in the principal stress orientations during the formation of the veins in this section, although there are no conjugate vein sets in the upper parts of the core.

Subhorizontal Microfractures

The variation in the intensity of the subhorizontal microfractures with depth is shown in Figure F100. No effort was made to interpret the distribution of these features. Similar small, white, subhorizontal joints and veins were also described during Leg 118 (Shipboard Scientific Party, 1989); all are probably drilling-induced or unloading features.

F100. Variation in subhorizontal microfracture intensity with depth, p. 204.

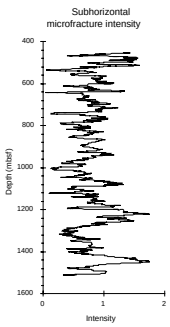

Microstructures

The gabbros of Hole 735B display a wide variety of microstructures, ranging from nearly undeformed igneous textures to late brittle features, illustrating the progression of deformation with time and cooling consistent with that interpreted macroscopically. For each shipboard thin section, we recorded the type and intensity of deformation on an intensity scale (Table T4, p. 42, in the "Explanatory Notes" chapter) from 1 to 6 (plastically undeformed to mylonitic or cataclastic); short descriptions of the main microstructural features are also included in the thin-section descriptions (see the "Core Descriptions" contents list).

Igneous Textures and the Transition to High-Temperature Crystal-Plastic Microstructures

Igneous textures that are completely free of any crystal-plastic overprint are extremely rare; where preserved, they are mainly found in fine-grained rocks. In the more common coarser grained rocks, the most pristine igneous textures consist of plagioclase with a few mechanical, tapered twins, undulose extinction, and/or subgrains (Fig. F101A, F101B, F101D, F101E, F101F). Olivine is often slightly deformed, as indicated by the common development of subgrains (Fig. F101F). Clinopyroxene is always undeformed. Fe-Ti oxides appear as aggregates or as interstitial phases, surrounding other grains or filling triple junctions. Igneous textures range from poikilitic (Fig. F101B), with mostly euhedral grains, to equilibrated (Figs. F101C, F101D, F101F), with mostly anhedral grains, 120° triple junctions, and curviplanar grain boundaries. A magmatic foliation (Fig. F101A), defined by shape-preferred orientation of plagioclase and pyroxene, is present in about 22% of the core (see "Magmatic Structures," p. 54), although it is sometimes difficult to see, especially in thin sections, because of coarse grain size. The transition from igneous textures to crystal-plastic deformation textures is marked by the increasing abundance of mechanical twins, subgrains, and minor recrystallization in plagioclase.

F101. Igneous texture transition to crystal-fabric deformation, p. 205.

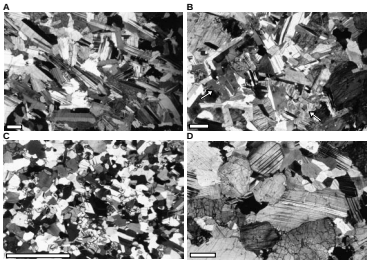

F102. High-temperature crystal-plastic microstructures, p. 207.

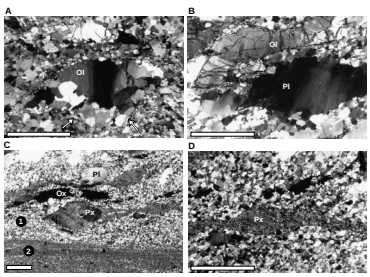

High-Temperature Crystal-Plastic Microstructures

Crystal-plastic deformation often results in extensive dynamic recrystallization of olivine (Fig. F102A, F102C, F102D) and plagioclase

(Fig. F102B, F102C, F102D). Clinopyroxene is typically undeformed, or slightly kinked in the less-deformed rocks, although we observed some subgrains in the lower 50 m of the core. In more deformed facies, clinopyroxene shows greater recrystallization and appears as porphyroclasts with recrystallized mantles and tails (Fig. F102C, F102D). Where Fe-Ti oxides are abundant in the highly deformed intervals, they appear as flattened ribbons (Fig. F102C), with subgrains and recrystallized grains that can be seen in reflected light. The smallest recrystallized grains are observed in the highly localized deformation bands (Fig. F102C).

Lower Temperature/Higher Stress Crystal-Plastic Microstructures and Semi-Brittle Microstructures

As temperature decreased, crystal-plastic deformation was localized into narrow shear zones, which often grade into semi-brittle faults. All minerals appear as a fine-grained recrystallized matrix surrounding porphyroclasts (Fig. F88A, F88B, F88C, F88D, F88E). Plagioclase porphyroclasts are strongly deformed, displaying subgrains, undulose extinction, subgrain boundaries, and microcracks (Fig. F101A, F101B, F101C, F101D, F101E). Amphibole frequently replaces clinopyroxene in recrystallized tails around porphyroclasts (Fig. F88A, F88F) or occurs as highly deformed, very fine-grained bands (Fig. F88B, F88F). Semi-brittle shear zones are often associated with Fe-Ti oxides (see "Crystal-Plastic Structures," p. 56), the latter including numerous small recrystallized ribbons and individual grains of plagioclase (Fig. F88C, F88D, F88E). In some thin sections, Fe-Ti oxides locally crosscut crystal-plastic fabrics, including aligned recrystallized plagioclase grains, and then fill microcracks in plagioclase porphyroclasts (Fig. F88D).

Brittle Microstructures

Numerous brittle features are observed in Hole 735B (see "Brittle Deformation," p. 59), ranging from early magmatic veins and breccias to late hydrothermal veins and faults. Figure F91 illustrates a few brittle microstructures.

Correlation between Microscopic and Macroscopic Observations

Microstructural observations of the deformation fabrics in gabbros from Hole 735B are consistent with structures observed macroscopically. This conclusion is supported by a comparison of macroscopic fabric intensities to thin-section analyses (Fig. F103). For example, in rocks for which no magmatic foliation is observed macroscopically, 150 of 168 display no magmatic foliation at the thin-section scale. Similarly, for rocks with a moderate to strong magmatic fabric, 23 of 29 display a magmatic foliation at the thin-section scale (Fig. F103A). A stacked histogram of observations of the intensity of crystal-plastic deformation illustrates that the dominant thin-section intensity corresponds to the macroscopic deformation intensity (Fig. F103B). For example, 100 of 147 rocks with no macroscopic crystal-plastic fabric (macroscopic fabric intensity = 0) show no evidence of plastic deformation at the thin-section scale, with the exception of the development of mechanical twins in plagioclase or subgrains in olivine or plagioclase. Similarly, all rocks with a macroscopic fabric intensity greater than 2 show either porphy-

F103. Intensity correlations between macroscopic and microscopic fabrics, p. 208.

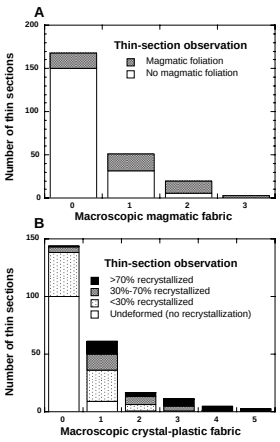

roclastic (30%–70% recrystallization) or mylonitic (>70% recrystallization) fabrics at the thin-section scale (Fig. F103B). Not surprisingly, the greatest discrepancies between the macroscopic and microscopic observations arise for rocks with weak deformation fabrics. A number of factors, including coarse-grain size and heterogeneous deformation, are likely causes for these discrepancies.

Discussion

The structures described in the gabbros of Hole 735B result from the evolution of deformation conditions with time and range from magmatic fabrics to late brittle faults and veins. Crosscutting relationships between the structures outlined above are described in hand samples as part of the VCDs (see "Overview of Macroscopic Core Descriptions," p. 13, in the "Explanatory Notes" chapter, and file X-CUT.XLS in "Appendix," p. 31, in the "Leg 176 Summary" chapter) they are briefly summarized below. We then discuss correlations between some of the structures described in the previous subsections.

Summary of the Crosscutting Relationships

Igneous textures, with or without a magmatic fabric, are overprinted by crystal-plastic fabrics. The latter is always localized into relatively narrow zones (see "Crystal-Plastic Structures," p. 56). The stronger the foliation, the thinner the zone of plastic deformation. High-temperature crystal-plastic foliations are locally overprinted by lower temperature/higher stress crystal-plastic shear zones, often semi-brittle, and/or associated with hydrothermal alteration, as recognized both in hand specimen and thin section. Many of these have a reverse sense of shear in the core reference frame; some of them grade into faults. However, between 450 and 700 mbsf, most shear zones are normal. Brittle deformation always postdates the crystal-plastic deformation, except for early felsic veins and associated magmatic breccias (see "Brittle Deformation," p. 59). Later, more evolved felsic veins and associated breccias generally crosscut the crystal-plastic fabrics and are not plastically deformed. Other brittle features include hydrothermal breccias, veins with different mineral assemblages (see "Metamorphic Petrology," p. 33, and "Brittle Deformation," p. 59), and faults. Faults have different crosscutting relationships with veins, depending on whether they developed after crystal-plastic or semi-brittle shear zones, or after veins (e.g., faults overprinting smectite veins are very common in the lower half of the hole; see "Brittle Deformation," p. 59). In the last 50 m of the Leg 118 cores, which were relogged during Leg 176, a few faults appear to be overprinted by crystal-plastic deformation (e.g., in Section 118-735B-85R-6); only one fault in Leg 176 cores was overprinted by crystal-plastic deformation (in Section 176-735B-147R-6).

Relationships of Fine-Grained Igneous Intrusions with Magmatic and Crystal-Plastic Fabrics

Fine-grained intervals (microgabbros) are present throughout the entire core recovered at Hole 735B. The microgabbros display various types of contacts with the coarse-grained host rock, from very diffuse and irregular to sharp and straight, with various dips (Fig. F104). In the lowest 100 m, they are subvertical, generally a few centimeters thick (e.g., Fig. F104C, F104D). In many instances, they are clearly intrusive,

F104. Close-up photographs of microgabbro intrusions, p. 209.

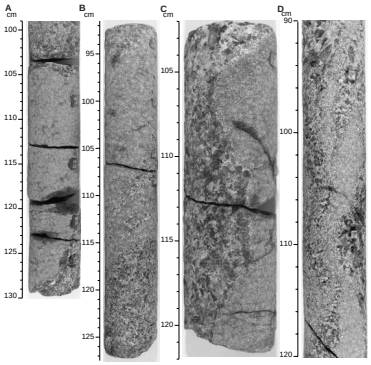

exhibiting a weak to moderate magmatic foliation parallel to the contacts with the undeformed coarse-grained host rock. In Section 176-735-191R-3, a layer of microgabbro, with a magmatic foliation parallel to the contact, intrudes and crosscuts at a high angle a pre-existing magmatic foliation in the coarse-grained host rock (see "Magmatic Structures," p. 54). Microgabbros do not intrude coarse-grained gabbro previously deformed plastically (i.e., no crystal-plastic foliation is crosscut by a contact with a fine-grained interval). On the other hand, crystal-plastic foliations locally overprint both the fine- and coarse-grained materials (e.g., Section 176-735B-191R-1). These relationships suggest that intrusion of microgabbros predated significant crystal-plastic deformation. The variable style of the contacts indicates that microgabbro intrusion took place in hot, sometimes partially molten host rock.

Correlation between Magmatic and Crystal-Plastic Fabrics

An intriguing feature observed throughout portions of the weakly deformed intervals of the core is a positive correlation between both the intensity and orientation of crystal-plastic fabrics and pre-existing magmatic foliations (Fig. F79). This is particularly evident in the intervals 830–920 and 1300–1400 mbsf, where magmatic foliations are locally overprinted by relatively weak crystal-plastic fabrics. As discussed in the previous section, thin-section observations are generally consistent with interpretations made on hand specimen. We analyzed all 40 thin sections of rocks that displayed a crystal-plastic overprint of a magmatic foliation in hand specimens. Of these, the majority illustrated a magmatic foliation defined by plagioclase that contains deformation twins, subgrains, and minor recrystallization, and olivine that exhibits weak subgrain development and minor recrystallization. Pyroxene in these samples may be locally recrystallized, contain subgrains, or exhibit slight undulose extinction, but it is generally interstitial and undeformed. No magmatic foliation could be identified in a subset of the 40 samples; the majority of these samples were >30% recrystallized, thus a preserved magmatic foliation could not be identified.

There are a number of explanations for the correlation in intensity and orientation between magmatic and weak crystal-plastic fabrics. Crystal-plastic deformation may occur easily because of the existence of a mechanical anisotropy (i.e., a magmatic foliation). For example, the easiest slip system to activate in plagioclase is the b-plane in the [a] direction (i.e., [010],[100]; Ji and Mainprice, 1988), which is parallel to the long dimension of crystals aligned during formation of a magmatic foliation.

Foliation development may occur across the transition from magmatic to crystal-plastic conditions as temperatures decrease and the melt phase is either expelled by compaction or crystallizes in situ. Such overprinting relationships have been described in granitoids (e.g., Blumenfeld and Bouchez, 1988; Paterson et al., 1989; Miller and Paterson, 1994) and are interpreted to form first by magmatic strain, and then by crystal-plastic processes as the melt fraction decreases and the framework minerals accommodate further strain.

Association between Crystal-Plastic Deformation and the Presence of Oxides

As was also observed during Legs 118 and 153 (Dick et al., 1991a; Agar and Lloyd, 1997), there is generally a strong association between regions rich in oxide and regions with moderate to strong crystal-plastic deformation. The variation in oxide content with depth in Hole 735B is compared to the variation in deformation intensity in Figure F105. Although the association is strong, there are numerous exceptions to the relationship, especially toward the bottom of Hole 735B. For example, in the interval between 1350 and 1320 mbsf, there are several regions with a moderate deformation fabric intensity and low proportions of oxides. Similarly, in the interval between 1200 and 1300 mbsf, there are several regions with a considerable amount of oxide and little or no crystal-plastic deformation; a good example of this situation occurs in Section 176-735B-153R-6 (1002 mbsf), in which a 30-cm-thick oxide-rich interval is free of crystal-plastic foliation, except for a weak foliation, developed over a few centimeters at the bottom, adjacent to the boundary with an undeformed olivine gabbro below. These observations suggest that the strong association between the presence of oxide and crystal-plastic fabric intensity is related to the localization of deformation in regions with a high concentration of highly fractionated melts. Once deformation is localized in a melt-rich region, the existence of low effective pressure may induce "magma-fracturing," potentially leading to a local increase in porosity and, therefore, permeability, promoting enhanced melt migration along the shear zone. In many occurrences, crystal-plastic and/or cataclastic deformation is concentrated in oxide-rich intervals (Fig. F88C, F88D, F88E); the absence of annealing in these textures suggests that this deformation occurs in the solid state, well below the gabbro solidus (see also Agar and Lloyd, 1997).

F105. Plot of correlation between oxide presence and crystal-plastic deformation intensity, p. 210.

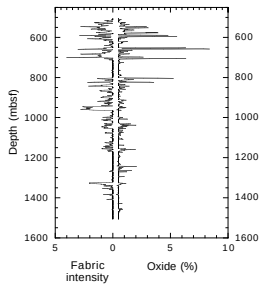

Correlation between Amphibole Veins and Crystal-Plastic Deformation

Both amphibole-bearing shear zones and amphibole veins are abundant at depths between 450 and 700 mbsf, suggesting a correlation between these features at a 100-m scale (see also Cannat et al., 1991; Dick et al., 1991a). The highest density of amphibole veins occurs in a region with the highest intensity of amphibolite to transitional greenschist grade semi-brittle deformation that is later overprinted by cataclastic deformation at lower temperature greenschist grade (Figs. F86B, F106). These observations indicate that deformation remains localized in the same region from granulite to lower temperature greenschist grade conditions. The strong correlation between deformed intervals and amphibole veins is much weaker or absent at length scales less than ~10 m (Fig. F106). The angle between the dip of amphibole veins and crystal-plastic foliations is shown in Figure F107. A majority of amphibole veins are roughly perpendicular to the crystal-plastic foliation, although the angle is variable.

F106. Comparison of amphibole veins and crystal-plastic fabric and fault intensity, p. 211.

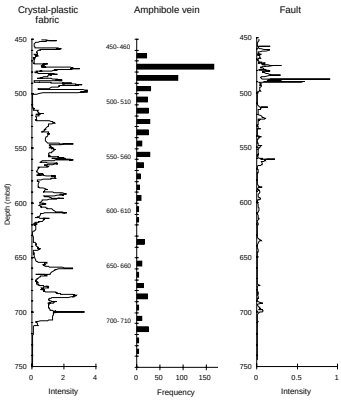

F107. Histogram of the distribution of angles between amphibole veins and crystal-plastic foliations, 450–850 mbsf, p. 212.

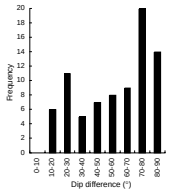

Comparison with Structures at Fast-Spreading Ridges and in Ophiolites

Gabbroic rocks recovered in Hole 735B display a much wider spectrum of structures and microstructures than gabbros of fast-spreading

environments. The upper gabbros cored during Leg 147 in Hess Deep (Gillis, Mével, Allan, et al., 1993) and the gabbros of ophiolites inferred to derive from fast-spreading ridges, such as the Oman ophiolite (e.g., Nicolas, 1989), do not have extensive crystal-plastic fabrics. The lack of planar and continuous igneous layering also contrasts with the layered gabbros observed in the lower two-thirds of the Oman ophiolite gabbro crust (Nicolas et al., 1996). Some structural characteristics such as the lack of well-developed layering, size of igneous intrusions, and large-scale tectonics of Hole 735B rocks are similar to observations in ophiolites inferred to have formed in a slow-spreading environment, such as the Trinity ophiolite (e.g., Boudier et al., 1989) or the Josephine ophiolite (e.g., Alexander and Harper, 1992). However, the general decrease in crystal-plastic deformation with depth in the core has not been described for these ophiolites.

Summary

Gabbroic rocks cored during Leg 176 at Hole 735B display magmatic, crystal-plastic, and brittle deformation features, as well as associated crosscutting relationships consistent with synkinematic cooling and extension in an ocean ridge environment. The following observations provide a basis for interpreting the conditions of deformation during evolution of this block of lower oceanic crust:

1. Thick intervals of the core (up to ~150 m) are comparatively free of deformation and are either structurally isotropic or contain local intervals with weak to moderate magmatic foliation.
2. Primary igneous fabrics are cut by high-temperature shear zones as much as 30 m thick, and these in turn are sometimes overprinted by lower temperature crystal-plastic, semi-brittle, or cataclastic shear zones.
3. Brittle magmatic deformation is represented by felsic magmatic breccias and veins found throughout the upper 1100 m and by decreases in abundance toward the bottom of the hole.
4. The transition from crystal-plastic to brittle deformation is associated with hydrothermal alteration at amphibolite to transitional greenschist-facies conditions.
5. Intense cataclasis is extremely localized downhole into zones of variable thickness (up to several centimeters thick).
6. Metamorphic veins show a wide variation in abundance and a general decrease in dip downhole; steeply dipping amphibole veins are common to 800 mbsf; moderately dipping smectite veins dominate between 800 and 1500 mbsf.

Additional observations relevant to the structural evolution of the Hole 735B tectonic block include the following:

7. The strong preferred orientation of both the deformation fabric and the average declination of the remanent magnetic vector indicates that the foliation has a relatively consistent orientation in the hole.
8. There is a strong association between regions rich in Fe-Ti oxides and regions with strong crystal-plastic deformation. The relationship between crystal-plastic deformation and the concentration of oxide-rich zones, however, is not unique. Macro- and microstructural observations indicate that

a. Oxide-rich zones occur as late-crystallizing interstitial material in undeformed zones,
b. Oxide-rich zones are frequently spatially associated with faults and crystal-plastic shear zones,
c. Lower temperature crystal-plastic and cataclastic deformation locally overprints some oxide zones,
d. Oxides locally cut high-temperature crystal-plastic fabrics along shear zones, and
e. Many oxide-bearing shear zones cut through oxide-poor undeformed gabbros.

9. Based on thickness and fracture intensity of recovered cataclastic rocks, there are two major zones (560 and 690–700 mbsf) and several minor zones of cataclasis (including 490, 1076, and 1100–1120 mbsf). The sense and magnitude of displacement on these faults is unknown; they are likely associated with uplift of the Atlantis Bank. An additional structural break, a 20-m-thick high-temperature shear zone, is located between 945 and 964 mbsf.
10. Numerous reverse-sense shear zones are observed in the interval 900–1100 mbsf.
11. The discontinuity at 560 m corresponds with the seismic reflector of Swift et al. (1991).

These observations indicate that the processes that control crustal accretion at slow-spreading ridges are strongly influenced by localized deformation at conditions ranging from magmatic to low-temperature cataclastic. The correlation between structural domains and igneous intervals are consistent with this segment of the Southwest Indian Ridge not having a steady-state magma source. Rather, intrusion and deformation are likely episodic phenomena that may occur separately or synchronously, but at different rates. In many cases, zones of localized deformation remained active over a wide range of conditions (e.g., cataclastic overprint of oxide-rich crystal-plastic shear zones that were initially active under partially molten conditions) and possibly for a much longer duration than igneous intrusion. The abundance of crystal-plastic deformation is in contrast to observations at faster spreading rates (e.g., Hess Deep and the Oman ophiolite) and is generally consistent with the paradigm of the spreading rate dependence of crustal accretion at ocean ridges.

PALEOMAGNETISM

Introduction

The vertical structure of the sources of lineated marine magnetic anomalies have remained poorly known ever since the recognition, more than 30 yr ago, that the ocean crust records reversals of the geomagnetic field. Inferences on the magnetization of lower crustal rocks from studies of dredged rocks (Fox and Opdyke, 1973; Kent et al., 1978) are ambiguous because these surficial samples have been subjected to varying degrees of seawater alteration that may have significantly affected the magnetic properties. To date, Hole 735B constitutes by far the deepest penetration into plutonic basement and thus arguably pro-

vides the best available information on the magnetization of gabbroic rocks generated at slowly spreading ridge crests.

During Leg 118, ~500 m of gabbroic rock was drilled in Hole 735B, with a high recovery rate of ~87%. Both discrete sample magnetizations and logging data from Hole 735B during Leg 118 indicate a stable inclination with reversed polarity, consistent with the location of the site, which was mapped within sea-surface magnetic Anomaly 5r (Dick et al., 1991b). The average inclination of 71.3° (+0.4°/–11.0°) (using the inclination-only averaging technique of McFadden and Reid, 1982) is approximately 20° steeper than the expected inclination (≈51°) for the latitude of the rift valley at 32°S. The average in situ natural remanent magnetization (NRM) estimated for Leg 118 gabbroic rocks (~2.5 A/m; Pariso and Johnson, 1993), together with the relatively high ratio of remanent to induced magnetization, suggests that gabbros may constitute a significant source for lineated marine magnetic anomalies (Kikawa and Pariso, 1991; Kikawa and Ozawa, 1992; Pariso and Johnson, 1993). Indeed, they apparently constitute the sole source of lineated sea-surface anomalies observed near Site 735 where there are no overlying basalts (Dick et al., 1991b).

During Leg 176, Hole 735B was deepened to 1508 mbsf, again with a high core recovery of 86%. Magnetic measurements were made on minicores as well as on half and whole cores. Magnetic susceptibilities were measured on all whole cores before they were split. Remanence measurements were conducted on the archive halves with stepwise alternating-field (AF) demagnetization. We collected 346 discrete samples for magnetic studies that included remanence measurements, AF and thermal demagnetization, and determination of the anisotropy of magnetic susceptibility.

Whole-Core Measurements

Susceptibility

The susceptibility (κ) of Leg 176 whole cores was measured at a 4-cm interval with a Bartington MS2C Sensor (80-mm diameter) integrated in the MST system (see **"Physical Properties,"** p. 77). Susceptibilities were also measured (at a 2-cm interval) on archive-half cores from the lowermost 50 m of core recovered during Leg 118. The dynamic range of the sensor is 1×10^{-6} to 1×10^{-1} (SI). This is multiplied by a geometric calibration constant (C) that depends on the core diameter. For a whole core with a diameter of 66 mm, C = 0.66. We use this correction factor even though the core diameter is variable and generally less than 60 mm. All readings in excess of 0.1 (SI) are clipped, such that a susceptibility of 0.11 results in a stored value of 0.01, for example. Because this clipping effect has been noted for several core pieces, care should be taken when interpreting the width of individual high-susceptibility zones as well as in the calculation of average susceptibility. Similarly, the inherent smoothing imparted by the large sensor diameter (the response function has a half width of ~5 cm) and the relatively coarse measurement spacing (4 cm) limit the resolution of narrow features with magnetic susceptibility above background levels.

For most of the gabbros measured during Leg 176, the susceptibility is proportional to the magnetite content. Magnetite has a susceptibility of $\kappa \approx 3$ (SI units) with little dependence on grain size (Heider et al., 1996). In contrast, the susceptibilities of other ferrimagnetic minerals likely to occur in gabbroic rocks (e.g., pyrrhotite, hematite, and

ilmenite) are 1–3 orders of magnitude smaller than that of magnetite. The susceptibility of paramagnetic silicates is to a good approximation proportional to their iron content (1% FeO corresponds to $\kappa \approx 6 \times 10^{-5}$ (SI); Collinson, 1983). Therefore, the contribution of silicate minerals to the susceptibility of gabbroic rocks recovered during Leg 176 is unlikely to exceed 10^{-3} (SI).

The downhole variation of susceptibility as determined with the whole core sensor is displayed in "Physical Properties," p. 77. This record has been cleaned for edge effects; however, the clipping effect for the highest values (κ = > 0.1) has not been taken into account. The main characteristics of the susceptibility data are short-wavelength (<0.1 m) spikes and an overall downhole decrease of mean susceptibilities. This is further illustrated by the variation of mean susceptibility, calculated over 20-m intervals (Fig. F108; see also "Physical Properties," p. 77). The average susceptibility for Leg 176 Hole 735B whole cores is $\kappa_{ave} = 5.37 \times 10^{-3}$ (±7.1), after filtering out data within 5 cm of a core gap and correcting for the geometric factor C, described above, which is related to the core diameter. This value is similar to the average value ($\kappa_{ave} = 7.4 \times 10^{-3}$ SI) calculated for the minicores (see below) for the same depth range 500–1500 mbsf and slightly lower than the average value ($\kappa_{ave} = 23.6 \times 10^{-3}$) for Leg 118 minicore measurements (0–500 mbsf).

F108. Variation in average magnetic susceptibility, p. 213.

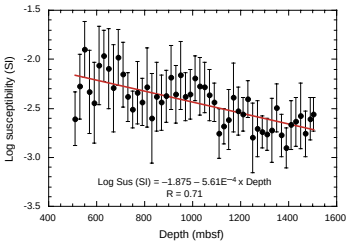

Remanence Measurements

Several problems were encountered during remanence measurements on the archive halves with the pass-through magnetometer. The largest intensities of magnetization that can be measured on half cores are on the order of 5–10 A/m (depending on direction) at the slowest possible tray speed of 1 cm/s, the limiting factor being the slew-rate of the superconducting quantum interference device (SQUID) sensors. Therefore, some pieces with higher magnetization had to be removed for NRM measurements. These pieces were generally replaced for the first demagnetization step. Well into the leg we discovered that the magnetometer software had an error that resulted in false directional readings. The Y-axis calibration constant had the wrong sign, resulting in declinations being west instead of east. This error apparently has been present since the installation of the present LabView software for the 2G magnetometer during Leg 169. A good deal of time was spent correcting the data already acquired and uploading these data to the JANUS database.

Remanence measurements were performed at 2-cm intervals for all archive halves. AF demagnetization steps were typically 5, 10, 15, 20 mT for Cores 176-735B-89R through 168R and 10, 20, 30, and 40 mT for Cores 176-735B-169R through 210R after we realized that 20 mT might not suffice to remove secondary drilling-related overprints completely. The archive-half core remanence data were also filtered to remove edge effects (similarly to that for the susceptibility whole-core measurements) owing to the response functions of the SQUID sensors, which have half widths of ~10 cm. Therefore, only data from core pieces longer than 15 cm were considered, and from these pieces only measurements more than 5 cm from the end of pieces were retained. Fisher average directions were calculated for all pieces greater than 15 cm in length.

The resulting downhole variation of NRM declination, inclination, and intensity are displayed in Figure F109. NRM inclinations for archive-half cores measured during Leg 176 (below 500 mbsf) are pre-

F109. Declination, inclination, and intensity of natural remanent magnetization of gabbroic rocks, p. 214.

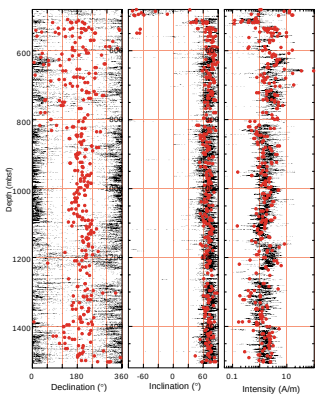

dominantly positive and steep. In contrast, initial inclinations measured on half cores from Leg 118 (above 500 mbsf) are dominantly negative, reflecting the presence of a substantial upward-directed, drilling-related overprint (Robinson, Von Herzen, et al., 1989). The small number of negative inclinations evident in the lower portion of the hole are almost always related to pieces archived and/or measured in an inverted position. NRM declinations from archive-half cores tend to be clustered near 360°, an unexpected result for cores that are azimuthally unoriented. Comparison of the NRM from a whole core before splitting and the archive-half core after splitting suggests that the declination clustering may be an artifact resulting from a drilling-related overprint (Fig. F110). The declination of the whole core contrasts strongly with that of the half core because the latter clusters near 360° as a result of the radial overprint, whereas whole-core declinations are not confined. The inclination for the whole core is generally steeper than for the half cores because the radial components cancel out. The prevalence of NRM declinations near 360° in the archive-half cores is also well illustrated by the distribution of average NRM declinations from more than 1900 core pieces (Fig. F111A).

Average declinations calculated from archive-half core pieces generally become more scattered after the removal of the overprint by 20 mT demagnetization (Fig. F112). However, a significant concentration of declination values is evident near 260° (Fig. F111B). As discussed more fully below, this preferred orientation of declination is identical to that determined on minicores. As NRM declinations of minicore samples (from the working half) are biased toward 180° by the radial overprint, the correspondence between the stable remanent declinations in minicores and the archive-half core data suggests that the radial overprint has been largely removed by AF demagnetization at 20 mT. The simple arithmetic average inclination value for the filtered half-core data of Leg 176 is 71.8° ± 13.3°, with no apparent downhole trend but with significant scatter.

F110. NRM comparison for whole core and archive half, p. 215.

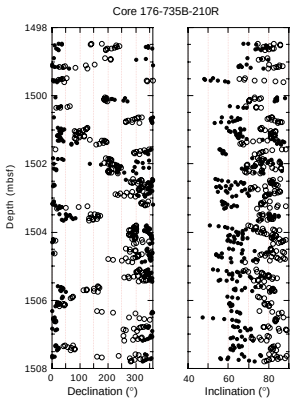

F111. Histogram of average declinations of NRM and remanence after demagnetization, p. 216.

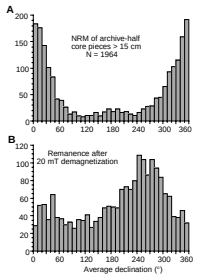

F112. Declination, inclination and intensity of remanence after 20 mT demagnetization, p. 217.

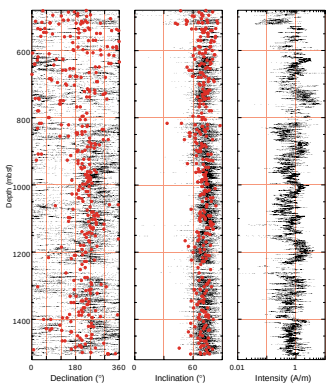

Discrete Sample Measurements

Natural Remanent Magnetization, Intensity, and Direction

The natural remanent magnetization (NRM) is often considered to be a good indicator of the in situ magnetization, which is the only relevant parameter for comparison with magnetic anomalies. Unfortunately, the NRM of a significant number of the hundreds of minicores measured during Leg 176 (Table T12) was affected by a secondary magnetization with apparent radial symmetry that was probably acquired during the drilling process. Many of Leg 118 gabbros also show evidence of a significant secondary drilling-induced magnetization, although the orientation of the secondary component in this case was vertically upward (Kikawa and Pariso, 1991; Pariso and Johnson, 1993). Because of the prevalence of secondary magnetizations, the NRM intensity and direction from Hole 735B minicores should be viewed with some caution.

NRM inclinations from discrete samples from Leg 176 are generally similar to values (near 70°) determined from the archive halves (Fig. F109). In contrast, NRM declinations from minicore samples tend to lie near 180°, providing nearly a mirror image of the declination data from the archive halves (Fig. F109). Since remanent magnetization induced by drilling is radially directed about the axis of the core, the concentra-

tion of declination values near 180° in working half minicores likely represents the complementary signal to the overprint observed in the archive halves. However, declination bias for minicore sample NRMs is more difficult to demonstrate because the stable remanence directions from both minicores and archive halves are preferentially located near 260° as a result of systematic splitting of the cores relative to mesoscopic structural features such as rock foliations. NRM intensities for Leg 176 minicores vary from 0.114 to 95.9 A/m, a range of ~3 orders of magnitude, but show no consistent trend downhole (Figs. **F113, F114A**). The range in NRM intensities is smaller than that observed for Leg 118 gabbros (from 0.00026 to 131 A/m), which have more scattered NRM intensity values. The arithmetic and geometric means calculated for Leg 176 gabbros are 2.54 (±5.77) A/m and 1.58 A/m (±0.39 log units), respectively.

Magnetic Susceptibility

Values for magnetic susceptibility for discrete samples are plotted vs. depth in Figure **F113** and listed in Table **T12.** The susceptibility values vary from 8.12×10^{-4} to 0.123, a range of about 3 orders of magnitude, and have an arithmetic mean of $\kappa_{arth} = 7.39 \times 10^{-3}$ and a geometric mean of $\kappa_{geom} = 4.65 \times 10^{-3}$ (Fig. **F114B**). These two mean values are smaller than those calculated for Leg 118 gabbros ($\kappa_{arth} = 2.37 \times 10^{-2}$; $\kappa_{geom} = 8.75 \times 10^{-3}$). Furthermore, susceptibilities for samples from Leg 176 are less scattered than those for Leg 118 gabbros and slightly decrease with depth (Fig. **F113**).

Königsberger Ratio

The Königsberger ratio, or Q-factor, is the ratio of remanent over induced intensities of magnetization, $Q = NRM/\kappa \times H$. We used the value of the ambient geomagnetic field at Site 735 (H = 30 A/m) for our calculation. As discussed later, a large number of the samples have secondary overprinting probably acquired during drilling. Therefore, care should be taken when considering the calculated Q values. However, as Figure **F114C** shows, most samples have a Q-factor much larger than 1. The arithmetic mean (13.4 ± 9.45) indicates that induced magnetizations contribute relatively little to the magnetic anomalies at the surface and in the borehole. Including the Leg 118 data reduces the arithmetic mean to 10.9 because of the lower Q values for Leg 118 (Q_{mean} = 7.4). For Hole 735B, Q values increase with depth (Fig. **F113**), primarily reflecting the decrease in susceptibility with depth.

Demagnetization Data and Characteristic Magnetization

More than half of the discrete samples analyzed during Leg 176 were collected as paired minicores in conjunction with shipboard thin-section and XRF samples. One minicore from each pair was subjected to thermal demagnetization, and the other to AF demagnetization. Adjacent minicores yield essentially the same remanence directions (Fig. **F115A, F115B, F115C, F115D**). Most discrete samples from Leg 176 have two magnetization components (Fig. **F115**): one with low stability that is apparently related to the drilling process, the other with higher stability and steeper inclinations. Samples in which the near-vertical, low-stability component predominates, presumably related to drilling, are prevalent in gabbros sampled during Leg 118, yet they are almost

T12. Magnetic properties of discrete samples, **p. 282.**

F113. Variation of NRM, volume susceptibility, Königsberger ratio (Q), and median destructive field from discrete minicore samples, **p. 218.**

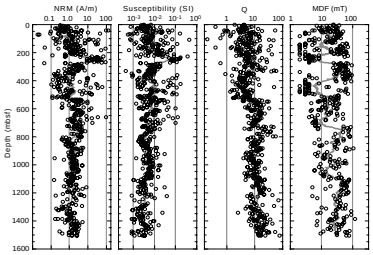

F114. Distribution of logarithm of NRM, volume susceptibility, Q, and inclination of gabbroic rocks, **p. 219.**

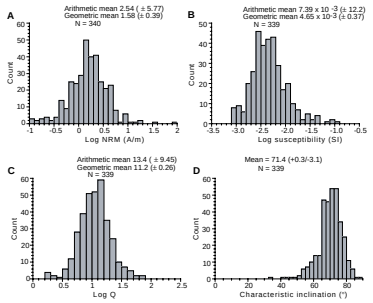

F115. Representative vector endpoint diagrams for gabbroic minicore samples with AF and thermal demagnetization results, **p. 220.**

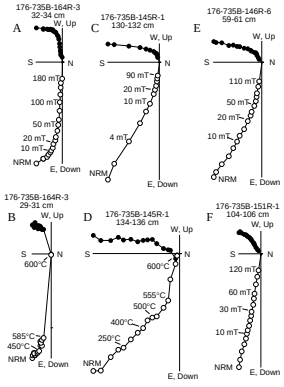

entirely absent in gabbros of Leg 176. Instead, although most samples from the lower kilometer of Hole 735B have low stability of magnetization, they have a southerly declination and moderate but variable inclination. In most cases, AF demagnetization at 10–20 mT (or temperatures of ~500°C) is sufficient to remove this secondary-magnetization component (Fig. F115). In a smaller number of samples, AF demagnetization at 40–50 mT was required to remove this component (Fig. F115E). Identification of this secondary component was hampered when it was subparallel to the primary remanence direction (Fig. F115F). Most samples have both a very "hard" component of magnetic remanence (typically with high and sharp unblocking temperatures; Fig. F115A, F115B) and a "softer" magnetic component with a wider spectrum of unblocking temperatures (Fig. F115C, F115D). Nevertheless, the average demagnetization characteristics are fairly hard, as reflected in the high median destructive fields (MDF; Fig. F113). We note that temperature readings of the Schönstedt thermal demagnetizer TSD-1 are probably too low by about 20°C because the magnetite-bearing gabbros require settings of 590° to 600°C for complete demagnetization, depending on location within the oven.

The mean characteristic inclination for Leg 176 discrete samples is 71.4° (+0.3°/–3.1°) calculated by the method of McFadden and Reid (1982; Fig. F114D). This is 5° steeper than the average reported for the upper 500 m of Hole 735B drilled during Leg 118 (Kikawa and Pariso, 1991; Pariso and Johnson, 1993). However, our recalculation of the Leg 118 data also applying the McFadden and Reid (1982) method results in an average inclination value of 71.3° (+0.4°/–11.0°), which is statistically indistinguishable from that calculated from the Leg 176 samples. The previously quoted shallower inclination from Leg 118 gabbros was evidently the arithmetic mean.

Drilling-Induced Overprint

The radial direction of the drilling-induced overprint is nicely illustrated in Figure F116. Four samples were taken from one section of the working half. One minicore was drilled in the center (as usual), and then cut in two pieces, an outer and an inner specimen. Two other minicores were laterally offset to the sides of the piece. Upon AF demagnetization, all samples revealed the same primary component. However, the degree and orientation of the overprint varies with location. The direction of the secondary component changes from southeast for the sample at the left, to south for the centered samples, to southwest for the sample to the right. This is consistent with a radial direction of the overprinting field and is in agreement with the measurements on the archive halves (Fig. F109).

We measured magnetic fields in and around drill bits, bottom-hole assemblies (BHAs), and drill pipes. The magnetic fields of half a dozen measured roller cone bits were uniformly low with fields smaller than 0.5 mT. Joints of BHAs had fields up to 2 mT in the center and up to ~5 mT right on the edges, although the cored material was never close enough to these edges to have experienced the latter, higher field. One joint of a BHA was measured before and after magnafluxing. The field after magnafluxing was actually smaller than before, probably because the applied field was of opposite polarity to the BHA's remanence. The largest fields were measured on joints of regular drill pipes, with 5 mT at the center and >10 mT on the edges. Each drill pipe constitutes approximately an along-axis magnetized dipole. If all connected pipes are of

F116. Vector end-point diagrams of gabbroic minicore samples, showing radial orientation of the low-stability magnetization component, p. 221.

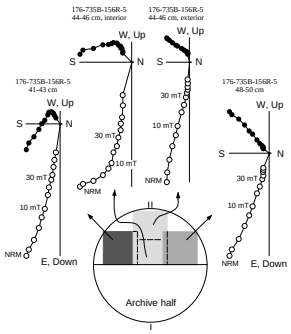

the same polarity, then the magnetic flux closes at joints, and the field in the interior should decrease. However, when pipes of opposite polarity are connected, the field intensity at joints will increase, and the field lines may point radially in (and out at the outside). We think that this situation is the most likely cause for the radial nature of the secondary overprint on drill-core magnetizations.

Anisotropy of Magnetic Susceptibility

The anisotropy of magnetic susceptibility (AMS) has been measured on all minicore samples with the Kappabridge KLY-2 by applying the measuring scheme for the ANISO20 program with measurements in 15 different orientations (Table T13). The program calculates the susceptibility tensor as well as several derived parameters characterizing the susceptibility ellipsoid. The degree of anisotropy (*P*) is expressed by the ratio γ_1/γ_3, where γ_1 and γ_3 are the maximum and minimum eigenvalues, respectively, of the susceptibility tensor. The shape of the susceptibility tensor is conveniently expressed by the shape parameter $T = (2\eta_2 - \eta_1 - \eta_3)/(\eta_1 - \eta_3)$, where $\eta_i = \ln \kappa_i$ (Tarling and Hrouda, 1993). The shape parameter varies between –1 and +1, with the former value representing a perfectly prolate ellipsoid and the latter reflecting an oblate ellipsoid. The direction of the principal axes is given by the eigenvectors κ_{max}, κ_{int}, and κ_{min}.

T13. Magnetic anisotropy from discrete samples, p. 288.

Most samples exhibit significant anisotropy with an average $P = 1.11 \pm 0.05$ and values as high as 1.5 (Fig. F117; Table T13). Anisotropies decrease below 1000 mbsf and increase again below 1400 mbsf. The AMS is predominantly oblate also down to 1000 mbsf and again below 1400 mbsf, whereas prolate anisotropies are more abundant between 1000 and 1400 mbsf. At first inspection, the orientation of the eigenvectors appears to be randomly scattered. (Fig. F117). However, the dip of κ_{max} is mostly below 30° and rarely exceeds 60°. The κ_{min} inclinations range up to 90° with clear clustering at ~45° for the shear zone at 960 mbsf.

F117. Anisotropy of magnetic susceptibility of minicore samples, p. 222.

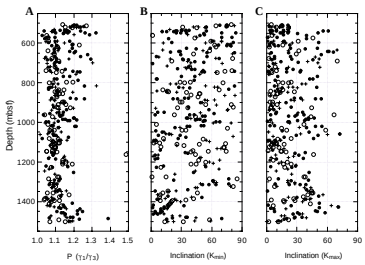

Discussion

The magnetic properties of Leg 176 Hole 735B drill cores are well characterized by a large number of measurements on discrete samples and the entire archive half. The average NRM intensity of Leg 176 minicores is 2.5 A/m, which is less than the average of 6.4 A/m for the upper 500 m cored during Leg 118. However, the Leg 118 samples carried a significant drilling-induced overprint, and the mean effective remanent magnetization was estimated to be 2.5 A/m (Pariso and Johnson, 1993). A drilling-induced component is also apparent for Leg 176 samples as a radial overprint; however, the magnitude appears to be smaller than for Leg 118 samples. Despite the fact that oxide gabbros occur predominantly in the upper part of the hole, there is no general decrease of NRM downhole. On the other hand, susceptibility values decrease slightly downhole (Fig. F113). Consequently, the ratio of remanent and induced magnetization, the Q-factor, increases with depth (Fig. F113). This indicates a decrease in size of the magnetite grains because their magnetic "hardness" increases with decreasing size. The MDF increases accordingly with depth. Q-factor, MDF, and the demagnetization characteristics in general describe very stable remanent magnetization. Moreover, the high and often very sharp blocking temperatures suggest

relatively rapid acquisition of thermoremanence during cooling of the gabbros.

The gabbros thus constitute an ideal source for marine magnetic anomalies. An average gabbroic layer magnetization of 2.5 A/m together with a layer thickness of 3–5 km would in many places suffice to cause the surface anomalies or at least dominate over the contributions from the extrusive basalts and the sheeted dikes. However, a variety of effects including mixed polarity, elevated temperature, and greater source depth might reduce the contribution of these lower crustal lithologies to sea-surface anomalies observed elsewhere.

The primary remanence isolated through AF and thermal demagnetization has reversed polarity throughout the hole with an average inclination of ~71° and no observable downhole trend. This average value of 71° (not adjusted for any deviation of the drill hole from vertical) determined for archive halves and minicores of Hole 735B is about 20° steeper than the expected inclination (~52°) from an axial geocentric dipole. A tectonic tilt for the gabbroic section of 19° ± 5° (depending on the deviation of the hole from vertical), since the time of remanence acquisition near the rift axis, can be deduced.

The rather large scatter of inclinations (and declinations) within a piece would conventionally be explained by secular variation of the geomagnetic field. However, for very slowly cooled rocks such as gabbros, secular variation with periods up to a few thousand years should average out, and more uniform directions have to be expected. Additionally, the often pronounced magnetic anisotropy as determined by AMS measurements must have deflected the NRM from the field direction during thermoremanence acquisition. Alternatively, if significant quantities of magnetite grains crystallized as a result of metamorphism below the Curie temperature (T_c = 575°C), then these grains acquired a chemical remanence that may not average the secular variation of the geomagnetic field. Furthermore, stress and deformation that occurred below the blocking temperatures may have caused the directional quality of the paleomagnetic signal to deteriorate.

The magnetic anisotropy as determined by AMS measurements on discrete samples is fairly pronounced for most of them. The underlying physical mechanism for magnetic anisotropy is not yet understood. It may be related to a preferred orientation of elongate magnetite grains or to an alignment of magnetite grains in chains or planar structures along grain boundaries between or along crystallographic planes within silicate crystals. In any case, the AMS signal results predominantly from magnetite grains because they dominate the susceptibility signal even for the most weakly magnetic gabbros. At present, the relationship between AMS orientation and other structural features such as magmatic fabric and oriented faults and veins is not obvious on the large scale.

The consistent declination data suggest that gross reorientation of structural features in the core may be possible (Cannat and Pariso, 1991). This assumes that the characteristic remanence was originally parallel to the reversed polarity geocentric axial dipole (GAD) direction (180°, +51°). Such reorientation is subject to a number of uncertainties. Because the measured inclinations are significantly steeper than the expected GAD inclination (~51°), complex rotations about plunging rotation axes are not only possible, but likely. Nonetheless, the prevalence of stable declinations near 260° from both archive-half cores and minicores suggests a possible first-order reorientation of the core coordinate system. Assuming a south-pointing characteristic remanence

declination, the mean declination of 260° would be restored to 180° by a counterclockwise rotation of ~80°. Structural planar features (magmatic foliation and crystal-plastic fabric) that preferentially dip toward 90° in the core reference frame would thus dip preferentially toward the axial rift in the north after this same counterclockwise rotation.

PHYSICAL PROPERTIES

Natural Gamma-Ray (NGR) Logging

All cores drilled during Leg 176 were measured using the natural gamma ray (NGR) logger on the multisensor track system (MST) at intervals of 4 cm with a time period of 4 s. Results were output in counts per second (cps). We recorded 22,940 points with a mean value of 12.58 ± 1.52 cps. Count rates did not vary significantly between zones of intact core, zones of broken core, and empty liner sections. Thus, the native radioactivity of the gabbroic rocks recovered from Hole 735B was indistinguishable from the background radiation limits within the core laboratory of *JOIDES Resolution*. Nevertheless, we continued NGR recording so as not to miss any zone of markedly different radioactive properties. However, no such zone was ever encountered. The results from the NGR system therefore do not greatly assist geological interpretation of Hole 735B.

GRAPE Logging

All Leg 176 cores were measured using the gamma-ray densiometry logger (GRAPE) on the MST at intervals of 4 cm with a time period of 4 s, with results output in grams per cubic centimeter (g/cm³). Again, 22,994 points were recorded with a mean of 2.20 ± 0.81 g/cm³.

The GRAPE system used on *JOIDES Resolution* is designed chiefly to measure sedimentary materials that fill the core liner along its length. Rotary-cored hard rocks are of a significantly narrower diameter than the core liner; this diameter also varies considerably along the length of the core. Consequently, the GRAPE system cannot compensate for the smaller-diameter core and therefore underestimates the density of the material. The changing diameter of the core is not directly recorded in any way, preventing a simple correction of the data for the smaller diameter of hard-rock cores.

GRAPE data are recorded continuously along core sections and can be acquired over solid cores, broken cores, and empty core liner. Before analysis, GRAPE data should be filtered with respect to the piece log. A comparison of the GRAPE density points to the measured densities of the nearest minicores (see **"Index Properties,"** p. 79) shows a very poor correlation (Fig. **F118**). There is no significant trend other than a systematic shift of ~0.5 g/cm³ between the two data sets.

F118. Comparison of GRAPE density and bulk density, **p. 223.**

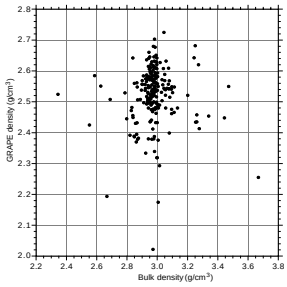

Magnetic Susceptibility

Magnetic susceptibility is particularly sensitive to grains of magnetite larger than ~10 µm and can be used to identify iron-rich zones in the rock, such as oxide-rich gabbros and felsic veins. Magnetic susceptibility is also used to compute the Königsberger ratio, which is the ratio of remnant to induced magnetization in the rock. Magnetic susceptibility values were acquired on the MST at 4-cm intervals for the cored mate-

rial. The Bartington response function of the MS2C meter used for measuring magnetic susceptibility is shown in Figure **F119.**

Analysis of the MST magnetic susceptibility data provides an interesting correspondence with the petrology, but there are some conventions that need to be mentioned. First, the readings from the MST saturate at machine values greater than 10,000. For example, a true value of 12,000 would appear as 2000 in the data set. Care should be taken in interpreting these saturated values. Second, machine values are converted to volume-normalized SI units by multiplying by 0.66 × 10^{-5}. This is a geometrical factor that depends on the fact that the cores have a radius of 66 mm, the radius of a full core liner. Values in SI units are incorrect to the extent that the core, or rubble, in the liner is less than this diameter. Also, spot measurements of whole-round core give diameters of 58.5 to 59.5 mm, less than the nominal 66 mm. The third issue is perhaps most important. The MST takes a measurement every 4 cm from the top to the bottom of a section. Sometimes there is no rock at the measurement point. For example, there are gaps at the plastic dividers between pieces. Also, when rubble is acquired it is unevenly distributed in the liner. Finally, we measured the half-width of a point element of susceptible material (a steel nail) during the cruise on the MST, and it was about 5 cm. For a rock of even the nominal 66 mm radius to yield its true volume-normalized value requires a sample at least 10 cm long. Data listed in Table **T14** (also in ASCII format in the **TABLES** directory) have been cleaned only to the extent that obvious errors, such as inverted pieces of rock, have been deleted. Otherwise, all data are reported in machine units and without regard to core diameter.

In Figure **F120,** we plot the magnetic susceptibility of the first data set (Table **T14,** also in ASCII format in the **TABLES** directory) as a function of depth. In this linear plot, clear spikes in magnetic susceptibility occur at depths where oxide minerals, notably magnetite, are present in the rock. The figure shows more than 20,000 data points acquired over the 1-km interval drilled during Leg 176. The number of spikes decreases with depth, indicating a decrease in the frequency of occurrence of oxide-rich intervals with depth (see Fig. **F108**). The figure also shows that the predominant mode of occurrence of oxide gabbros is as vary narrow seams, many of them a little thicker than the "point source" used to produce a 5-cm "half-width" response.

Magnetic susceptibility is a useful tool in identifying the petrological properties of the rock. With a value every 4 cm, the data density is greater than thin-section or chemical analysis of core can provide, and the resolution is better than can be conveniently handled by visual inspection. Magnetic susceptibility can help the petrologist identify thin or obscure regions of magnetite content. This is demonstrated in Figure **F121,** where we show the susceptibility as a function of depth for a single core about 9.5 m long. This is a preliminary study, but at first glance there is a striking correlation between spikes in the magnetic susceptibility, which exceed 2000 machine units, and both narrow intervals rich in oxide minerals and veins as identified in the vein log (see **"Igneous Petrology,"** p. 12). In addition to the spikes, there is a deterministic low-amplitude signal (less than about 1000 machine units) with a wavelength of a few meters that may reflect small but systematic variations in low proportions of oxide minerals in such rocks as olivine gabbros and troctolites. This background level also appears to diminish with depth.

F119. Response from functions of the Bartington MS2C sensor, **p. 224.**

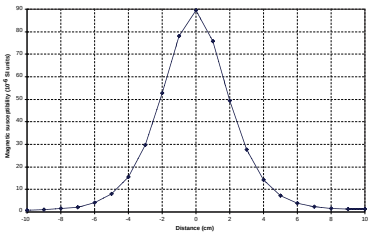

T14. Magnetic susceptibility of principal lithologies, **p. 300.**

F120. Raw magnetic susceptibility of Hole 735B, **p. 225.**

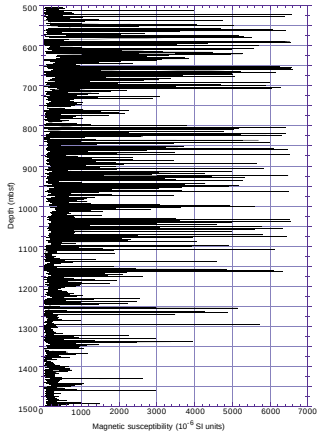

F121. Magnetic susceptibility of Core 176-735B-161R, **p. 226.**

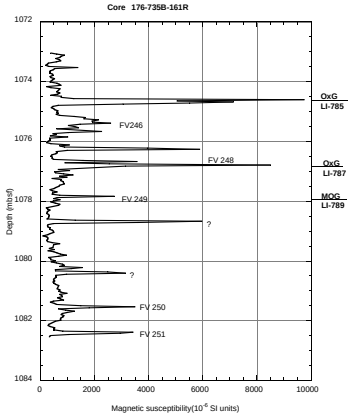

Index Properties

Mass and volumetric measurements were made on 218 minicores at irregularly spaced intervals (Table T15, also in ASCII format in the TABLES directory). Measurements were performed as described in "Index Properties," p. 21, in the "Explanatory Notes" chapter. Measurements of wet and dry mass were begun on the Scitech balance within the physical properties laboratory. After completion of ~50 measurements, we concluded that the balance was unable to measure masses in excess of 30 g to the required precision; this limit included the majority of the minicores measured up to that point. Samples measured after this discovery were measured for both wet and dry mass using a more accurate balance. The earlier samples were also remeasured dry, resaturated, and remeasured wet. We could not demonstrate whether previously dried cores resaturated.

Figure F122 shows the full data distribution for bulk and grain density minicores measured during Leg 176. The mean bulk density for the Leg 176 minicores is 2.979 ± 0.10 g/cm³ with the mean grain density of 2.991 ± 0.107 g/cm³. The mean porosity for the Leg 176 minicores is 0.649 ± 2.884%; the population is heavily skewed by both the large number of minimal porosities and the small number of porosities significantly greater than 1%. Direct comparison with the index properties recorded during Leg 118 is not possible because the bulk densities recorded for that leg were calculated using wet volume measurement. The values are, however, very similar.

Table T16, shows the physical properties of the principal lithologies of Hole 735B computed from both Leg 118 and 176 samples. Discussion of variation of density with lithology is problematic because 219 of the 347 minicores measured were of olivine gabbros. Oxide gabbronorite and oxide gabbro have higher densities (3.09 ± 0.08 g/cm³ and 3.21 ± 0.06 g/cm³, respectively) than olivine gabbros (2.96 ± 0.10 g/cm³) owing to the high density of oxide minerals. Two samples have densities >3.4 g/cm³. They cannot be closely correlated with zones of alteration seen in thin sections, and there is no obvious reason for these very high densities recorded in the shipboard data.

Comparison of the density profile with the interpreted VSP results for Hole 735B from Leg 118 (Swift et al., 1991) shows some coincidence (Fig. F123). The interpreted reflector at 225–250 mbsf (meters below seafloor) has a significant higher density than surrounding rocks because of the abundance of oxide mineral in Unit IV, Massive Oxide Gabbro (Shipboard Scientific Party, 1989). This also occurs to a lesser degree in the amphibolite shear zone at 50–70 mbsf, where there is also a pronounced mineral fabric. However, no similar zones of mineralization could be seen at the levels of the other two reflectors encountered by Leg 176 coring (560 and 760–825 mbsf). It therefore seems likely that these two reflectors represent structural changes, such as large-scale zones of fracturing, rather than changes in mineralogy. This is further suggested by the low percentage of recovery (Fig. F124) across these two zones.

Densities in the Leg 176 cores are less variable than in the upper 500 m. The density profile (Fig. F123) for the Leg 176 cores can be divided into three main regions. Between 500 and ~780 mbsf the rocks show considerable variation in both lithology and bulk density (between 2.8 and 3.3 g/cm³). Below 780 mbsf the rock composition is largely olivine gabbro with minor gabbro and orthopyroxene-bearing gabbro. These rocks show a far more consistent range of densities (mostly between 2.8

T15. Sample bulk and grain densities, p. 301.

F122. Bulk and grain density of minicores, p. 227.

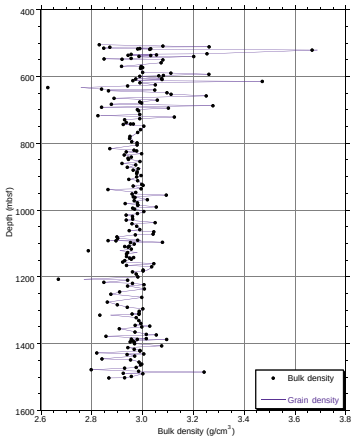

T16. Physical properties of principal lithologies, p. 302.

F123. Bulk density of principal lithologies, p. 228.

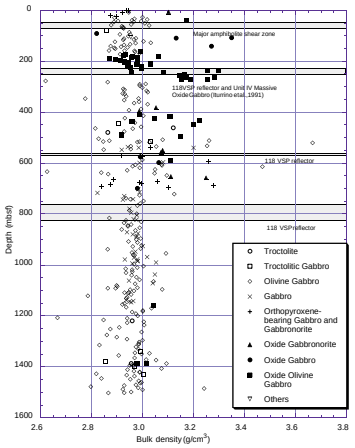

and 2.9 g/cm³). Below 1200 mbsf the rock is almost exclusively olivine gabbro, but increasing variations in the relative proportions of plagioclase and olivine in olivine gabbros and troctolites cause a greater scatter of densities (between 2.8 and 3.0 g/cm³). The mean densities of the deepest rocks are slightly lower than those above owing to the increasing proportion of plagioclase.

Thermal Conductivity

Thermal conductivity measurements were made at 219 irregularly spaced intervals through the borehole section. The measurements were made using the TK04 meter (see **"Physical Properties,"** p. 17, in the "Explanatory Notes" chapter). To minimize the experimental error, five measurements were made on each sample and the mean value was recorded. Where the five values of the measurements varied by more than 0.2 W/(m·K) the sample was remeasured. The measurement needles were tightly strapped to samples during measurements to ensure a good thermal contact; the most significant source of error during these experiments was the strap coming loose during the measurement cycle.

The thermal conductivity of 219 data points over the section is 2.276 ± 0.214 W/(m·K) (Table **T17,** also in ASCII format in the **TABLES** directory). This compares with a mean value obtained during Leg 118 of 2.21 ± 0.22 W/(m·K). During Leg 118, thermal conductivity measurements were made both parallel and perpendicular to the axis of the core. We could not make similar measurements during Leg 176 because the needles used by the TK04 meter are 10 cm in length, which is greater than the width of the sawed core face.

Two felsic veins sampled for thermal conductivity had a mean value of 1.98 W/(m·K), a significant contrast to the host rock (shown in the "Others" lithology column in Table **T16**). Troctolites also have lower thermal conductivities than most of the rocks, with a mean conductivity of 2.100 ± 0.100 W/(m·K). Figure **F125,** on which thermal conductivity is plotted vs. depth, shows no evidence for the threefold division of the borehole seen in the density profile.

Compressional Velocity

Seismic velocities are the basis of the first-order description of ocean crust in terms of Layer 2 (2500–5500 m/s), Layer 3 (6500–7000 m/s), and the mantle (7800–8300 m/s). Attempts to correlate the layers with lithology are constrained by observations of compressional velocities in minicores under pressure. The gabbros acquired from Hole 735B during Legs 118 and 176 clearly have velocities representative of seismic Layer 3.

During Leg 176, the compressional velocities of 217 minicores averaged 6777 ± 292 m/s (Table **T18,** also in ASCII format in the **TABLES** directory). This value is comparable to the velocities measured during Leg 118, is representative of seismic Layer 3 in the ocean crust, and is typical of gabbro and metagabbro. The velocities were measured at room temperature and pressure. Studies of the Leg 118 cores showed that increasing pressure to values appropriate for the in situ lower crust raises velocities by as much as 400 m/s (Iturrino et al., 1991). Cracking and fracturing in the gabbros at a scale larger than the minicores, as has been observed in this hole, would act to decrease the velocity that would be observed on seismic refraction experiments.

F124. Percentage recovery downhole in Hole 735B, **p. 229.**

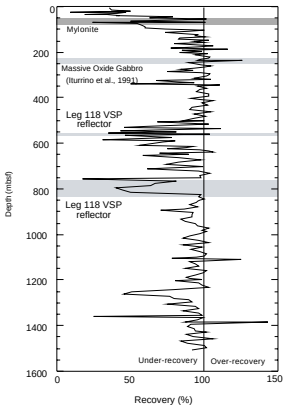

T17. Thermal conductivities, **p. 303.**

F125. Thermal conductivity of principal lithologies, **p. 230.**

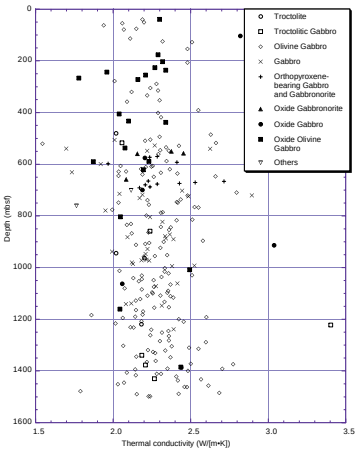

T18. Compressional velocity, **p. 307.**

Compressional velocities measured from minicores show no marked changes in the vicinity of the seismic reflectors interpreted from the Leg 118 VSP except for the massive oxide gabbro interval Unit IV (Fig. F126). The smoothing of the cut faces of the minicores, required for accurate velocity measurements, stresses the samples and causes breakage in fractured rock. Therefore, samples are specifically chosen in cohesive rather than fractured rock to prevent this failure. The minicores taken from the zones of these reflectors, therefore, are not representative of the whole rock, but of undeformed rock, either analogous to the rocks before the deformation episode or lithologies that are resistant to deformation. The low core recovery in the reflector zones indicates that the seismic reflectors are zones of fractured rock. Once again, Figure F126 does not show the threefold division of the borehole seen in the density profile.

F126. Compressional velocity of principal lithologies, p. 231.

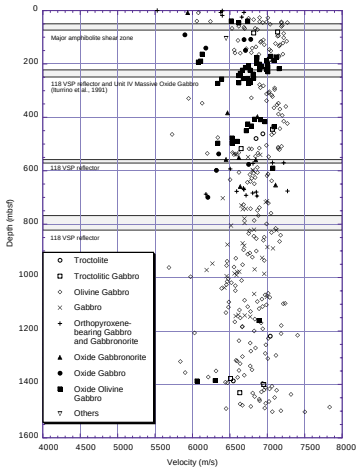

Electrical Resistivity

A knowledge of the electrical resistivity of the lithologies represented by minicores is necessary to infer porosity from electrical resistivity logs.

A few test measurements of electrical resistivity on minicores were made. These were all based on the "Meissner" cell, a device designed and built on board *JOIDES Resolution*. The device uses spring pressure to attach electrodes to either face of a minicore. The faces of the core are saturated with seawater to improve the contact of the electrodes. The sides of the core are wrapped in insulating Teflon tape to restrict the current from passing down the wet sides of the minicore. The resistance between the electrodes was measured on a Wayne-Kerr 6424 meter using differential inputs. Only aluminum standards were available to calibrate the device. These are inappropriate because aluminum is a near perfect conductor and dry igneous rocks are near perfect insulators. Better standards are required in the future for testing these devices

Straight DC resistance measurements were performed. A small number of minicores (20) were tested, giving results of about 3600 Ωm, comparable to logging results from Leg 118 (Table T19, also in ASCII format in the TABLES directory). However, values were both time and frequency dependent. As there was considerable variability in our results and no way of calibrating the system, there was little point in continuing with the measurements.

T19. Resistivity measurements, p. 313.

DOWNHOLE LOGGING

Operations

Initial Logging Program

When the ship reached Site 735, Hole 735B was reentered, a logging BHA was set at 49 mbsf, and two logging tool strings were deployed. The first tool string contained density (HLDS), porosity (APS), resistivity (DLL), spectral gamma-ray (HNGS), and temperature (TLT) probes as well as a one-arm caliper. The second logging run consisted of the NGT, DSI, and FMS.

First Run: HNGS-APS-HLDS-DLL-TLT

The tool string was assembled with an 80-ft bridle, necessary for the deep current return of the DLL, and lowered to 9 mbsf, or approximately 40 m above the bottom of the logging BHA. At this depth, the tool string was kept stationary for 8.5 min to allow the temperature probe to reach thermal equilibrium. After the temperature station, the tool was lowered to 1220.5 mbsf at a logging speed 180 m/hr. Immediately after we started lowering the tool string, an open-line message from the deep laterolog was recorded, meaning that this tool was not properly grounded. Even after exchanging panels in the MAXIS unit and checking the electrical grounds, the problem persisted, so the deployment continued. We began the up-log from the bottom of the hole at a speed of 500 m/hr. At 385 mbsf the density measurements from the HLDS became erratic and the long-spacing spectra ceased to work properly.

The tools checked perfectly in combination aboard the ship before deployment; however, the DLL problem surfaced after it came in contact with seawater. After checking the electronics thoroughly, we found that the specific density tools (HLDS and HLDT) used in ODP operations utilize channel 10 for the caliper electrical ground, and the DLL assumes that this channel is open. This tool string configuration is commonly used in industry wells, but the modifications made to the slimmer version of density tools, which are needed for the smaller-diameter holes drilled by ODP, make this configuration incompatible. Therefore, this tool string configuration cannot be used in future ODP logging operations unless modifications are made.

The quality of the porosity, temperature, shallow-resistivity, and gamma-ray measurements is good. The portions of the density data below 385 mbsf seem to be good, but the data above this depth and the deep resistivity measurements are poor.

Second Run: NGT-Centralizer-DSI-FMS

The 80-ft bridle used in the first run was exchanged for a conventional cable head before deployment. After rig-up and on-deck calibrations, the tool string was lowered to 492 mbsf at a speed of 1600 m/hr. Once on bottom, the first of two planned passes began at a speed of 300 m/hr. As soon as the FMS arms were open, the data being monitored at the MAXIS unit showed very poor images and an automatic "EMEX saturated, increase gain and reconnect EMEX" message was recorded. After adjusting gains to maximum and minimum values and then checking electrical grounds and offset settings, the problem persisted. Nevertheless, we decided to continue acquiring the sonic data and caliper information before retrieving the tool string.

At this point we began to decrease the logging speed because of telemetry transmission problems. The problems persisted until reaching 275 mbsf, where telemetry was lost for the entire tool string. The FMS arms were closed manually but no confirmation of their status was obtained until 30 m before reentering the BHA. After the tool string was retrieved safely, we determined that the telemetry problem was in the configuration of the computer in the MAXIS unit. A few hours before reentering the hole, the air conditioning system in the MAXIS unit had leaked water onto the main computer panels, shorting out parts of the main computer system including the main screen and intercom. At the beginning of logging operations, the companion computer had to be

used for monitoring the downhole logs, and the configuration was not properly optimized for handling the large amounts of data generated from the FMS-DSI combination. At this point we also thought that the problems with the FMS logs were due to an exposed joint. In preparing for the next logging opportunity later during the cruise, the computer configuration problems were corrected and all the tools were thoroughly checked individually and in combination.

Final Logging Program

Although Hole 735B was drilled to 1508 mbsf, about 1400 m of drill pipe had broken off in the hole and only 500 m of pipe was recovered, leaving approximately 600 m of the hole open for logging. Of this, ~500 m had been logged during Leg 118. At the conclusion of fishing operations, the logging BHA was set at 50 mbsf and four logging tool strings were deployed during an approximate total operational time of 42 hr. The first tool string consisted of density (HLDT), caliper, porosity (APS), and spectral gamma-ray (HNGS) probes. The second logging run consisted of an NGT, DSI, GPIT, and FMS probes. The third tool string was composed of NGT, GPIT, and DLL probes. The fourth and final run consisted of the Schlumberger BGKT three-component VSP tool. A modified Kinley sub was placed at 19.5 m above the bottom of the BHA. The inside diameter of this sub had to be modified at the beginning of the leg from 3.810 in to 3.918 in to allow the larger diameter VSP tool (3.85 in) to be deployed. This sub is routinely placed in the BHA during logging operations in case there is a need to cut the logging cable and retrieve the tool.

First Run: HNGS-Bowspring-APS-Caliper-HLDT

During the first run, good density, porosity, and gamma-ray measurements were obtained from the bottom of the logging BHA at 50 to 595 mbsf, or 10 m above the hole obstruction. Measurements were obtained at a logging speed of 500 m/hr starting with a short repeat section from 170 mbsf to 30 m above seafloor at the beginning of the deployment to determine the depth to seafloor from gamma-ray measurements inside the pipe. This repeat was also performed at the beginning of logging to allow enough time for the formation to recover from the neutron activation produced by the minitron in the APS tool before obtaining the main logs in the top section of the hole. The DLL probe was excluded from this first tool string because configuration problems with the density tool (HLDT and HLDS) were encountered at the beginning of the leg.

Second Run: NGT-Centralizer-DSI-FMS

The second run produced good sonic log data, whereas we encountered problems with the FMS. The tool string was set at 270 mbsf for a 7-min station without the wireline heave compensator (WHC) and a 5-min station with the WHC to record acceleration with the GPIT to test the efficiency of the WHC. The DSI recorded cross-dipole and *P*- and *S*-wave modes during the first pass and cross-dipole, upper dipole, and Stoneley modes during the second pass. The data seem to be good, and postcruise processing will be performed to produce final results.

After this second string was lowered, the arms of the FMS were opened at 200 mbsf to test the quality of the FMS log. The data were

poor and similar to the images obtained at the beginning of the leg. After considerable time was spent testing different gain options, the tool string was brought to the rig floor and replaced with a second FMS probe, in order to rule out any potential problems with the first tool. The second deployment initially went to 270 mbsf to test the performance of the second FMS. The results from the second tool were similar to those recorded with the first. After we logged from 270 to 210 mbsf and tried all possible gain-control and offset-configuration settings, the same automatic EMEX saturation message obtained during the previous runs was recorded. The tool string was lowered to 595 mbsf for the first of two passes in the open section of the hole at a logging speed of 225 m/hr. The poor performance of both FMS tools may have been caused by several factors: (1) the tools could not respond quickly enough to the extreme resistivity contrasts between the oxide gabbros (≤10 Ωm) and the olivine gabbros (≥10,000 Ωm); (2) the resistivity contrast between the olivine gabbros (low conductivity) and the borehole fluid (high conductivity) caused the current to travel along the borehole instead of penetrating the formation, thus causing the EMEX current to saturate the measuring electrodes; and (3) the low resolution of the MAXIS displays were degraded to the point where assessments of data quality control during logging operations were not possible. Extensive postcruise data processing was performed, however, and some useful information was obtained.

Third Run: NGT-GPIT-DLL

Cable heads were changed before the deployment of this tool string in order to use the 80-ft bridle necessary for the DLL. The deployment of the third tool string resulted in very good resistivity data. The tool string was set at 270 mbsf for a 48-min station without the WHC and an 8-min station with the WHC to record acceleration with the GPIT in order to test the efficiency of the WHC. The long station without the WHC was because of problems getting the WHC to engage. After several attempts and extensive checks of the WHC system, the WHC began to work properly, and we were able to continue operations. We began logging downward, but there were problems with the quality of the shallow resistivity measurements, and the tool string was brought up to the rig floor. The fiberglass sleeve covering the DLL joint was taped in place to ensure that no current was returning to the tool due to the high conductivity of the Fe-Ti oxides, and the tool was lowered once again. We acquired good shallow and deep profiles from 50 to 595 mbsf at a logging speed of 1500 m/hr.

Fourth Run: VSP

The deployment of the Schlumberger BGKT three-component VSP tool and data acquisition system was successful even though operational problems were encountered during the experiment. Other components of the VSP operation consisted of a 1000-in^3 air gun, a 400-in^3 water gun, and an over-the-side (OTS) source monitoring hydrophone. These three elements were suspended from the Number 3 crane, aft of the rig floor on the port side.

The objectives of the VSP were (1) to cover the 100-m section between 600 and 500 mbsf, (2) to identify seismic reflectors below the 1500-m depth of the hole, and (3) to provide high-quality data for seismic attenuation studies.

Three test phases were conducted in advance of the downhole VSP operation. Before the cruise, a 2-day orientation was held at the Schlumberger Houston District Offshore office on 29 and 30 September. The other two test phases were on board *JOIDES Resolution*. On 9 November, an 80-in^3 water gun was lowered from the fantail to test the Schlumberger firing box, the blast phone configuration, and the MAXIS acquisition system. On 24 November, we tested the 1000-in^3 air gun, the 400-in^3 water gun, and the OTS hydrophone as they were suspended from the Number 3 crane. These tests went well, and in both sets of tests, data sets were acquired and used in an attempt to decipher the Schlumberger SEG-Y format. Before the experiment, we arranged to have logs of engine room and dynamic positioning activity during the experiment.

The VSP tool was rigged up with the 80-ft bridle used during the DLL run, and approximately an hour was spent testing the system on the rig floor. Because there was considerable ship vibration, all channels were overloaded, and it was difficult to test the tool on deck. However, a test of the clamping arm was performed, and the VSP acquisition software was initialized before the deployment. The tool was deployed to 595 mbsf at a speed of 480 m/hr. As the light weight of the tool (253 lb) could not be monitored in the tension measurements at the logging winch, the noise that the geophones recorded during deployment was monitored with a speaker at the MAXIS unit to ensure that the tool did not get hung up in ledges while the wireline was being lowered. In addition, 30 gpm of drilling fluid was pumped while the tool was inside the pipe to help the tool past the Kinley sub.

The 1000-in^3 air gun, a 400-in^3 water gun, and the OTS monitoring hydrophone were lowered into the water after the tool passed the Kinley sub and while the tool was still being lowered to the bottom. When the tool reached the bottom, the guns, the clamping arm, the three orthogonal components, and the monitoring hydrophone were tested for signal quality and gain controls. At this point, the OTS monitoring hydrophone was not working properly. It was brought back to the ship, an electrical short was fixed, and the hydrophone was lowered once again to a depth of 300 mbsl. During the tests and the duration of the experiment, the y-component of the tool did not work properly; postcruise data processing will determine if any of the data from this channel is useful. However, the y-component apparently had cross-talk with the z-component (same character as the z-component with 60-Hz noise superimposed on it), and it is more than likely that the signals from this channel are not useful.

The advantage of having horizontal channels on a normal-incidence VSP is that the instrument can detect vertically traveling shear waves that may be generated by scattering near the seafloor. This was documented during previous VSP experiments at Hole 504B. Because the x-component was functioning and this one channel could provide some information on the shear wave arrivals, we decided it was not worth retrieving the tool to the rig floor and losing more time attempting to fix the y-channel. Aside from the y-channel problem, good signals from the air gun on both the x and z components were recorded. However, signals from the water gun, which is a source with lower amplitude and higher frequency, were weak and only sporadically detected. This was consistent with the observations from Leg 118, during which similar effects were attributed to the high seismic attenuation of these lower crustal rocks. However, we expected to see the water gun return signals get stronger shallower in the hole. Postcruise processing may improve

the water gun return signals beyond those which we observed during the experiment.

Data were recorded at 5-m intervals for the bottommost 50 m, at 10-m intervals for the following 50 m, and at 100-m intervals for the upper 500 m of the open hole. While lowering the OTS hydrophone to its operating depth of 300 mbsl, the cable ran off the sheave and lodged around the axle. Further lowering or raising the hydrophone could not be done without swinging the crane in and taking the air guns out of the water. Because time was running short (estimates were that we would require at least 11 hr of shooting for a complete VSP over the 600-m section of open hole), we began the VSP experiment with the tool clamped at 587 mbsf. Stations at 594, 591, and 588 mbsf had been acquired earlier during testing. The shooting procedure consisted of clamping at a depth, slacking the cable 2–3 m to isolate the tool from cable vibration, and then recording 10 air gun and 10 water gun shots at each level. VSP data were then acquired at depths of 587, 584, 579, and 574 mbsf.

At the beginning of the experiment, the weather conditions were clear and calm with a gentle, long-wavelength swell. However, wind speed and swells increased through the evening. The captain was concerned that weather conditions were deteriorating. Because the currents had been strong and variable throughout the cruise at this site and the hydrophone cable was off the sheave, we would not have been able to retrieve the hydrophone quickly should the cable come near the thrusters and screws. There was also concern that should the cable break at the sheave, remotely operated vehicle operations at this site, planned for late 1998, would be jeopardized. VSP operations were immediately suspended, and, with the assistance of ODP technicians and Sedco personnel, the hydrophone and cable were brought back on board. Under stronger winds and light rain, the OTS hydrophone was secured on deck, and the guns were redeployed. The entire operation was completed in 1 hr. Shooting was interrupted on two more occasions: once to adjust the pressure to recock the water gun, and then again to reattach an air gun hose.

VSP data acquired at 5-m intervals between 594 and 544 mbsf and at 10-m intervals between 544 and 494 mbsf give a good coverage over the new section of hole. As the BGKT tool did not show appreciably better results than the Leg 118 VSP, we decided not to redo the VSP in the upper 500 m. To compare the response between the Leg 118 and Leg 176 VSPs over the upper 500 m of the hole, stations at 100-m intervals between 494 and 94 mbsf were recorded. At the end of the VSP operations, a total of 525 air gun and water gun shots had been fired.

A problem with the VSP data acquisition during this experiment was the presence of noise generated by the pipe banging in the hole. If shots went off during quiet periods, good records were obtained, whereas if shots went off during noisy periods, the noise obscured the shot. Given the larger-than-normal outside diameter of the BGKT tool and the style of reentry cone at Hole 735B, we had no options for reducing pipe noise.

Transcription of data from Schlumberger SEG-Y format (TIF files) and an SEG-Y format that we could read on board the ship was a recurring problem throughout VSP planning, operations, and shipboard analysis. With the help of software specialists at the Woods Hole Oceanographic Institution, data files were translated from the Schlumberger files to a format that could be recognized by the shipboard software package. However, problems still exist in getting the identical waveforms that are

produced by the MAXIS. Proper transcription from Schlumberger format to a UNIX-based SEG-Y format at the Lamont-Doherty Earth Observatory will be necessary before any significant processing can occur.

Borehole Condition and Log Data Quality

Shipboard analysis of logging data and cores recovered during Leg 118 and Leg 176 shows that Hole 735B consists of definable units and horizons, reflecting differing influences of magmatic, structural, and metamorphic processes within the lower crustal gabbroic rocks drilled at this site. A selection of most of the logs acquired during Leg 176 is presented in Figures **F127, F128, F129, F130, F131.** The interval displayed in these figures corresponds to approximately the 545 m of open hole (50–595 mbsf) above the 900 m of pipe still in the borehole and the depth below the logging BHA. Most logs were also run through the BHA to the seafloor, and repeat passes were made for quality control, but these are not shown. Two caliper logs from the FMS (Fig. **F127**) illustrate two orthogonal dimensions of the borehole with depth. The diameter of Hole 735B generally varies between 10.4 and 15 in, with the largest diameters occurring at approximately 100 and 560 mbsf. Otherwise, the condition of Hole 735B is generally adequate for the acquisition of good logging data. In several sections, the borehole seems to be slightly elliptical in cross section. Only a few intervals have large systematic differences between the two calipers. These intervals are approximately at 100, 485, and 560 mbsf and have a maximum difference of 1.2 in. The orientation of the calipers with respect to magnetic north (P1AZ) illustrates that the tool followed almost identical paths during the two full passes with the FMS. This small rate of rotation may be indicative of hole ellipticity, deviation, or directional borehole damage caused by the extensive fishing operations conducted near the end of the leg.

The HLDS, HLDT, and FMS logs from initial and final logging programs show variations of ~2 in greater than the caliper measurements from Leg 118. The tools deployed during Leg 176 were recalibrated after logging operations, and they appear to be correct. A closer inspection of the Leg 118 caliper log suggests that these measurements are somewhat questionable because in many instances they are less than the bit diameter.

Figure **F127** also shows the hole deviation and azimuth logs obtained with the GPIT. Hole 735B shows a deviation approximately varying from 7.1° at 95 mbsf to 5.1° at 545 mbsf. Below 545 mbsf, the hole deviates more, which may be a result of the fishing operations. This slight hole deviation did not affect the operation of the logging tools or the data quality. The direction of this deviation rotates from N3°E at 95 mbsf to ~N35°E at 595 mbsf. The abundance of magnetic minerals in Hole 735B seems to have an influence in the azimuth measurements obtained with the GPIT magnetometer. This is most evident in the inflections measured in Unit 4 from 233 to 278 mbsf. However, the azimuth values obtained in Unit 5 from 325 to 400 mbsf should be more reliable, because this unit has a relatively low abundance of magnetic minerals, as already shown in the susceptibility log obtained during Leg 118 (Shipboard Scientific Party, 1989).

F127. Composite illustration showing the FMS calipers in Track 1, p. 232.

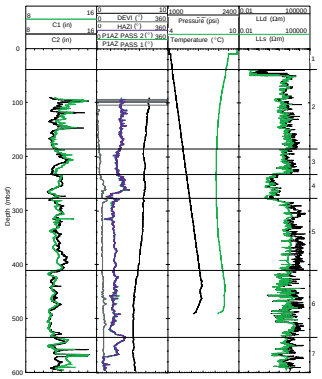

F128. Downhole logs of density, porosity, spectral and computed gamma ray, thorium, uranium, and potassium for Legs 118 and 176, p. 233.

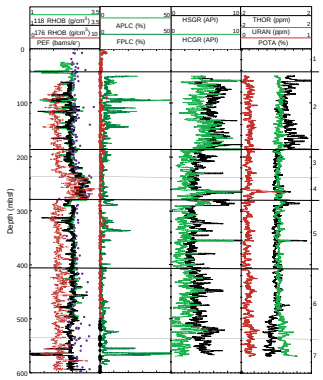

F129. Downhole logs of resistivity, density, porosity, and FMS calipers, p. 234.

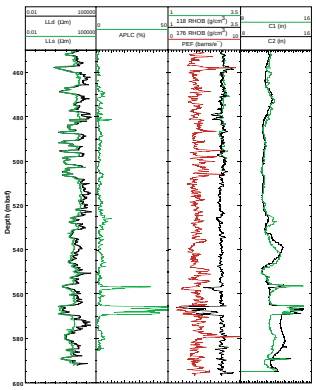

Temperature Measurements

Temperature measurements obtained with the Lamont-Doherty memory temperature tool (TLT) at the beginning of the leg show that the hole is nearly isothermal for 500 m. A slight but steady decrease in temperature of approximately 0.8°C from 8.9°C at 49 mbsf to 8.1°C at 240 mbsf is observed and followed by a steady increase of up to 0.8°C at a depth of approximately 445 mbsf. Below 445 mbsf, temperature and pressure fluctuations were recorded. These fluctuations may be attributed to difficulties trying to reach the bottom of the hole. The average temperature for the entire upper 500 m of Hole 735B is 8.5°C.

Nuclear Measurements

The bulk density (RHOB) of the formation and the photoelectric factor (PEF) were measured using the HLDT and are shown in Figure F128 (Track 1). Density values range from 1.47 to 3.27 g/cm³ with a mean value for the entire logged section of 2.88 g/cm³. Low values are related to fractures filled with seawater or to enlarged sections of the hole. The olivine gabbros of Unit 5 exhibit a range of values from 2.25 to 2.98 g/cm³ with a mean of 2.88 g/cm³, whereas the oxide gabbros of Unit 4 show a range of values from 2.95 to 3.27 g/cm³ with a mean of 3.09 g/cm³. The PEF varies from 1.10 to 9.84 barns/e⁻, which is indicative of the lithologic variations observed in this lower oceanic crustal section. Variations in the density profile correspond to variations in oxide mineralogy (Shipboard Scientific Party, 1989) and increases in porosity (Fig. F128, Track 2). Density values from discrete laboratory measurements show a fairly good correlation with log measurements, exhibiting slightly higher values in the upper 500 m of the hole and more scatter at the bottom of the logged section.

The porosity measurements in the logged section of the hole show variations between 0.03% and 57.37% with a mean value for the entire section of 3.34%. High values correspond to borehole washouts or fractures and generally correlate with low peaks in the density log. Several isolated zones corresponding to high porosity and low density occur in the upper 450 m of the hole and were previously documented as high permeability zones from results of Packer experiments (Shipboard Scientific Party, 1989). Below 450 mbsf, several zones showing decreases in resistivity and density and increases in porosity and borehole size were observed (Fig. F129). As shown in Figure F130, the higher porosity and lower resistivity may correspond to the higher deformation intensity observed in this section of the hole (see "Structural Geology," p. 54, and "Metamorphic Petrology," p. 33). Discrete laboratory measurements do not correlate well with the porosity logs. This may be a direct cause of sampling bias, because fractured intervals are usually poorly recovered and the rocks that are recovered have veins and fractures that are not often sampled for measurements of physical properties.

The spectral gamma-ray logs were measured with both the NGT and HNGS tools (see "Principles and Uses of the Tools," p. 21, in the "Explanatory Notes" chapter). Profiles from both tools show excellent correlations; therefore, for simplicity, only the profiles obtained with the HGNS are shown in Figure F128 (Tracks 3 and 4). The total spectral gamma ray (HSGR) varies from 1.8 to 16.9 API in the open section of Hole 735B. The contributions to the natural radioactivity observed in the HSGR and the computed gamma-ray (HCGR) vary throughout the hole. In Unit 2 from 58 to 186 mbsf, most of the contributions seem to

F130. Downhole logs of resistivity, fault intensity, and porosity, p. 235.

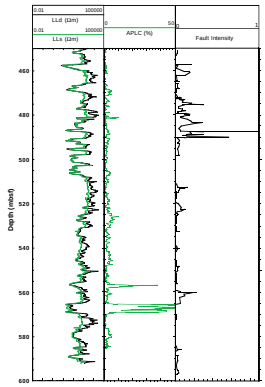

F131. Downhole logs of FMS calipers and shear-wave measurements, p. 236.

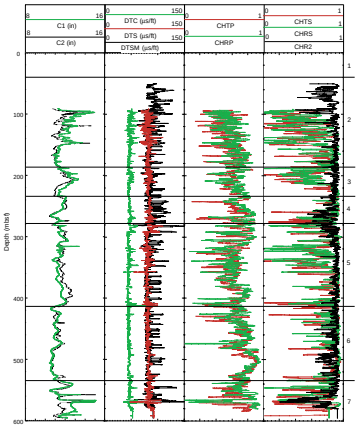

be related to an increase in thorium content toward the base of this unit. In Unit 3 from 186 to 239 mbsf, the variations are mostly caused by small increases in both potassium and thorium. Unit 4 from 250 to 278 mbsf is characterized by sharp increases in potassium and smaller variations in thorium, whereas the natural radioactivity of Unit 5 from 281 to 403 mbsf is mainly caused by increases in thorium and uranium. The base of Unit 6 from 488 to 536 mbsf is characterized by a decrease in thorium with increases in both potassium and uranium decay series. Potassium is highly mobile in oceanic crustal environments during low-temperature alteration processes; therefore, the HSGR and potassium logs are good indicators of alteration.

Sonic Measurements

The sonic logs recorded with the DSI tool represent the first use of this tool in the lower oceanic crust. The data obtained during the second logging run at both the beginning and the end of the leg were recorded during three separate passes of the tool through the section of open hole. In total, five different modes of the DSI using different acoustic sources allowed the acquisition of both compressional and shear waveforms (see **"Principles and Uses of the Tools,"** p. 21, in the "Explanatory Notes" chapter). Both high-frequency compressional and shear modes as well as the low-frequency dipole mode produced good sonic waveforms. Preliminary processing of compressional (DTC) and shear (DTS) traveltimes was completed on board *JOIDES Resolution* using Slowness-Time-Coherence (STC) software on the Schlumberger MAXIS acquisition system (Kimball and Marzetta, 1984). Postcruise processing must also be applied to the dipole data to account for dispersion effects, which may reduce the traveltimes by 2%–6% (Brie and Saiki, 1996). The low-frequency Stoneley mode also produced high-quality waveforms.

The delta-transit-time compressional (DTC) and delta-transit-time shear (DTS) logs from the monopole source and the delta-transit-time shear measurements (DTSM) from the dipole source are shown in Figure **F131.** The DTC trends were computed using a high-frequency source over a range from 35 to 150 µs/ft, whereas the DTS trends were computed using a low-frequency source over a range from 40 to 200 µs/ft. Coherence of the transmitter and receiver combinations for the compressional (CHTP and CHRP) and shear-wave (CHTS and CHRS) logs from the monopole source is degraded in washouts and with excursions in borehole size at several intervals. The dipole-shear waveforms (CHR2) have systematically higher coherence than the high-frequency compressional and high-frequency shear waveforms, which in part is the result of less scattering from small fractures.

Compressional and shear traveltime logs show generally uniform values throughout the 550 m of section logged. Variations correlate with changes in both resistivity and density measurements. The largest variation in both compressional and shear traveltimes is observed at approximately 565 mbsf. This apparent low-velocity, low-density zone, which also correlates with high-porosity and caliper readings, may be responsible for the reflector identified during Leg 118 (Swift et al., 1991) at this depth. The average compressional and shear-wave velocities obtained from the monopole source are 6516 m/s and 3697 m/s. The average shear-wave velocity obtained from the dipole source is 3504 m/s. However, these values have not been corrected for dispersion effects, and postcruise processing may have a significant effect on the final results.

Electrical Resistivity Measurements

Electrical resistivity measurements and images were obtained with the DLL and FMS probes in Hole 735B during Leg 176, recording two different electrical logs and one type of formation image. As shown in Figure F127 (Track 4), the laterolog deep (LLd) and shallow (LLs) measurements give similar results, with the lowest values being obtained in the Fe-Ti oxide gabbros of Unit 4. Several other low-resistivity measurements were recorded throughout the upper 600 m of the hole, and they correlate with density and porosity variations discussed below.

The quality of the FMS images from both passes at the end of the leg was poor and required extensive postcruise processing. In formations with resistivities greater than 10,000 Ωm, such as these, the FMS current will tend to flow into the mud and along the borehole fluid rather than into the formation (Schlumberger, pers. comm., 1997). A future alternative to this problem in high resistivity environments may be to increase the mud resistivity by pumping fresh-water mud into the hole with the goal of increasing the mud resistivity from 0.1 to ≥2 Ωm.

The following postcruise corrections and processing were made to the FMS data:

1. Speed corrections were applied to the data to correct the fact that measurements attributed to a cable depth are actually acquired at a somewhat different depth. This is essentially a depth correction but is also referred to as a speed correction because the depth error would not exist if the tool traveled at the same speed as the cable at the surface winch. The integration of the cable speed and the z-axis accelerometer data were used to estimate the speed and depth of the tool.
2. Because the tool was sticking for short intervals (i.e., the tool remained stationary while the cable moved for a short distance), a sticking detection threshold and recovery speed factors were applied to correct the fact that in these zones the information from the cable depth and the integration of the accelerometer data are in conflict. The former indicated that the tool is moving at a cable speed, whereas the latter showed that the tool velocity was not changing.
3. The average response of all the buttons in each pad were equalized to account for the difference in gain and offset of the preamplification circuits associated with each button, differences in standoff according to button location due to mismatch of borehole and pad curvature, and the difference in application pressure between pads.
4. A faulty button detection and correction was made specially for pad 4 because approximately 95% of the buttons failed. This correction interpolated the faulty button values using the values of adjacent good buttons.
5. The button response is controlled by the EMEX voltage which is applied between the button electrode and the return electrode. Because of the EMEX saturation messages were recorded during this particular logging run, a voltage correction was applied where the button response was divided by the EMEX voltage channel so that the response corresponds more closely to the conductivity of the formation.
6. Imaging enhancing techniques were used for data display by using the method of histogram equalization. This technique en-

hances the depiction of details in an image by optimizing the color usage (i.e., the use of colors available with equal frequency). The technique was used in two ways for highlighting different features: static normalization, which is a global optimization with a window covering the entire logged interval, and dynamic normalization, which is a local optimization with separate normalization computations repeated at regularly spaced positions using a 5-m sliding window.

A comparison of the FMS raw and processed data shown in Figure F132 illustrates the difficulties in monitoring data quality during the logging runs and the subsequent improvement. A preliminary interpretation of the processed FMS images revealed strike orientations as well as dip azimuth and magnitude for several hundred structural features. However, two main factors may influence the overall orientation of these features after more detailed postcruise interpretation and processing is performed. First, these orientations were obtained from sinusoid fits based on the assumption that the features were planar. Second, these picks may be significantly influenced by the high concentration and magnetization of the Fe-Ti oxide minerals present throughout the logged interval (Fig. F127). The degree to which the GPIT magnetometer is influenced by the high magnetization of the oxide gabbros will be investigated at a later date. The preliminary strike orientation of the majority of the features range from 280° to 310°. The dip azimuth of these features ranges from 340° to 20°, with several features also dipping from 180° to 220° and the magnitudes mostly ranging from 10° to 50°.

Examples of some of the features identified in the FMS images are displayed in Figures F133, F134, and F135. A 25-m interval from 273 to 297 mbsf shows the variations in character observed in the transition from oxide gabbros of Unit IV, through the breccia zone at the base of Unit IV, and into the olivine gabbros of Unit V. Alternating intervals of olivine and oxide gabbros are observed from 273 to 280 mbsf. The transition from the oxide gabbros into the magmatic breccia zone shows some deformation at the base of Unit IV with most of the features approximately dipping between 17° to 22° (Fig. F133A). Besides the large resistivity contrast between the interlayered subunits of Unit IV, one of the most noticeable features is the abrupt contact between the magmatic breccia zone and the olivine gabbros of Unit V (Fig. F133) at ~292 mbsf.

Several structural features and lithologic boundaries are clearly observed in the bottommost 100 m of the FMS logs (Figs. F134, F135). Highly conductive zones at 557 and 566 mbsf (Fig. F134) may correspond to zones of intense deformation. These 1 m and 4 m zones seem to correlate with high core fault intensity measurements (see "Structural Geology," p. 54). Lithologic boundaries are also observed in Figure F135. Oxide gabbros in Sections 176-735B-99R-6 to 101R-2 (see the "Core Descriptions" contents list) seem to correspond to a 3-m low-resistivity interval ranging from 579 to 582 mbsf (Fig. F135A). A smaller 1-m interval at 590 mbsf (Fig. F135B) also seems to correlate with oxide olivine gabbros recovered from Sections 176-735B-101R-3 through 102R-1 (see the "Core Descriptions" contents list). Both of these intervals also seem to be characterized by strong deformation (Fig. F135A, F135B).

F132. Illustration showing image quality of raw and processed FMS data, p. 237.

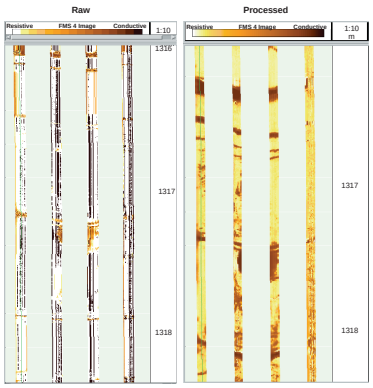

F133. FMS image showing 25 m of oxide gabbros and olivine gabbros, p. 238.

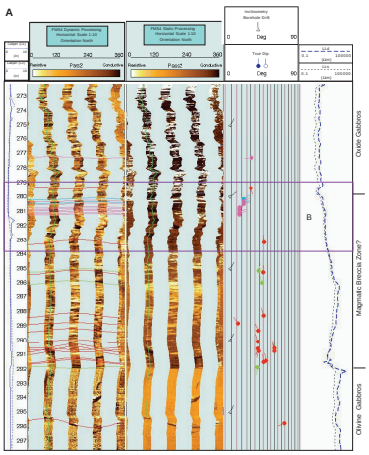

F134. FMS image showing 25-m interval with high core fault intensity, p. 240.

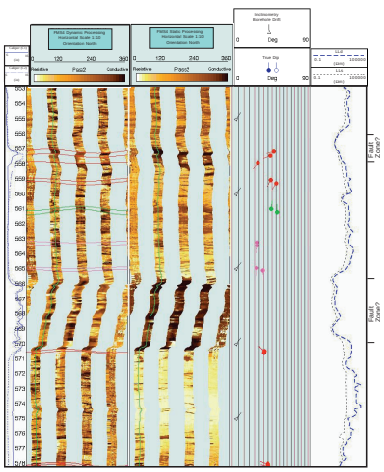

Core Imaging

During Leg 176, all whole-core pieces that could be successfully rotated through 360° were imaged on the DMT Digital Color CoreScan system. Contiguous pieces were imaged together wherever possible. In a number of cases, pieces with lengths in excess of 1 m were broken to fit the core scanner. One such piece (Samples 176-735B-150R-1, 0–77 cm, and 176-735B-150R-1, 77–147 cm) was originally 147 cm long. Pieces too small or uneven to be scanned effectively were also measured, to allow for them in the total core barrel lengths.

In total, more than 800 m of whole core was scanned in the unrolled mode. This accounts for approximately 93% of the material recovered during Leg 176. The scanned images were then integrated into core barrel lengths using the DMT CoreLog Software. The individual core images are imported into the CoreLog Software, then rotated so that the red china marker line, marked on the core by the structural geology team, is in the same orientation for each piece. The images can then be inserted together to reconstruct each core barrel length. Initial structural analysis of the images included the picking of pertinent structures, such as veins, fractures, and foliations. These are plotted by the software as sinusoids, from which the dip of the feature is calculated. Examples of the unrolled scanned images are shown in Figure F136. Figure F136A shows four smectite veins with dips ranging from 51° to 61°, and Figure F136B illustrates a highly foliated zone with thick mafic boundary layers. Preliminary reorientention of core pieces shows a good correlation between Leg 118 borehole televiewer (BHTV) data, unrolled core images, and Leg 176 FMS logs (Fig. F137). A westerly steeply dipping fracture is clearly identified in the core and the oriented logs. A second fracture is also identified in the FMS logs but not in the core or the BHTV image. These crosscutting fractures are dipping at 90° from each other but at this time, the lack of evidence for a second fracture in the recovered core and BHTV data prevents a classification as a conjugate pair of fractures. Final structural analysis and correlation with downhole logging data will be completed postcruise.

Approximately 48 m of split half-core was imaged in the slabbed scan mode. This represents only 5% of the core recovered. Slabbed Cores 176-735B-89R, 90R, 93R, 94R, 95R, 97R, 107R, 108R, 109R, 110R, and 111R were imaged in entirety. Selected pieces, with structural and igneous features of particular interest, were also imaged from Cores 176-735B-99R, 104R, 105R, 112R, 113R, 119R, 120R, and 121R.

F135. FMS image showing 25-m interval with structural features and lithologic boundaries, p. 241.

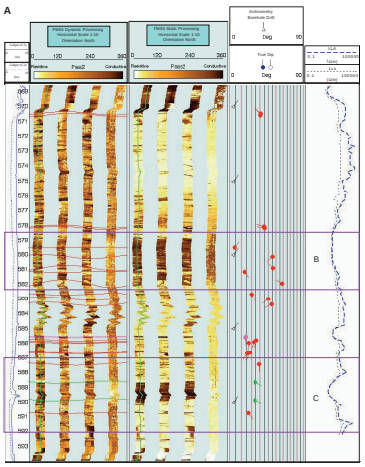

F136. Unrolled images from Hole 735B, p. 244.

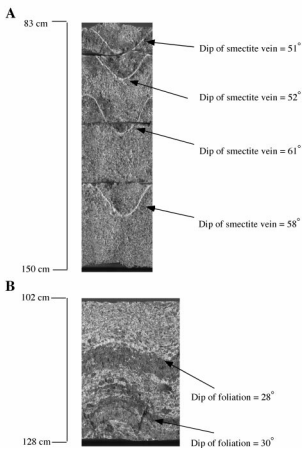

F137. Reorientation of a Core 118-735B-77R piece, p. 245.

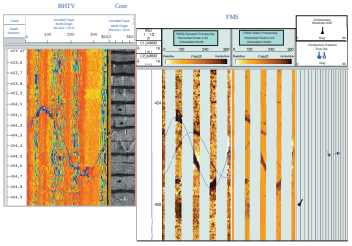

SHORE-BASED INTERPRETATION OF DOWNHOLE MEASUREMENTS AT ODP HOLE 735B[3]

A shore-based interpretation of wireline logs from ODP Hole 735B was conducted after Leg 176. The aim is to interpret logging data for a continuous lithologic reconstruction and to make the results available to the shipboard scientific party as a basis for further investigation. Similar studies were performed on several sites drilled during Leg 173 (Delius et al., 1998). Interpretation of downhole measurements provides information about the lithology, stratigraphy, and structure of the drilled lithology. This is especially important in holes with low core recovery. In holes with good core recovery, log interpretation may be based on a core-log correlation. Lithologic interpretation of logging data from Hole 735B was conducted to (1) identify the major rock

[3]A. Bartetzko, H. Delius, R. Pechnig, J. Wohlenberg, Lehr- und Forschungsgebiet für Angewandte Geophysik, Rheinisch-Westfälische Technische Hochschule Aachen, Lochnerstrasse 4-20, D-52056 Aachen, Federal Republic of Germany.
anne@sun.geophac.rwth.-aachen.de

types, (2) characterize the rock types by their in situ physical properties, and (3) reconstruct a continuous Electrofacies-Log (EFA-Log) lithologic profile.

Methods

The EFA-Log interpretation technique used in this study is a numerical procedure based on a core-log correlation to support geological interpretations. The calibration of the EFA-Logs was conducted before Leg 176 on the basis of the Leg 118 core and log data. After Leg 176, the calibration was checked with the new log data, and by using discriminant analysis, the interpretation was extended to the newly drilled section. These two steps, calibration and discriminant analysis, are explained below.

Calibration

Information about the lithology was taken from the core descriptions in Robinson, Von Herzen, et al. (1989) and the lithostratigraphy from Dick et al. (1991a). The aim of the calibration is (1) to determine the principal relations between the physical logs and the core lithology, (2) to find out which rock types can be distinguished using the logs (this is especially important in holes such as Hole 735B, in which most rock types are defined by mineralogical criteria), and (3) to define the electrofacies, the set of log responses that characterizes a rock type and distinguishes it from others (Serra, 1984). To derive relations between the lithologic characteristics and the tool responses, the data were displayed as two- or three-dimensional crossplots. Trends in the crossplots reflect the dependence of the tool responses on mineralogical, geochemical or structural variations in the rocks. In this way, definite log values are assigned to lithologic characteristics and each rock type is classified by an electrofacies (Pechnig et al., 1997).

After the calibration based on the Leg 118 data, the assignment of the electrofacies was checked with the Leg 176 log data. Only slight differences, mainly caused by different generations of tools used in the two legs, were observed. For example, during Leg 118 the Schlumberger compensated neutron tool was used to measure neutron porosity whereas during Leg 176 the Schlumberger APS was applied. The two tools are described in Eberli, Swart, Malone, et al. (1997). The transfer of the electrofacies to the newly drilled depth intervals was done by discriminant analysis. To do this, seven depth intervals characterized by well-defined, homogeneous electrofacies and a good correlation between cores and logs were chosen as key intervals. The key intervals are 85–95, 105.5–118, 130–139, 179–187, 242–295, 300–317, and 320–350 mbsf.

Discriminant Analysis

The discriminant analysis serves the following two objectives. First, it assesses the accuracy of a predefined classification. In this study, the predefined classification corresponds to the classification carried out in the calibration step. Second, the discriminant analysis gives a prediction for the classification of unclassified cases (Backhaus et al., 1989). This second objective is used here to predict and classify the new depth intervals. The analysis uses the logs to calculate linear discriminant functions that best separate the different electrofacies. These functions

are used to calculate the probability for electrofacies classification of a particular depth point. The following Leg 176 logs have been included into the discriminant analysis: electrical resistivity deep (LLd), neutron porosity (APLC), density (RHOB), photoelectric factor (PEF), capture cross section (SIGF), compressional wave velocity (V_p), shear wave velocity (V_p), and the caliper log from the FMS tool. Descriptions of the tools are given in **"Principles and Uses of the Tools,"** p. 21, in the "Explanatory Notes" chapter. Further information about the use of the discriminant analysis for the interpretation of well-logging data can be found in Doveton (1994).

After the transfer, the result of the discriminant analysis was checked and corrected. Attention was focused on depth intervals with borehole enlargements, alternating layers of small thickness, and low calculated probabilities for classification. Finally, a continuous synthetic lithologic log, the EFA-Log was established for the entire logged interval of the hole.

Results

We defined four electrofacies during the calibration with the Leg 118 data and transferred these electrofacies onto the entire logged interval of Leg 176. Figure **F138** shows the very good agreement between the logging data from Leg 118 and Leg 176. The data sets displayed in Figure **F138A** and **F138B** show nearly identical ranges and trends. The definition of the electrofacies with individual value ranges or trends in the logs is the same in the Leg 118 data, which were used for the calibration, and in the Leg 176 data.

F138. Relation of electrical resistivity deep vs. density, **p. 246.**

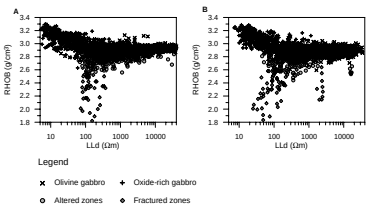

The electrofacies can be described and characterized as follows. Quantitatively, the most important electrofacies makes up 73% of the logged interval. The correlation with the cores shows that this electrofacies comprises a variety of gabbros. The classification of these rocks by the shipboard petrologic teams is based on varying amounts of plagioclase, olivine, orthopyroxene, and clinopyroxene (see **"Rock Classification,"** p. 5, in the "Explanatory Notes" chapter, this volume). These differences in mineralogy do not significantly affect the physical properties of the rocks; therefore, most of the gabbroic rocks cannot be resolved as individual electrofacies. This electrofacies is named olivine gabbro because olivine gabbro is the most abundant rock type. It is characterized by high electrical resistivities; the average value of the LLd is 3400 Ωm (Table **T20**). However, the values show a broad range from 100 to 34,000 Ωm. The log density values range from 2.7 to 3.1 g/cm³; the average value is 2.87 g/cm³. These broad ranges in resistivity and density are probably related to variations in mineral content or secondary mineralization.

T20. Average and standard deviation of log values, **p. 314.**

The oxide-rich gabbros form 19% of the EFA-Log. This electrofacies comprises rocks that are classified as different types of oxide gabbros in the core stratigraphy. Rocks with disseminated oxides could not be assigned to this electrofacies. The characteristic feature of the oxide-rich gabbroic rocks is the presence of Fe-Ti oxide minerals. The presence of these minerals causes the electrical resistivity to decrease because of electronic conduction (Pezard et al., 1991) and the density to increase because of the higher density of the ore minerals. Thus, electrical resistivities are very low, with an average value for the LLd of 135 Ωm. The density measurements are high and the values range from 2.7 to 3.3 g/cm³ with an average of 3.03 g/cm³. An additional log that shows very

characteristic responses for oxide gabbros is the photoelectric factor. The photoelectric factor depends on the average atomic number of the constituents of the rocks and is thus an indicator for mineralogy. The oxide-rich gabbros show higher values of the photoelectric factor than the olivine gabbros. The average value in the oxide-rich gabbros is 5.6 barns/e^-. In the olivine gabbros, it is 4 barns/e^-.

Altered zones form 5% of the EFA-Log. These rocks are characterized by intermediate neutron porosities with an average value of 9%. The neutron porosity log is sensitive to the hydrogen content of the formation. In these gabbroic rocks, hydrogen is bound in hydrous alteration minerals or in seawater that fills fractures. Frequently occurring hydrous alteration minerals are talc, clay minerals, smectites, and amphiboles (Robinson, Von Herzen, et al., 1989). Electrical resistivities are intermediate as well. The average value of the LLd is 920 Ωm. The density values are >2.5 g/cm³, with the average value being 2.7 g/cm³.

Fractured zones are of minor occurrence and make up 3% of the EFA-Log. They are identified by high neutron porosities (average = 23%), intermediate to low electrical resistivities (LLd average = 320 Ωm), and low density values (average = 2.41 g/cm³). Fractured zones are associated with depth intervals of reduced core recovery and borehole enlargements. The rocks are mostly disintegrated and saturated with seawater so that the log responses are strongly influenced by the presence of seawater. Some of the depth intervals that have been classified as fractured zones correspond to fault zones (e.g., at 560 mbsf; see **"Structural Geology,"** p. 54, **"Physical Properties,"** p. 77, and **"Downhole Logging,"** p. 81).

The electrical resistivity, density, neutron porosity, and photoelectric factor are the most important logs to distinguish between the electrofacies. Figure **F138** outlines the specific trends in the electrical resistivity and density for each electrofacies. Olivine gabbros show high electrical resistivities and density values that are typical of gabbros. In oxide-rich gabbros, the log responses clearly reflect the presence of the conductive and very dense oxide minerals. Electrical resistivity decreases, whereas the density increases. Altered and fractured zones are influenced by the presence of alteration minerals and seawater that fills fractures. Thus, electrical resistivities and densities are intermediate to low.

In Figure **F139** the EFA-Log summarizes the electrofacies stratigraphy for the logged interval compared to the actual lithostratigraphy (Dick et al., 1991a; see **"Igneous Petrology,"** p. 12, and the **"Core Descriptions"** contents list). The core observations show much greater variability than the EFA-Log because the logging data are unsuitable to distinguish differences in rock types based on slight variations in primary silicate mineralogy, grain size (e.g., the various types of microgabbro), or other macroscopic features (e.g., patchy olivine gabbro). Thus the 21 rock types observed on board were reduced in the EFA-Log to oxide-rich gabbro and olivine gabbro.

A very good correlation exists between the different types of oxide-rich gabbros in the core stratigraphy and in the EFA-Log. This not only applies for the correlation of single layers in the two profiles. The EFA-Log gives a very good estimate of the total amount of oxide-rich gabbros in the logged interval. Oxide-rich gabbros make up 19% of the EFA-Log and 17.7% of the core stratigraphy. However, in Figure **F139,** oxide gabbros and disseminated oxide gabbros have the same pattern so that in some depth intervals, these correlations are not obvious. This is especially the case between 170 and 223 mbsf, where most of the rocks

F139. The EFA-Log of Hole 735B, **p. 247.**

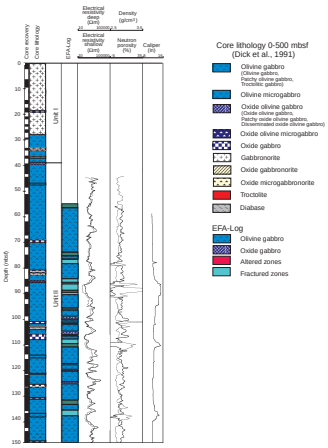

are disseminated oxide gabbros (Robinson, Von Herzen, et al., 1989). Rocks containing disseminated oxides can not be distinguished from olivine gabbros. The threshold value of 2% oxide content applied by the shipboard petrographic team to distinguish between disseminated and oxide-rich gabbros (**"Metamorphic Petrology,"** p. 10, in the "Explanatory Notes" chapter) apparently corresponds to the detection limit of the logs. Besides the lithologic information, the EFA-Log gives information about structural aspects such as alteration and fracturing. Altered zones often give hints for paleofluid circulation, whereas fractured zones can be related to recent pathways. This additional information may help to reconstruct a comprehensive model of the local geology.

REFERENCES

Agar, S.M., and Lloyd, G.E., 1997. Deformation of Fe-Ti oxides in gabbroic shear zones from the MARK area. *In* Karson, J.A., Cannat, M., Miller, D.J., and Elthon, D. (Eds.), *Proc. ODP, Sci. Results,* 153: College Station, TX (Ocean Drilling Program), 123–141.

Alexander, R.J., and Harper, G.D., 1992. The Josephine ophiolite: an ancient analogue for slow- to intermediate-spreading oceanic ridges. *In* Parson, L.M., Murton, B.J., and Browning, P. (Eds.), *Ophiolites and Their Modern Oceanic Analogues*. Geol. Soc. Spec. Publ. London, 60:3–38.

Alt, J.C., 1995. Subseafloor processes in mid-ocean ridge hydrothermal systems. *In* Humphris, S.E., Zierenberg, R., Mullineaux, L., and Thomson, R. (Eds.), *Seafloor Hydrothermal Systems: Physical, Chemical, Biological and Geological Interactions within Hydrothermal Systems*. Geophys. Monogr., Am. Geophys. Union, 91:85–114.

Alt, J.C., and Anderson, T.F., 1991. Mineralogy and isotopic composition of sulfur in layer 3 gabbros from the Indian Ocean, Hole 735B. *In* Von Herzen, R.P., Robinson, P.T., et al., *Proc. ODP, Sci. Results,* 118: College Station, TX (Ocean Drilling Program), 113–126.

Backhaus, K., Erichson, B., Plinke, W., Schuchard-Ficher, C., and Weiber, R., 1989. *Multivariate Analysemethoden* (5th ed.): Berlin (Springer-Verlag).

Barling, J., Hertogen, J., and Weis, D., 1997. Whole-rock geochemistry and Sr-, Nd-, and Pb-isotopic characteristics of undeformed, deformed, and recrystallized gabbros from Sites 921, 922, and 923 in the MARK area. *In* Karson, J.A., Cannat, M., Miller, D.J., and Elthon, D. (Eds.), *Proc. ODP, Sci. Results,* 153: College Station, TX (Ocean Drilling Program), 351–362.

Barton, P.B., Jr., and Skinner, B.J., 1979. Sulfide mineral stabilities. *In* Barnes, H. L. (Ed.), *Geochemistry of Hydrothermal Ore Deposits* (2nd ed.): New York (Wiley), 278–403.

Bloomer, S.H., Meyer, P.S., Dick, H.J.B., Ozawa, K., and Natland, J.H., 1991. Textural and mineralogic variations in gabbroic rocks from Hole 735B. *In* Von Herzen, R.P., Robinson, P.T., et al., *Proc. ODP, Sci. Results,* 118: College Station, TX (Ocean Drilling Program), 21–39.

Blumenfeld, P., and Bouchez, J.L., 1988. Shear criteria in granite and migmatite deformed in the magmatic and solid states. *J. Struct. Geol.,* 10:361–372.

Boudier, F., Le Sueur, E., and Nicolas, A., 1989. Structure of an atypical ophiolite: the Trinity Complex, eastern Klamath Mountains, California. *Geol. Soc. Am. Bull.,* 101:820–833.

Brie, A., and Saiki, Y., 1996. Practical dipole sonic dispersion correction. *Trans. Soc. Expl. Geophys.,* 178–181.

Cannat, M., Mével, C., and Stakes, D., 1991. Normal ductile shear zones at an oceanic spreading ridge: tectonic evolution of Site 735 gabbros (southwest Indian Ocean). *In* Von Herzen, R.P., Robinson, P.T., et al., *Proc. ODP, Sci. Results,* 118: College Station, TX (Ocean Drilling Program), 415–429.

Cannat, M., and Pariso, J., 1991. Partial reorientation of the deformational structures at Site 735 using paleodeclination measurements. *In* Von Herzen, R.P., Robinson, P.T., et al., *Proc. ODP, Sci. Results,* 118: College Station, TX (Ocean Drilling Program), 409–414.

Cawthorn, R.G., 1996. *Layered Intrusions:* New York (Elsevier).

Collinson, D.W., 1983. *Methods in Rock Magnetism and Palaeomagnetism: Techniques and Instrumentation:* London (Chapman and Hall).

Czamanske, G.K., and Moore, J.G., 1977. Composition and phase chemistry of sulfide globules in basalt from the Mid-Atlantic Ridge rift valley near 37°N lat. *Geol. Soc. Am. Bull.,* 88:587–599.

Delius, H., Hunze, S., Pechnig, R., Bartetzko, A., Wohlenberg, J., and Leg 173 Shipboard Scientific Party, 1998. Shore-based interpretation of downhole measure-

ments at ODP Sites 1065, 1068, and 1069. *In* Whitmarsh, R.B., Beslier, M.-O., Wallace, P.J. et al., *Proc. ODP, Init. Repts.* 173: College Station, TX (Ocean Drilling Program), 49–61.

Dick, H.J.B., Meyer, P.S., Bloomer, S., Kirby, S., Stakes, D., and Mawer, C., 1991a. Lithostratigraphic evolution of an in-situ section of oceanic Layer 3. *In* Von Herzen, R.P., Robinson, P.T., et al., *Proc. ODP, Sci. Results,* 118: College Station, TX (Ocean Drilling Program), 439–538.

Dick, H.J.B., Schouten, H., Meyer, P.S., Gallo, D.G., Bergh, H., Tyce, R., Patriat, P., Johnson, K.T.M., Snow, J., and Fisher, A., 1991b. Tectonic evolution of the Atlantis II Fracture Zone. *In* Von Herzen, R.P., Robinson, P.T., et al., *Proc. ODP, Sci. Results,* 118: College Station, TX (Ocean Drilling Program), 359–398.

Doveton, J.H., 1994. Geologic log analysis using computer methods. *AAPG Comp. Appl. Geol.,* 2.

Eberli, G.P., Swart, P.K., Malone, M.J., et al., 1997. *Proc. ODP, Init. Repts.,* 166: College Station, TX (Ocean Drilling Program).

Fox, P.J., and Opdyke, N.D., 1973. Geology of the oceanic crust: magnetic properties of oceanic rocks. *J. Geophys. Res.,* 78:5139–5154.

Früh-Green, G.L., Plas, A., and Dell' Angelo, L.N., 1996. Mineralogic and stable isotope record of polyphase alteration of upper crustal gabbros of the East Pacific Rise (Hess Deep, Site 984). *In* Mével, C., Gillis, K.M., Allan, J.F., and Meyer, P.S. (Eds.), *Proc. ODP, Sci. Results,* 147: College Station, TX (Ocean Drilling Program), 235–254.

Gallinatti, B.C, 1984. Initiation and collapse of active circulation in a hydrothermal system at the Mid-Atlantic Ridge, 23°N. *J. Geophys. Res.,* 89:3275–3289.

Gillis, K., Mével, C., Allan, J., et al., 1993. *Proc. ODP, Init. Repts.,* 147: College Station, TX (Ocean Drilling Program).

Gillis, K.M., 1996. Rare earth element constraints on the origin of amphibole in gabbroic rocks from Site 894, Hess Deep. *In* Mével, C., Gillis, K.M., Allan, J.F., and Meyer, P.S. (Eds.), *Proc. ODP, Sci. Results,* 147: College Station, TX (Ocean Drilling Program), 59–75.

Gillis, K.M., Thompson, G., and Kelley, D.S., 1993b. A view of the lower crustal component of hydrothermal systems at the Mid-Atlantic Ridge. *J. Geophys. Res.,* 98:19597–19619.

Grove, T.L., and Baker, M.B., 1984. Phase equilibrium controls on the tholeiitic versus calc-alkaline differentiation trends. *J. Geophys. Res.,* 89:3253–3274.

Grove, T.L., Kinzler, R.J., and Bryan, W.B., 1992. Fractionation of mid-ocean ridge basalt (MORB). *In* Morgan, J.P., Blackman, D.K., and Sinton, J.M. (Eds.), *Mantle Flow and Melt Generation at Mid-Ocean Ridges.* Geophys. Monogr., Am. Geophys. Union, 71:281–310.

Haggerty, S.E., 1991. Oxide textures: a mini-atlas. *In* Lindsley, D.H. (Ed.), *Oxide Minerals: Petrologic and Magnetic Significance.* Rev. Mineral., 25:129–219.

Hébert, R., and Constantin, M., 1991. Petrology of hydrothermal metamorphism of oceanic layer 3: implications for sulfide parageneses and redistribution. *Econ. Geol.,* 86:472–485.

Heider, F., Zitzelberger, A., and Fabian, K., 1996. Magnetic susceptibility and remanent coercive force in grown magnetite crystals from 0.1µm to 6 mm. *Phys. Earth Planet. Inter.,* 93:239–256.

Henderson, P., 1970. The significance of the mesostasis of basic layered igneous rocks. *J. Petrol.,* 11:463–473.

Hopkinson, L., and Roberts, S., 1995. Ridge axis deformation and coeval melt migration within layer 3 gabbros: evidence from the Lizard Complex. *U.K. Contrib. Mineral. Petrol.,* 121:126–138.

Iturrino, G.J., Christensen, N.I., Kirby, S., and Salisbury, M.H., 1991. Seismic velocities and elastic properties of oceanic gabbroic rocks from Hole 735B. *In* Von Herzen, R.P., Robinson, P.T., et al., *Proc. ODP, Sci. Results,* 118: College Station, TX (Ocean Drilling Program), 227–244.

Ji, S., and Mainprice, D., 1988. Natural deformation fabrics of plagioclase: implications for slip systems and seismic anisotropy. *Tectonophysics,* 147:145–163.

Juster, T.C., Grove, T.L., and Perfit, M.R., 1989. Experimental constraints on the generation of FeTi basalts, andesites, and rhyodacites at the Galapagos Spreading Center, 85°W and 95°W. *J. Geophys. Res.,* 94:9251–9274.

Kelley D.S., 1996. Methane-rich fluids in the oceanic crust. *J. Geophys. Res.,* 101:2943–2962.

————, 1997. Fluid evolution in slow-spreading environments. *In* Karson, J.A., Cannat, M., Miller, D.J., and Elthon, D. (Eds.), *Proc. ODP, Sci. Results,* 153: College Station, TX (Ocean Drilling Program), 399–415.

Kent, D.V., Honnorez, B.M., Opdyke, N.D., and Fox, P.J., 1978. Magnetic properties of dredged oceanic gabbros and source of marine magnetic anomalies. *Geophys. J. R. Astron. Soc.,* 55:513–537.

Kikawa, E., and Ozawa, K., 1992. Contribution of oceanic gabbros to sea-floor spreading magnetic anomalies. *Science,* 258:796–799.

Kikawa, E., and Pariso, J.E., 1991. Magnetic properties of gabbros from Hole 735B, Southwest Indian Ridge. *In* Von Herzen, R.P., Robinson, P.T., et al., *Proc. ODP, Sci. Results,* 118: College Station, TX (Ocean Drilling Program), 285–307.

Kimball, C.V., and Marzetta, T.L., 1984. Semblance processing of borehole acoustic array data. *Geophysics,* 49:274–281.

McFadden, P.L., and Reid, A.B., 1982. Analysis of paleomagnetic inclination data. *Geophys. J. R. Astron. Soc.,* 69:307–319.

Mével, C., 1987. Evolution of oceanic gabbros from DSDP Leg 82: influence of the fluid phase on metamorphic crystallizations. *Earth Planet. Sci. Lett.,* 83:67–79.

Mével, C., Cannat, M., Gente, P., Marion, E., Auzende, J.-M., and Karson, J.A., 1991. Emplacement of deep crustal and mantle rocks on the west median valley wall of the MARK area (MAR 23°N). *Tectonophysics,* 190:31–53.

Miller, B., and Paterson, S.R., 1994. The transition from magmatic to high-temperature solid-state deformation: implications from the Mount Stuart batholith, Washington. *J. Struct. Geol.,* 16:853–865.

Muller, M.R., Robinson, C.J., Minshull, R.S., and Bickle, M.J., 1997. Thin crust beneath ocean drilling program borehole 735B at the Southwest Indian Ridge? *Earth Planet. Sci. Lett.,* 148:93–108.

Natland, J.H., Meyer, P.S., Dick, H.J.B., and Bloomer, S.H., 1991. Magmatic oxides and sulfides in gabbroic rocks from Hole 735B and the later development of the liquid line of descent. *In* Von Herzen, R.P., Robinson, P.T., et al., *Proc. ODP, Sci. Results,* 118: College Station, TX (Ocean Drilling Program), 75–111.

Nicolas, A., 1989. *Structure of Ophiolites and Dynamics of the Oceanic Lithosphere:* Dordrecht (Kluwer).

Nicolas, A., Boudier, F., and Ildefonse, B., 1996. Variable crustal thickness in the Oman ophiolite: implication for oceanic crust. *J. Geophys. Res.,* 101:17941–17950.

Ozawa, K., Meyer, P.S., and Bloomer, S.H., 1991. Mineralogy and textures of iron-titanium oxide gabbros and associated olivine gabbros from Hole 735B. *In* Von Herzen, R.P., Robinson, P.T., et al., *Proc. ODP, Sci. Results,* 118: College Station, TX (Ocean Drilling Program), 41–73.

Pariso, J.E., and Johnson, H.P., 1993. Do layer 3 rocks make a significant contribution to marine magnetic anomalies? In situ magnetization of gabbros at Ocean Drilling Program Hole 735B. *J. Geophys. Res.,* 98:16033–16052.

Pariso, J.E., Scott, J.H., Kikawa, E., and Johnson, H.P., 1991. A magnetic logging study of Hole 735B gabbros at the Southwest Indian Ridge. *In* Von Herzen, R.P., Robinson, P.T., et al., *Proc. ODP, Sci. Results,* 118: College Station, TX (Ocean Drilling Program), 309–321.

Paterson, S.R., Vernon, R.H., and Tobisch, O.T., 1989. A review of criteria for the identification of magmatic and tectonic foliations in granitoids. *J. Struct. Geol.,* 11:349–363

Pechnig, R., Haverkamp, S., Wohlenberg, J., Zimmermann, J., and Burkhardt, H., 1997. Integrated log interpretation in the German Deep Drilling Program: lithology, porosity and fracture zones. *J Geophys. Res.,* 102:18363–18390.

Pezard, P.A., Howard, J.J., and Goldberg, D., 1991. Electrical conduction in oceanic gabbros, Hole 735B, Southwest Indian Ridge. *In* Von Herzen, R.P., Robinson, P.T., et al., *Proc. ODP, Sci. Results,* 118: College Station, TX (Ocean Drilling Program), 323–331.

Robinson, P.T., Dick, H.J.B., and Von Herzen, R.P., 1991. Metamorphism and alteration in oceanic layer 3: Hole 735B. *In* Von Herzen, R.P., Robinson, P.T., et al., *Proc. ODP, Sci. Results,* 118: College Station, TX (Ocean Drilling Program), 541–552.

Robinson, P.T., Von Herzen, R., et al., 1989. *Proc. ODP, Init. Repts.,* 118: College Station, TX (Ocean Drilling Program).

Serra, O., 1984. *Fundamentals of Well-Log Interpretation (Vol. 1): The Acquisition of Logging Data:* Dev. Pet. Sci., 15A: Amsterdam (Elsevier).

Shipboard Scientific Party, 1989. Site 735. *In* Robinson, P.T., Von Herzen, R., et al., *Proc. ODP, Init. Repts.,* 118: College Station, TX (Ocean Drilling Program), 89–222.

Sinton, J.M., and Detrick, R.S., 1992. Mid-ocean ridge magma chambers. *J. Geophys. Res.,* 97:197–216.

Stakes, D., Mével, C., Cannat, M., and Chaput, T., 1991. Metamorphic stratigraphy of Hole 735B. *In* Von Herzen, R.P., Robinson, P.T., et al., *Proc. ODP, Sci. Results,* 118: College Station, TX (Ocean Drilling Program), 153–180.

Swift, S.A., Hoskins, H., and Stephen, R.A., 1991. Seismic stratigraphy in a transverse ridge, Atlantis II Fracture Zone. *In* Von Herzen, R.P., Robinson, P.T., et al., *Proc. ODP, Sci. Results,* 118: College Station, TX (Ocean Drilling Program), 219–226.

Tarling, D.H., and Hrouda, F., 1993. *The Magnetic Anisotropy of Rocks:* London (Chapman and Hall).

Toplis, M.J., and Carroll, M.R., 1995. An experimental study of the influence of oxygen fugacity on Fe-Ti oxide stability, phase relations, and mineral-melt equilibria in ferro-basaltic systems. *J. Petrol.,* 36:1137–1170.

Vanko, D.A., and Stakes, D.S., 1991. Fluids in oceanic layer 3: evidence from veined rocks, Hole 735B, Southwest Indian Ridge. *In* Von Herzen, R.P., Robinson, P.T., et al., *Proc. ODP, Sci. Results,* 118: College Station, TX (Ocean Drilling Program), 181–215.

Wager, L.R., and Brown, G.M., 1968. *Layered Igneous Rocks:* London (Oliver and Boyd).

Wager, L.R., Brown, G.M., and Wadsworth, W.J., 1960. Types of igneous cumulates. *J. Petrol.,* 1:73–85.

Figure F1. A photomosaic of the hard-rock base at Hole 735B installed during Leg 118. The smaller image to the left shows the hole itself through the open throat of the base. The base is 17 ft by 17 ft by 11 ft high. The mosaic was constructed from frames grabbed from a video sequence obtained near the seafloor using the Canadian *ROPOS* in the spring of 1998. The survey was carried out using the vessel *James Clark Ross* of the British Antarctic Survey. The figure was provided courtesy of the expedition's co-chief scientists, H.J.B. Dick, P.T. Robinson, C. MacLeod, and S. Allerton.

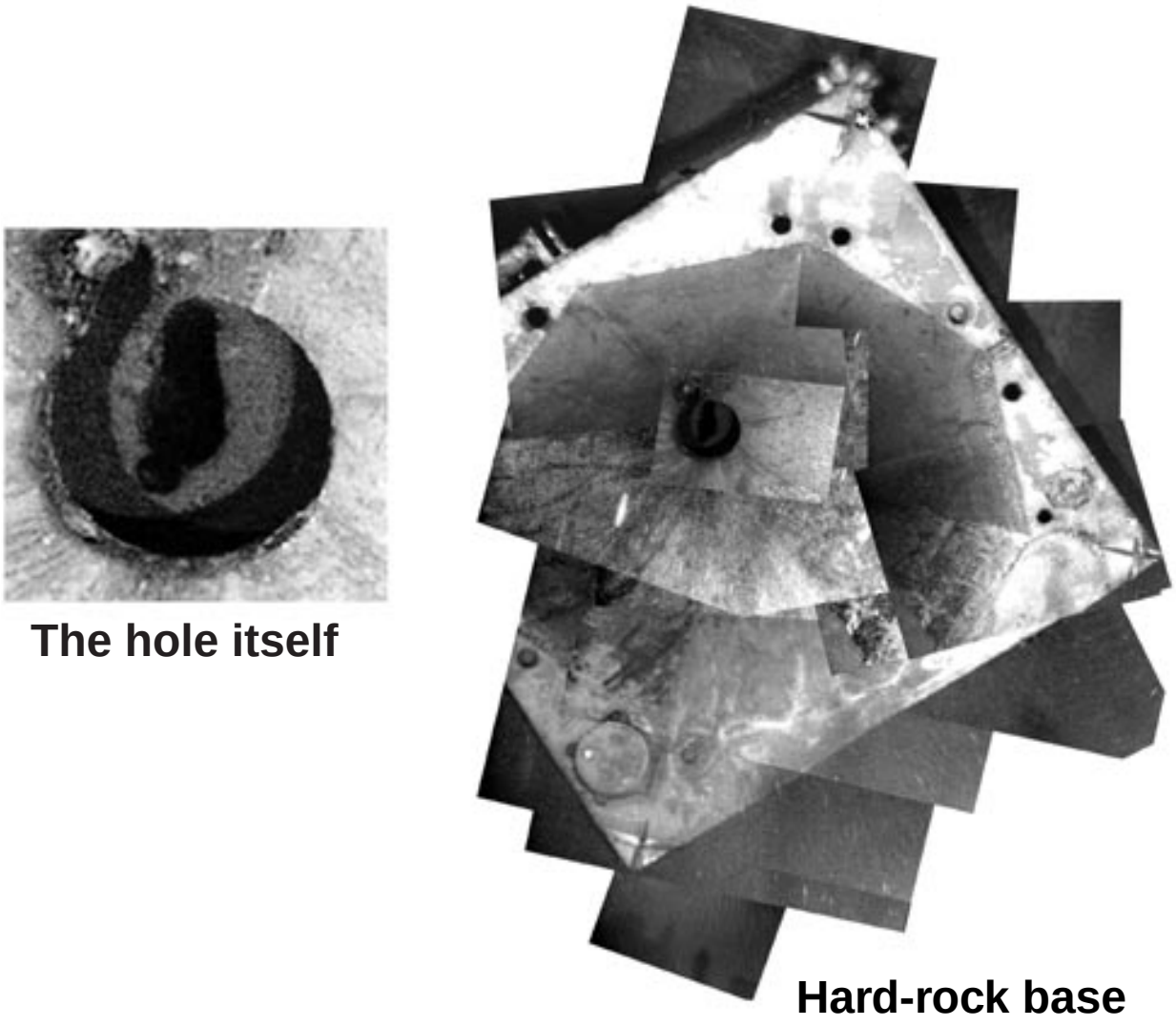

Figure F2. Lithostratigraphic variations in Hole 735B including the core recovered during Legs 118 and 176. **A.** Relative abundances of rock types averaged over 20 intervals. Lithologic boundaries of Units VII through XII of Leg 176 are shown together with those of Units I through VI of Leg 118 (in italics). Cross-hatched area indicates the extent of a large crystal-plastic shear zone. Troctolitic gabbro encompasses both troctolites and troctolitic gabbro. Oxide gabbro combines oxide gabbro, oxide olivine gabbro, and oxide troctolitic gabbro. Gabbronorite includes orthopyroxene-bearing gabbro and gabbronorite, and orthopyroxene-bearing oxide gabbro and gabbronorite. **B.** Occurrence of intervals of pegmatitic gabbro. **C.** Occurrence of microgabbro. **D.** Occurrence of igneous layering.

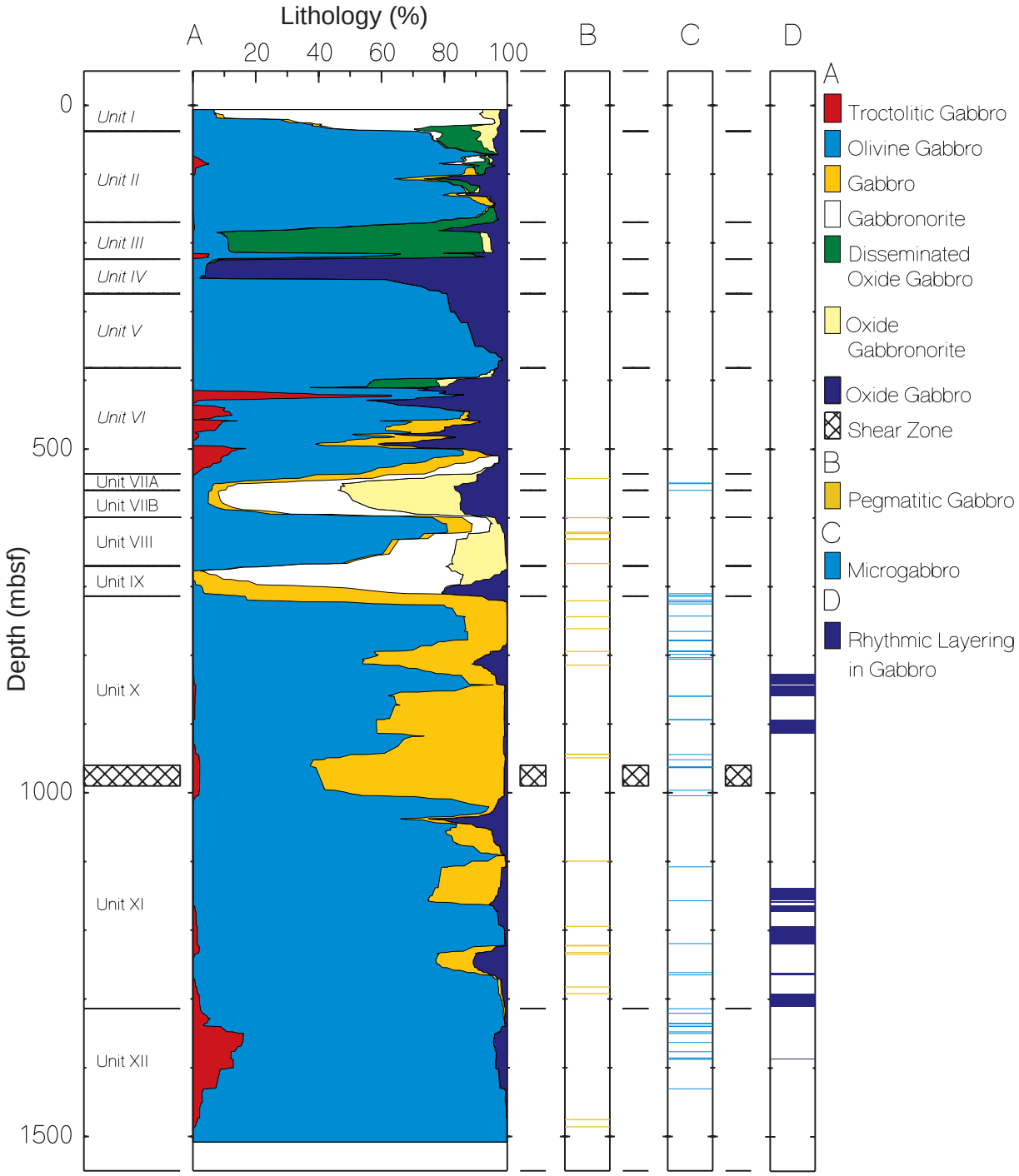

Figure F3. Relative abundances of olivine, plagioclase, and augite for the 456 lithologic intervals drilled during Leg 176. Modal compositions are determined macroscopically and represent the averages of each interval.

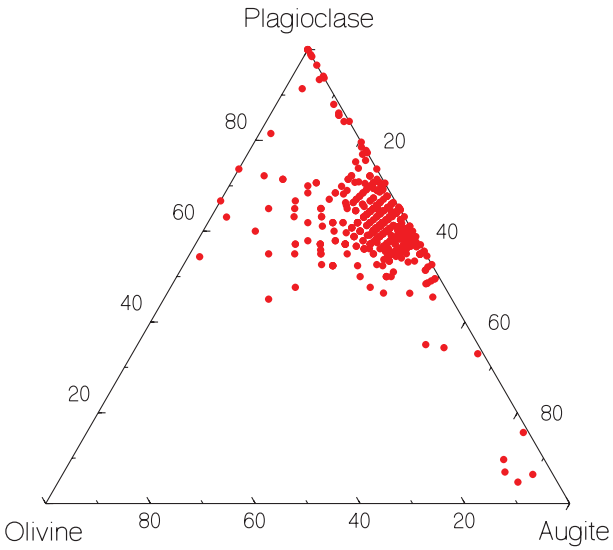

Figure F4. Relative abundances of orthopyroxene, plagioclase, and augite in the 456 lithologic intervals drilled during Leg 176. Modal compositions are determined macroscopically and represent the averages of each interval.

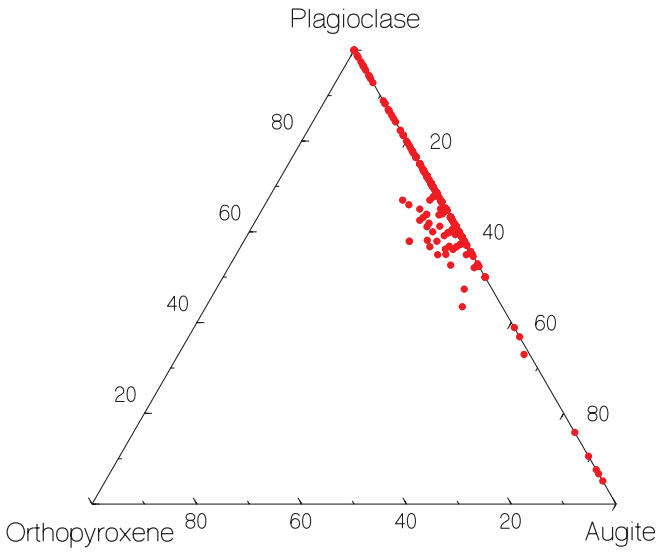

Figure F5. Olivine gabbro with ophitic texture (interval 176-735B-106R-3, 113–121 cm).

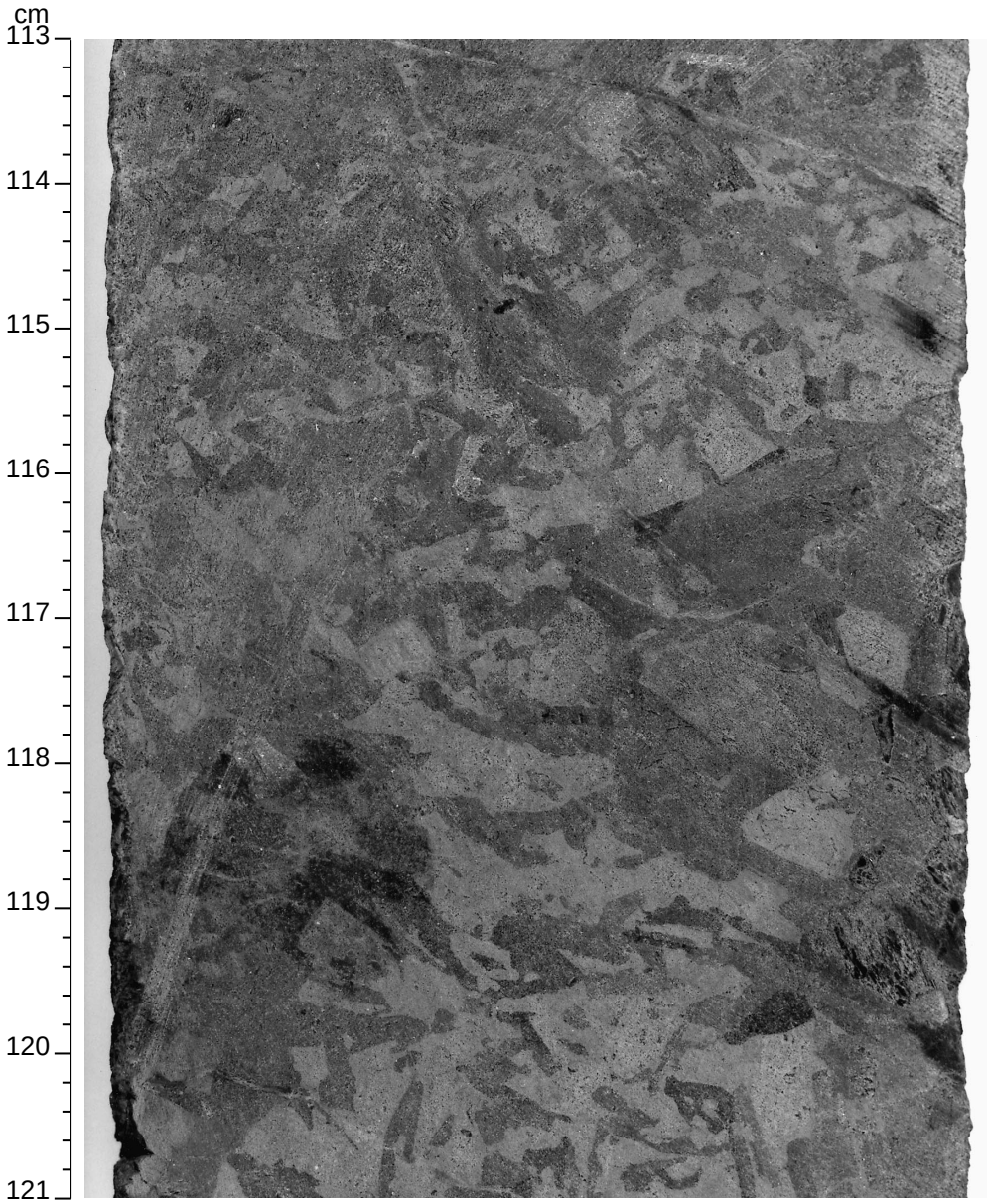

Figure F6. Coarse-grained olivine gabbro with intergranular texture (interval 176-735B-107R-1, 42–54 cm).

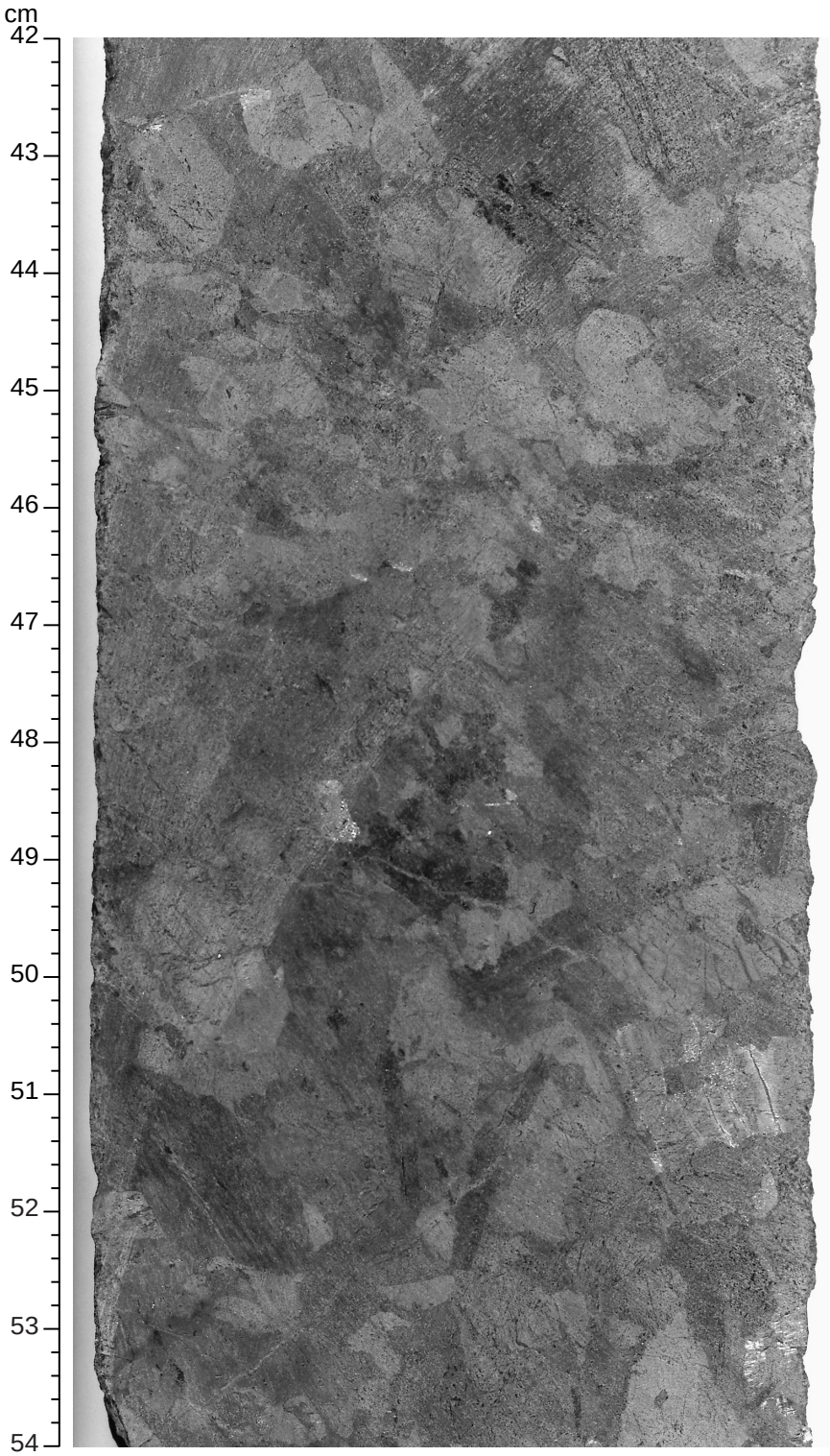

Figure F7. Contact between troctolitic microgabbro and olivine gabbro with morphology typical of the upper part of the Leg 176 core (interval 176-735B-178R-7, 20–30 cm).

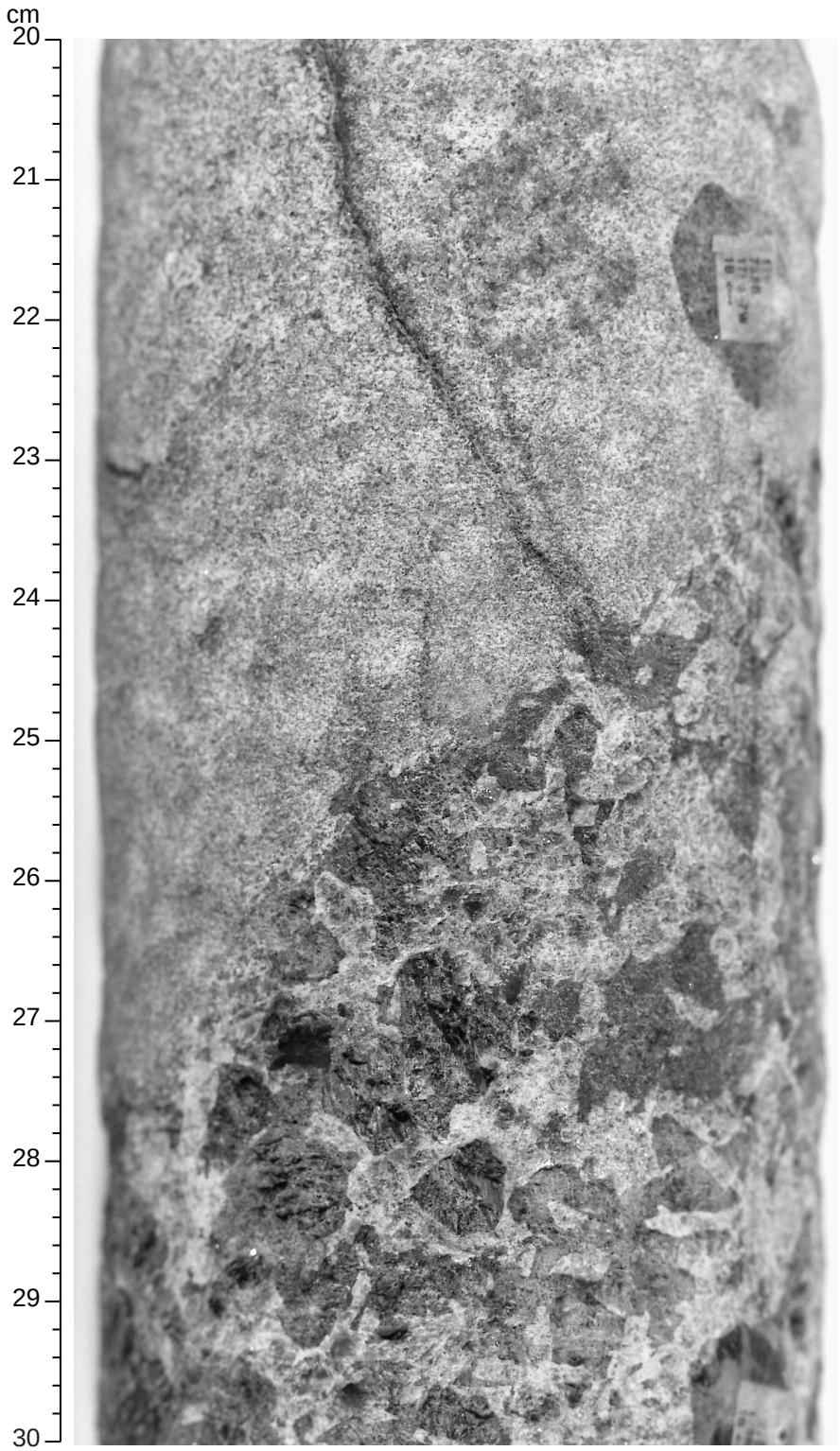

Figure F8. Microgabbro intruding olivine gabbro with morphology typical of the lower part of the Leg 176 core (Sections 176-735B-189R-3 through 189R-4).

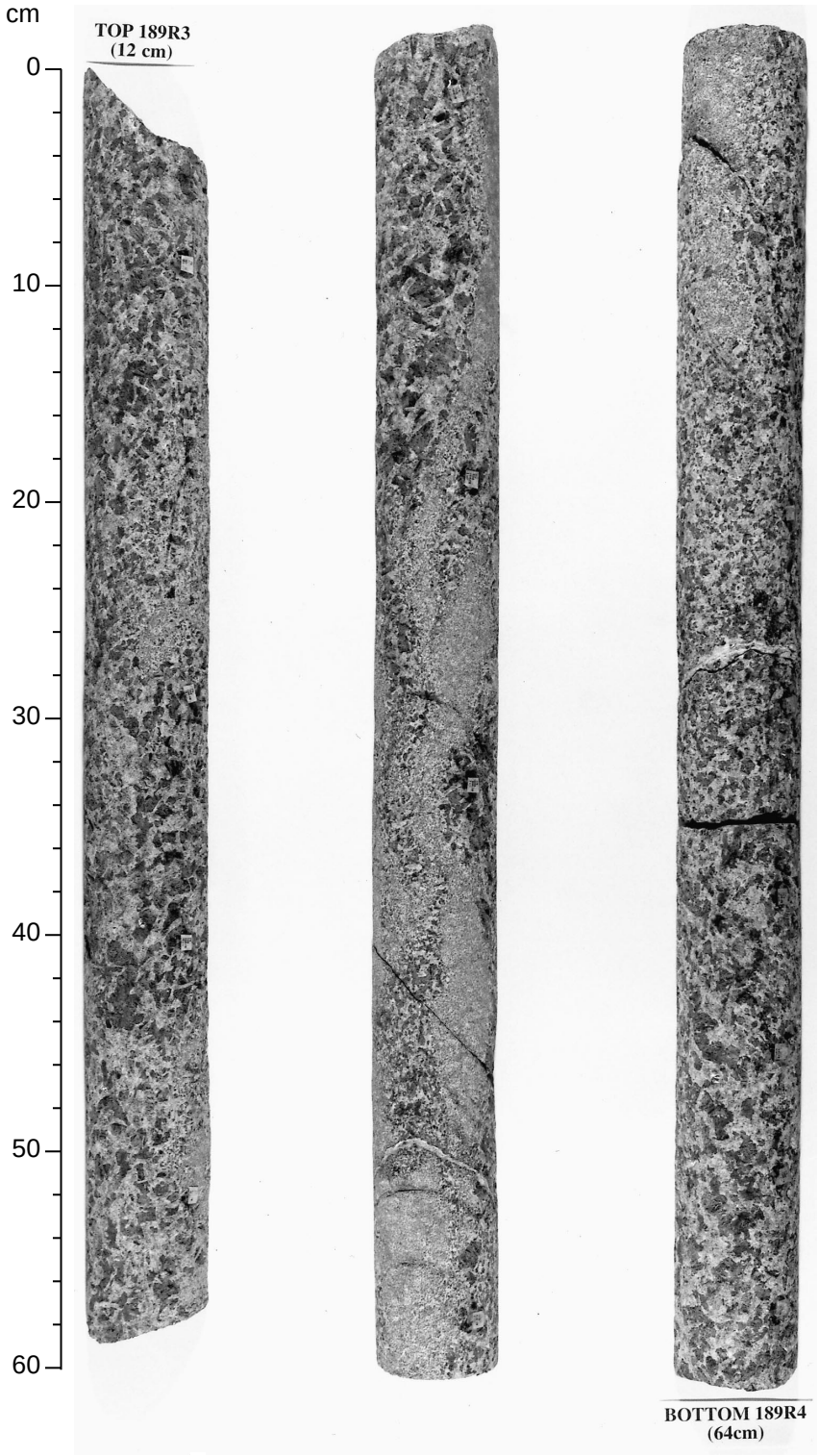

Figure F9. Gabbro with variable texture (interval 176-735B-194R-3, 0–50 cm).

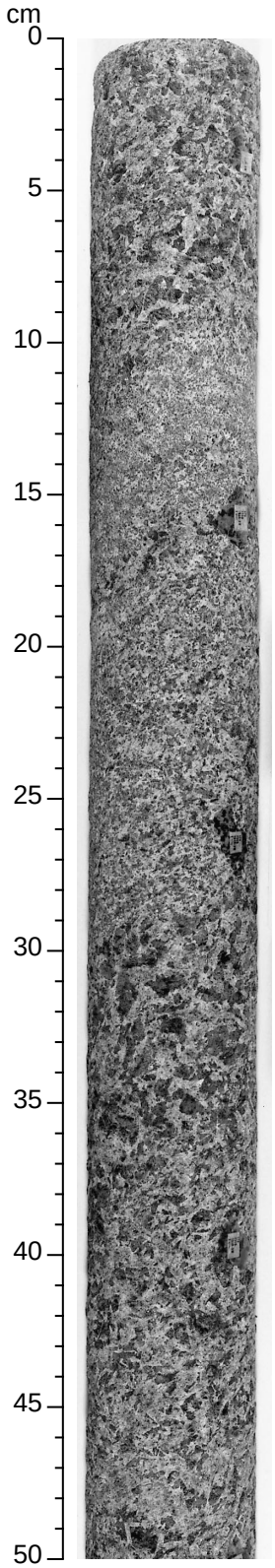

Figure F10. Typical olivine gabbro (interval 176-735B-195R-8, 0–36 cm).

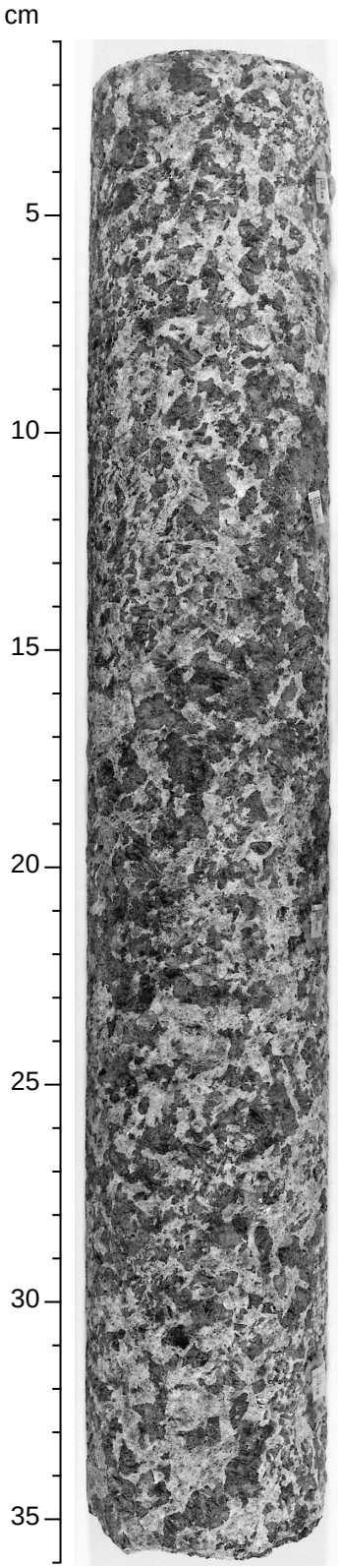

Figure F11. Typical gabbro (interval 176-735B-196R-6, 6–35 cm).

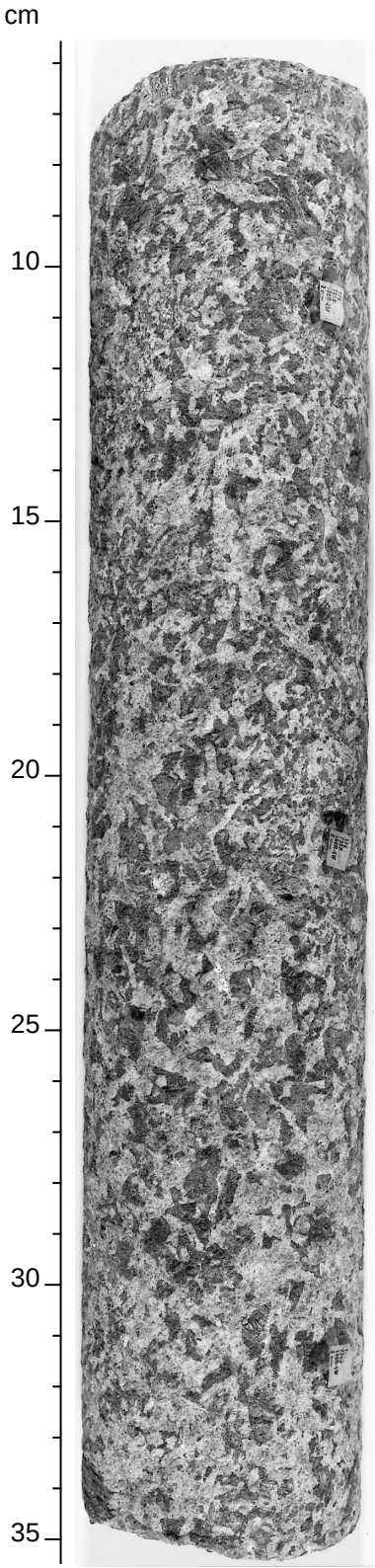

Figure F12. Schematic representation of intrusive contact types. **A.** Intrusive contact with broken country rock grain boundaries and finer grained zone at the intrusive margin. **B.** Sutured contact showing infilling of intrusive lithology around grain boundaries of the country rock.

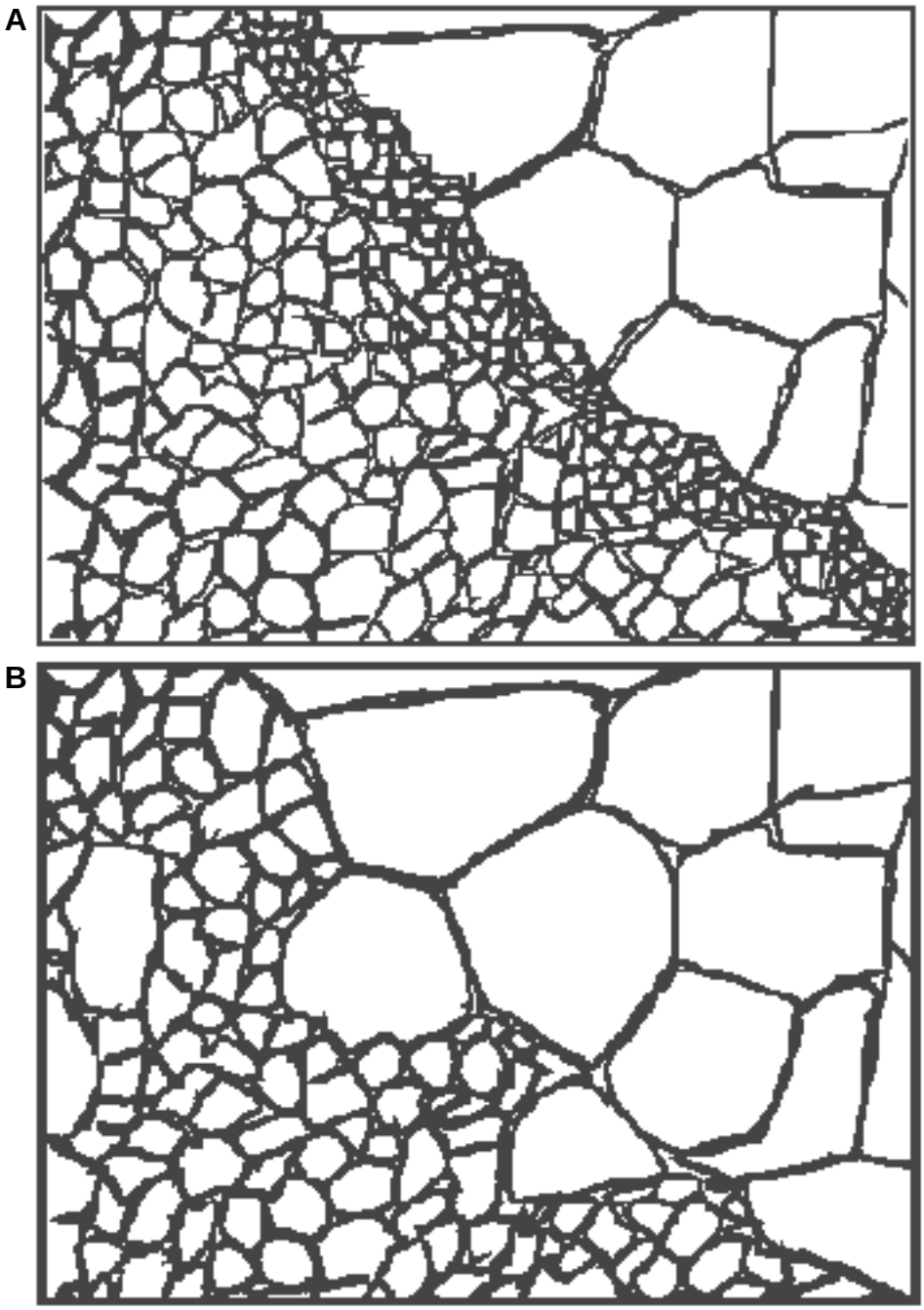

Figure F13. Correlation of grain size between plagioclase, olivine, and clinopyroxene as measured in 146 thin sections of relatively undeformed samples using a micrometer ocular for scale. Olivine gabbro includes troctolitic gabbro, gabbronorite includes orthopyroxene-bearing gabbro. A good correlation between the grain sizes of the three minerals is apparent except for the coarser grain-size range (>15 to 20 mm), where the correlation is less clear. This breakdown at higher grain sizes is probably the result of the truncation at the limit of the thin section of larger crystals. **A.** Olivine vs. plagioclase. **B.** Augite vs. olivine. **C.** Augite vs. plagioclase.

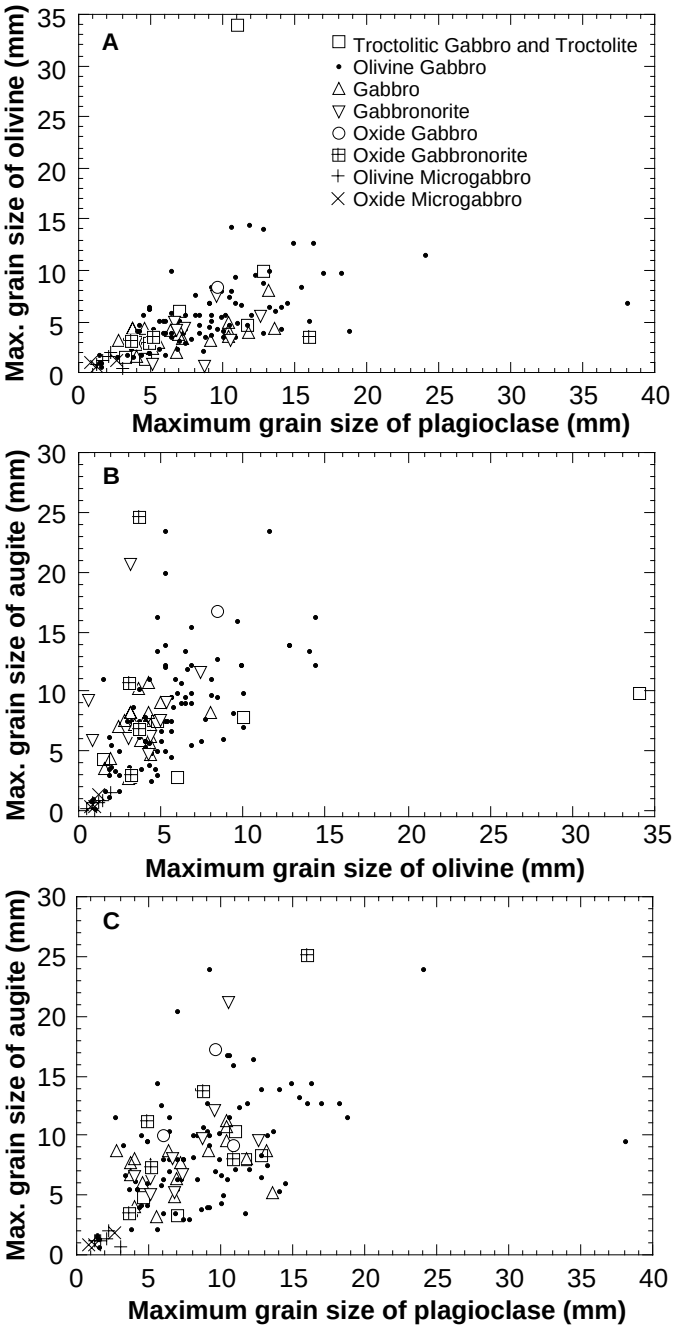

Figure F14. Variations of the average maximum grain sizes of plagioclase, augite, olivine, and whole rock with depth in Hole 735B plotted by interval (456 points). Rock averages were calculated at each interval from the maximum grain sizes reported for each mineral weighted according to the mode. Also plotted is a smoothed line calculated as a running average over 10-m intervals. Major peaks in average grain size are noted at 510, 635, 825, 940, 100, 1215, 1300, 1425, and 1480 mbsf.

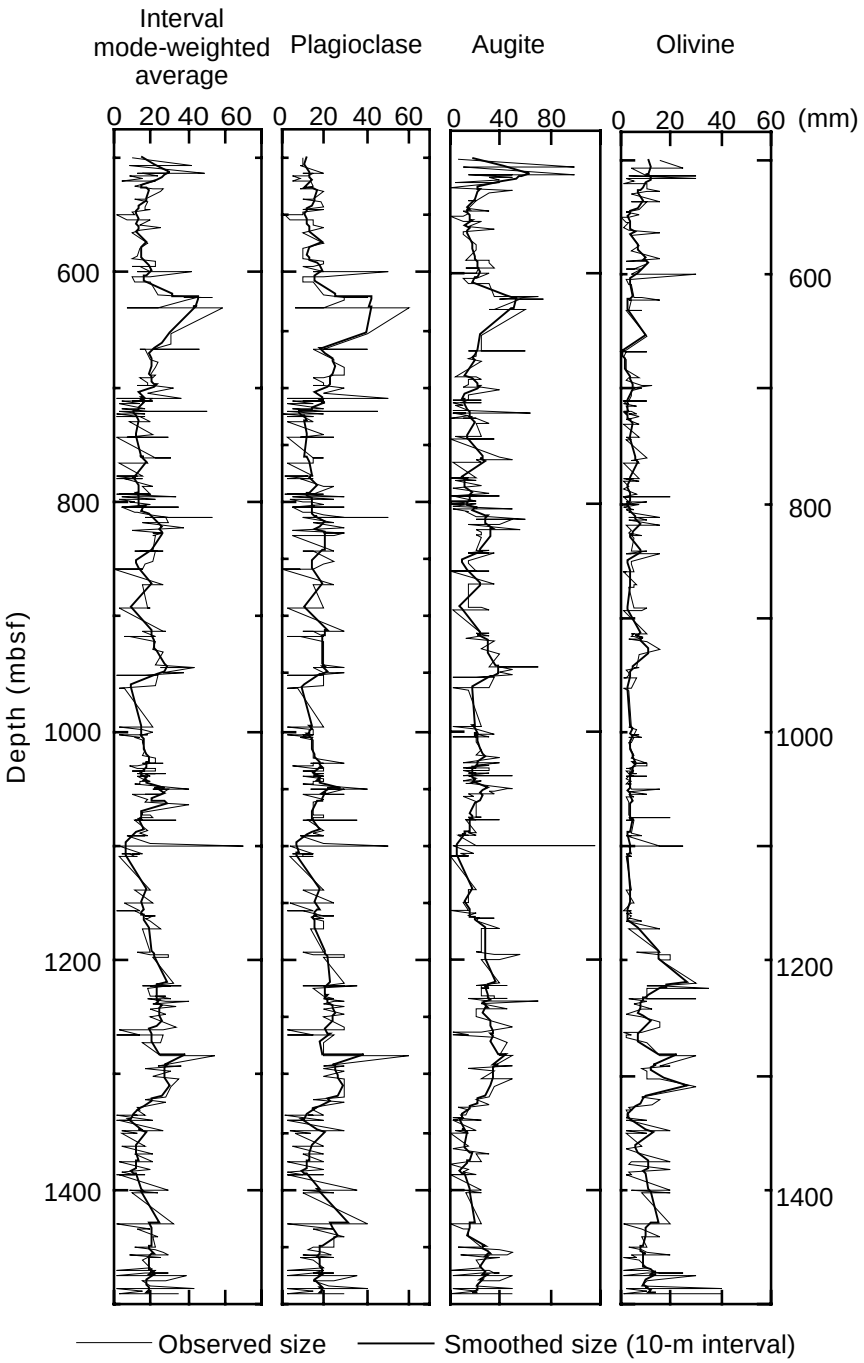

Figure F15. A. Plot of modal percent clinopyroxene vs. modal percent olivine in Leg 176 samples measured in thin section. **B.** Plot of modal percent clinopyroxene vs. modal percent plagioclase in Leg 176 samples measured in thin section. Gabbronorite and oxide gabbronorite include orthopyroxene-bearing gabbro and gabbronorite. Orthopyroxene-bearing gabbros and oxide orthopyroxene-bearing gabbros are grouped with gabbronorite and oxide gabbronorite, respectively.

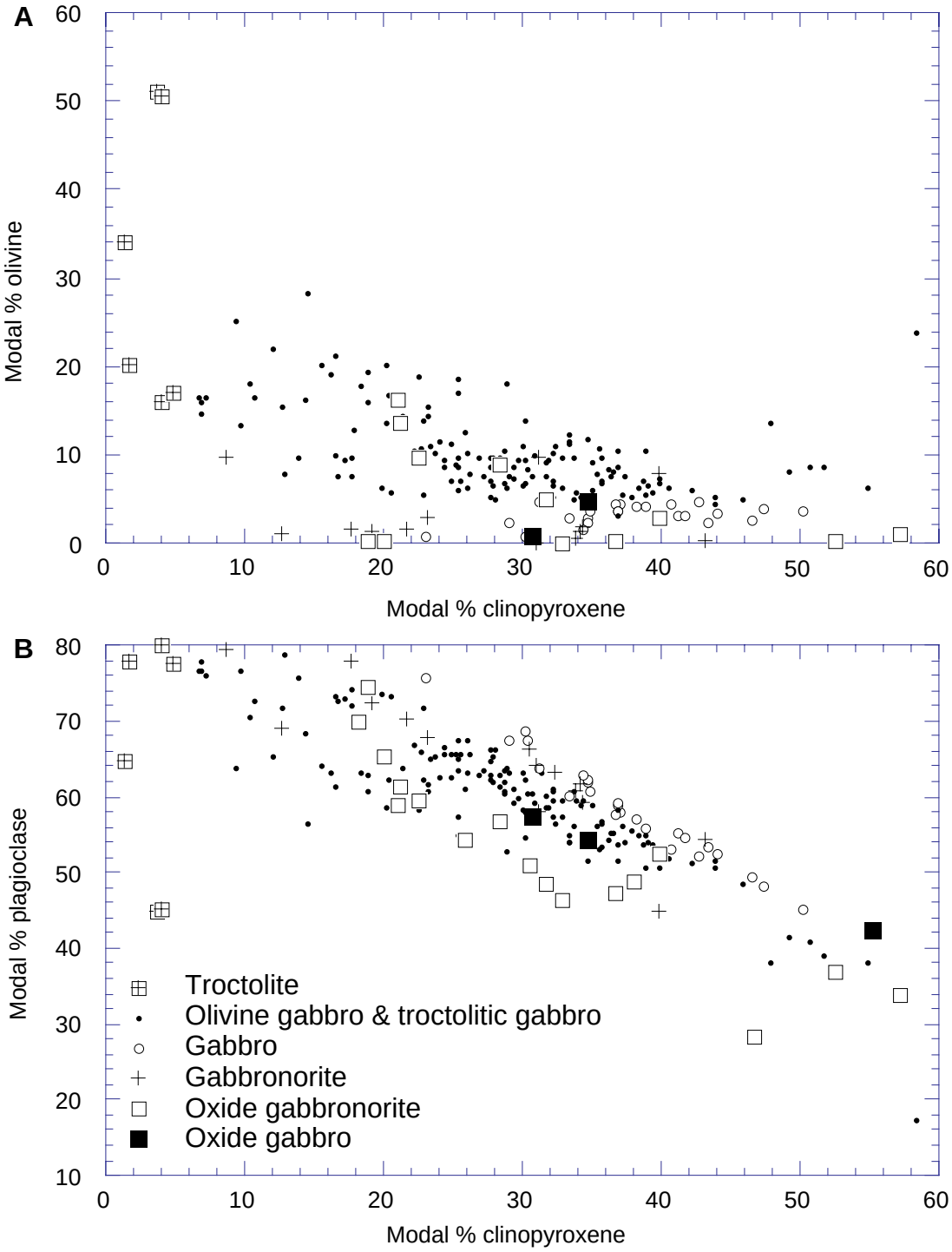

Figure F16. Photomicrograph in cross-polarized light of two types of exsolution textures in augite (Sample 176-735B-138R-7, 0–4 cm). On the left, the augite has abundant fine-scale, planar exsolution; on the right, the augite has course tabular exsolution. Both textures are formed by the exsolution of low-Ca pyroxene in an augite host. Field of view = 2.8 mm.

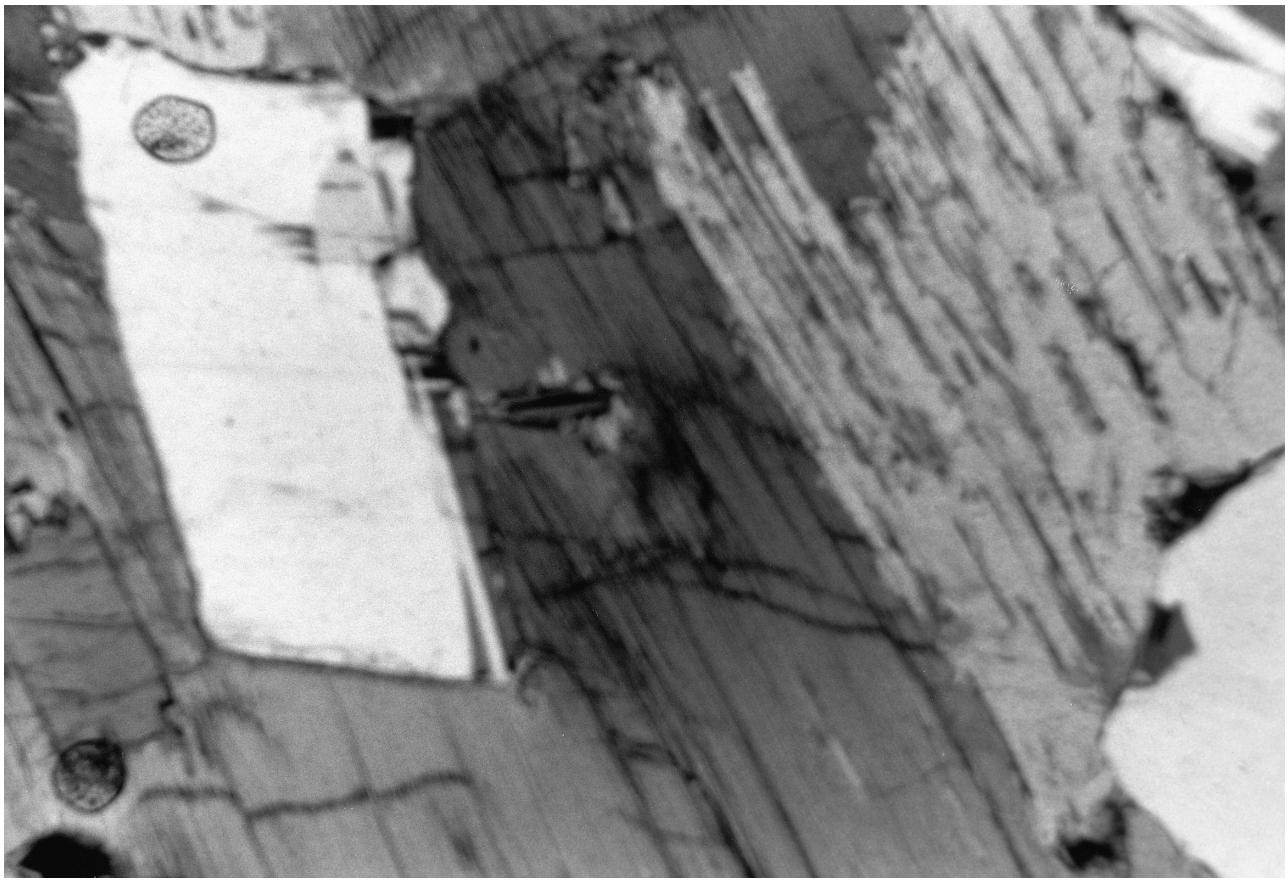

Figure F17. Photomicrograph of dark brown rods and opaque dendritic patches in olivine in thin section (Sample 176-735B-132R-3, 36–39 cm). Field of view = 0.7 mm.

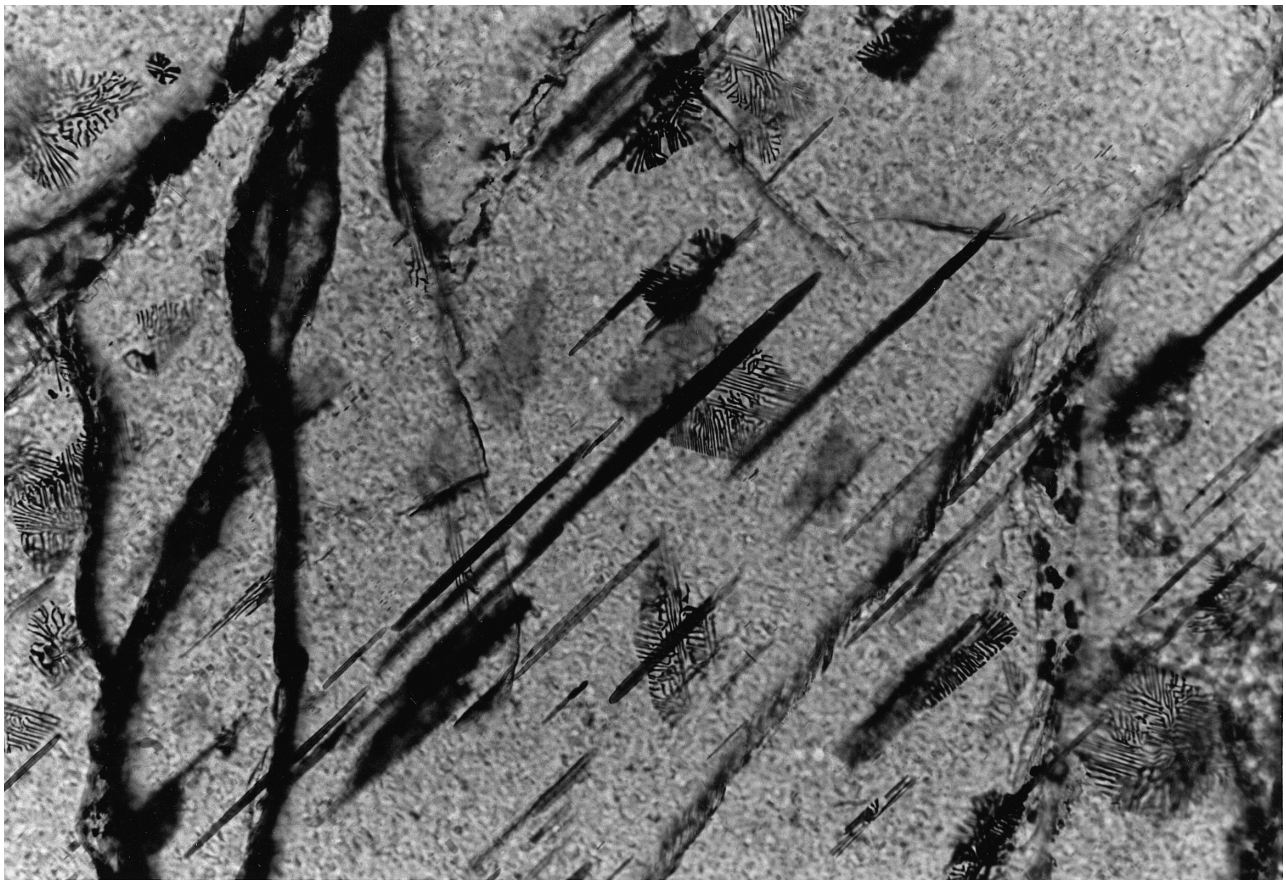

Figure F18. Photomicrograph of opaque needles in plagioclase in thin section (Sample 176-735B-137R-3, 34–38 cm). Field of view = 0.3 mm.

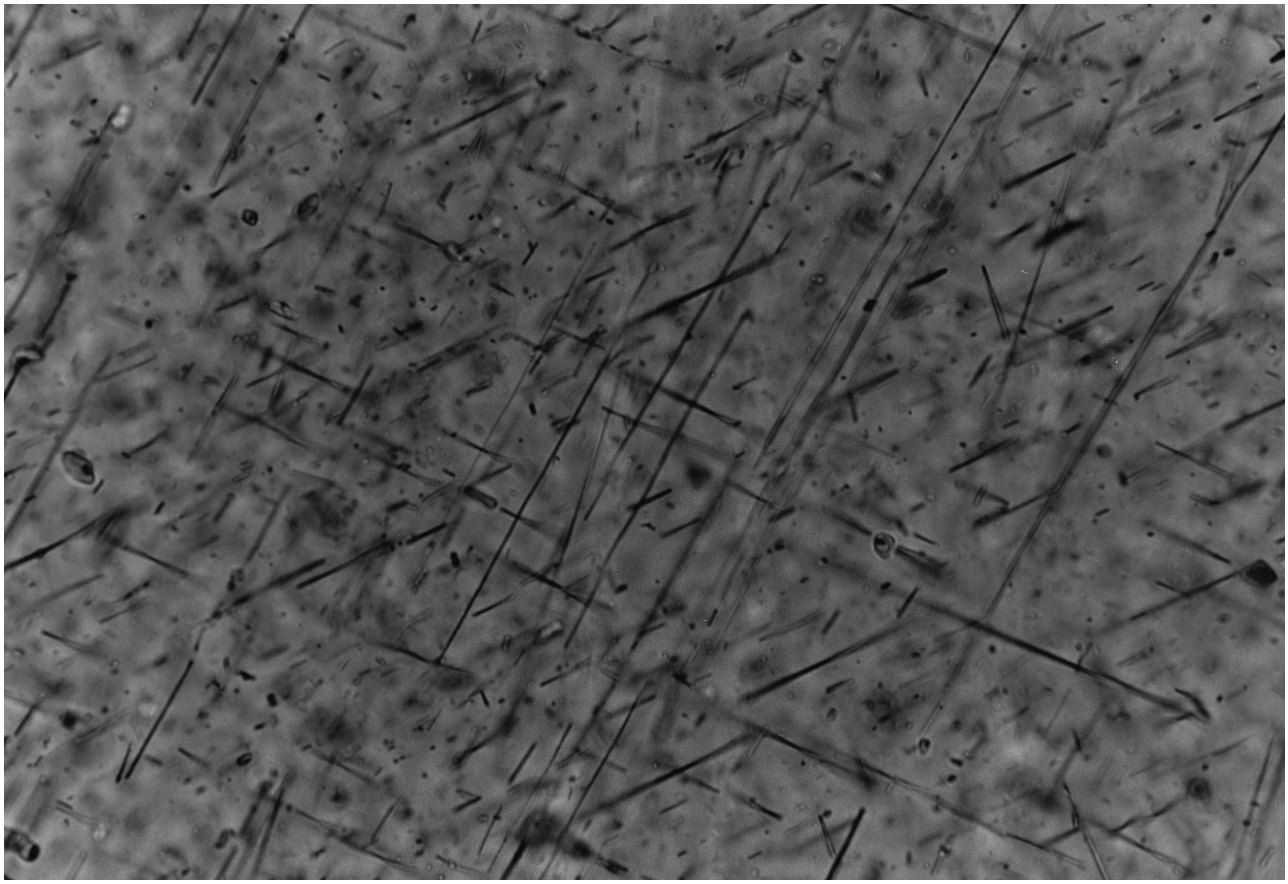

Figure F19. A. Augite/plagioclase vs. CaO/Al_2O_3 for Leg 176 rocks. **B.** TiO_2 (wt%) vs. oxide (vol%) mode of Leg 176 rocks. Modes by point counting and chemical analysis by X-ray fluorescence on samples adjacent to the thin-section billets. Gabbronorite and oxide gabbronorite include orthopyroxene-bearing gabbro and gabbronorite.

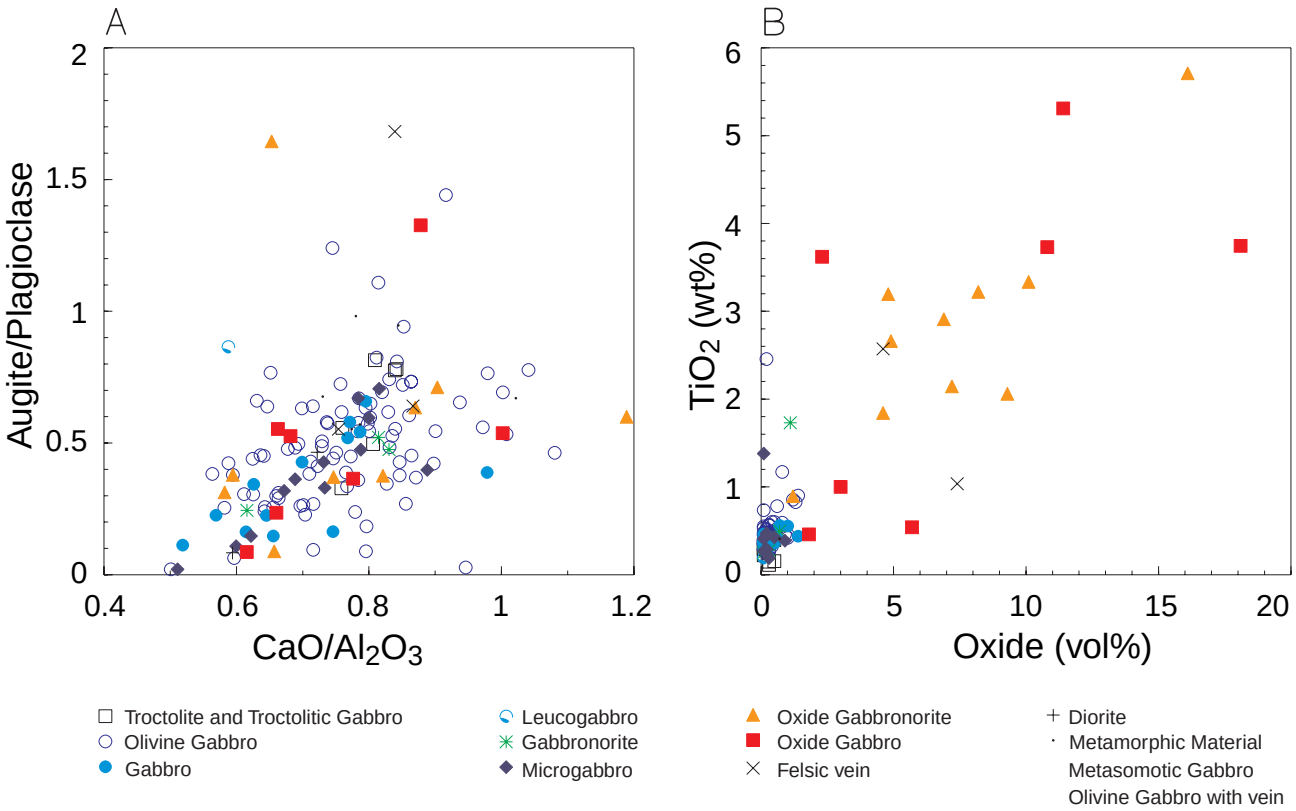

Figure F20. Ca# vs. Mg# for Leg 176 rocks. Individual analysis has same symbols as in Figure F19, p. 119. Averages for rock types are shown as large diamonds with ±1 standard deviation bars. Mg# was calculated assuming Fe^{2+} is 90% of total Fe.

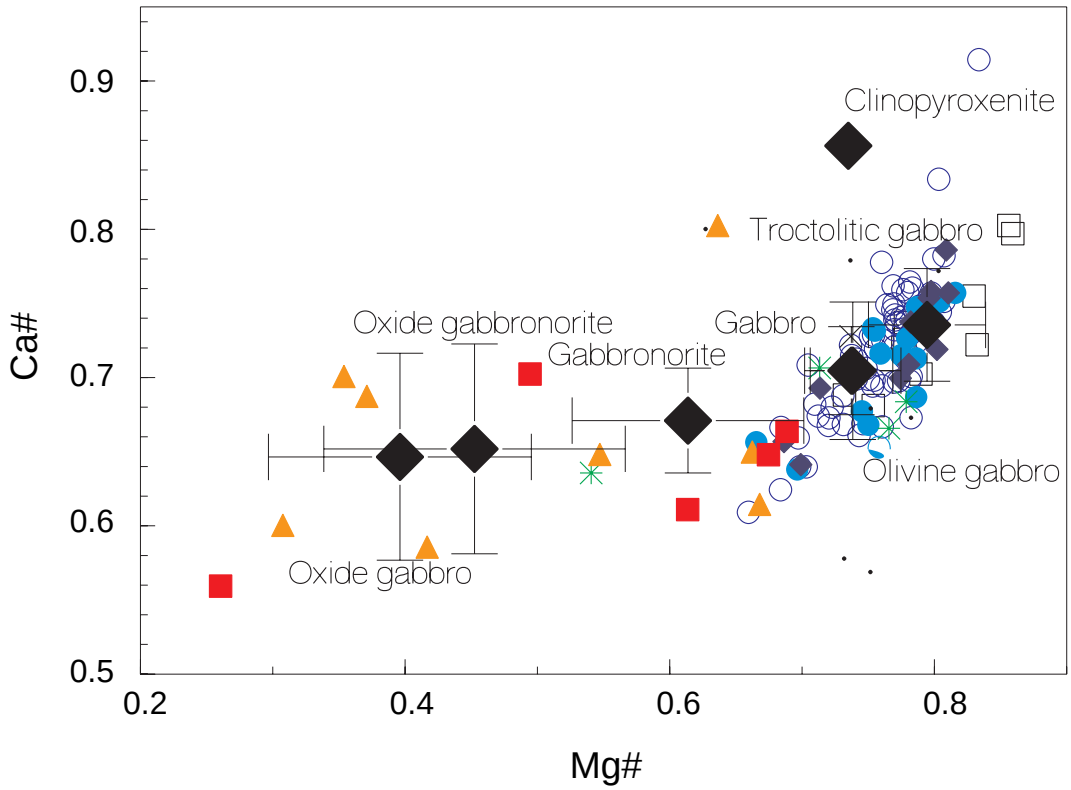

Figure F21. TiO_2 vs. Ca# for Leg 176 rocks. Symbols are the same as in Figure F19, p. 119. See text for explanation.

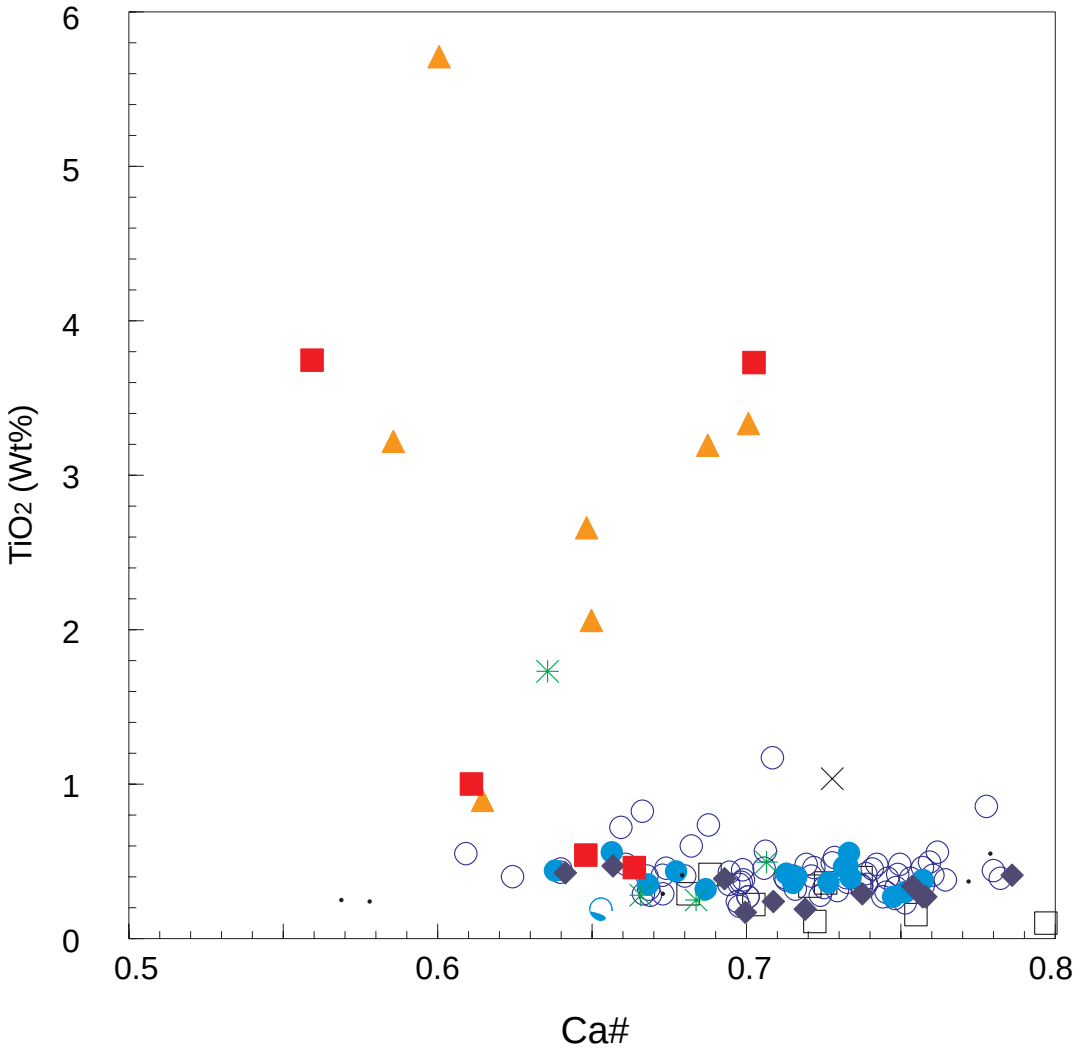

Figure F22. Plot of oxide abundance vs. depth in the Hole 735B cores. The light dashed lines show opaque abundances averaged over 1-cm segments of the core; the darker solid line indicates the average amount of opaques per meter in the core calculated as a running average of the 1-cm data. In most of the coarse-grained gabbros, the amount of opaque material could not be accurately determined at abundances of 0.5% or less, and a nominal value of 0.5% was reported for these samples. As a result, the apparent lower boundary for average oxide abundance at ~0.5% is artificial.

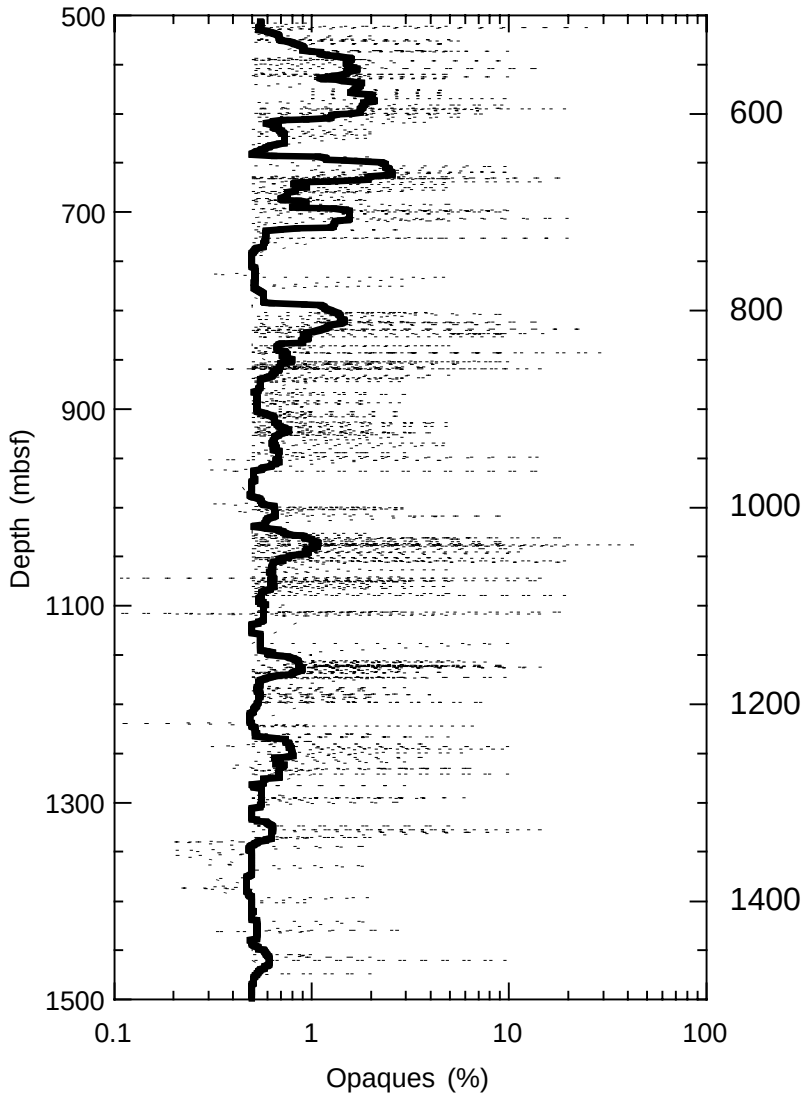

Figure F23. Scan of a thin section (Sample 176-735B-133R-1, 100–104 cm) of an oxide-rich gabbro with a typical texture in which deformed porphyroclasts of olivine, augite, and plagioclase are surrounded by a matrix of undeformed oxides. Scales are in centimeters.

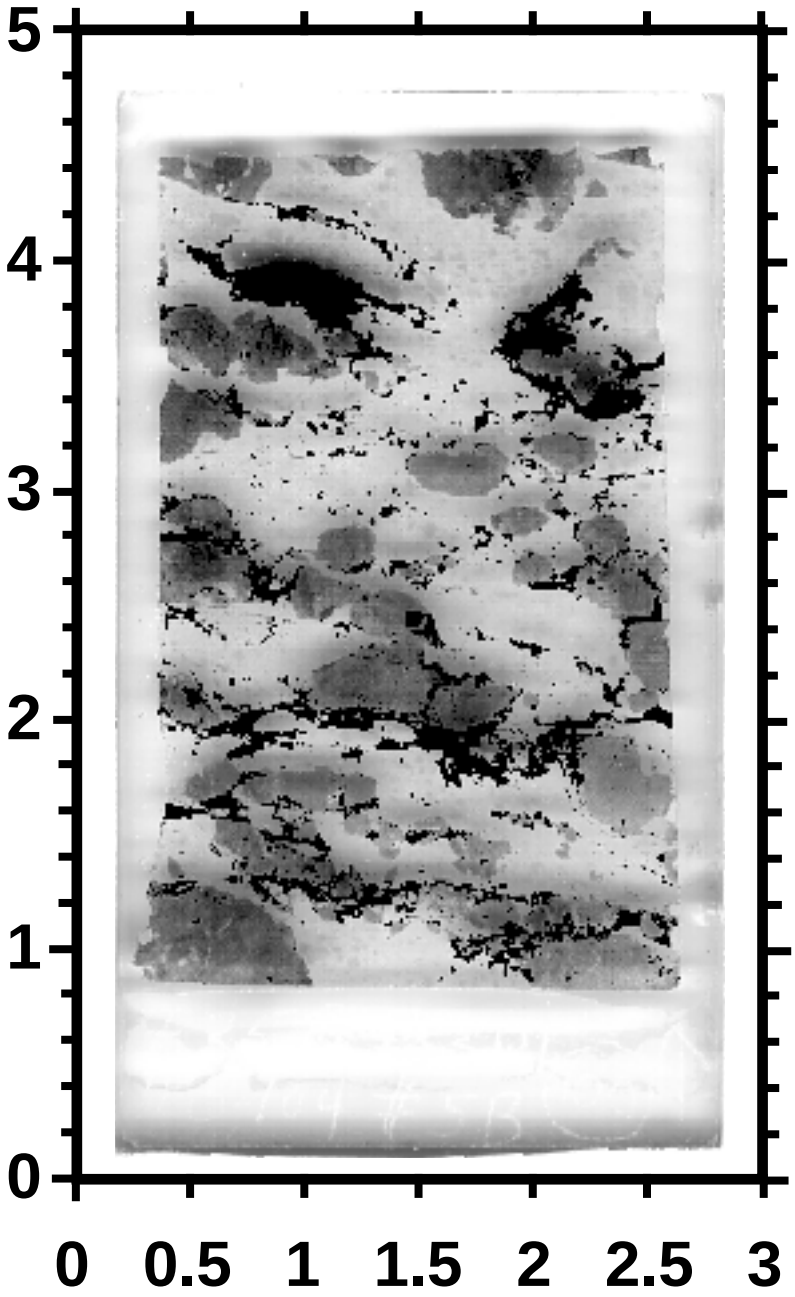

Figure F24. Scan of a thin section (Sample 176-735B-97R-3, 75–77 cm) of an oxide-rich gabbro with a typical texture in which sheared lenses of opaques are smeared out along the foliation in deformed oxide gabbro. Scales are in centimeters.

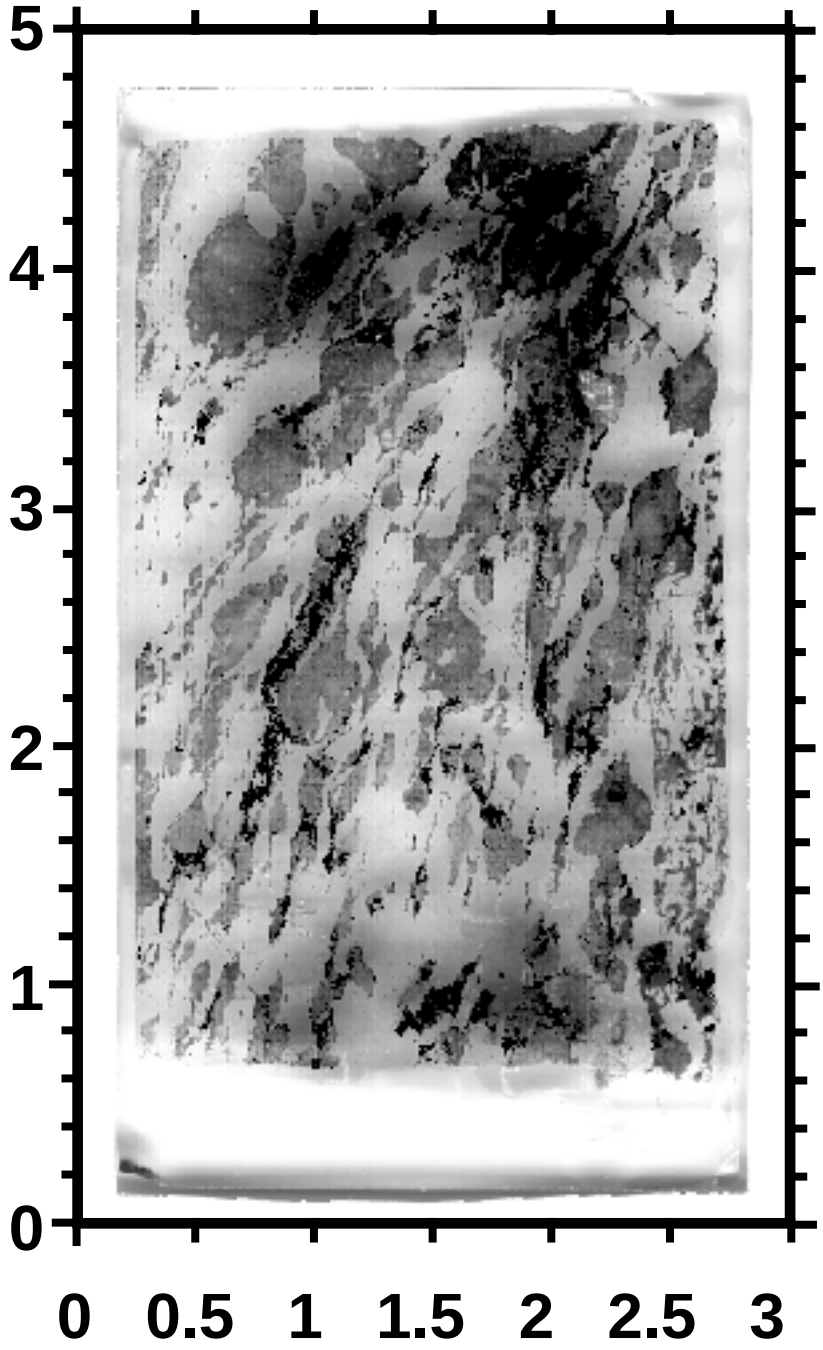

Figure F25. Scan of a thin section (Sample 176-735B-130R-4, 123–127 cm) of an olivine gabbro with an oxide-rich gabbro seam where undeformed subhedral to anhedral crystals of olivine, augite, and plagioclase are surrounded by a matrix of undeformed oxide gabbro. Scales are in centimeters.

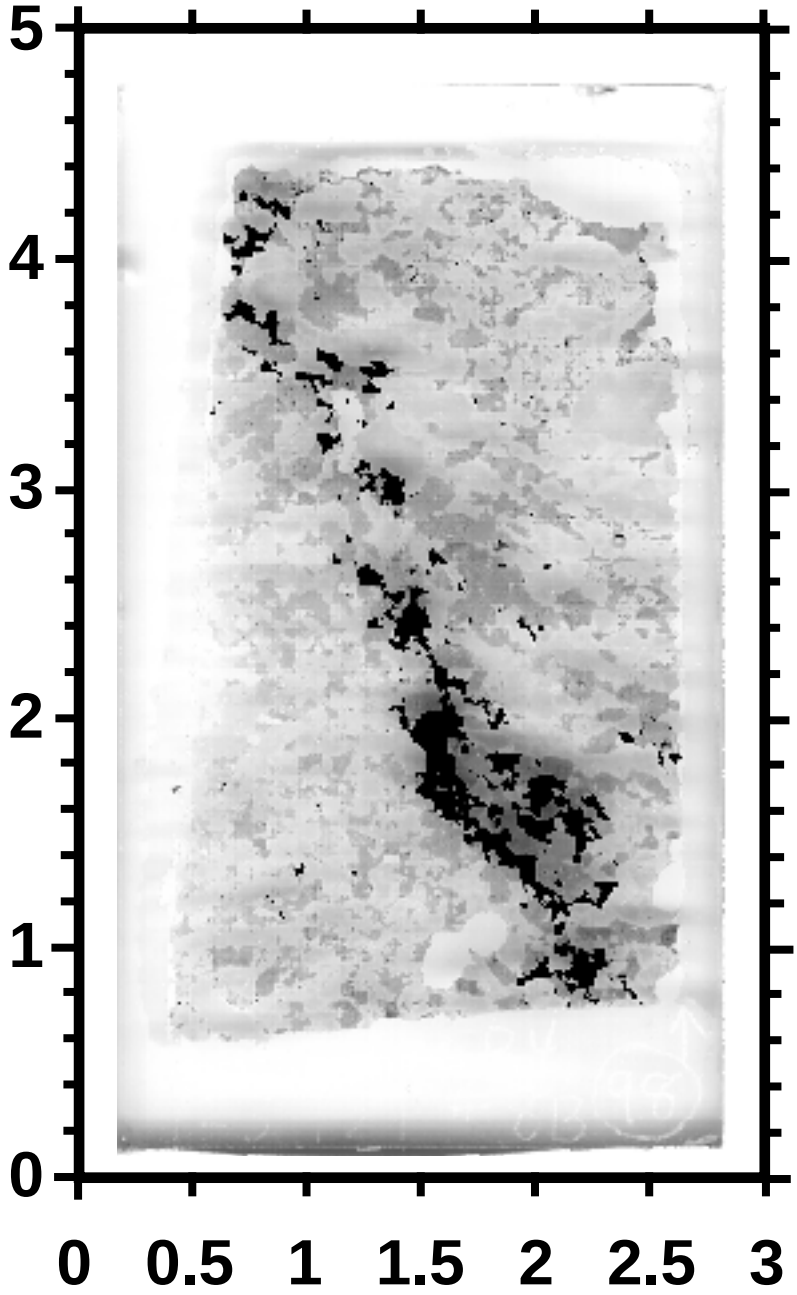

Figure F26. Plot of average intensity of deformation (left curve) and average oxide abundance (right curve) for the Leg 176 core. Both curves are based on running averages over 1-m intervals. Deformation intensity is based on a scale from 1 to 5 (see Fig. **F105,** p. 210).

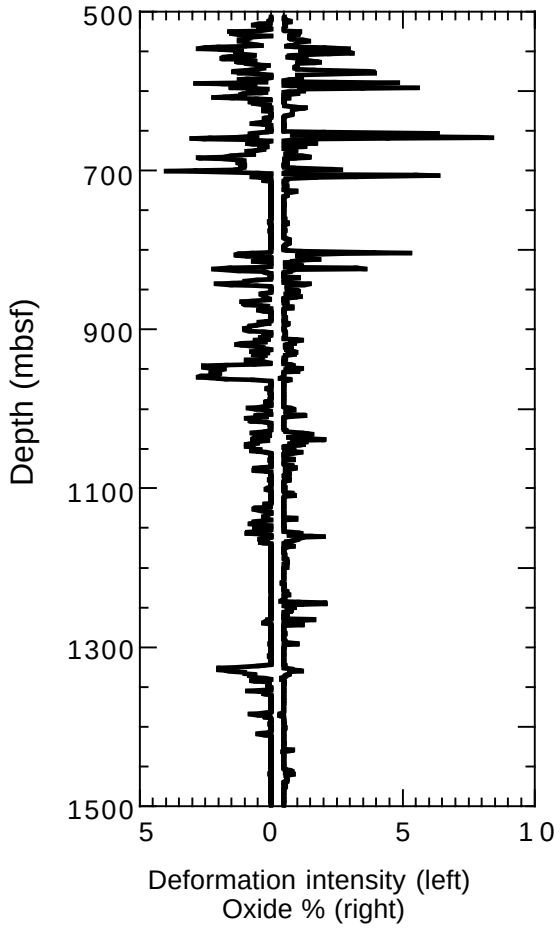

Figure F27. A. A troctolite (Sample 175-735B-91R-5, 105–107 cm) with olivine (prominent cracks, high relief), Cr-spinel (white), and plagioclase (gray, low relief), observed in reflected light. The olivine grain at the lower right, and the larger of the two intermediate spinels, have traces of ilmenite against them. Field of view = 2.8 mm. **B.** Elongate needles and aggregates of secondary magnetite set within amphibole in the center of an altered olivine grain. Olivine gabbro host (Sample 118-735B-85R-3, 47–54 cm), in reflected light. Field of view = 0.7 mm. **C.** Rods of ilmenite, interpreted as relict, coarse, exsolution lamellae, in green amphibole within an amphibolized clinopyroxene (Sample 176-735B-90R-1, 121–126 cm), in reflected light. Field of view = 1.4 mm. **D.** Rounded sulfide containing both pyrrhotite and chalcopyrite enclosed in ilmenite in an oxide ferrogabbro (Sample 118-735B-79R-7, 115–118 cm), in reflected light. Field of view = 0.7 mm. (Continued on next page.)

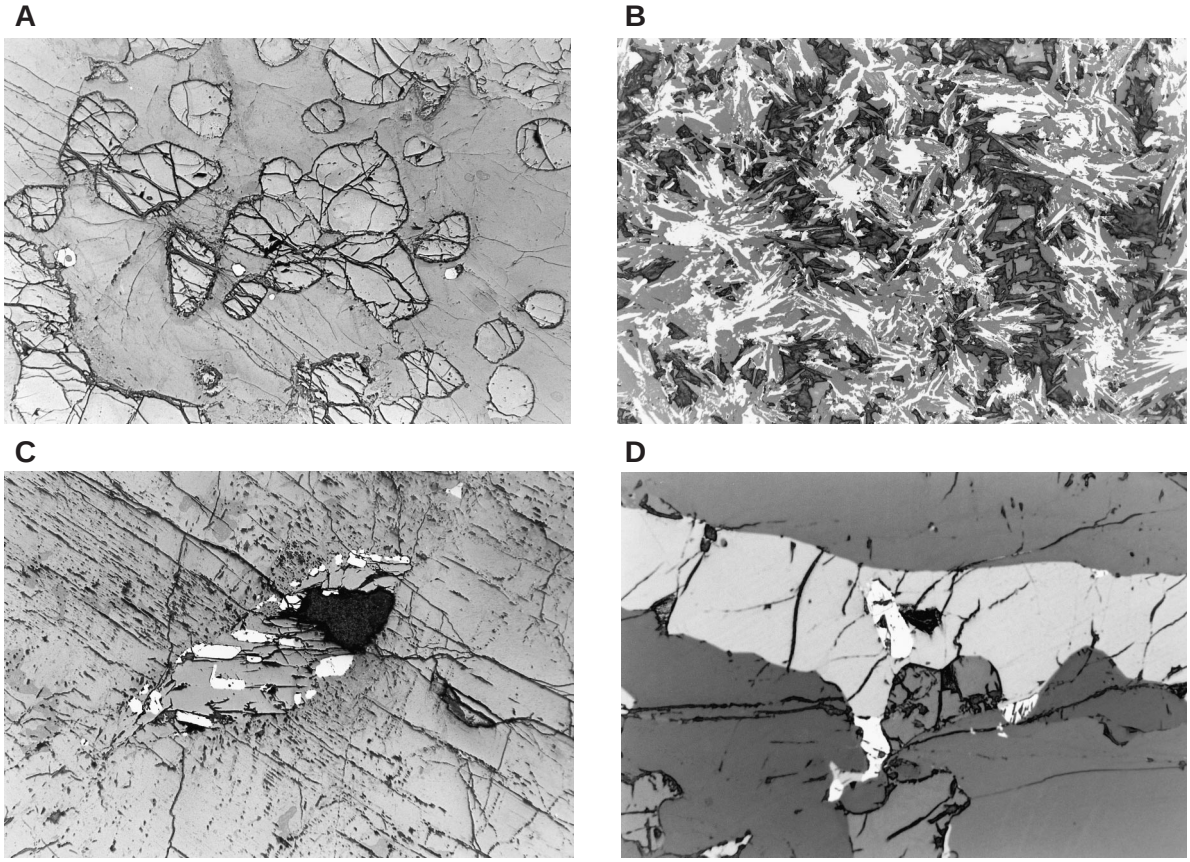

Figure F27 (continued). E. Intergrown oxides and sulfides (black) surrounded by brown amphibole (dark gray), in between clinopyroxene with some intergrown amphibole (bottom) and plagioclase (top; Sample 176-735B-94R-3, 119–121 cm), in plane-polarized light. Field of view = 0.7 mm. **F.** Same as E, except photographed in combined transmitted and reflected light. With reflected light, the opaque clump is seen to consist of sulfides (light gray) and ilmenite (darker gray). The smooth sulfide is pyrrhotite. The more irregular sulfide at center right is chalcopyrite.

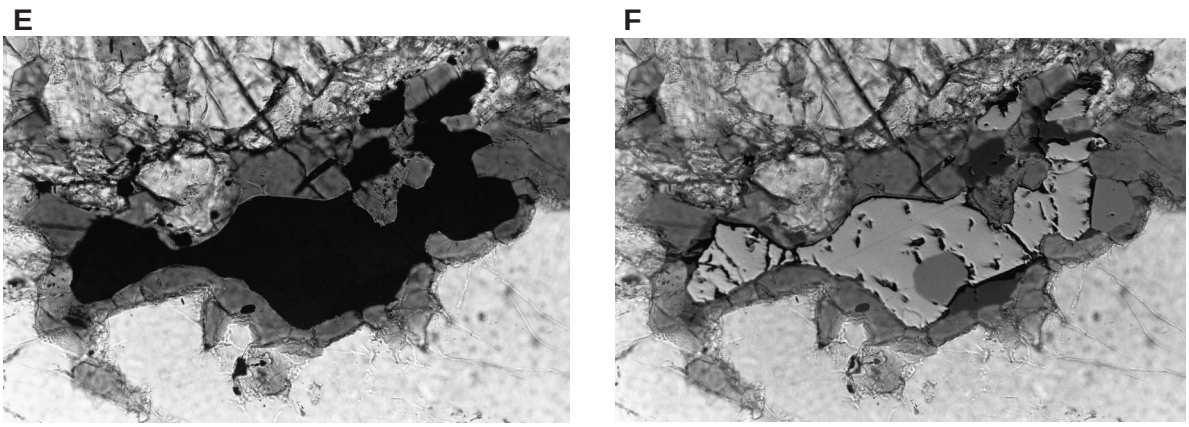

Figure F28. A. Troctolite showing the presence of rims of brown amphibole (gray), locally containing sulfides (black), adjacent to many olivine grains (Sample 118-735B-79R-7, 115–118 cm), in plane-polarized light. Field of view = 5.6 mm. **B.** Complex ilmenite-olivine symplectite (Sample 176-735B-153R-2, 24–28 cm) in reflected light. The bright grain along the crack at lower left is a sulfide. Field of view = 0.28 mm. **C.** Intricate intergrowth of clinopyroxene with ilmenite (black) and brown amphibole (gray) in, and in widened faceted cavities along cleavage (Sample 176-735B-153R-2, 24–28 cm), in plane-polarized light. Field of view = 0.70 mm. **D.** Cr-spinel (medium gray) in plagioclase, partly jacketed with ilmenite (white; Sample 176-735B-91R-1, 105–107 cm), in reflected light. Field of view = 0.28 mm. (Continued on next page.)

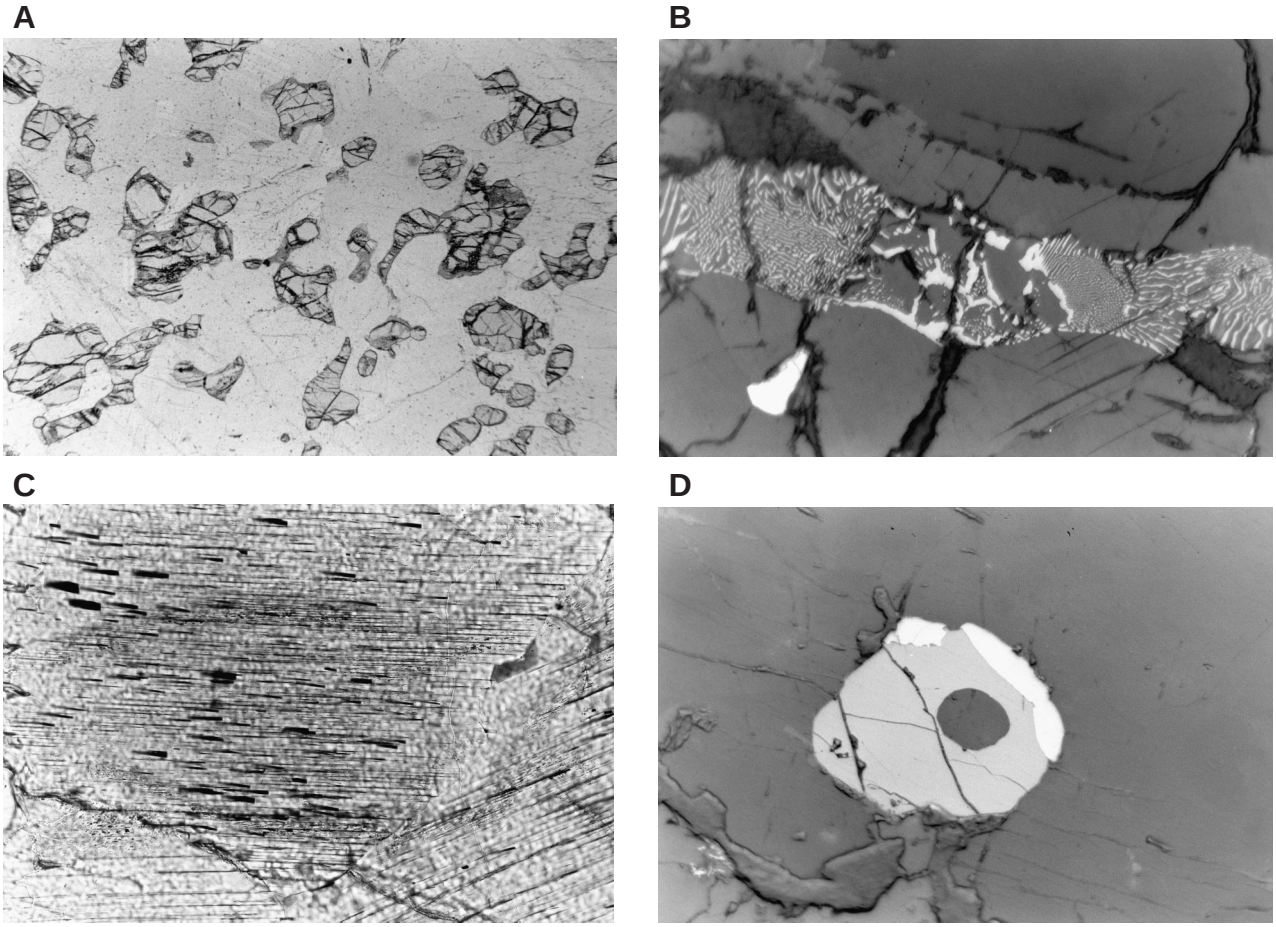

Figure F28 (continued). E. Cr-spinel (medium gray) in plagioclase, with minor ferrichromite alteration at upper right, partly enclosing interpenetrating ilmenite (white). The thin darker gray rim is brown amphibole. Same sample as in D. Field of view = 0.28 mm.

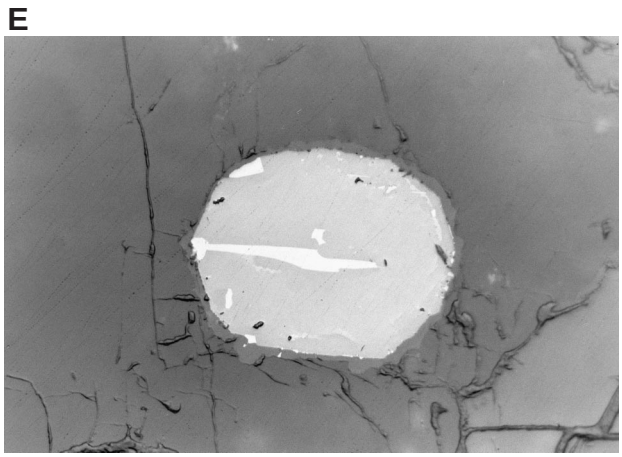

Figure F29. Downhole felsic vein intensity (vol%) averaged over every 10 m of core. Despite the scatter, the overall felsic vein abundance decreases with increasing depth. In the entire 1003.05 m of Leg 176 core, 203 felsic veins or sets of veins were recognized. The total accumulative length of the felsic veins is 5.43 m, which makes up ~0.54% of the total volume of the core recovered. Leg 118 data from the upper 500 m of Hole 735B are plotted for comparison (data from Dick et al., [1991a]). Presence of felsic veins in upper 70 m of the Leg 118 section is obscured by deformation (H. Dick, pers. comm., 1997).

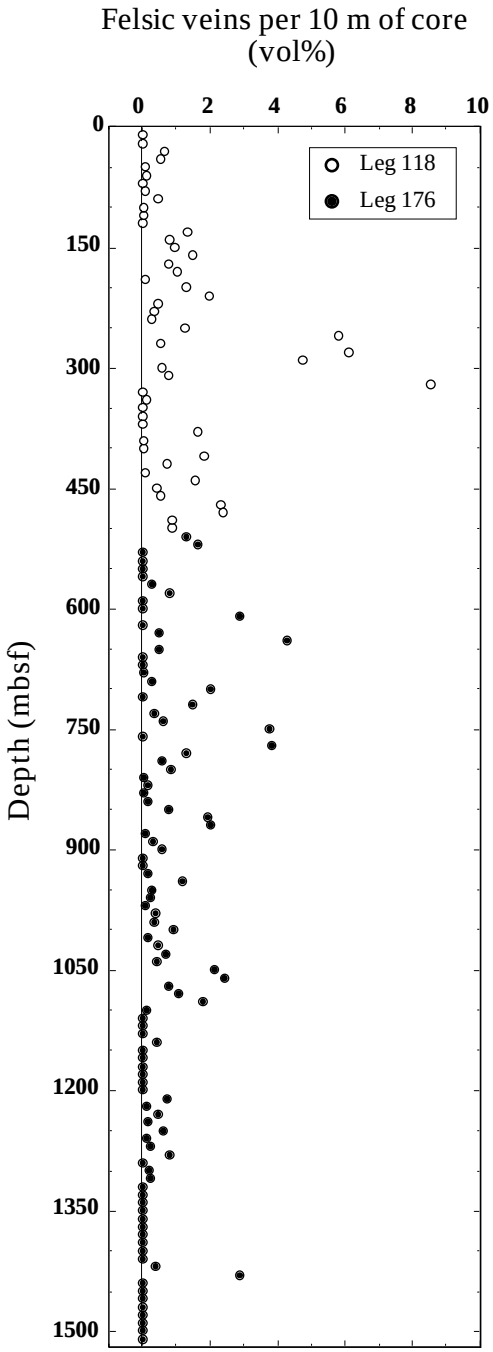

Figure F30. Core photograph of interval 176-735B-110R-4, 0–38 cm, showing a representative igneous felsic vein with sharp intrusive contacts. The felsic vein is a medium-grained leucodiorite dominated by plagioclase with disseminated green amphibole.

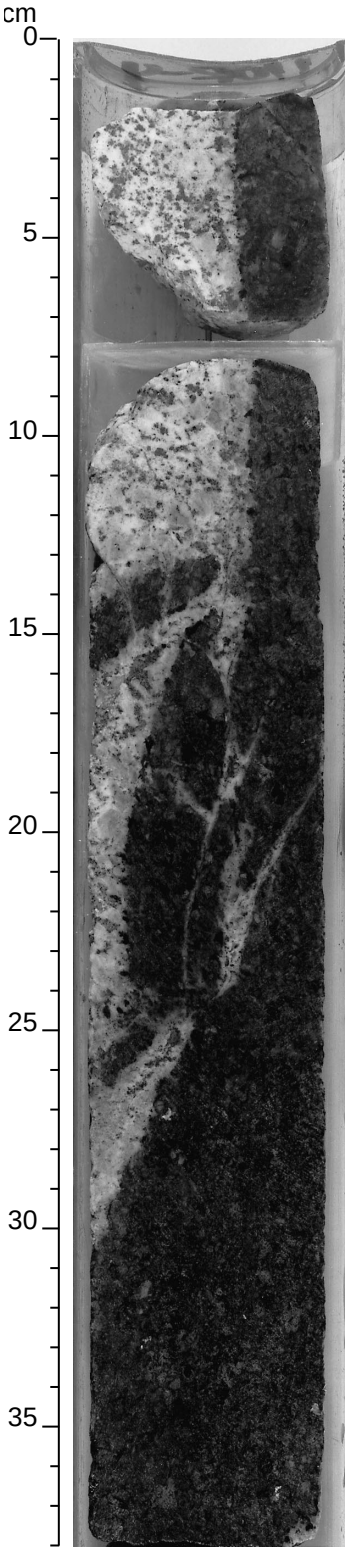

Figure F31. Core photographs showing grain-size layering. **A.** Rhythmic grain-size layering in Section 176-735B-171R-4. **B.** Coarse-grained layer in medium-grained gabbro in Section 176-735B-186R-4. Arrows indicate the bases of three graded layers.

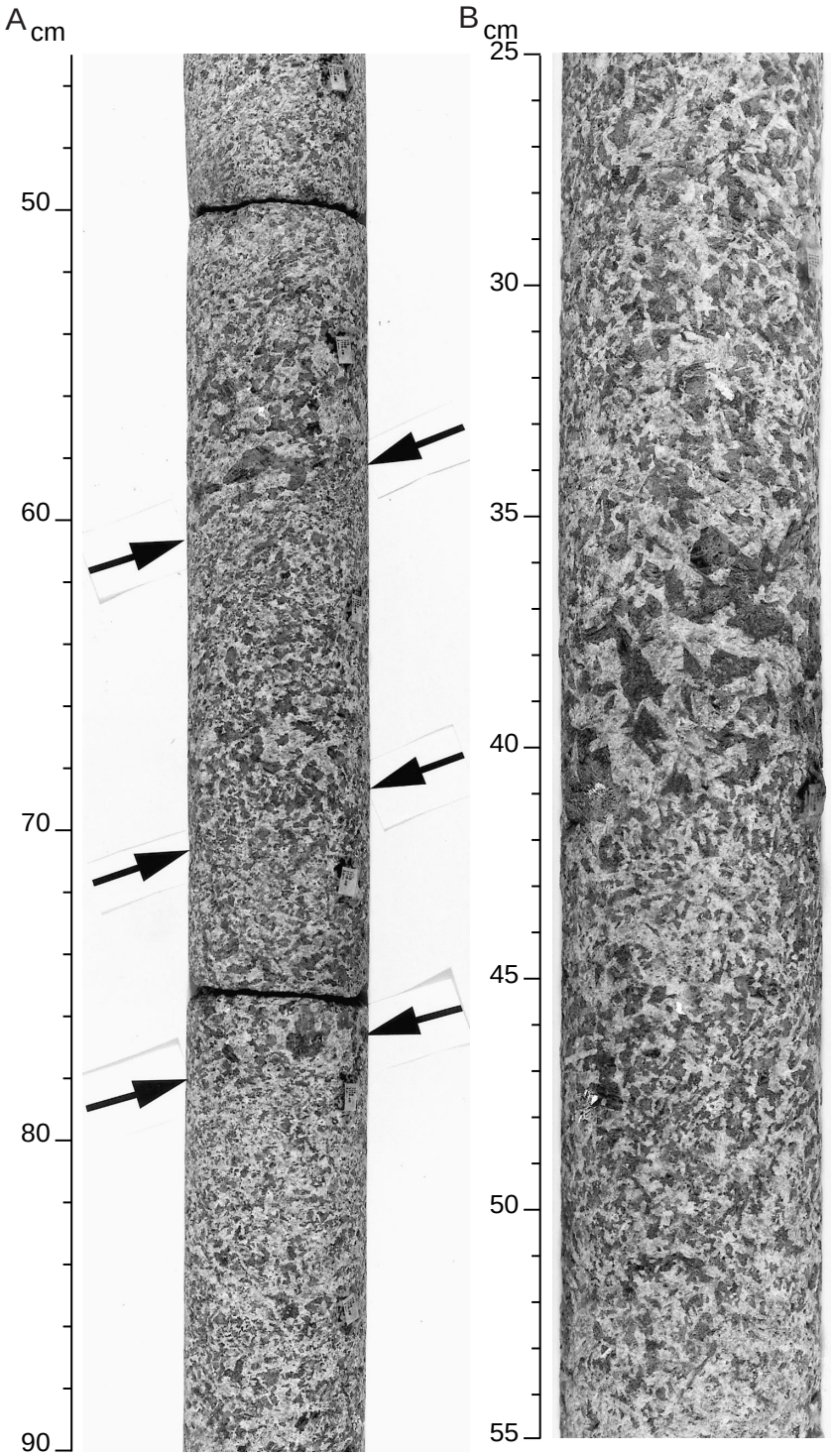

Figure F32. Histogram of layer thickness in the interval from Section 176-735B-134R-4 to Section 135R-2.

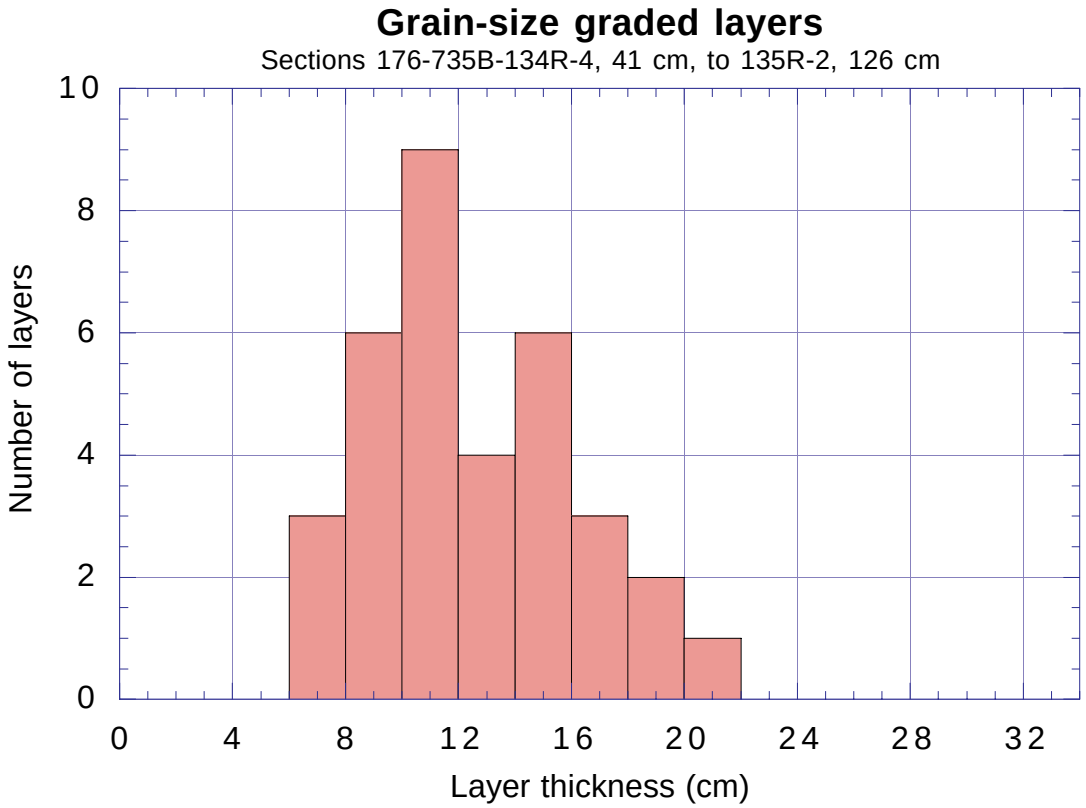

Figure F33. Distribution of the dominant secondary phases in Hole 735B. Estimates were obtained from visual core observation and refer to the rock recovery in each core section (see the **"Core Descriptions"** contents list). The mineral phases are grouped according to the grade of metamorphism.

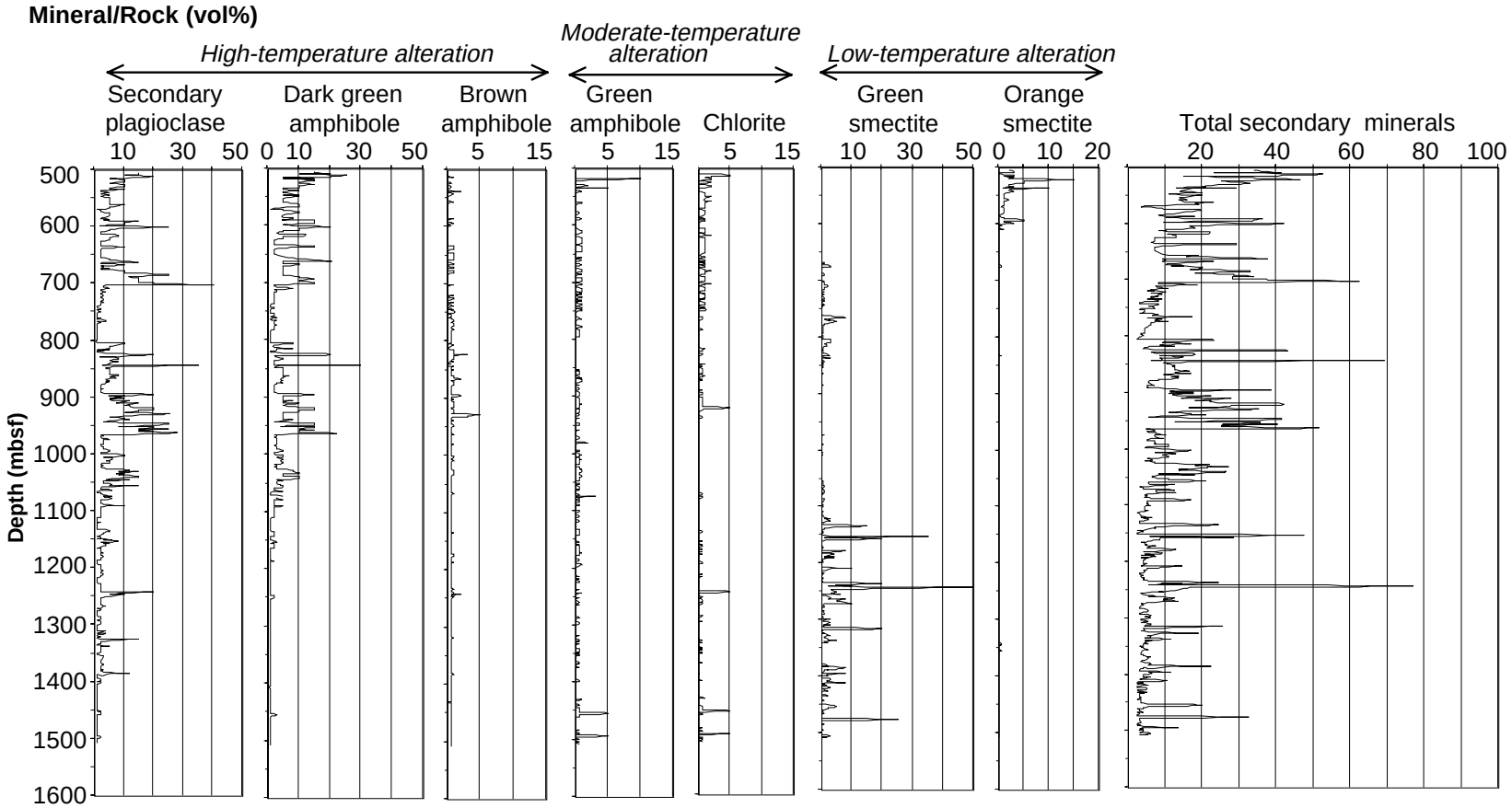

Figure F34. Amount of alteration (vol%) vs. depth in Hole 735B (see the "Core Descriptions" contents list). The percentages were estimated by visual observation of the core, and metamorphic units are defined in the visual core descriptions. **A.** Rock alteration percent. The thick gray line is a running average (window: 10 samples). **B.** Percent of plagioclase alteration. Note that background hydrothermal and dynamically recrystallized plagioclase are not distinguished in hand specimens of deformed gabbros (e.g., 880–1070 mbsf). **C.** Percent of olivine alteration. **D.** Percent of clinopyroxene alteration. Note that orthopyroxene is not distinguished from clinopyroxene.

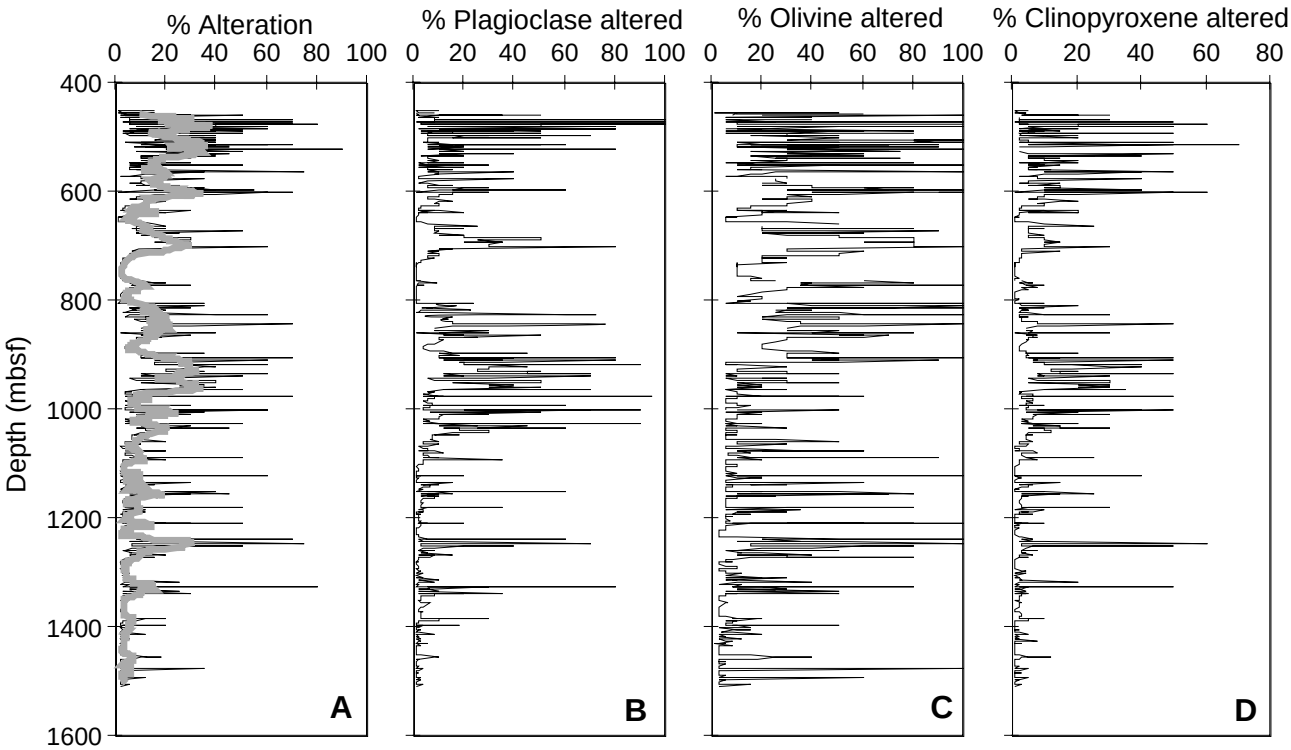

Figure F35. (**A**) Total degree of alteration (vol% secondary phases) compared with (**B**) the total abundance of veins per section. The shaded areas represent a zone of intense crystal-plastic deformation that terminates at the base of a reverse shear zone at 960 mbsf (lowest arrow). The two upper arrows indicate fault zones at 550 and 690 mbsf. Note that the abundance of veins is low in the zone of high crystal-plastic deformation between 800 and 960 mbsf.

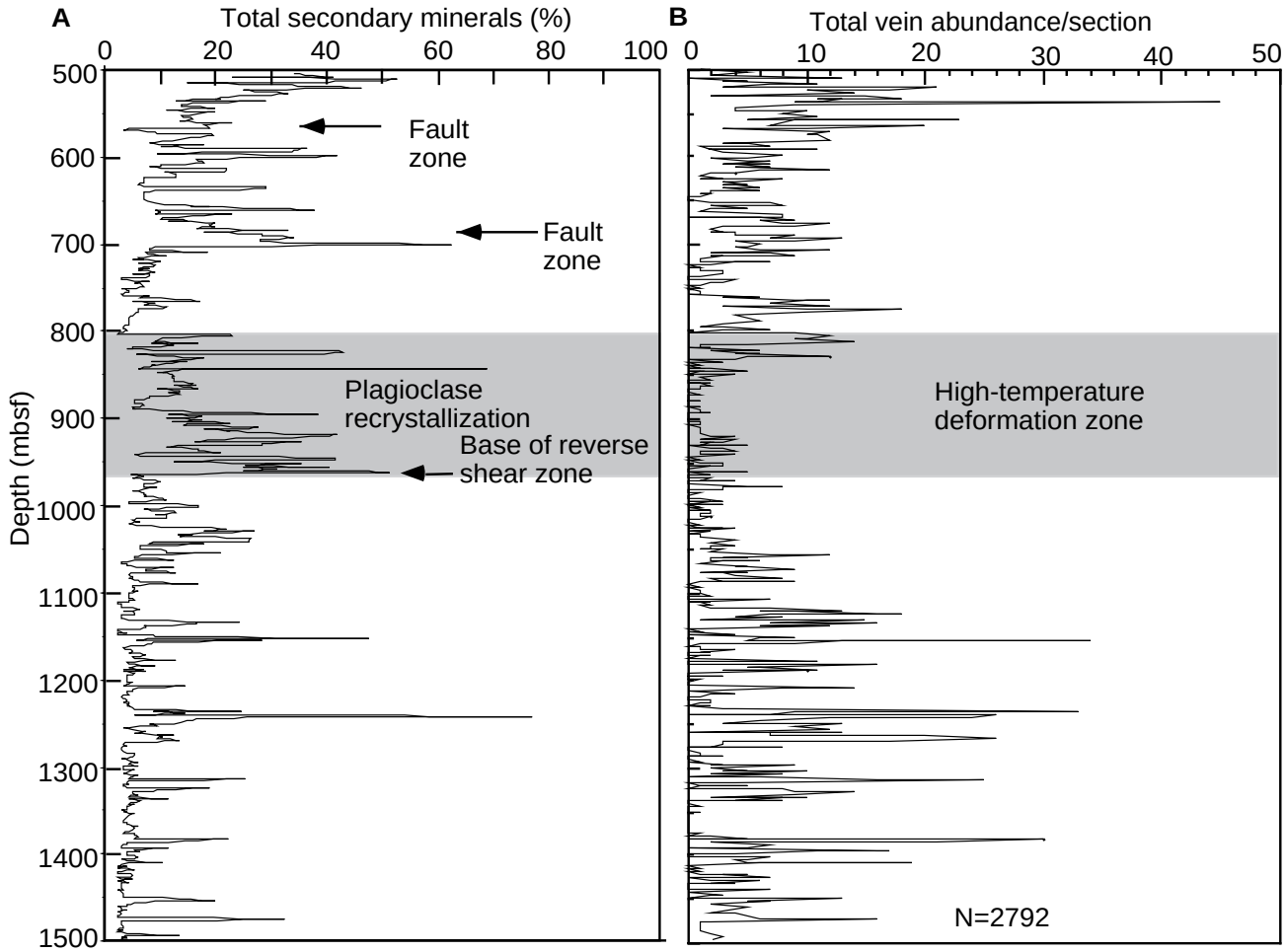

Figure F36. Downhole distribution of secondary phases in Hole 735B related to the variation in total rock alteration with depth. Data are from thin-section observations (see the **"Core Descriptions"** contents list).

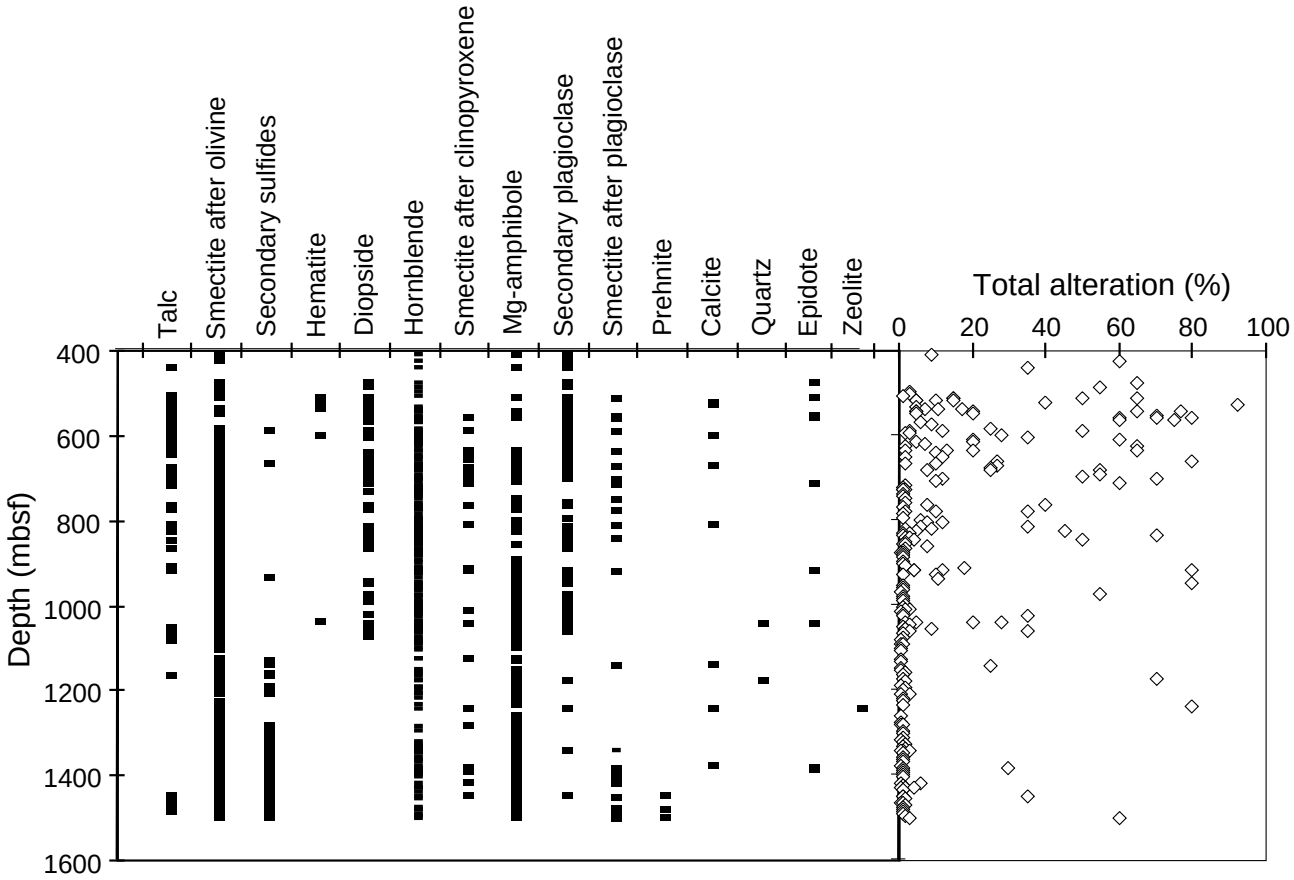

Figure F37. Visual estimation of olivine alteration in thin sections from Hole 735B vs. depth. **A.** Average degree of alteration of olivine. **B.** Percentage of talc after olivine in the secondary mineral assemblage. Magnetite is generally associated with talc. **C.** Percentage of smectite after olivine in the secondary mineral assemblage. Variable amounts of sulfide minerals or carbonate + oxyhydroxide are commonly intergrown with smectite. **D.** Percentage of amphibole after olivine in the secondary mineral assemblage. Amphibole forms microcrystalline reaction rims around olivine.

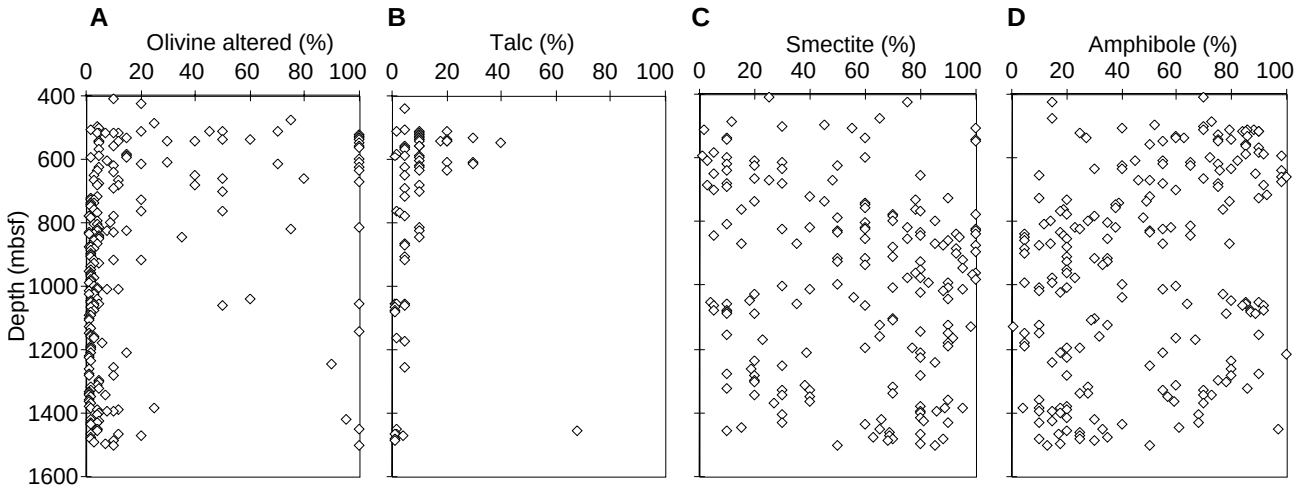

Figure F38. Visual estimation of clinopyroxene alteration in thin sections from Hole 735B vs. depth. **A.** Average alteration of pyroxene. **B.** Percentage of secondary clinopyroxene in the secondary mineral assemblage. **C.** Percentage of brown amphibole after clinopyroxene in the secondary mineral assemblage. **D.** Percentage of green amphibole after clinopyroxene in the secondary mineral assemblage.

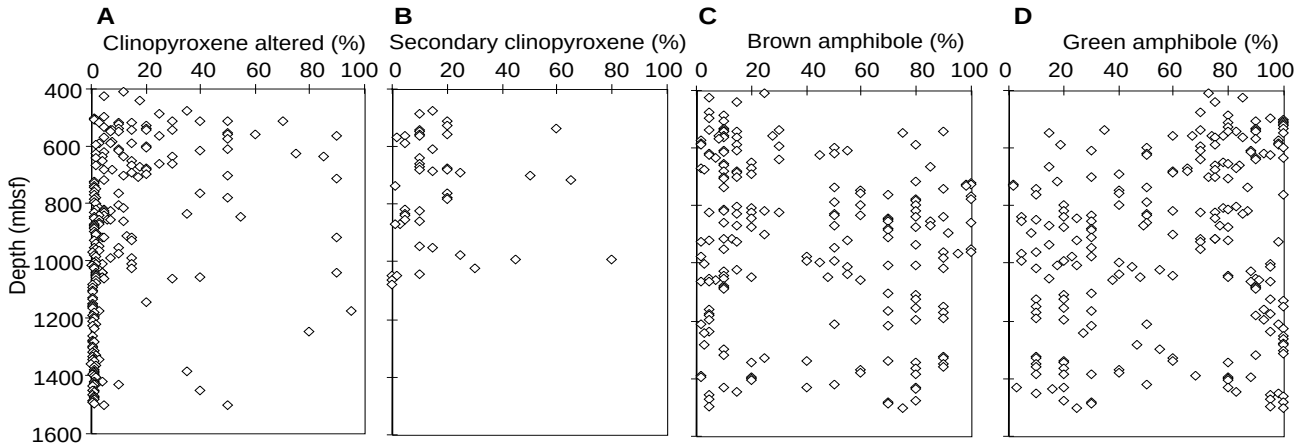

Figure F39. Visual estimation of plagioclase alteration in thin sections from Hole 735B vs. depth. **A.** Average alteration of plagioclase. **B.** Percentage of secondary plagioclase in the secondary mineral assemblage. **C.** Percentage of smectite after plagioclase in the secondary mineral assemblage. **D.** Percentage of actinolite after plagioclase in the secondary mineral assemblage.

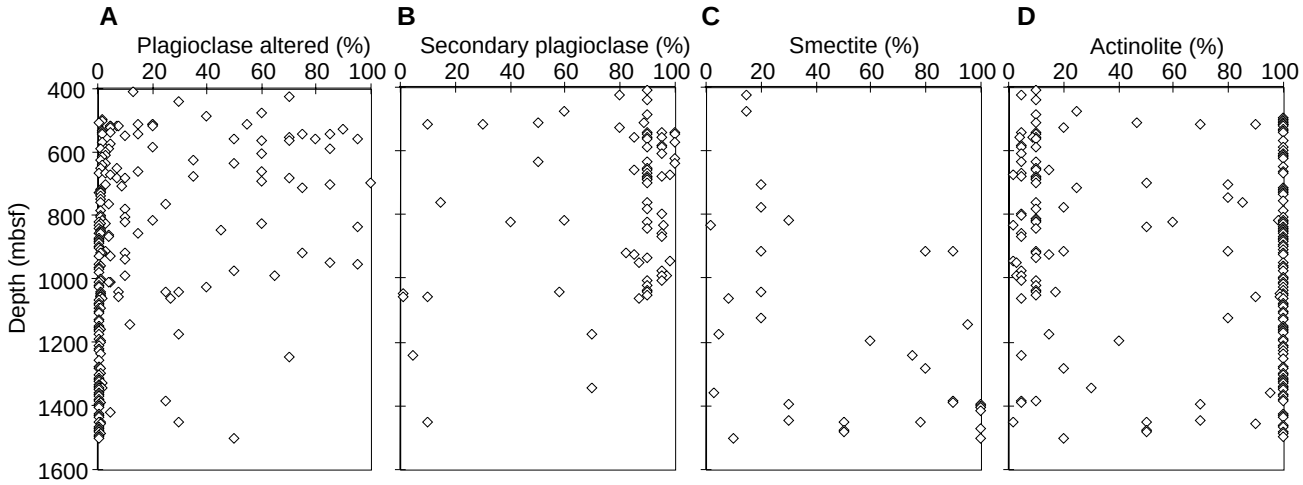

Figure F40. Close-up photograph of coarse-grained highly altered Fe-Ti gabbro (Sample 176-735B-181R-2 [Piece 9C and 9D, 100–112 cm]; 1244 mbsf) showing alteration of olivine and pyroxene (dark grains), of orthopyroxene (brilliant crystals) and plagioclase (from fresh light-gray Ca-plagioclase to milky-white Na-rich species). Olivine and clinopyroxene are mostly altered to smectite + sulfide. Minor talc + oxide and chlorite form after olivine and orthopyroxene. Plagioclase shows variable coloration from dark gray to milky white when pseudomorphed by albite. Note veins of dark green smectites, particularly at the top of the photo (cut side of the core section).

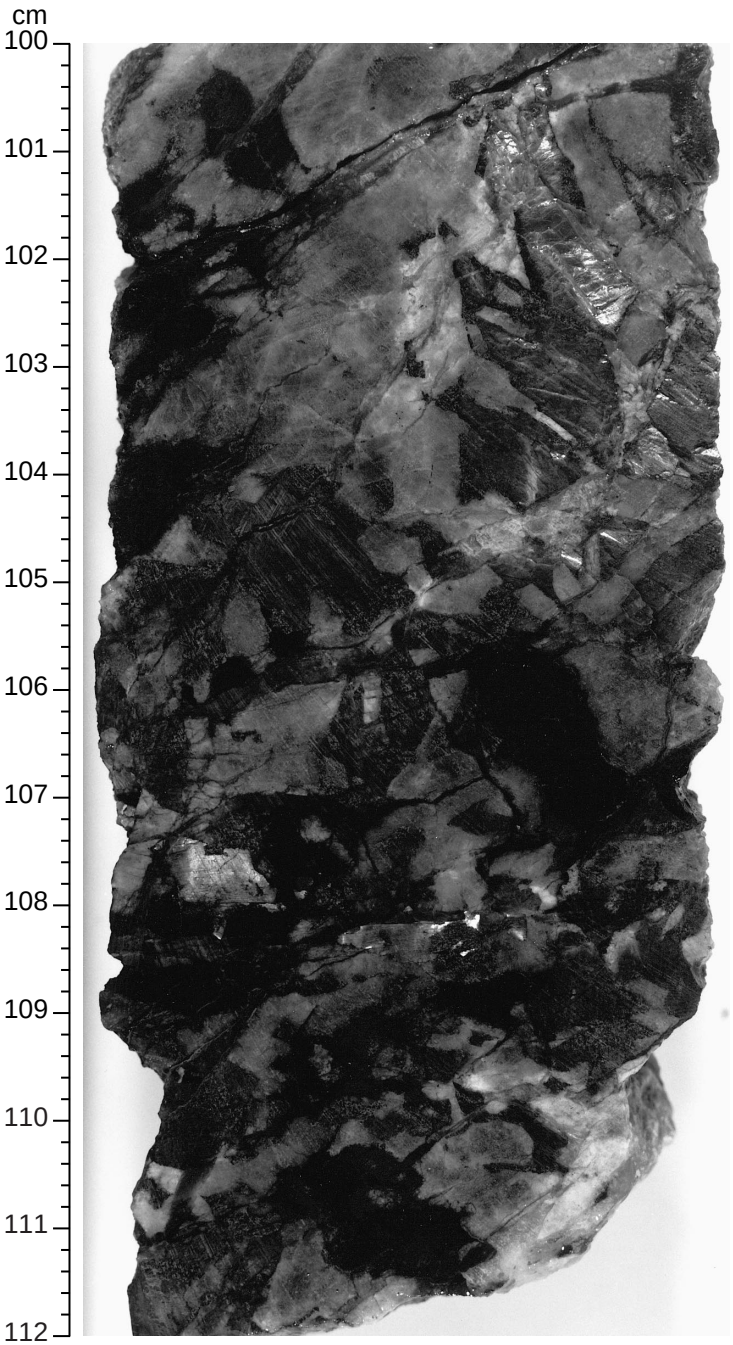

Figure F41. Close-up photograph of slightly altered Fe-Ti gabbronorite (Sample 176-735B-114R-2 [Piece 3C, 60–70 cm]; 655 mbsf) showing dark amphibole needles on the back side of the core. Note the dark gray alteration halos around grains (medium gray) of olivine (chlorite-smectite and minor amphibole) and pyroxene (mainly amphibole). Primary plagioclase is light gray and secondary plagioclase is white.

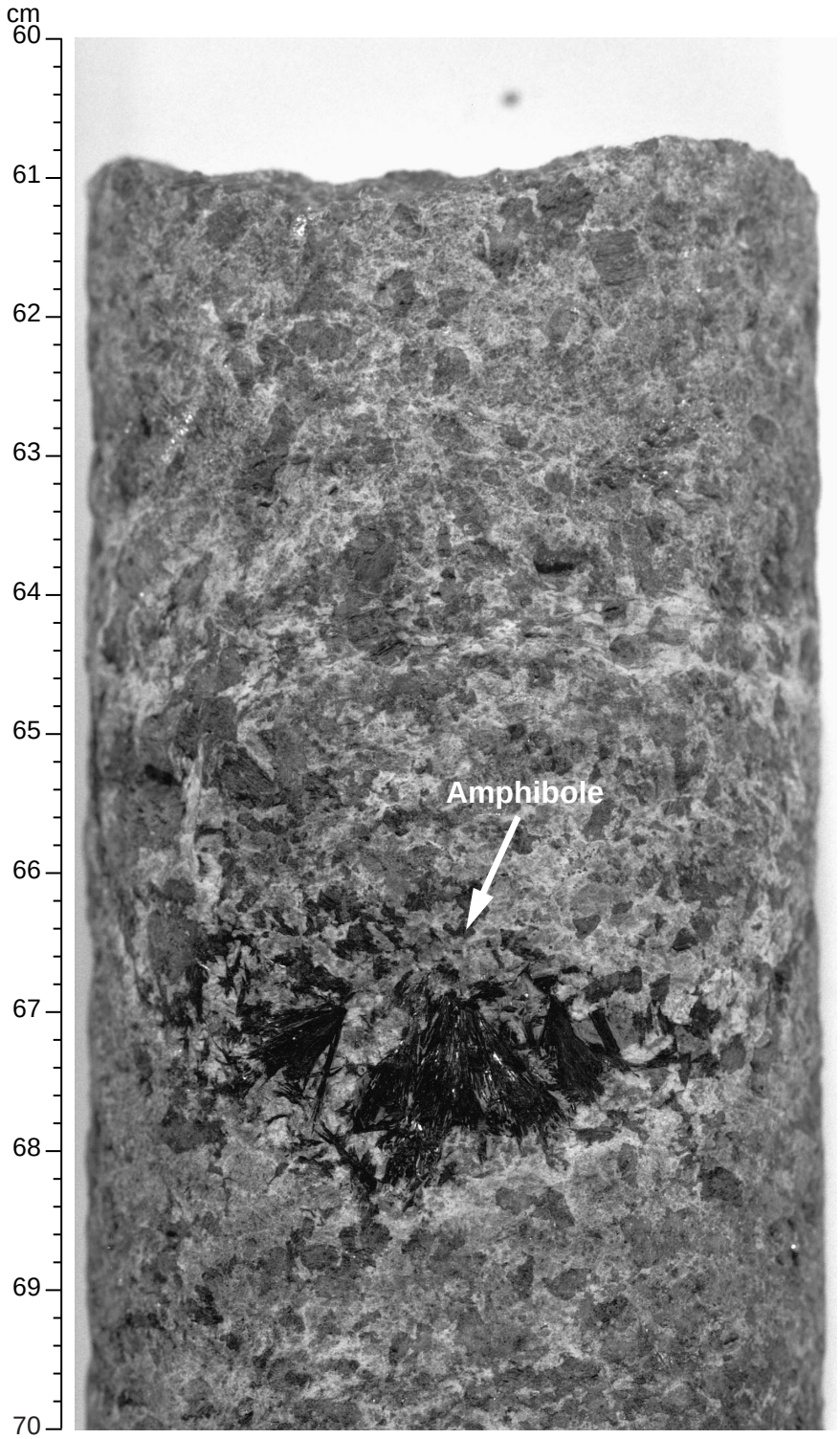

Figure F42. X-ray diffraction profile of vein-forming smectite, prehnite, and pumpellyite(?) in Sample 176-735B-190R-3 (Piece 3, 35–40 cm; 1329 mbsf).

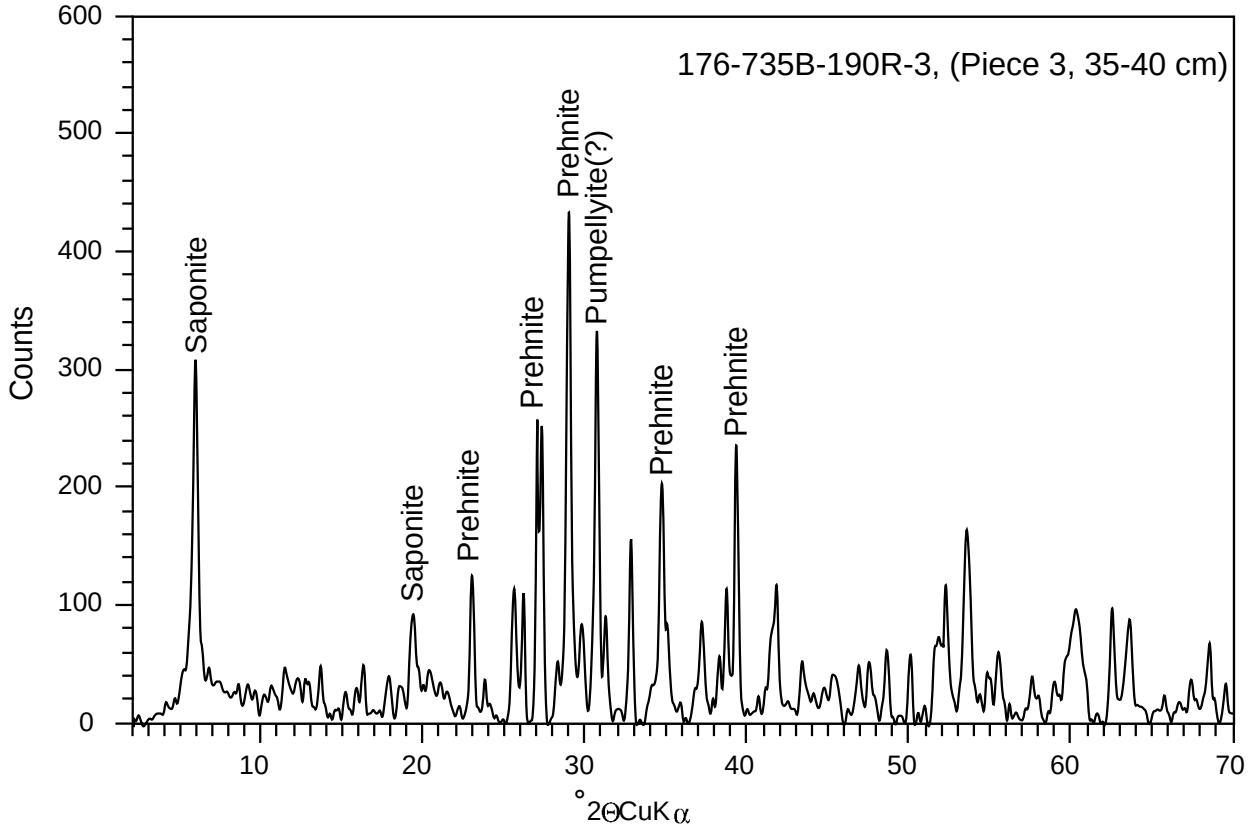

Figure F43. X-ray diffraction profile of vein-forming zeolite in Sample 176-735B-188R-6 (Piece 7, 98–102 cm; 1314 mbsf). The zeolite is probably natrolite, but it could possibly be scolecite.

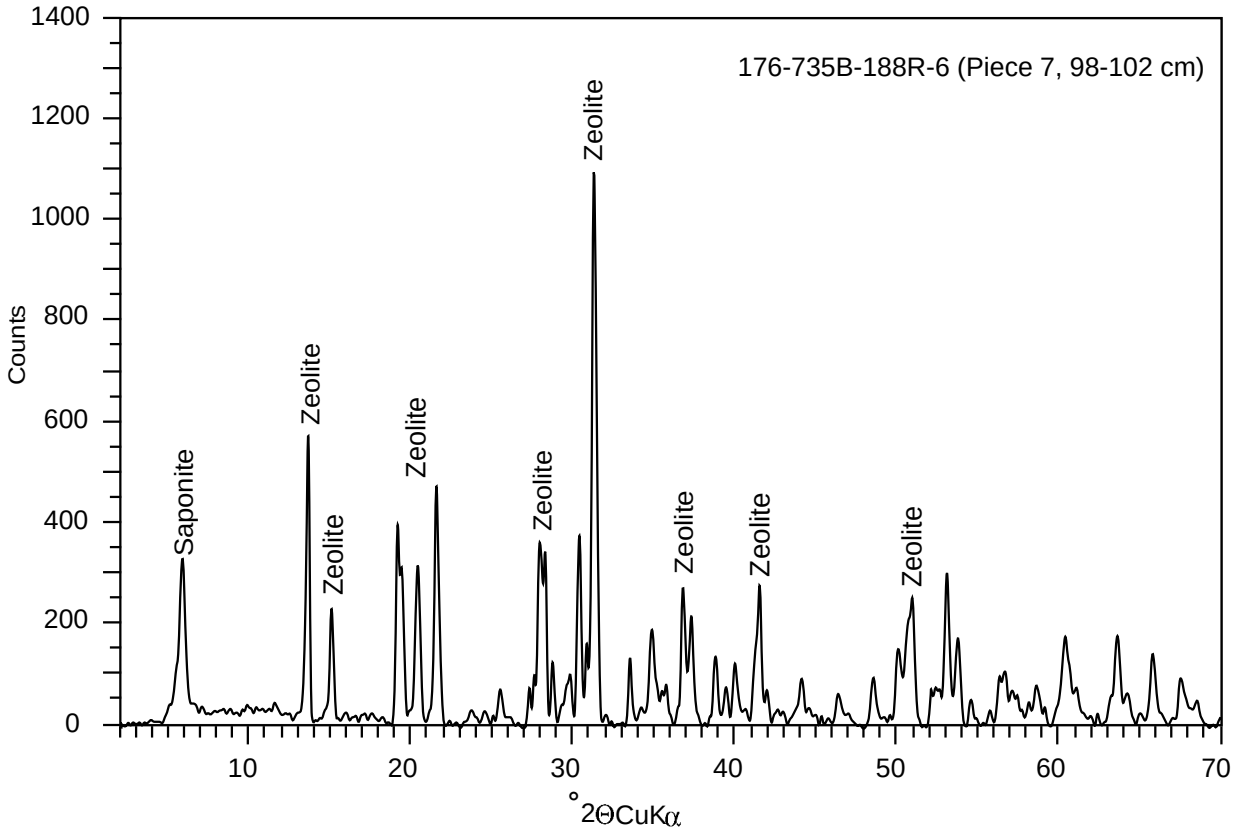

Figure F44. Vein of pale-green smectite in Sample 176-735B-133R-7 (Piece 1, 126–137 cm). Olivine, plagioclase, and clinopyroxene are highly altered to smectite in the alteration halo. Altered plagioclase appears pale green, olivine dark, and altered clinopyroxene brown or has brilliant reflectance at greater distance from the vein (incipient alteration).

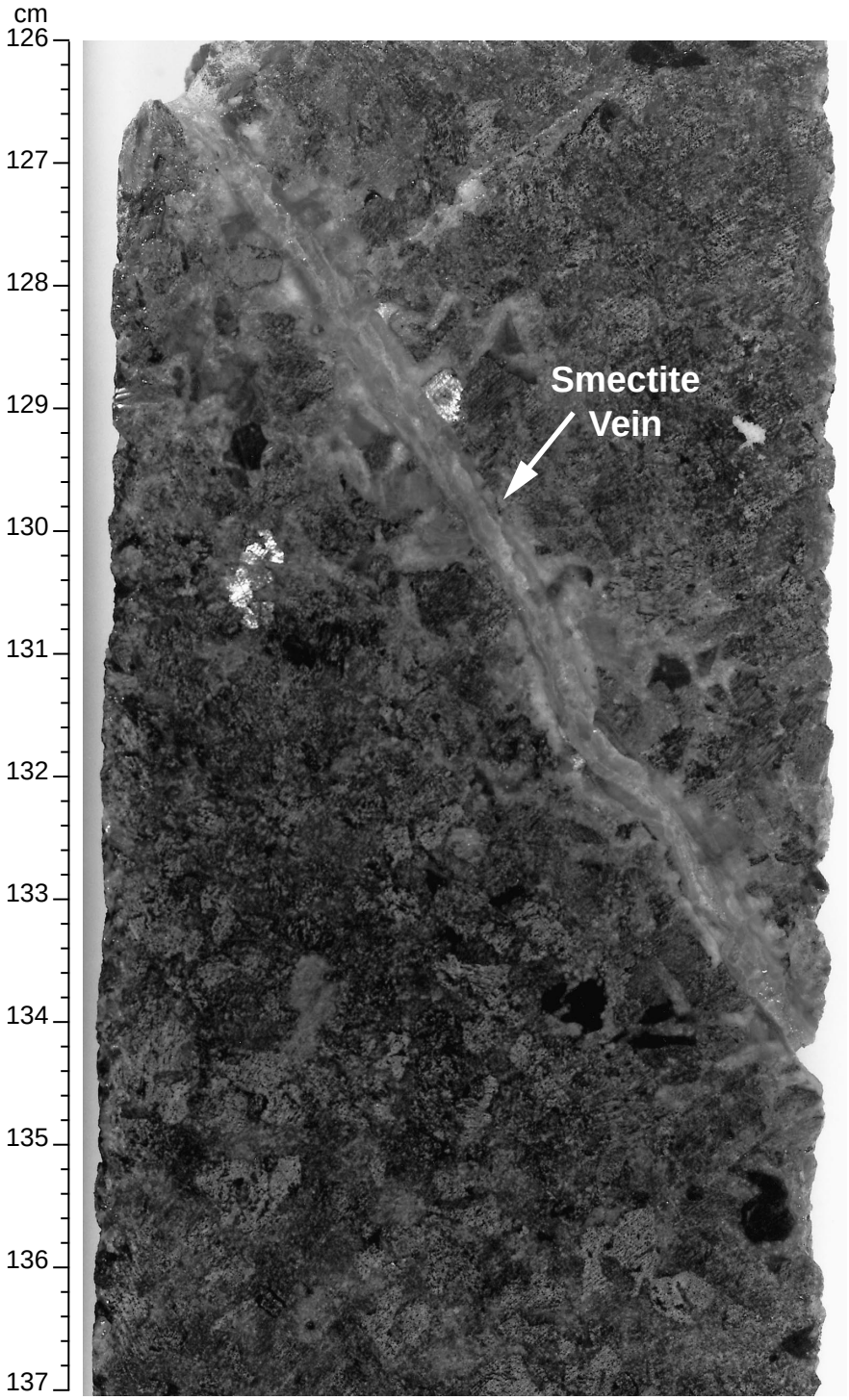

Figure F45. Close-up photograph of highly altered mylonitized and net-veined trondhjemitic-gabbro (Sample 176-735B-119R-1 [Piece 9, 90–100 cm]; 701 mbsf). Note the abundance of recrystallized plagioclase (white) parallel to the foliation and dark gray alteration rims around pyroxene and olivine porphyroclasts and along the tails (mainly amphibole and neoblasts of olivine and pyroxene). Some Ca-plagioclase porphyroclasts appear light gray in the plagioclase bands.

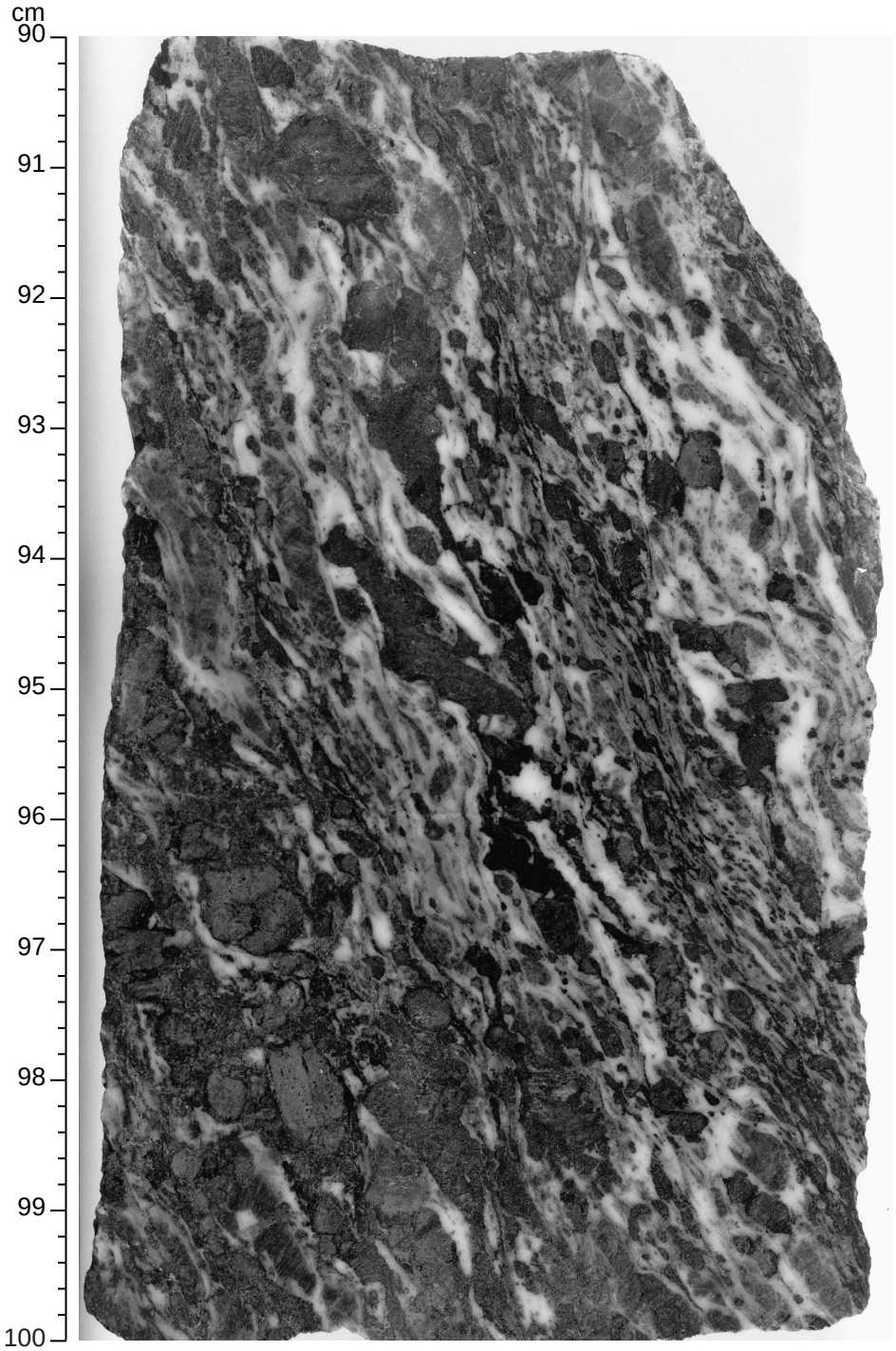

Figure F46. A. Sample 176-735B-133R-5 (Piece 3, 113–116 cm): large crystal of olivine in fresh olivine gabbro showing irregular cracks lined with smectite and finely disseminated oxide. **B.** Sample 176-735B-94R-1 (Piece 1F, 81–85 cm): partly altered olivine crystal in olivine gabbro. Note core of fresh olivine rimmed by dark smectite, which, in turn, is rimmed with a mixture of talc, Mg-amphibole, and disseminated oxide. **C.** Sample 176-735B-92R-1 (Piece 6B, 60–62 cm): large olivine grain enclosing a clinopyroxene grain with excellent cleavage. Note abundance of irregular cracks in the olivine and their paucity in the pyroxene, and the total absence of alteration in the pyroxene. Scale bars = 1 mm.

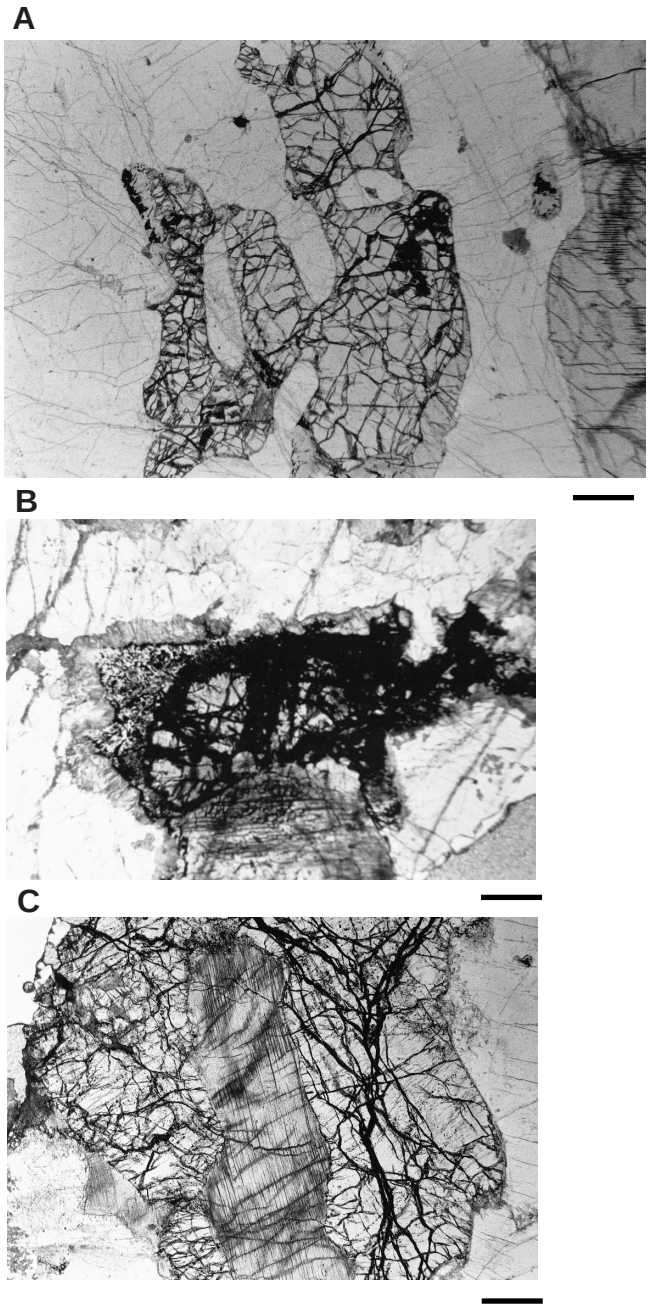

Figure F47. A. Distribution of total veins by percentage of core in gabbroic rocks recovered during Leg 118 and 176. **B.** Distribution of felsic, plagioclase, and plagioclase + amphibole veins by percentage of core. Below 1250 mbsf, felsic veins are rare. **C.** Distribution of plagioclase + diopside and diopside veins by percentage of core. Below 750 mbsf, diopside and plagioclase + diopside veins do not occur. **D.** Distribution of amphibole veins by percentage of core. Below 600 mbsf, amphibole veins are rare. **E.** Distribution of carbonate and smectite veins downsection. **F.** Distribution of chlorite and zeolite veins downsection.

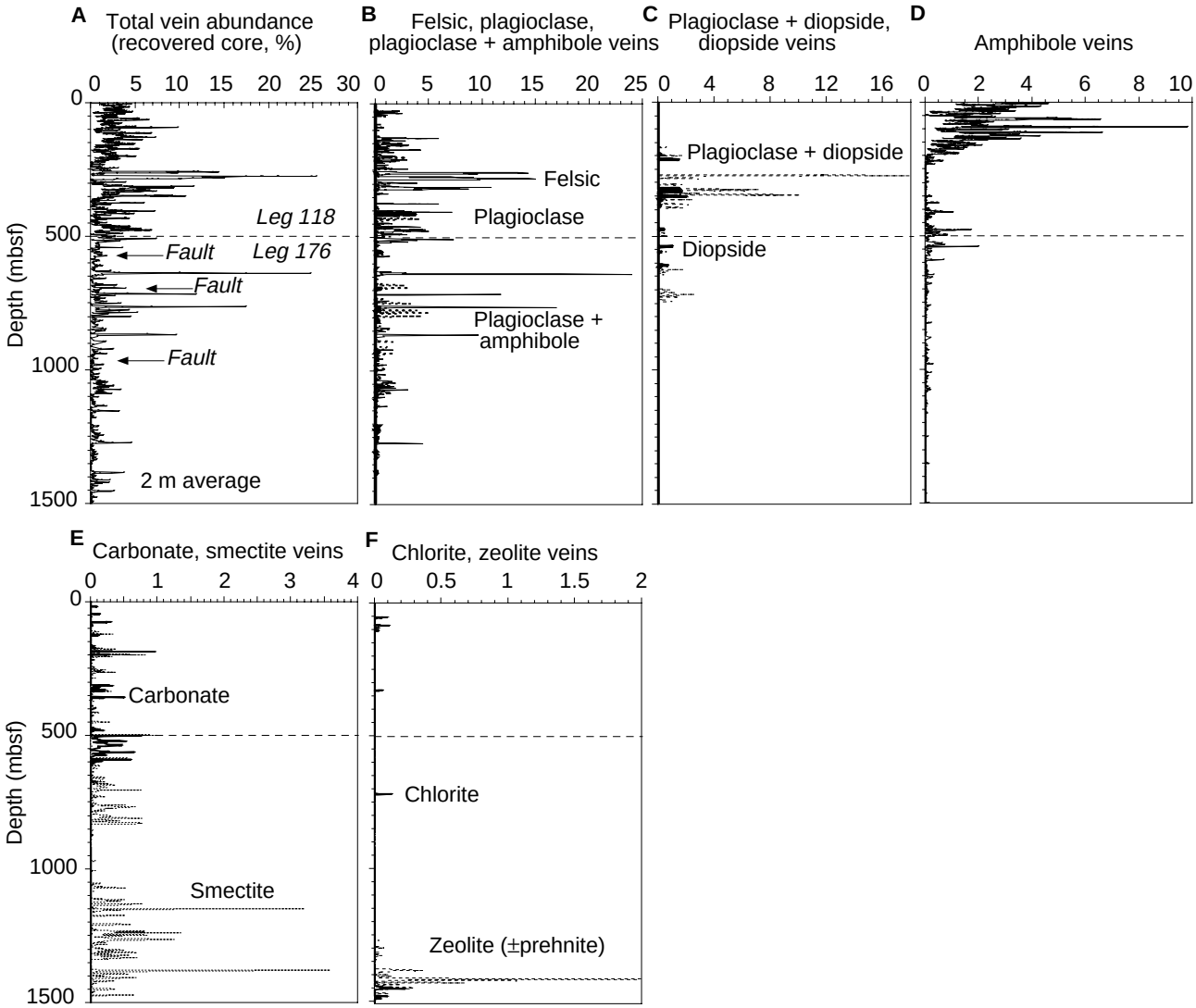

Figure F48. Proportion of the vein types in Hole 735B relative to the total amount of veins (%). The data set is for core from 500 to 1508 mbsf recovered during Leg 176. **A.** Number of veins of each type. **B.** Vein type by area percentage. The data were obtained by systematic counting of the veins and measuring their width and length in the core.

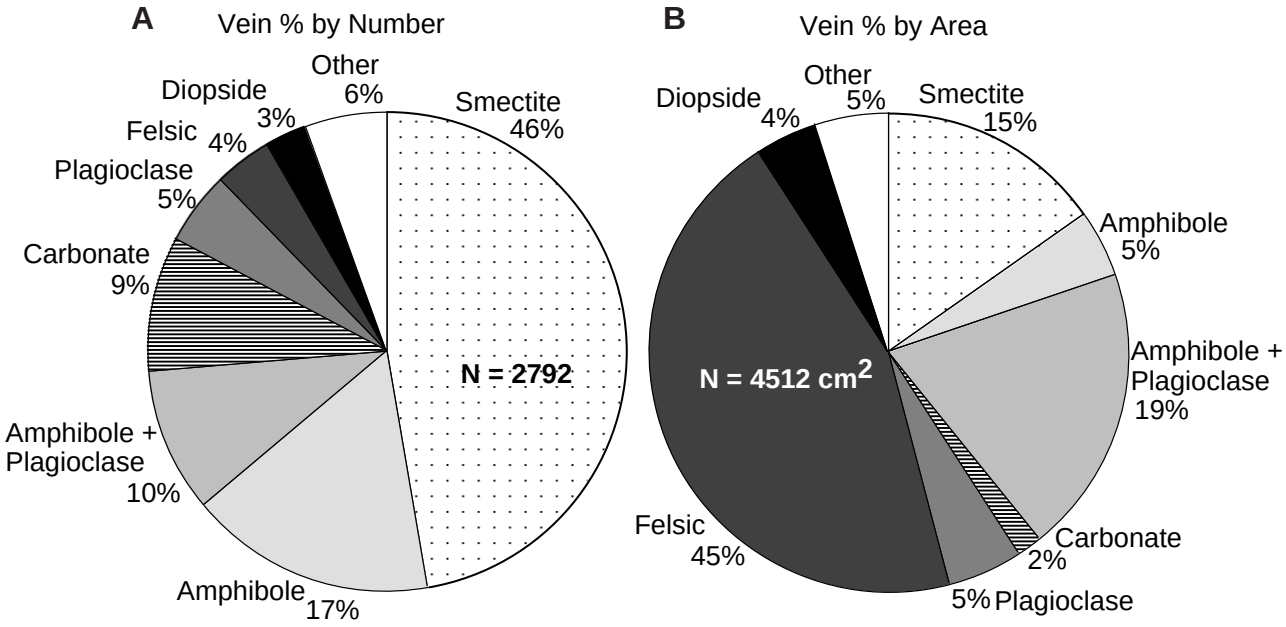

Figure F49. Extensively altered felsic vein in Sample 176-735B-160R-6 (Piece 6, 118–134 cm). Plagioclase is highly altered to secondary plagioclase, prehnite(?), and zeolite. Clinopyroxene is pervasively replaced by amphibole and chlorite. This vein also contains biotite, apatite, and trace amounts of quartz; magnetite is common along the vein margins, both in the vein and wall rock.

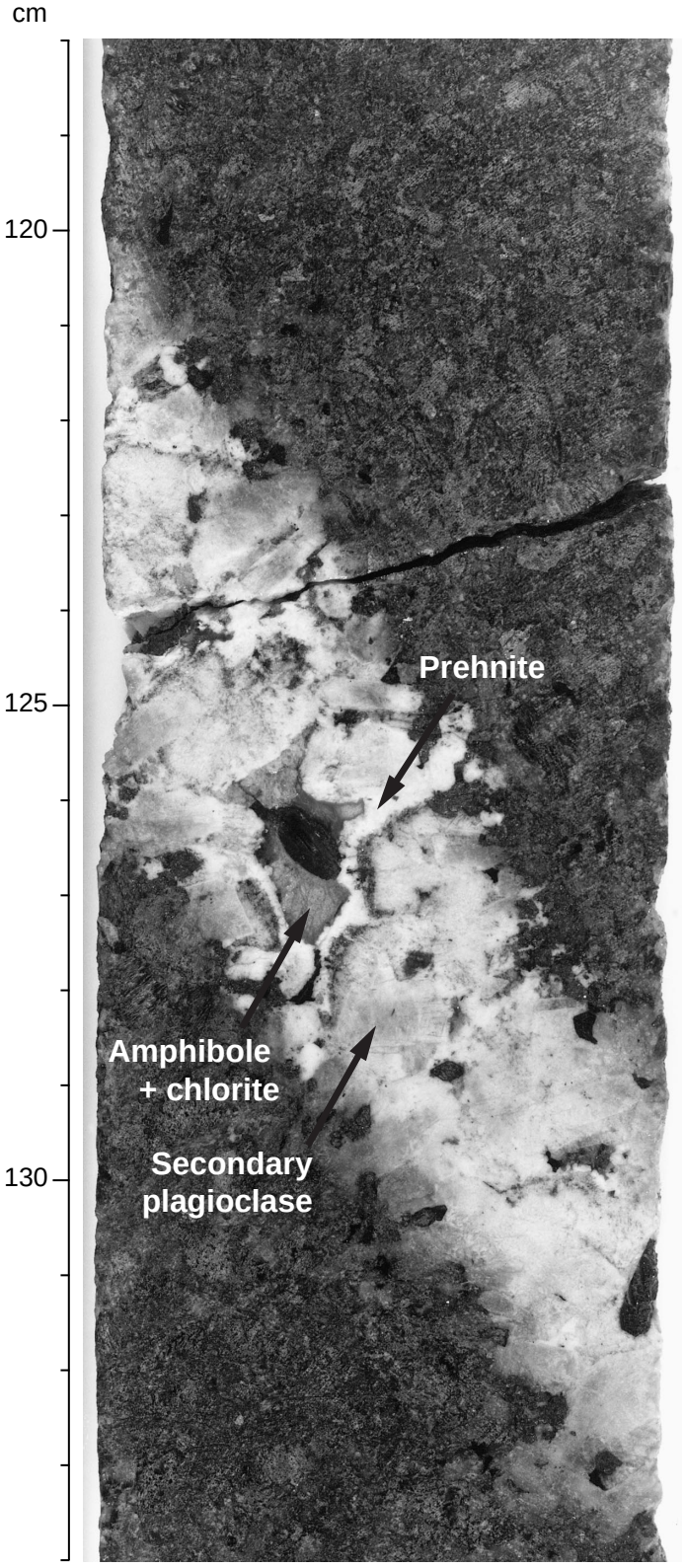

Figure F50. Typical zoned felsic vein in Sample 176-735B-90R-1 (Piece 1C, 37–60 cm). The vein contains an amphibole- and clinopyroxene-rich core, with a plagioclase- and quartz-rich margin. There is a weakly developed halo at the vein margin associated with alteration of plagioclase and pyroxene in the wall rock to secondary plagioclase and amphibole, respectively.

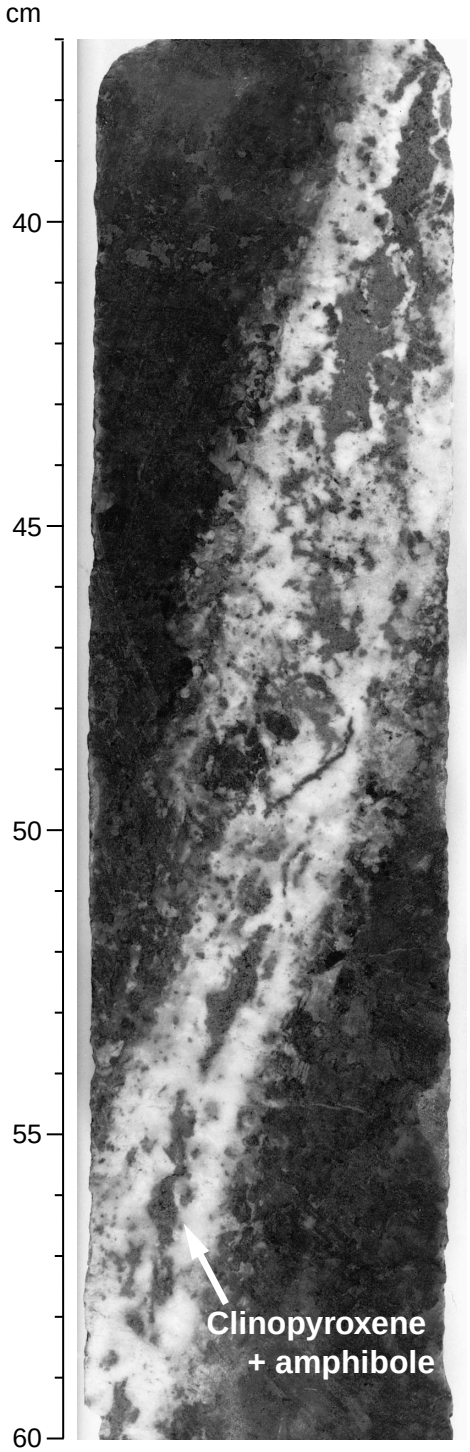

Figure F51. A. Sample 176-735B-110R-2 (Piece 3C, 101–104 cm): large euhedral grain of titanite in a diopside vein. The tip of the titanite crystal projects into a patch of chlorite. **B.** Sample 176-735B-144R-6 (Piece 5B, 89–92 cm): large crystals of green amphibole and titanite in a felsic vein. **C.** Sample 176-735B-99R-4 (Piece 6, 108–111 cm): mymekitic intergrowth of quartz and feldspar in a felsic vein. **D.** Sample 176-735B-157R-5 (Piece 8, 134–140 cm): euhedral zircon crystal associated with large crystals of brown biotite in a sheared zone in olivine gabbro. Scale bars = 0.5 mm.

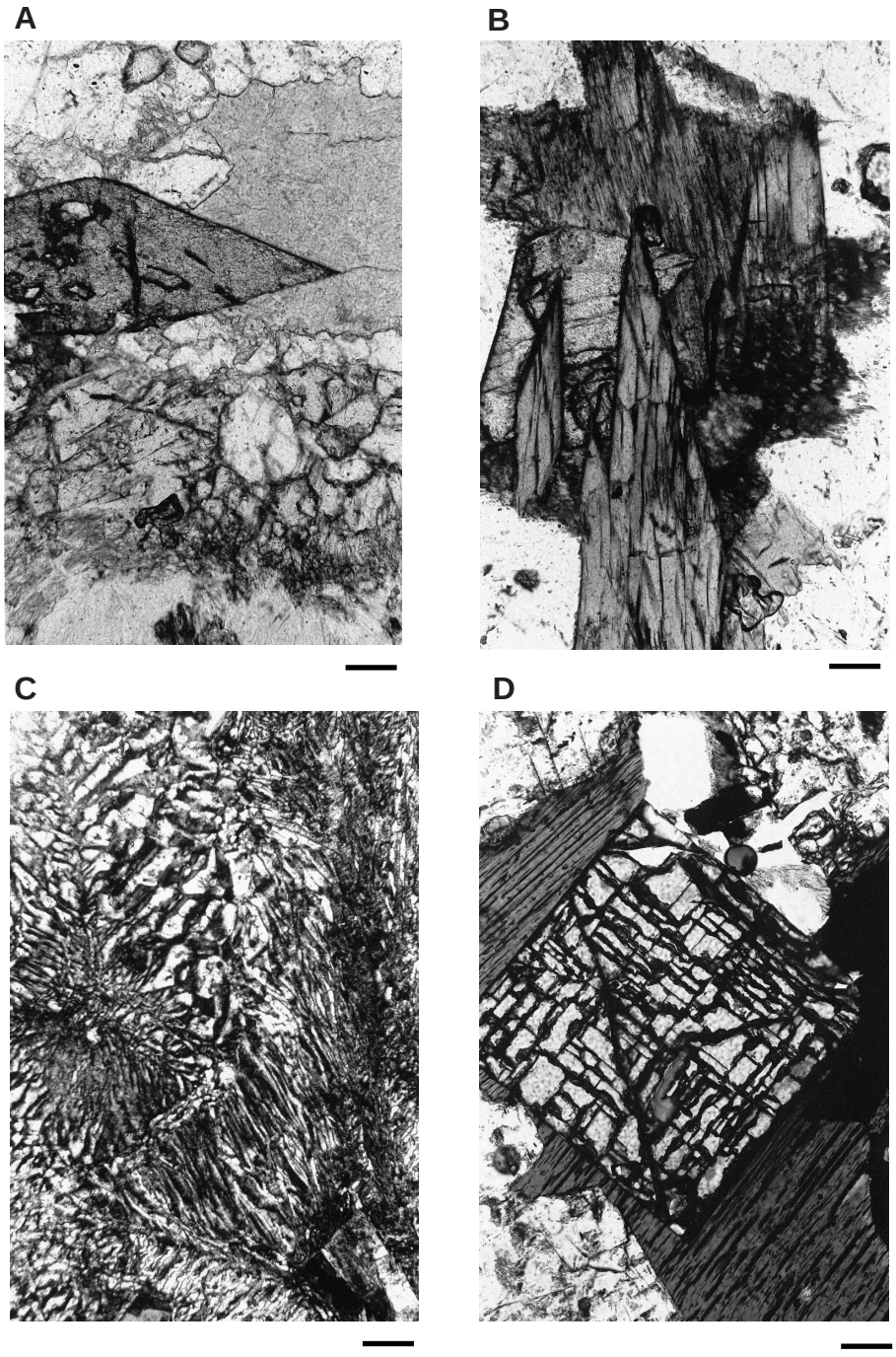

Figure F52. Dioritic vein in Sample 176-735B-110R-4 (Pieces 1–2A, 1–38 cm). Some fine amphibole + plagioclase veins measured in the core may represent small splays off larger vein networks (arrow).

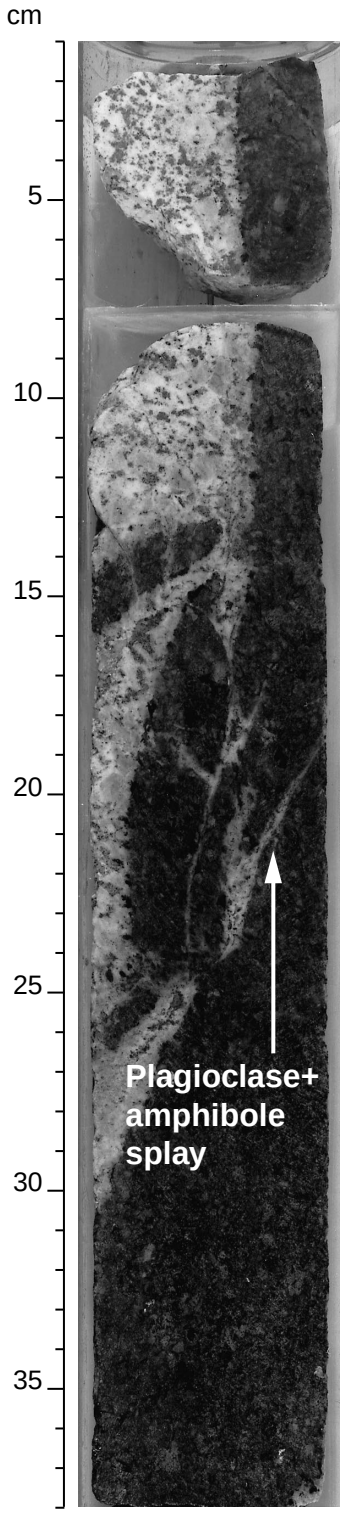

Figure F53. Plagioclase + amphibole vein network in Sample 176-735B-110R-2 (Pieces 9B and 9C, 120–149 cm). The anastomosing vein network is rooted in a small brecciated zone at the base of the section, which is continuous into Section 176-735B-110R-3.

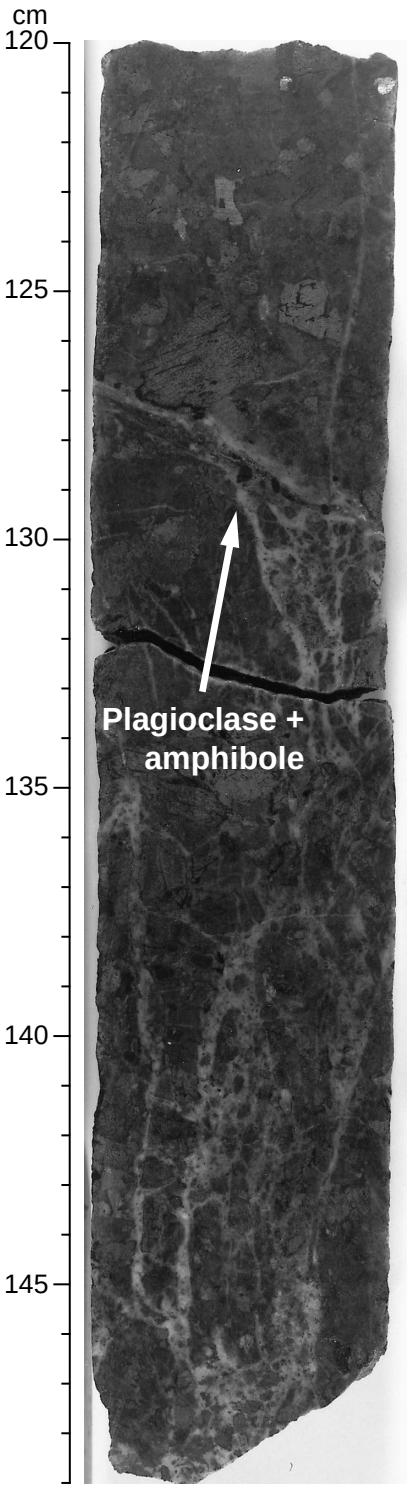

Figure F54. Highly zoned amphibole + plagioclase vein in Sample 176-735B-121R-1 (Pieces 3C and 3D, 64–95 cm). The vein contains an amphibole-rich core rimmed by plagioclase. A weakly developed alteration halo, which is defined by secondary plagioclase and amphibole, extends into the host rock.

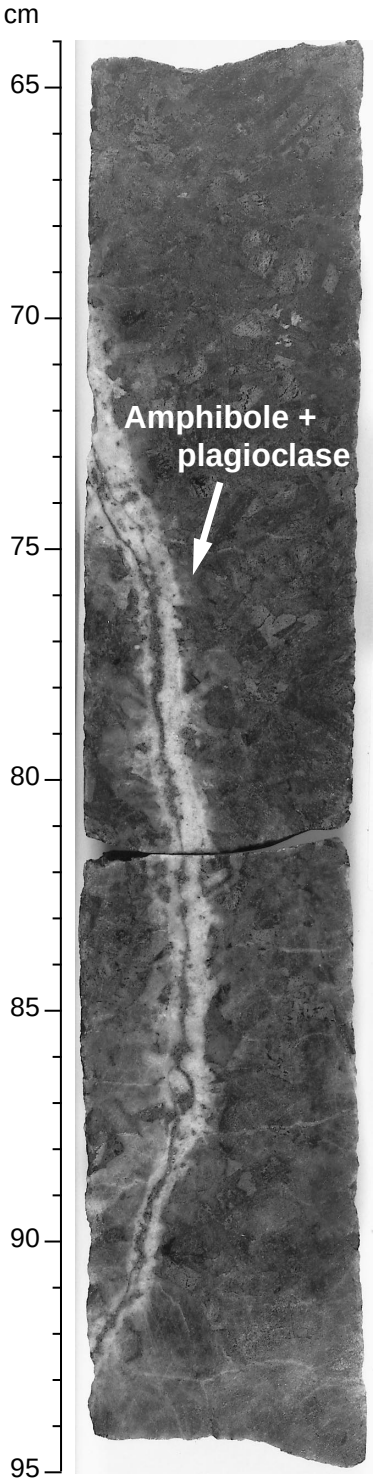

Figure F55. Highly zoned diopside + plagioclase vein in Sample 176-735B-94R-2 (Piece 1A, 13–21 cm). A diopside-rich core is rimmed by altered plagioclase. A narrow alteration halo, which is composed of secondary plagioclase, amphibole, and fine-grained oxide minerals, extends into the wall rock.

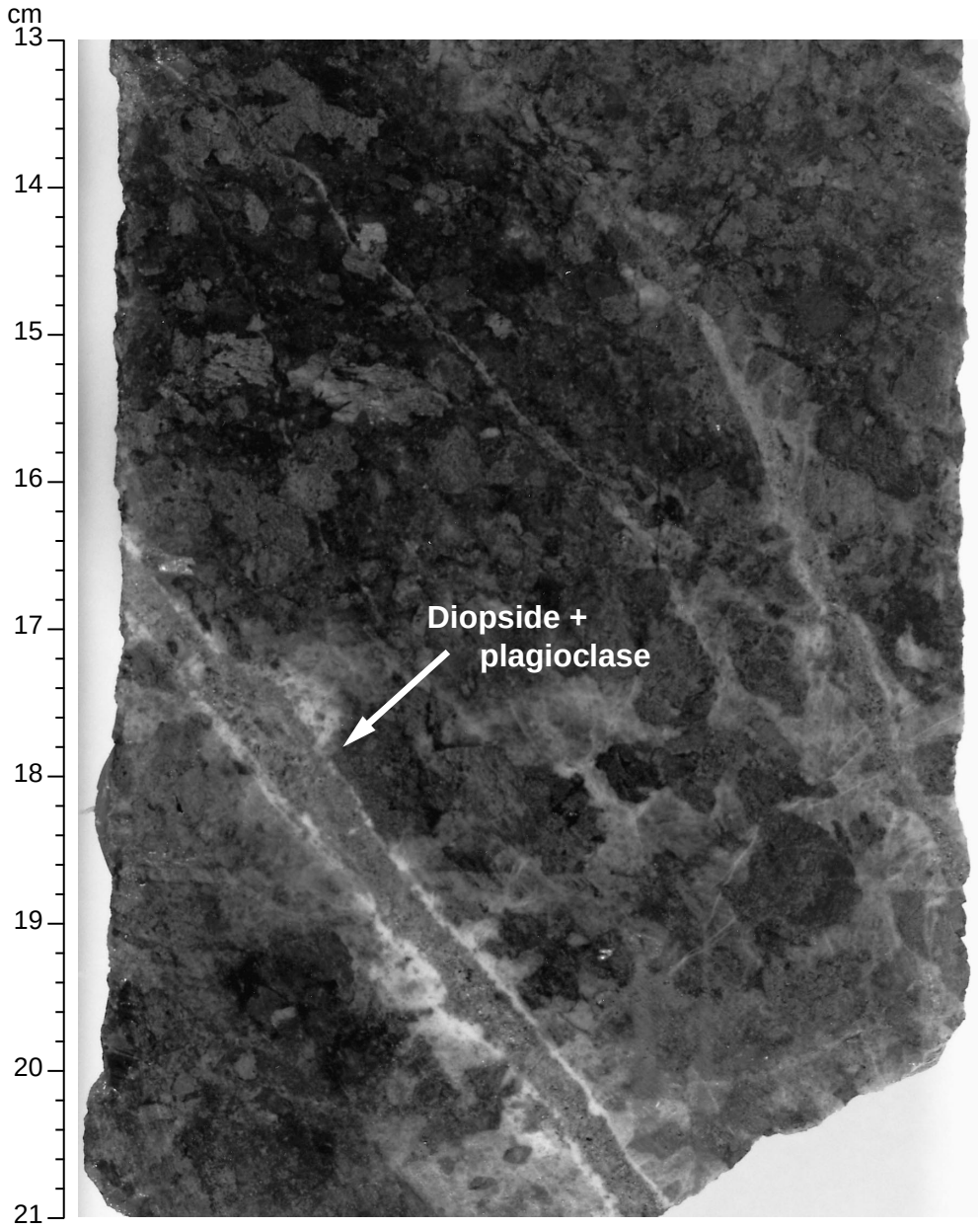

Figure F56. Subvertical amphibole vein in Sample 176-735B-148R-5, 92–112 cm.

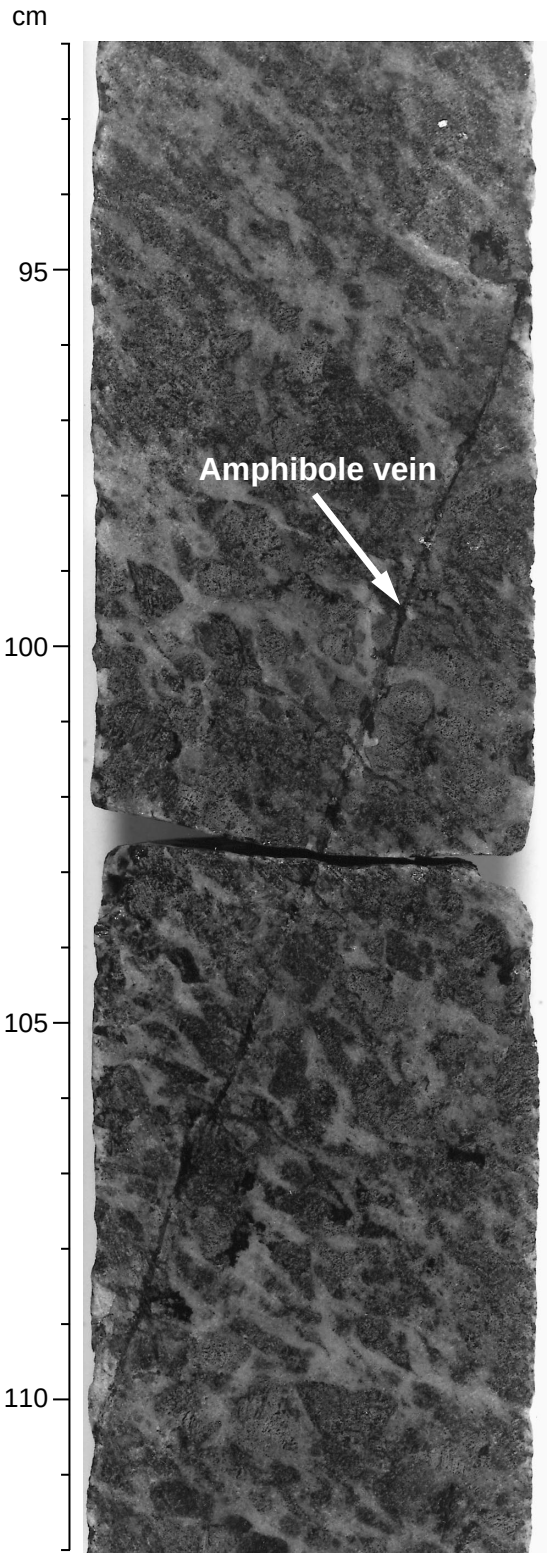

Figure F57. Subvertical anastomosing amphibole vein network in Sample 176-735B-92R-1 (Piece 3A, 10–15 cm). The vein network cuts strongly developed crystal-plastic deformation. Although this style of vein network is relatively common in the upper sections of core recovered during Leg 118, it is rare in gabbroic rocks recovered from below 500 mbsf.

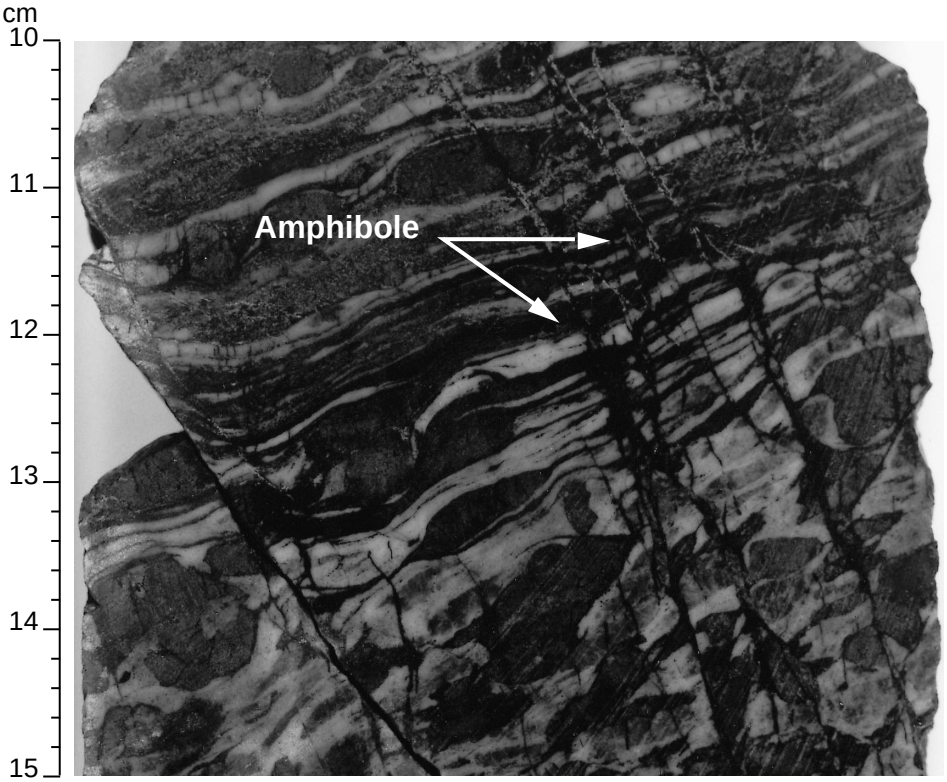

Figure F58. A. Sample 176-735B-92R-1 (Piece 3A, 12–15 cm): amphibole vein cutting and offsetting foliation in an amphibole gneiss. **B.** Sample 176-735B-132R-1 (Piece 11A, 66–68 cm): smectite vein cutting plagioclase. Note platy structure of smectite and orientation of plates normal to the vein wall. Scale bars = 0.5 mm.

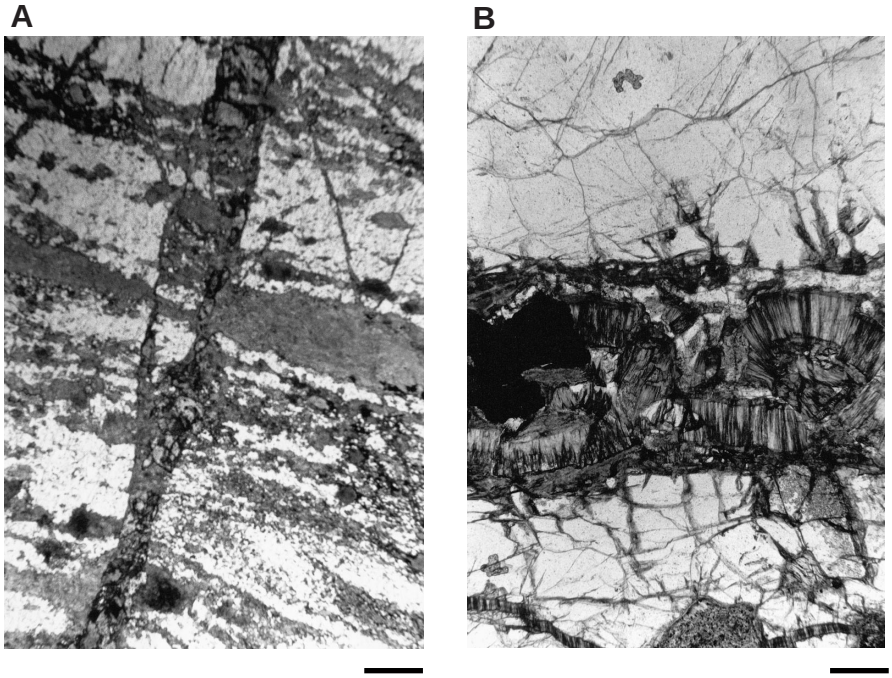

Figure F59. A subvertical set of amphibole veins with very well developed alteration halos that are composed of secondary plagioclase and amphibole (Sample 176-735B-133R-3 [Piece 1, 16–37 cm]). Extensive alteration halos are rare in rocks recovered during Leg 176.

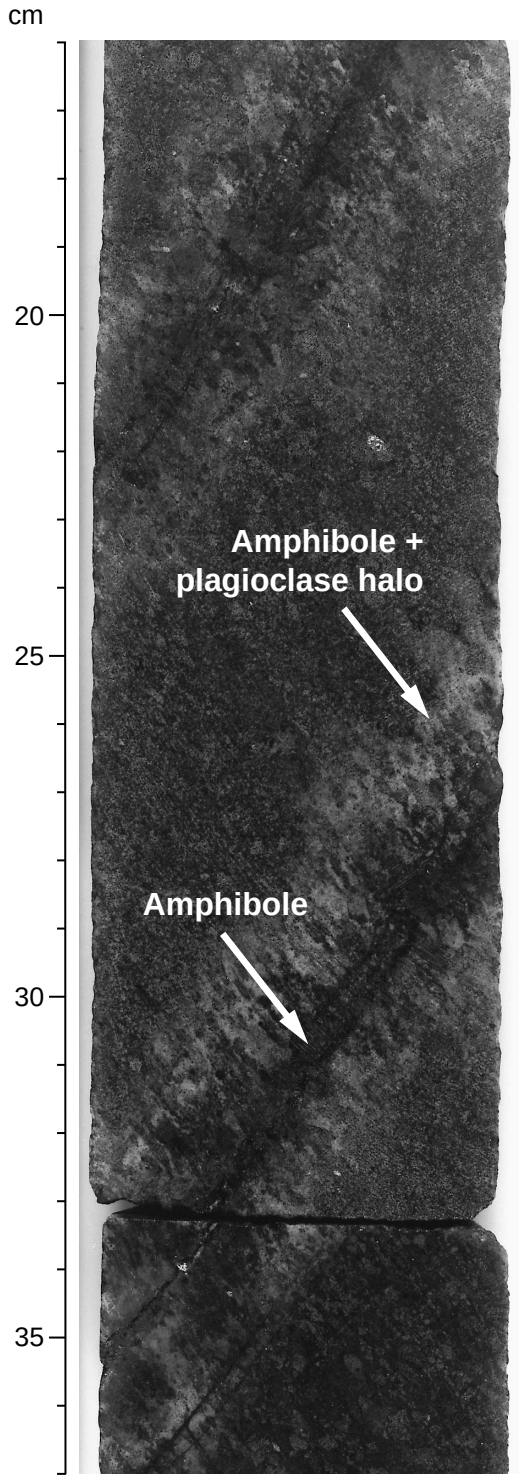

Figure F60. Carbonate veinlet and vug in Sample 176-735B-93R-1 (Piece 6, 74–93 cm).

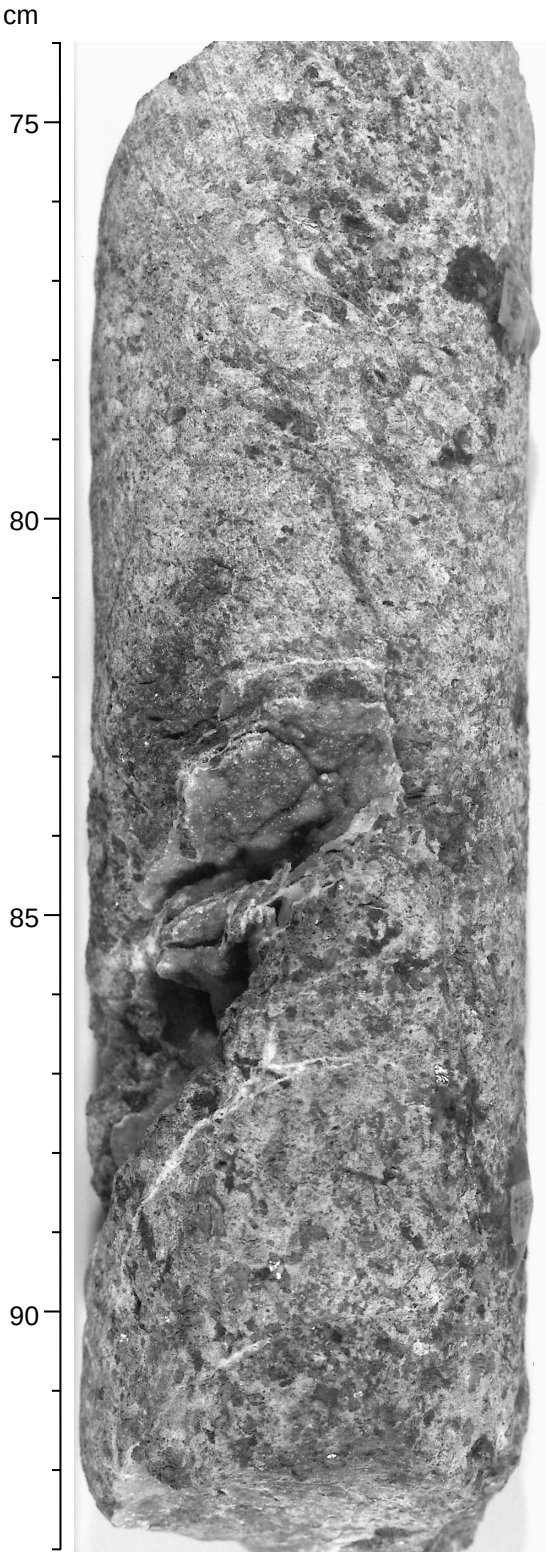

Figure F61. X-ray diffraction profile of vein-forming material (smectite + carbonate) in Sample 176-735B-128R-4 (Piece 10, 118–122 cm; 781 mbsf).

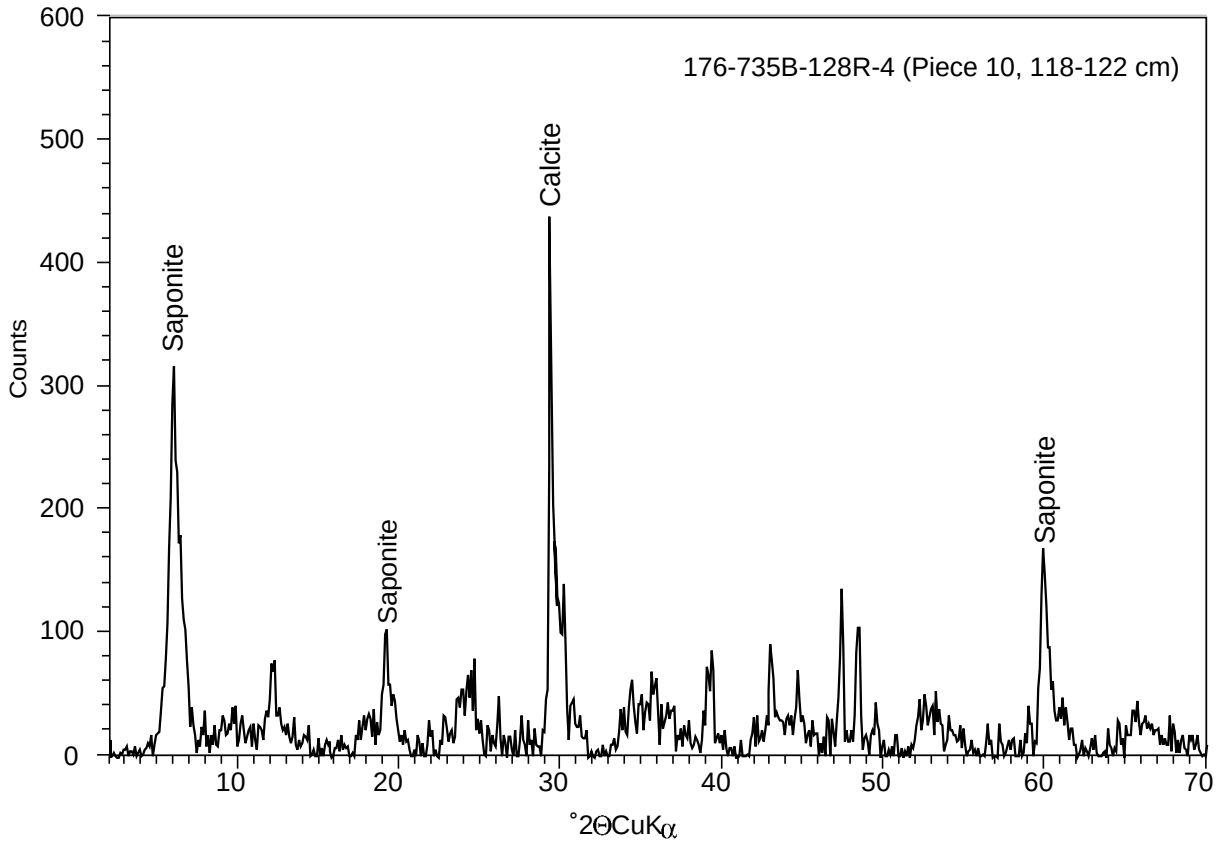

Figure F62. Vertical veins of chlorite and amphibole crosscut by near horizontal smectite veins in Sample 176-735B-205R-2 (Piece 1, 48–68 cm). The rock is significantly altered along the chlorite + actinolite veins. Olivine is almost completely replaced by chlorite/smectite in the center and talc, amphibole, and oxides in the outer parts. Clinopyroxene and plagioclase are slightly altered in the halo. Some of the vertical chlorite + amphibole veins were reopened and filled with smectite.

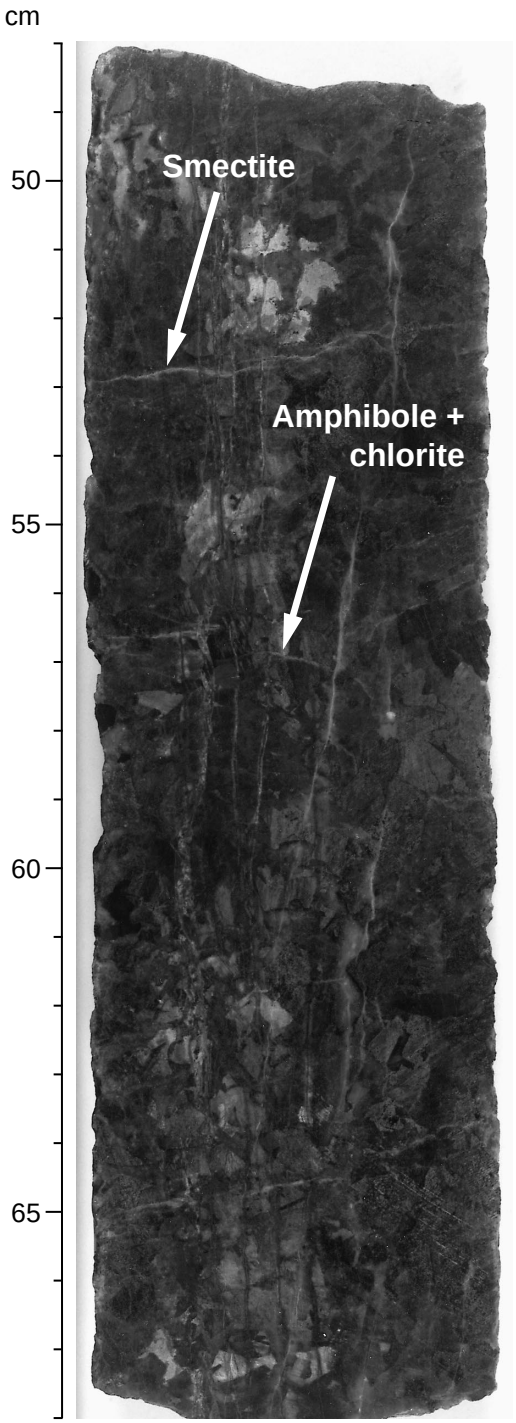

Figure F63. Rare epidote (+amphibole) vein in Sample 176-735B-114R-3 (Pieces 3A and 3B, 86–98 cm). The vein is composed of fine- to medium-grained granular epidote with minor green amphibole.

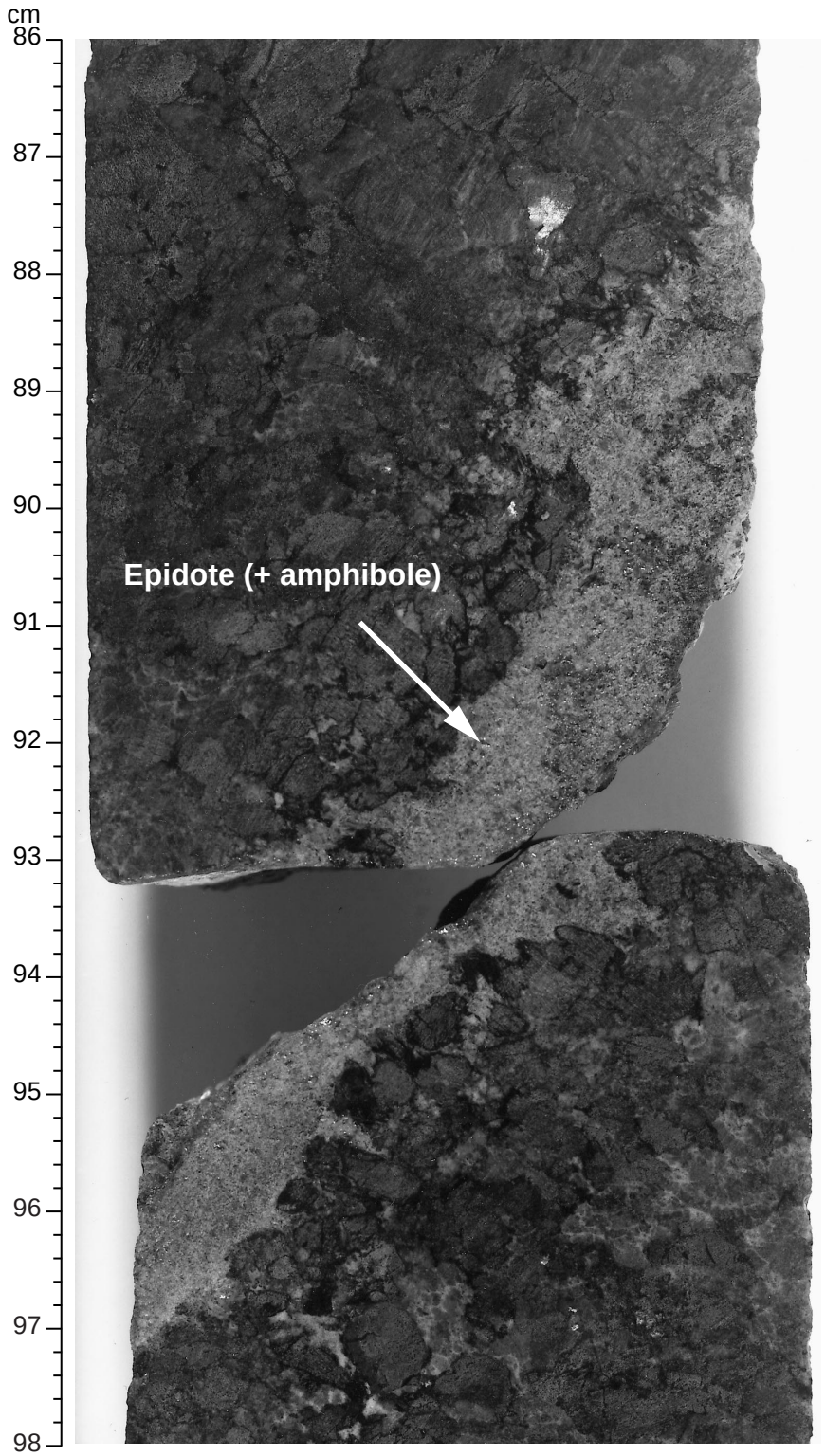

Figure F64. Downhole variation of Mg# from 500 to 1508 mbsf in Hole 735B drilled during Leg 176. Samples are subdivided mainly on the basis of TiO_2. Filled diamonds = troctolite, troctolitic gabbro, and olivine gabbro having <0.4 wt% TiO_2; half-filled diamonds = gabbro, gabbronorite, and disseminated oxide gabbro having between 0.4 and 1.0 wt% TiO_2; open diamonds = oxide gabbro with more than 1.0 wt% TiO_2; half-filled squares = felsic samples or hybrid samples with a significant felsic component; half-filled circle = strongly altered. Sample 176-735B-91R-3, 92–100 cm.

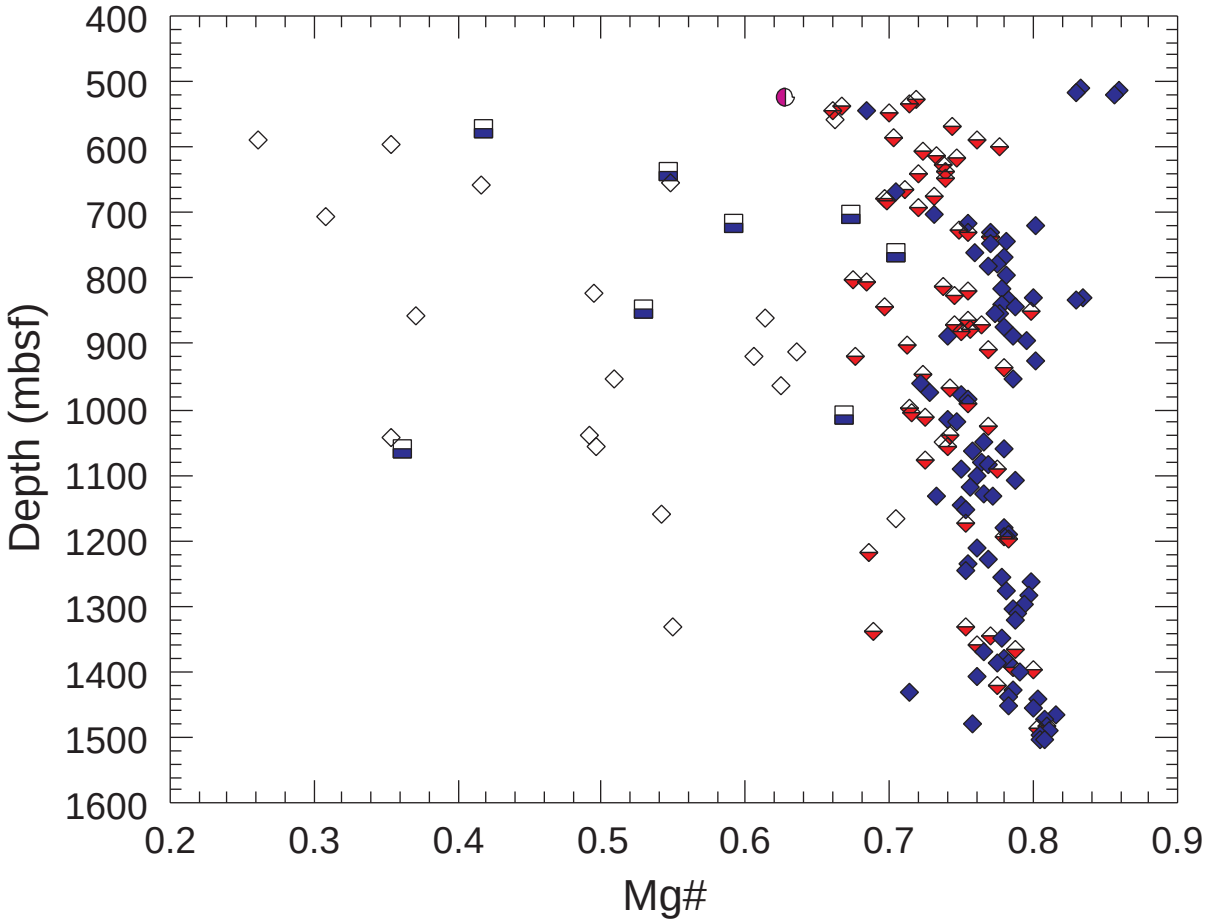

Figure F65. Variation of TiO_2 content with An/(An+Ab) ratio of Leg176 gabbros. An and Ab are the normative anorthite and albite content. Symbols are as in Figure F64, p. 166.

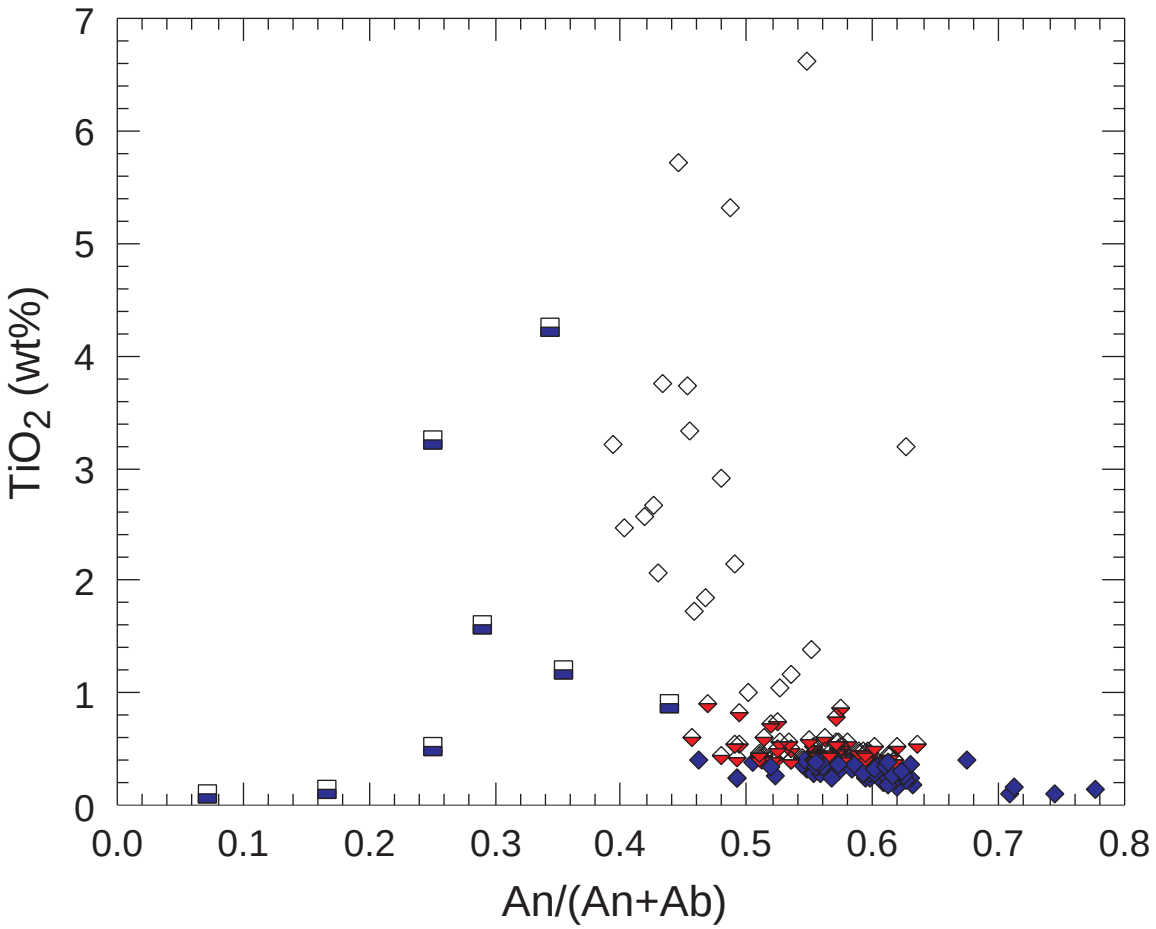

Figure F66. Variation of nickel concentration with MgO content in Leg 176 gabbros with <0.4 wt% TiO_2 and 0.4–1.0 wt% TiO_2. The Ni contents of gabbros are mainly controlled by olivine. Symbols are as in Figure F64, p. 166.

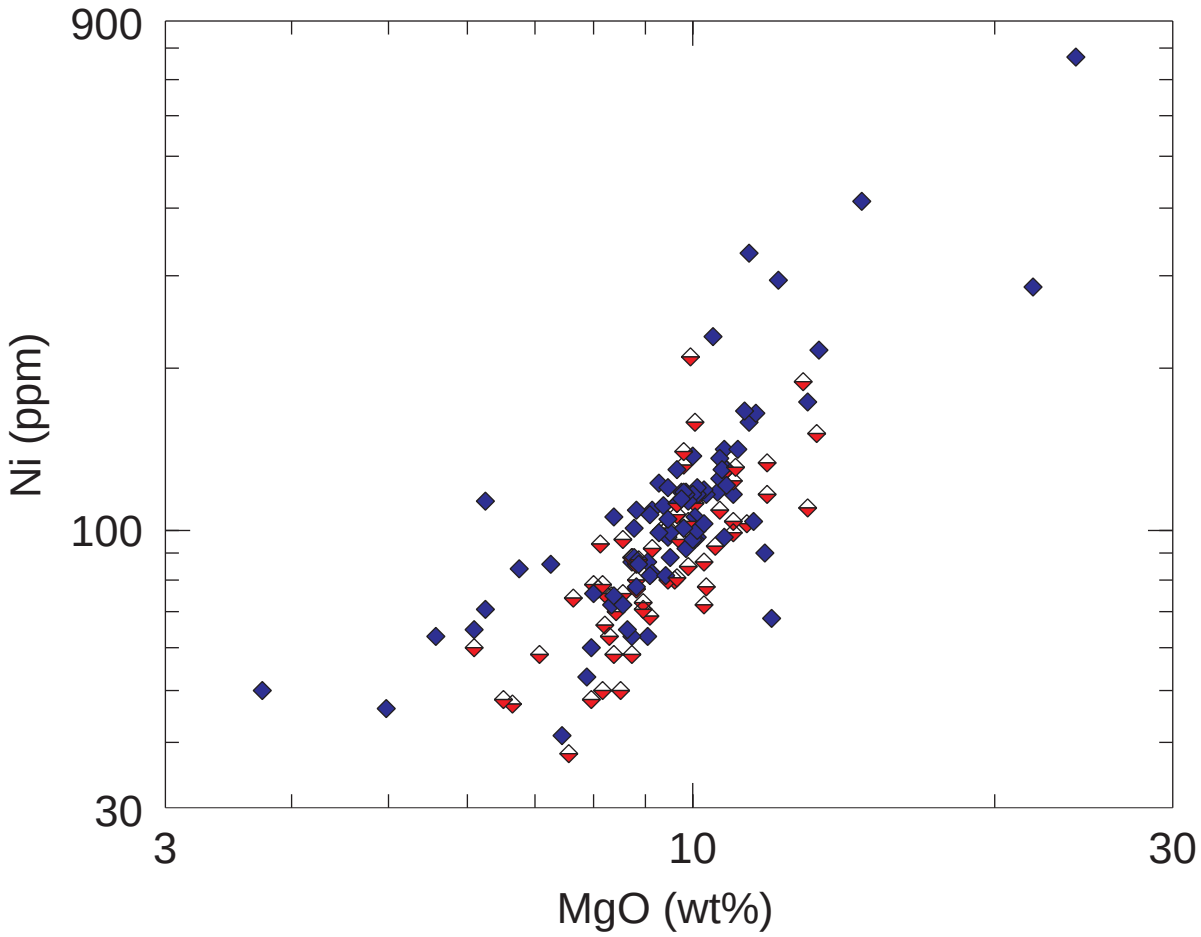

Figure F67. Variation of chromium concentration with MgO content in Leg 176 gabbros. The variation of Cr is more complex than that of Ni (Fig. F66, p. 168) because Cr is controlled by both clinopyroxene and Cr-spinels. Symbols are as in Figure F64, p. 166.

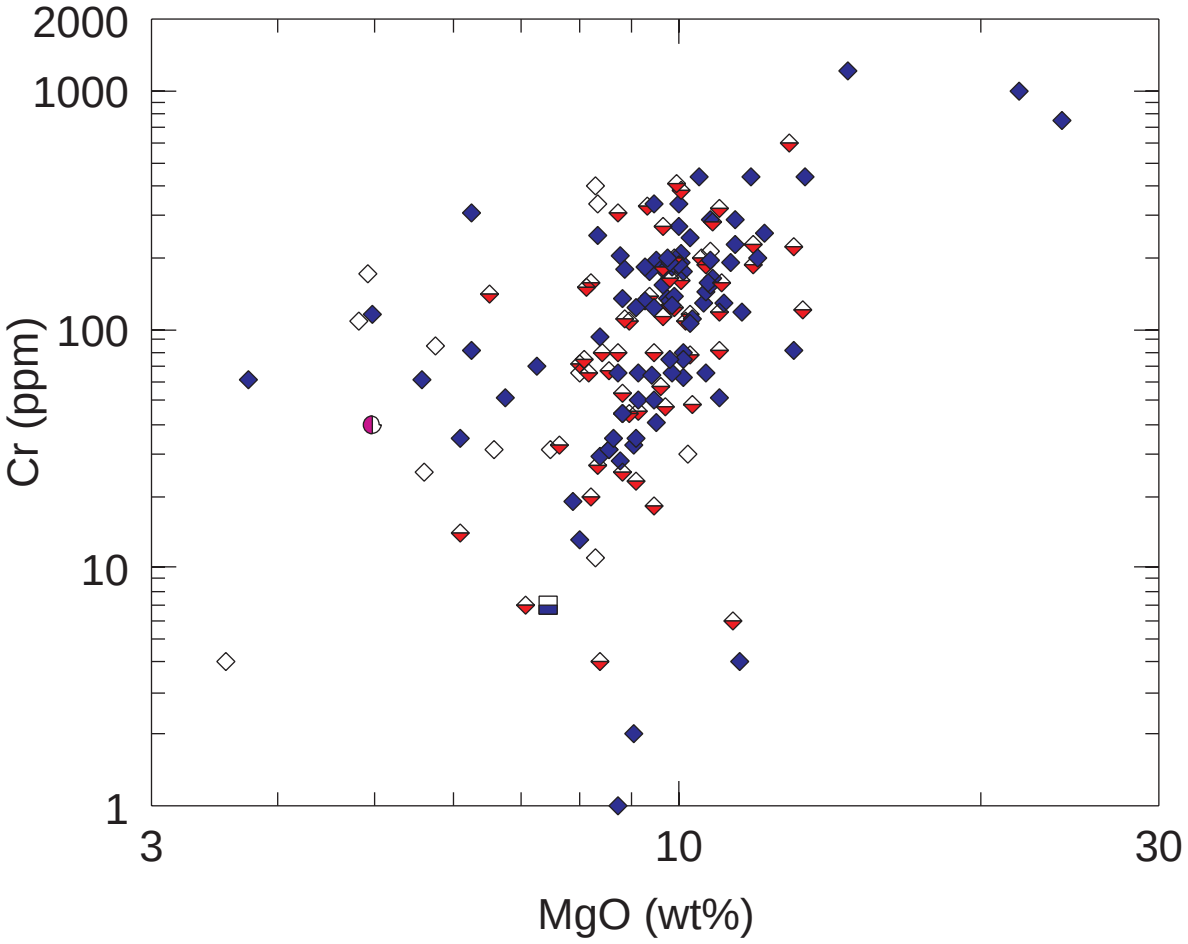

Figure F68. Variation of zinc concentration with total iron content (expressed as Fe_2O_3). The elements zinc and iron correlate very well over a large concentration range in gabbroic rocks drilled during Leg 176. Apparently Zn substitutes for Fe^{2+} in silicate phases and oxide minerals. Symbols are as in Figure F64, p. 166.

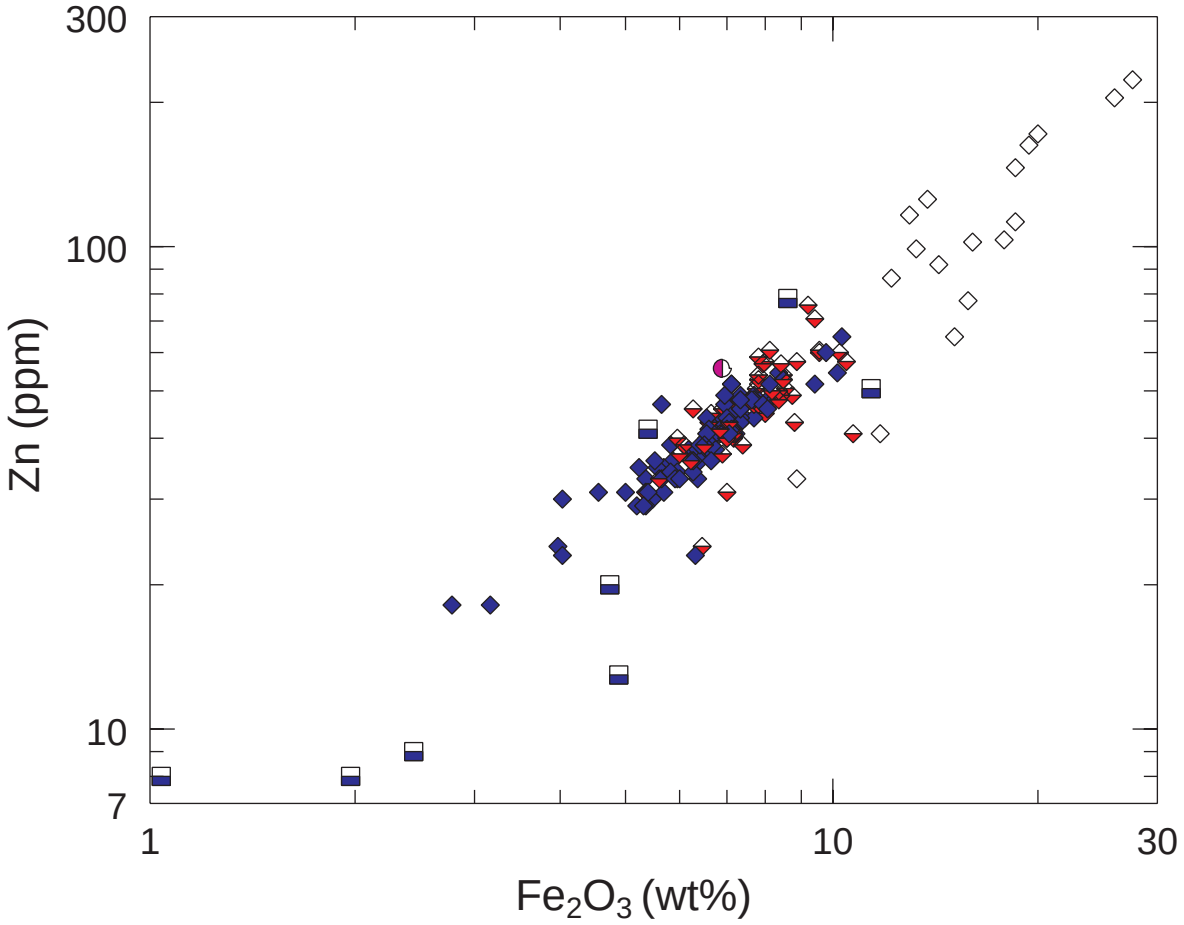

Figure F69. Vanadium vs. titanium in Leg 176 gabbros. The trace element vanadium correlates fairly well with TiO_2 in oxide-poor and in oxide-rich gabbros. The correlation for felsic rocks is poor.

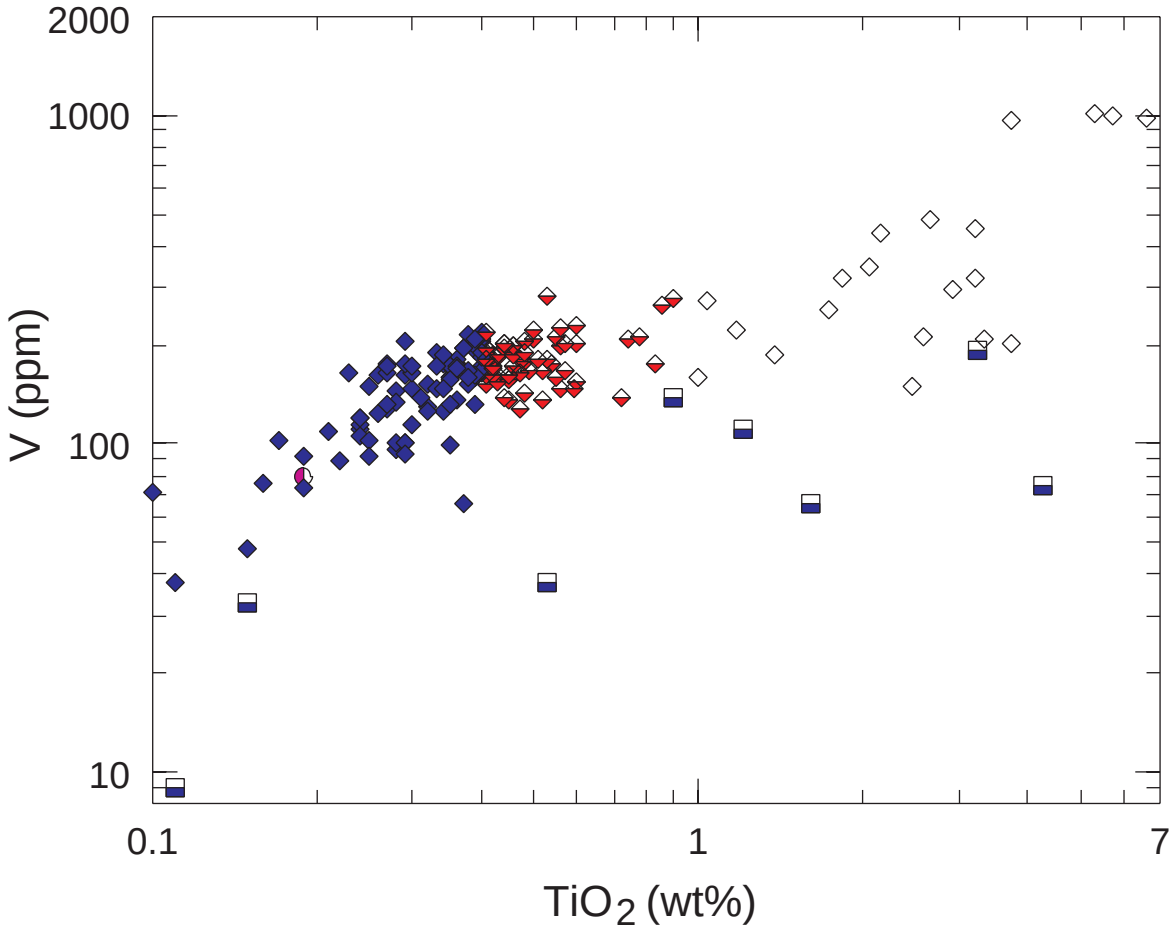

Figure F70. Variation of vanadium with titanium (<2 wt%) in Leg 176 gabbros. Symbols are as in Figure F64, p. 166. Filled triangle = basalt dike Sample 118-735B-23R-4, 83–86 cm; Leg 118 shipboard sample analysis. Cpx = estimate of average Ti,V composition of clinopyroxene in oceanic gabbros. The variation of vanadium concentration with TiO_2 content shows an inflection at ~0.4 wt% TiO_2, which marks a change in the processes controlling the V and Ti in gabbroic rocks. The Ti-poor samples lie on a mixing line between clinopyroxene, the main Ti and V host phase in these gabbros, and olivine and plagioclase that are virtually devoid of these elements. Samples having >0.4 wt% TiO_2 have lower V/Ti ratios, due to either trapping of interstitial liquid or accumulation of Ti-rich oxide minerals.

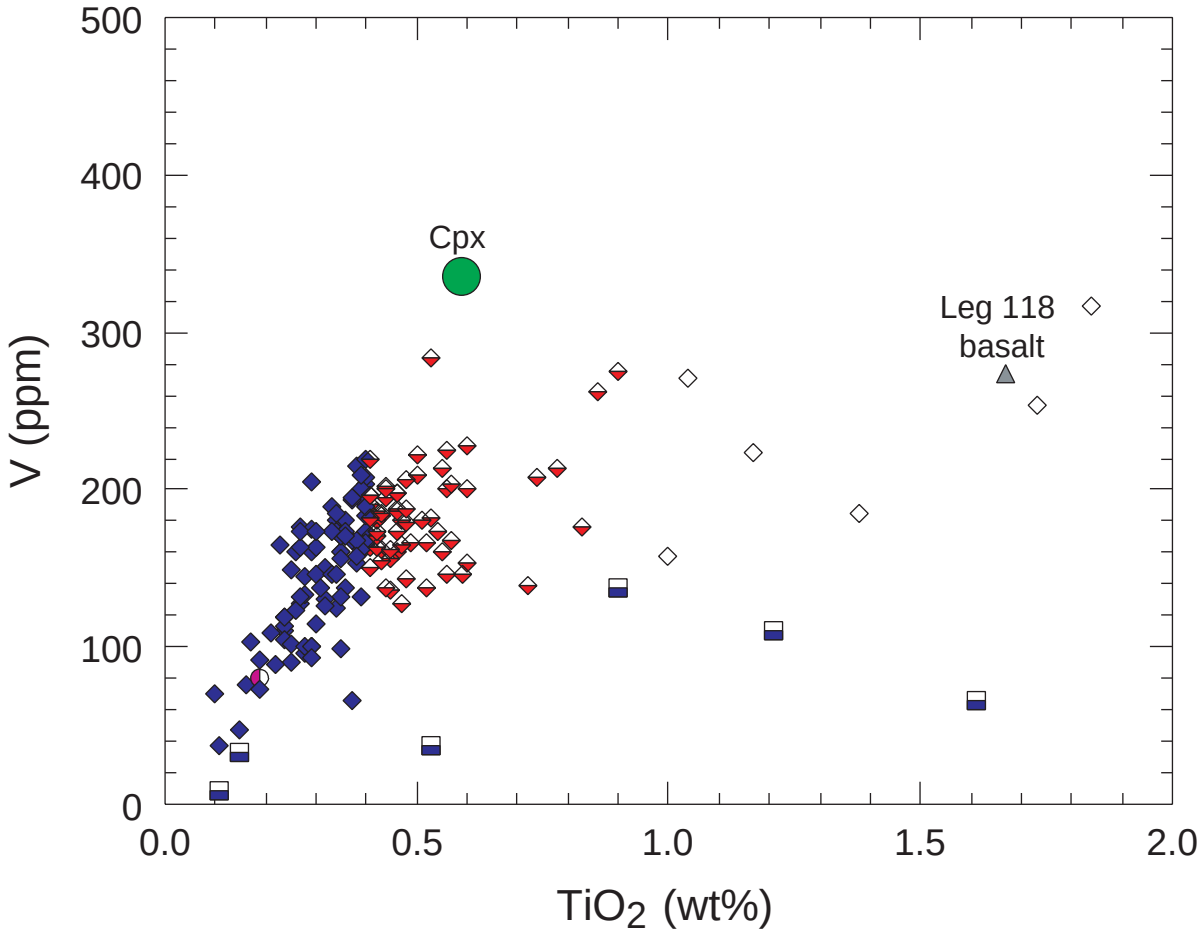

Figure F71. The strontium content of Leg 176 gabbros vs. Al_2O_3/MgO ratio. This chemical parameter is a measure of the relative abundance of plagioclase, which is the main host phase of strontium. Symbols are as in Figure F64, p. 166.

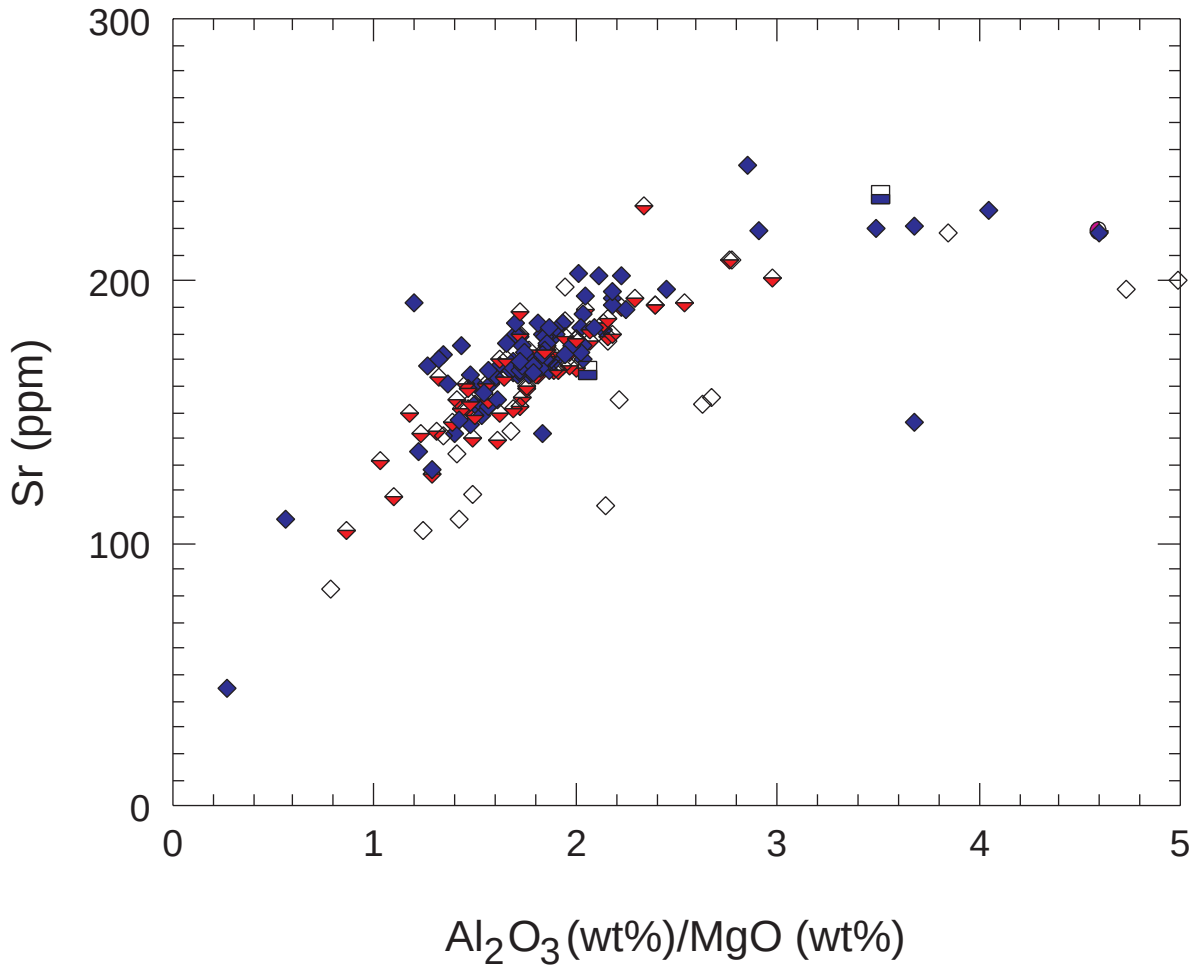

Figure F72. Variation of Sr/Al ratio with An/(An+Ab) ratio. The partitioning of Sr into plagioclase apparently increases with increasing albite content of plagioclase. Strongly differentiated felsic samples have low Sr content due to depletion of the liquids by plagioclase fractionation. Symbols are as in Figure F64, p. 166.

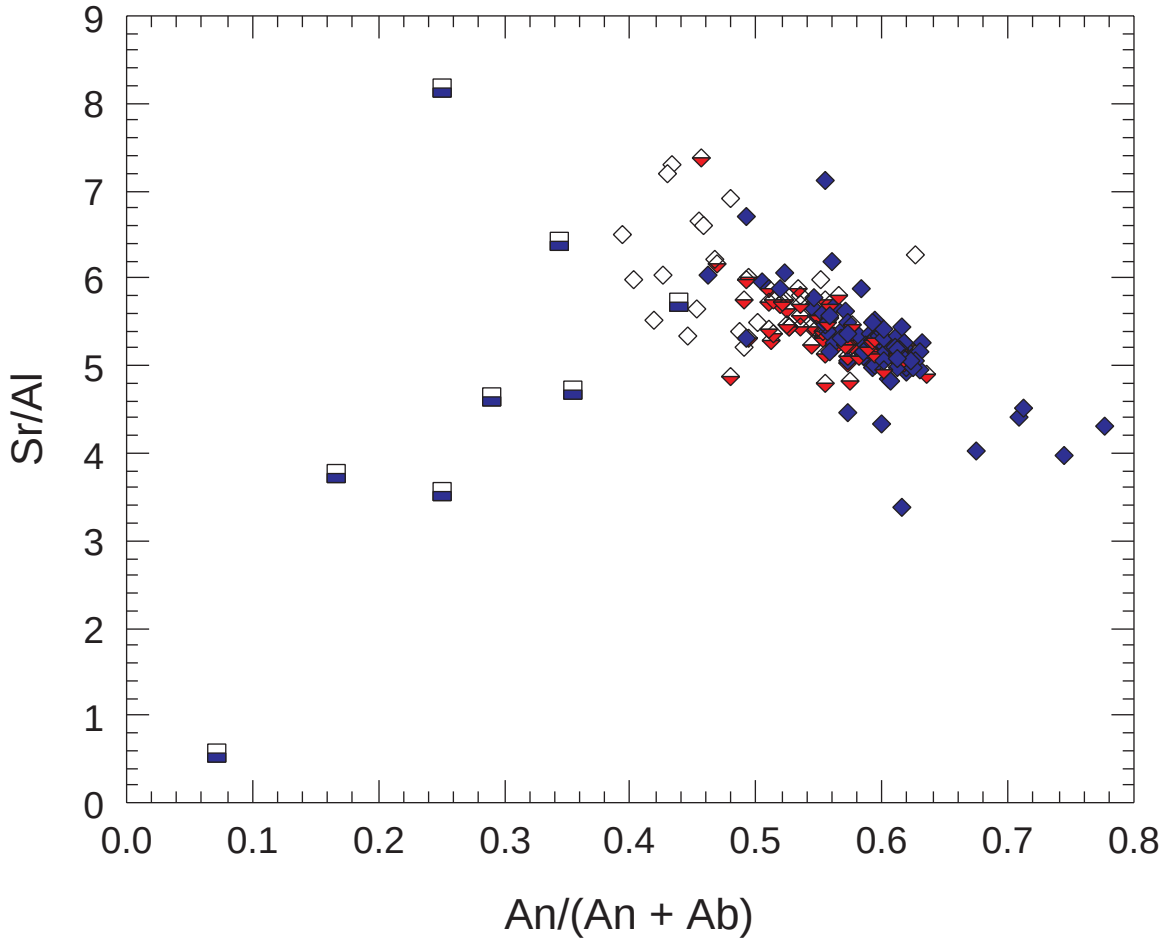

Figure F73. Chemical stratigraphy of Hole 735B from 500 to 1508 mbsf, based on the composition of gabbros with <1 wt% TiO_2. The troctolitic samples recovered between 500 and 520 mbsf belong to lithologic Unit VI defined by the Leg 118 shipboard party. The boundaries between successive units are based solely on abrupt changes in chemical composition except for the boundary at 800 mbsf. However, the boundaries also coincide with changes in lithologic, alteration, and structural properties. Symbols are as in Figure F64, p. 166.

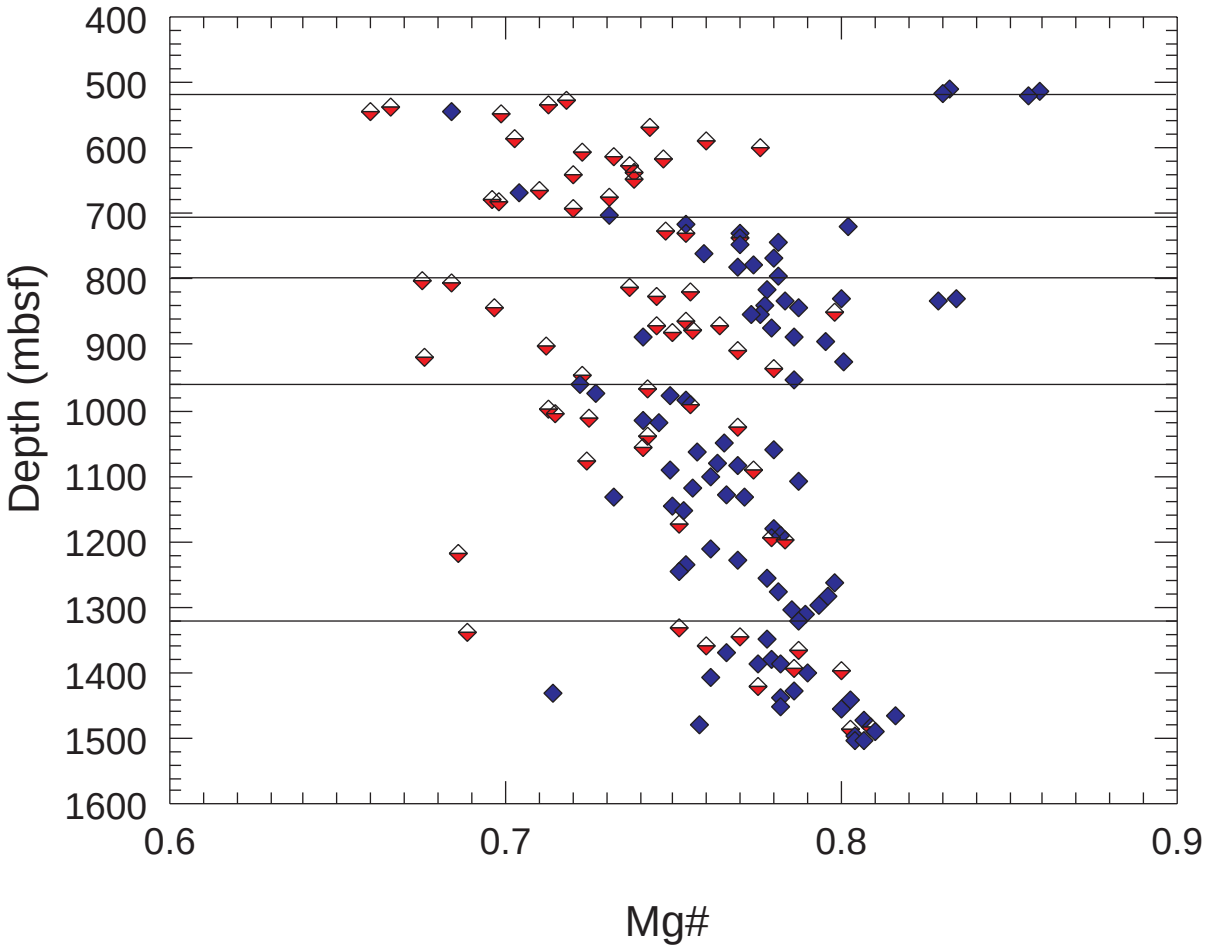

Figure F74. Downhole variation of the Mg# over the entire depth of Hole 735B (Legs 118 and 176) based on 357 whole-rock analyses (see text for sources). The section consists of a stack of a number of chemical/magmatic units, which, in most cases, exhibit an evolution from more primitive gabbro at the bottom to more differentiated members at the top. Symbols are as in Figure F64, p. 166. Filled triangle = basalt dike Sample 118-735B-23R-4, 83–86 cm.

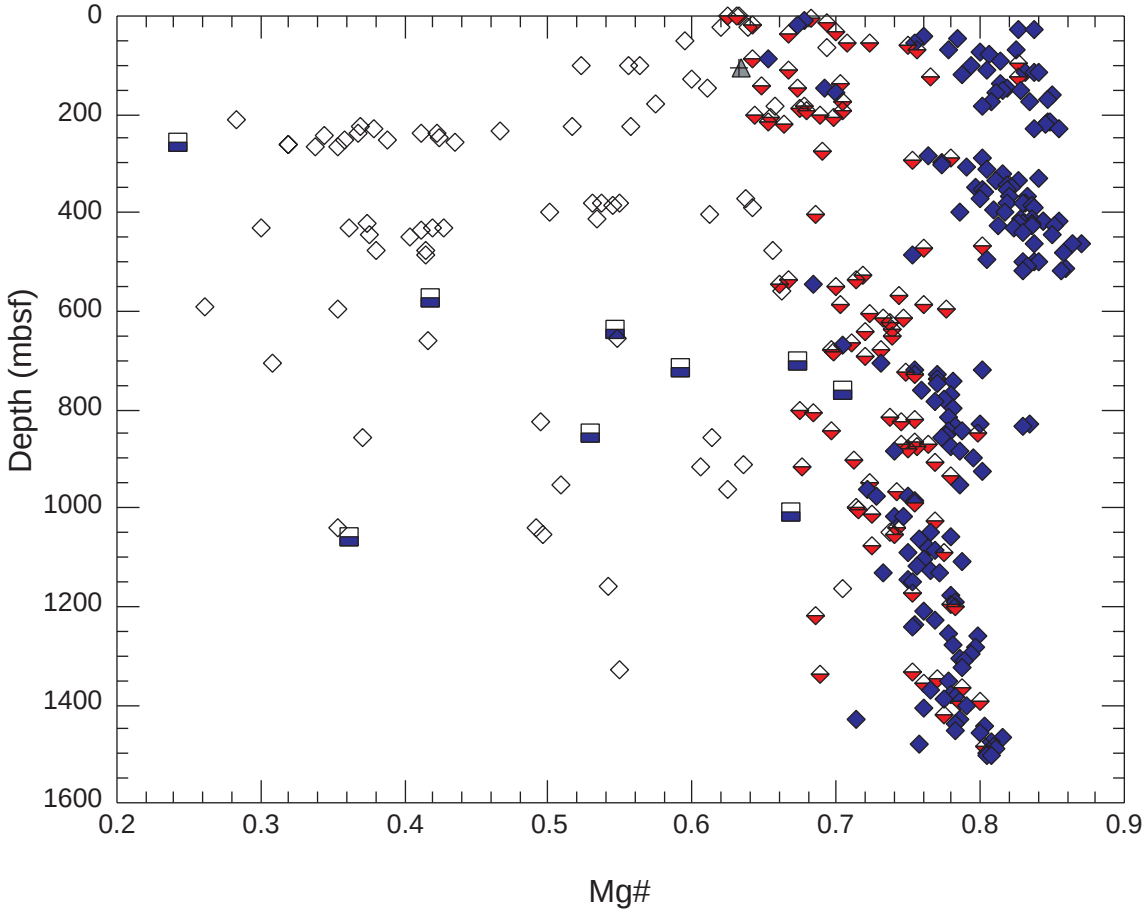

Figure F75. Downhole variation of the TiO_2 content over the entire depth of Hole 735B (Legs 118 and 176) based on 357 whole-rock analyses (see text for sources). Note the logarithmic scale of the X axis. Leg 118 Unit IV (224 to 274 mbsf) is largely made up of massive oxide-rich gabbros. Leg 118 Unit VI (382 to 520 mbsf) spans the whole range of TiO_2 content, from Ti-poor troctolites to oxide gabbros that occur as seams dispersed in rather primitive gabbro. The abundance of Fe-Ti-rich intervals appears to decline with depth in Hole 735B. Symbols are as in Figures F64, p. 166, and F74, p. 176.

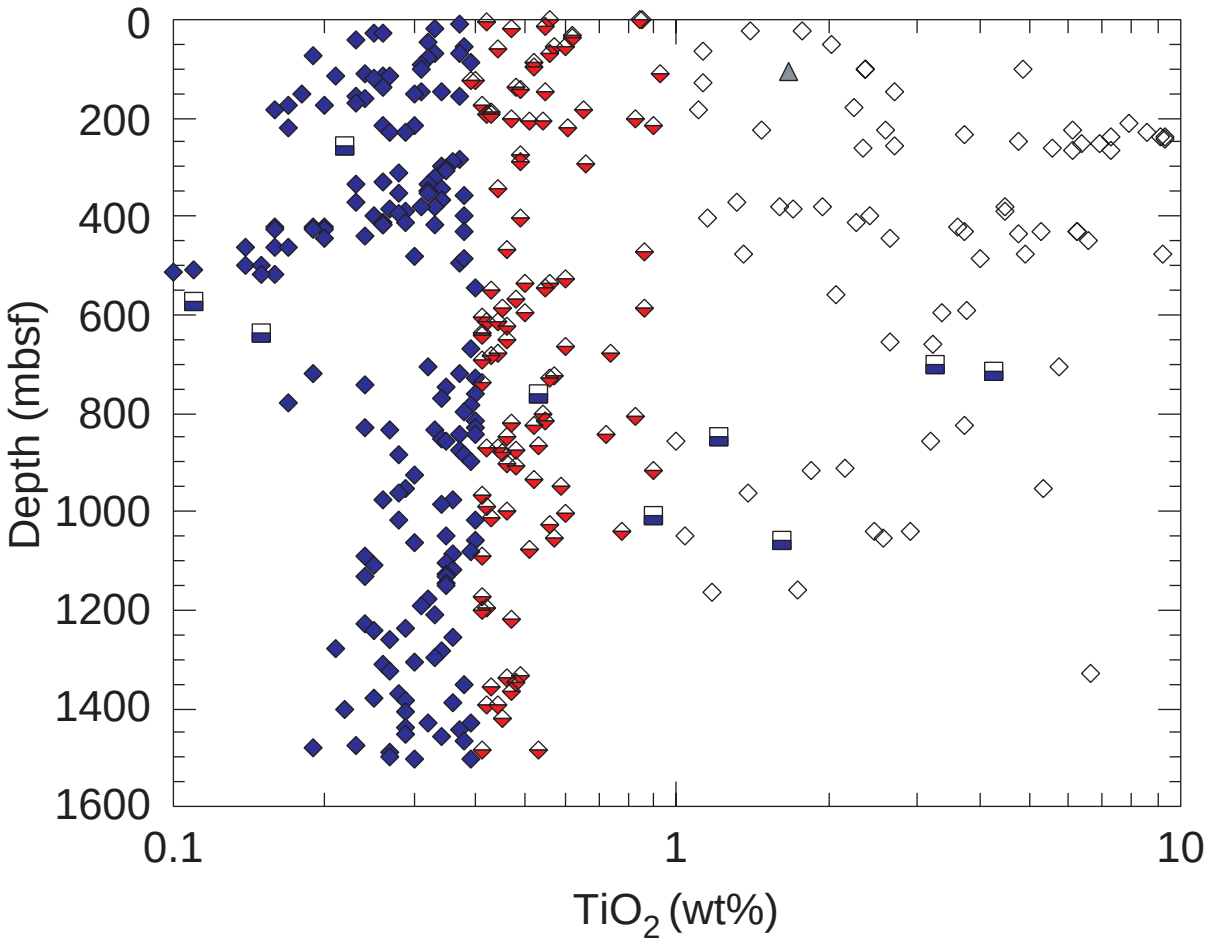

Figure F76. Downhole variation of the abundance of the trace element yttrium over the entire depth of Hole 735B (Legs 118 and 176) based on 357 whole-rock analyses (see text for sources). The yttrium data have been recast as logarithmic chondrite-normalized values for ready comparison with the normalized abundances of heavy REE, for which yttrium is a proxy. The clinopyroxene-poor troctolites from Leg 118 Units III and VI are depleted in yttrium and, by inference, heavy REE and other incompatible trace elements. However, these elements are highly enriched in the felsic veins and many oxide-rich gabbros. Symbols are as in Figure F64, p. 166.

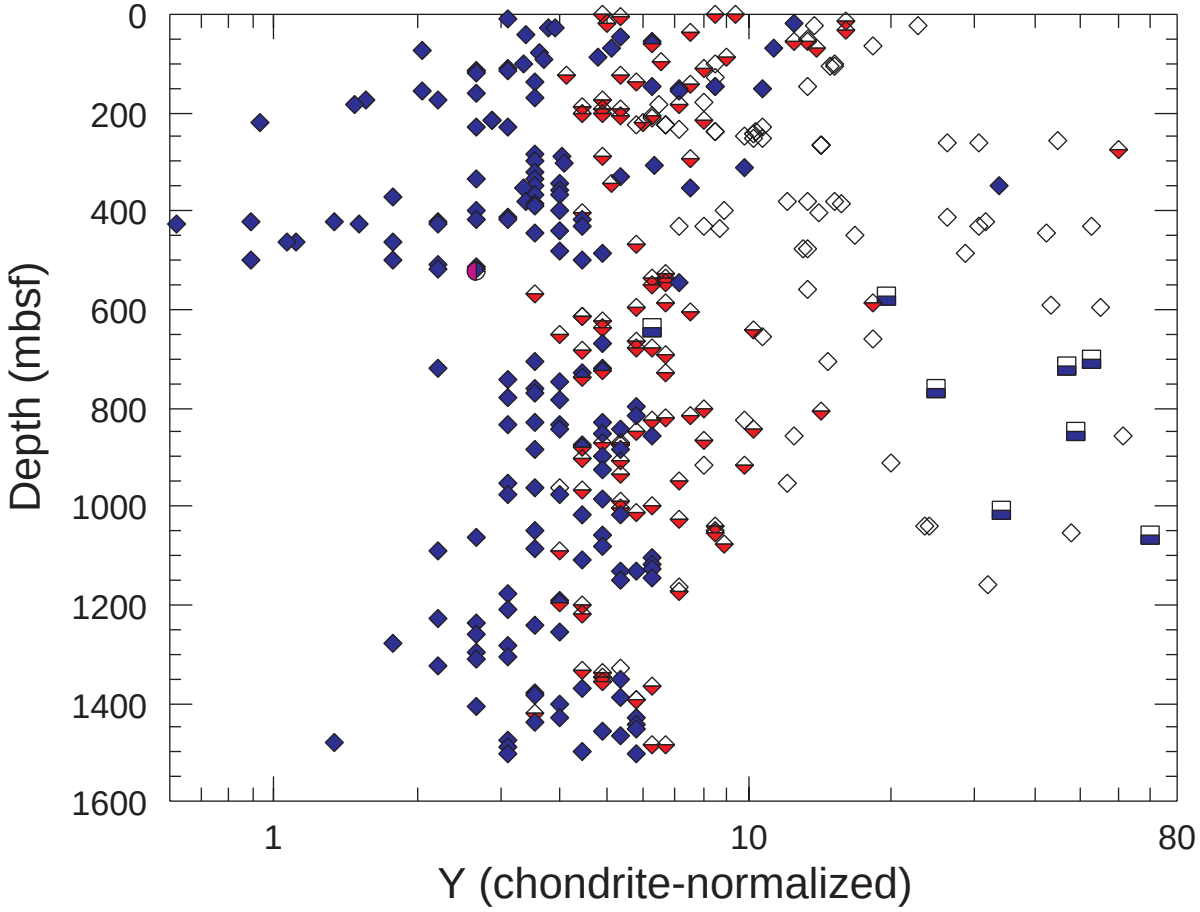

Figure F77. Number of measurements of magmatic fabric intensity and corresponding percentage of core length in which each fabric intensity was observed in hand specimen.

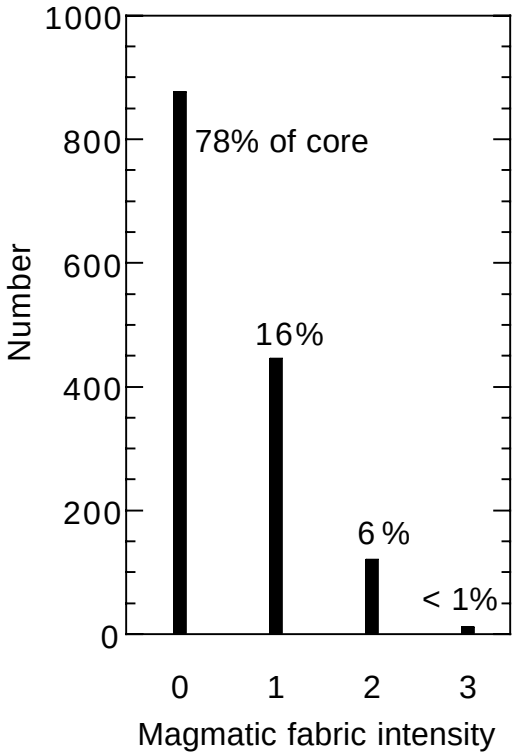

Figure F78. A. Variation of magmatic foliation fabric intensity (running average) with depth. **B.** Variation of magmatic foliation dip vs. depth.

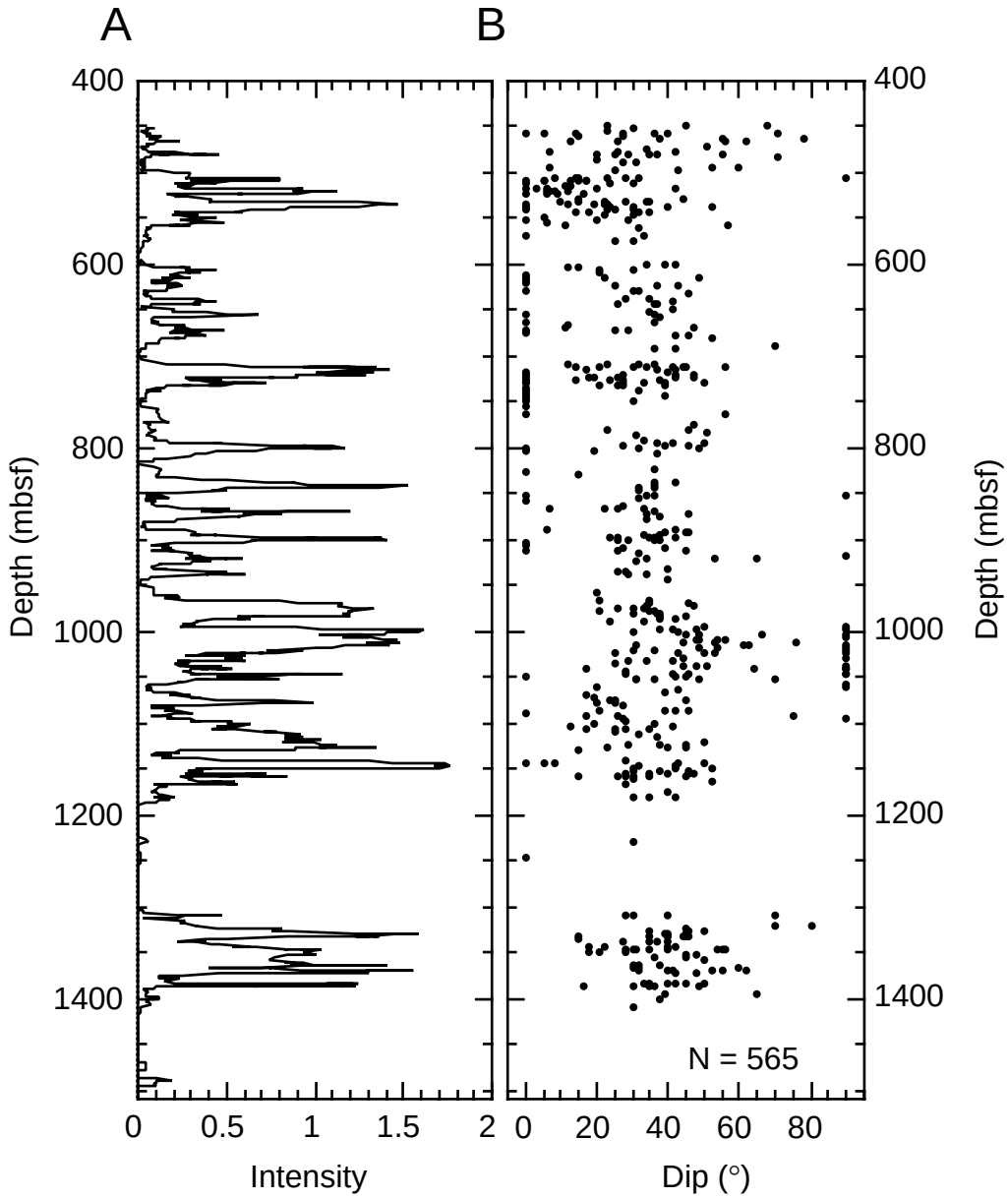

Figure F79. Correlation between magmatic and crystal-plastic fabrics. **A.** Fabric intensities (running averages) vs. depth for magmatic and crystal-plastic foliations. Lower hemisphere projection contoured at 2× uniform distribution: **B.** Poles of magmatic foliations clustering with a trend and plunge of 270/40 (565 points). **C.** Poles of crystal-plastic foliations clustering with a trend and plunge of X/Y (436 points).

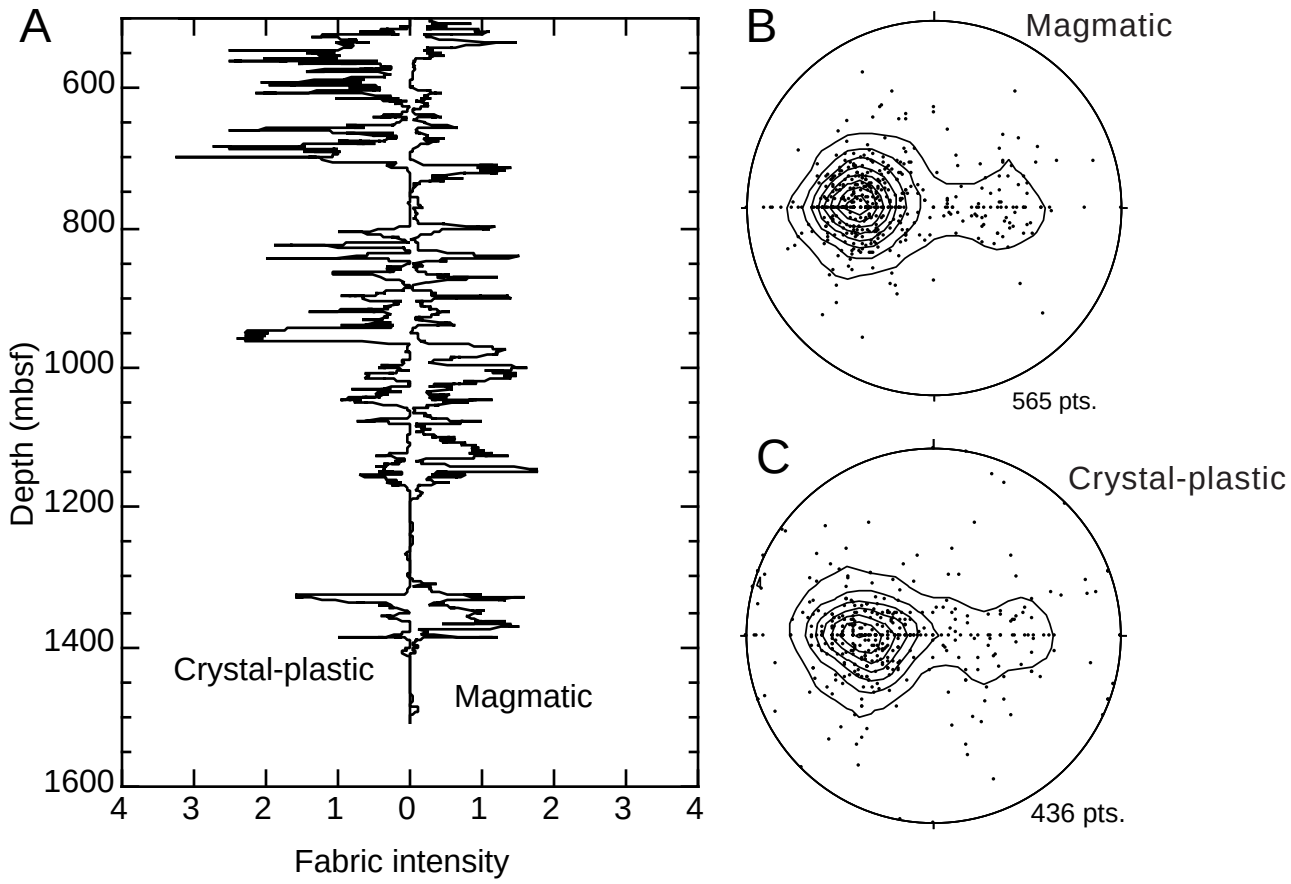

Figure F80. A. Variation in dip of igneous layers with depth. **B.** Number of measured igneous layers/50-m interval (total number of measured layers = 56).

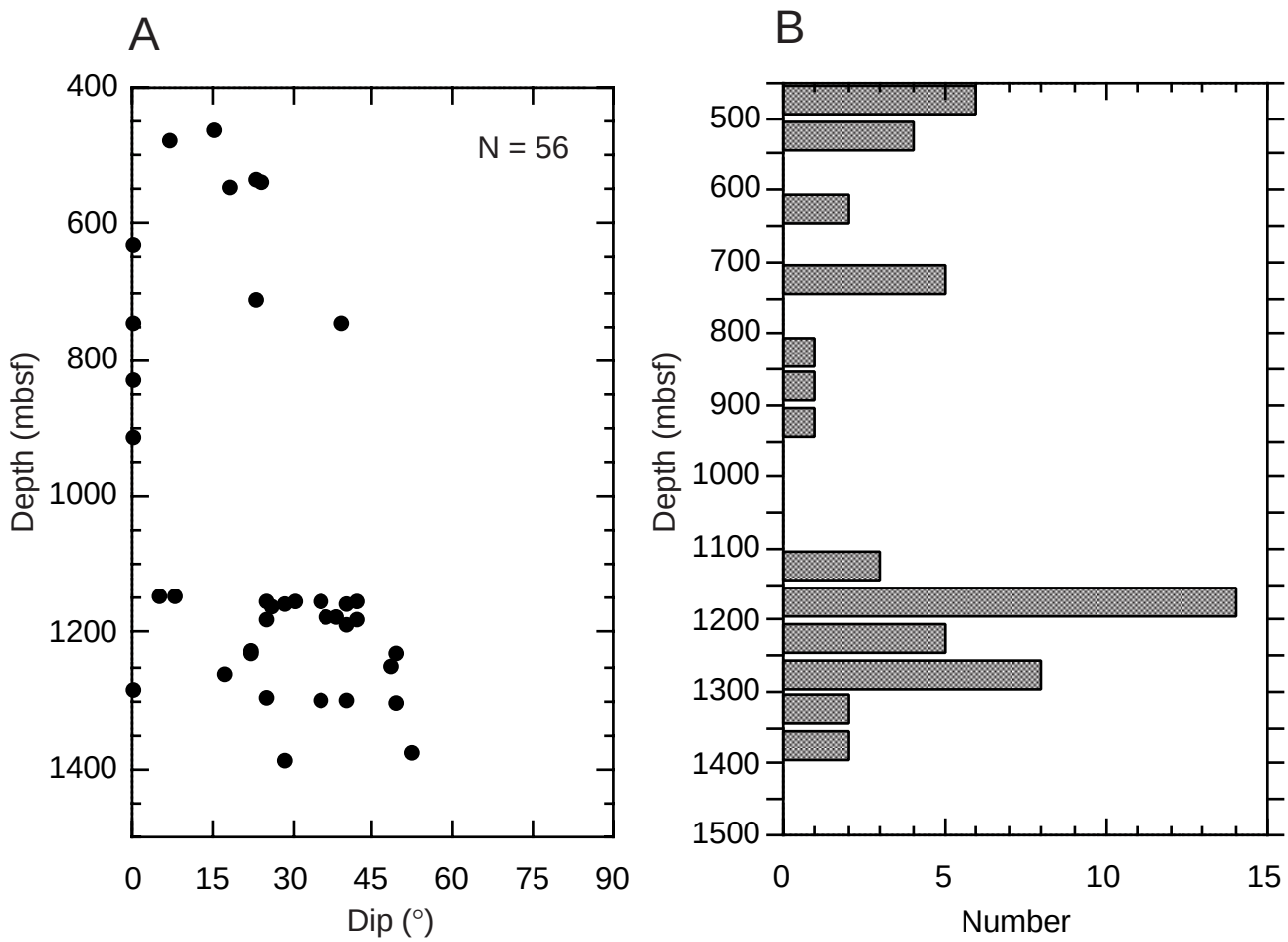

Figure F81. Variation in dip of igneous contacts with depth. Solid circle = intrusive, open triangle = tectonic, solid triangle = tectonic with reverse sense of displacement. Location of unmeasured contacts shown in box on right; solid square = not recovered/not preserved, open square = gradational.

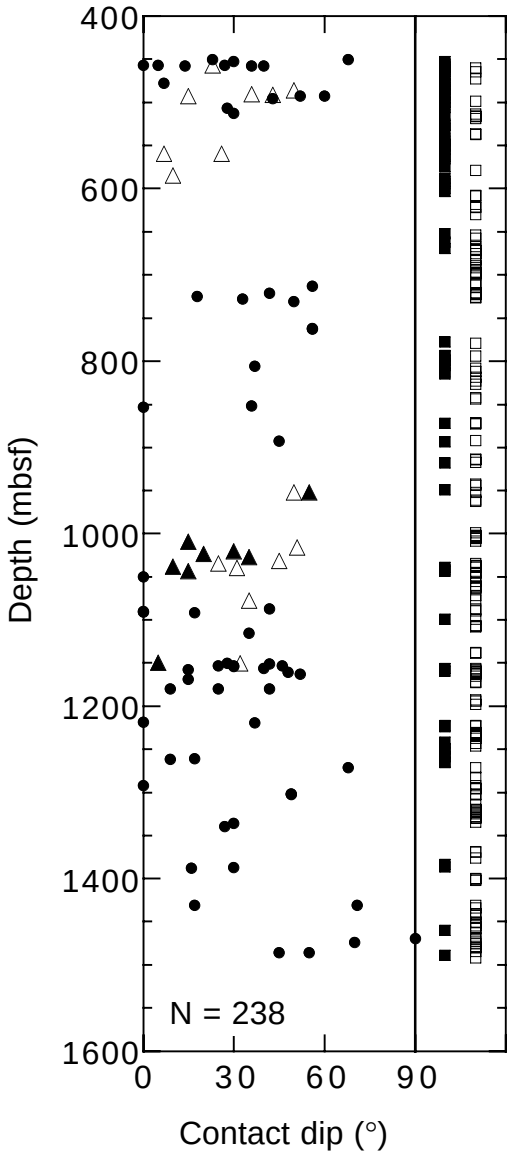

Figure F82. Variation in crystal-plastic deformation intensity and orientation of crystal-plastic foliation with depth. **A.** Plot of average deformation intensity vs. depth including data from Leg 118 (Dick et al., 1991a). The locations of major faults (dashed lines) and a major shear zone (solid line) are also shown. **B.** Plot of the dip of the crystal-plastic foliation in the core reference frame vs. depth, including data from Leg 118 (Dick et al., 1991a).

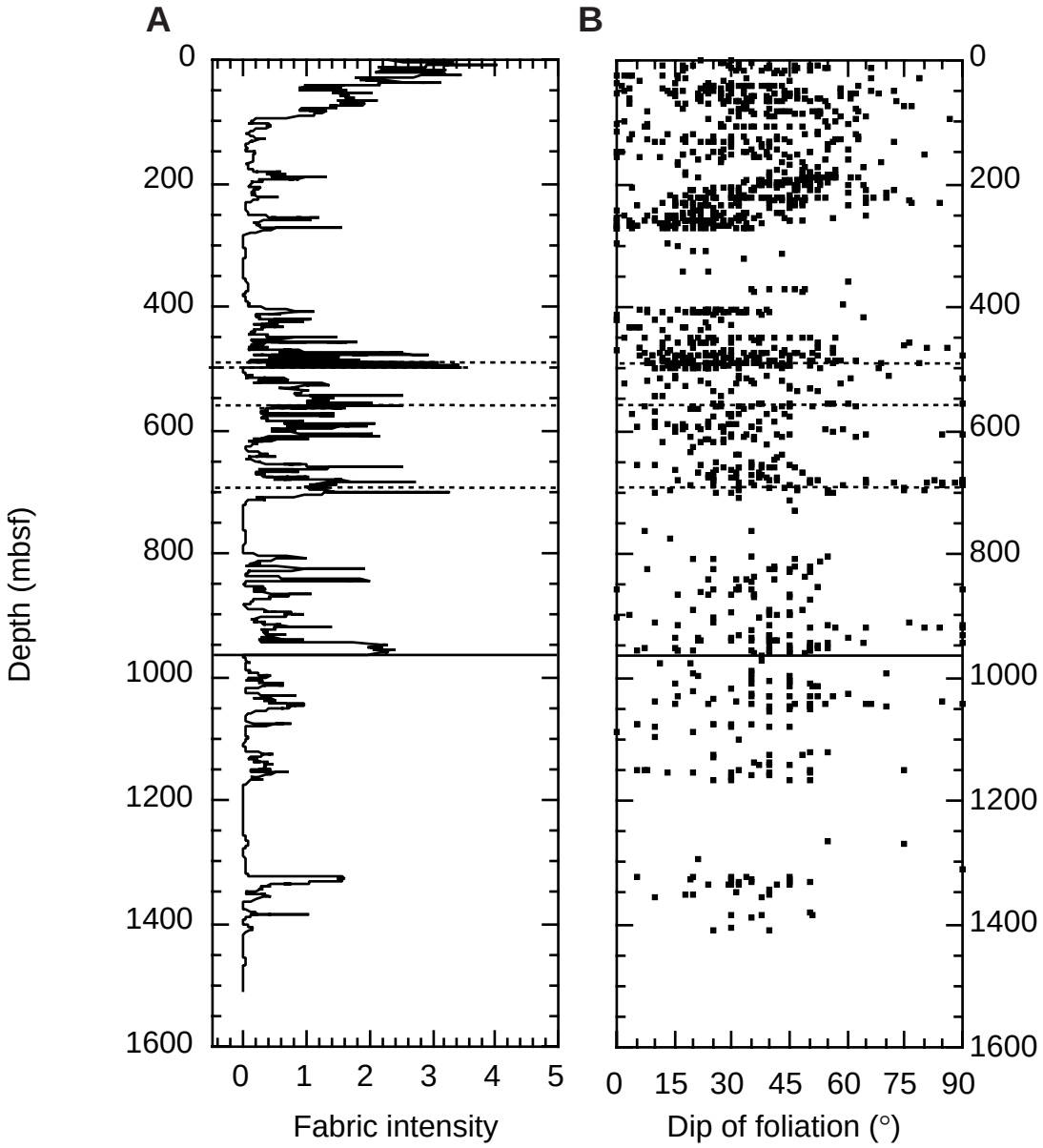

Figure F83. Comparison of crystal-plastic deformation intensity logged for the interval between 450 and 500 mbsf in Hole 735B during Legs 118 and 176 (see text). The deformation intensity for Leg 176 is an 11-cell running average of the crystal-plastic deformation log (see PLASTIC.XLS spreadsheet in **"Appendix,"** p. 31, in the "Leg 176 Summary" chapter), whereas the intensity from Leg 118 represent "visual averages" of ~1- to 2-m intervals.

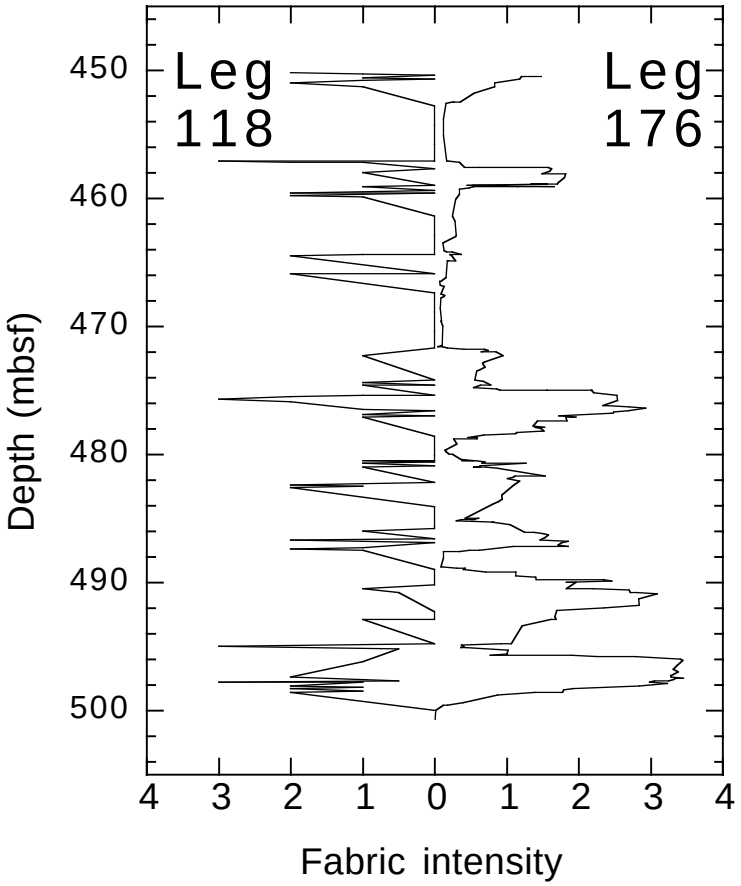

Figure F84. Number of core intervals vs. crystal-plastic deformation intensity; the percentage of the core with a particular intensity is also indicated.

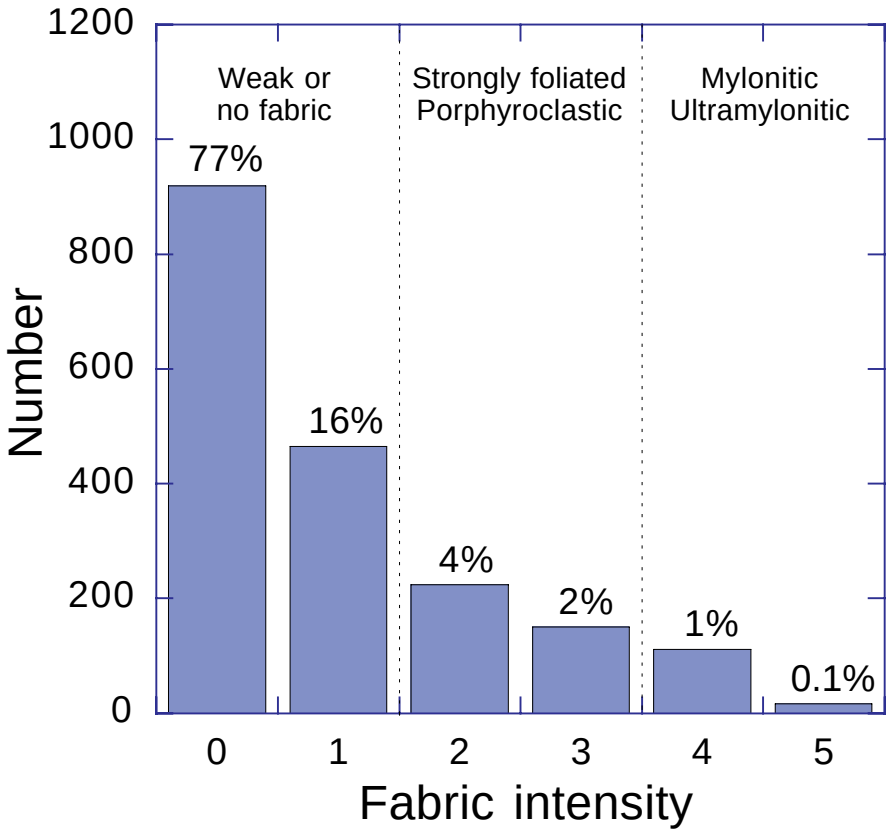

Figure F85. Mylonite at the base of a 20-m-thick shear zone extending from 945 to 964 mbsf (interval 176-735B-149R-3, 48–94 cm).

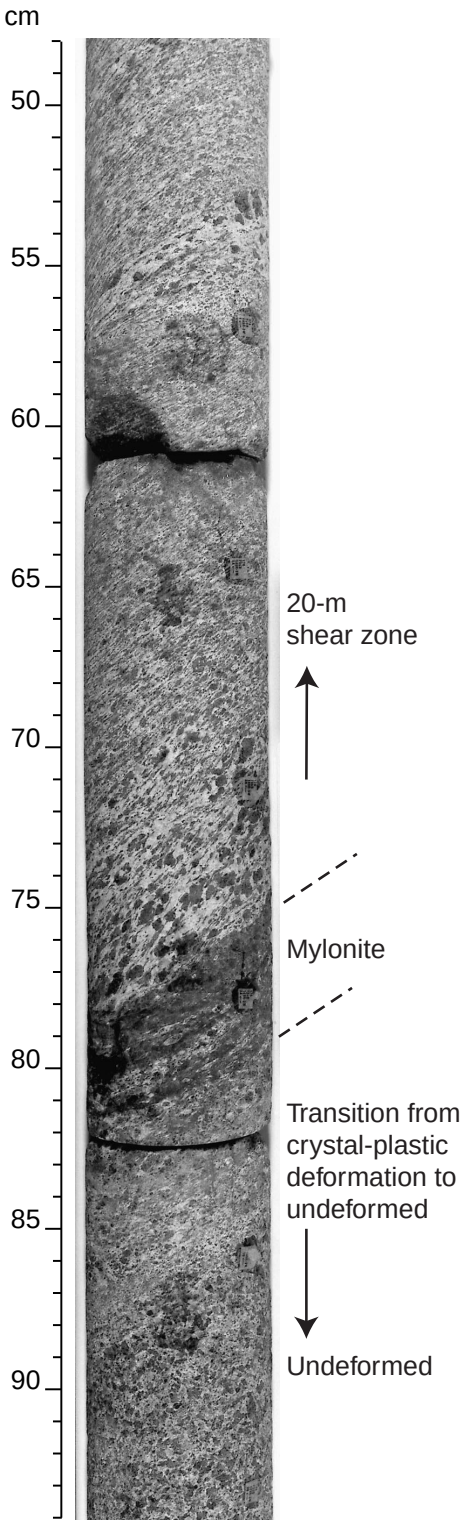

Figure F86. Variation in the dip of different categories of crystal-plastic foliation with depth. **A.** Mylonitic foliations (fabric intensity ≥4). **B.** Retrograde (mainly amphibolite to transitional greenschist grade) and semi-brittle shear zones. **C.** Shear zones with normal and reverse sense of shear in the core reference frame. The location of major faults (dashed lines) and a major reverse shear zone (solid line; see Fig. F85, p. 187) are shown in all three plots.

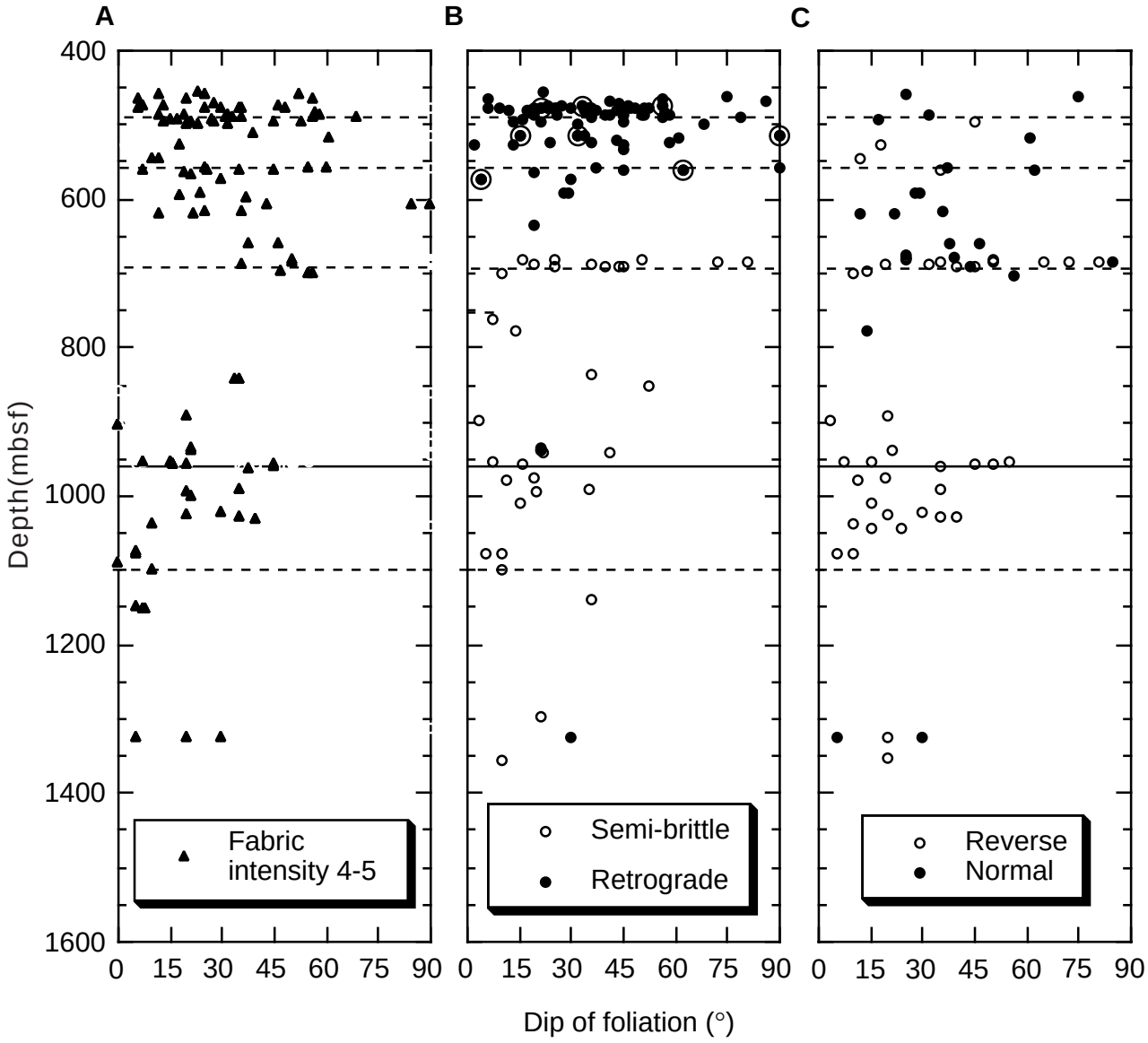

Figure F87. Close-up core photos of typical veined sections. **A.** Characteristic amphibole vein array from the upper part of the section (interval 176-735B-92R-1, 10–15 cm), showing steeply dipping, parallel veins, often slightly faulted. **B.** Characteristic smectite veining in the central part of the section (interval 176-735B-133R-7, 84–98 cm) with moderate dips and associated subhorizontal microfracturing. Scale bar in both = 5 cm.

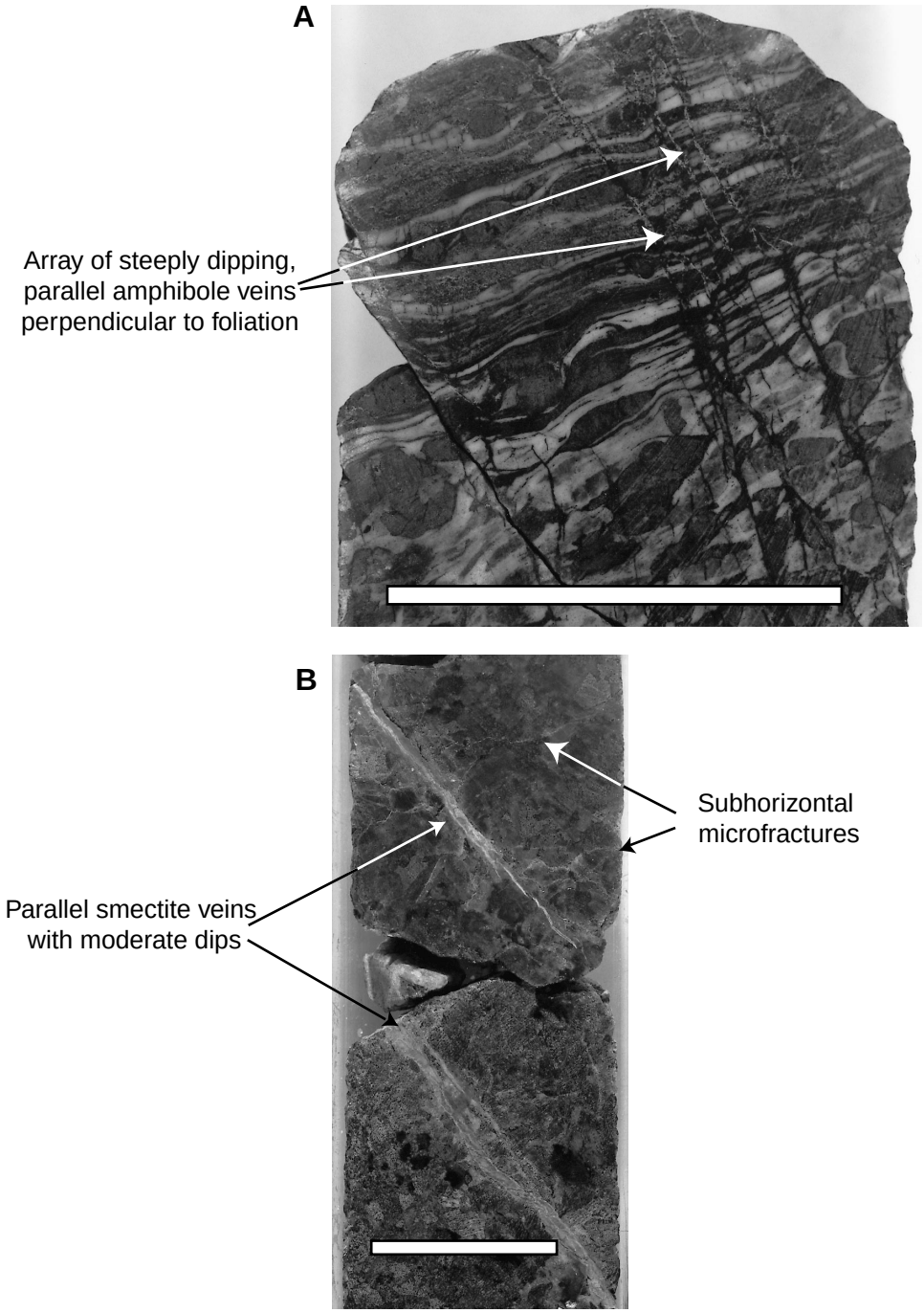

Figure F88. Low-temperature crystal-plastic and semi-brittle microstructures. Scale bars are 2 mm. **A.** The large pyroxene porphyroclast has a tail of small recrystallized pyroxene grains + amphiboles (1). An elongated plagioclase ribbon (2) is surrounded by a fine-grained recrystallized plagioclase matrix. In the latter, the finest grained zones are semi-brittle shear zones rich in amphibole. Sample 176-735B-92R-1 (Piece 3A, 12–15 cm). **B.** Localized semi-brittle shear zone (shown by the arrow), with a very fine grained size, overprinting a previously localized high-temperature shear zone (fine-grained recrystallized matrix). Sample 176-735B-95R-1 (Piece 8, 123–125 cm). **C.** Localized anastomosing shear zones, with Fe-Ti oxides and small, recrystallized plagioclase grains, wrapping around deformed plagioclase porphyroclasts. Sample 176-735B-90R-4 (Piece 4B, 112–116 cm). **D.** Close-up of (C), showing the fine-grained Fe-Ti oxide-plagioclase matrix around plagioclase porphyroclasts. Deformation in the plagioclase porphyroclasts is semi-brittle (undulose extinction, recrystallization, and microcracks). The arrow shows an area where oxides appear to cut the recrystallized mantle of the plagioclase porphyroclast and fill the crack in the same plagioclase. Sample 176-735B-90R-4 (Piece 4B, 112–116 cm). (Continued on next page.)

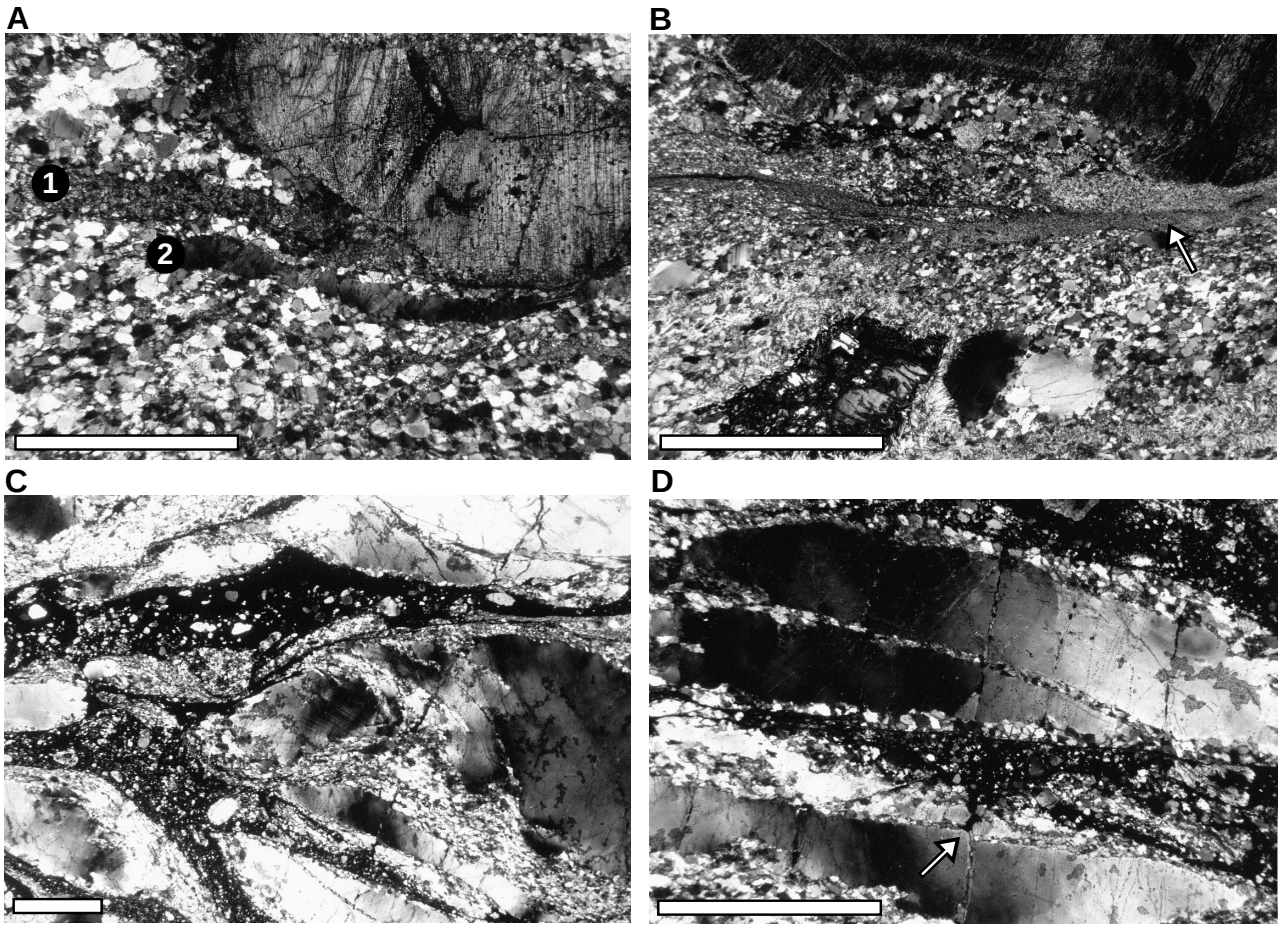

Figure F88 (continued). E. Semi-brittle fault (shown by the arrow) in an oxide gabbro, crosscutting a plagioclase porphyroclast. Sample 176-735B-97R-1 (Piece 2C, 120–125 cm). **F.** Strong crystal-plastic foliation, outlined by amphibole (plane-polarized light). The pyroxenes are almost completely replaced by amphiboles in both the very fine-grained recrystallized bands (1), and the tails of the porphyroclast (2). The crystal-plastic foliation is cut by a fault that also contains amphiboles (subvertical on the photo, shown by the arrow). Sample 176-735B-92R-1 (Piece 3A, 12–15 cm).

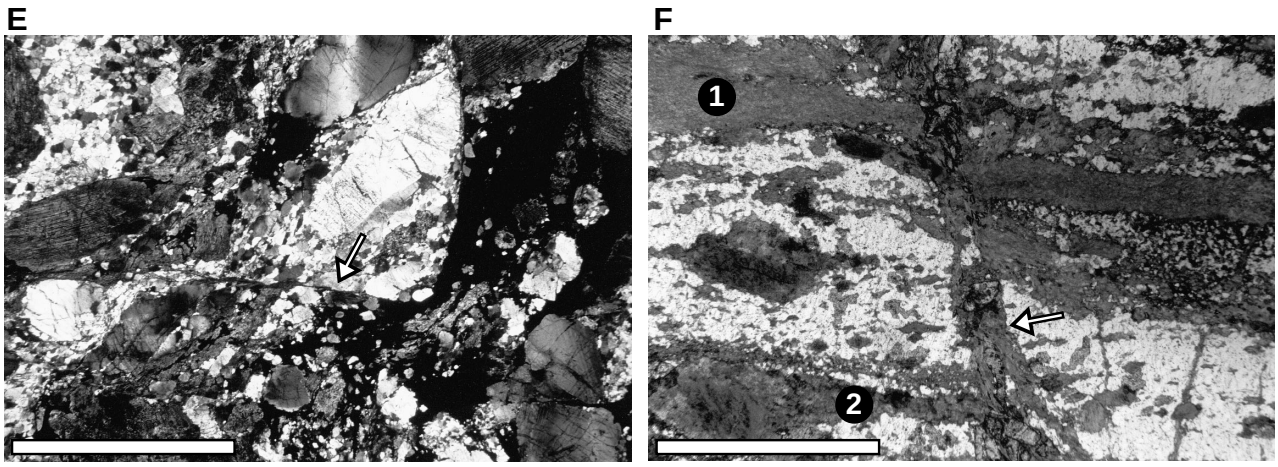

Figure F89. Close-up photograph of reverse shear zone from Section 176-735B-155R-1.

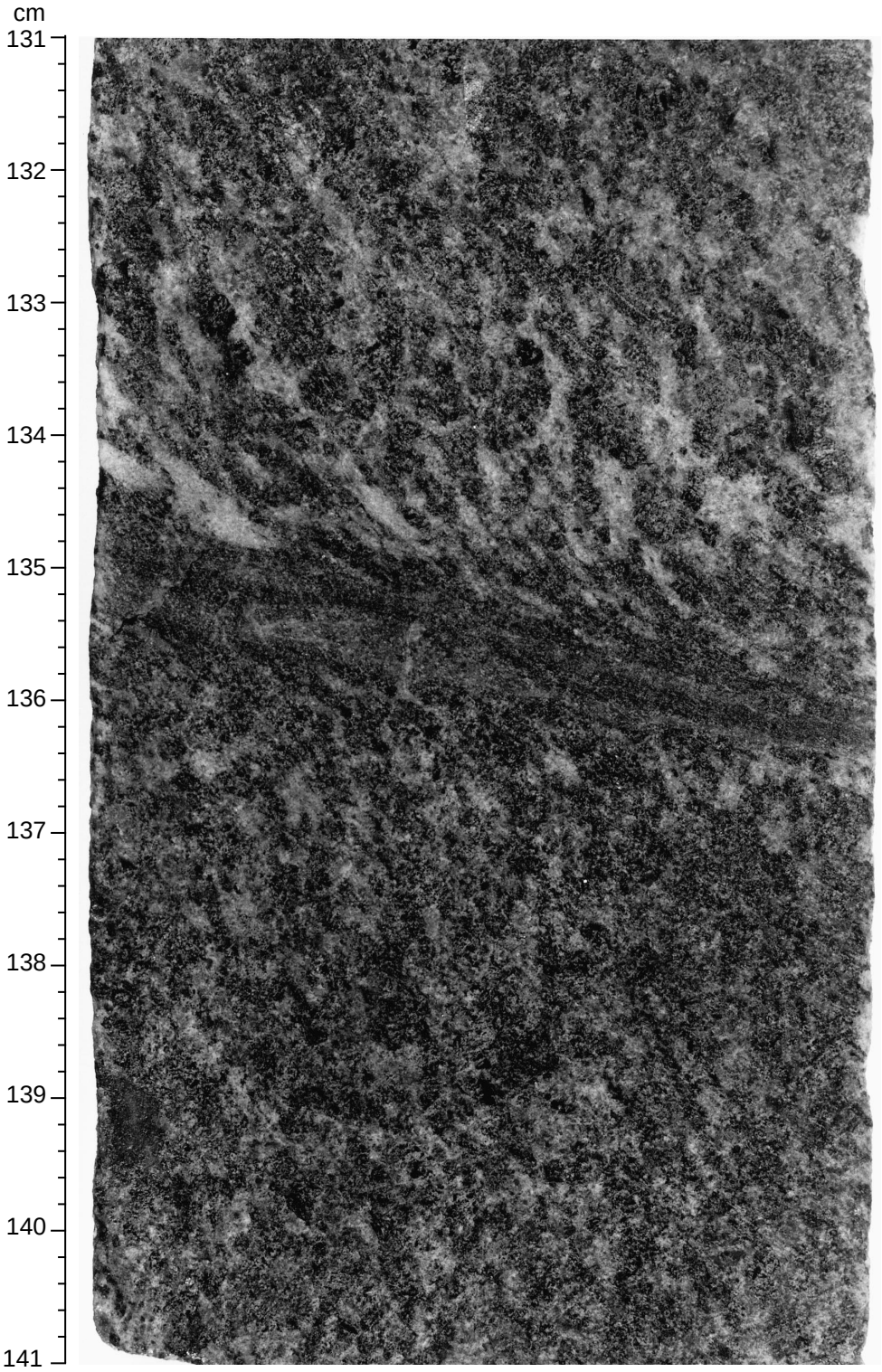

Figure F90. A. Downhole variability of the number of magmatic breccias/10-m interval based on visual core descriptions. **B.** Lower hemisphere, equal area stereoplot of poles of contacts for all magmatic breccias (*N* = 88).

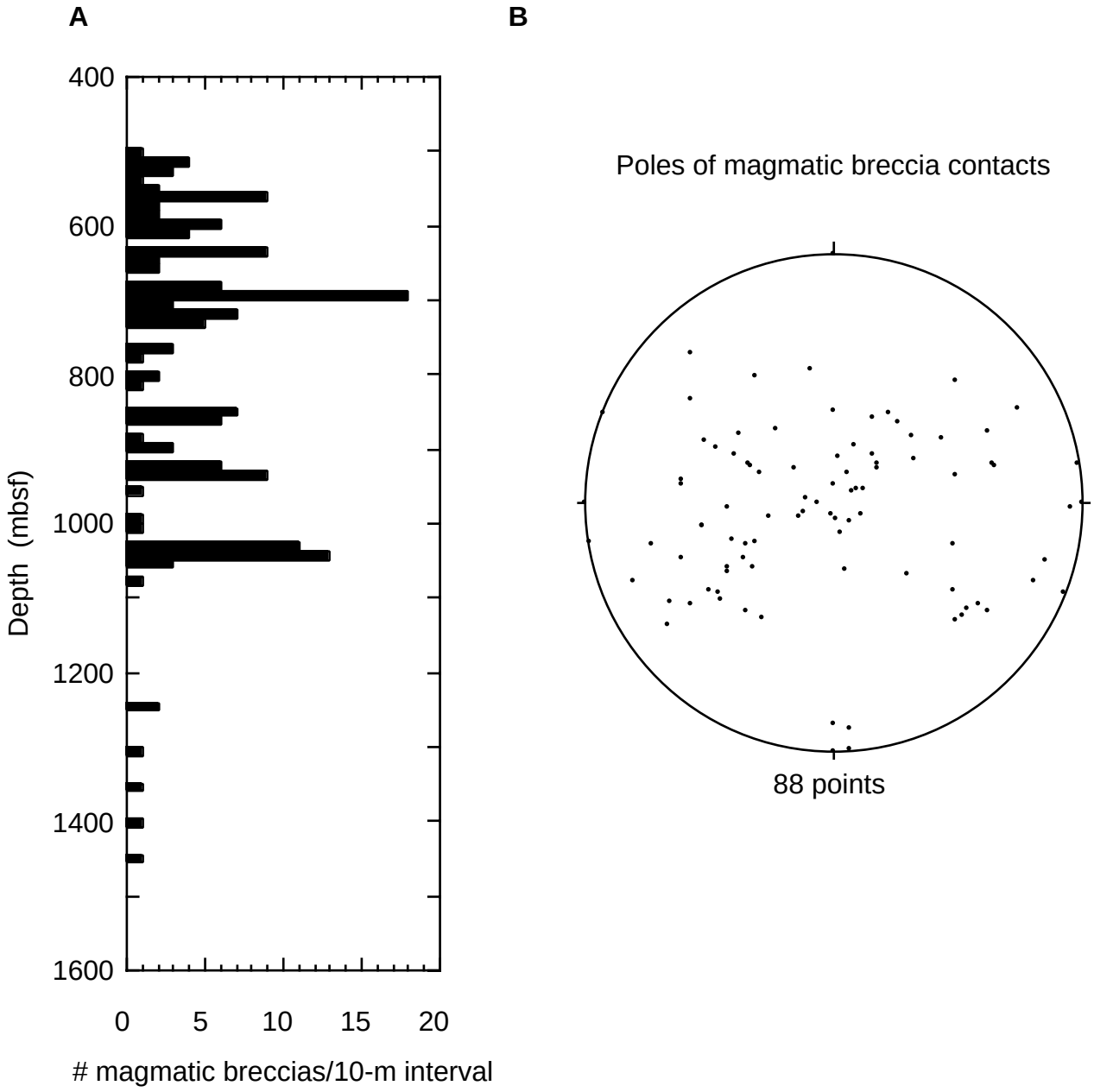

Figure F91. Brittle microstructures in cross-polarized transmitted light. Scale bars are 2 mm. **A.** Felsic vein crosscutting an undeformed igneous texture. The plagioclase in the veins is euhedral to subhedral and zoned. Sample 176-735B-172R-3 (Piece 2A, 70–76 cm). **B.** Thin amphibole vein (shown by the arrows) crosscutting large, slightly deformed plagioclase grains. Sample 176-735B-95R-3 (Piece 1C, 24–29 cm). **C.** Two calcite veins (nearly horizontal in the photo). The upper vein (1) may be a fault; it is filled with small, equigranular crystals. The lower vein (2) displays a crack-seal structure. Sample 176-735B-132R-1 (Piece 11A, 66–70 cm). **D.** Cataclasite, with a calcite matrix and angular clasts with a large range in grain size. Sample 176-735B-91R-3 (Piece 1D, 92–95 cm).

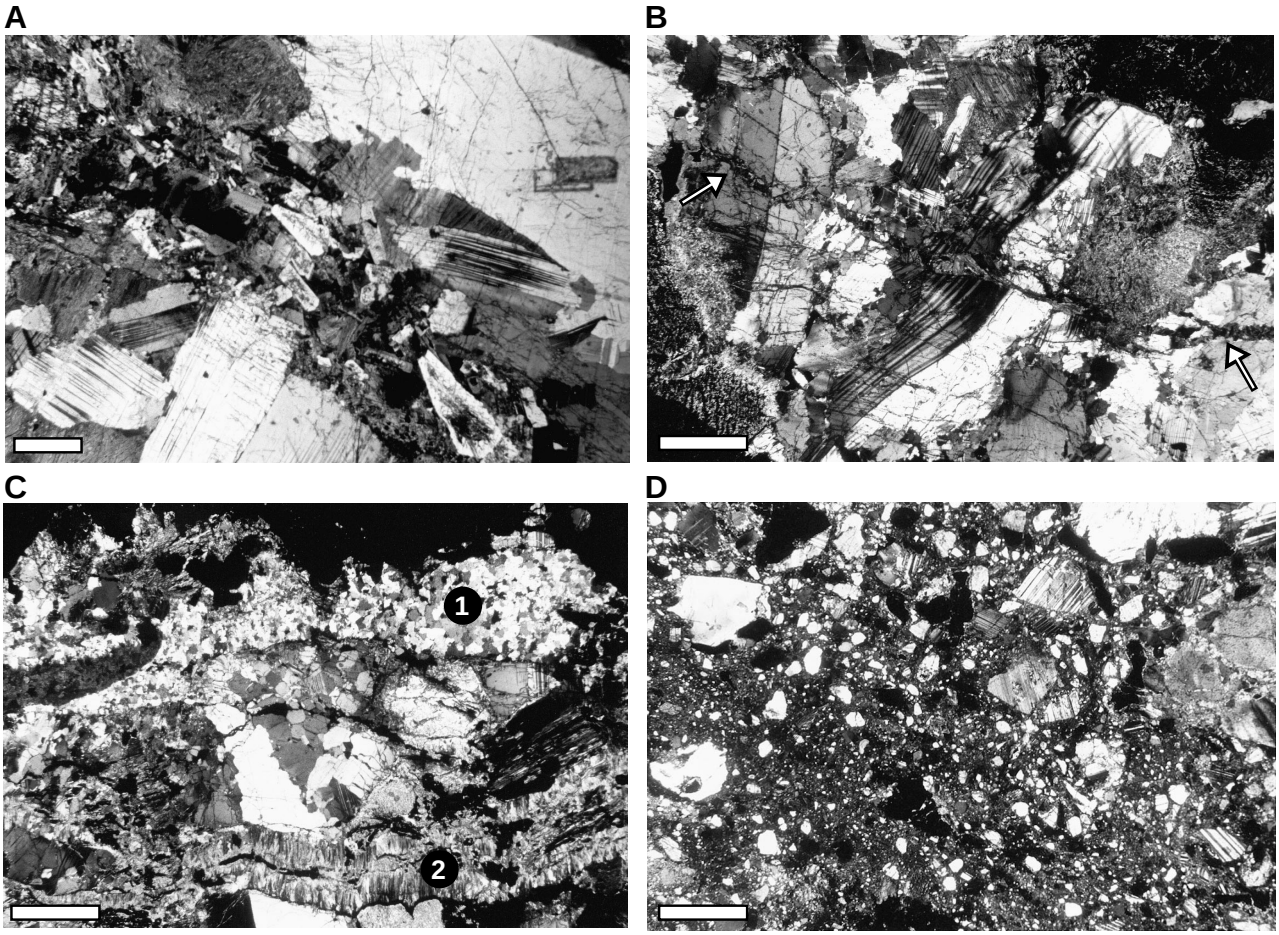

Figure F92. Core photographs of magmatic and tectonic breccia. **A.** Interval 176-735B-104R-2, 92–104.5 cm. Dark xenoliths of wall-rock gabbro have been rotated by intrusion of the light-colored felsic material. **B.** Interval 176-735B-110R-3, 1–10 cm. Xenoliths of host gabbro and individual pyroxene grains sit in a matrix of coarse-grained plagioclase, quartz, alkali feldspar, and euhedral biotite. **C.** Interval 176-735B-119R-1, 77.5–89 cm. Early magmatic breccia cut by well-developed crystal-plastic fabric. **D.** Interval 176-735B-97R-4, 121–126.5 cm. Cataclasite with fractured clasts of gabbro enclosed in a fine-grained matrix dominated by chlorite and amphibole, indicative of greenschist facies metamorphic conditions during deformation.

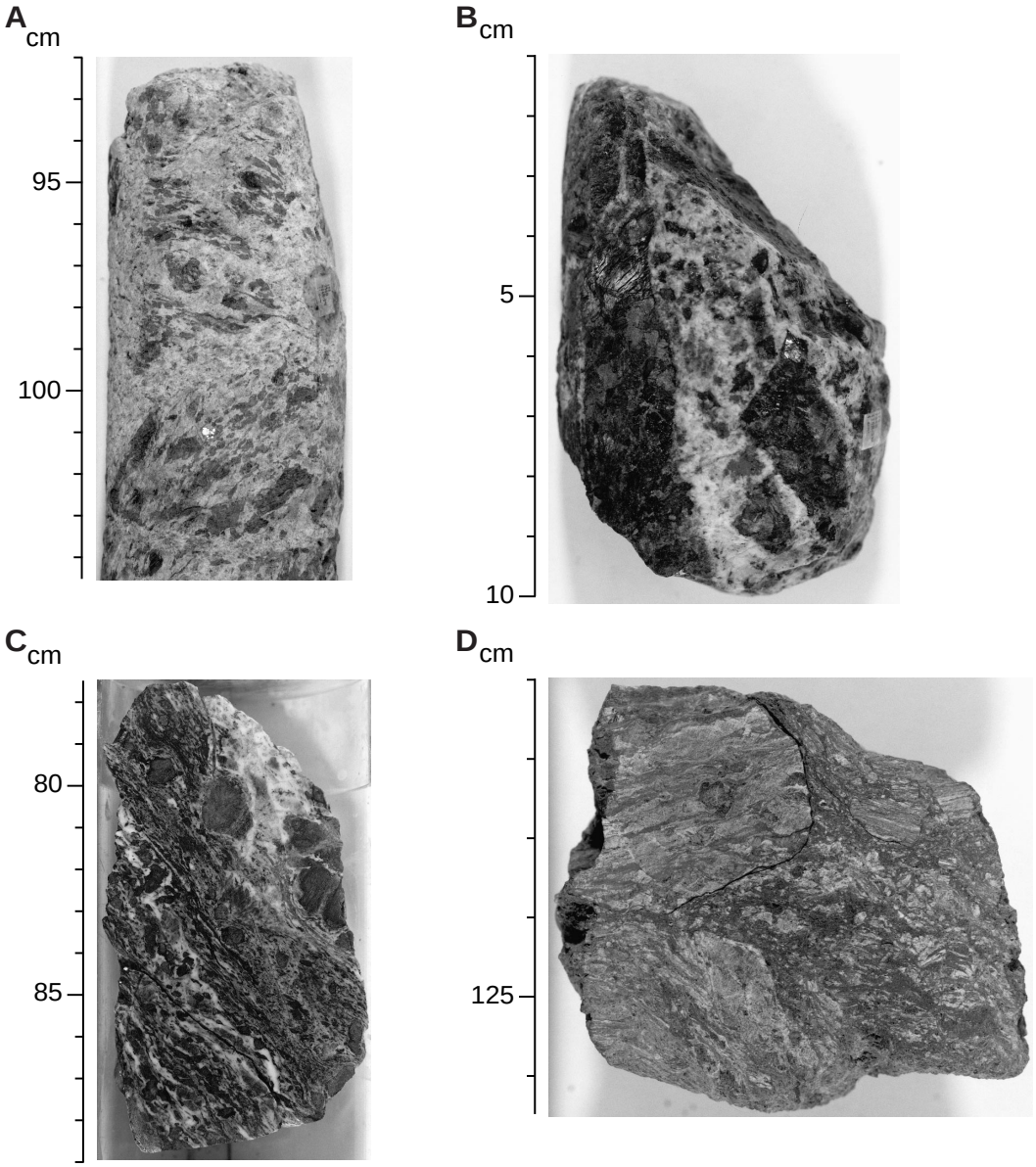

Figure F93. A. Downhole variability of the average intensity of cataclasis from visual core descriptions. Section includes relogged core from 118-735B-82R-6 through 88N (depths from 450 to 500 mbsf). **B.** Enlarged section showing downhole variability of the average intensity of cataclasis from visual core descriptions, highlighting the major fault zones (490, 560, and 690–700 mbsf). **C.** Downhole variability of fault dip from visual core descriptions. Note that zones of intense cataclasis show a wide range in dip angle.

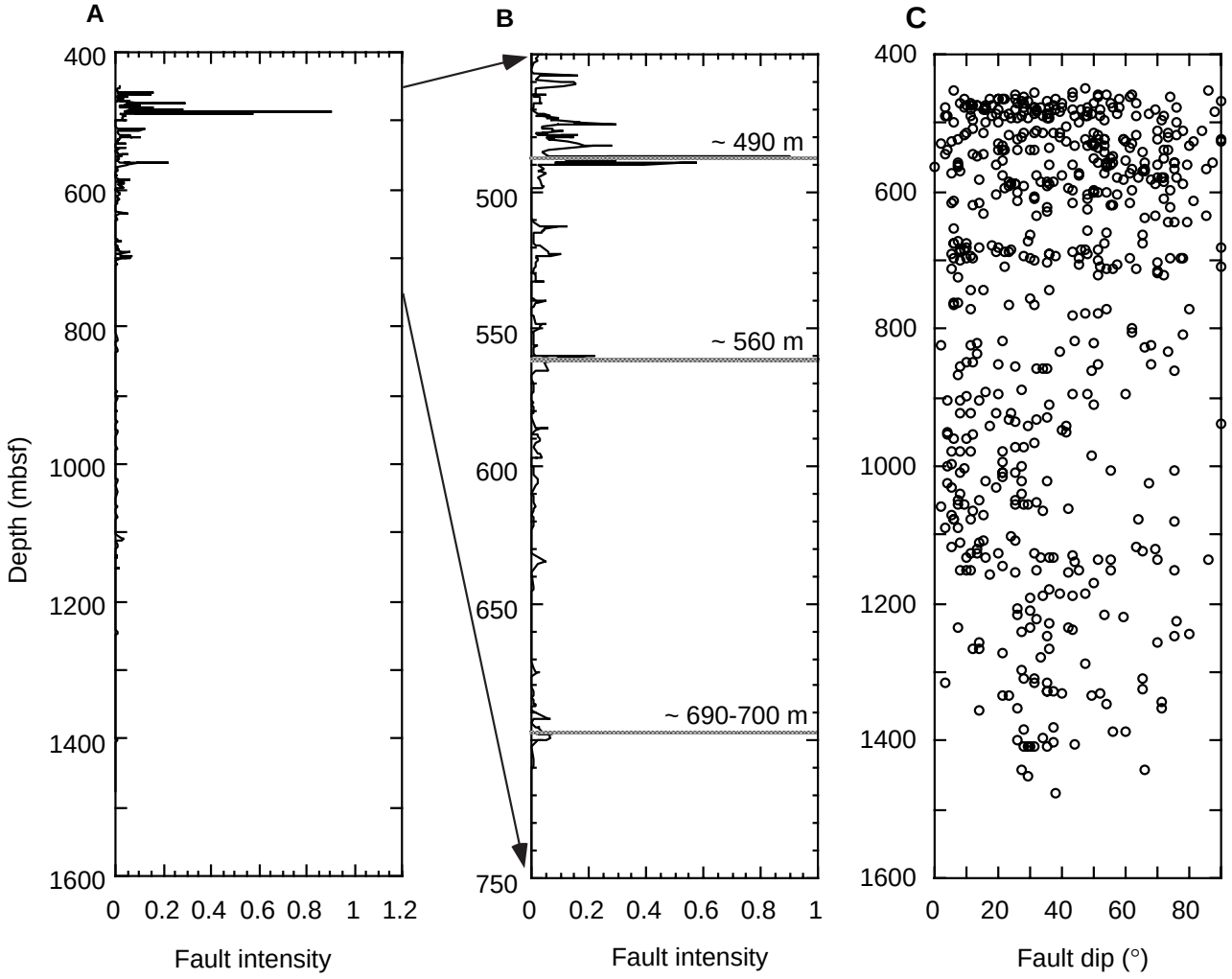

Figure F94. Lower hemisphere, equal area stereographic plot of poles of all faults (N = 599). Maximum concentration at 90° indicates a preferred subhorizontal fault orientation within the lower 1000 m of Hole 735B.

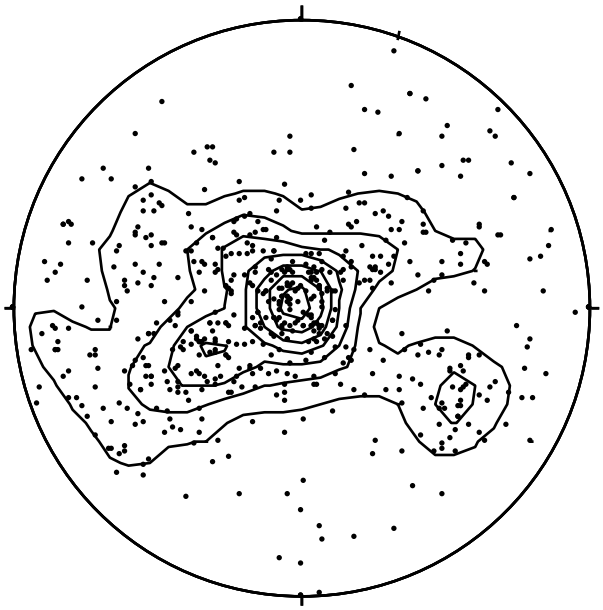

Figure F95. Fault displacements **A.** Sense of slip (*N* = 599). **B.** Slip direction based on pitch of slickenside striae from fault surfaces (*N* = 383).

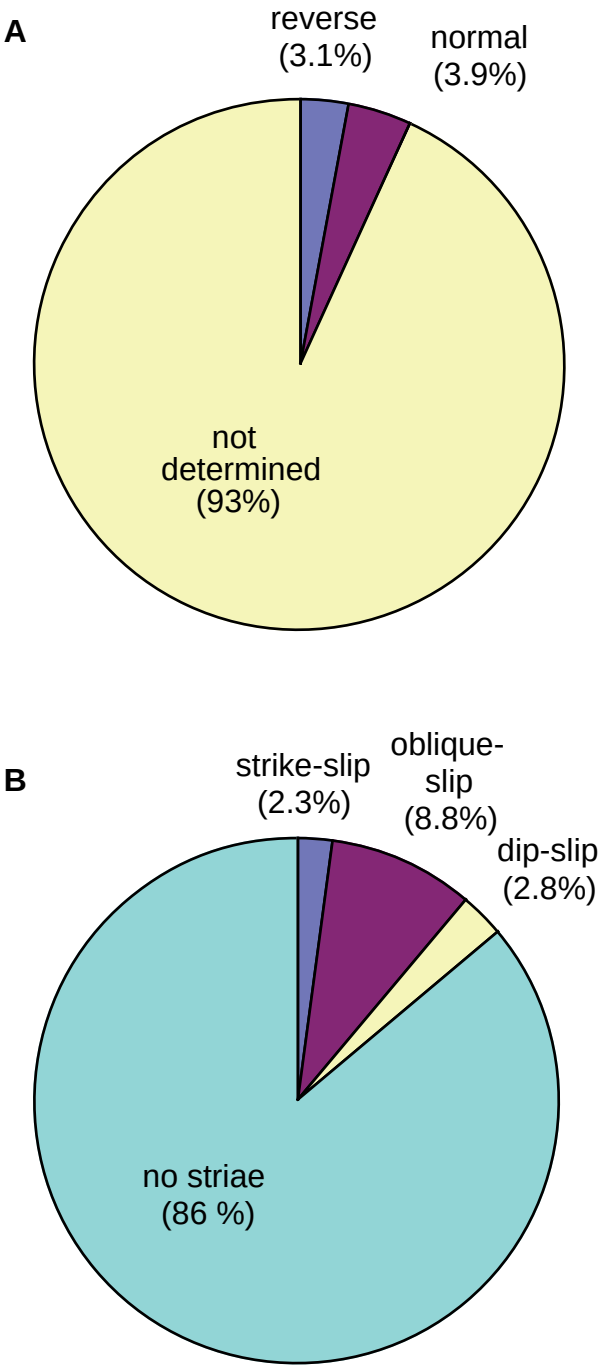

Figure F96. Core recovery plotted against depth for the entire 1500 m at Hole 735B. Also shown are the Leg 118 VSP reflectors (Swift et al., 1991). F = cataclastic fault (dashed lines), SZ = crystal-plastic shear zone.

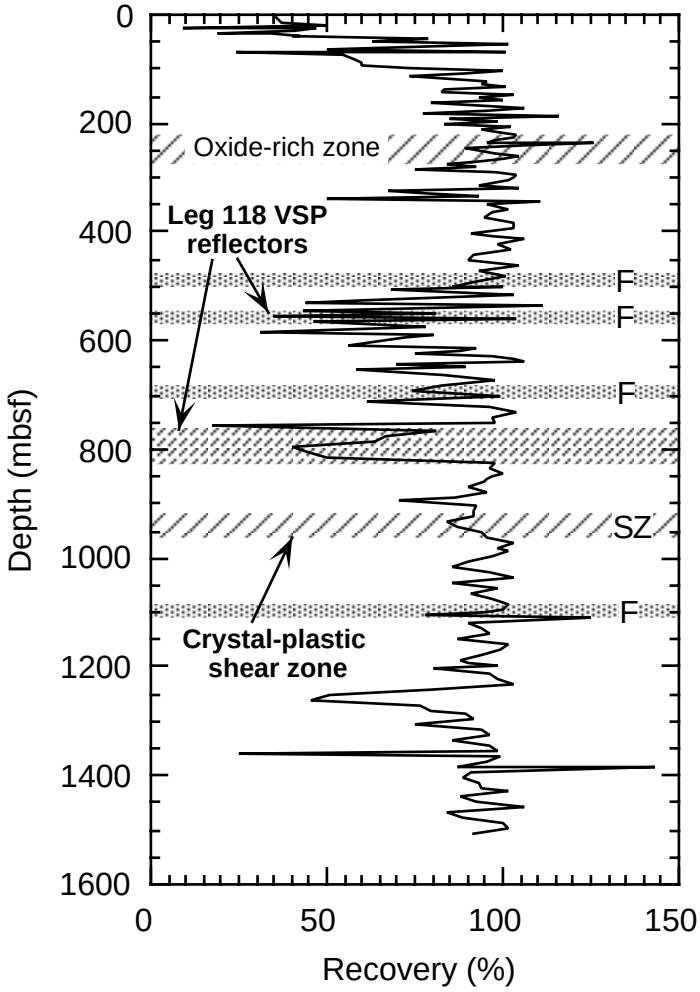

Figure F97. A. Variation in vein intensity with depth in Hole 735B. The scale is taken from the intensity scale as described in "Structural Geology," p. 13, in the "Explanatory Notes" chapter, and is based on vein density. Data from Leg 118 have been included and scaled to match the data from Leg 176. The Leg 176 values are averaged over 31 structural intervals. The dashed, horizontal lines mark the positions of major faults; the solid, horizontal line marks the position of the major ductile shear zone. **B.** Variation in vein dip with depth in Hole 735B (*N* = 3245).

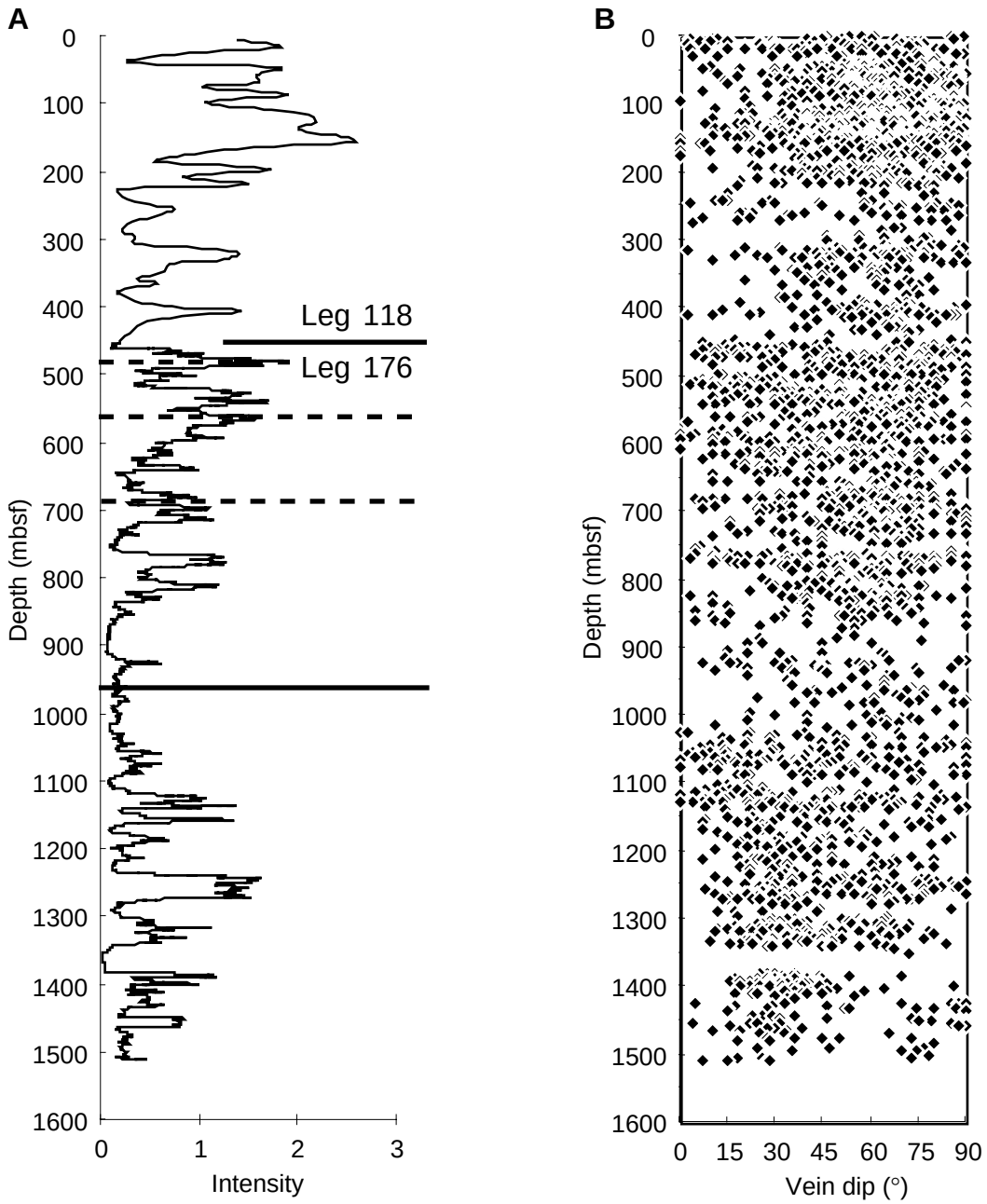

Figure F98. Distribution of dips for each of the major vein types (see text for classification) and variation in dip with depth. **A.** Dip of magmatic veins. **B.** Variation in dip of magmatic veins with depth. **C.** Dip of amphibole veins. **D.** Variation in dip of amphibole veins with depth. (Continued on next page).

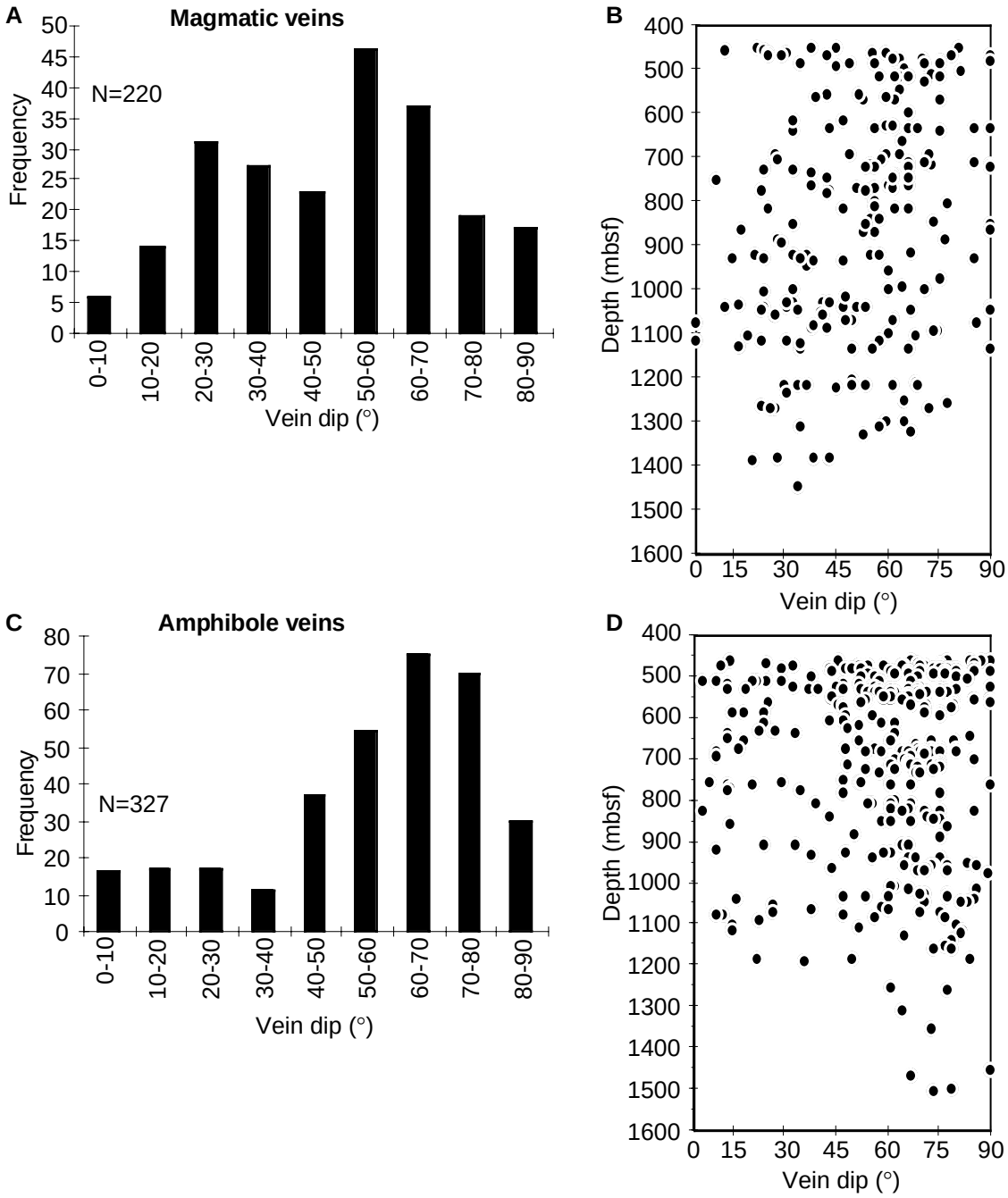

Figure F98 (continued). **E.** Dip of carbonate veins. **F.** Variation in dip of carbonate veins with depth. **G.** Dip of smectite/zeolite veins. **H.** Variation in dip of smectite/zeolite veins with depth.

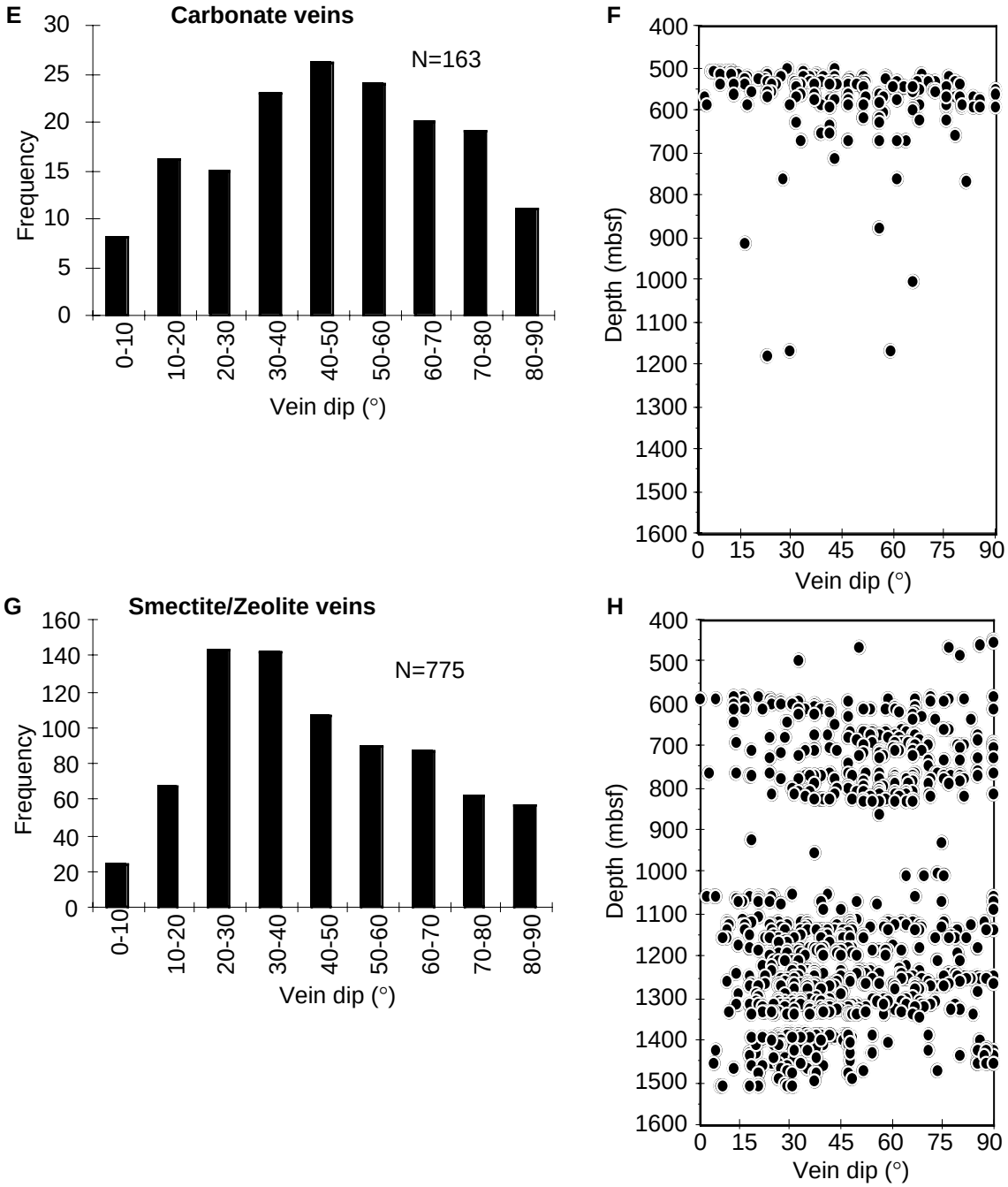

Figure F99. Variation in vein dip with depth. Data shown in Figure F94, p. 197, between 450 and 1508 mbsf have been grouped into 50-m intervals, plotted using a stereonet program, and contoured. The intensity of any contour maximum for each interval has been used to determine the size of each symbol: large symbols indicate a high intensity of points around that dip value; smaller symbols indicate a wider spread of dip values. Several contoured maxima may be present in any one interval.

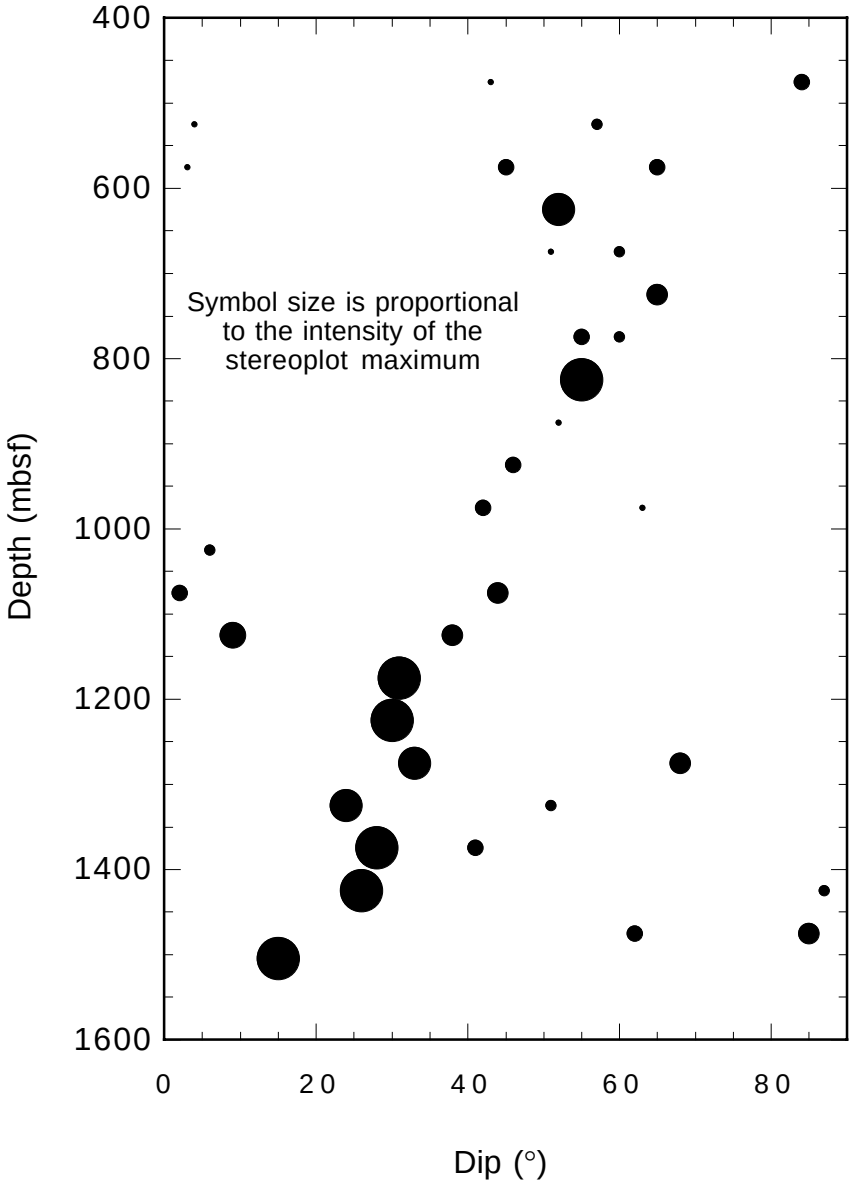

Figure F100. Variation in subhorizontal microfracture intensity with depth. The intensity scale, based on microfracture density, is outlined in **"Structural Geology,"** p. 13, in the "Explanatory Notes" chapter.

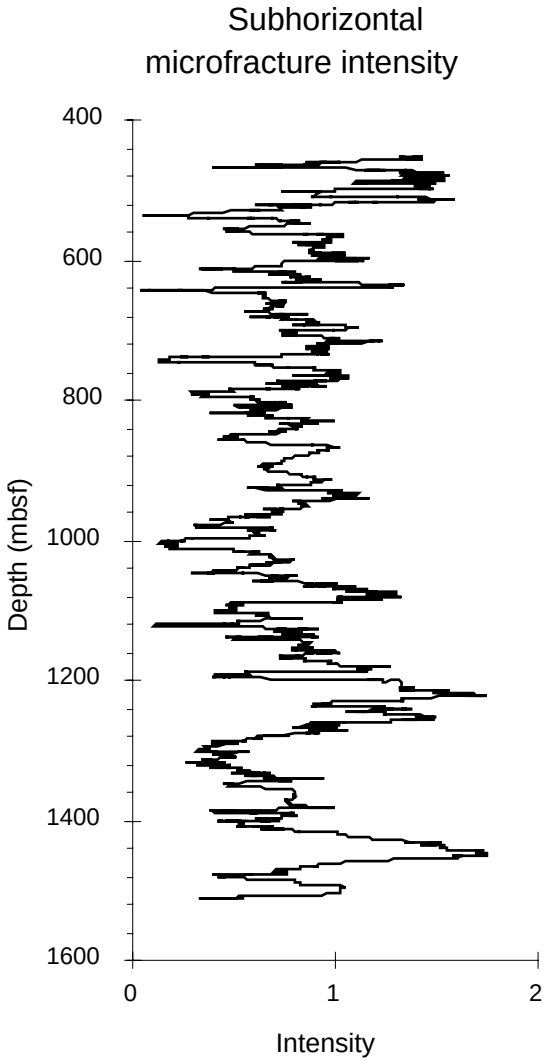

Figure F101. Igneous textures and fabrics in cross-polarized light illustrating the transition to crystal-plastic deformation. Scale bars are 2 mm. **A.** Magmatic foliation, defined by the shape-preferred orientation of plagioclase laths. A few mechanical twins are present in the plagioclase, and the grain boundaries are slightly serrated (onset of high-temperature crystal-plastic deformation). Sample 176-735B-89R-2 (Piece 1, 4–8 cm). **B.** Nearly undeformed igneous texture; the only traces of deformation are minor undulose extinction and mechanical twins in plagioclase, and subgrains in olivine. Clinopyroxene is typically undeformed and poikilitic. Sample 176-735B-121R-8 (Piece 2B, 68–72 cm). **C.** Equilibrated, fine-grained, igneous texture. All grains are undeformed. Sample 176-735B-121R-2 (Piece 2B, 40–43 cm). **D.** Equilibrated, coarse-grained, igneous texture. Most grains are anhedral, with curviplanar grain boundaries and 120° triple junctions. A few mechanical twins and minor undulose extinction are present in the plagioclase. Sample 176-735B-132R-5 (Piece 2, 95–100 cm). (Continued on next page.)

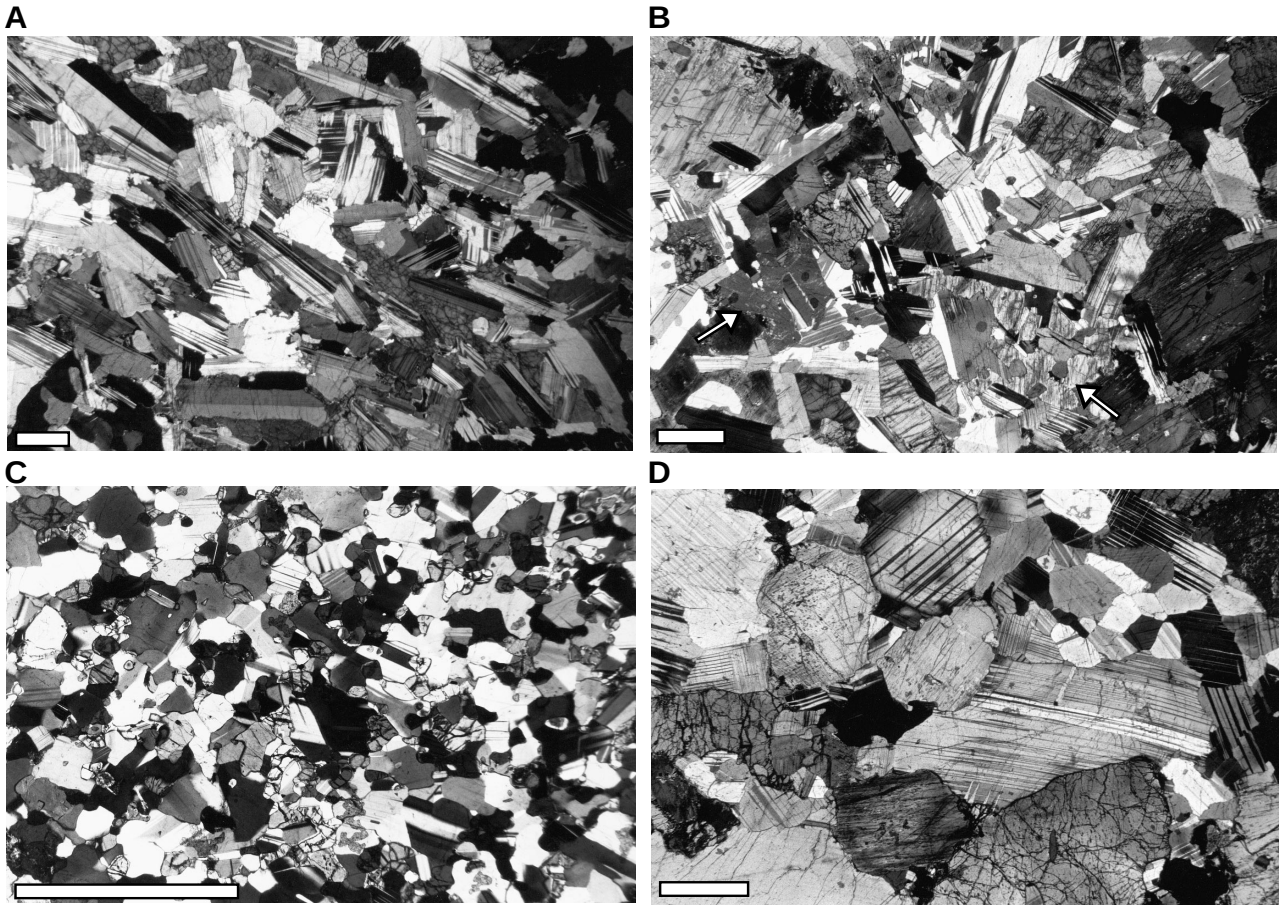

Figure F101 (continued). E. Subgrains and mechanical twins in a large plagioclase lath (Pl). Sample 176-735B-185R-5 (Piece 1, 2–6 cm). **F.** Subgrains in a large olivine crystal (Ol) in an equilibrated igneous texture. Sample 176-735B-140R-1 (Piece 3A, 24–28 cm).

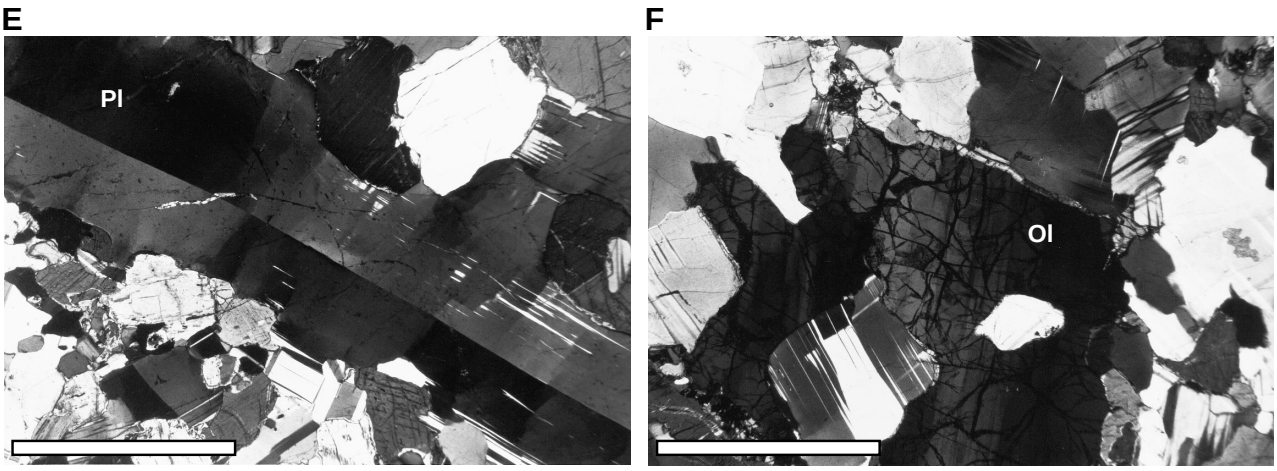

Figure F102. High-temperature crystal-plastic microstructures in cross-polarized light. Scale bars are 2 mm. **A.** Olivine (Ol) porphyroclast, with subgrains, bordered by recrystallized olivine grains, in a matrix of fine-grained recrystallized plagioclase. Sample 176-735B-135R-1 (Piece 2E, 98–102 cm). **B.** Plagioclase (Pl) porphyroclast, bordered by recrystallized plagioclase grains, next to an elongate olivine porphyroclast (Ol). Sample 176-735B-104R-2 (Piece 6B, 45–47 cm). **C.** Mylonitic (1) to ultramylonitic (2) foliation, with a matrix of recrystallized plagioclase, olivine, and pyroxene. The mylonite contains plagioclase (Pl), pyroxene (Px), and oxide (Ox) porphyroclasts or ribbons. The pyroxene porphyroclasts have very elongated recrystallized tails. Sample 176-735B-155R-6 (Piece 5B, 118–122 cm). **D.** Close-up of (C), showing a small plagioclase ribbon, a pyroxene (Px) porphyroclast with recrystallized mantle and tails, and a Fe-Ti oxide ribbon, in a fine-grained recrystallized matrix. Sample 176-735B-155R-6 (Piece 5B, 118–122 cm).

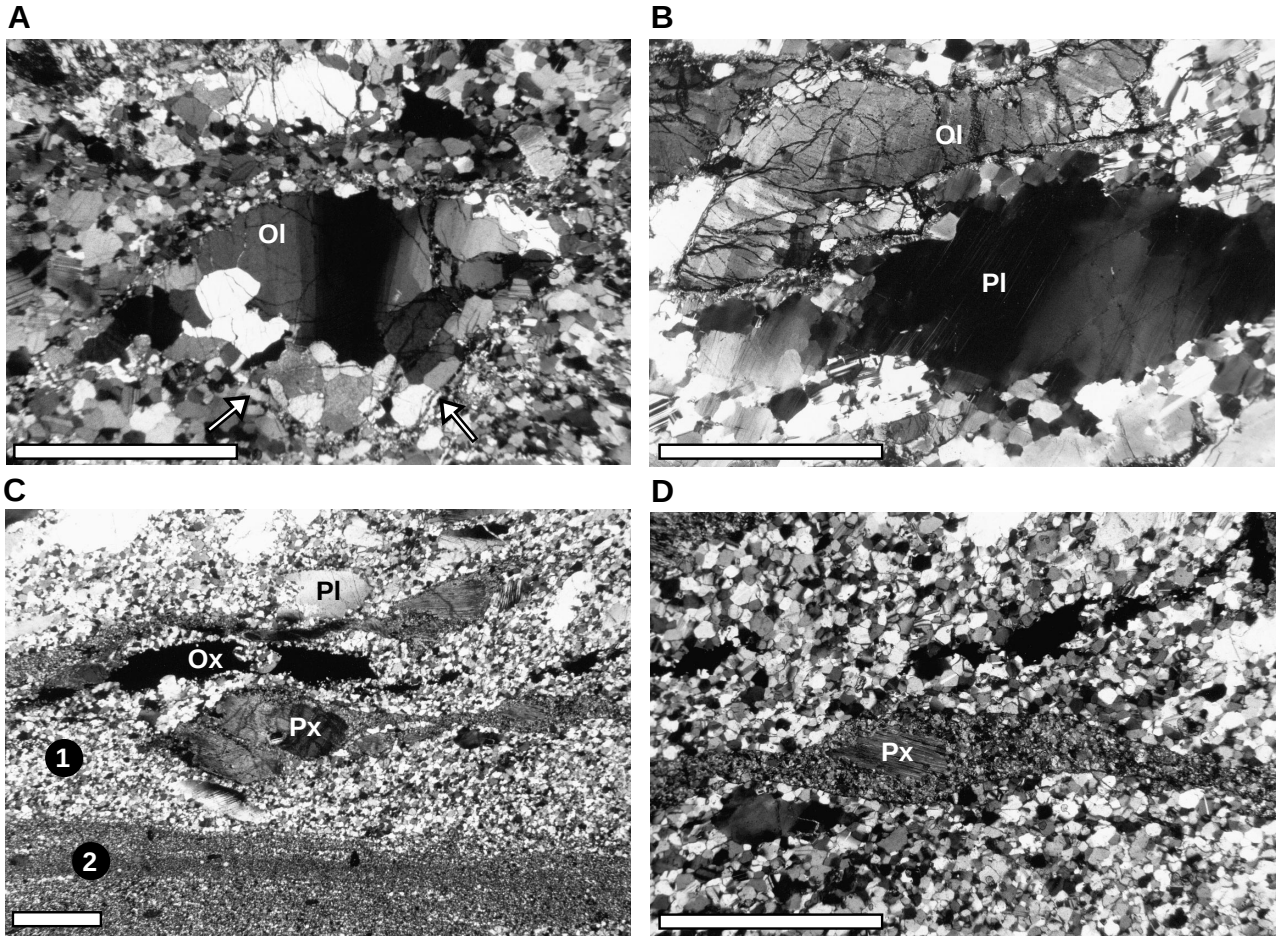

Figure F103. Correlation between recorded intensities of macroscopic (hand specimen) and microscopic (thin sections) fabrics. **A.** Magmatic fabric. **B.** Crystal-plastic fabric.

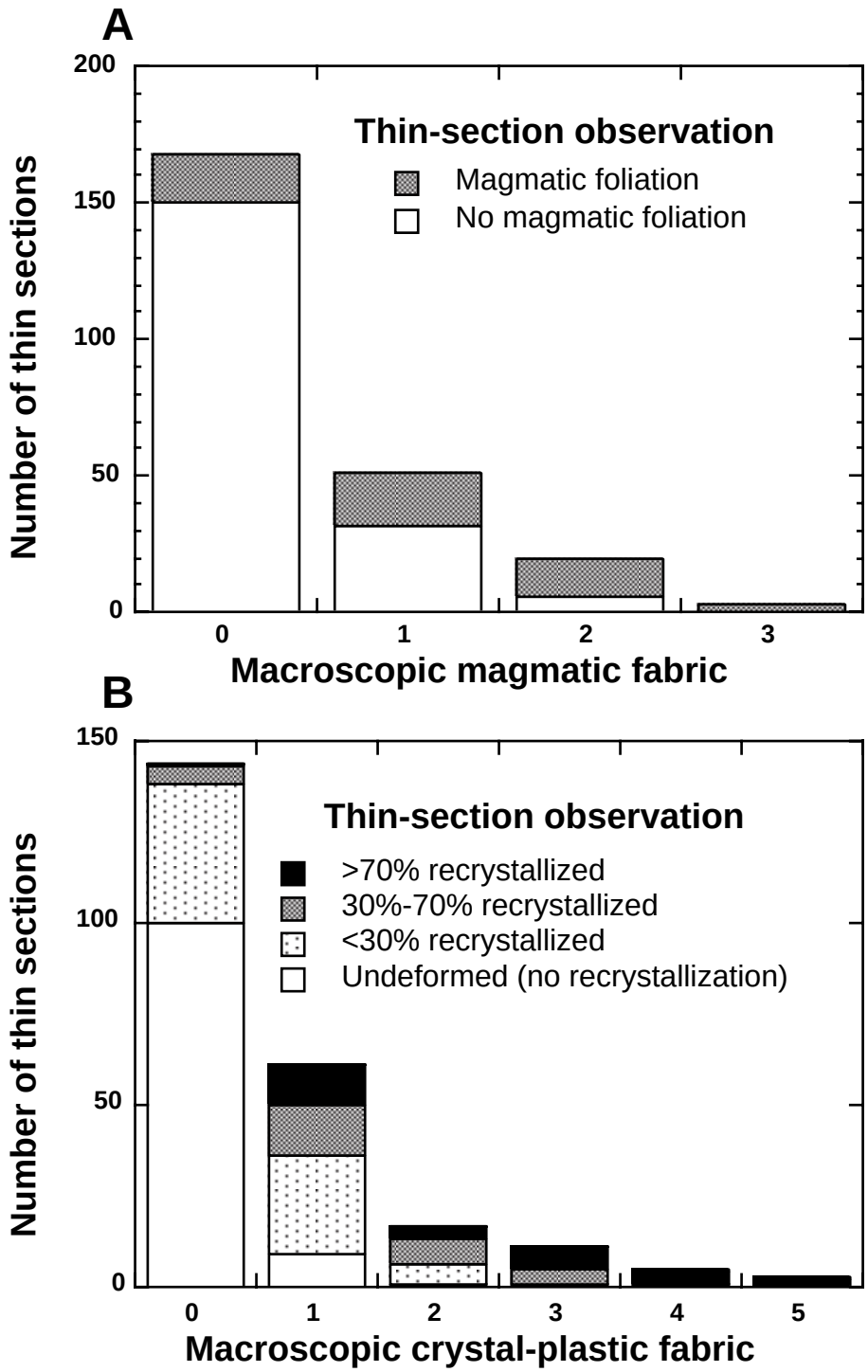

Figure F104. Microgabbro intrusions. **A.** The contacts of the coarse-grained gabbro with the microgabbro are sharp, but irregular, with variable dips (interval 176-735B-137R-6, 99–130 cm). **B.** The intrusive nature of the microgabbro is illustrated by a weak magmatic foliation and a few deformed schlieren of coarse-grained host rock, both parallel to the contacts (interval 176-735B-165R-3, 91.5–127.5 cm). **C.** The contact of the microgabbro with the coarse-grained gabbro is subvertical; it is overprinted by a felsic vein at the top of the piece (interval 176-735B-202R-7, 102–122 cm). **D.** The contacts of the microgabbro with the coarse-grained gabbro are subvertical and sinuous. The fine-grained layer is locally 1 cm thick (interval 176-735B-189R-3, 90–120 cm).

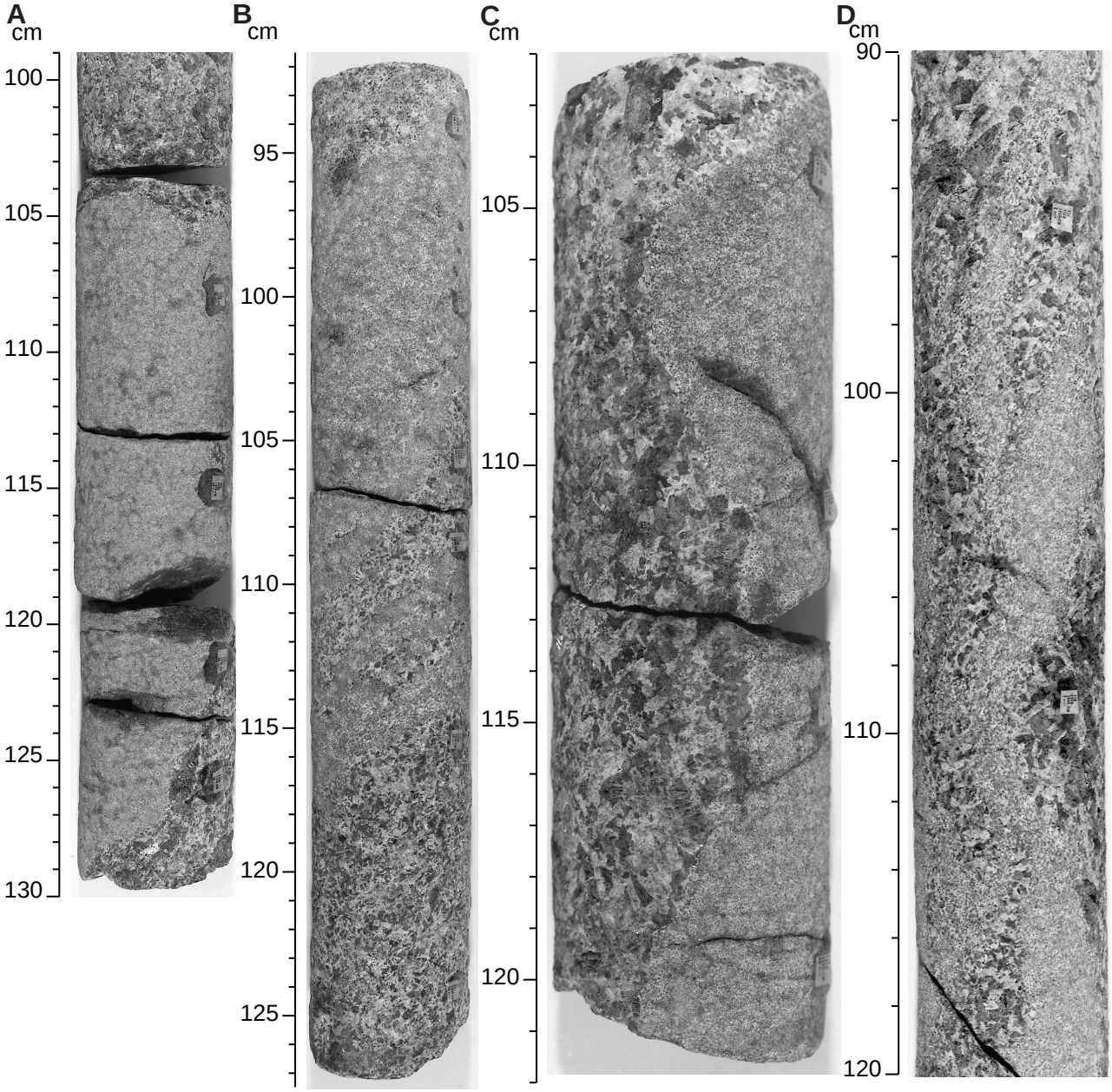

Figure F105. Correlation between the presence of oxide and the intensity of crystal-plastic deformation intensity.

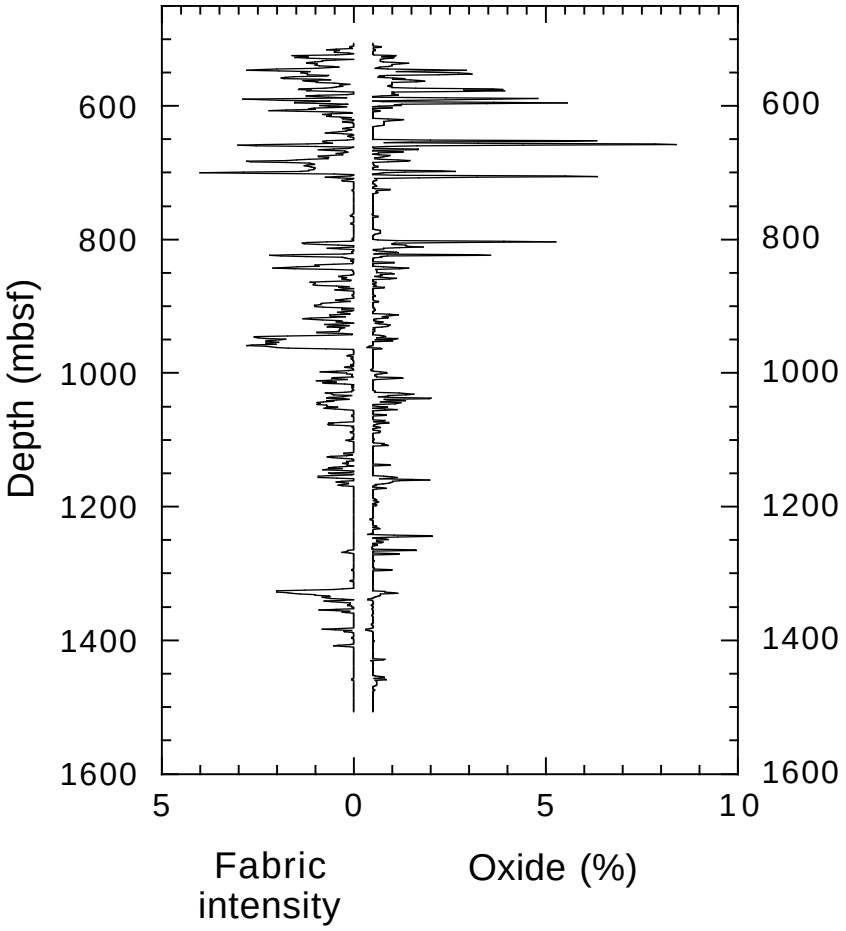

Figure F106. Comparison between the abundance of amphibole veins and the intensity of both crystal-plastic fabric and faults with depth.

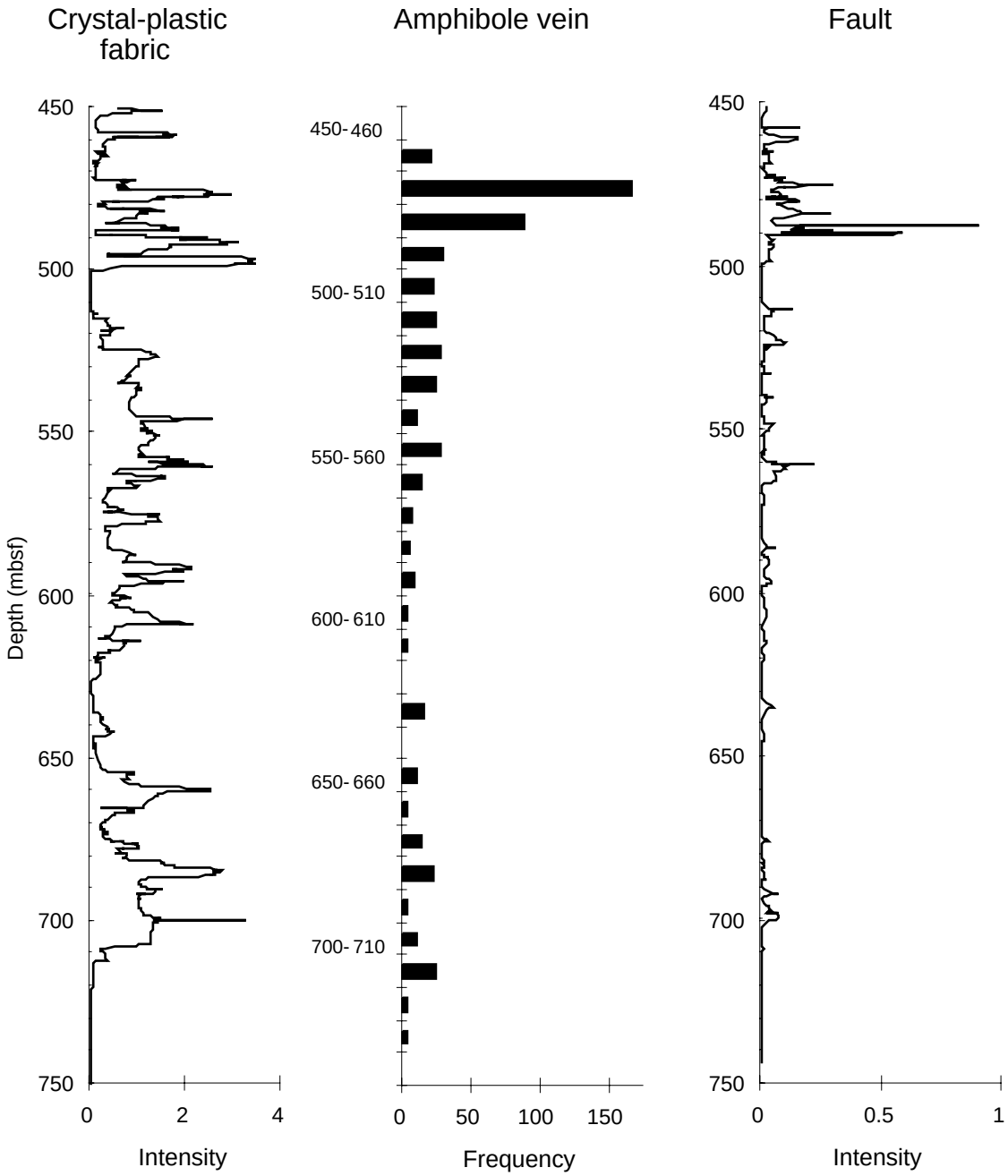

Figure F107. Distribution of angles (by 10° classes) between amphibole veins and crystal-plastic foliations for the interval 450 to 850 mbsf (*N* = 80).

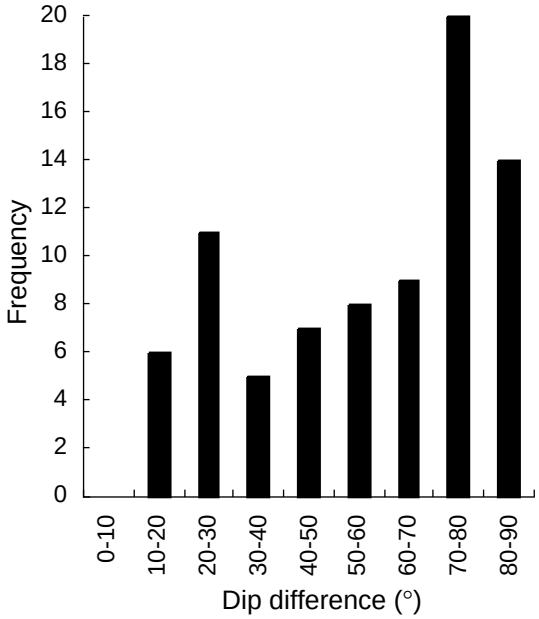

Figure F108. Variation in average magnetic susceptibility with depth in Leg 176 Hole 735B. Points represent values of geometric means (±1 σ error bars) for 20-m intervals, calculated from the filtered susceptibility data. One σ error on slope is 1.26×10^{-4}.

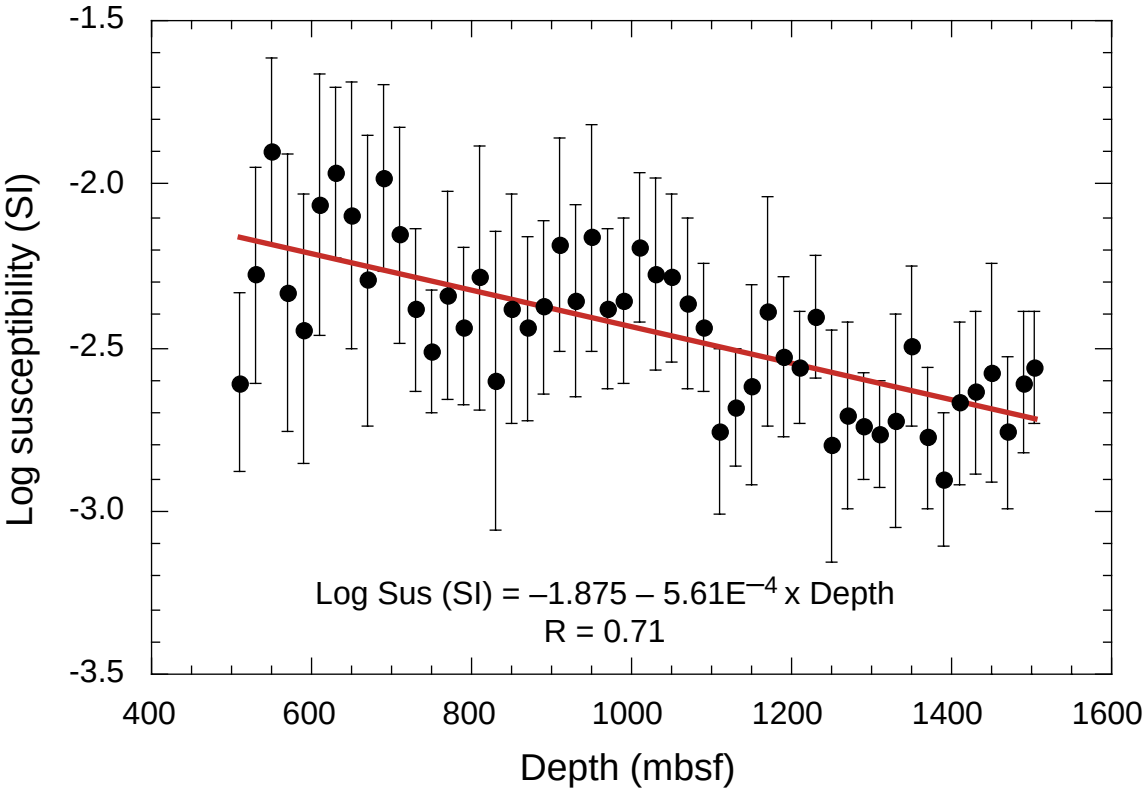

Figure F109. Declination, inclination, and intensity of the natural remanent magnetization (NRM) of gabbroic rocks from Hole 735B. Fine dots represent remanence determined from measurement of the archive halves, using only continuous core pieces greater than 15 cm in length and excluding data from within 5 cm of piece ends. Larger solid circles represent results from discrete minicore samples. Depths used are standard curated depths, linearly adjusted to remove overlap where curated lengths exceed the length of the drilled interval.

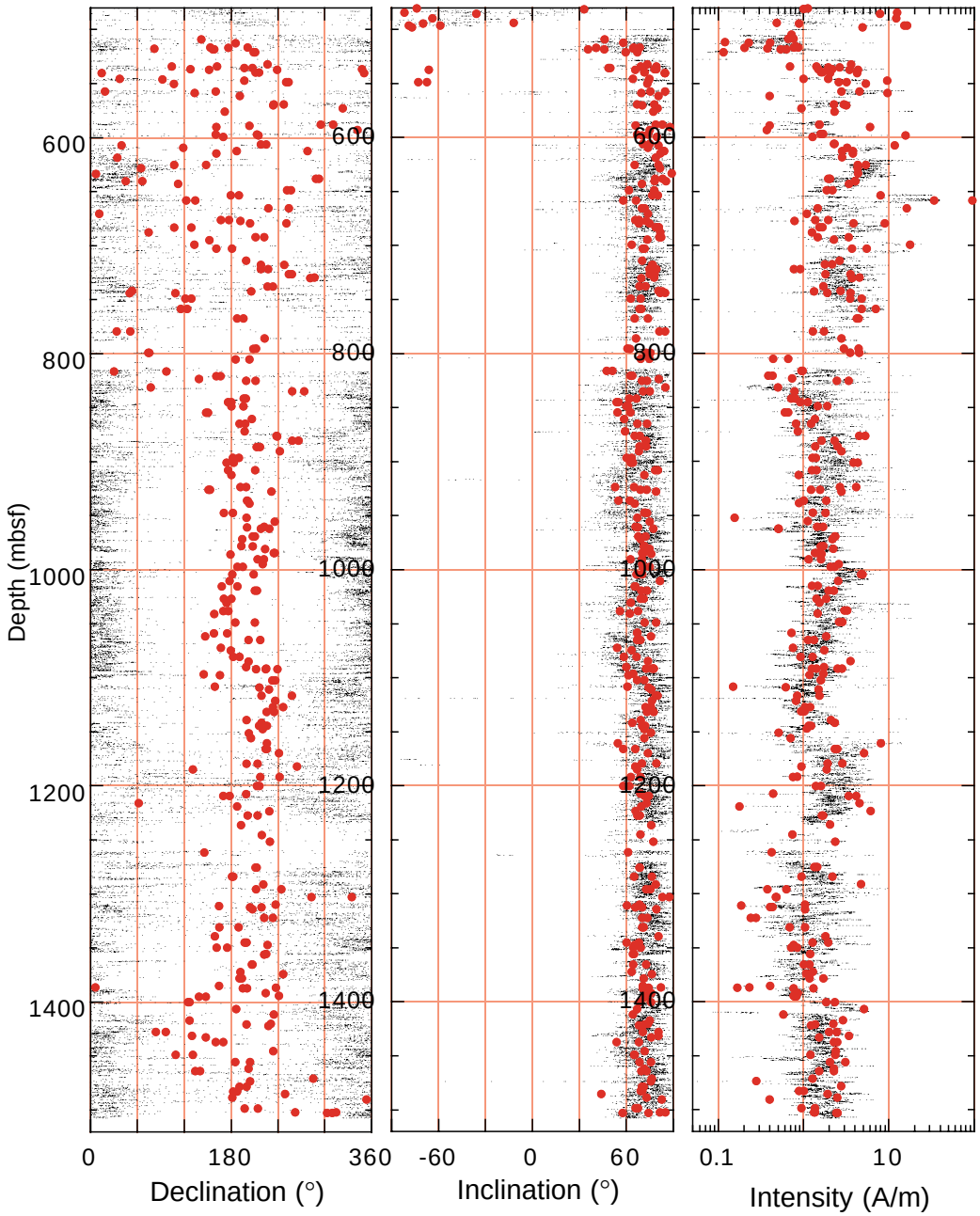

Figure F110. Comparison of the declinations and inclinations of natural remanent magnetization for whole core (open circles) and archive half (solid circles) illustrating the presence of drilling-related secondary magnetization. Data have been filtered to include only continuous core pieces greater than 15 cm in length and to exclude data from within 5 cm of piece ends. Depths refer to standard curated depths.

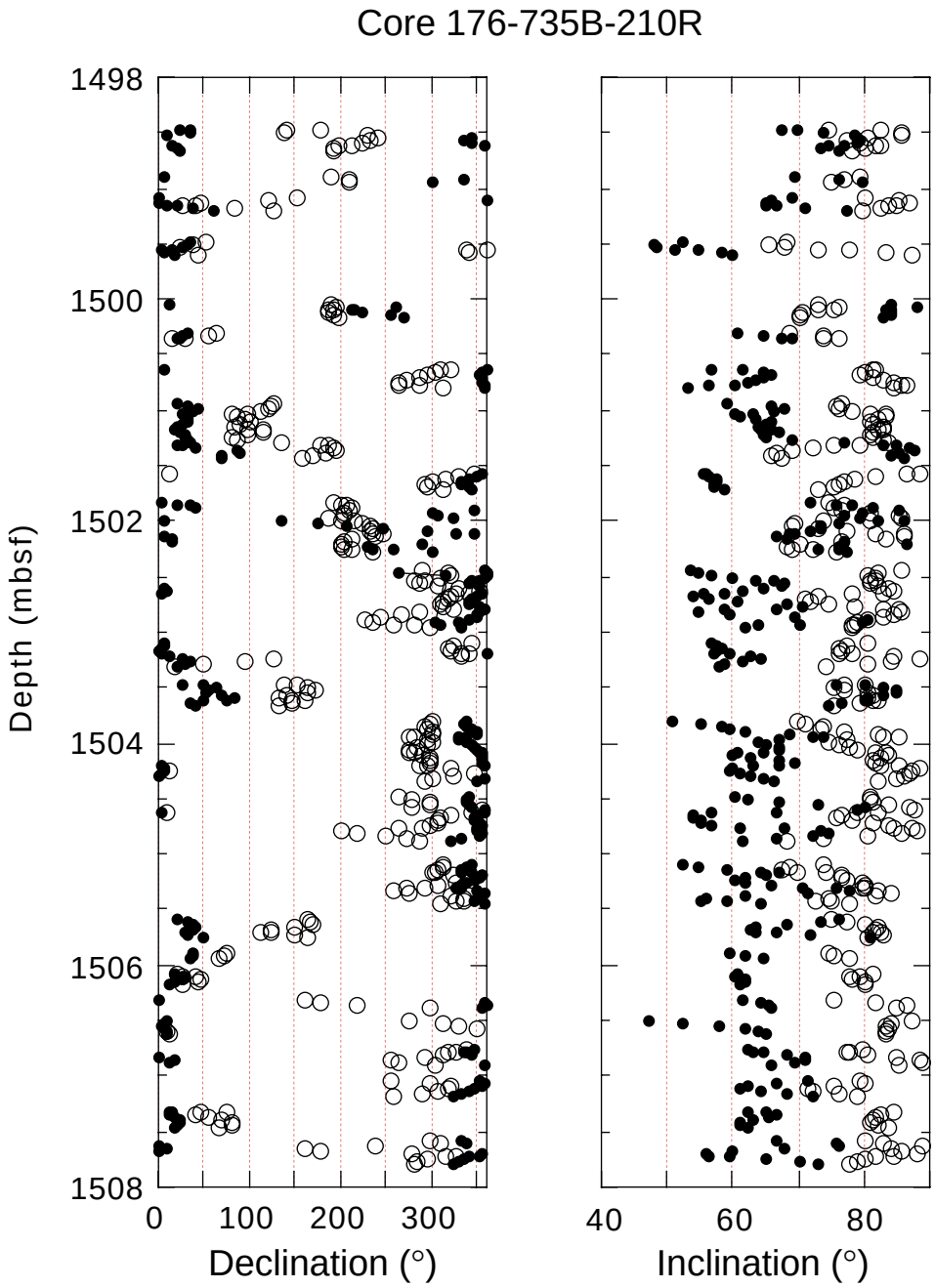

Figure F111. Histograms of average declinations of (**A**) natural remanent magnetization and (**B**) remanence after demagnetization at 20 mT as determined from archive-half core pieces greater than 15 cm in length.

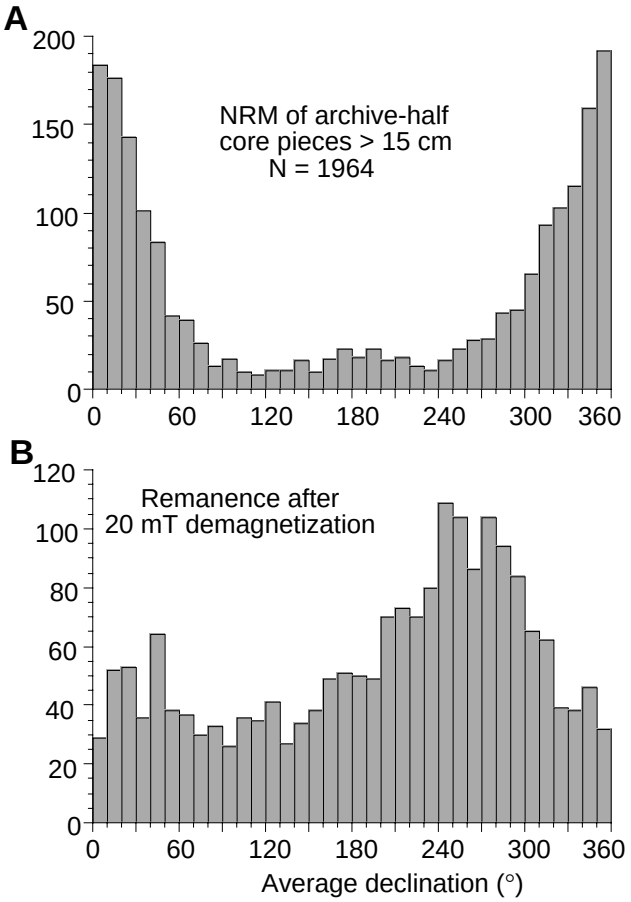

Figure F112. Declination, inclination, and intensity of remanence after 20 mT demagnetization for gabbroic rocks from Hole 735B. Fine dots represent remanence determined from measurement of the archive-half cores, using only continuous core pieces greater than 15 cm in length and excluding data from within 5 cm of piece ends. Larger solid circles represent best fit directions determined from stepwise demagnetization of discrete minicore samples. Depths used are standard curated depths, linearly adjusted to remove overlap where curated lengths exceed the length of the drilled interval.

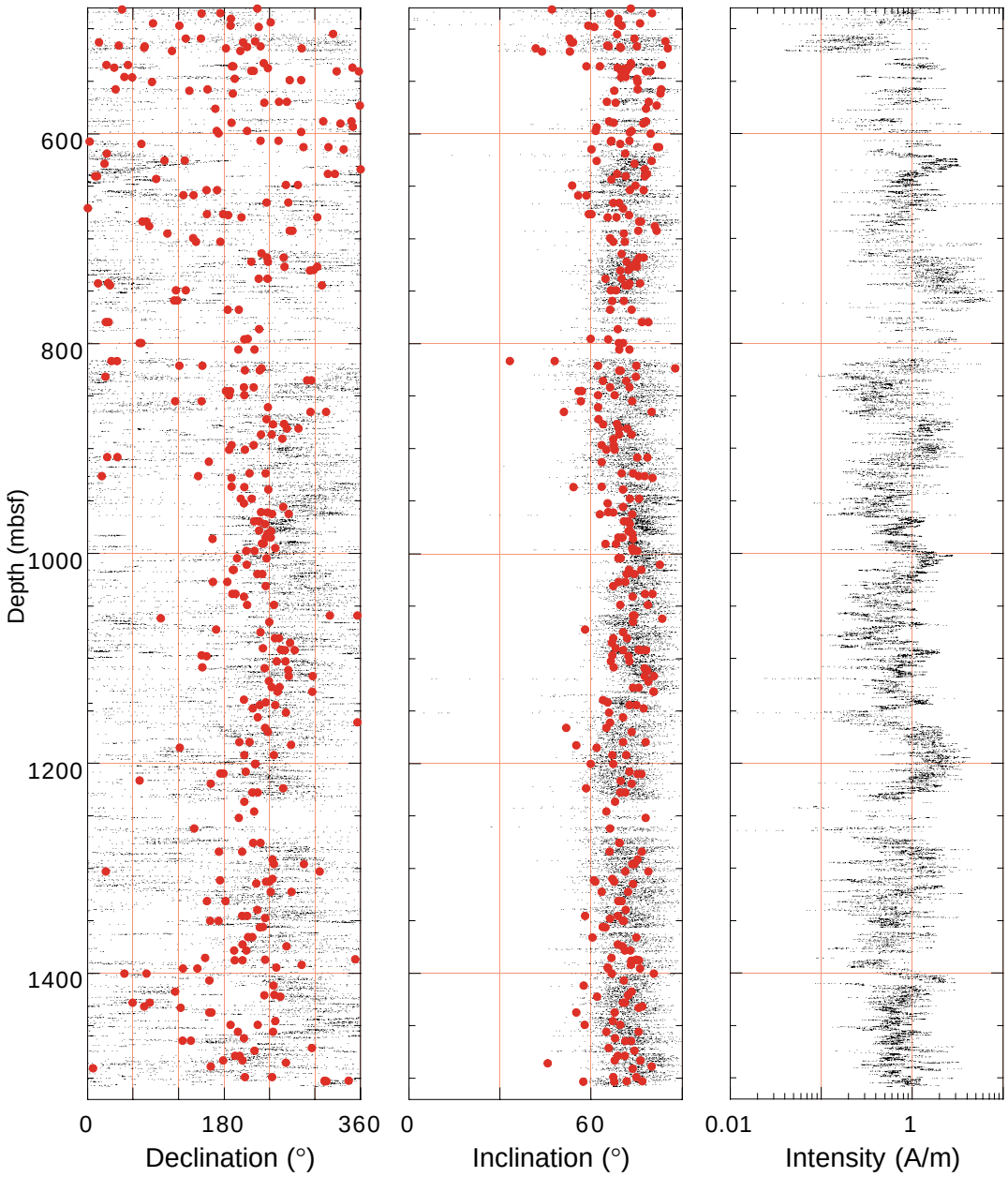

Figure F113. Downhole variation of natural remanent magnetization (NRM), volume susceptibility, Königsberger ratio (Q), and median destructive field (MDF) determined from discrete minicore samples from Hole 735B. Data above 500 mbsf are from minicore samples from Leg 118 (Robinson, Von Herzen, et al., 1991; Kikawa and Pariso, 1991; Pariso and Johnson, 1993). Note that depths refer to standard curated depths. Thick gray lines represent a 20-point running mean of the discrete sample data.

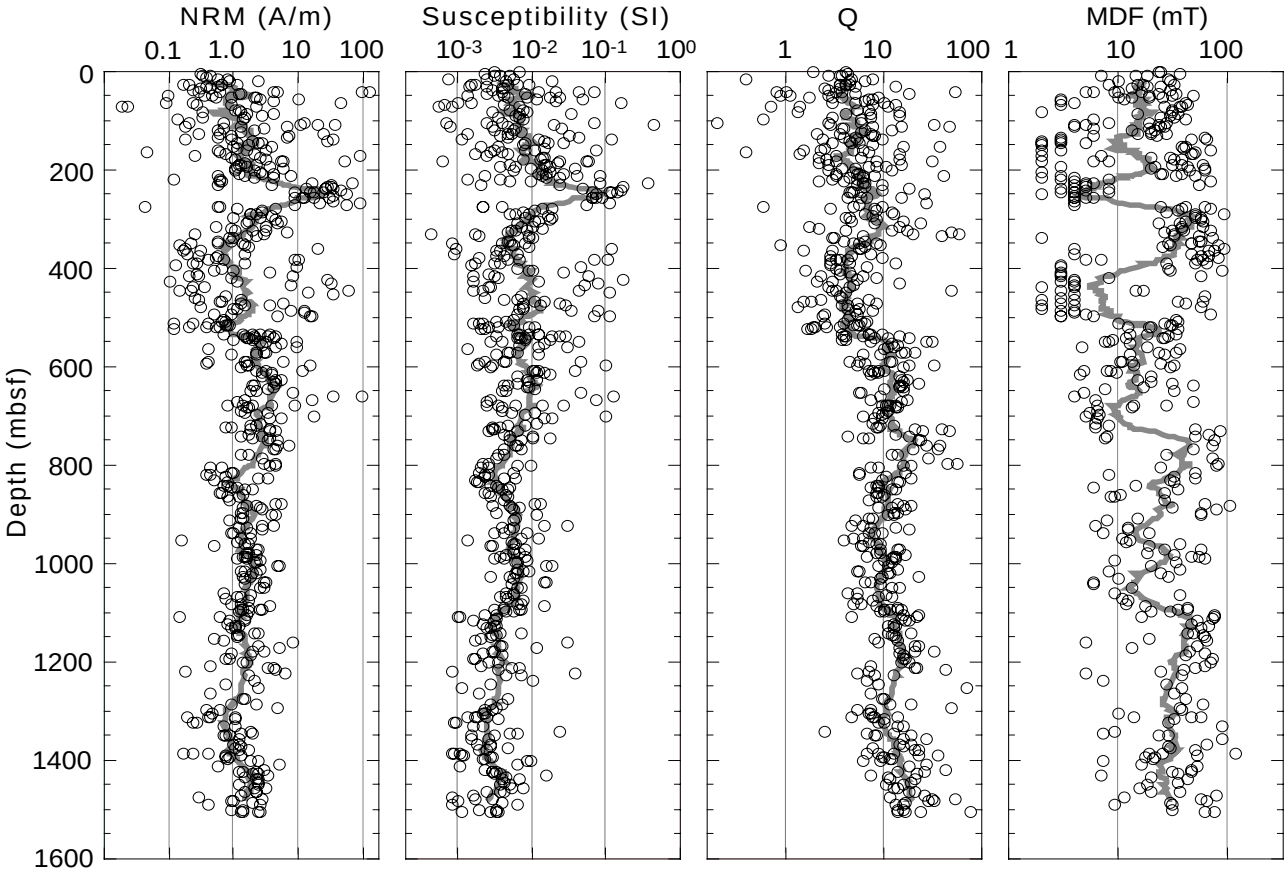

Figure F114. Distribution of (**A**) logarithm of natural remanent magnetization (NRM), (**B**) logarithm of volume susceptibility, (**C**) logarithm of Königsberger ratio (Q), and (**D**) characteristic inclination determined from gabbroic minicores from Leg 176. Arithmetic mean (one standard deviation) and geometric mean (one standard deviation in log units) are given for NRM, susceptibility, and Q. Mean characteristic inclination and asymmetric 95% confidence limits from inclination-only technique of McFadden and Reid (1982).

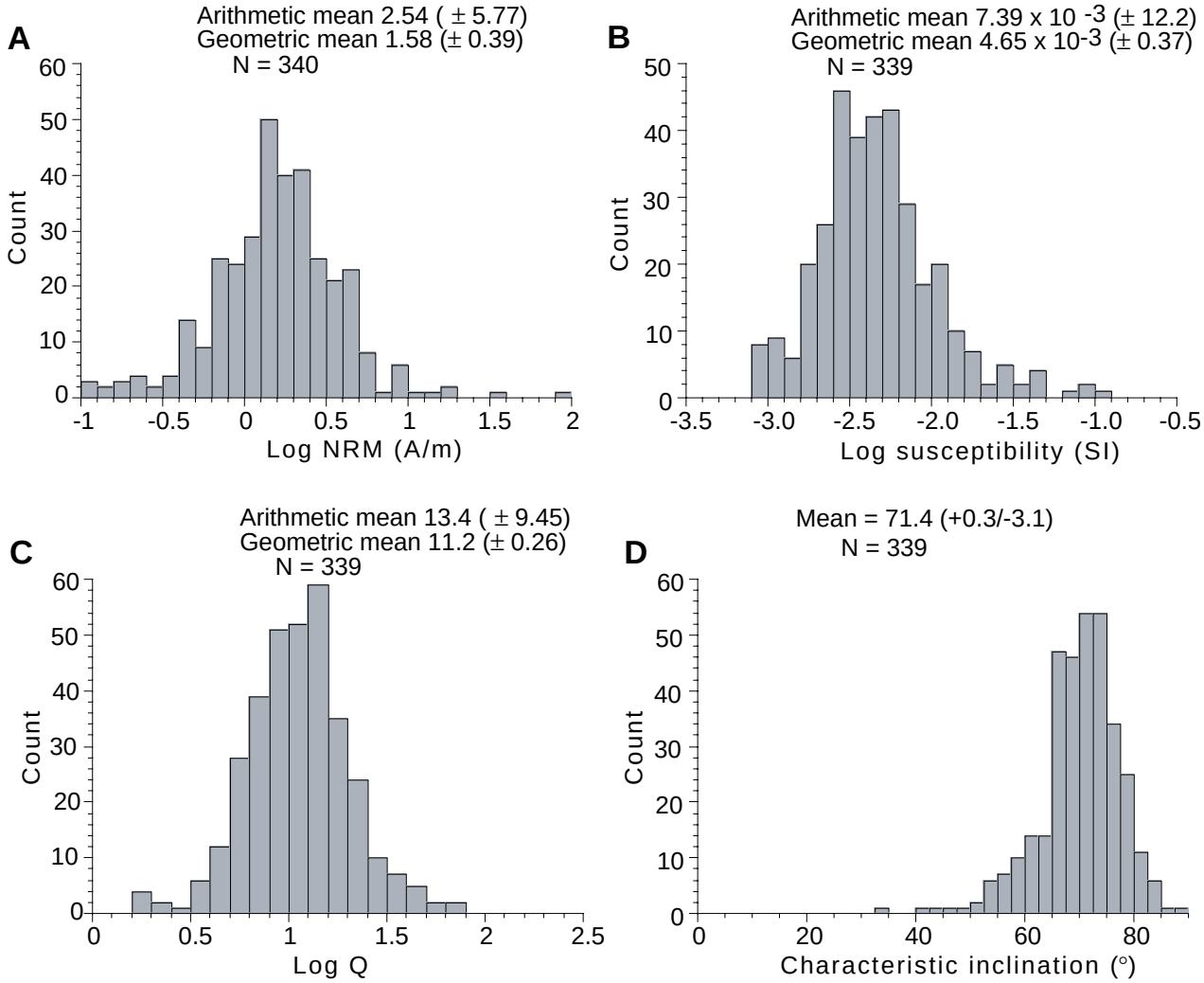

Figure F115. Representative vector end-point diagrams for gabbroic minicore samples from Leg 176. Alternating-field and thermal demagnetization results from adjacent minicores illustrating (**A, B**) minor and (**C, D**) more substantial southward-directed secondary magnetization component. This southward-directed secondary component occasionally is stable to AF fields as high as 50 mT (**E**) or may not be evident at all if the secondary magnetization is (sub)parallel to the characteristic magnetization direction (**F**). Solid circles are the projections of the remanent magnetization onto the horizontal plane, and open circles are the projection onto the vertical plane.

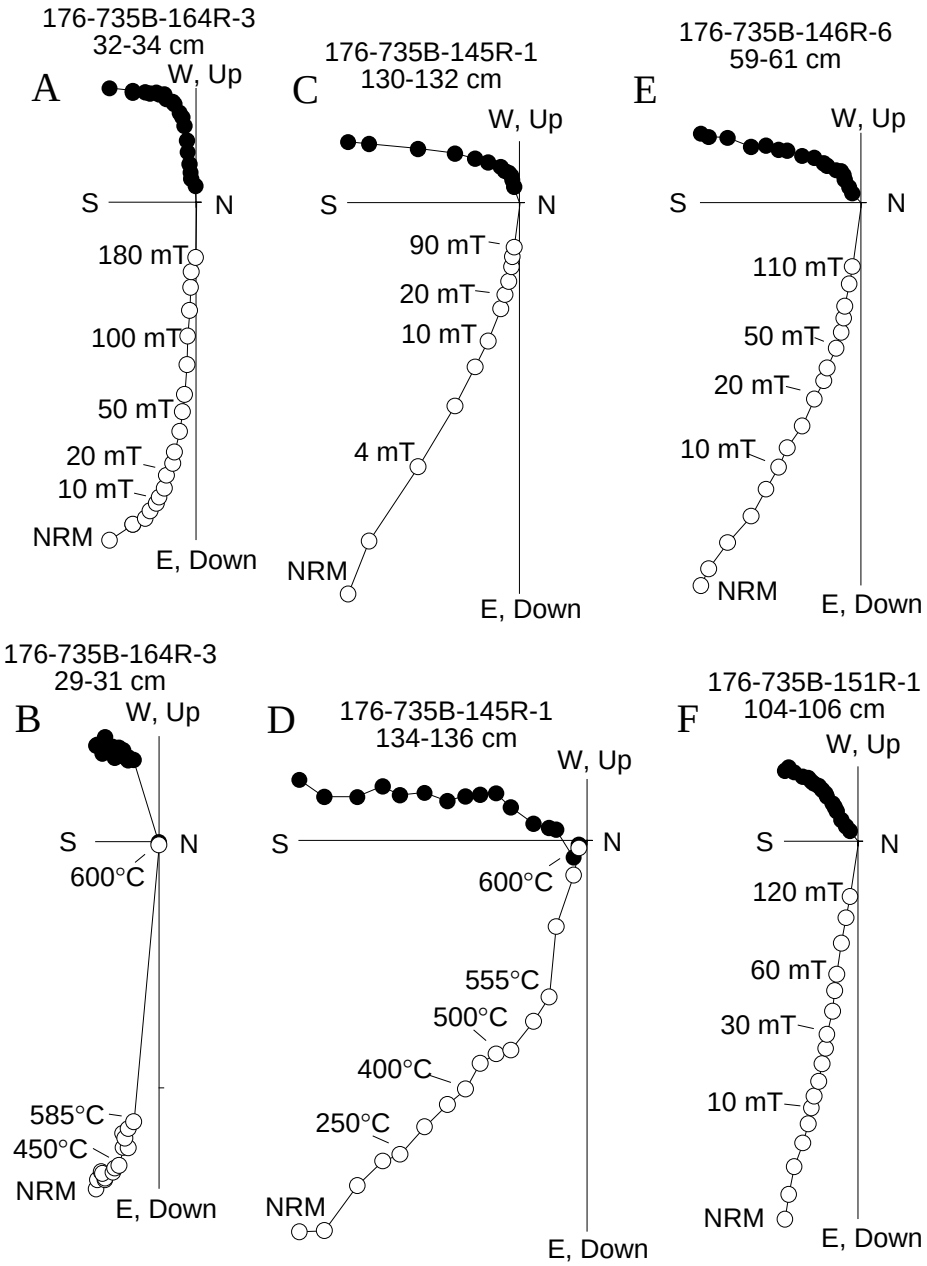

Figure F116. Vector end-point diagrams for minicore samples from Section 176-735B-156R-5 (Piece 2A), illustrating apparent radial orientation of the low-stability magnetization component. The sample from 41–43 cm was slightly offset to left of the center line in the working half (i.e., toward azimuth of 270° in core reference frame). The sample from 48–50 cm was slightly offset toward azimuth of 90°. The sample from 44–46 cm was taken from the center of the working half and subsequently subdivided into an interior and an exterior sample. Solid circles are the projections of the remanent magnetization onto the horizontal plane, and open circles are the projection onto the vertical plane.

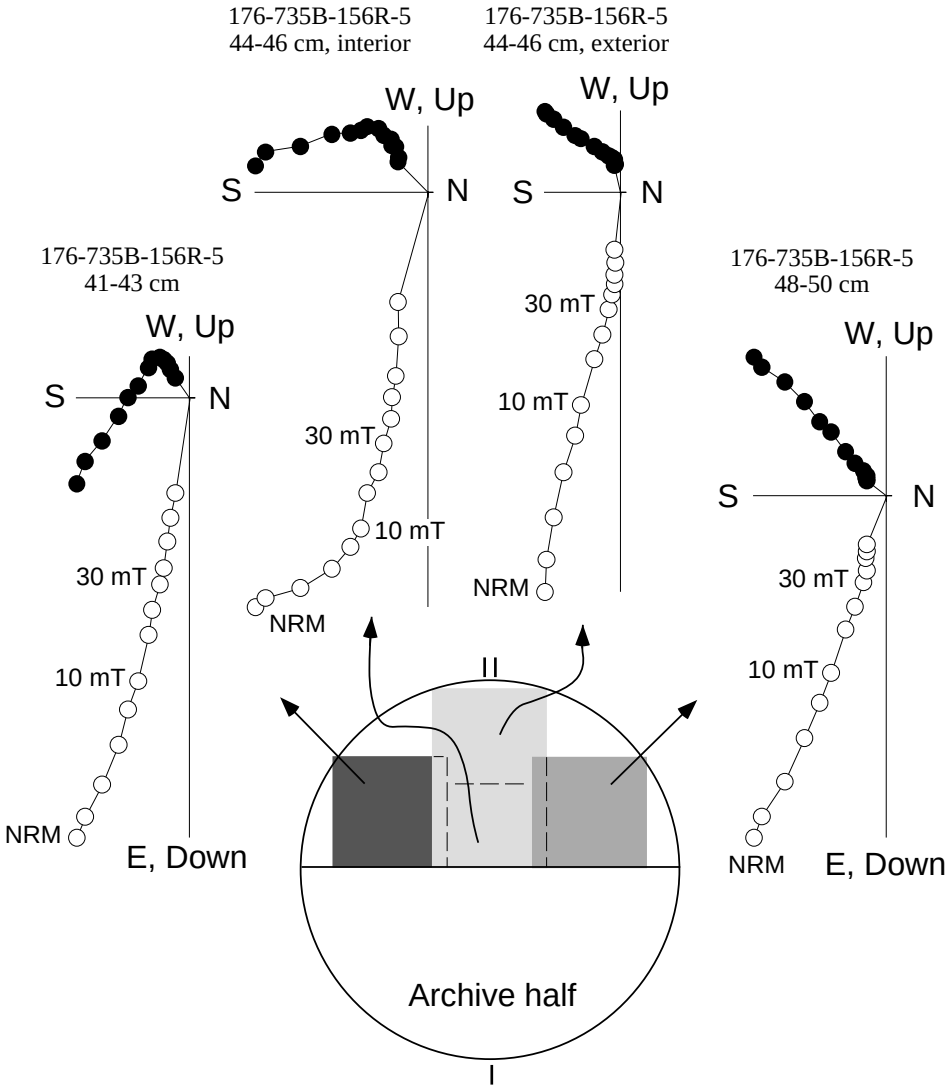

Figure F117. Anisotropy of magnetic susceptibility (AMS) results from minicore samples from Leg 176. **(A)** Degree of anisotropy (P, where P is the ratio of the maximum eigenvalue (γ_1) to the minimum eigenvalue (γ_3) of the AMS tensor), **(B)** inclination of the minimum eigenvector (K_{min}), and **(C)** inclination of the maximum eigenvector (K_{max}) are shown as a function of depth. Prolate ($T < -0.2$), neutral ($-0.2 < T < 0.2$), and oblate ($T > 0.2$) samples are indicated by open circles, plus signs, and solid circles, respectively. See text for explanation of shape parameter T. Note that depths refer to standard curated depths.

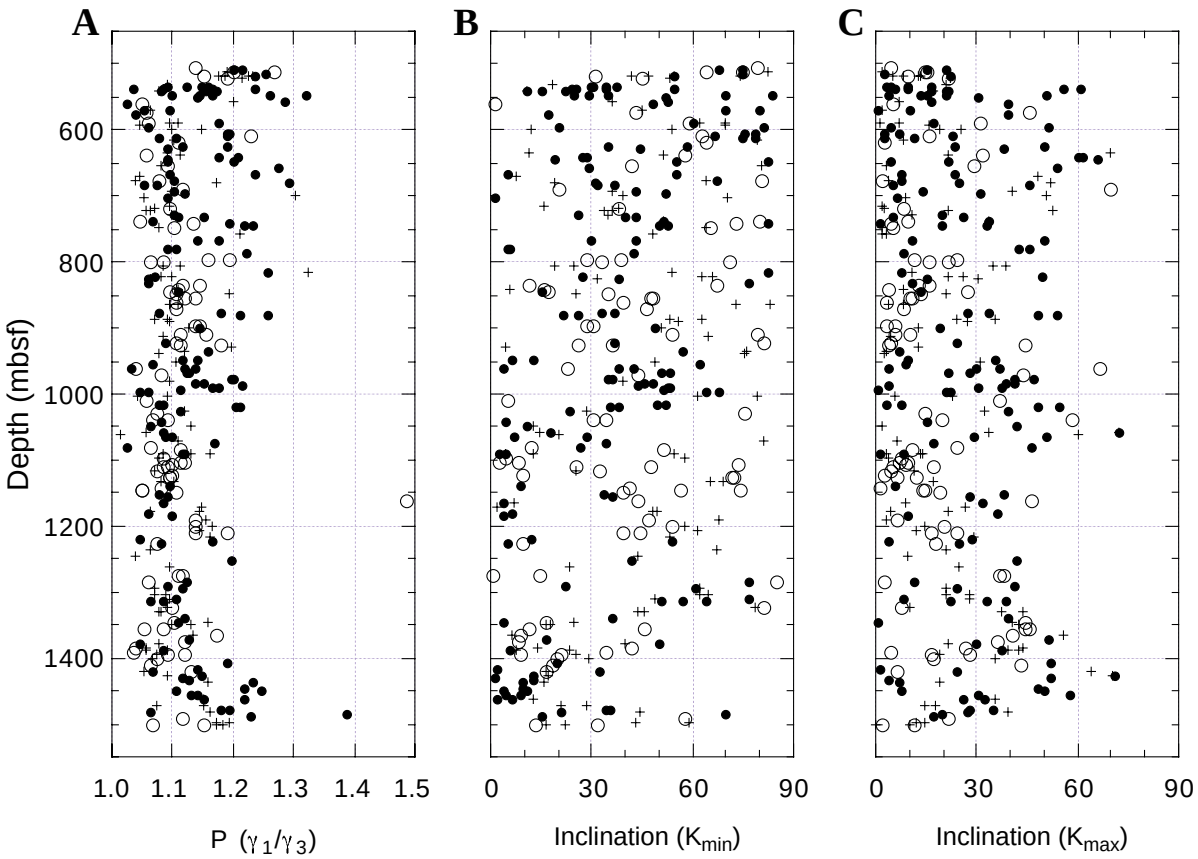

Figure F118. A comparison of GRAPE density and bulk density for Hole 735B.

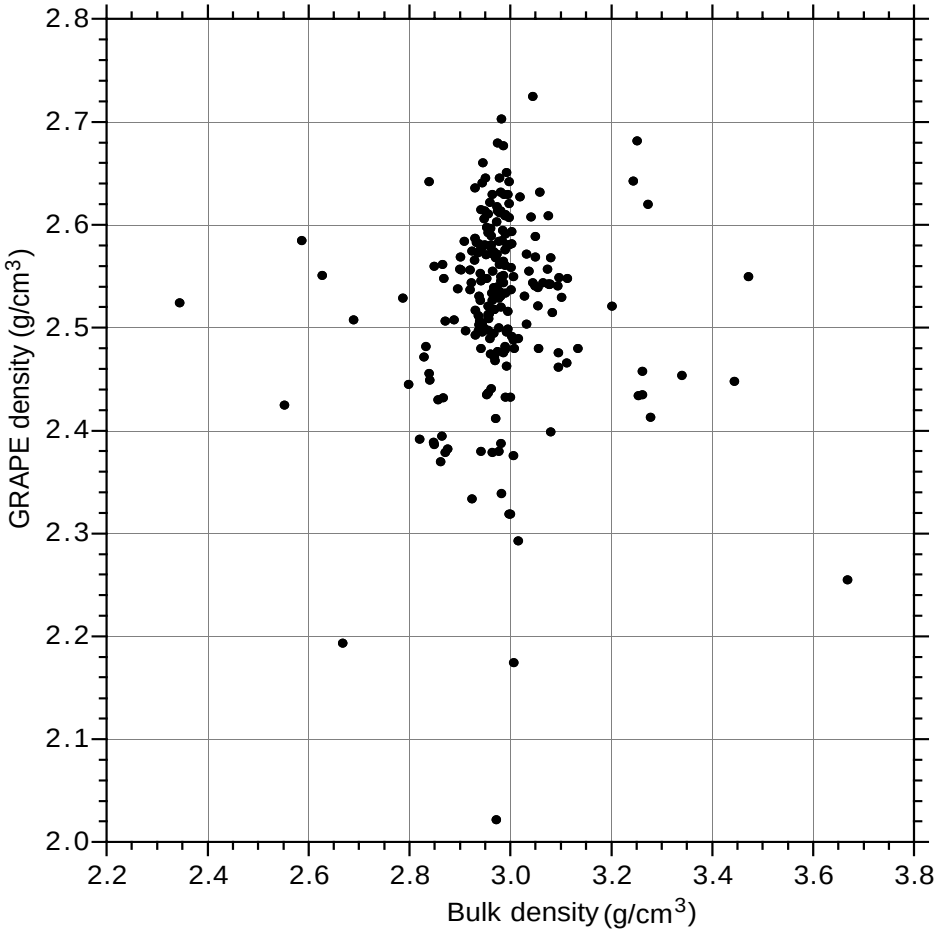

Figure F119. Response functions of the Bartington MS2C sensor.

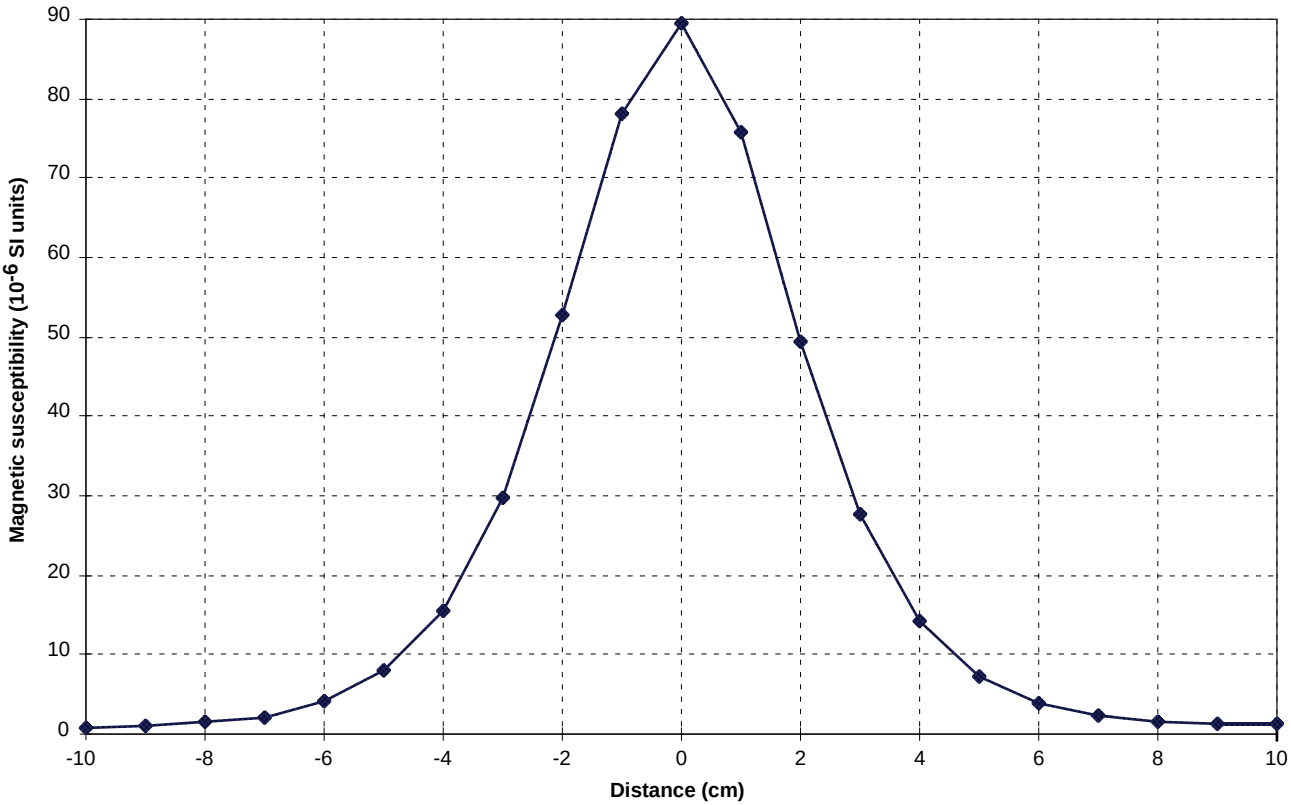

Figure F120. Raw magnetic susceptibility of Hole 735B.

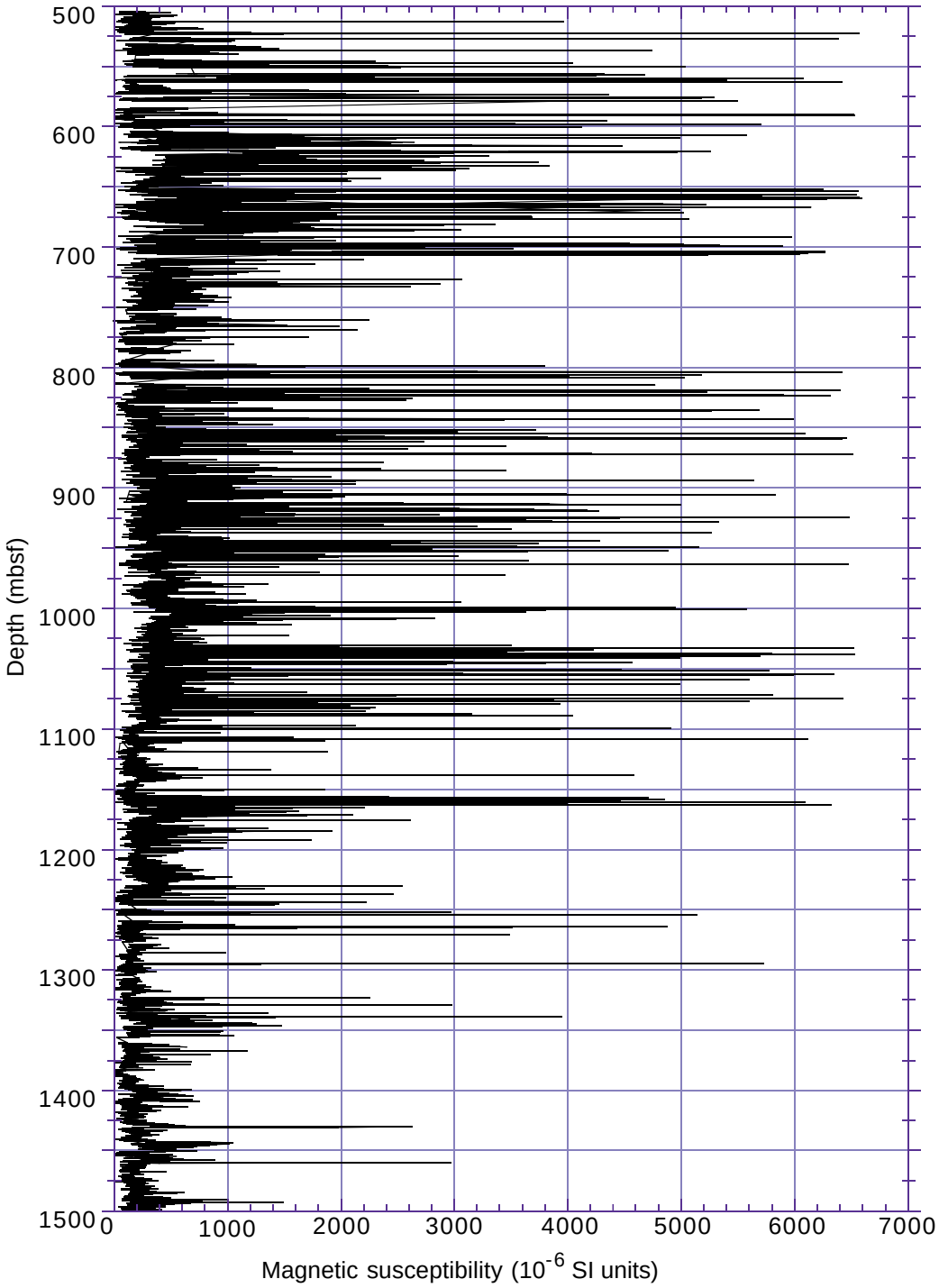

Figure F121. Magnetic susceptibility of Core 176-735B-161R. Locations of felsic veins numbers 246, 248, 249, 250, 251, and lithologic intervals 785 and 787 correlate directly with susceptibility peaks, Lithologic intervals 785 and 787 are 8- and 13-cm-thick oxide gabbros with 5 and 3 modal% opaques, respectively. Uncorrelated peaks likely correspond to oxide-rich intervals thinner than 5 cm, which were not logged.

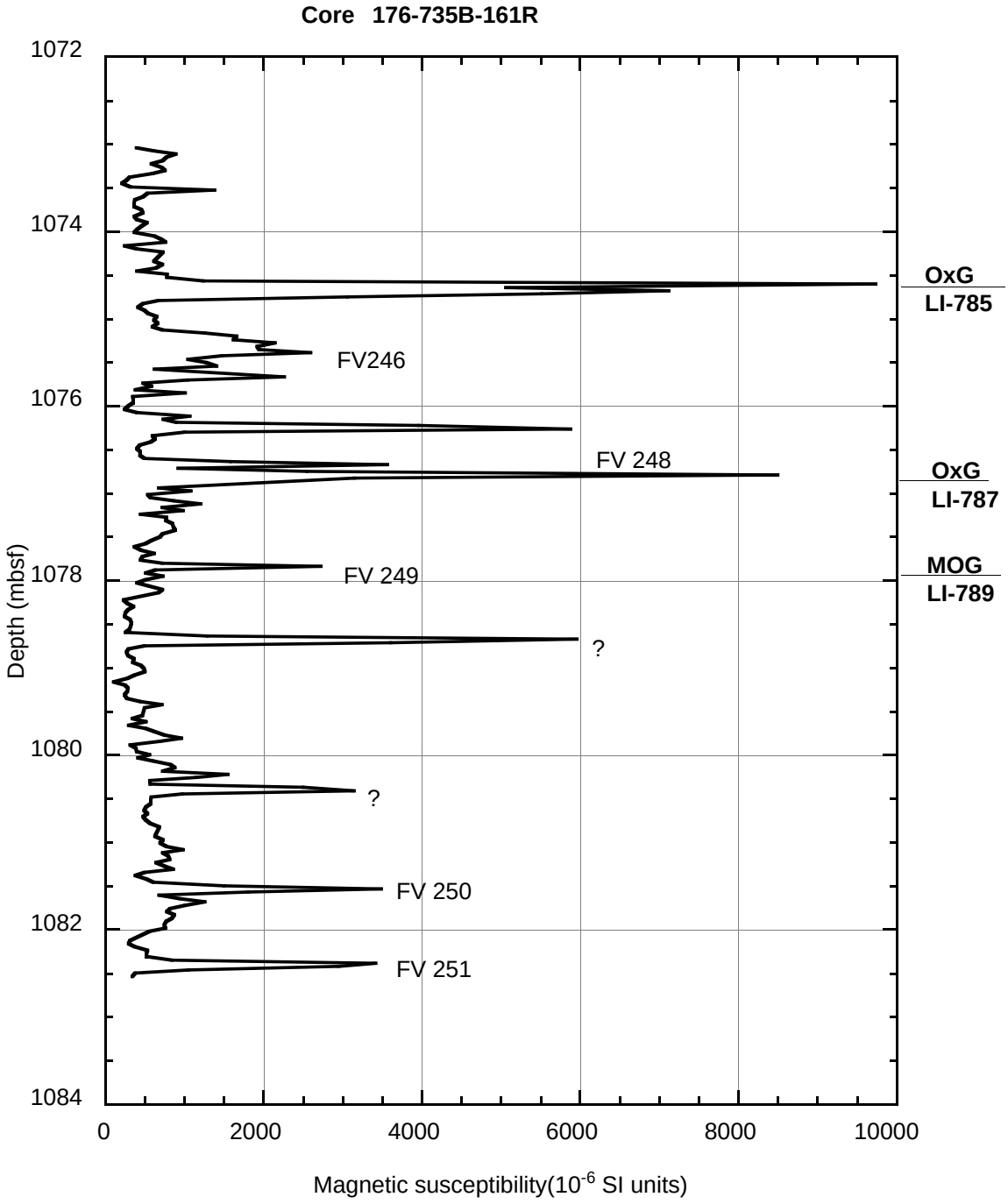

Figure F122. Bulk and grain density of minicores from Hole 735B.

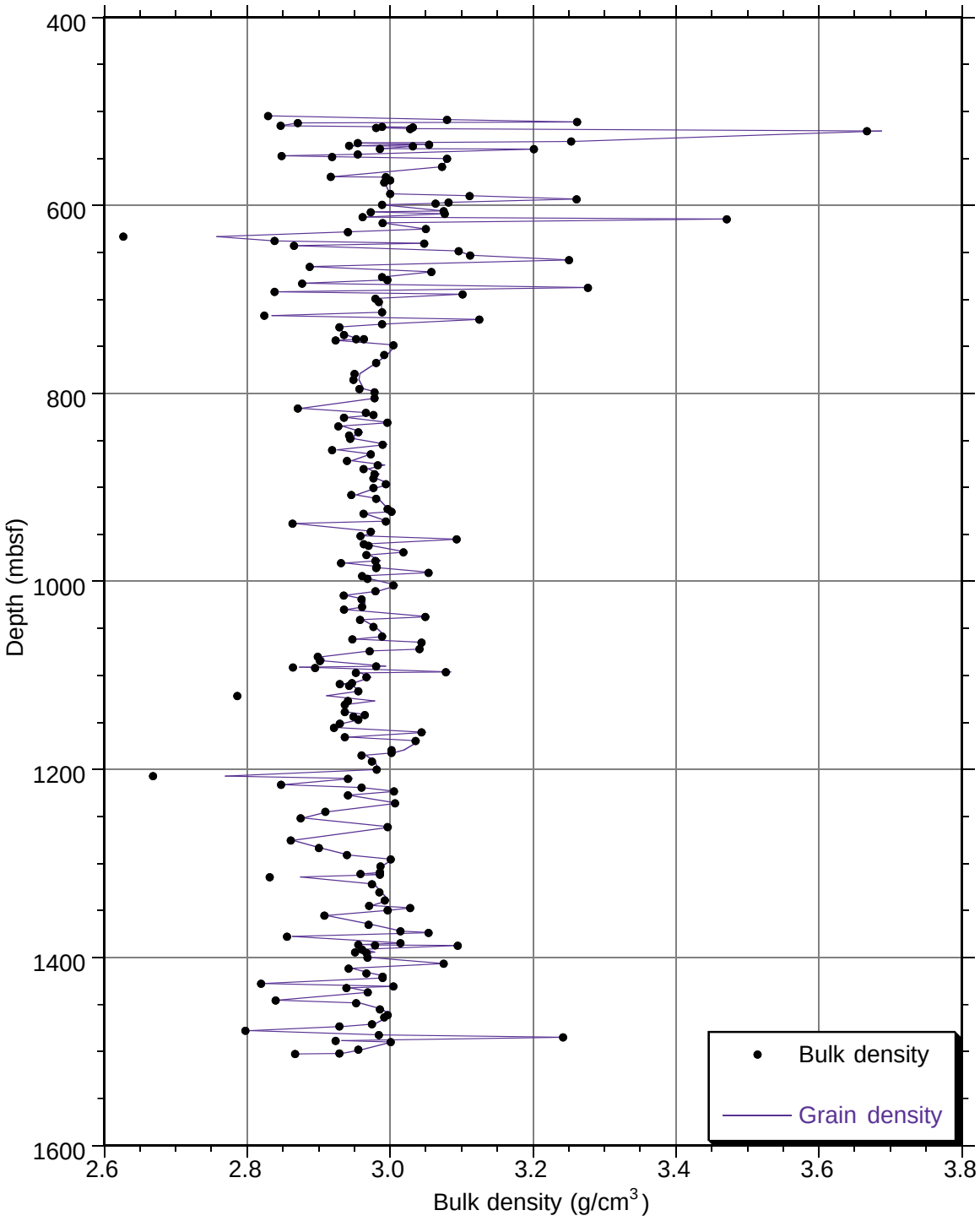

Figure F123. Bulk density of principal lithologies for Hole 735B.

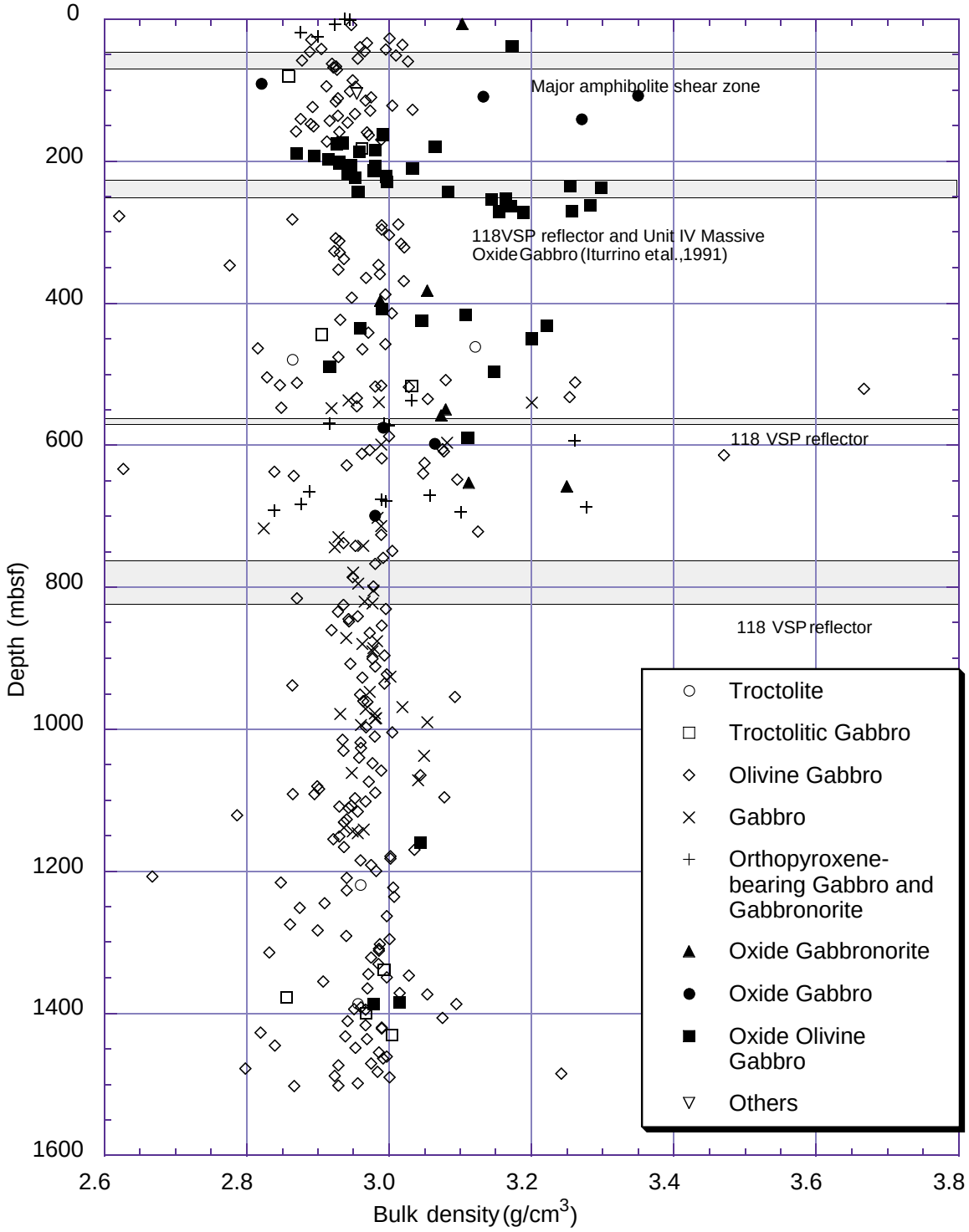

Figure F124. Percentage recovery downhole in Hole 735B. The bottom-hole assembly in the upper 100 m of the hole was not buried, causing poor recovery in that interval.

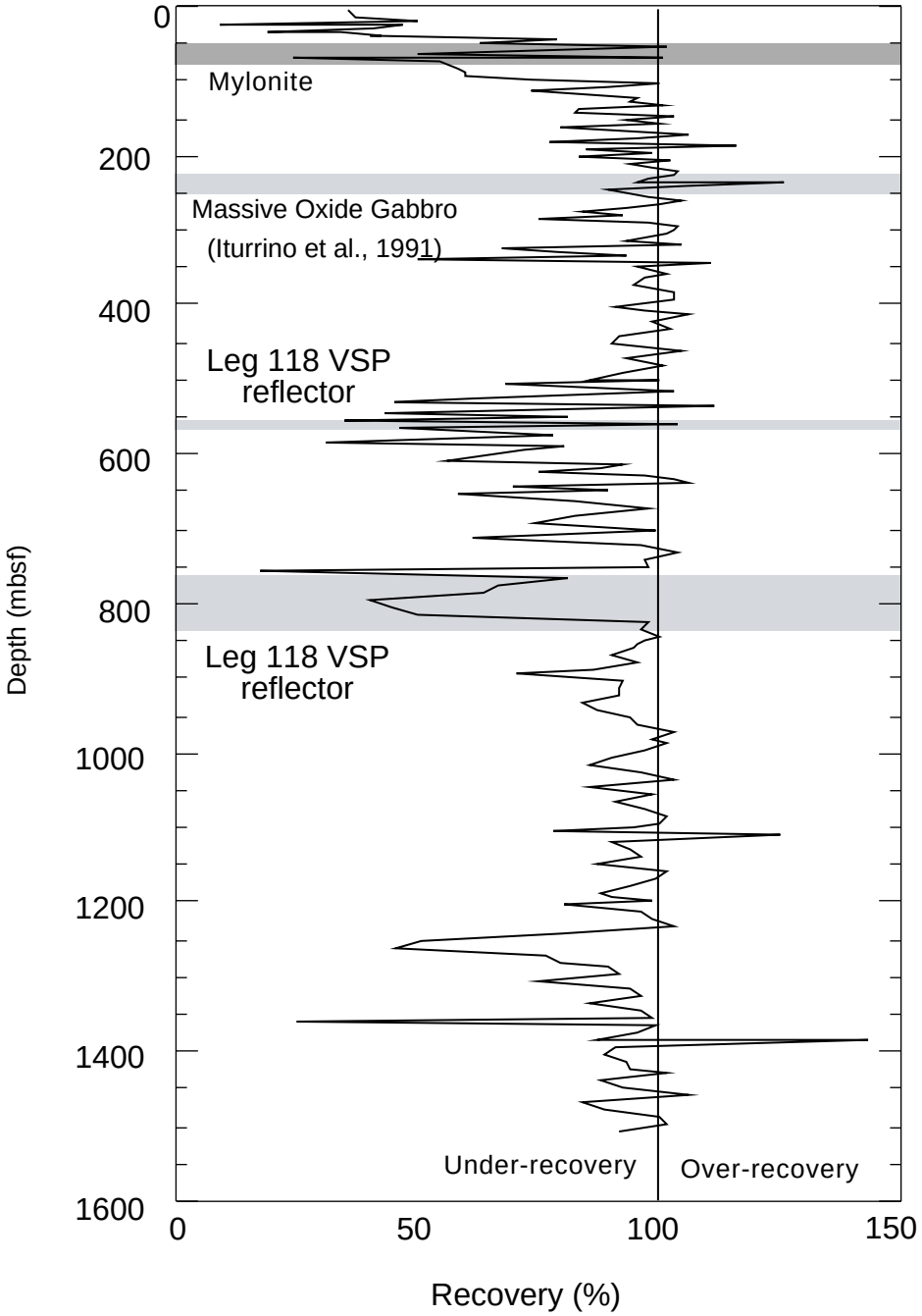

Figure F125. Thermal conductivity of principal lithologies for Hole 735B.

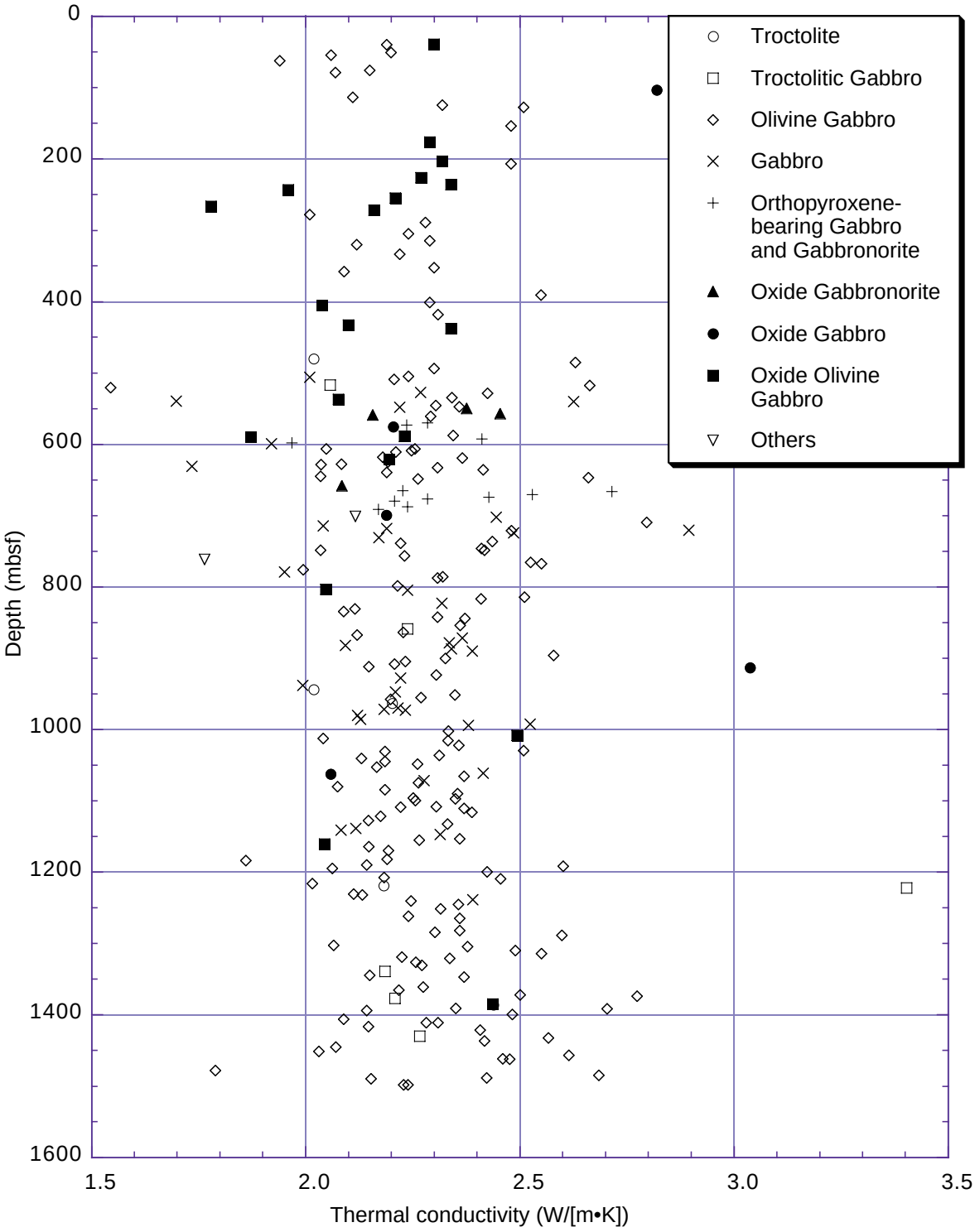

Figure F126. Compressional velocity of principal lithologies for Hole 735B.

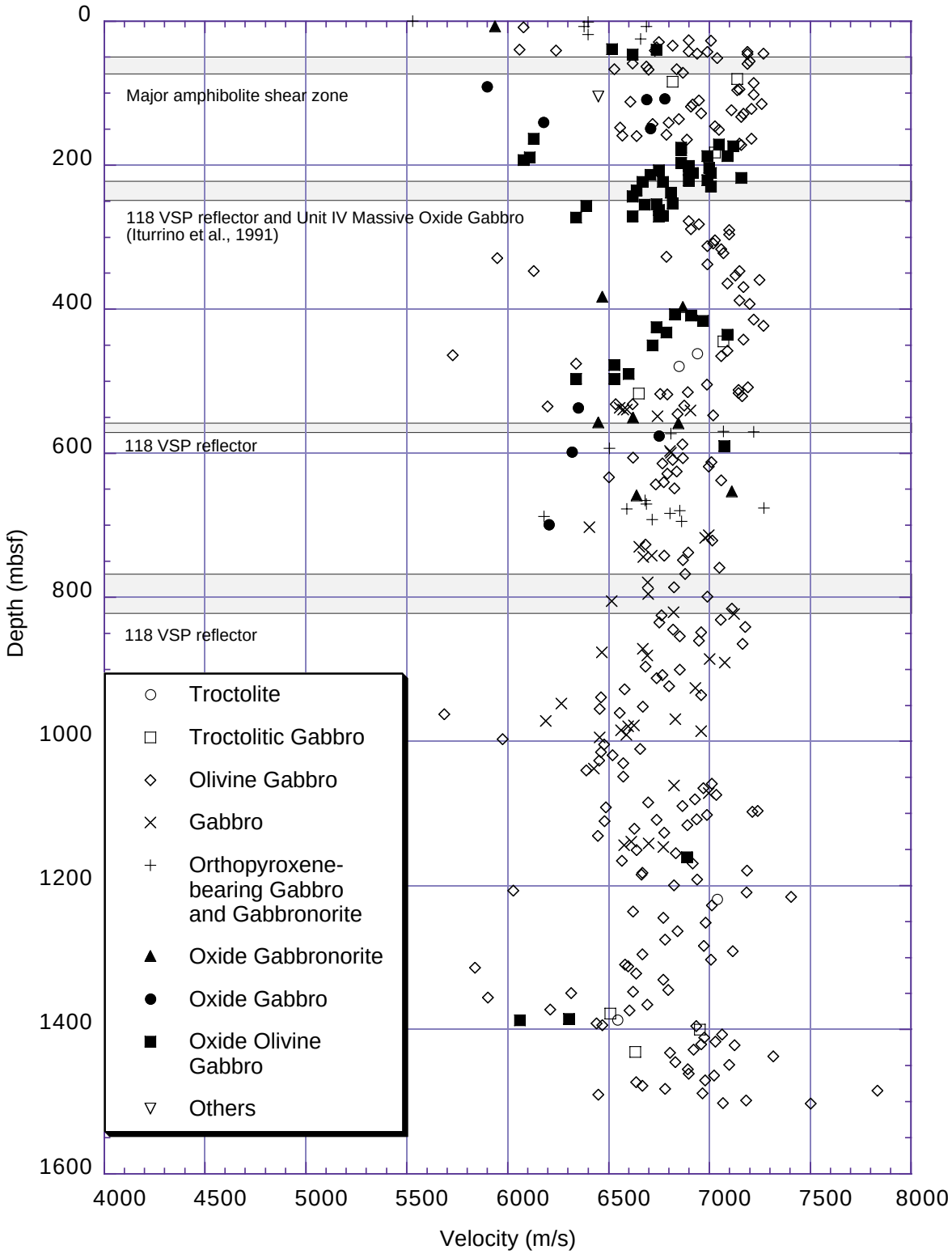

Figure F127. Composite illustration of Hole 735B logs showing the FMS calipers (C1 and C2) in Track 1; hole deviation (DEVI), hole azimuth (HAZI), and FMS pad 1 azimuth for both passes in Track 2; borehole pressure and temperature in Track 3; and laterolog deep (LLs) and shallow (LLs) measurements in Track 4. The bottom scale in the plot axis shows the scale increments for the bottommost curves displayed above the plot; the top scale shows the increments for the topmost curves shown above the plot.

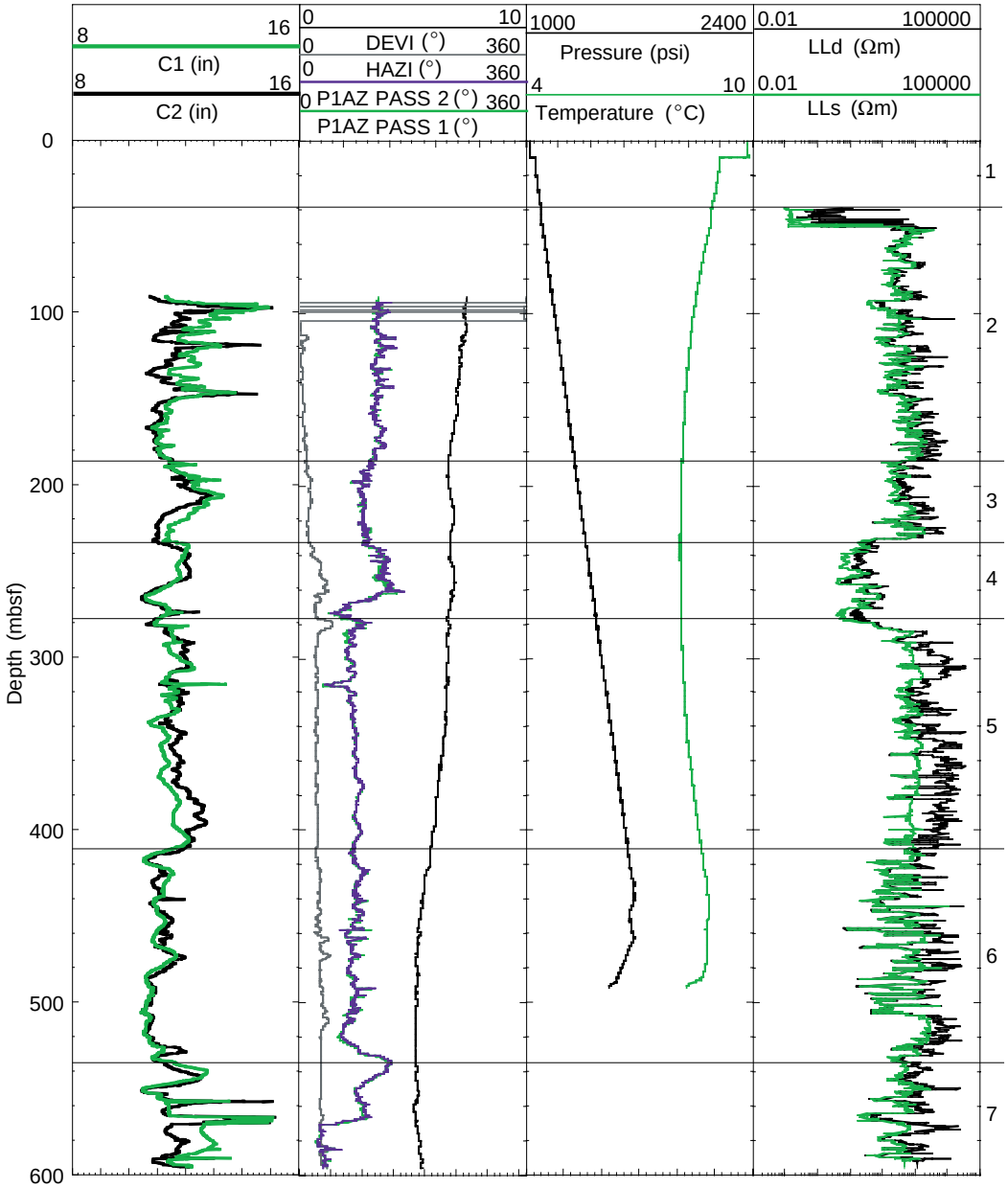

Figure F128. Downhole logs for Hole 735B showing the Leg 118 density (118 RHOB), Leg 176 density (176 RHOB), Legs 118 and 176 discrete laboratory measurements, and photoelectric effect (PEF) in Track 1; array epithermal porosity (APLC), Far/Near detector porosity (FPLC), and Legs 118 and 176 discrete laboratory porosity measurements in Track 2; spectral gamma ray (HSGR) and computed gamma ray (HCGR) in Track 3; and thorium (THOR), uranium (URAN), and potassium (POTA) in Track 4. The bottom scale in the plot axis shows the scale increments for the bottommost curves displayed above the plot; the top scale shows the increments for the topmost curves shown above the plot.

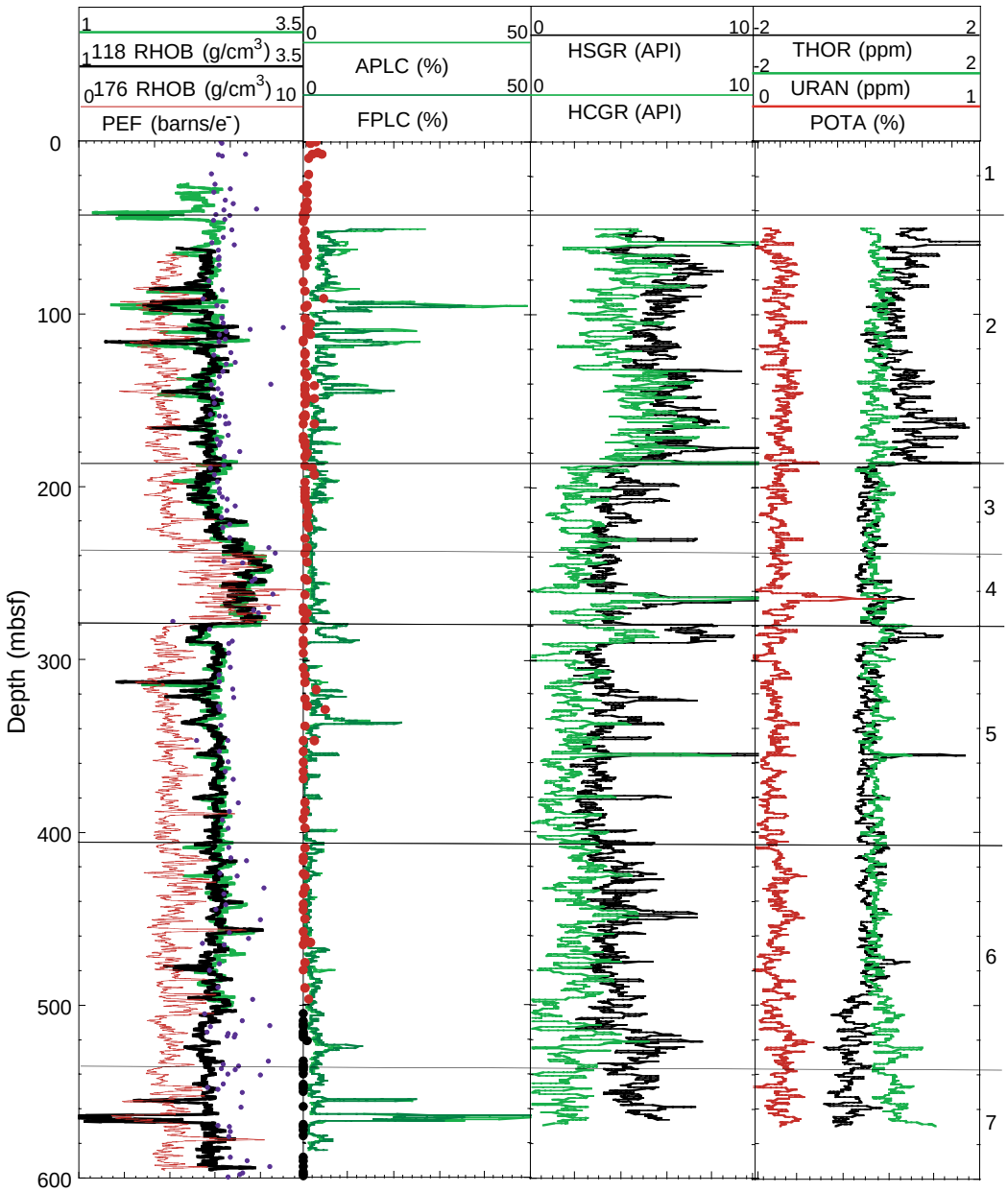

Figure F129. Expanded section of the bottommost 150 m of open hole logged at the end of Leg 176 showing deep (LLd) and shallow (LLs) resistivity in Track 1; array epithermal porosity (APLC) in Track 2; Legs 118 and 176 density (118 RHOB and 176 RHOB), and photoelectric effect (PEF) in Track 3; and FMS calipers (C1 and C2) in Track 4.

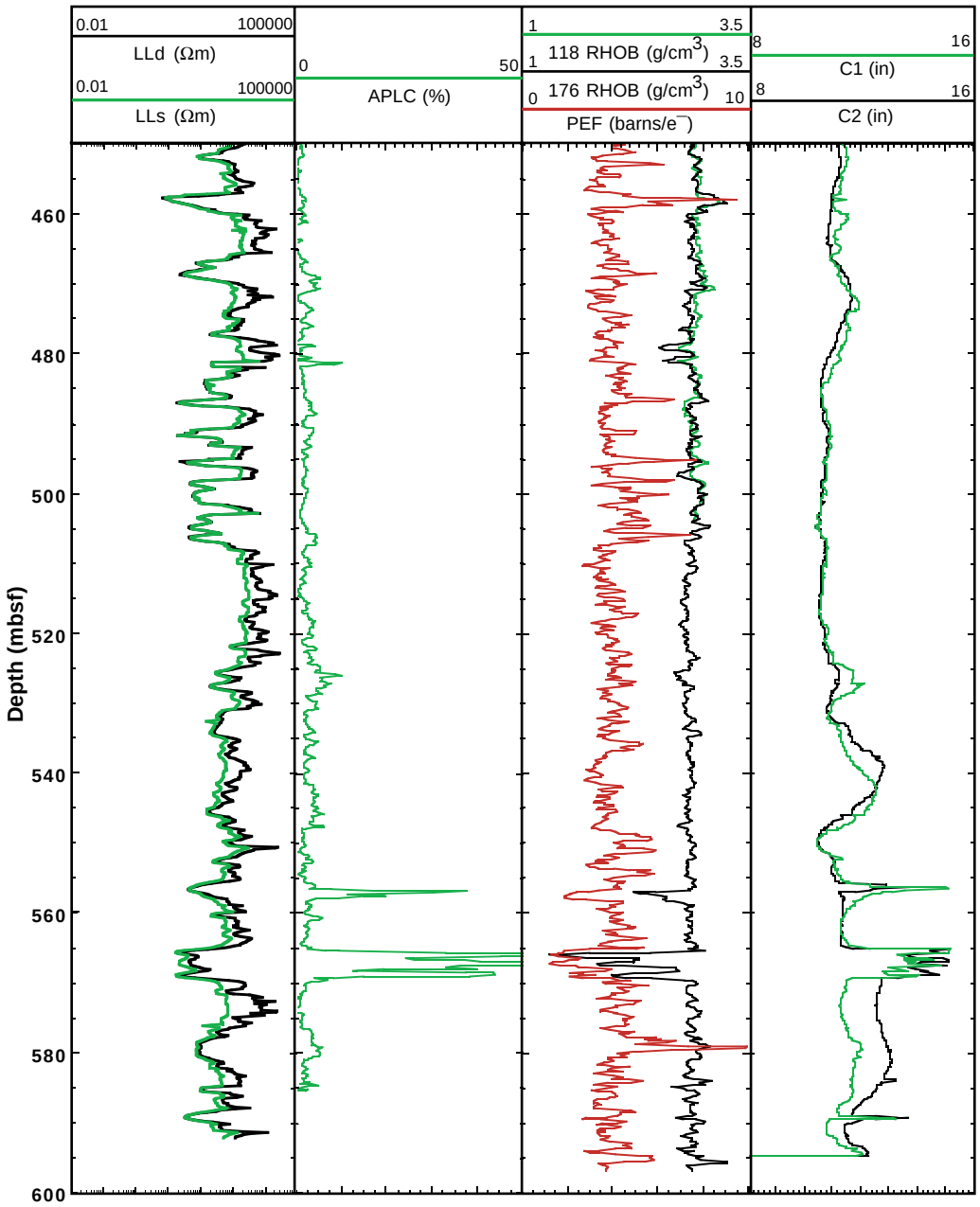

Figure F130. Expanded section of the bottommost 150 m of open hole logged at the end of Leg 176 showing deep (LLd) and shallow (LLs) resistivity in Track 1; array epithermal porosity (APLC) in Track 2; and fault intensity from core observations in Track 3.

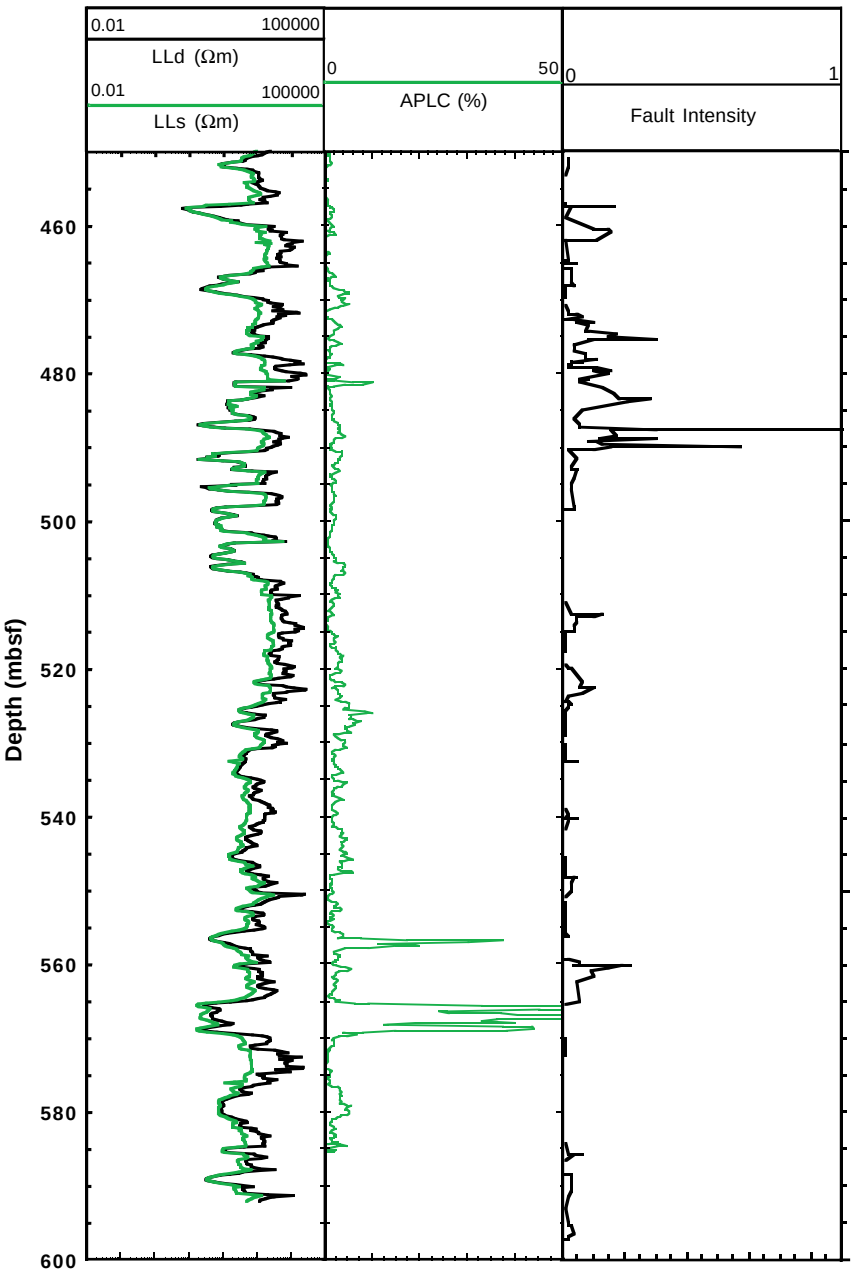

Figure F131. Downhole logs for Hole 735B showing the FMS calipers (C1 and C2) in Track 1; traveltime for compressional (DTC) and shear waves (DTS) generated with the DSI monopole source and shear-wave traveltimes produced with the DSI dipole source in Track 2; transmitter and receiver coherence for the high-frequency compressional wave monopole source (CHTP and CHRP) in Track 3; and transmitter and receiver coherence produced by the high-frequency shear-wave monopole source (CHTS and CHRS) as well as coherence from the low-frequency shear-wave dipole source (CHR2) in Track 4. The numbers on the right side of the figure are the logging units that correspond to the lithostratigraphic units identified in the Hole 735B cores.

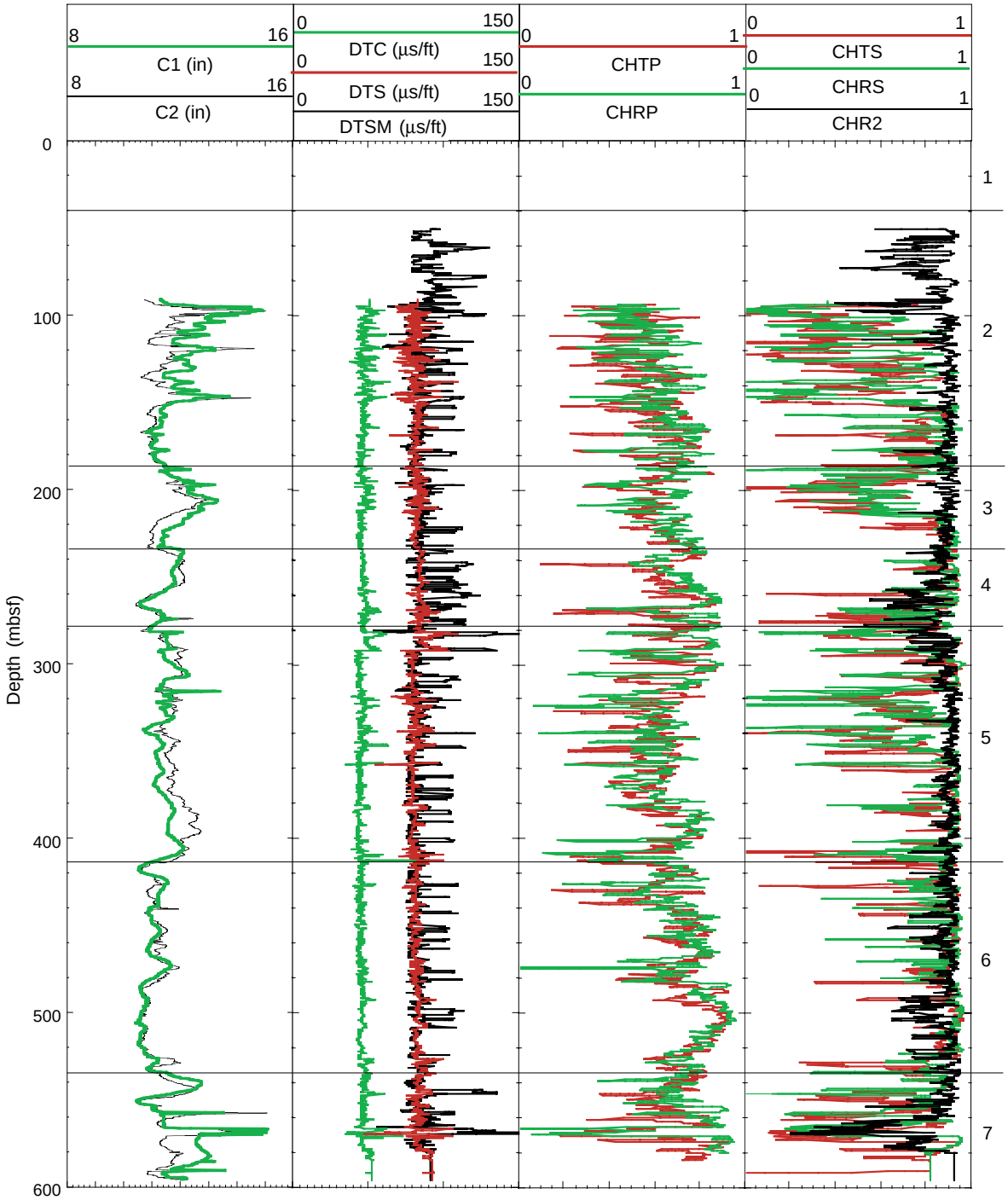

Figure F132. Illustration showing the difference in image quality between the raw and processed FMS data. The raw data was being monitored for quality control and tool performance during the logging run.

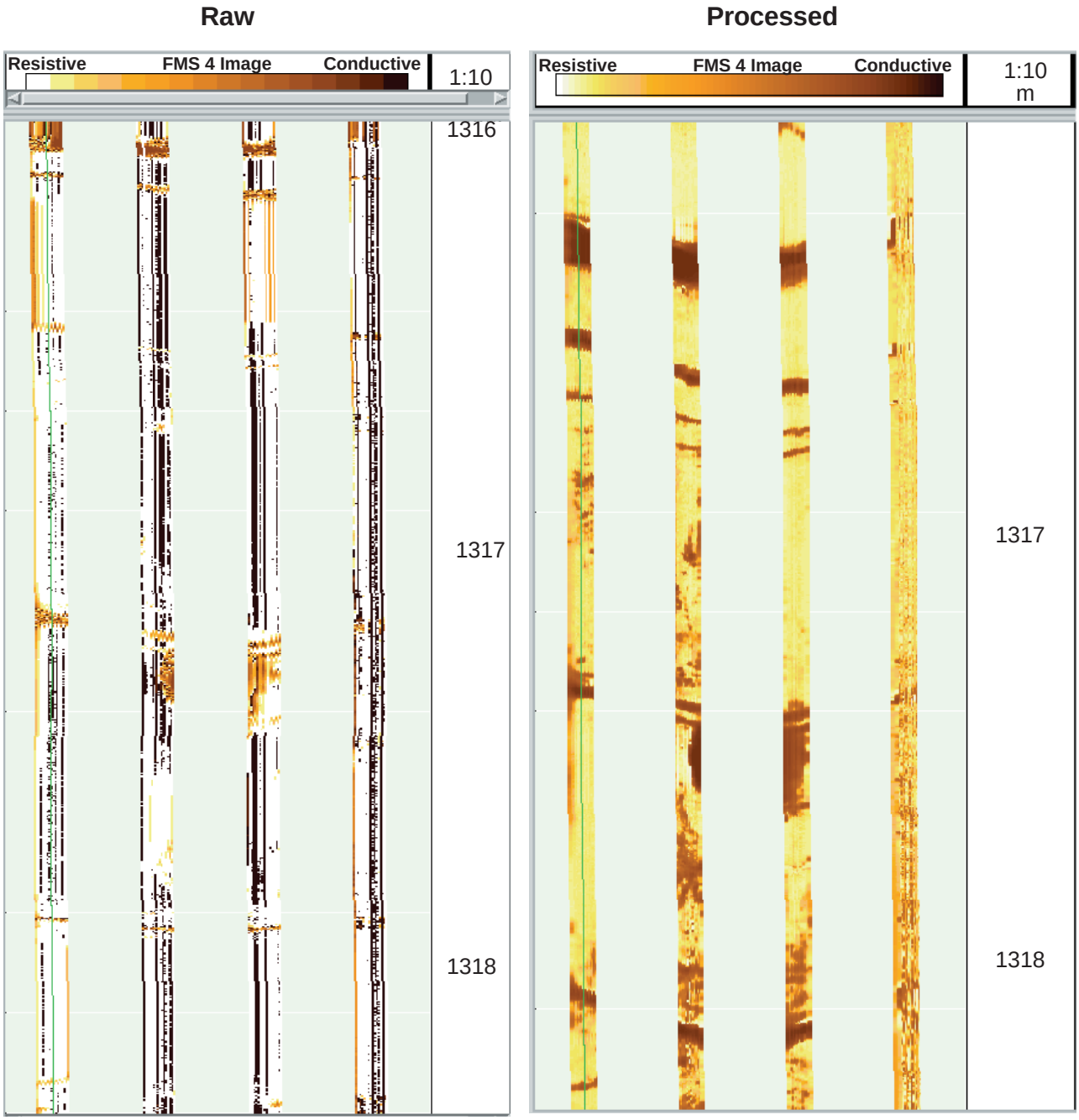

Figure F133. A. FMS image showing a 25-m interval that includes the transition from the oxide gabbros of Unit IV, through the breccia zone and into the olivine gabbros of Unit V. This figure also includes a depth scale in mbsf; caliper data from the FMS; dynamic and static processed FMS images; borehole drift and structural dips and azimuth; and deep and shallow resistivity logs from the DLL. (Continued on next page.)

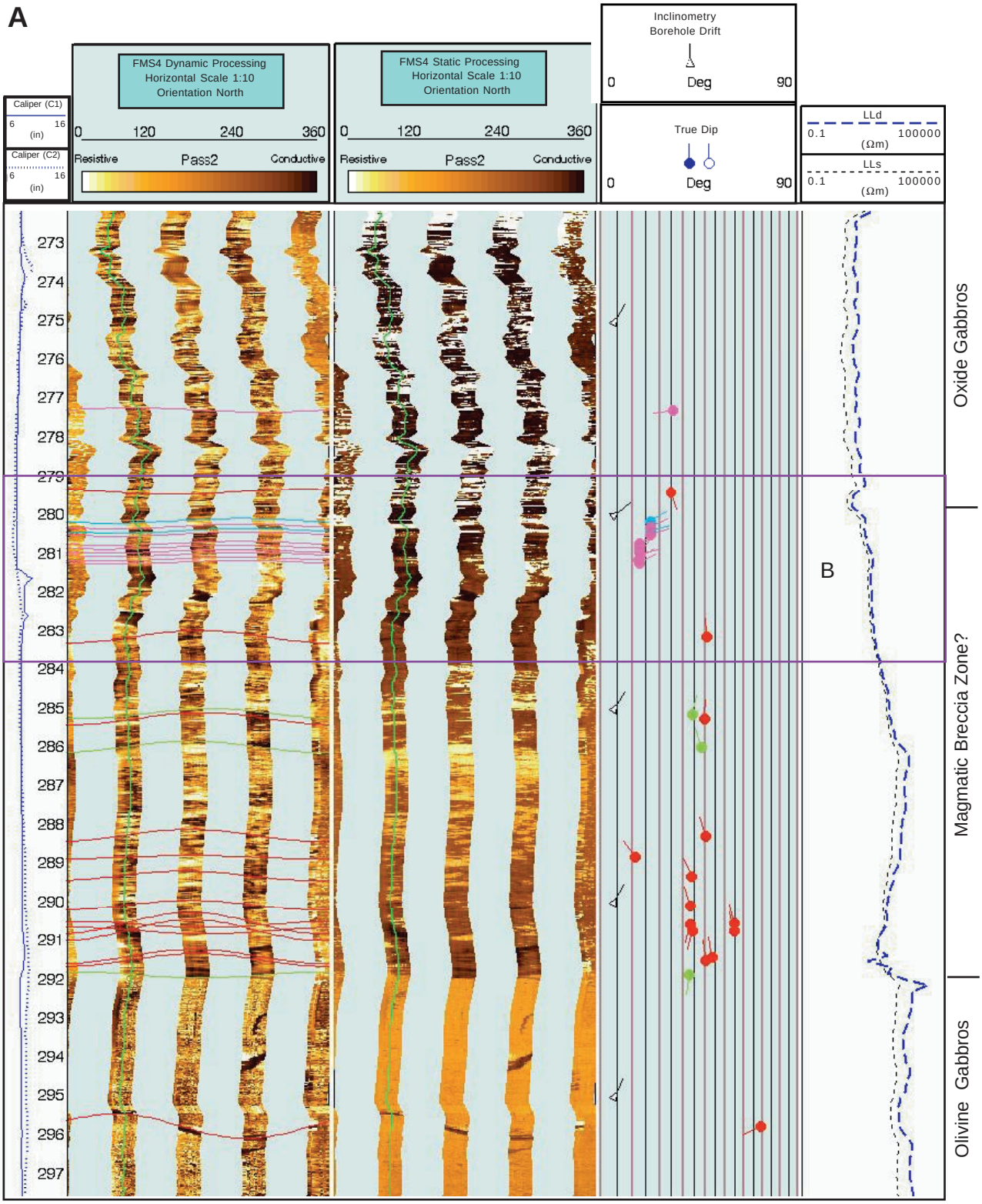

Figure F133 (continued). B. FMS image showing an expanded 4-m interval of the transition between the oxide gabbros and the breccia zone.

B

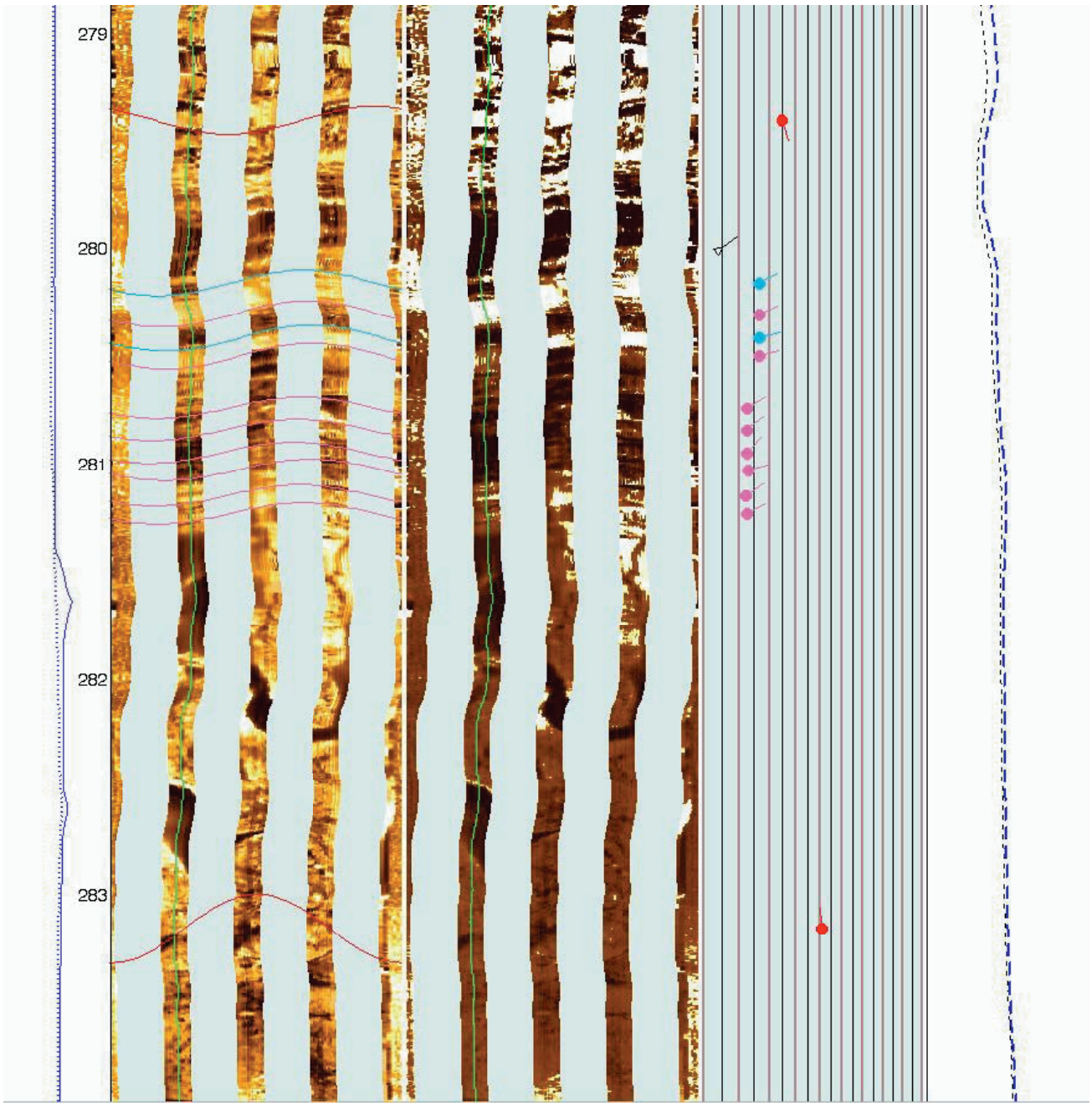

Figure F134. FMS image showing a 25-m interval that includes several structural features which correlate with high core fault intensity measurements. This figure also includes a depth scale in mbsf; caliper data from the FMS; dynamic and static processed FMS images; borehole drift and structural dips and azimuth; and deep and shallow resistivity logs from the DLL.

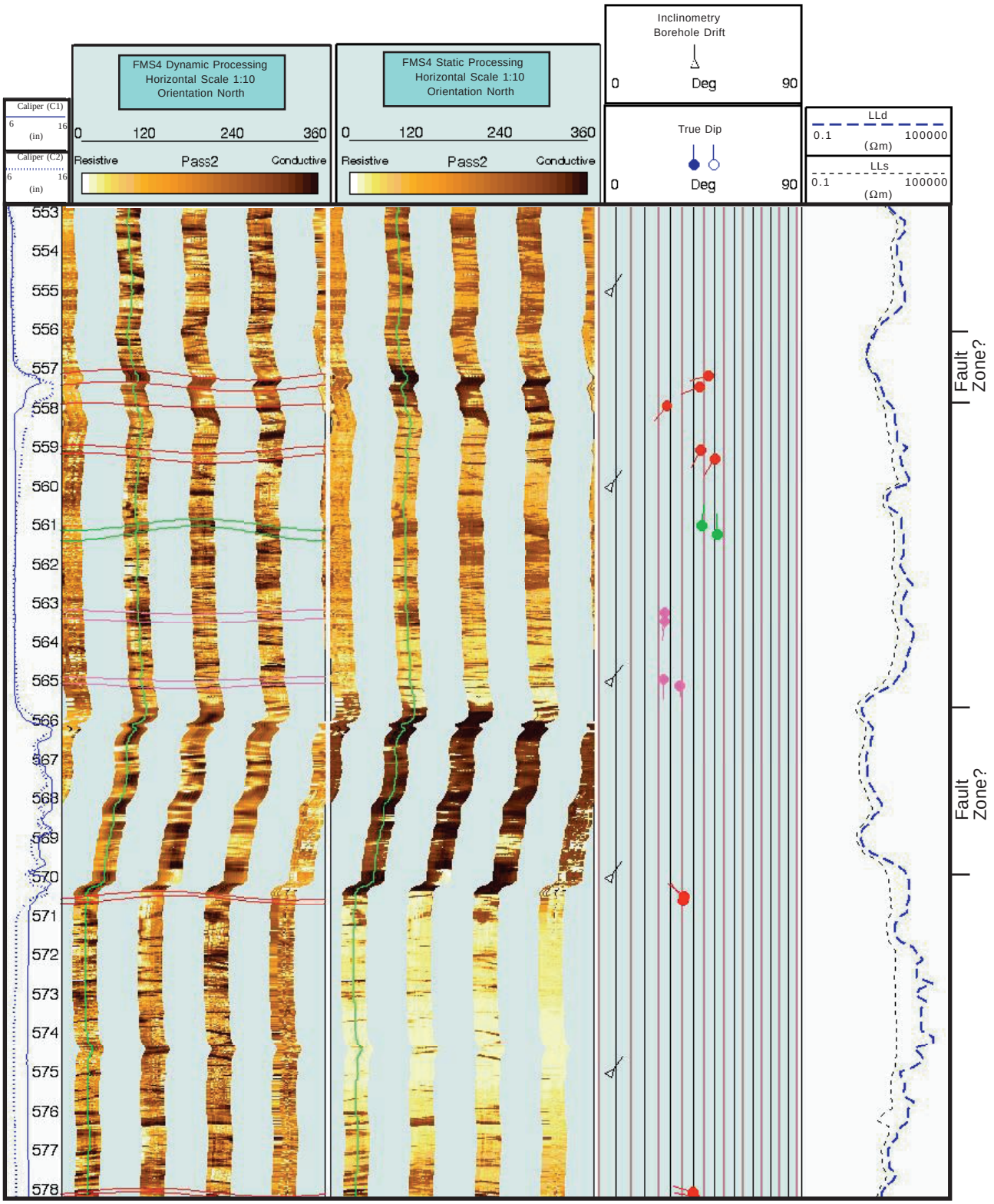

Figure F135. A. FMS image showing the bottommost 25-m logged interval that includes structural features and lithological boundaries. This figure also includes a depth scale in mbsf; caliper data from the FMS; dynamic and static processed FMS images; borehole drift and structural dips and azimuth; and deep and shallow resistivity logs from the DLL. (Continued on next two pages.)

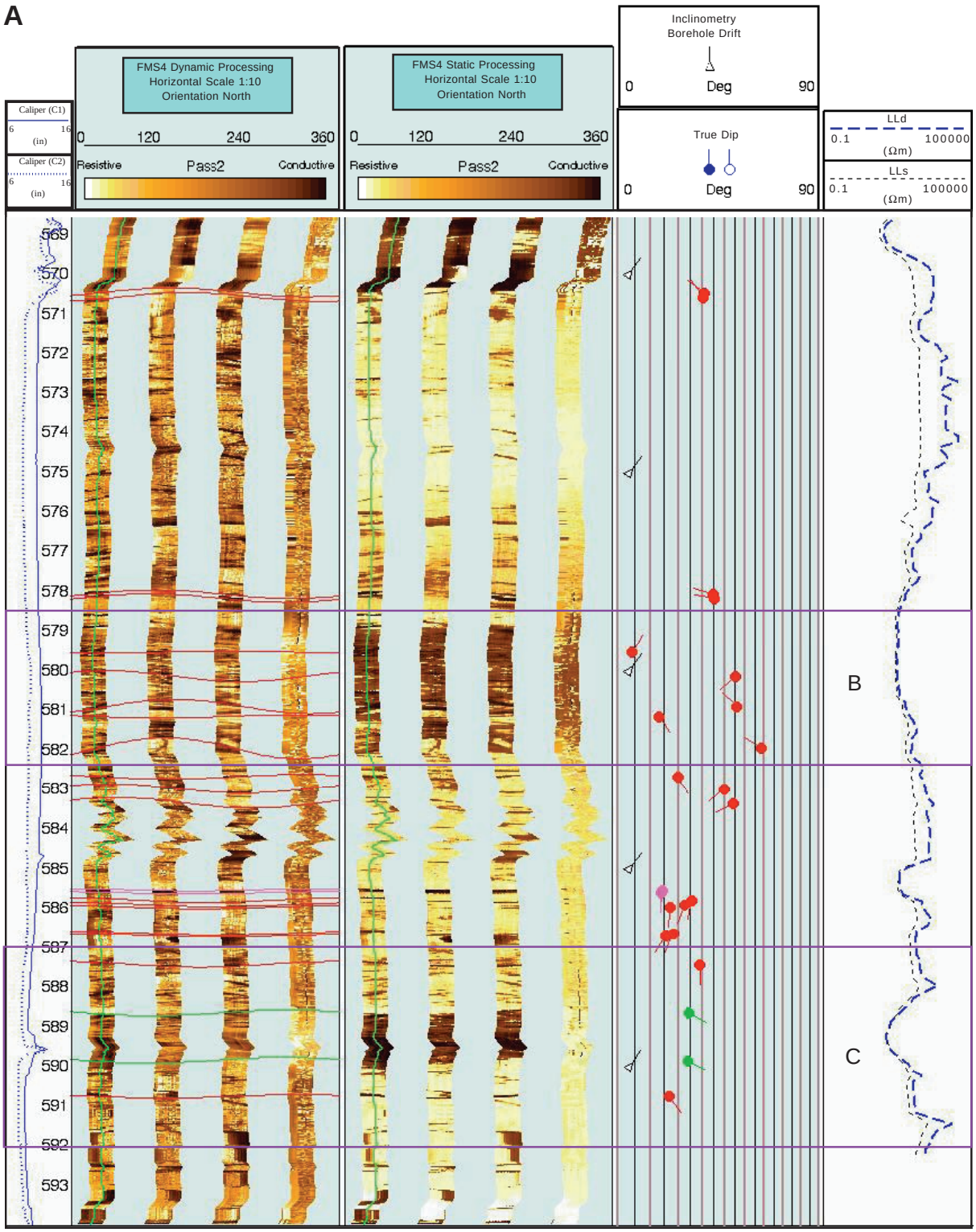

Figure F135 (continued). B. FMS image of a 4-m interval showing resistivity contrasts that seem to correlate with lithological boundaries and structural features observed in Sections 176-735B-99R-6 to 101R-2.

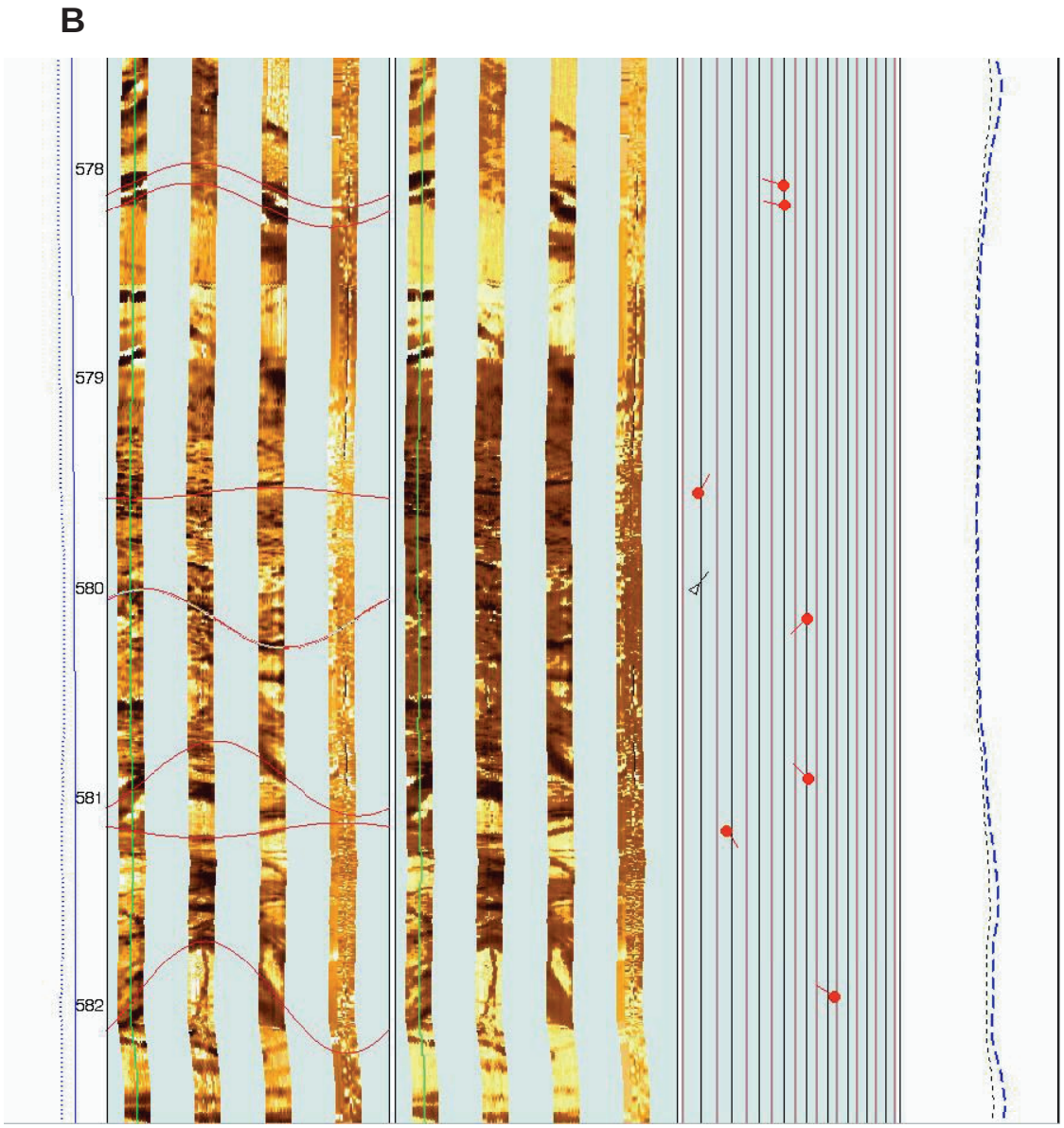

Figure F135 (continued). C. FMS image of a 4-m interval showing resistivity contrasts that seem to correlate with lithological boundaries and structural features observed in Sections 176-735B-101R-3 through 102R-1.

C

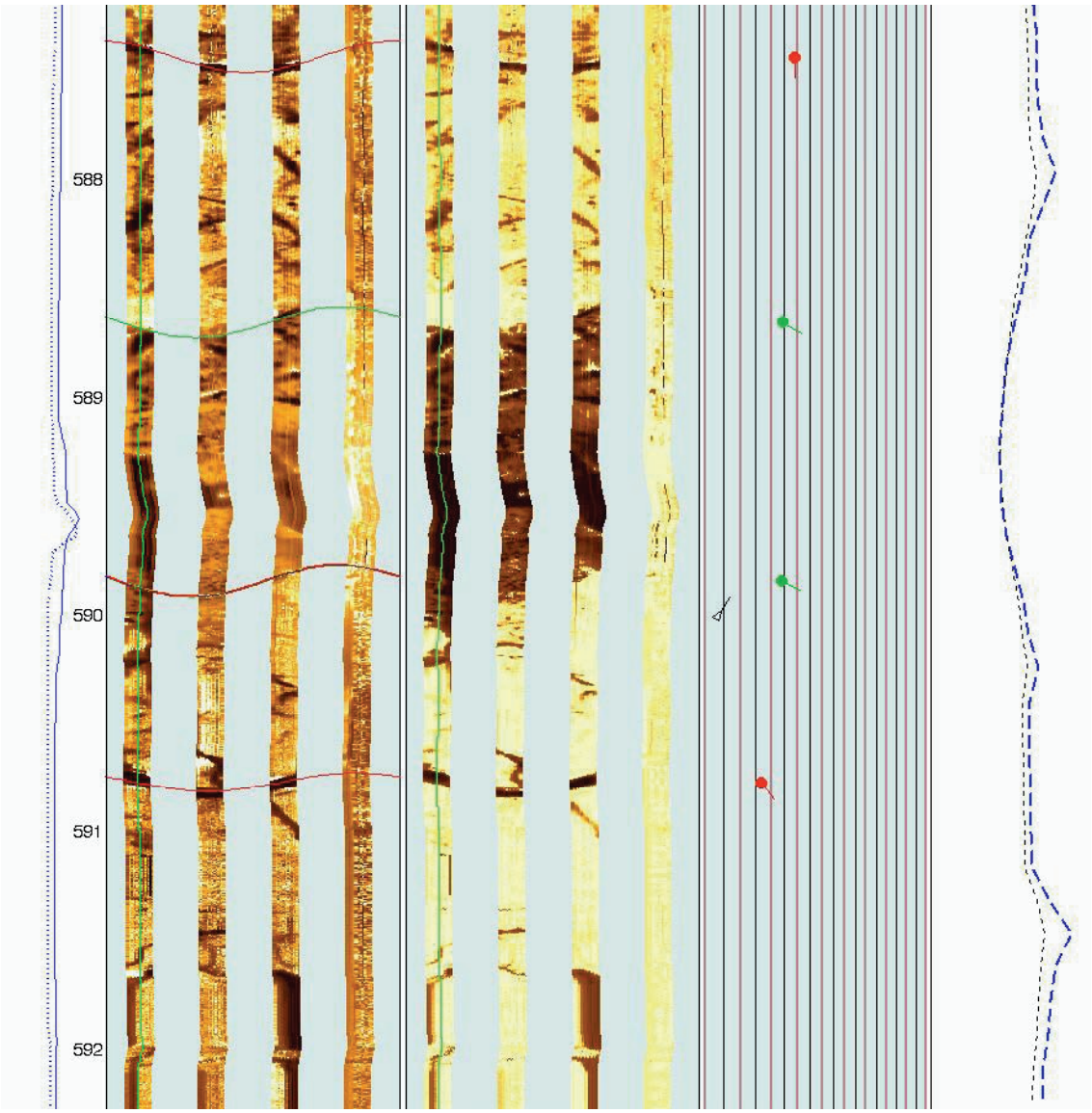

Figure F136. Unrolled images from Hole 735B. **A.** Sample 176-735B-133R-7, 83–150 cm. **B.** Sample 176-735B-135R-1, 102–128 cm. Dips of veins and foliations were determined using the DMT software CoreLog.

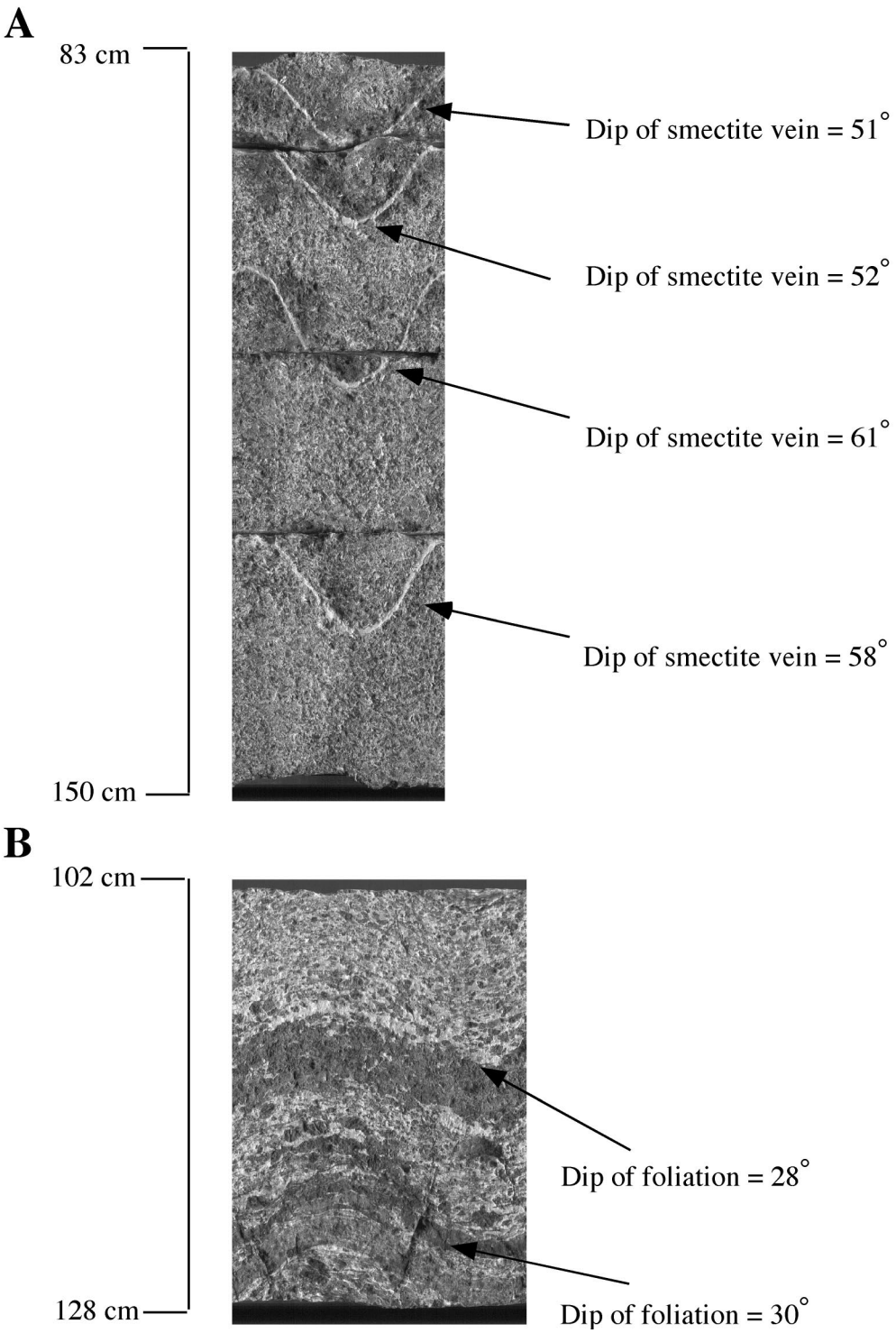

Figure F137. Reorientation of a Core 118-735B-77R piece by direct correlation with Leg 118 BHTV data and Leg 176 FMS logs. One fracture is correlated between BHTV data, core images, and FMS logs, but a second fracture observed in the FMS images is not apparent in the BHTV log or the recovered core.

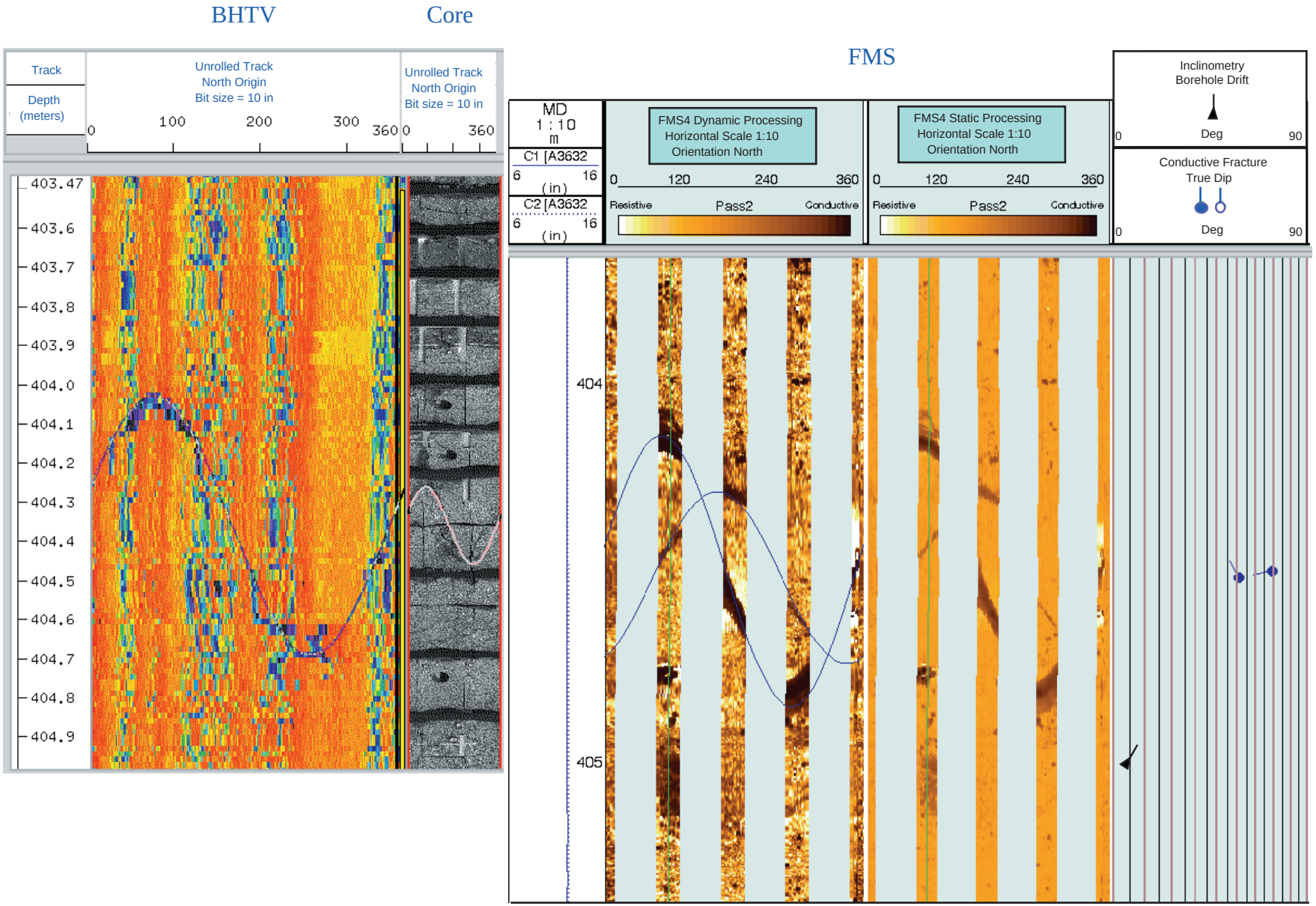

Figure F138. Relation of electrical resistivity deep (LLd) vs. density (RHOB) used for the definition of the electrofacies. **A.** Electrofacies based on the calibration between core information and Leg 118 logging data. The crossplot contains all data from 50 to 480 mbsf. **B.** Electrofacies after transfer by discriminant analysis using Leg 176 data. The crossplot contains all data from 95 to 575 mbsf. The comparison of the crossplots shows only slight differences between the logging data from the different legs and that the classification of the electrofacies is very similar.

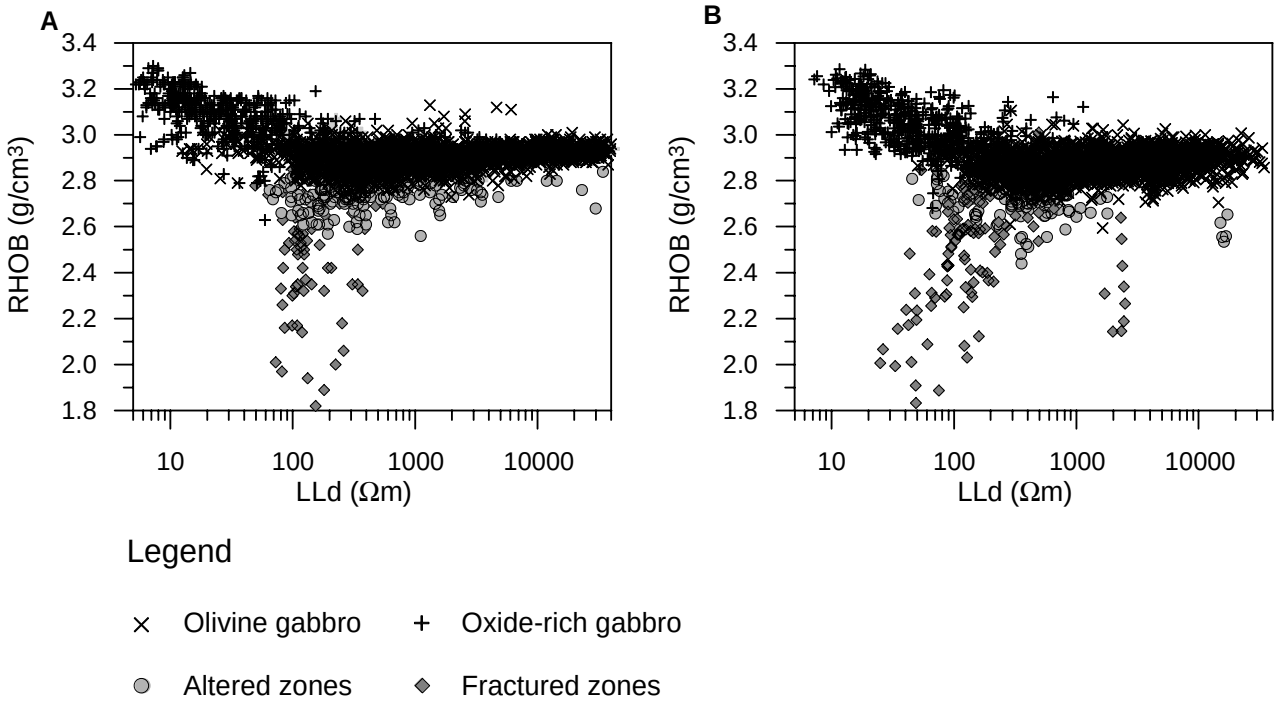

Figure F139. The EFA-Log of Hole 735B based on Leg 176 logging data. The column to the left shows the core recovery (Robinson, Von Herzen, et al., 1989; also see "Operations Narrative," p. 3). The second column contains the core lithology based on data from Dick et al. (1991a), between 10 and 500 mbsf, and from core descriptions (see the "Core Descriptions" contents list), between 500 and 600 mbsf. Layers with thicknesses <0.5 m are not displayed. In the third column, the EFA-Log is presented. The three columns on the right show some of the most important logs for distinguishing the electrofacies, electrical resistivity (deep [LLd] and shallow [LLs]), the density log RHOB, the neutron porosity log APLC, and the caliper log. Colors and patterns are chosen according to Figure F8, p. 52, in the "Leg 176 Summary" chapter and the barrel sheets (see the "Core Descriptions" contents list). All logging data have been shifted with a constant amount of 8.85 m upward to move them to core depth. The upper boundary of Unit IV served as reference depth for this shift. **(Continued on next four pages.)**

Figure F139 (continued).

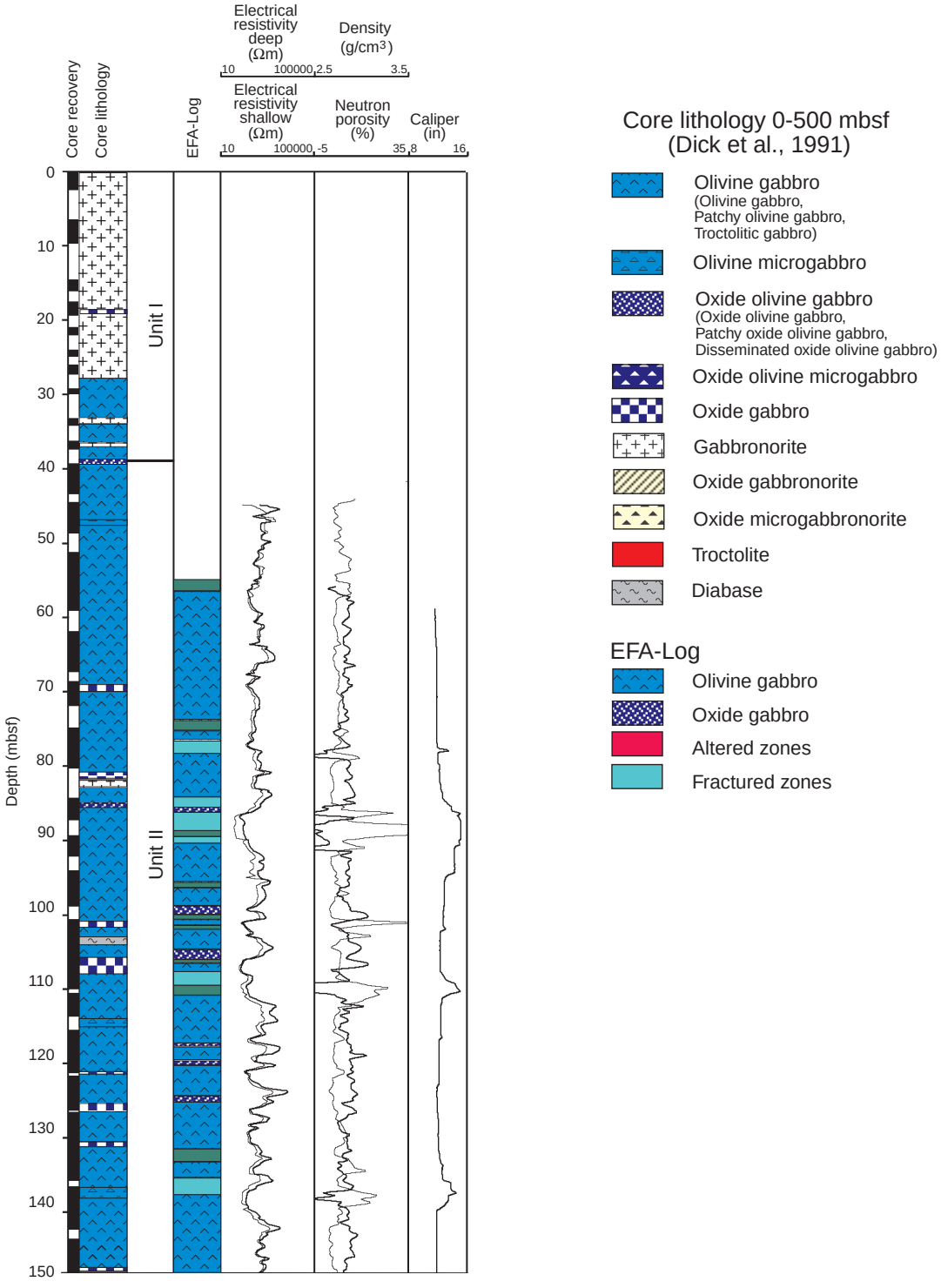

Figure F139 (continued).

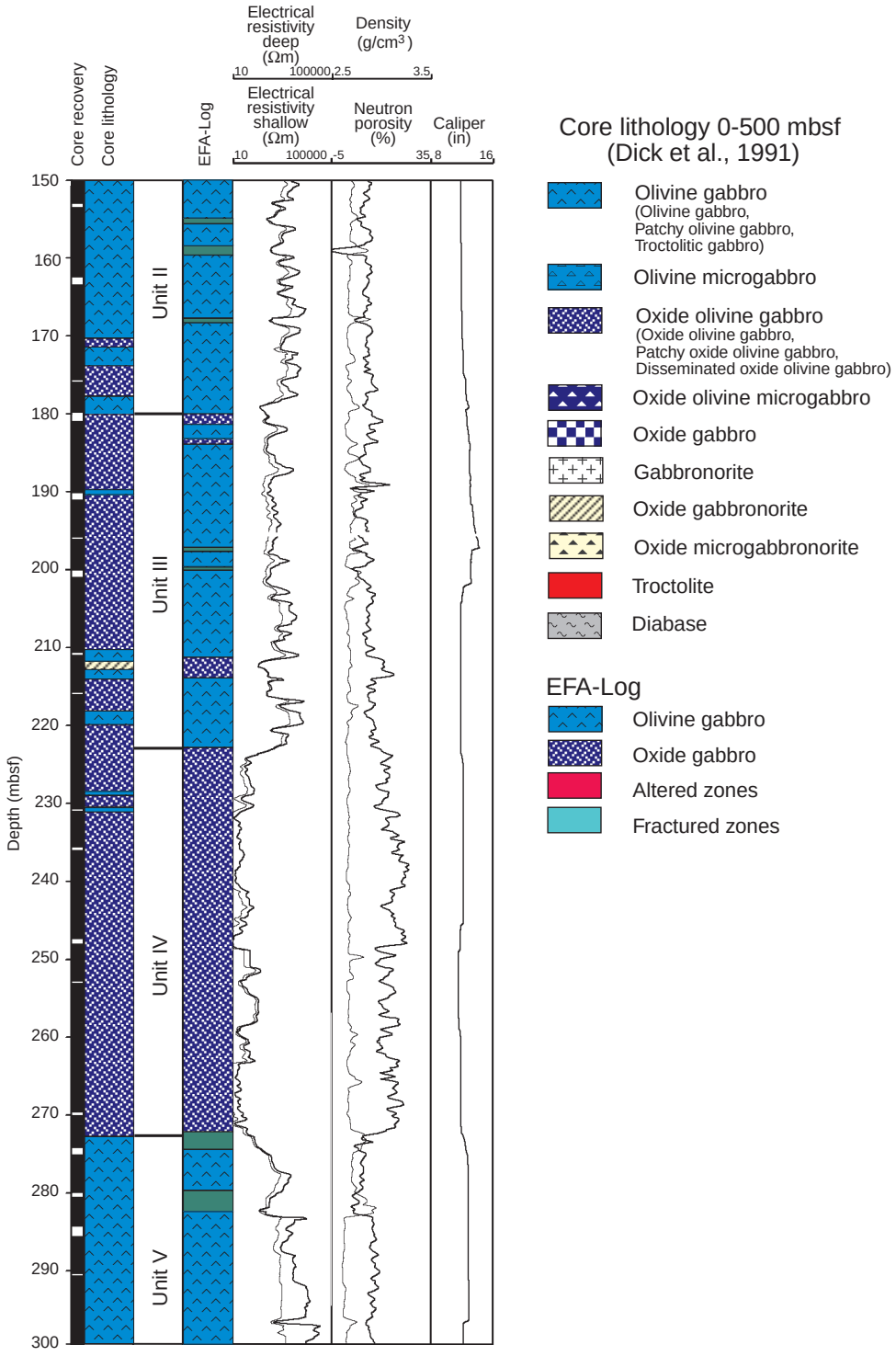

Figure F139 (continued).

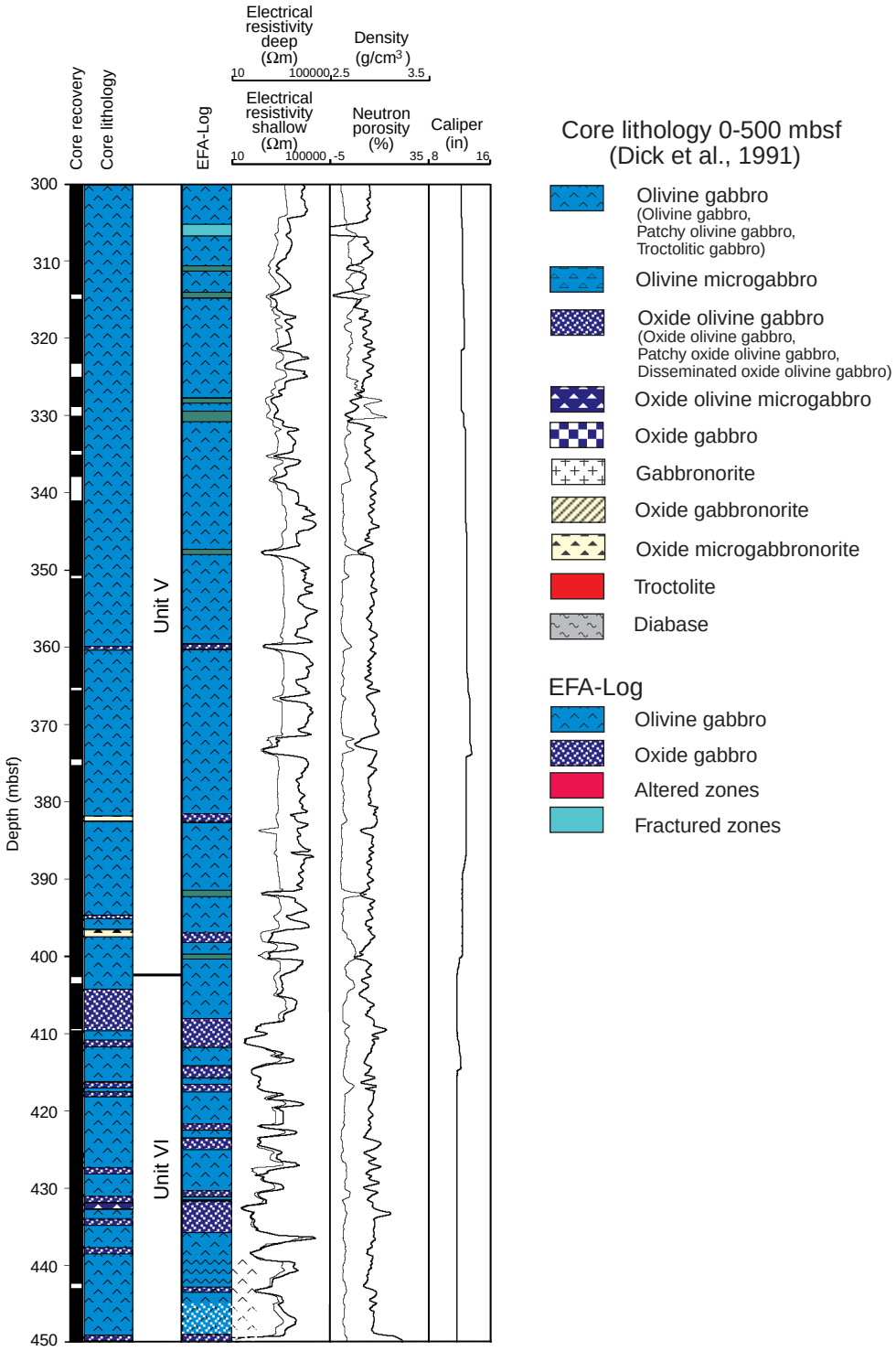

Figure F139 (continued).

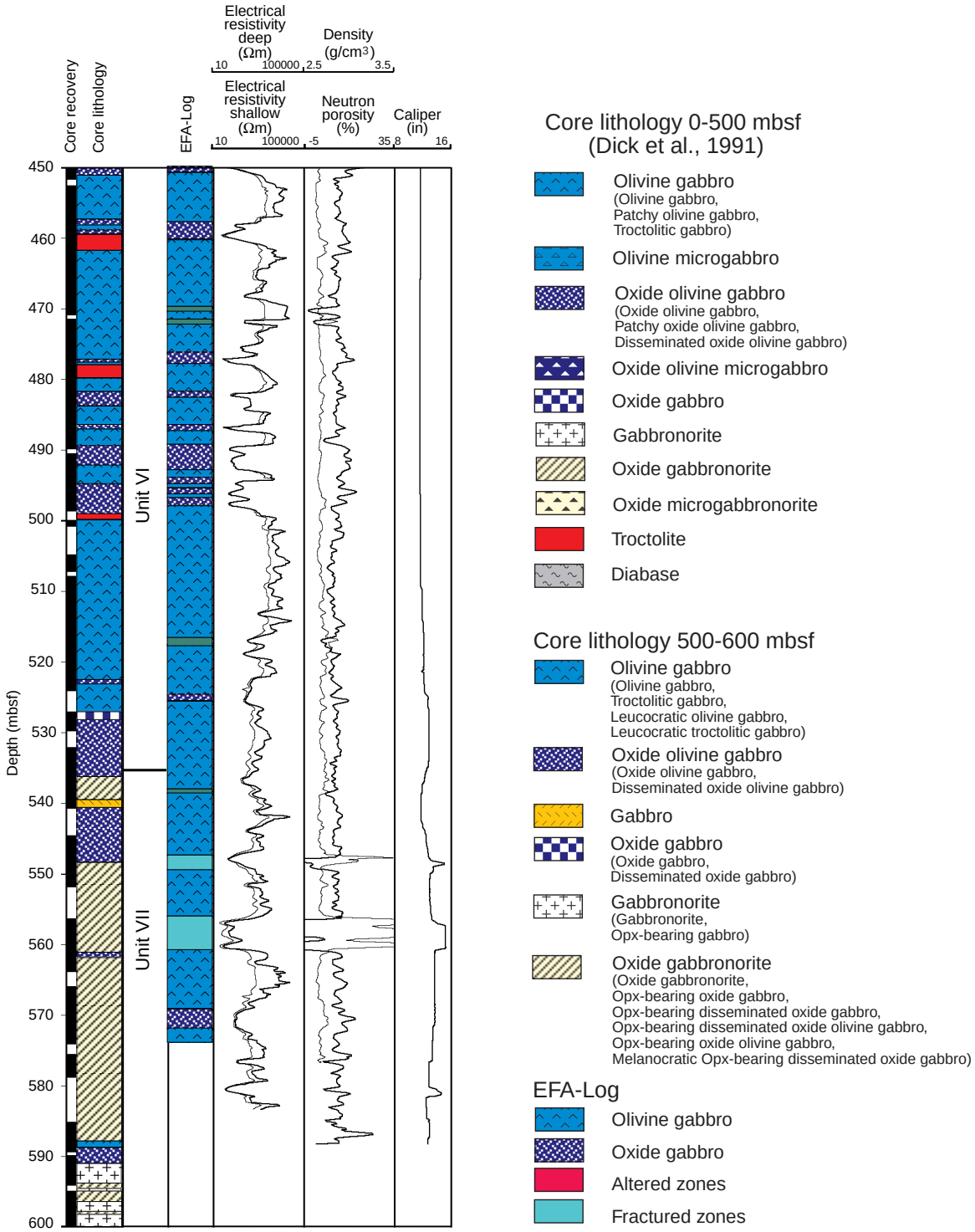

Table T1. Coring summary for Hole 735B. (Continued on next page.)

Core	Date (1997)	Time (UTC)	Depth (mbsf)	Length cored (m)	Length recovered (m)	Recovery (%)
176-735B-						
89R	Oct 26	0815	504.8-507.8	3.0	2.05	68.3
90R	Oct 26	1220	507.8-517.4	9.6	9.88	102.9
91R	Oct 26	1640	517.4-527.0	9.6	5.87	61.1
92R	Oct 26	1955	527.0-532.1	5.1	2.23	43.7
93R	Oct 26	2320	532.1-536.6	4.5	5.02	111.6
94R	Oct 27	0430	536.6-544.6	8.0	3.48	43.5
95R	Oct 27	0800	544.6-548.3	3.7	3.00	81.1
96R	Oct 27	1945	548.3-556.3	8.0	2.79	34.9
97R	Oct 28	0900	556.3-561.0	4.7	4.89	104.0
98R	Oct 28	1105	561.0-565.9	4.9	2.28	46.5
99R	Oct 28	1600	565.9-575.5	9.6	7.49	78.0
100R	Oct 28	2010	575.5-585.1	9.6	3.00	31.3
101R	Oct 28	2330	585.1-589.9	4.8	3.86	80.4
102R	Oct 29	0200	589.9-594.8	4.9	3.53	72.0
103R	Oct 29	0525	594.8-604.3	9.5	5.81	61.2
104R	Oct 29	0740	604.3-608.8	4.5	2.53	56.2
105R	Oct 29	1125	608.8-613.9	5.1	4.70	92.2
106R	Oct 29	1440	613.9-619.5	5.6	4.91	87.7
107R	Oct 29	1645	619.5-623.5	4.0	3.01	75.3
108R	Oct 29	2000	623.5-628.7	5.2	5.05	97.1
109R	Oct 29	2250	628.7-633.1	4.4	4.55	103.4
110R	Oct 30	0140	633.1-638.0	4.9	5.18	105.7
111R	Oct 30	0415	638.0-642.7	4.7	3.26	69.4
112R	Oct 30	2035	642.7-647.7	5.0	4.48	89.6
113R	Oct 30	2350	647.7-652.4	4.7	2.76	58.7
114R	Oct 31	0515	652.4-662.0	9.6	7.92	82.5
115R	Oct 31	1020	662.0-671.6	9.6	9.42	98.1
116R	Oct 31	1450	671.6-681.2	9.6	7.96	82.9
117R	Oct 31	2020	681.2-690.8	9.6	7.13	74.3
118R	Nov 1	0130	690.8-700.4	9.6	9.50	99.0
119R	Nov 1	0440	700.4-710.0	9.6	5.88	61.3
120R	Nov 1	0850	710.0-719.7	9.7	9.27	95.6
121R	Nov 1	1350	719.7-729.4	9.7	10.04	103.5
122R	Nov 1	1750	729.4-739.0	9.6	9.28	96.7
123R	Nov 1	2135	739.0-748.7	9.7	9.46	97.5
124R	Nov 1	2340	748.7-752.1	3.4	3.33	97.9
125R	Nov 2	1440	752.1-755.3	3.2	0.57	17.8
126R	Nov 2	1805	755.3-764.9	9.6	7.90	82.3
127R	Nov 2	2110	764.9-774.5	9.6	6.38	66.5
128R	Nov 3	0045	774.5-784.2	9.7	6.16	63.5
129R	Nov 3	0510	784.2-793.9	9.7	3.90	40.2
130R	Nov 3	0935	793.9-803.5	9.6	4.30	44.8
131R	Nov 3	1220	803.5-813.2	9.7	4.83	49.8
132R	Nov 3	1630	813.2-822.9	9.7	9.46	97.5
133R	Nov 3	2035	822.9-832.6	9.7	9.34	96.3
134R	Nov 4	0100	832.6-842.2	9.6	9.60	100.0
135R	Nov 4	0400	842.2-846.9	4.7	4.57	97.2
136R	Nov 4	0625	846.9-851.8	4.9	4.69	95.7
137R	Nov 4	1055	851.8-861.4	9.6	9.10	94.8
138R	Nov 4	1535	861.4-871.1	9.7	8.78	90.5
139R	Nov 4	1940	871.1-880.3	9.2	8.79	95.5
140R	Nov 4	2345	880.3-889.3	9.0	7.78	86.4
141R	Nov 6	1745	889.3-892.9	3.6	2.54	70.6
142R	Nov 6	2240	892.9-902.6	9.7	8.97	92.5
143R	Nov 7	0305	902.6-912.3	9.7	8.86	91.3
144R	Nov 7	0745	912.3-921.9	9.6	8.81	91.8
145R	Nov 7	1200	921.9-931.5	9.6	8.10	84.4
146R	Nov 7	1700	931.5-941.2	9.7	8.48	87.4
147R	Nov 7	2240	941.2-950.9	9.7	9.08	93.6
148R	Nov 8	0500	950.9-960.5	9.6	9.18	95.6
149R	Nov 8	1130	960.5-970.1	9.6	9.90	103.1
150R	Nov 8	1720	970.1-979.8	9.7	9.56	98.6
151R	Nov 8	2240	979.8-987.5	7.7	7.80	101.3
152R	Nov 9	1415	987.5-995.7	8.2	7.96	97.1
153R	Nov 9	1935	995.7-1005.3	9.6	8.65	90.1
154R	Nov 10	0100	1005.3-1015.0	9.7	8.34	86.0
155R	Nov 10	0645	1015.0-1024.7	9.7	9.34	96.3

Table T1 (continued).

Core	Date (1997)	Time (UTC)	Depth (mbsf)	Length cored (m)	Length recovered (m)	Recovery (%)
156R	Nov 10	1150	1024.7-1034.3	9.6	9.86	102.7
157R	Nov 10	1600	1034.3-1044.0	9.7	8.33	85.9
158R	Nov 10	2015	1044.0-1053.7	9.7	9.54	98.4
159R	Nov 11	0000	1053.7-1063.4	9.7	8.83	91.0
160R	Nov 11	0430	1063.4-1073.0	9.6	9.33	97.2
161R	Nov 11	0840	1073.0-1082.6	9.6	9.77	101.8
162R	Nov 11	1250	1082.6-1092.2	9.6	9.59	99.9
163R	Nov 11	1655	1092.2-1099.4	7.2	6.81	94.6
164R	Nov 12	0750	1099.4-1105.3	5.9	4.61	78.1
165R	Nov 12	1150	1105.3-1110.9	5.6	7.00	125.0
166R	Nov 12	1600	1110.9-1120.5	9.6	8.65	90.1
167R	Nov 12	2055	1120.5-1130.1	9.6	9.05	94.3
168R	Nov 13	0100	1130.1-1139.7	9.6	9.21	95.9
169R	Nov 13	0605	1139.7-1149.3	9.6	8.39	87.4
170R	Nov 13	0950	1149.3-1159.0	9.7	9.86	101.6
171R	Nov 13	1435	1159.0-1168.7	9.7	9.66	99.6
172R	Nov 13	1820	1168.7-1178.4	9.7	9.14	94.2
173R	Nov 13	2115	1178.4-1188.1	9.7	8.54	88.0
174R	Nov 13	2315	1188.1-1191.1	3.0	2.70	90.0
175R	Nov 14	1240	1191.1-1196.7	5.6	5.52	98.6
176R	Nov 14	1500	1196.7-1201.7	5.0	4.00	80.0
177R	Nov 14	1805	1201.7-1211.3	9.6	9.23	96.1
178R	Nov 14	2130	1211.3-1220.9	9.6	9.48	98.8
179R	Nov 15	0055	1220.9-1230.5	9.6	9.92	103.3
180R	Nov 15	0415	1230.5-1240.2	9.7	7.74	79.8
181R	Nov 15	0640	1240.2-1249.9	9.7	4.89	50.4
182R	Nov 15	0925	1249.9-1259.6	9.7	4.44	45.8
183R	Nov 15	1250	1259.6-1269.2	9.6	7.34	76.5
184R	Nov 15	1635	1269.2-1278.8	9.6	7.67	79.9
185R	Nov 15	2030	1278.8-1288.4	9.6	8.61	89.7
186R	Nov 15	2350	1288.4-1297.2	8.8	8.09	91.9
187R	Nov 16	0500	1297.2-1306.9	9.7	7.25	74.7
188R	Nov 16	0905	1306.9-1316.5	9.6	9.05	94.3
189R	Nov 16	1415	1316.5-1326.1	9.6	9.22	96.0
190R	Nov 16	1915	1326.1-1335.7	9.6	8.22	85.6
191R	Nov 17	0025	1335.7-1345.3	9.6	9.22	96.0
192R	Nov 17	0520	1345.3-1355.0	9.7	9.52	98.1
193R	Nov 17	0840	1355.0-1360.6	5.6	1.39	24.8
194R	Nov 18	0250	1360.6-1364.1	3.5	3.48	99.4
195R	Nov 18	0710	1364.1-1373.7	9.6	9.13	95.1
196R	Nov 18	1115	1373.7-1383.3	9.6	8.39	87.4
197R	Nov 18	1420	1383.3-1386.4	3.1	4.44	143.2
198R	Nov 20	0400	1386.4-1392.4	6.0	5.47	91.2
199R	Nov 20	0630	1392.4-1402.0	9.6	8.50	88.5
200R	Nov 20	0925	1402.0-1411.6	9.6	8.98	93.5
201R	Nov 20	1245	1411.6-1421.2	9.6	9.00	93.8
202R	Nov 20	1630	1421.2-1430.8	9.6	9.75	101.6
203R	Nov 20	2000	1430.8-1440.5	9.7	8.50	87.6
204R	Nov 20	2340	1440.5-1450.2	9.7	8.99	92.7
205R	Nov 21	0325	1450.2-1459.9	9.7	10.32	106.4
206R	Nov 21	0705	1459.9-1469.5	9.6	8.07	84.1
207R	Nov 21	1015	1469.5-1479.1	9.6	8.51	88.6
208R	Nov 21	1450	1479.1-1488.7	9.6	9.57	99.7
209R	Nov 21	1900	1488.7-1498.3	9.6	9.77	101.8
210R	Nov 21	2305	1498.3-1508.0	9.7	8.93	92.1
			Coring totals:	1003.2	865.99	86.3
			Drilled:	504.8		
			Total:	1508.0		

Note: UTC = Universal Time Coordinated. Cores 1R through 88R were drilled during Leg 118.

Table T2. Operations parameters for Hole 735B. (Continued on next page.)

Location			Time			
Latitude	Longitude	Territorial jurisdiction	Start hole	Spud hole	End hole	Total
			1345	N/A	1900	917.3 hr
32°43.3928′S	57°15.9606′E	International	24 Oct 97	N/A	1 Dec 97	38.2 days

Drill pipe depths			
Water depth (mbsl)	Seafloor depth (mbrf)	Penetration depth (mbsf)	Total depth (mbrf)
720.6	731.0	1508.0/606.01	2239.0/1337.01

Bit data

	Bit size	Make	Model no.	Jets	Serial no.	Cumulative time (hr)	Cumulative depth (m)
Core Bit 1	9⅞	RBI	C-7	4x16	BM109	25.9	51.5
Core Bit 2	9⅞	RBI	C-7	4x16	BM111	36.0	86.4
Core Bit 3	9⅞	RBI	C-7	4x16	BM114	43.8	109.4
Core Bit 4	9⅞	RBI	C-7	4x16	BM113	46.8	137.2
Core Bit 5	9⅞	RBI	C-7	4x16	BM115	47.3	98.2
Core Bit 6	9⅞	RBI	C-7	4x16	BM110	45.9	111.9
Core Bit 7	9⅞	RBI	C-7	4x16	BM108	33.3	91.7
Core Bit 8	9⅞	RBI	C-7	4x16	BM107	53.8	169.5
Core Bit 9	9⅞	RBI	C-7	4x16	BM106	8.8	25.8
Core Bit 10	9⅞	RBI	C-7	4x16	BM112	33.9	121.6

Beacon data

		Model	Serial no.	Frequency	Power	Deployed	Recovered	Total time (hr)
Primary #1	Datasonics	354M	2025	16.0 kHz	208 dB	1825/24 Oct 97	1730/1 Dec 97	911.3
Backup #2	Datasonics	354M	2040	14.0 kHz	205 dB	1345/24 Oct 97	1645/1 Dec 97	915.0

Bottom-hole assembly (BHA)

Coring: bit, bit sub, outer core barrel, top sub, head sub, 10 each 8¼-in drill collars, tapered drill collar, two stands of 5½-in drill pipe, cross-over
Fishing: overshot with bit sub as required, 10-ft 8¼-in drill collar pup, 2-8 each 8¼-in drill collars, tapered drill collar, two stands of 5½-in drill pipe, cross-over
Logging: reentry clean out bit, two each 8¼-in drill collars, landing/saver sub with modified landing ring for VSP, tapered drill collar, two stands of 5½ in drill pipe, cross-over
(Note: A total of three sets of drilling jars were used [placed in BHA with two collars above] until the units developed cracks and were taken out of service.)

Downhole tools/measurements (Orientation, temperature, water sampler, etc.)

Phase I of logging was conducted to 492 mbsf prior to coring. The BHA was placed at 49 mbsf and three tool strings were deployed: (1) natural gamma (NGS), accelerator porosity (APS), hostile environment lithodensity (HLDS), dual laterolog (DLL) and temperature tool; (2) NGS, dipole shear sonic imager (DSI) and Formation MicroScanner (FMS). This run was aborted due to data acquisition difficulties; (3) NGT, general purpose inclinometry tool (GPIT), and DLL. After drill pipe failure, Phase II logging went to 595 mbsf. This consisted of four tool string deployments with the following tools: (1) HLDT, caliper, APS, and HNGS; (2) NGT, DSI, GPIT, and FMS (same problem as before with FMS data); (3) NGT, GPIT, and DLL; (4) Schlumberger VSP-ASI.

Drilling/coring statistics

Coring system	Bit number	Number of cores	Depth cored (m)	Core recovered (m)	Core recovery (%)	Core drilled (m)	Total (m)	Average (Range of ROP)
RCB	1	8	51.5	34.32	66.6%	0.0	51.5	2.0 (1.3-2.9)
RCB	2	15	86.4	64.05	74.1%	0.0	86.4	2.4 (1.3-4.9)
RCB	3	13	109.4	96.43	88.1%	0.0	109.4	2.5 (2.1-4.3)
RCB	4	16	137.2	106.15	77.4%	0.0	137.2	2.9 (1.9-4.9)
RCB	5	11	98.2	91.28	93.0%	0.0	98.2	2.1 (1.6-2.6)
RCB	6	12	111.9	106.35	95.0%	0.0	111.9	2.4 (1.9-3.2)
RCB	7	11	91.7	86.81	94.7%	0.0	91.7	2.8 (1.8-4.3)
RCB	8	19	169.5	140.80	83.1%	0.0	169.5	3.1 (2.1-6.1)
RCB	9	4	25.8	25.44	98.6%	0.0	25.8	2.9 (2.0-3.2)
RCB	10	13	121.6	114.36	94.0%	0.0	121.6	3.6 (2.9-5.2)

Formation data

Cored interval (mbsf)	Nature	Description	Comments
0-500.7	Cored during Leg 118	Gabbro/olivine gabbro	Lower 0.7 m cored with 3.75 NCB.
504.8-1508.0	Cored during Leg 176	Gabbro/olivine gabbro	Leg 176 tagged 4.8 m deeper than Leg 118.

Table T2 (continued).

Mud/cement usage
Bentonite gel mud weeps were pumped in volumes of 20-30 bbl every other core or after every core if rapid ROP or other hole conditions warranted.
Weather/seas
Weather and sea state were variable throughout the leg. Large, long period swells from the south were prevalent most of the leg, creating large vessel heave (2-3 m). Swells were often from two different directions and when coupled with the moderate wind (20-30 kt) and erratic current (1-2 kt from a northerly or southerly direction) they created some difficulty for the DP operators in minimizing roll/pitch. Gale force 8/9 winds and seas were experienced at times during the leg. Because of the shallow water there were several yellow and red positioning alerts.

Note: The two tricone drill bits and two reentry cleanout bits for logging were excluded from this list because there was no applicable wear, hours, or footage. Pin failure resulted in a total of 26 stands, 5-in drill pipe, and 172 m of BHA left in hole.

Table T3. Abundance, mode, and chemical composition of the major rock types of Leg 176. (Continued on next 3 pages.)

Rock type	Fraction of core	Number of intervals	Details			
Troctolitic gabbro and troctolite	1.9 vol%	19 of troctolitic gabbro 4 of troctolite	Mode			
			%	Plagioclase	Clinopyroxene	Olivine
			Average	64	10	26
			Maximum	80	15	40
			Minimum	45	0	12
			Grain size			
			mm	Plagioclase	Clinopyroxene	Olivine
			Avg max/1 SD	8/8	9/9	7/8
			Avg min/1 SD	2/2	2/2	1/1
			Chemical composition (10 analyses)			
			Wt%	SiO_2	TiO_2	Al_2O_3
			Average	49.58	0.24	18.13
			Standard deviation	2.79	0.12	2.23
			Maximum	52.65	0.42	22.05
			Minimum	43.82	0.09	13.37
Olivine gabbro	69.9 vol%	255	Mode			
			%	Plagioclase	Clinopyroxene	Olivine
			Average	59	30	10
			Maximum	75	60	35
			Minimum	35	15	4
			Grain size			
			mm	Plagioclase	Clinopyroxene	Olivine
			Avg max/1 SD	8/8	9/9	7/8
			Avg min/1 SD	2/2	2/2	1/1
			Chemical composition (62 analyses)			
			Wt%	SiO_2	TiO_2	Al_2O_3
			Average	51.94	0.44	16.40
			Standard deviation	0.98	0.17	1.90
			Maximum	54.46	1.17	21.23
			Minimum	49.52	0.15	5.91
Gabbro	14.9 vol%	71	Mode			
			%	Plagioclase	Clinopyroxene	Olivine
			Average	61	34	3
			Maximum	85	50	5
			Minimum	48	10	0
			Grain size			
			mm	Plagioclase	Clinopyroxene	Olivine
			Avg max/1 SD	16/11	24/19	4/3
			Avg min/1 SD	4/3	3/2	1/0
			Chemical composition (11 analyses)			
			Wt%	SiO_2	TiO_2	Al_2O_3
			Average	52.43	0.43	17.12
			Standard deviation	0.63	0.07	1.09
			Maximum	53.56	0.56	19.30
			Minimum	51.43	0.35	14.96
Gabbronorite and ortho-pyroxene-bearing gabbro	5.6 vol%	12	Mode			
			%	Plagioclase	Clinopyroxene	Olivine
			Average	56	34	2
			Maximum	65	45	6
			Minimum	40	30	1
			Grain size			
			mm	Plagioclase	Clinopyroxene	Olivine
			Avg max/1 SD	23/7	23/13	3/3
			Avg min/1 SD	6/2	2/1	1/0
			Chemical composition (two analyses)			
			Wt%	SiO_2	TiO_2	Al_2O_3
			Average	50.89	1.11	14.97
			Standard deviation	1.22	0.62	0.78
			Maximum	52.11	1.73	15.75
			Minimum	49.67	0.5	14.19

Table T3 (continued).

Troctolitic gabbro and troctolite

Mode

%	Orthopyroxene	Oxide
Average	0	0.4
Maximum	0	0.5
Minimum	0	0.1

Chemical composition (10 analyses)

Wt%	Fe_2O_3tot	MnO	MgO	CaO	Na_2O	K_2O	P_2O_5	Sum	LOI	Mg#	Ca#
Average	6.69	0.11	12.39	11.73	2.38	0.06	0.01	101.32	1.24	79.44	73.55
Standard deviation	1.19	0.02	4.30	1.65	0.61	0.06	0.01	1.37	1.68	4.43	3.80
Maximum	9.41	0.14	24.03	13.83	3.15	0.20	0.03	103.62	5.94	85.21	80.25
Minimum	5.35	0.09	8.42	7.94	1.08	0.01	0.00	99.45	0.01	72.06	68.11

Olivine gabbro

Mode

%	Orthopyroxene	Oxide
Average		0.5
Maximum		2
Minimum		0.5

Chemical composition (62 analyses)

Wt%	Fe_2O_3tot	MnO	MgO	CaO	Na_2O	K_2O	P_2O_5	Sum	LOI	Mg#	Ca#
Average	7.42	0.14	9.67	12.57	2.91	0.04	0.02	101.56	0.15	73.84	70.46
Standard deviation	1.12	0.02	2.08	0.99	0.46	0.04	0.02	1.20	0.24	3.64	4.64
Maximum	10.36	0.18	21.80	15.07	3.86	0.27	0.10	103.76	0.87	82.54	91.44
Minimum	4.56	0.06	6.08	9.63	0.73	0.00	0.00	98.72	-0.43	64.65	60.91

Gabbro

Mode

%	Orthopyroxene	Oxide
Average	1	0.6
Maximum	1	1
Minimum	0	0.4

Chemical composition (11 analyses)

Wt%	Fe_2O_3tot	MnO	MgO	CaO	Na_2O	K_2O	P_2O_5	Sum	LOI	Mg#	Ca#
Average	6.65	0.13	8.55	13.14	3.04	0.04	0.02	101.56	0.14	73.73	70.46
Standard deviation	0.65	0.01	0.99	0.69	0.30	0.02	0.02	1.31	0.19	3.12	2.97
Maximum	7.81	0.14	10.31	14.24	3.50	0.08	0.07	103.06	0.61	77.70	73.37
Minimum	5.49	0.11	6.09	11.98	2.69	0.02	0.01	99.26	-0.09	65.25	65.64

Gabbronorite and ortho-pyroxene-bearing gabbro

Mode

%	Orthopyroxene	Oxide
Average	5	0.6
Maximum	10	0.8
Minimum	2	0.5

Chemical composition (two analyses)

Wt%	Fe_2O_3tot	MnO	MgO	CaO	Na_2O	K_2O	P_2O_5	Sum	LOI	Mg#	Ca#
Average	10.41	0.19	7.46	11.77	3.16	0.06	0.59	100.6	0.28	61.38	67.1
Standard deviation	2.6	0.05	0.89	1.32	0.15	0.01	0.57	0.22	0.48	8.75	3.54
Maximum	13.01	0.23	8.34	13.09	3.31	0.07	1.15	100.82	0.75	70.13	70.65
Minimum	7.82	0.14	6.57	10.45	3.01	0.06	0.02	100.38	-0.2	52.63	63.56

Table T3 (continued).

Rock type	Fraction of core	Number of intervals	Details

Oxide gabbronorite and ortho-pyroxene-bearing oxide gabbro — 2.7 vol% — 10

Mode

%	Plagioclase	Clinopyroxene	Olivine
Average	54	36	1
Maximum	60	45	3
Minimum	45	30	0

Grain size

mm	Plagioclase	Clinopyroxene	Olivine
Avg max/1 SD	22/13	27/18	2/3
Avg min/1 SD	4/2	3/3	1/1

Chemical composition (eight analyses)

Wt %	SiO_2	TiO_2	Al_2O_3
Average	46.38	3.13	12.53
Standard deviation	4.29	1.1	3.2
Maximum	53.25	5.71	18.55
Minimum	40.44	1.84	8.45

Oxide gabbro and disseminated oxide gabbro — 4.5 vol% — 100

Mode

%	Plagioclase	Clinopyroxene	Olivine
Average	60	30	3
Maximum	80	50	20
Minimum	30	5	0

Grain size

mm	Plagioclase	Clinopyroxene	Olivine
Avg max/1 SD	16/7	22/13	3/4
Avg min/1 SD	4/3	3/4	1/0

Chemical composition (four analyses)

Wt %	SiO_2	TiO_2	Al_2O_3
Average	45.53	4.1	12.12
Standard deviation	1.17	0.7	1.53
Maximum	46.85	5.31	14.27
Minimum	44.07	3.62	10.31

Clinopyroxenite — 0.04 vol% — 5

Mode

%	Plagioclase	Clinopyroxene	Olivine
Average	6	85	7
Maximum	10	93	9
Minimum	5	70	3

Grain size

mm	Plagioclase	Clinopyroxene	Olivine
Avg max/1 SD	8/2	26/6	3/2
Avg min/1 SD	3/1	5/3	1/0

Chemical composition (two analyses)

Wt %	SiO_2	TiO_2	Al_2O_3
Average	49.99	1.27	7.18
Standard deviation	0.47	0.87	1.27
Maximum	50.47	2.15	8.45
Minimum	49.52	0.4	5.91

Microgabbro — 2.4 vol% — 49

Mode

%	Plagioclase	Clinopyroxene	Olivine
Average	62	23	15
Maximum	75	40	40
Minimum	45	0	4

Grain size

mm	Plagioclase	Clinopyroxene	Olivine
Avg max/1 SD	7/6	12/18	4/4
Avg min/1 SD	1/1	1/1	1/0

Chemical composition (10 analyses) - includes two FeTi oxide gabbros, one gabbro, and seven olivine gabbros

Wt%	SiO_2	TiO_2	Al_2O_3
Average	51.6	0.49	17.01
Standard deviation	0.87	0.38	1.08
Maximum	52.95	1.38	19.53
Minimum	50.22	0.17	15.95

Table T3 (continued).

Oxide gabbronorite and Orthopyroxene-bearing oxide gabbro

Mode

%	Orthopyroxene	Oxide
Average	5	4.1
Maximum	10	8
Minimum	2	2

Chemical composition (eight analyses)

Wt %	Fe_2O_3tot	MnO	MgO	CaO	Na_2O	K_2O	P_2O_5	Sum	LOI	Mg#	Ca#
Average	17.9	0.26	6.45	10.33	3.03	0.09	0.85	100.95	0.38	45.25	65.19
Standard deviation	6.18	0.07	1.93	1.68	0.68	0.04	1.08	0.27	0.39	11.39	7.08
Maximum	27.66	0.37	10.77	13.36	4.23	0.18	3	101.35	1	62.28	80.26
Minimum	7.34	0.13	4.82	7.67	1.82	0.04	0.01	100.4	-0.19	29.54	58.5

Oxide gabbro and disseminated oxide gabbro

Mode

%	Orthopyroxene	Oxide
Average	1	5.1
Maximum	1	25
Minimum	0	2

Chemical composition (four analyses)

Wt %	Fe_2O_3tot	MnO	MgO	CaO	Na_2O	K_2O	P_2O_5	Sum	LOI	Mg#	Ca#
Average	18.85	0.26	5.91	10.21	3.12	0.08	0.61	100.79	0.25	39.61	64.64
Standard deviation	0.78	0.02	2.09	0.79	0.72	0.05	0.73	0.58	0.31	9.93	6.96
Maximum	19.98	0.3	8.26	11.22	4.06	0.17	1.82	101.35	0.55	49.42	72.58
Minimum	17.82	0.24	3.02	9.32	2.24	0.03	0.01	99.83	-0.25	24.96	55.93

Clinopyroxenite

Mode

%	Orthopyroxene	Oxide
Average	0	2.5
Maximum	0	4
Minimum	0	1

Chemical composition (two analyses)

Wt %	Fe_2O_3tot	MnO	MgO	CaO	Na_2O	K_2O	P_2O_5	Sum	LOI	Mg#	Ca#
Average	12.25	0.22	16.29	13.69	1.27	0.02	0.04	102.23	0.81	0.73	0.86
Standard deviation	2.11	0.04	5.52	0.33	0.55	0.02	0.03	1.43	0.2	0.1	0.05
Maximum	14.36	0.27	21.8	14.03	1.82	0.04	0.08	103.66	1	0.83	0.91
Minimum	10.15	0.18	10.77	13.36	0.73	0	0.01	100.8	0.61	0.64	0.8

Microgabbro

Mode

%	Orthopyroxene	Oxide
Average		0.5
Maximum		1
Minimum		0.1

Chemical composition (10 analyses) - includes two FeTi oxide gabbros, one gabbro, and seven olivine gabbros

Wt%	Fe_2O_3tot	MnO	MgO	CaO	Na_2O	K_2O	P_2O_5	Sum	LOI	Mg#	Ca#
Average	8.18	0.15	9.53	12.26	3.01	0.04	0.02	102.29	0.17	71.82	69.1
Standard deviation	2.13	0.03	1.58	1.36	0.39	0.04	0.02	1	0.24	6.95	4.35
Maximum	12.24	0.2	13.37	14.35	3.58	0.15	0.06	104.68	0.76	79.26	75.81
Minimum	5.93	0.12	7.55	9.61	2.42	0.01	0	100.74	-0.18	59.99	61.09

Note: SD = standard deviation

Table T4. Total mode and chemical composition of the Leg 176 core from 500 to 1508 mbsf.

	Plagioclase	Augite	Olivine	Orthopyroxene	Oxide
Macroscopic* mode:	59.5	30.1	8.8	0.3	0.76
Microscopic† mode:	58.9	30.6	8.2	0.6	0.79
Bulk composition**					
		Leg 118	Leg 176	Hole 735B	
Depth (mbsf):		0-500	500-1508	0-1508	
SiO_2 (wt%):		49.4	50.8	50.3	
TiO_2 (wt%):		1.4	0.7	0.9	
Al_2O_3 (wt%):		15.7	16.0	15.9	
Fe_2O_3, total (wt%):		9.6	8.1	8.6	
MnO (wt%):		0.6	0.1	0.1	
MgO (wt%):		9.1	9.1	9.1	
CaO (wt%):		12.1	12.3	12.2	
Na_2O (wt%):		2.7	2.9	2.8	
K_2O (wt%):		0.1	0.0	0.1	
P_2O_5 (wt%):		0.0	0.1	0.1	
Total (wt%):		100.3	100.0	100.1	
Mg# (Fe^{2+} 90% of Fe)		67.6	71.6	69.9	

Note: Also given is the Leg 118 data (Dick et al., 1991) and the weighted average for the entire Hole 735B. * = Average weighted mode from macroscopic estimations of 458 intervals (volume percent). † = Average weighted mode from averages of rock types derived by point counting in 220 thin sections (volume percent). ** = Average weighted chemical composition from averages of rock types characterized in thin sections and normalized to 100%.

Table T5. Lithologic units of Leg 176: limits and characterization. (Continued on next 2 pages.)

Igneous units of Leg 176: Hole 735B from 500 to 1508 mbsl.

Unit	Top (mbsf)	Bottom (mbsf)	Extent (m)	Rel.vol. (%)	Top igneous interval	Bottom igneous interval	Number of intervals
VI: Compound olivine gabbro	500	536	36	3.6	495	511	17
	End Leg 118				Continued from Leg 118		
VII: Gabbronorite and oxide gabbronorite	536	599	63	6.3	512	546	35
VIII: Olivine gabbro	599	670	71	7.0	547	568	22
IX: Gabbronorite and gabbro	670	714	44	4.4	569	600	32
X: Olivine gabbro and gabbro	714	960	246	24.4	601	716	116
XI: Olivine gabbro	960	1314	354	35.1	717	880	164
XII: Olivine gabbro and troctolitic gabbro	1314	1508	194	19.2	881	952	72
	Bottom of Hole 735B				Continues		
Total			1008	100			458

Note: * = For Unit VI (450-536 mbsf): 6% troctolitic gabbro, 63% olivine gabbro, 15% gabbro, 16% oxide gabbro.

Table T5 (continued).

Unit	Relative abundance of rock types	Subophitic texture	Proportion	Remarks
VI: Compound olivine gabbro	Olivine gabbro and troctolite common. Gabbronorite absent. Decreasing oxide gabbro.	Common	35%	
VII: Gabbronorite and oxide gabbronorite	Gabbronorite, oxide gabbronorite, and oxide gabbro are common. Major fault at 560 mbsf divides Subunits VIIA and VIIB. Olivine gabbro absent in top of Subunit VIIB.	Absent in Subunit VIIA, present in VIIB	5%	
VIII: Olivine gabbro	Olivine gabbro abundant. Gabbronoritic rocks make up 25% of unit, the majority being oxide rich.	Common	27%	Pegmatic intervals common.
IX: Gabbronorite and gabbro	Olivine gabbro absent. Gabbronorite abundant at top of unit, decreasing to zero at bottom. Oxide gabbro and gabbronorite present.	Absent	0%	Small size of intervals. Absence of pegmatic gabbro and microgabbro intervals.
X: Olivine gabbro and gabbro	Olivine gabbro dominating and gabbro common. Oxide gabbro rare.	Occurs	10%	Microgabbros abundant at top of unit.
XI: Olivine gabbro	Olivine gabbro predominant, oxide gabbro present throughout.	Rare	4%	Olivine gabbro intervals relatively large? Abundant oxide gabbro intrusion around 1020 m.
XII: Olivine gabbro and troctolitic gabbro	Olivine gabbro >90 vol%. Troctolitic gabbro present.	Common	21%	Abundant microgabbros 1310-1390 m.
Total				

Table T5 (continued).

Unit	Abundance of rock types (vol%)						Intervals/m
	Troctolitic	Olivine gabbro	Gabbro	Gabbronorite	Oxide gabbronorite	Oxide gabbro	
VI: Compound olivine gabbro	9 (*)	74	14			3	0.5
VII: Gabbronorite and oxide gabbronorite		6	11	41	28	14	0.6
VIII: Olivine gabbro		73	2	11	13	1	0.3
IX: Gabbronorite and gabbro		2	23	61	4	10	0.7
X: Olivine gabbro and gabbro	tr	70	29			1	0.5
XI: Olivine gabbro	1	79	16			4	0.5
XII: Olivine gabbro and troctolitic gabbro	6	92				2	0.4
Total							

Table T6. Contact types by lithology.

Lithology	Sutured	Sharp	Intrusive	Tectonic	Gradational	Not preserved	Not recovered	Totals
Oxide gabbro*	40	5	3	11	98	5	32	194
Gabbronorite†	6	13	0	1	24	0	12	56
Melanogabbro**	6	2	0	0	2	0	0	10
Microgabbro	52	1	8	4	17	2	14	98
Olivine gabbro	161	17	7	34	223	3	54	499
Troctolitic gabbro	8	4	2	0	19	0	6	39
Unknown	3	4	4	0	9	0	0	20
Totals:	276	46	24	50	392	10	118	916

Notes: Each contact is listed once for each bordering lithology, resulting in a total that is twice the number of lithologic intervals. * = oxide gabbro and disseminated oxide gabbro, † = orthopyroxene-bearing gabbro and gabbronorite, ** = disseminated oxide microgabbro and microgabbro.

Table T7. Average primary modes of Leg 176 rocks determined by point counting.

Rock type	*N*	Plagioclase	Olivine	Clinopyroxene	Orthopyroxene	Opaques	Amphibole	Apatite
Troctolite	7	66.6	30.4	2.8	0.0	0.2	0.0	0.0
Troctolitic gabbro	12	72.8	16.1	10.7	0.1	0.2	0.1	0.0
Olivine gabbro	118	59.5	9.8	29.9	0.2	0.3	0.3	0.0
Olivine microgabbro	11	58.4	8.8	32.1	0.1	0.2	0.4	0.0
Gabbro	25	58.5	3.3	37.5	0.2	0.4	0.3	0.0
Gabbronorite*	15	64.6	2.7	27.5	3.5	0.7	0.8	0.0
Oxide gabbronorite†	13	50.6	0.8	34.5	3.5	9.4	0.4	0.5
Oxide gabbro**	3	51.4	1.9	40.2	0.2	6.3	0.1	0.5
Oxide microgabbro	5	58.5	10.9	25.8	1.5	1.8	1.4	0.1

Note: * = orthopyroxene-bearing gabbro, † = orthopyroxene-bearing oxide gabbro, ** = disseminated oxide gabbro.

Table T8. Summary of alteration minerals and conditions of formation.

	Metamorphic minerals																				
	800°–400°C						400°–150°C								150°–0°C						
Igneous minerals	Diopside	Secondary plagioclase	Brown amphibole	Dark green amphibole	Talc	Magnetite	Green amphibole	Chlorite	Oxides	Quartz	Albite	Titanite	Epidote	Prehnite	Sulfide	Zeolite	Green smectite	Sulfide	Orange smectite	Carbonate	Hematite	Oxyhydroxides
Olivine			o	O	O	O	o	o	o						o		O	O	o	o	o	o
Clinopyroxene	O		O	O	o	o	O	O	o								o	o	o	o	o	o
Orthopyroxene			o	O	o	o	O	o	o								o	o	o	o	o	
Plagioclase		O					o	o		o	o		o	o		o	O					
Hornblende				O		o	O	?	o								O	o				?
Oxides						?		?				o										

Notes: Symbols = presence of secondary mineral phases. O = secondary minerals that commonly replace a primary phase; o = less common replacement. ? = secondary minerals after primary phases that were difficult to identify in hand specimen.

Table T9. Summary of vein types.

Vein type	Total	Vein (%)	Area (cm^2)	Area (%)
Smectite	1316	47.13	684.44	15.17
Amphibole	471	16.87	208.14	4.61
Plagioclase + amphibole	269	9.63	871.45	19.31
Carbonate	254	9.10	81.85	1.81
Plagioclase	138	4.94	223.08	4.94
Felsic	114	4.08	2023.45	44.85
Zeolite	51	1.83	26.93	0.60
Clinopyroxene + plagioclase	40	1.43	171.32	3.80
Smectite + carbonate	35	1.25	24.89	0.55
Clinopyroxene	27	0.97	16.59	0.37
Smectite + zeolite	22	0.79	63.93	1.42
Chlorite	17	0.61	9.95	0.22
Amphibole + chlorite	13	0.47	37.68	0.84
Quartz	8	0.29	20.60	0.46
Clinopyroxene + amphibole	5	0.18	5.90	0.13
Carbonate + oxide	4	0.14	14.40	0.32
Epidote	3	0.11	14.15	0.31
Smectite + amphibole	2	0.07	8.10	0.18
Amphibole + carbonate	1	0.04	2.60	0.06
Aragonite(?)	1	0.04	0.12	0.00
Chlorite + zeolite	1	0.04	2.40	0.05
Total veins	2792	100.00	4511.97	100.00

Table T10. Chemical composition of samples from Hole 735B. (Continued on next 12 pages.)

	118-735B								176-735B						
Hole:	B	B	B	B	B	B	B	B	B	B	B	B	B	B	B
Core:	74	78	79	82	85	86	87	88	90	90	90	91	91	92	93
Type:	R	R	R	R	R	R	R	N	R	R	R	R	R	R	R
Section:	6	1	7	1	3	4	6	1	1	4	7	1	3	1	3
Top (cm):	45	114	115	13	47	78	98	48	115	41	55	105	92	25	85
Bottom (cm):	51	118	118	16	54	81	102	51	121	47	62	114	100	30	92
Piece:	4A	5A	10	2A	1F	4B	13	2B	2	1B	1B	3B	1D	4	1E
Depth (mbsf):	382.2	410.5	423.9	443.1	474.7	486.1	499.1	500.5	508.9	512.0	515.8	518.9	522.5	527.5	534.7
Li_Int:					460	474	491a	495	497a	497a	501	504	506	509	510
Rock type:	OxGa	OxGa	OxGa	OxGa	OxGa	OlGa	OlGa	Troc	Troc	TrocGa	Troc	Troc	altGa	Ga	Ga
SiO_2 (wt%):	52.01	48.83	46.48	49.44	46.86	51.53	49.64	46.86	48.10	48.42	48.38	43.82	44.48	54.26	52.11
TiO_2 (wt%):	1.60	2.26	3.62	2.66	4.91	0.38	0.15	0.09	0.11	0.10	0.16	0.15	0.19	0.60	0.50
Al_2O_3 (wt%):	14.82	14.05	12.79	13.30	13.70	16.33	19.21	20.45	22.05	18.01	19.72	13.37	22.89	16.46	15.75
Fe_2O_3 (wt%):	12.24	14.45	19.01	16.82	17.62	7.62	5.48	6.01	5.35	5.64	5.81	9.41	6.91	6.46	7.82
MnO (wt%):	0.21	0.22	0.30	0.26	0.25	0.13	0.10	0.09	0.09	0.09	0.10	0.14	0.11	0.11	0.14
MgO (wt%):	6.43	7.07	4.87	4.34	4.66	9.90	11.37	13.50	11.39	14.77	12.17	24.03	4.98	7.05	8.34
CaO (wt%):	10.25	10.90	9.59	9.27	9.04	12.67	12.34	10.24	11.27	11.83	11.76	7.94	18.96	12.72	13.09
Na_2O (wt%):	3.65	3.16	3.56	3.99	3.67	2.85	2.43	2.14	2.40	1.67	2.11	1.08	2.62	3.86	3.01
K_2O (wt%):	0.07	0.10	0.07	0.13	0.05	0.05	0.04	0.06	0.01	0.20	0.03	0.01	0.21	0.05	0.06
P_2O_5 (wt%):	0.09	0.43	0.57	0.49	0.11	0.01	0.01	0.01	0.01	0.00	0.01	0.01	0.13	0.02	0.02
Total (wt%):	101.37	101.47	100.86	100.70	100.87	101.47	100.77	99.45	100.76	100.72	100.24	99.95	101.47	101.58	100.82
LOI:	0.33	0.04	0.44	0.28	–0.18	–0.61	–0.87	–1.30	–0.60	–2.22	–0.57	–1.36	–9.24	–1.68	–0.75
FeO(tit):	8.31	10.03	12.63	11.01	11.62	5.96	ND	5.10	4.47	4.54	5.13	8.00	1.42	4.66	5.34
$\%Fe^{2+}$:	75	77	74	73	73	87	ND	96	93	91	99	96	25	82	77
Mg-value:	0.58	0.56	0.41	0.41	0.42	0.75	ND	0.82	0.82	0.85	0.81	0.84	0.85	0.73	0.73
Mg#:	0.550	0.533	0.374	0.376	0.381	0.752	0.829	0.840	0.832	0.859	0.830	0.856	0.627	0.718	0.713
Ca#:	0.608	0.656	0.598	0.562	0.576	0.711	0.737	0.726	0.722	0.797	0.755	0.802	0.800	0.645	0.706
V (ppm):	311	180	220	188	504	165	81	30	38	71	76	48	80	228	209
Cr (ppm):	168	417	0	14	0	283	820	194	228	1202	251	742	40	7	27
Ni (ppm):	59	101	64	42	35	114	287	410	329	413	294	770	276	58	75
Cu (ppm):	54	108	119	70	107	20	22	80	86	105	46	60	70	10	58
Zn (ppm):	87	117	166	161	99	46	34	39	33	47	39	52	56	24	47
Rb (ppm):	2	3	2	3	2	2	2	1	1	2	2	2	5	1	1
Sr (ppm):	171	151	164	158	159	166	168	175	184	135	168	109	219	229	166
Y (ppm):	30	59	71	95	30	11	10	4	5	6	6	5	6	15	14
Zr (ppm):	81	92	89	250	93	25	29	19	21	21	22	15	28	41	33
Nb (ppm):	1	5	7	6	3	0	0	0	1	1	0	0	0	0	0

Notes: Li_Int = lithologic interval (see **"Igneous Petrology,"** p. 12). Rock type = rock names assigned on the basis of modal data determined by point counting. Troc = troctolite; TrocGa = troctolitic gabbro; OlGa = olivine gabbro; Ga = gabbro; DiOlGa = disseminated oxide olivine gabbro; OxGa = oxide gabbro; LeuGa = leucocratic gabbro; OpxOxGa = orthopyroxene-bearing oxide gabbro; altGa = heavily altered gabbro; felsic = diorite or plagiogranite; mixed = intimately mixed felsic and mafic components. Major elements determined on ignited powder; %FeO(tit) and minor and trace elements on powder dried at 110°C. Concentration units: weight percent for major element oxides, LOI and FeO(tit); parts per million for minor and trace elements. LOI = weight loss on ignition; negative values = loss of weight; positive values = gain of weight, i.e., oxygen uptake > volatile loss. FeO(tit) = weight percent ferrous iron oxide determined by redox titration. $\%Fe^{2+}$ = percentage of total iron present as ferrous iron, calculated from FeO(tit) and Fe_2O_3 determined by X-ray fluorescence. Mg-value = Mg-number, calculated from $\%Fe^{2+}$. Mg# = Mg-number, calculated value for ferrous iron set equal to 85% of total iron. Ca# = (Ca/Ca+Na) molar; ND = not determined.

Table T10 (continued).

	176-735B														
Hole:	B	B	B	B	B	B	B	B	B	B	B	B	B	B	B
Core:	94	95	95	96	97	99	99	101	101	102	103	103	104	105	106
Type:	R	R	R	R	R	R	R	R	R	R	R	R	R	R	R
Section:	1	1	2	1	1	3	4	1	3	1	1	2	2	3	2
Top (cm):	36	115	82	25	125	72	106	63	30	17	72	80	45	93	21
Bottom (cm):	43	125	88	32	130	78	108	68	36	23	80	86	48	99	26
Piece:	1B	8	1D	4	2C	5	6	7B	1D	3	6A	3E	6B	7	1C
Depth (mbsf):	537.3	545.3	545.9	548.9	557.4	570.2	572.1	585.8	588.3	590.1	595.8	598.0	607.2	612.4	615.5
Li_Int:	514	517	518	521	526	532	532	535	536	537	541	542	548	550	550
Rock type:	Ga	OlGa	OlGa	OlGa	OxGa	OlGa	Felsic	OlGa	DiOlGa	OxGa	OxGa	OlGa	OlGa	TrocGa	TrocGa
SiO_2 (wt%):	51.93	52.97	52.69	52.95	52.27	51.78	74.85	52.29	51.17	44.72	41.24	52.35	52.79	51.73	52.90
TiO_2 (wt%):	0.56	0.55	0.40	0.43	2.06	0.48	0.11	0.45	0.86	3.75	3.34	0.50	0.41	0.42	0.44
Al_2O_3 (wt%):	18.09	18.31	15.90	16.81	14.57	18.44	14.86	15.08	12.95	14.27	8.68	14.75	15.95	16.86	16.18
Fe_2O_3 (wt%):	7.14	7.96	8.04	7.57	8.88	6.89	1.04	9.22	8.72	19.98	25.92	6.65	8.12	7.19	7.04
MnO (wt%):	0.12	0.15	0.15	0.15	0.14	0.12	0.04	0.17	0.16	0.26	0.37	0.13	0.16	0.13	0.13
MgO (wt%):	6.09	6.62	7.45	7.55	7.47	8.55	0.32	9.37	11.85	3.02	6.09	9.89	9.08	8.42	8.94
CaO (wt%):	11.98	10.89	11.02	11.57	12.23	11.73	0.66	10.61	13.99	9.32	10.32	14.45	12.50	12.57	13.16
Na_2O (wt%):	3.47	3.86	3.67	3.58	3.64	3.33	5.05	3.30	2.21	4.06	2.44	2.53	3.25	3.15	3.27
K_2O (wt%):	0.08	0.27	0.06	0.15	0.06	0.06	3.97	0.17	0.07	0.17	0.18	0.04	0.05	0.05	0.08
P_2O_5 (wt%):	0.05	0.03	0.00	0.01	0.04	0.03	0.01	0.04	0.07	1.82	2.20	0.03	0.01	0.01	0.01
Total (wt%):	99.48	101.59	99.36	100.74	101.35	101.40	100.91	100.69	102.04	101.35	100.76	101.31	102.31	100.50	102.13
LOI:	–0.61	–0.58	–0.28	–0.11	–0.63	0.19	0.19	–0.18	–0.07	–0.55	–0.84	–0.26	–0.33	–0.65	–0.92
FeO(tit):	4.28	6.19	6.80	6.03	6.54	5.60	0.70	7.56	6.96	7.99	12.79	5.57	6.38	5.68	5.14
$\%Fe^{2+}$:	67	87	94	89	82	90	75	91	89	45	55	93	88	88	82
Mg-value:	0.72	0.65	0.66	0.69	0.67	0.73	0.45	0.69	0.75	0.40	0.46	0.76	0.72	0.72	0.75
Mg#:	0.666	0.660	0.684	0.699	0.662	0.743	0.418	0.703	0.760	0.261	0.354	0.776	0.723	0.732	0.747
Ca#:	0.656	0.609	0.624	0.641	0.650	0.661	0.067	0.640	0.778	0.559	0.701	0.759	0.680	0.688	0.690
V (ppm):	146	160	204	184	343	143	9	136	262	203	209	222	190	181	195
Cr (ppm):	14	0	0	0	31	31	0	136	225	0	0	124	23	79	107
Ni (ppm):	60	47	41	38	60	96	7	99	116	17	24	85	69	70	73
Cu (ppm):	29	72	29	30	13	65	27	49	50	76	102	62	72	27	24
Zn (ppm):	52	58	48	45	33	46	8	76	49	171	203	41	47	40	31
Rb (ppm):	2	2	1	2	1	0	27	0	0	3	3	0	0	0	0
Sr (ppm):	201	208	181	190	198	179	16	139	118	197	109	140	159	167	164
Y (ppm):	15	15	16	14	30	8	44	41	15	97	124	13	17	10	10
Zr (ppm):	52	81	29	37	95	34	166	134	47	62	88	45	28	25	27
Nb (ppm):	0	0	0	0	2	2	11	5	2	5	6	3	3	2	2

Table T10 (continued).

176-735B														
Hole:	B	B	B	B	B	B	B	B	B	B	B	B	B	B
Core:	108	110	110	111	113	114	114	115	115	116	116	117	118	119
Type:	R	R	R	R	R	R	R	R	R	R	R	R	R	R
Section:	2	4	4	2	1	1	5	3	6	4	6	2	1	1
Top (cm):	44	0	56	101	97	92	23	75	23	67	92	42	138	72
Bottom (cm):	50	5	63	105	100	96	29	81	29	74	99	48	148	77
Piece:	2	1	2B	3	4B	6C	1B	2C	2	4A	7A	3A	7E	7
Depth (mbsf):	625.4	637.1	637.6	641.3	649.3	653.5	659.5	665.5	668.9	676.7	680.0	683.5	692.1	701.4
Li_Int:	556	560	560	560	560	561	563	564	568	573	575	577	581	588
Rock type:	OlGa	Felsic	OlGa	OlGa	OlGa	OpxOxGa	OpxOxGa	DiOlGa	OlGa	OlGa	Ga	OlGa	OlGa	Felsic
SiO_2 (wt%):	52.09	61.35	51.55	51.89	51.26	49.10	48.03	51.64	52.71	52.83	52.75	52.45	51.85	56.94
TiO_2 (wt%):	0.46	0.15	0.41	0.41	0.46	2.66	3.22	0.60	0.39	0.74	0.44	0.43	0.41	3.25
Al_2O_3 (wt%):	14.99	18.67	15.04	16.86	16.55	11.75	12.64	17.88	17.17	16.55	17.29	16.99	14.99	15.08
Fe_2O_3 (wt%):	8.55	4.73	7.98	7.73	8.42	16.08	18.60	7.83	7.70	7.05	8.51	8.36	10.28	4.86
MnO (wt%):	0.16	0.08	0.15	0.14	0.15	0.27	0.31	0.14	0.14	0.14	0.15	0.15	0.17	0.10
MgO (wt%):	10.26	2.44	9.62	8.54	10.17	8.34	5.70	8.21	7.85	8.21	8.37	8.29	11.33	4.29
CaO (wt%):	12.82	2.61	12.73	11.97	12.35	9.86	8.80	12.31	11.43	12.95	11.26	11.19	10.73	10.08
Na_2O (wt%):	2.73	7.71	2.81	3.22	2.85	2.96	3.44	3.17	3.55	3.25	3.53	3.48	2.95	5.58
K_2O (wt%):	0.03	0.01	0.03	0.07	0.02	0.06	0.07	0.05	0.07	0.05	0.05	0.05	0.10	0.11
P_2O_5 (wt%):	0.02	0.00	0.01	0.02	0.02	0.03	0.28	0.02	0.01	0.02	0.01	0.02	0.01	1.00
Total (wt%):	102.10	97.74	100.32	100.82	102.23	101.09	101.08	101.85	101.01	101.78	102.35	101.40	102.81	101.27
LOI:	–0.04	–1.11	–0.25	–0.15	0.08	0.20	0.22	0.11	–0.19	–0.44	0.21	–0.24	–0.06	–1.31
FeO(tit):	6.89	3.81	6.70	6.17	7.23	11.70	11.70	6.31	6.43	5.63	6.89	6.87	7.98	3.89
$\%Fe^{2+}$:	90	91	94	89	95	81	70	89	93	89	90	92	86	90
Mg-value:	0.73	0.53	0.72	0.71	0.72	0.56	0.47	0.70	0.68	0.72	0.68	0.68	0.72	0.66
Mg#:	0.737	0.546	0.738	0.720	0.738	0.547	0.417	0.710	0.704	0.731	0.696	0.698	0.720	0.673
Ca#:	0.722	0.158	0.715	0.673	0.706	0.648	0.586	0.682	0.640	0.688	0.638	0.640	0.668	0.500
V (ppm):	198	33	197	169	161	481	318	154	160	208	202	162	163	193
Cr (ppm):	115	0	57	67	108	0	0	156	19	20	4	0	6	0
Ni (ppm):	87	17	80	76	116	40	29	76	53	66	58	63	103	44
Cu (ppm):	64	6	99	96	143	69	81	52	35	69	48	52	69	10
Zn (ppm):	51	20	45	51	49	102	145	53	49	43	54	50	60	13
Rb (ppm):	1	0	0	0	0	1	1	1	0	1	0	0	0	0
Sr (ppm):	151	133	155	173	170	134	155	180	193	177	177	189	163	233
Y (ppm):	11	14	11	23	9	24	41	13	11	13	14	10	15	119
Zr (ppm):	28	279	24	260	29	53	74	42	31	39	45	27	35	1015
Nb (ppm):	3	5	2	4	3	2	6	3	3	3	2	2	2	25

Table T10 (continued).

	176-735B														
Hole:	B	B	B	B	B	B	B	B	B	B	B	B	B	B	B
Core:	119	119	120	120	121	121	121	122	122	123	124	126	126	127	128
Type:	R	R	R	R	R	R	R	R	R	R	R	R	R	R	R
Section:	2	4	4	6	2	5	8	2	7	4	1	3	5	3	2
Top (cm):	93	5	62	35	43	106	72	0	13	82	32	82	91	0	133
Bottom (cm):	99	11	67	41	47	111	77	7	19	89	38	88	97	6	137
Piece:	8B	1	6	1B	2C	1G	2B	1A	1	2B	2A	2B	2B	1	13A
Depth (mbsf):	703.6	706.4	714.9	717.4	721.5	726.0	729.2	730.7	737.8	744.0	749.0	759.5	762.6	768.3	778.4
Li_Int:	589	590	601	601	606	611	615	615	617	621	622	622	625	628	631
Rock type:	OlGa	OxGa	Felsic	OlGa	OlGa	OlGa	OlGa	Ga	OlGa	OlGa	OlGa	OlGa	Felsic	OlGa	OlGa
SiO_2 (wt%):	52.68	40.44	56.64	52.33	50.22	51.95	52.48	52.43	52.43	51.21	52.22	52.41	61.44	52.16	51.51
TiO_2 (wt%):	0.32	5.71	4.25	0.37	0.19	0.57	0.40	0.56	0.41	0.24	0.35	0.40	0.53	0.34	0.17
Al_2O_3 (wt%):	17.78	11.32	20.03	17.35	16.86	17.30	16.66	16.14	17.09	18.48	15.90	17.35	20.80	15.53	19.53
Fe_2O_3 (wt%):	7.47	27.66	2.43	7.05	7.70	7.68	6.88	7.11	6.74	7.04	7.37	6.76	1.97	7.32	6.55
MnO (wt%):	0.13	0.32	0.06	0.13	0.13	0.14	0.13	0.14	0.13	0.13	0.14	0.13	0.05	0.14	0.12
MgO (wt%):	8.71	5.27	1.51	9.29	13.37	9.79	9.88	9.33	9.68	10.74	10.58	9.15	2.02	11.13	9.64
CaO (wt%):	11.95	7.67	9.47	12.53	11.19	12.66	13.52	13.76	13.26	12.11	13.42	13.18	4.72	13.64	12.31
Na_2O (wt%):	3.28	2.82	6.08	2.99	2.42	2.91	2.73	2.77	2.84	2.75	2.62	2.89	7.66	2.42	2.92
K_2O (wt%):	0.09	0.05	0.12	0.03	0.01	0.04	0.03	0.04	0.03	0.02	0.02	0.03	0.22	0.02	0.02
P_2O_5 (wt%):	0.01	0.10	0.30	0.02	0.01	0.08	0.02	0.02	0.03	0.03	0.01	0.02	0.01	0.01	0.00
Total (wt%):	102.40	101.35	100.88	102.08	102.08	103.10	102.71	102.28	102.62	102.74	102.62	102.29	99.40	102.69	102.76
LOI:	–0.58	0.68	–0.66	–0.63	–0.06	–0.04	–0.13	–0.17	–0.20	–0.24	–0.21	–0.02	–0.79	–0.40	–0.76
FeO(tit):	5.55	14.47	1.55	6.25	6.50	6.08	5.41	5.76	5.35	5.70	5.68	5.33	1.42	5.42	5.58
$\%Fe^{2+}$:	83	58	71	99	94	88	88	90	88	90	86	88	81	83	95
Mg-value:	0.74	0.40	0.63	0.72	0.79	0.74	0.76	0.74	0.76	0.77	0.77	0.75	0.72	0.78	0.75
Mg#:	0.731	0.308	0.591	0.754	0.802	0.748	0.770	0.754	0.770	0.781	0.770	0.759	0.705	0.780	0.774
Ca#:	0.668	0.600	0.463	0.698	0.719	0.706	0.732	0.733	0.721	0.709	0.739	0.716	0.254	0.757	0.700
V (ppm):	151	991	75	168	92	168	173	200	170	111	173	165	38	180	103
Cr (ppm):	65	0	0	132	438	125	183	329	112	286	130	66	0	128	152
Ni (ppm):	87	57	15	122	216	132	117	100	107	142	117	109	14	142	129
Cu (ppm):	30	162	7	121	109	95	109	85	69	85	88	99	4	133	117
Zn (ppm):	44	221	9	47	44	48	43	47	41	41	44	41	8	43	40
Rb (ppm):	0	1	0	0	0	0	0	0	0	0	0	0	0	0	1
Sr (ppm):	187	114	243	166	168	174	165	156	170	179	153	169	140	142	182
Y (ppm):	8	33	105	11	5	11	10	15	10	7	9	8	56	8	7
Zr (ppm):	22	99	247	28	15	48	29	40	32	27	23	26	140	20	16
Nb (ppm):	1	4	36	1	1	2	1	0	1	1	1	0	11	1	0

Table T10 (continued).

	176-735B														
Hole:	B	B	B	B	B	B	B	B	B	B	B	B	B	B	B
Core:	128	130	130	131	132	132	132	133	133	133	133	133	134	134	135
Type:	R	R	R	R	R	R	R	R	R	R	R	R	R	R	R
Section:	4	2	4	2	1	3	6	1	2	5	5	7	2	7	1
Top (cm):	67	35	121	25	62	39	81	100	117	81	111	127	105	71	97
Bottom (cm):	73	40	127	30	70	49	87	107	123	87	116	130	110	77	103
Piece:	7	3	8B	3	11A	2	2	5B	5	2G	3	1H	2D	1B	2E
Depth (mbsf):	781.7	796.5	802.5	806.4	813.8	816.3	820.2	823.9	825.4	829.2	829.5	832.4	834.9	841.3	843.1
Li_Int:	634	642	647	650	655	658	660	661	662	667	668	668	668	668	671
Rock type:	OlGa	OlGa	Ga	OlGa	Ga	TrocGa	Ga	OxGa	OlGa	OlGa	OlGa	OlGa	OlGa	OlGa	OlGa
SiO_2 (wt%):	52.08	52.52	52.69	52.30	49.53	52.61	52.10	46.85	52.04	50.47	51.26	52.85	51.37	51.58	52.72
TiO_2 (wt%):	0.39	0.38	0.54	0.83	0.55	0.40	0.47	3.73	0.52	0.40	0.24	0.33	0.27	0.37	0.72
Al_2O_3 (wt%):	15.85	14.99	15.95	15.16	13.62	17.37	17.16	11.13	17.03	5.91	18.46	15.19	19.18	16.70	17.12
Fe_2O_3 (wt%):	7.24	6.61	9.56	9.46	8.79	6.29	6.59	17.82	7.31	10.15	5.84	5.68	5.69	7.13	8.11
MnO (wt%):	0.14	0.14	0.18	0.18	0.24	0.12	0.13	0.25	0.13	0.18	0.11	0.14	0.11	0.13	0.15
MgO (wt%):	10.32	10.13	8.50	8.79	10.54	9.47	8.72	7.48	9.14	21.80	10.03	11.78	8.79	10.64	8.00
CaO (wt%):	13.64	14.57	11.41	11.64	15.25	13.83	13.89	11.22	12.45	14.03	13.02	14.57	12.66	12.90	11.96
Na_2O (wt%):	2.57	2.48	3.43	3.22	2.39	2.73	2.82	2.63	3.09	0.73	2.66	2.62	2.99	2.60	3.42
K_2O (wt%):	0.02	0.02	0.05	0.11	0.05	0.15	0.03	0.04	0.05	0.00	0.01	0.02	0.02	0.02	0.07
P_2O_5 (wt%):	0.01	0.01	0.02	0.07	0.06	0.02	0.01	0.01	0.03	0.01	0.01	0.01	0.01	0.01	0.10
Total (wt%):	102.26	101.84	102.32	101.73	101.00	102.97	101.89	101.14	101.76	103.66	101.62	103.17	101.08	102.05	102.35
LOI:	–0.20	–0.29	–0.03	–0.37	–5.01	–0.73	–0.32	0.27	–0.26	–0.61	–0.25	–3.97	–0.19	–0.11	0.07
FeO(tit):	5.72	5.45	7.91	8.10	3.95	5.13	5.20	11.17	6.03	7.81	4.83	3.67	4.93	5.93	6.36
$\%Fe^{2+}$:	88	92	92	96	53	91	88	69	92	86	92	75	96	93	87
Mg-value:	0.76	0.77	0.66	0.66	0.82	0.77	0.75	0.54	0.73	0.83	0.79	0.85	0.76	0.76	0.69
Mg#:	0.769	0.781	0.675	0.684	0.737	0.778	0.755	0.494	0.745	0.834	0.800	0.829	0.783	0.777	0.697
Ca#:	0.746	0.764	0.648	0.666	0.779	0.737	0.732	0.702	0.690	0.914	0.730	0.754	0.701	0.733	0.659
V (ppm):	193	215	174	176	213	208	181	970	167	220	119	189	127	66	139
Cr (ppm):	110	175	0	54	200	333	306	0	45	1003	338	432	135	142	72
Ni (ppm):	116	97	50	86	93	97	89	60	92	286	137	90	109	125	79
Cu (ppm):	100	67	38	47	82	34	112	63	61	110	99	49	76	82	40
Zn (ppm):	41	38	60	71	43	36	43	103	48	55	36	31	35	45	61
Rb (ppm):	0	2	3	2	0	2	3	0	0	0	0	0	0	0	3
Sr (ppm):	149	145	173	152	126	142	168	119	171	45	180	128	191	152	184
Y (ppm):	9	13	18	32	17	13	15	22	14	11	8	9	7	9	23
Zr (ppm):	23	24	37	100	56	35	31	39	45	19	22	21	26	26	66
Nb (ppm):	1	1	1	3	1	1	1	1	1	0	0	1	1	0	0

Table T10 (continued).

	176-735B														
Hole:	B	B	B	B	B	B	B	B	B	B	B	B	B	B	B
Core:	135	135	136	137	137	137	137	138	138	138	139	139	140	140	140
Type:	R	R	R	R	R	R	R	R	R	R	R	R	R	R	R
Section:	3	3	2	3	3	5	6	3	7	7	4	4	1	5	5
Top (cm):	12	98	62	34	126	33	117	65	0	11	68	120	17	19	33
Bottom (cm):	17	99	67	39	131	38	121	74	9	18	74	125	24	26	39
Piece:	1	6	1B	2A	4A	1B	5B	2A	1	1	3	4	3A	1	2
Depth (mbsf):	844.9	845.7	848.7	854.4	855.3	857.2	859.3	864.8	869.8	869.9	875.9	876.4	880.5	886.5	886.6
Li_Int:	675	675	675	679	679	679	680	683	683	683	687	687	687	687	687
Rock type:	Ga	Mixed	OlGa	TrocGa	OlGa	OxGa	OxGa	OlGa	Ga	OlGa	Ga	OlGa	OlGa	OlGa	OlGa
SiO_2 (wt%):	53.28	57.56	52.30	52.65	51.88	42.18	50.83	52.52	52.70	50.48	52.85	53.15	51.89	51.26	51.09
TiO_2 (wt%):	0.40	1.21	0.46	0.34	0.35	3.20	1.00	0.53	0.44	0.42	0.37	0.48	0.45	0.38	0.28
Al_2O_3 (wt%):	17.84	21.33	15.72	18.35	18.26	12.93	16.16	15.53	19.30	13.69	16.30	16.86	17.58	16.42	17.20
Fe_2O_3 (wt%):	5.53	5.39	5.95	6.50	7.36	19.40	12.24	8.35	6.43	9.59	6.29	6.65	7.36	8.36	6.18
MnO (wt%):	0.12	0.09	0.12	0.12	0.13	0.23	0.20	0.15	0.12	0.17	0.13	0.13	0.13	0.15	0.11
MgO (wt%):	8.76	2.60	10.05	9.66	10.74	4.91	8.34	10.98	8.07	13.32	9.53	8.81	9.48	10.26	9.76
CaO (wt%):	14.24	7.17	14.15	13.14	12.05	12.12	9.61	12.87	12.48	12.37	13.73	13.85	12.70	12.23	13.05
Na_2O (wt%):	2.86	6.24	2.51	2.82	2.89	3.05	3.38	2.65	3.29	2.29	2.86	2.99	3.03	2.91	2.75
K_2O (wt%):	0.03	0.42	0.02	0.03	0.03	0.07	0.07	0.06	0.05	0.03	0.01	0.03	0.03	0.05	0.01
P_2O_5 (wt%):	0.02	0.29	0.02	0.02	0.09	3.00	0.06	0.06	0.07	0.03	0.00	0.01	0.02	0.03	0.01
Total (wt%):	103.06	102.28	101.29	103.62	103.76	101.07	101.88	103.68	102.93	102.36	102.05	102.94	102.65	102.03	100.44
LOI:	–0.17	–0.33	–0.21	0.01	–0.08	0.31	0.23	–0.12	–0.05	0.06	–0.02	–0.06	–0.06	0.02	–0.07
FeO(tit):	4.66	3.63	5.05	5.58	5.84	9.45	9.26	6.96	5.22	7.85	5.11	5.09	5.80	6.49	5.48
$\%Fe^{2+}$:	94	75	95	95	88	54	84	93	90	91	90	85	88	86	99
Mg-value:	0.77	0.56	0.78	0.76	0.77	0.48	0.62	0.74	0.73	0.75	0.77	0.76	0.74	0.74	0.76
Mg#:	0.787	0.529	0.798	0.776	0.773	0.371	0.614	0.754	0.745	0.764	0.779	0.756	0.750	0.741	0.786
Ca#:	0.734	0.388	0.757	0.721	0.698	0.687	0.611	0.729	0.677	0.749	0.726	0.719	0.699	0.699	0.724
V (ppm):	167	111	188	125	99	450	158	182	138	170	194	206	157	153	145
Cr (ppm):	201	0	161	179	153	171	333	119	74	120	41	44	80	106	135
Ni (ppm):	101	43	112	112	131	80	153	104	77	152	89	77	101	119	117
Cu (ppm):	114	221	74	75	45	109	54	62	66	133	83	79	77	64	111
Zn (ppm):	35	42	40	39	49	162	86	48	39	61	36	45	46	55	38
Rb (ppm):	2	3	2	3	2	0	0	0	0	0	0	0	0	0	0
Sr (ppm):	175	190	155	180	180	153	168	155	191	132	164	166	174	163	171
Y (ppm):	12	110	13	11	14	139	28	18	11	12	10	12	10	12	8
Zr (ppm):	29	406	34	30	72	98	105	70	58	37	20	28	28	38	20
Nb (ppm):	0	11	0	0	0	5	0	0	0	0	0	0	0	0	0

Table T10 (continued).

176-735B														
Hole:	B	B	B	B	B	B	B	B	B	B	B	B	B	B
Core:	142	142	143	144	144	144	145	146	147	148	148	148	149	149
Type:	R	R	R	R	R	R	R	R	R	R	R	R	R	R
Section:	3	7	5	1	4	5	4	4	6	1	1	7	2	7
Top (cm):	92	15	40	142	95	0	38	118	45	101	127	112	55	121
Bottom (cm):	97	18	47	150	103	9	44	124	54	103	132	118	60	126
Piece:	4B	1	2A	3E	2B	1	1	3	2A	2G	3B	4	2	2
Depth (mbsf):	896.7	901.2	908.5	913.7	917.4	917.9	926.4	936.7	947.4	951.9	952.1	960.4	962.3	968.7
Li_Int:	693	693	693	694	700	701	703	703	710	713	715	716	717	719
Rock type:	OlGa	OlGa	OlGa	OpxOxGa	OlGa	OxGa	OlGa	OlGa	OlGa	Ga	OxGa	OlGa	OlGa	OlGa
SiO_2 (wt%):	52.72	52.71	50.80	49.52	54.46	53.25	51.01	49.21	51.56	51.74	44.07	50.01	50.54	51.28
TiO_2 (wt%):	0.39	0.46	0.48	2.15	0.90	1.84	0.30	0.52	0.59	0.29	5.31	0.28	1.38	0.41
Al_2O_3 (wt%):	16.98	18.26	15.50	8.45	16.49	18.55	17.08	15.16	16.97	16.95	10.31	16.55	16.38	15.64
Fe_2O_3 (wt%):	5.00	7.18	7.56	14.36	7.27	7.34	6.58	8.44	7.78	6.36	18.60	10.36	11.77	7.66
MnO (wt%):	0.11	0.13	0.14	0.27	0.06	0.13	0.12	0.14	0.14	0.12	0.24	0.16	0.18	0.14
MgO (wt%):	8.33	7.62	10.82	10.77	6.50	4.82	11.38	12.87	8.72	10.05	8.26	11.53	8.43	9.45
CaO (wt%):	15.07	12.44	13.50	13.36	12.62	10.79	13.10	11.90	11.86	13.47	10.73	9.63	12.63	12.54
Na_2O (wt%):	2.73	3.33	2.49	1.82	3.75	4.23	2.55	2.27	3.12	2.69	2.24	3.01	3.33	2.84
K_2O (wt%):	0.02	0.04	0.02	0.04	0.08	0.12	0.04	0.02	0.05	0.01	0.03	0.03	0.03	0.02
P_2O_5 (wt%):	0.02	0.01	0.03	0.08	0.01	0.01	0.05	0.03	0.03	0.00	0.04	0.01	0.01	0.01
Total (wt%):	101.36	102.16	101.33	100.80	102.14	101.08	102.21	100.56	100.82	101.68	99.83	101.57	104.68	99.99
LOI:	–0.22	0.01	–0.10	1.00	0.05	0.00	–0.21	0.16	0.22	–0.03	0.25	0.43	0.18	0.16
FeO(tit):	4.39	5.38	6.52	11.15	5.71	6.01	5.42	7.19	6.53	5.55	12.62	8.73	5.67	6.28
$\%Fe^{2+}$:	98	83	96	85	87	91	92	95	93	97	75	93	53	91
Mg-value:	0.77	0.72	0.75	0.63	0.67	0.59	0.79	0.76	0.70	0.76	0.54	0.70	0.73	0.73
Mg#:	0.795	0.712	0.769	0.636	0.676	0.605	0.801	0.780	0.723	0.786	0.509	0.722	0.625	0.742
Ca#:	0.753	0.674	0.750	0.803	0.650	0.585	0.739	0.743	0.677	0.735	0.726	0.639	0.677	0.709
V (ppm):	200	173	179	441	275	317	146	137	147	161	1009	96	185	185
Cr (ppm):	249	33	279	214	139	109	285	609	79	190	11	4	0	18
Ni (ppm):	72	74	130	141	48	55	159	189	89	106	97	104	55	80
Cu (ppm):	55	61	68	200	31	55	34	74	56	106	150	88	56	86
Zn (ppm):	31	42	48	92	47	48	40	57	59	38	112	65	41	47
Rb (ppm):	0	0	0	0	0	0	0	0	1	0	2	0	0	1
Sr (ppm):	170	191	151	83	192	218	161	150	179	169	105	175	185	170
Y (ppm):	11	10	12	45	22	18	11	12	16	7	27	8	9	10
Zr (ppm):	27	22	32	85	39	79	38	41	44	20	80	30	23	23
Nb (ppm):	0	0	0	1	0	0	0	2	2	2	3	2	2	2

Table T10 (continued).

176-735B															
Hole:	B	B	B	B	B	B	B	B	B	B	B	B	B	B	B
Core:	150	150	151	152	153	153	154	154	155	155	156	157	157	157	158
Type:	R	R	R	R	R	R	R	R	R	R	R	R	R	R	R
Section:	4	7	4	3	2	7	3	5	1	4	2	3	4	5	4
Top (cm):	102	11	82	68	23	102	67	36	10	1	135	96	66	134	72
Bottom (cm):	107	18	87	72	28	110	72	40	14	6	142	103	72	140	78
Piece:	2	1	5	1	1	1C	4	1	2A	1	4	3	3	8	3
Depth (mbsf):	974.9	978.1	984.1	990.5	997.5	1005.0	1008.8	1011.2	1015.1	1019.3	1026.8	1038.4	1039.7	1042.0	1048.4
Li_Int:	719	719	719	719	721	727	730	731	731	732	734	754	759	760	768
Rock type:	OlGa	OlGa	OlGa	Ga	OlGa	OlGa	DiGa	Ga	OlGa	OlGa	OlGa	OlGa	OxGa	Mixed	OlGa
SiO_2 (wt%):	52.69	52.08	51.72	51.43	52.89	52.55	53.19	53.03	51.81	51.05	52.03	51.60	47.31	49.00	51.68
TiO_2 (wt%):	0.26	0.36	0.34	0.42	0.46	0.60	0.90	0.43	0.40	0.28	0.56	0.78	2.91	2.46	0.35
Al_2O_3 (wt%):	17.66	16.73	16.72	14.96	16.18	16.40	15.34	17.22	16.15	17.74	14.30	14.44	15.95	17.70	16.57
Fe_2O_3 (wt%):	6.95	7.03	6.86	7.81	8.18	7.58	8.63	7.03	7.10	6.96	7.19	8.88	13.85	15.17	6.57
MnO (wt%):	0.13	0.14	0.13	0.14	0.15	0.14	0.18	0.14	0.14	0.12	0.15	0.16	0.19	0.17	0.12
MgO (wt%):	7.93	9.02	9.04	10.31	8.71	8.17	7.45	7.96	8.71	8.77	10.26	10.98	5.74	3.55	9.15
CaO (wt%):	11.32	12.56	12.66	13.01	12.20	11.96	10.75	12.26	13.99	11.63	14.33	13.23	9.75	6.73	12.99
Na_2O (wt%):	3.50	3.13	2.97	2.69	3.31	3.32	3.73	3.43	3.12	3.18	2.48	2.49	3.51	4.58	2.90
K_2O (wt%):	0.03	0.02	0.02	0.02	0.04	0.04	0.18	0.03	0.02	0.02	0.02	0.06	0.10	0.74	0.02
P_2O_5 (wt%):	0.01	0.01	0.00	0.01	0.01	0.01	0.42	0.01	0.01	0.01	0.02	0.04	1.09	0.38	0.01
Total (wt%):	100.48	101.08	100.46	100.80	102.13	100.77	100.74	101.54	101.44	99.75	101.31	102.66	100.40	100.46	100.36
LOI:	–0.06	0.22	0.07	0.09	0.15	0.00	0.00	0.05	–0.07	–0.01	0.11	0.13	0.19	–0.07	–0.01
FeO(tit):	5.38	5.89	5.82	6.62	6.86	6.17	6.56	5.19	5.67	5.97	5.85	7.34	8.69	8.57	5.48
$\%Fe^{2+}$:	86	93	94	94	93	90	84	82	89	95	90	92	70	63	93
Mg-value:	0.72	0.73	0.73	0.74	0.69	0.70	0.67	0.73	0.73	0.72	0.76	0.73	0.54	0.42	0.75
Mg#:	0.727	0.749	0.754	0.755	0.713	0.715	0.668	0.725	0.741	0.746	0.769	0.742	0.491	0.353	0.765
Ca#:	0.641	0.689	0.702	0.728	0.671	0.666	0.614	0.664	0.712	0.669	0.762	0.746	0.605	0.448	0.712
V (ppm):	124	181	174	186	198	201	138	185	183	134	225	213	293	149	171
Cr (ppm):	0	2	33	48	0	0	7	0	1	28	78	82	86	4	50
Ni (ppm):	60	63	87	78	58	50	54	48	63	89	72	99	65	44	83
Cu (ppm):	45	72	81	73	78	50	82	51	72	71	72	76	108	93	72
Zn (ppm):	47	44	41	47	50	48	78	42	42	49	41	58	125	65	44
Rb (ppm):	0	0	0	0	0	1	2	1	1	2	2	2	1	6	0
Sr (ppm):	202	179	179	161	175	178	166	186	176	173	146	143	208	200	169
Y (ppm):	7	9	11	12	14	12	77	13	12	10	16	19	54	53	8
Zr (ppm):	21	22	21	25	29	24	162	24	22	22	34	75	101	995	22
Nb (ppm):	1	1	0	0	0	0	6	1	0	0	0	2	8	9	1

Table T10 (continued).

176-735B															
Hole:	B	B	B	B	B	B	B	B	B	B	B	B	B	B	B
Core:	158	159	159	159	159	160	161	161	162	162	162	164	165	166	167
Type:	R	R	R	R	R	R	R	R	R	R	R	R	R	R	R
Section:	5	2	2	4	4	2	4	6	2	8	8	3	3	5	6
Top (cm):	135	0	41	84	111	24	26	59	65	24	45	21	104	70	0
Bottom (cm):	148	7	47	89	116	28	35	64	71	29	50	29	106	77	6
Piece:	4	1A	2	3A	3B	1B	1C	3A	1C	1	1	1A	2A	3	1
Depth (mbsf):	1050.4	1055.0	1055.5	1058.8	1059.1	1065.1	1077.1	1080.1	1084.4	1091.3	1091.5	1102.8	1107.6	1116.9	1127.1
Li_Int:	769	774	774	776	776	780	788	790	790	797	798	802	805	810	810
Rock type:	OlGa	OlGa	Mixed	Ga	mixed	OlGa	OlGa	OlGa	OlGa	OlGa	OlGa	OlGa	OlGa	Ga	OlGa
SiO_2 (wt%):	51.56	51.32	48.35	51.80	57.17	53.46	52.42	51.42	50.30	53.00	52.94	51.26	52.50	52.09	52.57
TiO_2 (wt%):	1.04	0.57	2.57	0.40	1.61	0.30	0.51	0.39	0.36	0.24	0.41	0.35	0.25	0.36	0.35
Al_2O_3 (wt%):	13.71	14.51	14.99	16.51	16.54	21.23	15.91	15.97	16.20	19.60	15.71	16.09	17.70	16.26	15.77
Fe_2O_3 (wt%):	8.49	7.91	13.29	5.49	11.37	4.56	7.83	7.33	7.69	6.26	6.08	6.67	6.36	6.63	7.03
MnO (wt%):	0.16	0.15	0.18	0.11	0.12	0.09	0.15	0.14	0.13	0.12	0.13	0.13	0.12	0.13	0.14
MgO (wt%):	10.20	9.69	5.61	8.35	2.75	6.08	8.82	10.14	10.99	8.00	8.93	9.09	10.08	8.79	9.88
CaO (wt%):	12.97	12.53	9.21	13.71	5.57	12.48	12.31	12.56	11.95	12.07	14.10	12.65	13.75	13.33	13.24
Na_2O (wt%):	2.68	2.84	3.81	2.86	5.58	3.66	3.13	2.67	2.64	3.42	2.86	2.90	2.86	2.91	2.86
K_2O (wt%):	0.05	0.05	0.20	0.02	0.24	0.03	0.08	0.04	0.02	0.02	0.02	0.02	0.01	0.03	0.02
P_2O_5 (wt%):	0.08	0.02	0.39	0.01	0.29	0.01	0.06	0.03	0.01	0.01	0.01	0.01	0.01	0.01	0.01
Total (wt%):	100.92	99.59	98.60	99.26	101.24	101.90	101.22	100.69	100.29	102.74	101.19	99.17	103.64	100.54	101.87
LOI:	0.20	–0.16	–0.21	–0.21	–0.17	–0.08	–0.07	–0.11	–0.05	0.02	–0.14	–0.02	–0.14	–0.01	–0.03
FeO(tit):	6.50	6.00	7.88	4.90	5.85	3.75	6.27	5.47	6.34	5.60	5.06	5.36	5.08	5.25	5.36
$\%Fe^{2+}$:	85	84	66	99	57	91	89	83	92	99	93	89	89	88	85
Mg-value:	0.74	0.74	0.56	0.75	0.46	0.74	0.71	0.77	0.76	0.72	0.76	0.75	0.78	0.75	0.77
Mg#:	0.737	0.741	0.496	0.780	0.361	0.757	0.724	0.763	0.769	0.749	0.774	0.761	0.787	0.756	0.766
Ca#:	0.728	0.709	0.572	0.726	0.355	0.653	0.685	0.722	0.714	0.661	0.731	0.707	0.727	0.717	0.719
V (ppm):	271	203	210	189	66	115	181	162	137	114	196	160	149	171	160
Cr (ppm):	30	47	25	92	0	35	25	63	52	13	44	35	209	44	66
Ni (ppm):	78	96	62	75	26	65	80	116	116	76	71	82	96	78	92
Cu (ppm):	43	85	91	64	10	82	61	90	77	94	44	89	96	75	90
Zn (ppm):	53	57	99	36	51	31	54	46	48	36	39	40	33	39	40
Rb (ppm):	2	2	2	3	3	0	0	0	0	0	0	2	1	2	2
Sr (ppm):	141	149	156	175	145	220	164	161	164	197	160	164	167	170	163
Y (ppm):	19	19	108	11	158	6	20	11	8	5	9	14	10	14	14
Zr (ppm):	65	80	227	26	1252	27	109	45	24	20	26	25	18	29	25
Nb (ppm):	2	2	14	1	20	1	2	2	1	1	2	0	0	0	0

Table T10 (continued).

176-735B															
Hole:	B	B	B	B	B	B	B	B	B	B	B	B	B	B	B
Core:	168	168	169	170	171	171	172	173	175	175	176	177	178	179	180
Type:	R	R	R	R	R	R	R	R	R	R	R	R	R	R	R
Section:	2	3	4	2	2	5	3	1	1	4	3	6	6	5	5
Top (cm):	0	51	36	65	56	92	69	102	85	99	79	111	134	100	0
Bottom (cm):	6	56	45	69	62	99	76	111	91	117	86	118	136	106	8
Piece:	1	7	2A	3A	3	3	2A	8	4	2D	2A	4B	5B	3	1
Depth (mbsf):	1131.3	1133.3	1144.6	1151.0	1160.9	1165.5	1172.1	1179.5	1191.9	1195.6	1198.8	1209.6	1219.2	1227.0	1236.8
Li_Int:	810	810	812	814	822	829	829	831	831	835	837	837	838	845	853
Rock type:	OlGa	altGa	Ga	OlGa	OpxOxGa	OlGa	OlGa	OlGa	OlGa	OlGa	OlGa	OlGa	OlGa	OlGa	TrocGa
SiO_2 (wt%):	53.41	53.27	53.56	53.52	49.67	51.33	51.67	49.58	49.52	52.38	51.98	51.34	50.97	51.76	50.82
TiO_2 (wt%):	0.35	0.24	0.35	0.35	1.73	1.17	0.41	0.32	0.31	0.42	0.41	0.33	0.47	0.24	0.29
Al_2O_3 (wt%):	16.68	18.82	17.50	17.37	14.19	15.26	16.79	15.51	15.43	16.58	16.21	16.96	17.36	18.38	18.21
Fe_2O_3 (wt%):	6.49	7.15	6.65	6.58	13.01	7.82	6.25	7.61	7.35	7.03	7.08	7.92	10.74	7.07	8.13
MnO (wt%):	0.14	0.11	0.13	0.13	0.23	0.14	0.12	0.13	0.13	0.14	0.14	0.14	0.16	0.13	0.13
MgO (wt%):	9.40	8.37	8.56	8.62	6.57	8.00	8.12	11.59	11.30	10.64	10.98	10.82	10.08	10.12	10.68
CaO (wt%):	13.93	10.31	12.75	12.74	10.45	12.84	12.26	11.76	12.15	13.71	14.01	12.65	10.84	12.20	11.21
Na_2O (wt%):	2.75	4.16	3.50	3.10	3.31	2.92	3.20	2.58	2.49	2.68	2.44	2.65	3.13	2.93	2.90
K_2O (wt%):	0.03	0.61	0.05	0.03	0.07	0.04	0.07	0.02	0.02	0.03	0.02	0.03	0.04	0.03	0.04
P_2O_5 (wt%):	0.01	0.01	0.01	0.00	1.15	0.02	0.04	0.02	0.02	0.03	0.02	0.02	0.01	0.01	0.03
Total (wt%):	103.19	103.05	103.06	102.44	100.38	99.54	98.93	99.12	98.72	103.64	103.29	102.86	103.80	102.87	102.44
LOI:	–0.12	–5.15	–0.13	–0.03	0.20	0.01	–0.46	–0.75	–0.10	–0.42	–0.18	–0.50	0.10	–0.28	–0.14
FeO(tit):	4.96	3.52	5.11	5.10	9.23	7.02	5.44	6.22	6.12	5.66	5.79	4.92	5.79	5.66	6.30
$\%Fe^{2+}$:	85	58	86	86	79	100	97	92	93	90	91	69	60	89	86
Mg-value:	0.77	0.80	0.75	0.75	0.56	0.67	0.73	0.77	0.77	0.77	0.77	0.80	0.76	0.76	0.75
Mg#:	0.771	0.732	0.750	0.753	0.541	0.705	0.752	0.780	0.782	0.779	0.783	0.761	0.686	0.769	0.754
Ca#:	0.737	0.578	0.668	0.694	0.636	0.708	0.679	0.716	0.729	0.739	0.760	0.725	0.657	0.697	0.681
V (ppm):	171	105	156	132	254	223	151	130	138	163	182	146	128	119	101
Cr (ppm):	64	29	31	35	31	66	149	117	192	185	323	164	380	79	66
Ni (ppm):	82	106	72	65	72	99	94	165	167	109	123	121	159	120	136
Cu (ppm):	74	53	83	37	84	140	70	113	155	53	106	64	102	68	80
Zn (ppm):	38	52	39	42	116	52	46	48	48	40	43	47	41	41	52
Rb (ppm):	2	3	2	0	0	0	0	0	0	0	0	0	2	0	0
Sr (ppm):	165	189	194	203	177	167	181	172	161	161	154	166	180	184	184
Y (ppm):	13	12	14	12	72	16	16	7	9	9	10	7	10	5	6
Zr (ppm):	27	26	27	79	67	51	67	30	33	32	31	31	22	22	32
Nb (ppm):	0	0	0	3	4	2	3	1	1	2	2	2	0	2	2

Table T10 (continued).

176-735B															
Hole:	B	B	B	B	B	B	B	B	B	B	B	B	B	B	B
Core:	181	182	183	184	185	186	187	188	189	190	190	191	191	192	193
Type:	R	R	R	R	R	R	R	R	R	R	R	R	R	R	R
Section:	2	2	2	5	5	6	5	4	5	3	4	3	8	4	1
Top (cm):	83	99	16	55	2	40	54	102	1	68	70	83	31	54	88
Bottom (cm):	100	111	23	62	9	46	60	110	6	77	76	85	36	61	93
Piece:	9A	7	1B	3A	1	1	2B	2C	1A	5B	3	3C	2	2	3B
Depth (mbsf):	1243.8	1254.7	1261.5	1276.7	1284.3	1296.2	1304.2	1312.2	1322.2	1329.8	1331.4	1339.4	1345.1	1350.0	1358.5
Li_Int:	856	861	864	870	872	876	878	880	884	889	890	895	898	900	902
Rock type:	altGa	Troc	OlGa	OlGa	Ga	OlGa	OlGa	OlGa	OlGa	OxGa	OlGa	DiOlGa	OlGa	OlGa	OlGa
SiO_2 (wt%):	53.99	52.37	52.48	52.13	52.98	52.91	52.54	51.11	52.53	44.95	51.92	50.89	52.00	52.72	53.11
TiO_2 (wt%):	0.25	0.36	0.27	0.21	0.34	0.33	0.30	0.26	0.27	6.62	0.49	0.46	0.48	0.38	0.43
Al_2O_3 (wt%):	19.28	16.97	16.86	19.82	17.17	17.44	17.29	16.55	17.12	13.95	16.12	17.17	16.32	16.72	18.72
Fe_2O_3 (wt%):	5.20	6.55	5.93	5.92	5.61	5.78	6.41	6.69	6.25	15.84	8.49	10.52	6.88	6.73	5.99
MnO (wt%):	0.10	0.13	0.13	0.11	0.12	0.12	0.12	0.13	0.12	0.19	0.15	0.16	0.13	0.13	0.12
MgO (wt%):	6.75	9.83	10.02	9.08	9.39	9.51	10.03	10.72	9.89	8.29	11.02	9.98	9.90	10.10	8.15
CaO (wt%):	10.17	13.50	14.35	12.78	14.96	14.48	14.08	13.49	13.93	9.70	12.82	10.75	13.81	13.48	13.08
Na_2O (wt%):	4.26	2.82	2.53	3.06	2.70	2.69	2.66	2.51	2.60	2.58	2.65	3.01	2.65	3.00	3.18
K_2O (wt%):	1.63	0.03	0.01	0.02	0.02	0.02	0.02	0.01	0.01	0.04	0.03	0.03	0.04	0.04	0.04
P_2O_5 (wt%):	0.03	0.02	0.01	0.01	0.01	0.01	0.01	0.00	0.00	0.01	0.02	0.01	0.07	0.02	0.04
Total (wt%):	101.66	102.58	102.59	103.14	103.30	103.29	103.46	101.47	102.72	102.17	103.71	102.98	102.28	103.32	102.86
LOI:	–4.12	–0.22	–0.34	–0.21	–0.23	–0.08	–0.17	–0.37	–0.03	0.43	–0.07	0.14	–0.15	–0.09	–0.16
FeO(tit):	2.79	5.58	4.60	5.03	4.37	4.98	5.12	5.12	4.87	11.23	6.53	7.95	5.35	5.11	4.81
$\%Fe^{2+}$:	62	95	87	95	87	96	89	85	87	78	86	84	87	84	89
Mg-value:	0.81	0.76	0.79	0.76	0.79	0.77	0.78	0.79	0.78	0.57	0.75	0.69	0.77	0.78	0.75
Mg#:	0.752	0.778	0.798	0.781	0.796	0.793	0.785	0.789	0.787	0.550	0.752	0.689	0.770	0.778	0.760
Ca#:	0.569	0.726	0.758	0.698	0.754	0.748	0.745	0.748	0.747	0.675	0.728	0.664	0.742	0.713	0.694
V (ppm):	102	173	176	109	185	173	164	161	164	985	167	187	188	168	155
Cr (ppm):	52	131	268	124	174	196	188	157	137	401	155	410	197	74	66
Ni (ppm):	84	101	96	107	111	99	116	129	113	167	131	210	104	100	79
Cu (ppm):	35	58	66	62	106	67	102	90	102	134	80	91	59	69	49
Zn (ppm):	35	41	33	34	33	34	36	37	34	77	53	58	42	38	37
Rb (ppm):	7	0	0	0	0	0	0	0	0	1	0	2	0	2	1
Sr (ppm):	244	165	166	196	167	172	166	157	168	143	159	188	163	176	193
Y (ppm):	8	9	6	4	7	6	7	6	5	12	10	11	11	12	11
Zr (ppm):	78	34	18	17	19	21	19	16	15	90	29	23	50	28	33
Nb (ppm):	1	2	1	2	2	2	2	2	1	5	1	0	2	0	0

Table T10 (continued).

176-735B															
Hole:	B	B	B	B	B	B	B	B	B	B	B	B	B	B	B
Core:	195	195	196	197	198	199	199	199	200	201	202	202	203	204	205
Type:	R	R	R	R	R	R	R	R	R	R	R	R	R	R	R
Section:	2	4	4	3	1	2	2	6	4	7	5	8	5	7	2
Top (cm):	7	73	99	87	126	71	123	56	45	106	119	72	119	34	132
Bottom (cm):	13	79	106	89	132	77	129	63	52	112	124	74	126	42	142
Piece:	1	4	7B	5A	9B	2A	5	3	2A	4	2C	2	4	2	3
Depth (mbsf):	1365.6	1368.8	1378.3	1385.7	1387.6	1394.5	1395.0	1400.3	1406.6	1420.8	1427.6	1430.8	1437.7	1448.8	1452.7
Li_Int:	904	905	909	910	913	915	915	915	919	919	919	919	925	927	930
Rock type:	Ga	Ga	TrocGa	OlGa	Ga	Ga	OlGa	TrocGa	OlGa	OlGa	Ga	TrocGa	OlGa	OlGa	OlGa
SiO_2 (wt%):	53.00	52.84	52.14	52.73	52.56	52.35	51.57	49.90	52.04	52.61	54.33	49.83	52.57	52.36	52.57
TiO_2 (wt%):	0.47	0.28	0.25	0.29	0.36	0.42	0.44	0.22	0.29	0.45	0.32	0.39	0.29	0.37	0.29
Al_2O_3 (wt%):	17.73	22.61	20.04	17.11	17.06	16.62	14.63	17.14	21.07	17.75	22.86	17.99	22.93	16.58	22.93
Fe_2O_3 (wt%):	5.58	3.98	6.28	6.42	6.64	6.23	6.93	8.07	5.32	6.52	3.15	9.80	4.04	5.87	4.04
MnO (wt%):	0.12	0.08	0.11	0.12	0.13	0.12	0.13	0.13	0.09	0.13	0.08	0.16	0.08	0.12	0.08
MgO (wt%):	8.87	5.58	9.48	9.88	9.79	9.82	11.86	13.01	7.25	9.64	4.97	10.47	6.23	10.27	6.23
CaO (wt%):	14.19	12.87	12.01	13.73	13.31	13.53	14.31	11.02	12.38	13.91	14.29	11.19	12.92	14.64	12.92
Na_2O (wt%):	2.86	3.57	3.07	2.70	2.93	3.01	2.23	2.58	3.42	2.69	3.60	2.74	3.47	2.39	3.47
K_2O (wt%):	0.03	0.03	0.02	0.02	0.02	0.04	0.02	0.02	0.04	0.02	0.04	0.03	0.04	0.02	0.04
P_2O_5 (wt%):	0.04	0.02	0.01	0.00	0.01	0.01	0.01	0.01	0.02	0.01	0.01	0.02	0.02	0.01	0.02
Total (wt%):	102.89	101.86	103.41	103.00	102.81	102.15	102.13	102.10	101.92	103.73	103.65	102.62	102.59	102.63	102.59
LOI:	–0.13	–0.27	0.01	–0.14	–0.22	–2.73	–0.20	–0.15	–0.12	–0.32	–0.33	0.22	–0.39	–0.39	–0.39
FeO(tit):	4.50	3.32	4.97	5.13	5.23	4.08	5.46	6.23	4.20	4.79	2.47	7.81	3.06	4.61	3.60
$\%Fe^{2+}$:	90	93	88	89	88	75	88	86	88	82	87	88	85	88	99
Mg-value:	0.78	0.75	0.77	0.77	0.77	0.81	0.79	0.79	0.75	0.78	0.78	0.71	0.78	0.80	0.75
Mg#:	0.787	0.766	0.779	0.782	0.775	0.786	0.800	0.790	0.761	0.775	0.786	0.714	0.782	0.803	0.782
Ca#:	0.733	0.666	0.684	0.738	0.715	0.713	0.780	0.702	0.667	0.741	0.687	0.693	0.673	0.772	0.673
V (ppm):	165	100	91	175	170	173	201	89	100	162	126	132	93	195	205
Cr (ppm):	111	61	51	125	74	165	188	81	70	184	116	432	81	242	304
Ni (ppm):	88	63	120	116	101	140	133	174	86	112	46	229	71	103	113
Cu (ppm):	58	53	81	96	80	106	92	125	72	66	47	17	34	66	23
Zn (ppm):	33	24	36	39	36	36	37	46	31	39	18	60	23	33	30
Rb (ppm):	1	0	1	0	2	1	1	0	0	0	1	0	1	1	1
Sr (ppm):	178	227	202	175	173	151	142	170	219	174	218	169	221	155	146
Y (ppm):	14	10	8	8	12	13	13	9	6	8	9	13	8	13	13
Zr (ppm):	45	32	22	16	22	28	27	21	25	25	26	33	26	28	24
Nb (ppm):	0	0	0	1	0	0	0	0	1	1	0	1	0	0	0

Table T10 (continued).

	176-735B												
Hole:	B	B	B	B	B	B	B	B	B	B	B	B	B
Core:	205	206	207	207	208	208	209	209	210	200	200	210	210
Type:	R	R	R	R	R	R	R	R	R	R	R	R	R
Section:	4	4	4	7	4	5	2	8	4	2	8	4	4
Top (cm):	102	51	60	117	1	96	75	109	1	75	109	1	58
Bottom (cm):	111	57	62	123	7	102	77	117	7	77	117	7	65
Piece:	3B	2	1B	2B	1	3B	1E	4	1	1E	4	1	1
Depth (mbsf):	1455.1	1464.6	1473.9	1479.0	1482.6	1484.9	1490.4	1497.9	1502.5	1490.4	1497.9	1502.5	1503.0
Li_Int:	931	936	942	945	946	947	950	952	952	950	952	952	952
Rock type:	OlGa	Ga	OlGa	LeuGa	OlGa	OlGa	OlGa	OlGa	Ga	OlGa	OlGa	Ga	OlGa
SiO_2 (wt%):	52.82	52.75	52.71	53.70	53.20	52.73	53.26	52.31	53.48	53.26	52.31	53.48	52.79
TiO_2 (wt%):	0.34	0.38	0.23	0.19	0.41	0.53	0.27	0.27	0.30	0.27	0.27	0.30	0.39
Al_2O_3 (wt%):	18.46	14.30	17.58	25.26	15.66	11.21	17.50	17.68	18.03	17.50	17.68	18.03	15.29
Fe_2O_3 (wt%):	5.16	6.31	5.45	2.78	5.33	7.42	5.32	5.36	5.28	5.32	5.36	5.28	6.00
MnO (wt%):	0.11	0.14	0.11	0.07	0.12	0.16	0.11	0.11	0.11	0.11	0.11	0.11	0.13
MgO (wt%):	8.83	11.98	9.79	3.74	9.68	12.99	9.76	9.46	9.28	9.76	9.46	9.28	10.78
CaO (wt%):	14.38	14.61	14.06	13.10	15.69	16.06	14.50	14.11	14.60	14.60	14.11	14.60	15.21
Na_2O (wt%):	2.83	2.59	2.57	3.85	2.36	1.77	2.57	2.68	2.67	2.57	2.68	2.67	2.34
K_2O (wt%):	0.02	0.05	0.01	0.03	0.01	0.01	0.01	0.01	0.01	0.01	0.01	0.01	0.01
P_2O_5 (wt%):	0.01	0.01	0.00	0.01	0.01	0.01	0.00	0.01	0.00	0.00	0.01	0.00	0.01
Total (wt%):	102.96	103.12	102.51	102.73	102.47	102.89	103.30	102.00	103.76	103.30	102.00	103.76	102.95
LOI:	–0.41	–2.34	–0.24	–0.84	–0.36	–0.29	–0.15	–0.31	–0.31	0.16	0.31	–0.31	–0.23
FeO(tit):	4.13	3.61	4.21	2.27	4.07	5.94	4.38	4.53	4.01	4.38	4.53	4.01	4.88
$\%Fe^{2+}$:	89	65	86	92	85	89	92	94	85	92	94	85	91
Mg-value:	0.79	0.85	0.81	0.74	0.81	0.80	0.80	0.79	0.80	0.80	0.70	0.80	0.80
Mg#:	0.800	0.816	0.807	0.758	0.809	0.803	0.810	0.804	0.804	0.81	0.80	0.80	0.81
Ca#:	0.737	0.757	0.751	0.653	0.786	0.834	0.757	0.744	0.751	0.76	0.74	0.75	0.78
V (ppm):	147	158	165	73	220	283	173	132	173	173	132	173	209
Cr (ppm):	179	200	190	62	272	223	200	123	181	200	123	181	196
Ni (ppm):	86	68	118	50	81	110	114	105	99	114	105	99	97
Cu (ppm):	34	51	115	65	50	55	125	73	96	125	73	96	47
Zn (ppm):	29	23	30	18	31	39	29	31	29	29	31	29	33
Rb (ppm):	1	0	0	0	1	0	0	0	0	0	0	0	2
Sr (ppm):	182	192	168	248	150	105	165	182	172	165	182	172	147
Y (ppm):	11	12	7	3	14	15	7	10	7	7	10	7	13
Zr (ppm):	28	27	14	21	26	30	15	21	17	15	21	17	24
Nb (ppm):	0	0	2	1	1	1	0	0	2	0	0	2	0

Table T11. CO_2 and H_2O content of volatile-rich samples.

Core, section, interval (cm)	Piece	Depth (mbsf)	LOI (wt%)	CO_2 (wt%)	H_2O (wt%)
118-735B-					
88N-1, 48-51	2B	500.5	1.30	0.06	1.71
176-735B-					
90R-4, 41-47	1B	512.0	2.22	0.08	3.06
91R-3, 92-100	1D	522.5	9.24	6.92	3.16
92R-1, 25-30	4	527.5	1.68	0.71	1.21
119R-1, 72-77	7	701.4	1.31	0.63	0.87
132R-1, 62-70	11A	813.8	5.01	3.31	2.77
133R-7, 127-133	1H	832.4	3.97	0.36	3.59
168R-3, 51-56	7	1133.3	5.15	0.58	5.32
181R-2, 83-100	9A	1243.8	4.12	0.68	4.18
199R-2, 71-77	2A	1394.5	2.73	0.09	3.03

Notes: LOI = weight loss on ignition. CO_2 and H_2O determined using a CHNS gas analyzer.

Table T12. Summary of magnetic properties of discrete samples from Leg 176. (Continued on next 5 pages.)

Core, section, interval (cm)	Curated depth (mbsf)	NRM (A/m)	Volume susceptibility (10^{-6} SI)	Q	Best-fit direction							MDF (mT)	MDF′ (mT)
					N	Type	MAD	Declination (°)	Inclination (°)	Low	High		
176-735B-													
89R-1 (Piece 2, 19-21)	504.99	0.719	5,496	4.36	8	F	1.2	323.7	68.4	8	50	33.1	32.8
90R-1 (Piece 2, 115-117)	508.95	0.766	4,323	5.91	5	F	3.8	129.1	74.2	15	50	35.3	28.6
90R-1 (Piece 2, 119-121)	508.99	0.660	3,292	6.68	6	F	3.7	149.4	52.8	500	585		
90R-3 (Piece 2C, 95-97)	511.72	0.120	1,602	2.50	3	F	16.4	220.3	84.5	30	50	10.0	10.3
90R-4 (Piece 1B, 35-37)	512.34	0.406	2,142	6.32	7	F	2.4	15.0	53.4	12	60	26.0	25.9
90R-4 (Piece 1B, 38-40)	512.37	0.227	1,979	3.82	6	F	5.3	204.6	54.1	500	585		
90R-6 (Piece 5A, 105-107)	515.56	0.807	5,492	4.90	7	F	3.9	41.4	65.3	12	60	28.9	28.6
90R-7 (Piece 1B, 56-58)	516.49	0.773	4,920	5.24	5	F	4.4	75.2	75.0	30	80	31.2	23.9
90R-7 (Piece 1B, 59-61)	516.52	0.861	5,122	5.60	6	F	7.2	228.0	65.7	500	585		
90R-8 (Piece 1A, 27-29)	517.13	0.202	2,586	2.60	6	F	14.3	210.3	69.6	25	80	20.0	14.4
91R-1 (Piece 2B, 36-38)	517.76	0.373	3,532	3.52	10	F	3.6	74.5	69.7	8	60	19.1	23.0
91R-1 (Piece 3B, 108-110)	518.48	0.537	9,092	1.97	4	F	11.1	282.1	85.3	25	50	12.1	11.6
91R-1 (Piece 3B, 111-113)	518.51	0.627	10,997	1.90	6	F	12.7	182.1	41.6	500	585		
91R-3 (Piece 1E, 113-115)	521.08	0.114	2,257	1.68	6	F	5.7	110.9	53.0	20	60	34.7	47.7
91R-3 (Piece 1E, 116-118)	521.11	0.115	2,075	1.85	6	F	11.7	201.5	43.8	500	585		
92R-1 (Piece 6A, 39-41)	527.39												
93R-1 (Piece 3B, 33-35)	532.43												
93R-1 (Piece 3B, 36-38)	532.46	3.610	12,480	9.64	7	F	1.5	232.0	73.1	5	60	12.9	12.9
93R-2 (Piece 3, 94-96)	534.15	1.410	6,713	7.00	5	F	3.8	24.6	73.0	20	80	33.3	25.8
93R-2 (Piece 3, 97-99)	534.18	0.690	6,195	3.71	6	F	4.1	53.5	83.3	500	600		
93R-3 (Piece 1E, 85-87)	535.29	1.940	9,129	7.08	8	F	1.3	191.9	62.9	12	60	18.0	16.0
93R-3 (Piece 1E, 88-90)	535.32	2.650	11,910	7.42	6	F	2.1	190.3	58.5	500	600		
93R-5 (Piece 3, 33-35)	537.37	3.440	28,457	4.03					27.8	19.1			
93R-5 (Piece 3, 37-39)	537.41	4.370	23,292	6.25	9	F	5.0	237.8	70.9	300	585		
94R-1 (Piece 1B, 30-32)	536.90	2.140	18,064	3.95	5	F	2.4	35.0	72.2	20	80		
94R-1 (Piece 1B, 33-35)	536.93	1.480	3,388	14.56	8	F	1.8	348.7	68.6	400	600		
94R-3 (Piece 5, 52-54)	539.71	1.660	6,939	7.97	12	F	1.0	218.7	69.9	6	80	25.8	25.6
94R-3 (Piece 5, 55-57)	539.74	1.590	6,688	7.93	12	F	1.3	215.6	71.6	6	80	24.8	24.6
94R-3 (Piece 12, 116-118)	540.35	4.250	7,880	17.98	7	F	2.2	328.6	78.0	10	80	11.6	11.4
94R-3 (Piece 12, 123-125)	540.42	2.050	6,155	11.10	10	F	3.9	357.7	79.4	300	600		
95R-1 (Piece 8, 118-120)	545.78	1.950	17,145	3.79	7	F	2.2	48.4	71.4	10	40	8.9	8.8
95R-1 (Piece 8, 121-123)	545.81	1.000	8,200	4.07	9	F	7.7	58.5	69.8	400	600		
95R-3 (Piece 1C, 19-21)	547.58	9.490	43,856	7.21	7	F	1.5	193.9	75.1	10	70	7.5	7.5
96R-1 (Piece 4, 27-29)	548.57	2.590	2,797	30.87	9	F	2.3	266.3	–72.7	300	585		
96R-1 (Piece 4, 30-32)	548.60	3.230	3,890	27.68	5	F	2.1	281.4	–73.3	20	80	8.1	8.0
96R-2 (Piece 4, 49-51)	550.29	5.400	14,763	12.19	4	F	0.9	84.8	75.4	20	70	12.9	12.8
97R-1 (Piece 2C, 125-127)	557.55	2.770	6,741	13.70	6	F	3.1	36.9	83.1	450	585		
97R-1 (Piece 2C, 128-130)	557.58	4.530	12,098	12.48	8	F	1.0	157.5	75.3	5	80	18.2	18.2
97R-3 (Piece 1C, 26-28)	559.08	9.680	29,126	11.08	7	F	1.1	134.2	67.6	5	70	4.7	4.7
98R-1 (Piece 5B, 40-42)	561.40	0.402	1,311	10.22	13	F	1.0	191.6	82.8	6	80	35.5	35.0
99R-3 (Piece 5, 72-74)	569.53	2.980	4,840	20.52	8	F	1.8	262.7	79.0	15	80	33.3	32.3
99R-3 (Piece 5, 75-77)	569.56	2.260	5,083	14.82	6	F	4.0	252.4	65.1	450	585		
99R-4 (Piece 1C, 23-25)	570.25	3.150	6,267	16.75	11	F	1.7	232.9	68.1	8	80	23.1	22.7
99R-6 (Piece 3, 30-32)	573.04	0.940	3,363	9.32	9	F	1.7	358.7	81.6	12	80	26.3	25.7
100R-1 (Piece 3D, 43-45)	575.93	2.290	12,468	6.12	7	F	0.8	168.4	78.0	10	80	12.9	12.9
101R-3 (Piece 1D, 31-33)	587.93	1.520	4,398	11.52	4	F	3.6	347.6	65.9	20	70	13.2	13.4
101R-3 (Piece 1D, 34-36)	587.96	1.540	4,300	11.94	6	F	4.6	310.6	78.0	450	585		
101R-4 (Piece 1B, 27-29)	589.08	0.399	2,338	5.69	6	F	3.0	189.7	67.4	10	60	10.5	10.6
102R-1 (Piece 4A, 28-30)	590.18	6.000	45,000	4.44	7	F	1.7	333.3	77.1	20	80	10.7	10.5
102R-3 (Piece 6, 58-60)	593.36	0.372	1,971	6.29	7	F	4.6	349.5	61.8	20	80	24.2	24.1
103R-2 (Piece 3E, 81-83)	597.00	1.570	2,934	17.84	5	F	2.4	169.9	61.4	30	80	32.4	31.5
103R-2 (Piece 3E, 84-86)	597.03	1.690	1,775	31.74	6	F	2.0	209.8	73.3	450	585		
103R-3 (Piece 3D, 48-50)	598.13	15.700	97,735	5.35	7	F	1.1	281.2	72.7	40	180	13.8	13.1
103R-4 (Piece 4A, 31-33)	599.46	1.270	2,740	15.45	5	F	0.8	172.6	79.7	15	70	30.0	29.9
104R-2 (Piece 6B, 49-51)	606.29	2.280	10,723	7.09	5	F	2.2	251.9	72.6	15	70	8.6	8.5
104R-2 (Piece 6B, 52-54)	606.32	2.290	9,983	7.65	10	F	6.9	228.0	66.7	300	585		
104R-3 (Piece 1C, 36-38)	607.30	11.700	38,419	10.15	5	F	1.4	2.9	66.5	15	70	4.8	4.7
105R-1 (Piece 8B, 52-54)	609.32	3.250	12,537	8.64	5	F	1.6	70.7	69.6	20	80	7.7	7.6
105R-3 (Piece 7, 94-96)	612.63	2.830	11,611	8.12	5	F	2.3	317.4	81.7	20	80	9.6	9.4
105R-3 (Piece 7, 97-99)	612.66	3.810	14,205	8.94	9	F	7.1	284.3	82.3	300	585		
106R-1 (Piece 10, 73-75)	614.63	3.790	16,982	7.44	4	F	4.4	337.3	60.2	20	60	4.4	4.5
106R-4 (Piece 4B, 54-56)	618.63	2.830	6,506	14.50	10	F	1.7	25.6	71.3	10	90	19.9	19.4
108R-2 (Piece 2, 44-46)	625.41	5.360	11,723	15.24	12	F	1.5	127.8	79.8	4	70	14.7	14.5
108R-2 (Piece 2, 47-49)	625.44	4.320	8,384	17.17	6	F	4.8	101.7	61.8	450	585		
108R-4 (Piece 4, 87-89)	628.48	4.280	8,948	15.94	9	F	1.6	22.1	74.2	20	90	19.6	18.6
110R-1 (Piece 2D, 46-48)	633.56	4.360	6,464	22.48	8	F	2.6	359.8	77.6	40	120	30.1	29.2

Table T12 (continued).

Core, section, interval (cm)	Curated depth (mbsf)	NRM (A/m)	Volume susceptibility (10^{-6} SI)	Q	Best-fit direction							MDF (mT)	MDF′ (mT)
					N	Type	MAD	Declination (°)	Inclination (°)	Low	High		
110R-4 (Piece 2B, 57-59)	638.01	1.930	4,187	15.37	11	F	2.5	316.9	68.4	15	120	47.7	39.9
110R-4 (Piece 2B, 60-62)	638.04	2.040	4,815	14.12	7	F	2.0	325.8	78.3	450	600		
111R-2 (Piece 3, 105-107)	640.42	4.010	8,302	16.10	8	F	1.9	10.4	71.4	15	80	16.9	15.7
111R-2 (Piece 3, 108-110)	640.45	4.000	9,284	14.36	6	F	2.5	12.5	77.7	500	600		
112R-1 (Piece 3B, 54-56)	643.24	3.410	11,088	10.25	5	F	1.7	90.4	66.7	20	80	7.5	7.4
113R-1 (Piece 4B, 106-108)	648.76	1.870	3,872	16.10	5	F	1.2	261.7	53.7	15	70	31.5	30.4
113R-1 (Piece 4B, 109-111)	648.79	2.170	4,502	16.07	7	F	3.2	277.3	74.6	450	600		
114R-1 (Piece 6C, 97-99)	653.37	7.970	46,015	5.77	10	F	4.7	156.5	77.4	250	580		
114R-1 (Piece 6C, 100-102)	653.40	7.960	46,515	5.70	6	F	1.2	170.5	72.8	6	20	4.9	4.9
114R-5 (Piece 1B, 30-32)	658.51	95.900			10	F	3.8	126.1	55.7	300	600		
114R-5 (Piece 1B, 33-35)	658.54	33.900	122,622	9.22	6	F	1.0	139.5	58.4	6	20	4.0	4.3
115R-3 (Piece 2C, 70-72)	665.60	16.200	72,743	7.42	13	F	1.6	264.2	69.3	6	100	6.1	6.1
115R-3 (Piece 2C, 73-75)	665.63	1.470	2,799	17.51	11	F	2.8	235.8	67.2	250	600		
115R-7 (Piece 4, 44-46)	670.92	1.090	2,417	15.03	8	F	2.8	0.5	70.4	20	110	47.9	46.4
116R-4 (Piece 4A, 62-64)	676.39	1.940	5,909	10.94	10	F	2.7	178.7	60.2	300	600		
116R-4 (Piece 4A, 65-67)	676.42	1.380	3,510	13.11	6	F	3.1	156.9	59.2	25	70	13.6	13.5
116R-5 (Piece 1A, 7-9)	677.27	0.779	2,512	10.34	14	F	2.0	185.1	72.4	6	120	26.7	26.3
116R-6 (Piece 7A, 94-96)	679.56	8.980	26,571	11.27	13	F	5.3	202.7	68.3	200	600		
116R-6 (Piece 7A, 97-99)	679.59	3.870	13,610	9.48	4	F	3.1	302.4	65.5	20	70	6.3	6.3
117R-2 (Piece 3A, 49-51)	683.19	1.660	4,034	13.72	8	F	4.0	77.4	76.3	450	600		
117R-2 (Piece 3A, 52-54)	683.22	1.540	3,955	12.98	3	F	3.0	72.1	75.8	30	70	13.0	12.9
117R-5 (Piece 8, 91-93)	687.83	1.260	3,836	10.95	8	F	0.8	80.9	81.0	5	90	6.5	6.5
118R-1 (Piece 7E, 139-141)	692.19	3.370	10,903	10.30	7	F	1.1	269.9	75.5	12	50	5.4	5.4
118R-1 (Piece 7E, 142-144)	692.22	1.460	5,430	8.96	8	F	6.7	266.5	81.6	450	600		
118R-3 (Piece 6B, 90-92)	694.62	2.270	7,959	9.51	7	F	3.0	104.6	70.8	20	80	6.7	6.7
118R-6 (Piece 10, 112-114)	699.28	17.700	96,265	6.13	13	F	1.7	139.0	66.2	4	80	5.0	5.0
119R-2 (Piece 8B, 100-102)	702.71	5.490	18,872	9.70	6	F	1.7	142.4	67.2	20	60	6.4	6.3
119R-2 (Piece 8B, 103-105)	702.74	3.670	15,021	8.14	14	F	5.4	174.8	71.0	150	600		
120R-3 (Piece 6C, 98-100)	713.91	2.640	11,620	7.57	6	F	2.4	229.0	70.1	20	60	6.1	6.1
120R-6 (Piece 1B, 41-43)	717.63	2.160	7,835	9.19	5	F	1.7	236.3	77.4	20	80	8.1	8.1
120R-6 (Piece 1B, 44-46)	717.66	1.760	4,697	12.49	12	F	3.1	258.2	75.8	250	600		
121R-2 (Piece 2C, 49-51)	721.67	0.768	2,967	8.63	11	F	2.9	237.6	74.8	300	600		
121R-2 (Piece 2C, 52-54)	721.70	0.914	3,640	8.37	8	F	2.7	216.0	71.7	4	50	6.2	6.3
121R-5 (Piece 1G, 112-114)	726.64	1.800	2,905	20.66	3	F	4.0	302.6	75.1	50	90	50.6	46.5
121R-5 (Piece 1G, 115-117)	726.67	3.550	3,055	38.73	13	F	3.2	259.7	73.5	150	600		
121R-8 (Piece 2B, 62-64)	729.89	4.570	6,216	24.51	8	F	1.9	297.9	72.3	450	600		
121R-8 (Piece 2B, 65-67)	729.92	3.690	2,608	47.17	13	F	2.7	293.4	69.5	20	160	83.9	81.4
122R-7 (Piece 1, 8-10)	737.87	1.700	4,232	13.39	8	F	3.2	236.8	70.1	450	600		
122R-7 (Piece 1, 11-13)	737.90				7	F	2.6	225.2	64.6	10	90	65.3	64.0
123R-3 (Piece 1B, 39-41)	742.27	2.700	5,091	17.68	12	F	2.1	26.9	76.1	15	120	49.6	47.3
123R-3 (Piece 1B, 46-48)	742.34	1.310	10,331	4.23	8	F	2.2	13.4	72.5	20	80	7.7	7.4
123R-4 (Piece 2B, 76-78)	743.94	3.540	17,130	6.89	8	F	5.7	29.4	72.2	450	600		
123R-4 (Piece 2B, 79-81)	743.97	1.890	10,089	6.24	5	F	6.8	308.7	71.3	20	80	7.5	7.7
124R-1 (Piece 2A, 26-28)	748.96	4.770	7,182	22.14	6	F	1.6	116.5	66.4	520	600		
124R-1 (Piece 2A, 29-31)	748.99	3.480	4,946	23.45	9	F	1.3	129.1	68.2	8	110	73.8	72.6
126R-3 (Piece 2B, -79)	758.90	4.750	5,961	26.56	11	F	3.0	118.4	70.7	8	200	71.8	71.0
126R-3 (Piece 2B, 80-82)	758.93	7.020	6,302	37.13	12	F	2.9	114.0	67.0	250	600		
127R-3 (Piece 1, 6-8)	767.68	4.210	7,007	20.03	12	F	0.9	184.9	66.3	8	140	48.6	48.0
127R-3 (Piece 1, 10-12)	767.72	4.410	4,190	35.08	12	F	4.2	199.5	73.4	250	600		
128R-4 (Piece 7, 61-63)	779.52	1.290	3,500	12.29	10	F	2.1	24.3	76.7	15	100	27.6	26.4
128R-4 (Piece 7, 64-66)	779.55	1.730	4,189	13.77	8	F	1.9	27.4	78.8	450	600		
129R-2 (Piece 3A, 35-37)	785.95	2.800	3,329	28.04	14	F	3.4	225.7	68.7	10	130	72.6	70.8
130R-2 (Piece 3, 29-31)	795.48	2.980	2,217	44.80	12	F	2.2	210.7	59.8	250	600		
130R-2 (Piece 3, 32-34)	795.51	4.450	2,611	56.82	15	F	2.1	206.7	65.6	10	150	80.5	78.1
130R-4 (Piece 8B, 111-113)	799.25	4.490	9,541	15.69	8	F	1.1	68.4	70.5	450	600		
130R-4 (Piece 8B, 114-116)	799.28	3.510	6,179	18.93	13	F	1.9	70.7	69.1	15	150	77.5	75.2
131R-2 (Piece 3, 19-21)	805.19	0.439	2,016	7.26	13	F	4.5	198.9	69.2	250	600		
131R-2 (Piece 3, 22-24)	805.22	0.666	2,555	8.69	6	F	1.3	220.2	72.6	50	200	24.4	24.0
132R-3 (Piece 2, 28-30)	816.30	0.949	1,912	16.55	10	F	3.1	31.2	48.0	10	90	49.0	47.2
132R-3 (Piece 2, 31-33)	816.33	0.973	5,715	5.67	5	F	8.0	38.9	33.2	500	570		
132R-6 (Piece 2, 73-75)	820.48	0.384	2,327	5.50	5	F	3.7	120.8	74.8	20	60	8.1	8.1
132R-6 (Piece 2, 76-78)	820.51	0.431	2,626	5.47	13	F	11.2	151.4	62.2	200	600		
132R-8 (Piece 7B, 120-122)	823.37	0.732	2,280	10.70	8	F	2.8	229.1	87.7	20	120	32.0	31.6
133R-2 (Piece 5, 123-125)	825.47	2.450	4,299	19.00	13	F	4.9	207.5	69.2	150	585		
133R-2 (Piece 5, 126-128)	825.50	3.370	5,991	18.75	9	F	2.6	226.7	69.7	25	120	49.8	46.2
133R-7 (Piece 1A, 12-14)	831.38	0.495	1,733	9.52	9	F	2.1	23.5	74.7	25	120	29.2	26.7
134R-2 (Piece 2D, 99-101)	834.94	0.781	1,774	14.68	8	F	1.7	294.7	71.6	450	600		

Table T12 (continued).

Core, section, interval (cm)	Curated depth (mbsf)	NRM (A/m)	Volume susceptibility (10^{-6} SI)	Q	Best-fit direction							MDF (mT)	MDF′ (mT)
					N	Type	MAD	Declination (°)	Inclination (°)	Low	High		
134R-2 (Piece 2D, 102-104)	834.97	0.781	1,927	13.51	5	F	2.6	289.5	64.0	50	100	31.8	30.0
134R-7 (Piece 1B, 65-67)	841.43	0.711	2,690	8.81	4	F	4.2	218.8	72.6	30	80	14.4	14.0
134R-7 (Piece 1B, 68-70)	841.46	0.796	3,207	8.27	14	F	4.7	206.3	66.3	150	600		
135R-3 (Piece 1, 7-9)	845.12	1.110	5,108	7.24	7	F	2.0	182.1	56.9	8	30	5.9	5.9
135R-3 (Piece 1, 10-12)	845.15	0.911	3,477	8.73	15	F	3.8	187.6	55.8	100	600		
136R-2 (Piece 1B, 56-58)	848.69	1.470	4,029	12.16	9	F	2.6	206.8	67.8	15	120	34.3	33.9
136R-2 (Piece 1B, 59-61)	848.72	1.900	4,815	13.15	7	F	1.9	186.5	62.2	500	600		
137R-3 (Piece 2A, 40-42)	854.52	0.665	2,598	8.53	13	F	3.2	150.1	56.6	200	600		
137R-3 (Piece 2A, 43-45)	854.55	0.599	2,311	8.64	6	F	1.3	115.2	73.5	20	80	26.5	25.5
137R-7 (Piece 6, 70-72)	860.52	1.360	4,465	10.15	6	F	2.3	237.7	62.2	15	60	10.5	9.9
138R-3 (Piece 2B, 77-79)	864.75	0.813	2,784	9.73	7	F	2.8	293.7	51.0	50	160	9.0	9.3
138R-3 (Piece 2B, 80-82)	864.78	1.230	4,827	8.49	6	F	3.1	314.1	79.9	25	80	8.6	8.4
139R-1 (Piece 4, 84-86)	871.94	0.849	4,122	6.87	10	F	3.2	235.8	62.4	25	140	25.9	21.8
139R-4 (Piece 4, 110-112)	876.41	5.280	12,683	13.88	10	F	1.7	258.9	68.4	15	160	61.5	56.3
139R-4 (Piece 4, 113-115)	876.44	4.500	10,690	14.03	14	F	3.6	244.6	64.0	150	600		
140R-1 (Piece 3A, 29-31)	880.59	2.300	4,865	15.76	14	F	2.5	262.8	71.9	150	600		
140R-1 (Piece 3A, 32-34)	880.62	1.630	2,934	18.52	6	F	1.2	277.8	69.1	30	160	101.7	98.1
140R-5 (Piece 2, 40-42)	886.10	1.370	5,308	8.60	7	F	1.1	242.7	73.4	20	160	31.3	28.7
140R-5 (Piece 2, 43-45)	886.13	2.490	6,815	12.18	13	F	4.4	228.5	69.2	200	600		
141R-1 (Piece 7, 124-126)	890.54	2.770	5,623	16.42	13	F	2.0	256.4	67.3	12	150	76.2	74.2
142R-3 (Piece 4B, 86-88)	896.47	1.390	3,287	14.09	8	F	1.3	218.4	63.4	40	150	57.2	52.0
142R-3 (Piece 4B, 89-91)	896.50	1.270	3,360	12.60	8	F	2.2	189.8	67.4	450	600		
142R-7 (Piece 1, 9-11)	900.82	4.290	11,535	12.40	8	F	3.7	186.5	67.7	450	600		
142R-7 (Piece 1, 12-14)	900.85	3.830	11,774	10.84	9	F	1.1	207.4	65.0	30	140	57.2	41.4
143R-5 (Piece 1, 32-34)	908.20	1.250	5,923	7.03	5	F	3.8	39.4	78.5	520	585		
143R-5 (Piece 1, 35-37)	908.23	1.400	6,131	7.61	5	F	3.0	26.0	75.2	50	100	15.0	13.0
144R-1 (Piece 1, 13-15)	912.43	0.880	5,703	5.14	9	F	2.3	159.5	63.5	10	60	7.9	7.9
145R-1 (Piece 3, 130-132)	923.20	2.680	14,480	6.17	6	F	4.7	234.3	70.0	15	90	6.1	6.1
145R-1 (Piece 3, 134-136)	923.24	4.160	30,156	4.60	5	F	6.2	213.3	73.9	540	600		
145R-4 (Piece 1, 32-34)	926.06	1.560	4,025	12.92	2	A	3.3	145.5	75.6	70	90	12.1	12.1
145R-4 (Piece 1, 35-37)	926.09	1.230	5,554	7.38	4	F	4.1	18.6	77.7	540	585		
145R-5 (Piece 6, 83-85)	927.98	2.770	5,093	18.13	6	F	2.2	189.6	80.1	20	140	12.2	12.4
146R-4 (Piece 3, 111-113)	936.25	1.830	8,552	7.13	12	F	1.5	189.2	63.4	6	70	7.2	7.1
146R-4 (Piece 3, 114-116)	936.28	1.010	4,187	8.04	13	F	7.3	206.5	54.2	150	585		
146R-6 (Piece 1B, 59-61)	938.60	0.894	3,075	9.69	6	F	3.1	238.0	70.4	40	110	19.3	18.9
147R-6 (Piece 2A, 55-57)	947.49	1.290	6,967	6.17	8	F	2.4	216.6	75.8	30	130	10.8	10.7
147R-6 (Piece 2A, 58-60)	947.52	1.800	12,282	4.89	6	F	2.9	202.1	72.8	500	585		
148R-1 (Piece 2G, 101-103)	951.91	0.155	1,335	3.87	9	F	1.4	206.2	65.5	4	30	12.6	12.6
148R-4 (Piece 1A, 7-9)	955.34	1.110	5,378	6.88	7	F	6.6	257.8	70.5	30	100	11.6	11.6
148R-7 (Piece 4, 106-108)	960.54	1.680	6,034	9.28	11	F	5.5	228.3	65.6	250	585		
148R-7 (Piece 4, 109-111)	960.57	1.440	5,641	8.51	8	F	2.1	237.0	67.2	30	130	36.4	32.7
149R-2 (Piece 2, 49-51)	962.30	0.506	2,756	6.12	4	F	2.2	264.9	62.9	40	100	18.7	18.2
149R-2 (Piece 2, 52-54)	962.33	0.512	2,909	5.87	11	F	5.1	243.1	73.6	250	585		
149R-7 (Piece 2, 115-117)	969.13	2.340	5,588	13.96	11	F	4.2	219.2	70.7	250	585		
149R-7 (Piece 2, 117-119)	969.15	2.370	5,538	14.27	5	F	2.7	225.9	72.1	50	140	56.2	54.1
150R-2 (Piece 2A, 42-44)	971.87	2.180	8,030	9.05	5	F	0.6	234.1	72.7	20	100	26.4	23.9
150R-7 (Piece 1, 5-7)	978.21	1.700	6,900	8.21	6	F	1.7	225.9	72.8	500	585		
150R-7 (Piece 1, 8-10)	978.24	1.580	5,732	9.19	5	F	1.4	241.9	72.2	20	100	18.3	17.3
151R-1 (Piece 7, 104-106)	980.84	2.240	4,447	16.79	9	F	0.8	237.2	73.5	20	120	31.9	31.5
151R-4 (Piece 5, 88-90)	984.60	1.460	3,690	13.19	11	F	1.4	241.1	69.0	20	160	53.5	53.1
151R-4 (Piece 5, 91-93)	984.63	1.360	3,610	12.56	10	F	3.2	234.8	70.2	300	585		
151R-5 (Piece 8, 49-51)	985.71	1.630	7,983	6.81	16	F	1.8	164.6	73.8	6	140	45.6	43.9
152R-3 (Piece 1, 62-64)	990.56	1.600	4,092	13.03	16	F	2.9	229.9	64.7	6	150	61.2	57.0
152R-3 (Piece 1, 65-67)	990.59	1.150	3,130	12.25	7	F	2.4	232.6	68.2	450	585		
152R-6 (Piece 2, 62-64)	994.52	2.570	8,579	9.99	8	F	2.3	247.7	73.6	20	100	9.2	9.2
153R-2 (Piece 1, 18-20)	997.32	2.070	5,839	11.82	6	F	3.7	209.1	75.2	500	585		
153R-2 (Piece 1, 21-23)	997.35	2.310	6,501	11.84	8	F	1.4	219.9	73.8	40	120	33.8	32.5
153R-7 (Piece 1B, 96-98)	1004.44	4.730	18,336	8.60	6	F	3.3	197.0	69.7	500	585		
153R-7 (Piece 1B, 99-101)	1004.47	4.920	15,185	10.80	6	F	1.3	236.0	69.0	30	130	19.6	18.9
154R-5 (Piece 1, 32-34)	1010.59	2.550	6,293	13.51	8	F	1.9	209.6	82.6	40	130	35.9	35.6
155R-1 (Piece 2A, 16-18)	1015.16	1.260	7,667	5.48	6	F	3.6	191.3	76.5	500	585		
155R-1 (Piece 2A, 19-21)	1015.19	1.460	9,284	5.24	8	F	3.4	192.6	72.4	20	80	8.0	8.0
155R-4 (Piece 1, 7-9)	1019.34	2.280	6,496	11.70	8	F	4.1	230.3	74.3	25	120	23.8	24.1
155R-4 (Piece 1, 10-12)	1019.37	1.980	5,869	11.25	6	F	2.2	223.7	71.7	500	585		
156R-2 (Piece 4, 127-129)	1026.90	1.400	4,929	9.47	9	F	2.1	184.3	71.2	350	585		
156R-2 (Piece 4, 131-133)	1026.94	1.850	2,732	22.57	9	F	2.1	164.9	69.1	20	120	27.9	27.6
156R-5 (Piece 2B, 53-55)	1030.57	1.530	5,461	9.34	7	F	2.1	234.5	67.2	30	90	9.9	9.5

Table T12 (continued).

Core, section, interval (cm)	Curated depth (mbsf)	NRM (A/m)	Volume susceptibility (10^{-6} SI)	Q	Best-fit direction							MDF (mT)	MDF′ (mT)
					N	Type	MAD	Declination (°)	Inclination (°)	Low	High		
157R-3 (Piece 3, 89-91)	1038.16	3.240	14,906	7.25	7	F	2.6	195.1	80.1	15	60	6.0	6.0
157R-3 (Piece 3, 92-94)	1038.19	2.990	15,260	6.53	5	F	4.1	190.6	77.8	500	570		
157R-5 (Piece 4, 45-47)	1040.72	1.470	5,364	9.13	4	F	2.1	206.1	73.7	30	80	6.0	6.0
158R-4 (Piece 3, 65-67)	1048.63	2.600	7,193	12.05	7	F	0.9	209.9	69.6	15	90	13.4	13.0
158R-4 (Piece 3, 68-70)	1048.66	2.850	6,462	14.70	5	F	3.0	245.3	78.6	500	570		
159R-4 (Piece 3A, 89-91)	1058.73	0.720	5,566	4.31	6	F	11.0	319.3	73.8	450	570		
159R-4 (Piece 3A, 92-94)	1058.76	0.720	4,499	5.33	5	F	3.2	355.4	74.3	30	80	9.0	8.2
159R-6 (Piece 4A, 89-91)	1061.70	1.830	5,754	10.60	6	F	1.1	96.2	83.5	30	100	35.6	33.7
160R-2 (Piece 1B, 29-31)	1065.19	1.130	4,363	8.63	5	F	4.3	239.3	73.9	500	570		
160R-2 (Piece 1B, 32-34)	1065.22	1.310	3,604	12.12		Zapped at 100 mT							
160R-7 (Piece 1, 16-18)	1072.15	0.751	4,719	5.30	6	F	1.3	169.4	58.0	15	50	10.7	10.5
161R-2 (Piece 2, 20-22)	1074.59	1.750	7,737	7.54	6	F	0.9	227.7	70.5	30	100	12.1	10.5
161R-6 (Piece 3A, 65-67)	1080.59	0.924	6,224	4.95	5	F	2.7	247.0	67.3	500	570		
161R-6 (Piece 3A, 68-70)	1080.62	1.270	7,287	5.81	6	F	1.6	252.4	71.8	30	100	11.9	10.2
162R-2 (Piece 3, 93-95)	1084.78	3.570	14,212	8.37	6	F	4.2	266.7	66.8	30	100	17.4	15.6
162R-6 (Piece 3, 84-86)	1090.19	1.730	4,117	14.01	5	F	1.5	231.0	68.1	30	100	41.5	35.4
162R-8 (Piece 1, 30-32)	1091.70	1.410	3,077	15.27	5	F	1.7	254.7	75.6	30	100	43.0	41.4
162R-8 (Piece 1, 33-35)	1091.73	1.260	4,184	10.04	5	F	4.0	256.8	78.0	500	570		
162R-8 (Piece 1, 51-53)	1091.91	2.810	6,762	13.85	5	F	1.0	272.9	76.4	30	100	35.3	34.1
162R-8 (Piece 1, 54-56)	1091.94	2.490	7,232	11.48	5	F	4.7	260.1	70.5	500	570		
163R-4 (Piece 2A, 85-87)	1096.55	1.700	5,572	10.17	8	F	1.2	150.1	66.9	20	150	29.5	29.3
163R-5 (Piece 3B, 68-70)	1097.64	1.180	4,304	9.14	6	F	1.2	156.5	72.3	30	110	19.9	19.2
164R-3 (Piece 1A, 29-31)	1102.29	1.590	2,292	23.12	7	F	2.2	249.2	72.6	500	600		
164R-3 (Piece 1A, 32-34)	1102.32	1.570	3,245	16.13	8	F	1.3	261.1	66.5	40	160	74.1	67.8
165R-3 (Piece 2A, 104-106)	1108.32	0.148	1,039	4.75	6	F	3.8	151.4	67.4	15	50	15.9	15.7
165R-4 (Piece 2A, 39-41)	1108.98	0.621	975	21.23	10	F	1.2	233.4	77.7	20	140	74.6	71.5
166R-1 (Piece 4A, 21-23)	1111.11	1.500	3,341	14.96	11	F	1.6	264.1	78.5	30	180	71.7	66.8
166R-5 (Piece 3, 77-79)	1116.66	1.530	3,060	16.66	10	F	1.6	296.9	77.6	25	160	51.8	49.6
166R-5 (Piece 3, 81-83)	1116.70	0.846	1,583	17.82	6	F	2.7	264.8	80.6	520	600		
167R-1 (Piece 3D, 105-107)	1121.55	0.814	2,201	12.33	12	F	1.3	239.0	78.8	15	160	45.7	45.8
167R-6 (Piece 1, 7-9)	1127.32	1.190	3,069	12.92	7	F	5.1	252.6	75.6	500	600		
167R-6 (Piece 1, 10-12)	1127.35	1.040	3,206	10.81	8	F	2.2	242.7	73.9	50	180	67.1	64.8
168R-2 (Piece 1, 7-9)	1131.46	1.020	2,734	12.43	7	F	1.8	250.6	80.6	500	600		
168R-2 (Piece 1, 10-12)	1131.49	0.928	2,472	12.51	8	F	2.2	295.7	80.5	40	160	55.6	52.5
168R-7 (Piece 5, 74-76)	1139.39	2.080	3,618	19.16	9	F	1.7	206.3	64.0	20	120	42.1	41.5
169R-2 (Piece 3, 97-99)	1141.88	2.330	7,209	10.77	11	F	1.9	234.5	65.5	15	140	48.7	44.7
169R-4 (Piece 2A, 47-49)	1144.28	1.150	2,984	12.85	6	F	3.1	226.9	72.6	520	600		
169R-4 (Piece 2A, 50-52)	1144.31	1.220	3,310	12.28	13	F	1.4	247.6	74.9	20	180	59.5	56.1
169R-6 (Piece 3, 79-81)	1147.22	1.090	2,774	13.10	7	F	2.3	217.5	77.3	15	100	61.8	60.9
170R-2 (Piece 3A, 61-63)	1151.14	0.510	2,076	8.19	4	F	3.1	261.2	65.9	40	100	18.9	17.4
170R-5 (Piece 5, 106-108)	1155.70	0.704	1,727	13.59	6	F	1.3	224.2	70.4	20	120	64.4	62.9
171R-2 (Piece 2, 28-30)	1160.73	8.040	30,606	8.76	4	F	5.2	355.3	66.2	40	90	5.1	5.2
171R-5 (Piece 3, 102-104)	1165.93	2.470	3,606	22.83	9	F	2.4	234.1	51.8	10	150	51.7	50.9
171R-5 (Piece 3, 105-107)	1165.96	2.340	3,841	20.30	7	F	4.4	233.6	65.0	500	600		
172R-1 (Piece 6, 123-125)	1169.93	5.070	11,597	14.57	6	F	0.7	237.7	73.4	15	90	13.0	13.0
173R-1 (Piece 8, 96-98)	1179.36	1.910	3,039	20.95	6	F	1.6	199.7	77.9	15	90	44.6	44.3
173R-1 (Piece 8, 99-101)	1179.39	2.860	2,966	32.14	15	F	4.6	213.3	70.5	100	600		
173R-3 (Piece 4, 119-121)	1182.45	0.945	2,205	14.28	4	F	2.7	268.0	55.1	30	90	60.9	58.1
173R-5 (Piece 6, 84-86)	1184.87	1.870	4,038	15.44	11	F	1.5	121.5	61.8	25	120	41.2	39.0
175R-1 (Piece 4, 78-80)	1191.88	0.841	1,678	16.70	13	F	1.6	206.4	71.5	15	160	71.6	71.1
175R-1 (Piece 4, 81-83)	1191.91	0.748	1,609	15.50	6	F	4.6	245.6	67.0	500	585		
176R-3 (Piece 2A, 87-89)	1200.23	1.600	3,464	15.40	6	F	3.1	221.1	59.8	500	585		
176R-3 (Piece 2A, 90-92)	1200.26	1.390	2,554	18.14	13	F	1.9	220.4	67.2	15	160	68.0	63.8
177R-5 (Piece 2, 57-59)	1207.61	0.436	2,013	7.22	9	F	2.0	208.7	72.5	25	140	60.9	59.4
177R-6 (Piece 4B, 108-110)	1209.62	3.370	5,172	21.72	6	F	2.2	174.7	75.4	500	585		
177R-6 (Piece 4B, 119-121)	1209.73	4.130	6,777	20.31	11	F	1.1	179.1	76.6	12	130	49.4	49.3
178R-4 (Piece 5B, 113-115)	1216.34	4.540	3,528	42.89	7	F	0.6	68.4	69.7	15	100	39.4	38.8
178R-6 (Piece 5B, 134-136)	1219.40	0.176	834	7.03	4	F	2.2	162.0	73.3	100	200	24.1	24.2
179R-2 (Piece 6C, 130-132)	1223.40	6.110	38,383	5.31	9	F	1.3	257.5	58.3	20	90	5.1	5.1
179R-5 (Piece 3, 107-109)	1227.52	1.680	7,103	7.88	6	F	3.0	217.0	71.3	500	585		
179R-5 (Piece 3, 110-112)	1227.55	1.650	4,322	12.73	9	F	1.3	224.6	69.6	15	200	38.1	37.8
180R-5 (Piece 1, 10-12)	1236.38	2.050	10,312	6.63	9	F	2.6	206.4	67.9	12	80	7.3	7.3
181R-4 (Piece 8, 93-95)	1245.48	0.739	2,766	8.90	13	F	1.5	219.5	65.0	10	100	26.9	26.1
182R-2 (Piece 4, 65-67)	1251.97	2.370	1,126	70.16	6	F	1.3	199.6	77.9	50	140	37.8	37.4
183R-2 (Piece 2A, 75-77)	1261.76	0.419	1,875	7.45	11	F	3.3	140.6	66.3	15	140	31.8	31.6
184R-5 (Piece 3A, 65-67)	1275.55	1.340	4,698	9.51	10	F	1.8	228.1	69.4	15	120	40.2	38.3

Table T12 (continued).

Core, section, interval (cm)	Curated depth (mbsf)	NRM (A/m)	Volume susceptibility (10^{-6} SI)	Q	Best-fit direction							MDF (mT)	MDF′ (mT)
					N	Type	MAD	Declination (°)	Inclination (°)	Low	High		
184R-5 (Piece 3A, 67-69)	1275.57	1.450	4,750	10.18	6	F	3.6	217.8	69.3	500	585		
185R-5 (Piece 1, 11-13)	1283.88	0.939	2,690	11.64	8	F	5.0	203.5	76.7	500	600		
185R-5 (Piece 1, 14-16)	1283.91	2.190	3,881	18.81	12	F	2.5	172.8	66.0	20	140	58.9	59.2
186R-3 (Piece 1A, 21-23)	1291.38	4.700	3,195	49.03	8	F	1.5	243.8	75.4	25	120	36.6	35.6
186R-6 (Piece 1, 33-35)	1295.82	0.627	2,875	7.27	6	F	2.0	285.1	73.6	40	120	38.1	35.0
186R-6 (Piece 1, 36-38)	1295.85	0.376	2,315	5.41	8	F	5.5	245.6	74.3	500	600		
187R-5 (Piece 2B, 60-62)	1302.97	0.476	2,133	7.44	8	F	6.0	23.9	71.2	20	90	10.0	10.0
187R-5 (Piece 2B, 64-66)	1303.01	0.478	2,259	7.05	8	F	3.5	305.6	78.9	500	600		
188R-3 (Piece 1A, 10-12)	1309.94	1.030	2,470	13.90	14	F	2.6	243.5	67.0	10	140	55.8	53.8
188R-3 (Piece 1D, 127-129)	1311.11	0.185	1,315	4.69	10	F	4.8	174.4	60.8	6	50	13.7	17.7
188R-4 (Piece 2C, 112-114)	1312.33	0.431	1,859	7.73	8	F	4.9	235.0	61.3	500	600		
188R-4 (Piece 2C, 115-117)	1312.36	0.408	1,696	8.02	4	F	2.2	239.4	67.6	60	120	46.4	46.0
188R-6 (Piece 3, 54-56)	1314.52	1.040	3,462	10.01	6	F	2.4	222.4	73.8	30	150	32.1	33.2
189R-5 (Piece 1A, 7-9)	1322.19	0.240	891	8.98	6	F	2.8	269.0	63.4	30	150	28.1	25.9
189R-5 (Piece 1A, 9-11)	1322.21	0.275	916	10.01	8	F	3.2	241.2	72.1	500	600		
190R-4 (Piece 3, 64-66)	1330.87	0.683	1,625	14.01	7	F	2.2	181.9	70.0	500	600		
190R-4 (Piece 3, 67-69)	1330.90	1.030	2,149	15.98	7	F	1.0	157.2	69.0	30	200	89.0	87.6
191R-3 (Piece 3C, 83-85)	1339.40	1.790	24,132	2.47	7	F	2.5	224.0	71.4	30	200	9.1	9.1
191R-8 (Piece 1, 22-24)	1345.13	1.950	5,144	12.64	7	F	4.3	203.4	58.0	500	600		
191R-8 (Piece 1, 25-27)	1345.16	1.270	6,320	6.70	8	F	2.3	209.9	68.7	15	150	7.1	7.9
192R-2 (Piece 2, 72-74)	1347.52	0.759	3,082	8.21	12	F	1.5	233.9	66.3	10	120	23.6	23.4
192R-4 (Piece 2, 61-63)	1350.02	0.715	3,020	7.89	8	F	1.8	172.5	70.5	50	120	28.2	28.3
192R-4 (Piece 2, 64-66)	1350.05	0.839	1,494	18.72	7	F	2.2	161.7	70.7	500	600		
193R-1 (Piece 3B, 82-84)	1355.82	1.200	1,473	27.15	11	F	2.1	231.3	63.7	20	160	86.3	84.0
193R-1 (Piece 3B, 85-87)	1355.85	1.190	2,552	15.54	7	F	1.8	226.9	64.6	500	600		
195R-2 (Piece 1, 2-4)	1365.57	1.170	2,760	14.13	7	F	1.8	211.5	60.4	10	100	62.2	61.4
195R-2 (Piece 1, 5-7)	1365.60	1.010	1,778	18.94	7	F	2.2	217.3	74.9	500	600		
195R-7 (Piece 3, 38-40)	1372.24	1.290	2,720	15.81	7	F	4.9	204.1	68.8	30	120	28.6	28.2
196R-1 (Piece 3, 27-29)	1373.97	1.080	4,779	7.53	6	F	5.4	262.0	70.2	15	100	29.2	27.9
196R-4 (Piece 7A, 93-95)	1378.09	1.700	2,505	22.62	4	F	0.7	209.2	72.9	30	100	49.8	49.5
196R-4 (Piece 7A, 96-98)	1378.12	1.170	1,899	20.54	7	F	2.2	193.4	71.0	500	600		
197R-2 (Piece 7, 57-59)	1385.37	0.405	1,075	12.56	4	F	1.9	155.0	66.6	70	200	115.1	114.6
197R-3 (Piece 5A, 87-89)	1387.17	0.167	815	6.83	13	F	1.6	233.7	75.8	8	100	24.6	25.0
198R-1 (Piece 4, 17-19)	1386.57	0.230	886	8.66	7	F	3.5	352.8	74.8	25	100	19.3	19.2
198R-1 (Piece 9B, 117-119)	1387.57	1.300	1,195	36.26	7	F	2.0	204.1	73.9	500	600		
198R-1 (Piece 9B, 120-122)	1387.60	0.759	1,102	22.96	12	F	1.8	193.8	73.2	15	160	51.3	51.3
198R-4 (Piece 4, 105-107)	1391.69	0.852	2,868	9.90	4	F	3.3	282.0	73.1	40	100	17.4	16.8
199R-2 (Piece 2A, 79-81)	1394.56	0.766	2,705	9.44	8	F	2.9	248.3	65.4	20	100	21.0	20.4
199R-2 (Piece 5, 134-136)	1395.11	0.818	2,292	11.89	7	F	5.1	125.7	65.6	500	600		
199R-2 (Piece 5, 137-139)	1395.14	0.780	2,231	11.65	9	F	2.5	144.6	76.0	10	150	20.5	21.1
199R-6 (Piece 3, 49-51)	1400.12	2.320	8,596	9.00	7	F	6.0	77.8	80.6	500	600		
199R-6 (Piece 3, 53-55)	1400.16	1.830	9,823	6.21	4	A	3.0	48.2	66.8	40	100	7.2	7.6
200R-4 (Piece 2B, 58-60)	1406.78	5.100	6,377	26.66	7	F	1.3	160.4	70.8	25	100	16.2	16.5
201R-1 (Piece 1, 11-13)	1411.71	0.582	1,069	18.14	11	F	3.1	245.1	57.5	15	140	52.4	49.8
201R-5 (Piece 2A, 42-44)	1417.08	2.890	2,298	41.93	8	F	1.6	115.2	73.4	30	150	46.7	45.4
201R-7 (Piece 4, 113-115)	1420.72	2.230	2,887	25.75	7	F	1.5	246.5	72.2	40	150	46.2	45.7
201R-7 (Piece 4, 116-118)	1420.75	1.380	3,330	13.82	7	F	5.1	232.7	72.1	500	600		
202R-1 (Piece 3A, 80-82)	1422.00	1.230	2,949	13.90	7	F	1.8	254.0	62.0	30	120	30.1	25.4
202R-5 (Piece 2C, 109-111)	1427.88	1.990	3,023	21.94	10	F	1.8	59.0	71.0	15	120	34.0	30.4
202R-5 (Piece 2C, 112-114)	1427.91	2.450	3,760	21.72	7	F	5.1	81.7	70.4	500	600		
202R-8 (Piece 2, 72-74)	1431.27	3.430	15,937	7.17	4	A	0.7	74.3	76.8	25	50	7.0	7.0
203R-2 (Piece 1D, 62-64)	1432.73	1.520	4,549	11.14	6	F	1.8	122.7	75.7	40	120	19.7	19.2
203R-5 (Piece 4, 113-115)	1437.05	2.260	6,573	11.46	7	F	3.3	160.2	55.1	500	600		
203R-5 (Piece 4, 116-118)	1437.08	2.460	3,996	20.52	5	F	1.5	163.6	67.7	50	120	42.4	41.1
204R-4 (Piece 4, 117-119)	1445.62	2.380	4,113	19.29	6	F	1.7	247.3	67.1	20	150	34.1	33.4
204R-7 (Piece 2, 44-46)	1448.94	2.350	4,864	16.10	5	F	1.9	224.2	57.8	30	150	18.1	12.9
204R-7 (Piece 2, 47-49)	1448.97	1.210	3,810	10.59	6	A	2.6	188.3	69.6	500	590		
205R-4 (Piece 4A, 115-117)	1455.70	3.070	7,553	13.55	7	F	1.6	244.3	64.9	25	100	15.5	14.4
205R-4 (Piece 4A, 117-119)	1455.72	2.040	5,390	12.62	6	F	3.8	198.3	75.6	500	590		
206R-2 (Piece 2B, 83-85)	1461.79	2.260	4,139	18.20	12	F	1.5	205.7	67.9	10	120	19.4	19.1
206R-4 (Piece 2, 58-60)	1464.08	1.520	2,400	21.11	6	F	2.7	136.1	71.3	500	590		
206R-4 (Piece 2, 61-63)	1464.11	2.260	3,616	20.84	10	F	1.5	125.4	73.2	15	120	35.4	34.5
207R-2 (Piece 1, 19-21)	1471.11	1.270	1,618	26.16	10	F	2.4	295.2	65.7	20	140	76.1	73.3
207R-4 (Piece 1B, 60-62)	1473.67	0.280	812	11.49	7	F	2.1	219.7	74.3	15	60	11.3	11.3
207R-7 (Piece 2B, 110-112)	1478.42	2.740	1,712	53.34	12	F	1.5	200.4	71.0	10	120	55.0	53.8
207R-7 (Piece 2B, 113-115)	1478.45	2.750	2,960	30.97	6	F	2.1	194.3	68.7	500	590		
208R-4 (Piece 1, 9-11)	1482.73	0.891	1,027	28.92	6	F	1.6	178.8	67.8	500	590		
208R-4 (Piece 1, 12-14)	1482.76	1.010	1,027	32.77	4	F	3.0	204.2	76.2	30	100	62.1	61.3

Table T12 (continued).

Core, section, interval (cm)	Curated depth (mbsf)	NRM (A/m)	Volume susceptibility (10^{-6} SI)	Q	Best-fit direction							MDF (mT)	MDF′ (mT)
					N	Type	MAD	Declination (°)	Inclination (°)	Low	High		
208R-5 (Piece 3C, 106-108)	1485.20	1.920	3,860	16.58	6	F	9.4	261.6	45.6	15	100	29.1	32.1
208R-8 (Piece 2A, 65-67)	1488.72	2.480	6,190	13.36	5	F	4.5	162.3	79.9	20	100	9.0	9.0
209R-2 (Piece 1E, 75-77)	1490.49	0.400	854	15.60	8	F	1.9	7.2	73.7	15	80	30.8	29.1
209R-8 (Piece 4, 103-105)	1498.64	0.941	1,950	16.08	4	F	3.4	243.1	74.9	30	100	30.8	30.0
209R-8 (Piece 4, 106-108)	1498.67	1.350	3,231	13.93	6	F	7.7	207.1	67.2	500	590		
210R-4 (Piece 1, 8-10)	1502.46	1.360	2,701	16.78	6	F	3.6	312.3	76.8	500	590		
210R-4 (Piece 1, 11-13)	1502.49	1.320	3,236	13.60	4	F	2.1	344.0	71.7	30	100	61.5	50.9
210R-4 (Piece 1, 52-54)	1502.90	2.410	3,429	23.43	6	F	1.6	315.1	67.5	20	150	72.9	69.8
210R-4 (Piece 1, 55-57)	1502.93	2.490	1,108	74.93	6	F	3.1	312.2	57.4	500	590		

Notes: NRM = natural remanent magnetization. Q = NRM/susceptibility × H, where H is ambient field strength (30 A/m). Best-fit magnetization directions from principal component analysis (pca) of stepwise demagnetization data. N = number of points for pca; type of pca; F = free of origin, A = anchored to origin; MAD = maximum angular deviation of pca; Dec = declination of characteristic magnetization; Inc = inclination of characteristic magnetization; Low, High = beginning and ending treatment levels for pca (in mT or °C). MDF = median destructive field of NRM. MDF′ = median destructive field calculated from the sum of vector differences between successive demagnetization steps.

Table T13. Summary of magnetic anisotropy results from Leg 176 discrete samples. (Continued on next 11 pages.)

Core, section, interval (cm)	Curated depth (mbsf)	Volume susceptibility (10^{-6} SI)	γ_1	Declination (°)	Inclination (°)	γ_2	Declination (°)	Inclination (°)	γ_3	Declination (°)	Inclination (°)
176-735B-											
89R-1 (Piece 2, 19-21)	504.99	5,496	5,888	264.1	4.7	5,413	173.3	9.9	5,185	19.2	79.1
90R-1 (Piece 2, 115-117)	508.95	4,323	4,606	26.2	21.0	4,568	293.3	7.7	3,795	184.1	67.5
90R-1 (Piece 2, 119-121)	508.99	3,292	3,545	104.0	15.4	3,381	194.4	1.3	2,952	289.1	74.5
90R-3 (Piece 2C, 95-97)	511.72	1,602	1,738	158.5	1.9	1,607	248.8	7.6	1,461	54.7	82.2
90R-4 (Piece 1B, 35-37)	512.34	2,142	2,477	180.3	15.0	1,993	276.2	21.1	1,955	57.6	63.7
90R-4 (Piece 1B, 38-40)	512.37	1,979	2,174	170.3	14.7	1,949	261.2	3.6	1,813	4.6	74.9
90R-6 (Piece 5A, 105-107)	515.56	5,492	6,039	148.5	2.4	5,626	57.9	14.7	4,812	247.6	75.1
90R-7 (Piece 1B, 56-58)	516.49	4,920	5,360	138.5	22.4	5,069	36.8	26.3	4,332	263.4	54.3
90R-7 (Piece 1B, 59-61)	516.52	5,122	5,676	151.2	13.3	5,055	59.1	8.9	4,637	296.4	73.9
90R-8 (Piece 1A, 27-29)	517.13	2,586	2,791	109.0	12.5	2,597	10.8	32.8	2,372	216.9	54.3
91R-1 (Piece 2B, 36-38)	517.76	3,532	3,813	43.1	9.8	3,472	297.5	57.3	3,312	139.0	30.8
91R-1 (Piece 3B, 108-110)	518.48	9,092	9,846	114.3	8.5	9,125	212.1	42.0	8,305	15.2	46.8
91R-1 (Piece 3B, 111-113)	518.51	10,997	12,126	77.9	4.8	11,039	342.6	47.9	9,827	172.2	41.7
91R-3 (Piece 1E, 113-115)	521.08	2,257	2,481	186.0	22.0	2,249	83.6	28.0	2,041	308.5	53.1
91R-3 (Piece 1E, 116-118)	521.11	2,075	2,296	194.6	21.4	1,999	87.3	37.1	1,929	307.8	45.1
92R-1 (Piece 6A, 39-41)	527.39										
93R-1 (Piece 3B, 33-35)	532.43										
93R-1 (Piece 3B, 36-38)	532.46	12,480	13,012	223.4	21.1	12,493	358.1	61.2	11,934	125.9	18.6
93R-2 (Piece 3, 94-96)	534.15	6,713	7,066	50.9	16.5	6,925	165.2	54.4	6,147	310.8	30.6
93R-2 (Piece 3, 97-99)	534.18	6,195	6,523	50.7	9.8	6,425	157.1	58.5	5,637	315.1	29.6
93R-3 (Piece 1E, 85-87)	535.29	9,129	9,570	171.4	3.4	9,301	265.7	52.1	8,516	78.8	37.7
93R-3 (Piece 1E, 88-90)	535.32	11,910	12,390	346.0	4.5	11,998	249.5	55.4	11,341	79.1	34.2
93R-5 (Piece 3, 33-35)	537.37	28,457	30,101	252.5	61.0	29,447	6.6	12.7	25,823	102.8	25.6
93R-5 (Piece 3, 37-39)	537.41	23,292	25,464	301.6	55.9	23,823	174.0	22.5	20,589	73.3	24.2
94R-1 (Piece 1B, 30-32)	536.90	18,064	18,616	179.5	5.7	18,397	81.3	55.4	17,179	273.4	34.0
94R-1 (Piece 1B, 33-35)	536.93	3,388	3,442	63.4	9.5	3,399	326.9	34.1	3,323	166.8	54.2
94R-3 (Piece 5, 52-54)	539.71	6,939	7,184	8.7	21.2	6,996	228.0	63.4	6,637	104.8	15.3
94R-3 (Piece 5, 55-57)	539.74	6,688	6,923	7.3	17.2	6,717	221.2	69.5	6,423	100.7	10.7
94R-3 (Piece 12, 116-118)	540.35	7,880	8,396	4.8	16.7	8,095	150.0	69.9	7,150	271.6	10.8
94R-3 (Piece 12, 123-125)	540.42	6,155	6,555	355.2	21.3	6,233	124.9	58.6	5,678	256.2	22.0
95R-1 (Piece 8, 118-120)	545.78	17,145	19,163	311.6	13.2	17,773	45.2	15.0	14,501	182.0	69.8
95R-1 (Piece 8, 121-123)	545.81	8,200	9,011	319.5	3.6	8,444	49.8	5.3	7,145	195.5	83.6
95R-3 (Piece 1C, 19-21)	547.58	43,856	46,969	210.3	50.9	44,249	341.3	28.1	40,349	85.6	24.8
96R-1 (Piece 4, 27-29)	548.57	2,797	2,889	131.2	20.6	2,870	16.8	47.7	2,632	236.5	35.0
96R-1 (Piece 4, 30-32)	548.60	3,890	4,090	333.1	15.2	4,011	87.3	56.5	3,568	234.4	29.1
96R-2 (Piece 4, 49-51)	550.29	14,763	15,559	182.4	30.5	15,086	79.6	20.6	13,644	321.0	51.9
97R-1 (Piece 2C, 125-127)	557.55	6,741	7,540	27.6	16.7	6,820	128.5	32.2	5,864	274.3	52.7
97R-1 (Piece 2C, 128-130)	557.58	12,098	13,293	52.5	7.1	11,932	151.9	52.8	11,069	317.2	36.3
97R-3 (Piece 1C, 26-28)	559.08	29,126	29,870	82.7	5.3	29,025	275.4	84.6	28,484	172.8	1.2
98R-1 (Piece 5B, 40-42)	561.40	1,311	1,325	268.2	39.0	1,315	8.8	12.7	1,292	113.4	48.1
99R-3 (Piece 5, 72-74)	569.53	4,840	4,957	27.9	10.0	4,857	297.4	2.9	4,705	191.8	79.6
99R-3 (Piece 5, 75-77)	569.56	5,083	5,289	187.4	0.8	5,129	277.7	20.3	4,832	95.2	69.7
99R-4 (Piece 1C, 23-25)	570.25	6,267	6,446	245.6	2.1	6,284	337.8	45.1	6,072	153.5	44.9
99R-6 (Piece 3, 30-32)	573.04	3,363	3,472	343.5	45.5	3,328	243.5	9.6	3,289	144.4	42.9
100R-1 (Piece 3D, 43-45)	575.93	12,468	12,677	294.8	39.2	12,519	148.3	45.6	12,209	39.6	17.4
101R-3 (Piece 1D, 31-33)	587.93	4,398	4,588	225.8	1.4	4,418	135.1	27.8	4,187	318.6	62.2
101R-3 (Piece 1D, 34-36)	587.96	4,300	4,533	258.4	7.0	4,279	166.0	19.0	4,087	7.6	69.7
101R-4 (Piece 1B, 27-29)	589.08	2,338	2,424	219.8	31.1	2,303	129.8	0.0	2,287	39.8	58.9
102R-1 (Piece 4A, 28-30)	590.18	45,000	48,127	37.7	17.0	45,955	135.3	23.6	40,918	275.3	60.3
102R-3 (Piece 6, 58-60)	593.36	1,971	2,015	160.4	15.8	1,971	253.9	12.1	1,927	19.7	69.9
103R-2 (Piece 3E, 81-83)	597.00	2,934	3,001	258.4	4.3	2,970	348.9	7.7	2,830	139.7	81.1
103R-2 (Piece 3E, 84-86)	597.03	1,775	1,818	253.5	51.4	1,791	33.3	31.4	1,715	136.2	20.1
103R-3 (Piece 3D, 48-50)	598.13	97,735	104,384	221.4	25.5	97,985	119.1	24.0	90,837	351.8	53.7
103R-4 (Piece 4A, 31-33)	599.46	2,740	2,864	8.7	19.2	2,744	223.4	67.0	2,611	103.0	12.1
104R-2 (Piece 6B, 49-51)	606.29	10,723	11,429	28.4	6.9	11,142	297.3	9.2	9,598	154.8	78.5
104R-2 (Piece 6B, 52-54)	606.32	9,983	10,586	240.1	2.4	10,504	330.7	14.2	8,859	140.7	75.6
104R-3 (Piece 1C, 36-38)	607.30	38,419	42,770	30.7	15.7	37,709	127.0	21.3	34,779	267.2	63.0
105R-1 (Piece 8B, 52-54)	609.32	12,537	13,471	104.4	23.0	12,829	195.9	3.7	11,312	294.5	66.7
105R-3 (Piece 7, 94-96)	612.63	11,611	12,059	98.7	11.1	11,867	189.0	1.6	10,907	287.0	78.7
105R-3 (Piece 7, 97-99)	612.66	14,205	14,609	76.9	2.4	14,457	346.2	14.8	13,548	175.9	75.0
106R-1 (Piece 10, 73-75)	614.63	16,982	17,797	119.9	8.2	17,017	28.9	6.6	16,132	260.4	79.4
106R-4 (Piece 4B, 54-56)	618.63	6,506	6,931	258.7	2.7	6,331	350.1	26.1	6,257	163.3	63.8
108R-2 (Piece 2, 44-46)	625.41	11,723	12,548	221.1	50.3	12,085	110.7	16.2	10,537	8.9	35.1
108R-2 (Piece 2, 47-49)	625.44	8,384	8,804	159.7	23.6	8,465	259.0	20.2	7,884	25.1	58.1
108R-4 (Piece 4, 87-89)	628.48	8,948	9,235	92.3	38.1	9,134	199.9	21.0	8,476	312.0	44.5
110R-1 (Piece 2D, 46-48)	633.56	6,464	6,734	169.0	69.9	6,487	26.8	16.1	6,172	293.4	11.6

Table T13 (continued).

Core, section, interval (cm)	L	F	P	T
176-735B-				
89R-1 (Piece 2, 19-21)	1.088	1.044	1.136	–0.323
90R-1 (Piece 2, 115-117)	1.008	1.204	1.214	0.914
90R-1 (Piece 2, 119-121)	1.048	1.145	1.201	0.483
90R-3 (Piece 2C, 95-97)	1.082	1.100	1.190	0.097
90R-4 (Piece 1B, 35-37)	1.243	1.019	1.267	–0.838
90R-4 (Piece 1B, 38-40)	1.115	1.075	1.199	–0.203
90R-6 (Piece 5A, 105-107)	1.074	1.169	1.255	0.375
90R-7 (Piece 1B, 56-58)	1.057	1.170	1.237	0.475
90R-7 (Piece 1B, 59-61)	1.123	1.090	1.224	–0.147
90R-8 (Piece 1A, 27-29)	1.075	1.095	1.177	0.116
91R-1 (Piece 2B, 36-38)	1.098	1.048	1.151	–0.331
91R-1 (Piece 3B, 108-110)	1.079	1.099	1.185	0.106
91R-1 (Piece 3B, 111-113)	1.098	1.123	1.234	0.107
91R-3 (Piece 1E, 113-115)	1.103	1.102	1.215	–0.008
91R-3 (Piece 1E, 116-118)	1.149	1.036	1.190	–0.594
92R-1 (Piece 6A, 39-41)				
93R-1 (Piece 3B, 33-35)				
93R-1 (Piece 3B, 36-38)	1.042	1.047	1.090	0.059
93R-2 (Piece 3, 94-96)	1.020	1.127	1.149	0.710
93R-2 (Piece 3, 97-99)	1.015	1.140	1.157	0.794
93R-3 (Piece 1E, 85-87)	1.029	1.092	1.124	0.511
93R-3 (Piece 1E, 88-90)	1.033	1.058	1.092	0.272
93R-5 (Piece 3, 33-35)	1.022	1.140	1.166	0.713
93R-5 (Piece 3, 37-39)	1.069	1.157	1.237	0.373
94R-1 (Piece 1B, 30-32)	1.012	1.071	1.084	0.705
94R-1 (Piece 1B, 33-35)	1.013	1.023	1.036	0.282
94R-3 (Piece 5, 52-54)	1.027	1.054	1.082	0.331
94R-3 (Piece 5, 55-57)	1.031	1.046	1.078	0.194
94R-3 (Piece 12, 116-118)	1.037	1.132	1.174	0.545
94R-3 (Piece 12, 123-125)	1.052	1.098	1.155	0.299
95R-1 (Piece 8, 118-120)	1.078	1.226	1.322	0.460
95R-1 (Piece 8, 121-123)	1.067	1.182	1.261	0.440
95R-3 (Piece 1C, 19-21)	1.061	1.097	1.164	0.215
96R-1 (Piece 4, 27-29)	1.007	1.090	1.097	0.858
96R-1 (Piece 4, 30-32)	1.020	1.124	1.146	0.713
96R-2 (Piece 4, 49-51)	1.031	1.106	1.140	0.530
97R-1 (Piece 2C, 125-127)	1.106	1.163	1.286	0.202
97R-1 (Piece 2C, 128-130)	1.114	1.078	1.201	–0.179
97R-3 (Piece 1C, 26-28)	1.029	1.019	1.049	–0.207
98R-1 (Piece 5B, 40-42)	1.007	1.017	1.025	0.400
99R-3 (Piece 5, 72-74)	1.021	1.032	1.053	0.220
99R-3 (Piece 5, 75-77)	1.031	1.061	1.095	0.318
99R-4 (Piece 1C, 23-25)	1.026	1.035	1.062	0.144
99R-6 (Piece 3, 30-32)	1.043	1.012	1.056	–0.566
100R-1 (Piece 3D, 43-45)	1.013	1.025	1.038	0.334
101R-3 (Piece 1D, 31-33)	1.038	1.055	1.096	0.177
101R-3 (Piece 1D, 34-36)	1.059	1.047	1.109	–0.113
101R-4 (Piece 1B, 27-29)	1.053	1.007	1.060	–0.759
102R-1 (Piece 4A, 28-30)	1.047	1.123	1.176	0.431
102R-3 (Piece 6, 58-60)	1.022	1.023	1.046	0.018
103R-2 (Piece 3E, 81-83)	1.010	1.049	1.060	0.644
103R-2 (Piece 3E, 84-86)	1.015	1.045	1.060	0.496
103R-3 (Piece 3D, 48-50)	1.065	1.079	1.149	0.090
103R-4 (Piece 4A, 31-33)	1.044	1.051	1.097	0.079
104R-2 (Piece 6B, 49-51)	1.026	1.161	1.191	0.709
104R-2 (Piece 6B, 52-54)	1.008	1.186	1.195	0.913
104R-3 (Piece 1C, 36-38)	1.134	1.084	1.230	–0.218
105R-1 (Piece 8B, 52-54)	1.050	1.134	1.191	0.441
105R-3 (Piece 7, 94-96)	1.016	1.088	1.106	0.680
105R-3 (Piece 7, 97-99)	1.010	1.067	1.078	0.723
106R-1 (Piece 10, 73-75)	1.046	1.055	1.103	0.088
106R-4 (Piece 4B, 54-56)	1.095	1.012	1.108	–0.770
108R-2 (Piece 2, 44-46)	1.038	1.147	1.191	0.570
108R-2 (Piece 2, 47-49)	1.040	1.074	1.117	0.288
108R-4 (Piece 4, 87-89)	1.011	1.078	1.090	0.743
110R-1 (Piece 2D, 46-48)	1.038	1.051	1.091	0.143

Table T13 (continued).

Core, section, interval (cm)	Curated depth (mbsf)	Volume susceptibility (10^{-6} SI)	γ_1	Declination (°)	Inclination (°)	γ_2	Declination (°)	Inclination (°)	γ_3	Declination (°)	Inclination (°)
110R-4 (Piece 2B, 57-59)	638.01	4,187	4,322	0.0	31.8	4,148	93.8	6.1	4,091	193.5	57.5
110R-4 (Piece 2B, 60-62)	638.04	4,815	5,095	15.2	21.5	4,778	118.7	30.7	4,573	256.0	51.1
111R-2 (Piece 3, 105-107)	640.42	8,302	8,949	83.1	61.4	8,558	349.3	2.1	7,400	258.2	28.5
111R-2 (Piece 3, 108-110)	640.45	9,284	9,869	67.3	60.1	9,584	177.6	11.3	8,398	273.5	27.3
112R-1 (Piece 3B, 54-56)	643.24	11,088	11,483	110.6	66.0	11,262	234.3	13.8	10,520	329.2	19.2
113R-1 (Piece 4B, 106-108)	648.76	3,872	4,161	265.0	4.3	3,993	355.4	5.9	3,463	139.4	82.7
113R-1 (Piece 4B, 109-111)	648.79	4,502	4,687	356.9	21.3	4,534	97.9	26.2	4,286	232.8	55.1
114R-1 (Piece 6C, 97-99)	653.37	46,015	47,794	276.1	3.2	45,990	6.6	8.6	44,261	165.9	80.8
114R-1 (Piece 6C, 100-102)	653.40	46,515	48,712	171.9	29.0	46,181	59.8	34.2	44,654	292.0	42.1
114R-5 (Piece 1B, 30-32)	658.51	0		0		0					
114R-5 (Piece 1B, 33-35)	658.54	122,622	134,686	109.7	53.6	127,461	350.8	19.6	105,720	249.3	29.3
115R-3 (Piece 2C, 70-72)	665.60	72,743	79,656	298.5	23.5	74,056	39.9	24.5	64,515	170.3	54.9
115R-3 (Piece 2C, 73-75)	665.63	2,799	2,889	56.5	7.6	2,866	203.1	81.0	2,641	325.8	4.9
115R-7 (Piece 4, 44-46)	670.92	2,417	2,470	18.0	48.4	2,418	182.5	40.5	2,364	279.2	7.8
116R-4 (Piece 4A, 62-64)	676.39	5,909	6,169	160.5	1.8	5,841	70.2	9.4	5,717	261.1	80.4
116R-4 (Piece 4A, 65-67)	676.42	3,510	3,656	184.1	7.9	3,557	91.0	21.0	3,317	293.6	67.4
116R-5 (Piece 1A, 7-9)	677.27	2,512	2,558	323.8	3.7	2,516	55.6	25.4	2,461	226.0	64.3
116R-6 (Piece 7A, 94-96)	679.56	26,571	29,552	264.2	24.9	27,271	142.9	48.2	22,889	10.4	31.1
116R-6 (Piece 7A, 97-99)	679.59	13,610	14,719	286.6	52.0	13,568	67.7	31.3	12,542	170.0	19.3
117R-2 (Piece 3A, 49-51)	683.19	4,034	4,154	210.1	4.9	4,085	113.6	53.0	3,864	303.8	36.6
117R-2 (Piece 3A, 52-54)	683.22	3,955	4,039	156.8	45.6	3,997	34.6	27.5	3,830	285.8	31.6
117R-5 (Piece 8, 91-93)	687.83	3,836	4,103	341.0	69.8	3,726	72.0	0.4	3,680	162.2	20.2
118R-1 (Piece 7E, 139-141)	692.19	10,903	11,447	82.1	40.5	10,853	324.1	28.8	10,409	210.5	36.1
118R-1 (Piece 7E, 142-144)	692.22	5,430	5,676	331.7	14.0	5,469	75.4	43.6	5,146	228.3	43.0
118R-3 (Piece 6B, 90-92)	694.62	7,959	8,314	134.8	31.2	8,129	237.4	19.8	7,433	354.6	51.8
118R-6 (Piece 10, 112-114)	699.28	96,265	108,497	108.6	50.4	97,116	204.0	4.4	83,182	297.6	39.2
119R-2 (Piece 8B, 100-102)	702.71	18,872	19,597	145.5	6.3	19,068	337.0	83.6	17,952	235.7	1.3
119R-2 (Piece 8B, 103-105)	702.74	15,021	15,391	117.9	8.7	15,050	25.1	17.3	14,622	233.7	70.5
120R-3 (Piece 6C, 98-100)	713.91	11,620	12,148	60.5	2.0	11,632	323.6	74.1	11,081	151.1	15.8
120R-6 (Piece 1B, 41-43)	717.63	7,835	8,089	247.0	2.7	7,845	153.5	52.0	7,570	339.1	37.8
120R-6 (Piece 1B, 44-46)	717.66	4,697	4,942	229.9	8.0	4,638	130.0	50.9	4,512	326.2	38.0
121R-2 (Piece 2C, 49-51)	721.67	2,967	3,064	163.3	52.3	2,957	265.0	8.9	2,881	1.6	36.2
121R-2 (Piece 2C, 52-54)	721.70	3,640	3,741	188.6	21.3	3,641	304.6	48.4	3,538	83.5	33.7
121R-5 (Piece 1G, 112-114)	726.64	2,905	3,034	306.3	19.4	2,923	183.9	56.6	2,757	46.2	26.0
121R-5 (Piece 1G, 115-117)	726.67	3,055	3,194	304.6	10.6	3,065	200.2	53.2	2,907	42.0	34.8
121R-8 (Piece 2B, 62-64)	729.89	6,216	6,497	317.4	4.9	6,290	222.3	46.6	5,859	52.0	43.0
121R-8 (Piece 2B, 65-67)	729.92	2,608	2,753	306.4	26.1	2,676	193.1	39.0	2,394	60.6	39.9
122R-7 (Piece 1, 8-10)	737.87	4,232	4,359	256.2	33.4	4,249	357.6	16.7	4,088	109.9	51.6
122R-7 (Piece 1, 11-13)	737.90	4,730	4,857	200.8	9.6	4,691	291.3	3.0	4,642	38.3	79.9
123R-3 (Piece 1B, 39-41)	742.27	5,091	5,442	204.9	4.5	5,035	113.6	16.7	4,795	309.4	72.6
123R-3 (Piece 1B, 46-48)	742.34	10,331	11,074	207.0	1.4	10,635	297.2	7.7	9,283	106.5	82.1
123R-4 (Piece 2B, 76-78)	743.94	17,130	18,335	13.7	32.7	18,174	117.2	20.0	14882	233.2	50.3
123R-4 (Piece 2B, 79-81)	743.97	10,089	10,802	110.1	19.6	10,593	8.1	30.3	8,871	228.0	52.7
124R-1 (Piece 2A, 26-28)	748.96	7182	7,461	98.1	2.1	7,169	189.1	26.0	6,917	3.8	63.9
124R-1 (Piece 2A, 29-31)	748.99	4,946	5,246	115.9	5.1	4,834	23.6	24.2	4,758	217.0	65.2
126R-3 (Piece 2B, 77-79)	758.90	5,961	6,531	275.1	3.3	5,954	182.1	41.9	5,396	8.8	47.9
126R-3 (Piece 2B, 80-82)	758.93	6,302	6,933	274.8	1.9	6,244	183.1	41.7	5,728	6.9	48.3
127R-3 (Piece 1, 6-8)	767.68	7,007	7,497	205.8	50.0	7,145	328.5	24.4	6,378	73.4	29.5
127R-3 (Piece 1,10-12)	767.72	4,190	4,447	346.3	10.9	4,229	245.2	45.2	3,896	86.6	42.8
128R-4 (Piece 7, 61-63)	779.52	3,500	3,608	199.7	42.6	3,586	9.9	47.0	3,305	105.2	4.9
128R-4 (Piece 7, 64-66)	779.55	4,189	4,370	208.2	45.9	4,240	39.0	43.5	3,957	303.8	5.4
129R-2 (Piece 3A, 35-37)	785.95	3,329	3,591	219.6	8.4	3,456	318.6	46.5	2,941	121.8	42.3
130R-2 (Piece 3, 29-31)	795.48	2,217	2,446	227.6	11.1	2,158	336.4	58.7	2,048	131.5	28.8
130R-2 (Piece 3, 32-34)	795.51	2,611	2,828	232.3	24.3	2,566	346.1	41.8	2,438	121.4	38.4
130R-4 (Piece 8B, 111-113)	799.25	9,541	9,909	102.8	16.0	9,412	195.7	10.2	9,301	316.9	70.9
130R-4 (Piece 8B, 114-116)	799.28	6,179	6,448	102.5	21.4	6,140	219.5	49.2	5,950	357.9	32.8
131R-2 (Piece 3, 19-21)	805.19	2,016	2,119	273.6	38.8	2,021	129.4	45.3	1,908	19.4	18.7
131R-2 (Piece 3, 22-24)	805.22	2,555	2,661	272.3	34.6	2,549	138.6	45.0	2,456	20.9	24.9
132R-3 (Piece 2, 28-30)	816.30	1,912	2,196	20.8	10.9	1,881	283.3	34.3	1,658	125.9	53.6
132R-3 (Piece 2, 31-33)	816.33	5,715	6,215	31.2	7.3	5,985	301.2	0.1	4,945	210.7	82.7
132R-6 (Piece 2, 73-75)	820.48	2,327	2,436	190.7	21.4	2,329	285.0	10.9	2,215	40.3	65.7
132R-6 (Piece 2, 76-78)	820.51	2,626	2,721	198.1	25.9	2,637	291.6	7.2	2,520	35.9	63.0
132R-8 (Piece 7B, 120-122)	823.37	2,280	2,343	101.2	49.7	2,313	333.4	27.5	2,185	228.0	27.0
133R-2 (Piece 5, 123-125)	825.47	4,299	4,444	170.8	30.2	4,282	47.3	43.5	4,171	281.7	31.5
133R-2 (Piece 5, 126-128)	825.50	5,991	6,138	192.1	15.3	6,046	84.4	48.0	5,788	294.4	38.0
133R-7 (Piece 1A, 12-14)	831.38	1,733	1,773	0.0	11.0	1,754	268.6	7.2	1,672	145.9	76.8
134R-2 (Piece 2D, 99-101)	834.94	1,774	1,900	339.0	15.9	1,716	196.0	70.4	1,705	72.2	11.2
134R-2 (Piece 2D, 102-104)	834.97	1,927	2,076	347.0	12.8	1,889	252.5	18.8	1,816	109.4	67.0

Table T13 (continued).

Core, section, interval (cm)	L	F	P	T
110R-4 (Piece 2B, 57-59)	1.042	1.014	1.057	–0.492
110R-4 (Piece 2B, 60-62)	1.066	1.045	1.114	–0.190
111R-2 (Piece 3, 105-107)	1.046	1.157	1.209	0.530
111R-2 (Piece 3, 108-110)	1.030	1.141	1.175	0.636
112R-1 (Piece 3B, 54-56)	1.020	1.071	1.092	0.557
113R-1 (Piece 4B, 106-108)	1.042	1.153	1.202	0.550
113R-1 (Piece 4B, 109-111)	1.034	1.058	1.093	0.258
114R-1 (Piece 6C, 97-99)	1.039	1.039	1.080	–0.002
114R-1 (Piece 6C, 100-102)	1.055	1.034	1.091	–0.227
114R-5 (Piece 1B, 30-32)				
114R-5 (Piece 1B, 33-35)	1.057	1.206	1.274	0.545
115R-3 (Piece 2C, 70-72)	1.076	1.148	1.235	0.308
115R-3 (Piece 2C, 73-75)	1.008	1.085	1.094	0.821
115R-7 (Piece 4, 44-46)	1.022	1.023	1.045	0.023
116R-4 (Piece 4A, 62-64)	1.056	1.022	1.079	–0.437
116R-4 (Piece 4A, 65-67)	1.028	1.072	1.102	0.435
116R-5 (Piece 1A, 7-9)	1.017	1.022	1.039	0.145
116R-6 (Piece 7A, 94-96)	1.084	1.191	1.291	0.371
116R-6 (Piece 7A, 97-99)	1.085	1.082	1.174	–0.017
117R-2 (Piece 3A, 49-51)	1.017	1.057	1.075	0.539
117R-2 (Piece 3A, 52-54)	1.010	1.044	1.054	0.608
117R-5 (Piece 8, 91-93)	1.101	1.012	1.115	–0.774
118R-1 (Piece 7E, 139-141)	1.055	1.043	1.100	–0.122
118R-1 (Piece 7E, 142-144)	1.038	1.063	1.103	0.243
118R-3 (Piece 6B, 90-92)	1.023	1.094	1.118	0.598
118R-6 (Piece 10, 112-114)	1.117	1.168	1.304	0.166
119R-2 (Piece 8B, 100-102)	1.028	1.062	1.092	0.376
119R-2 (Piece 8B, 103-105)	1.023	1.029	1.053	0.125
120R-3 (Piece 6C, 98-100)	1.044	1.050	1.096	0.054
120R-6 (Piece 1B, 41-43)	1.031	1.036	1.069	0.076
120R-6 (Piece 1B, 44-46)	1.065	1.028	1.095	–0.394
121R-2 (Piece 2C, 49-51)	1.036	1.026	1.063	–0.160
121R-2 (Piece 2C, 52-54)	1.027	1.029	1.057	0.028
121R-5 (Piece 1G, 112-114)	1.038	1.060	1.101	0.224
121R-5 (Piece 1G, 115-117)	1.042	1.055	1.099	0.128
121R-8 (Piece 2B, 62-64)	1.033	1.074	1.109	0.374
121R-8 (Piece 2B, 65-67)	1.029	1.118	1.150	0.593
122R-7 (Piece 1, 8-10)	1.026	1.040	1.066	0.210
122R-7 (Piece 1, 11-13)	1.035	1.011	1.046	–0.534
123R-3 (Piece 1B, 39-41)	1.081	1.050	1.135	–0.227
123R-3 (Piece 1B, 46-48)	1.041	1.146	1.193	0.542
123R-4 (Piece 2B, 76-78)	1.009	1.221	1.232	0.916
123R-4 (Piece 2B, 79-81)	1.020	1.194	1.218	0.802
124R-1 (Piece 2A, 26-28)	1.041	1.036	1.079	–0.055
124R-1 (Piece 2A, 29-31)	1.085	1.016	1.102	–0.677
126R-3 (Piece 2B, 77-79)	1.097	1.103	1.210	0.031
126R-3 (Piece 2B, 80-82)	1.110	1.090	1.210	–0.097
127R-3 (Piece 1, 6-8)	1.049	1.120	1.176	0.406
127R-3 (Piece 1,10-12)	1.052	1.085	1.141	0.240
128R-4 (Piece 7, 61-63)	1.006	1.085	1.092	0.857
128R-4 (Piece 7, 64-66)	1.031	1.072	1.104	0.393
129R-2 (Piece 3A, 35-37)	1.039	1.175	1.221	0.618
130R-2 (Piece 3, 29-31)	1.134	1.053	1.194	–0.415
130R-2 (Piece 3, 32-34)	1.102	1.052	1.160	–0.313
130R-4 (Piece 8B, 111-113)	1.053	1.012	1.065	–0.623
130R-4 (Piece 8B, 114-116)	1.050	1.032	1.084	–0.219
131R-2 (Piece 3, 19-21)	1.048	1.059	1.111	0.101
131R-2 (Piece 3, 22-24)	1.044	1.038	1.084	–0.078
132R-3 (Piece 2, 28-30)	1.168	1.135	1.325	–0.101
132R-3 (Piece 2, 31-33)	1.038	1.210	1.257	0.670
132R-6 (Piece 2, 73-75)	1.046	1.052	1.100	0.059
132R-6 (Piece 2, 76-78)	1.032	1.046	1.080	0.177
132R-8 (Piece 7B, 120-122)	1.013	1.059	1.072	0.634
133R-2 (Piece 5, 123-125)	1.038	1.027	1.065	–0.174
133R-2 (Piece 5, 126-128)	1.015	1.045	1.061	0.486
133R-7 (Piece 1A, 12-14)	1.011	1.049	1.060	0.639
134R-2 (Piece 2D, 99-101)	1.107	1.007	1.115	–0.876
134R-2 (Piece 2D, 102-104)	1.099	1.040	1.143	–0.412

Table T13 (continued).

Core, section, interval (cm)	Curated depth (mbsf)	Volume susceptibility (10^{-6} SI)	γ_1	Declination (°)	Inclination (°)	γ_2	Declination (°)	Inclination (°)	γ_3	Declination (°)	Inclination (°)
134R-7 (Piece 1B, 65-67)	841.43	2,690	2,860	91.4	3.8	2,634	348.6	73.6	2,576	182.5	16.0
134R-7 (Piece 1B, 68-70)	841.46	3,207	3,371	95.6	8.4	3,215	309.0	80.0	3,036	186.4	5.4
135R-3 (Piece 1, 7-9)	845.12	5,108	5,356	218.6	27.0	5,072	0.8	57.2	4,896	119.5	17.2
135R-3 (Piece 1, 10-12)	845.15	3,477	3,645	219.7	13.5	3,502	349.3	69.4	3,285	125.9	15.3
136R-2 (Piece 1B, 56-58)	848.69	4,029	4,259	221.8	13.3	3,971	114.2	51.9	3,857	321.3	34.9
136R-2 (Piece 1B, 59-61)	848.72	4,815	5,252	212.6	20.8	4,790	88.1	56.0	4,403	313.0	25.5
137R-3 (Piece 2A, 40-42)	854.52	2,598	2,815	178.7	10.4	2,505	79.7	40.5	2,472	280.3	47.6
137R-3 (Piece 2A, 43-45)	854.55	2,311	2469	185.7	11.0	2,258	285.0	39.9	2,205	83.3	48.0
137R-7 (Piece 6, 70-72)	860.52	4,465	4,751	243.8	3.2	4,350	337.7	50.3	4,294	151.2	39.5
138R-3 (Piece 2B, 77-79)	864.75	2,784	2,929	343.0	8.0	2,781	250.9	14.9	2,644	100.4	73.0
138R-3 (Piece 2B, 80-82)	864.78	4,827	5,054	325.5	3.9	4,812	235.1	5.8	4,616	89.0	83.0
139R-1 (Piece 4, 84-86)	871.94	4,122	4,394	271.8	8.0	4,003	9.1	42.5	3,969	173.3	46.4
139R-4 (Piece 4, 110-112)	876.41	12,683	13,637	252.3	27.1	12,844	12.8	44.8	11,566	142.9	33.0
139R-4 (Piece 4, 113-115)	876.44	10,690	11,055	257.3	33.4	10,764	15.4	35.6	10,251	137.8	36.8
140R-1 (Piece 3A, 29-31)	880.59	4,865	5,209	295.7	53.6	5,091	62.0	23.6	4,296	164.2	26.0
140R-1 (Piece 3A, 32-34)	880.62	2,934	3,190	292.5	48.4	3,077	70.8	33.6	2,535	176.1	21.6
140R-5 (Piece 2, 40-42)	886.10	5,308	5,545	285.1	24.3	5,304	189.9	11.3	5,076	76.9	62.9
140R-5 (Piece 2, 43-45)	886.13	6,815	7,045	252.9	35.2	6,808	156.4	9.1	6,592	54.0	53.3
141R-1 (Piece 7, 124-126)	890.54	5,623	5,891	259.7	27.5	5,603	360.0	19.0	5,377	120.2	55.6
142R-3 (Piece 4B, 86-88)	896.47	3,287	3,547	220.0	3.0	3,214	315.2	59.2	3,101	128.2	30.6
142R-3 (Piece 4B, 89-91)	896.50	3,360	3,626	32.4	5.4	3,266	132.2	61.1	3,187	299.5	28.3
142R-7 (Piece 1, 9-11)	900.82	11,535	12,216	212.9	18.8	11,718	316.9	35.3	10,670	100.2	48.5
142R-7 (Piece 1, 12-14)	900.85	11,774	12,456	188.4	12.8	11,826	288.1	36.5	11,039	82.4	50.6
143R-5 (Piece 1, 32-34)	908.20	5,923	6,271	14.5	6.0	5,861	108.8	35.6	5,638	276.3	53.8
143R-5 (Piece 1, 35-37)	908.23	6,131	6,644	39.0	9.9	5,993	129.8	4.8	5,756	245.3	79.0
144R-1 (Piece 1, 13-15)	912.43	5,703	5,948	240.7	4.5	5,678	332.8	24.6	5,484	141.0	64.9
145R-1 (Piece 3, 130-132)	923.20	14,480	15,015	96.8	24.0	14,607	341.6	43.6	13,818	206.2	36.8
145R-1 (Piece 3, 134-136)	923.24	30,156	31,899	263.7	4.2	29,754	354.3	8.1	28,815	146.8	80.9
145R-4 (Piece 1, 32-34)	926.06	4,025	4,277	154.4	44.2	3,955	270.3	24.2	3,842	19.4	36.0
145R-4 (Piece 1, 35-37)	926.09	5,554	6,077	31.9	3.8	5,436	129.8	63.9	5,148	300.1	25.7
145R-5 (Piece 6, 83-85)	927.98	5,093	5,578	251.5	12.5	5,041	91.0	76.8	4,660	342.5	4.3
146R-4 (Piece 3, 111-113)	936.25	8,552	9,012	225.5	2.9	8,597	316.2	13.5	8,048	123.6	76.1
146R-4 (Piece 3, 114-116)	936.28	4,187	4,469	232.1	7.0	4,235	326.5	31.9	3,856	131.1	57.1
146R-6 (Piece 1B, 59-61)	938.60	3,075	3,192	126.5	2.4	3,068	35.9	14.4	2,967	226.0	75.4
147R-6 (Piece 2A, 55-57)	947.49	6,967	7,287	184.6	9.5	7,093	58.4	74.1	6,522	276.7	12.6
147R-6 (Piece 2A, 58-60)	947.52	12,282	12,962	7.5	35.5	12,510	174.6	53.8	11,373	273.1	6.2
148R-1 (Piece 2G, 101-103)	951.91	1,335	1,404	283.8	30.9	1,329	178.3	24.1	1,271	57.3	49.0
148R-4 (Piece 1A, 7-9)	955.34	5,378	5,528	58.3	8.8	5,424	323.9	26.0	5,183	165.4	62.3
148R-7 (Piece 4, 106-108)	960.54	6,034	6,121	144.3	4.1	6,060	9.4	84.2	5,923	234.6	4.1
148R-7 (Piece 4, 109-111)	960.57	5,641	5,755	24.0	66.3	5,626	129.2	6.5	5,542	221.9	22.6
149R-2 (Piece 2, 49-51)	962.30	2,756	2,896	28.3	36.8	2,823	272.2	30.5	2,548	154.5	38.3
149R-2 (Piece 2, 52-54)	962.33	2,909	3,057	34.6	30.1	2,938	282.5	33.0	2,733	156.3	42.2
149R-7 (Piece 2, 115-117)	969.13	5,588	5,880	240.3	21.3	5,650	342.6	28.6	5,236	119.0	53.0
149R-7 (Piece 2, 117-119)	969.15	5,538	5,827	255.7	28.2	5,605	0.3	25.1	5,181	125.0	50.6
150R-2 (Piece 2A, 42-44)	971.87	8,030	8,416	261.0	44.0	7,898	159.5	11.6	7,775	58.2	43.6
150R-7 (Piece 1, 5-7)	978.21	6,900	7,410	246.4	41.2	7,096	4.4	28.2	6,193	117.2	35.9
150R-7 (Piece 1, 8-10)	978.24	5,732	6,157	237.1	46.6	5,914	352.5	22.1	5,124	99.1	35.1
151R-1 (Piece 7, 104-106)	980.84	4,447	4,642	264.6	42.1	4,456	17.1	23.0	4,242	127.3	39.1
151R-4 (Piece 5, 88-90)	984.60	3,690	3,868	270.4	41.1	3,806	5.8	6.1	3,395	102.7	48.3
151R-4 (Piece 5, 91-93)	984.63	3,610	3,790	243.3	38.6	3,746	348.7	18.4	3,295	98.6	45.6
151R-5 (Piece 8, 49-51)	985.71	7,983	8,536	304.5	4.0	8,387	210.3	45.8	7,026	38.3	43.9
152R-3 (Piece 1, 62-64)	990.56	4,092	4,378	247.1	30.3	4,176	348.7	19.0	3,721	106.0	53.1
152R-3 (Piece 1, 65-67)	990.59	3,130	3,327	263.4	37.4	3,206	171.8	2.1	2,856	79.1	52.5
152R-6 (Piece 2, 62-64)	994.52	8,579	8,989	328.2	0.5	8,677	237.8	38.9	8,071	58.9	51.1
153R-2 (Piece 1, 18-20)	997.32	5,839	5,964	277.1	22.2	5,856	186.4	1.8	5,697	92.1	67.7
153R-2 (Piece 1, 21-23)	997.35	6,501	6,668	278.2	20.6	6,548	182.3	15.1	6,288	58.7	64.0
153R-7 (Piece 1B, 96-98)	1004.44	18,336	18,697	97.2	6.0	18,353	6.2	8.6	17,959	221.7	79.4
153R-7 (Piece 1B, 99-101)	1004.47	15,185	15,825	270.8	23.0	15,225	7.6	15.5	14,506	128.7	61.7
154R-5 (Piece 1, 32-34)	1010.59	6,293	6,487	37.7	36.8	6,261	207.1	52.7	6,132	303.9	5.1
155R-1 (Piece 2A, 16-18)	1015.16	7,667	7,897	21.2	7.6	7,779	285.4	36.9	7,325	121.1	52.1
155R-1 (Piece 2A, 19-21)	1015.19	9,284	9,639	33.4	3.1	9,336	300.7	40.3	8,878	127.0	49.5
155R-4 (Piece 1, 7-9)	1019.34	6,496	6,982	285.7	54.2	6,708	15.7	0.0	5,797	105.7	35.8
155R-4 (Piece 1, 10-12)	1019.37	5,869	6,274	256.1	48.3	6,146	3.5	15.0	5,187	105.5	37.8
156R-2 (Piece 4, 127-129)	1026.90	2,800	2,932	203.6	39.0	2,833	340.7	42.1	2,636	93.4	23.2
156R-2 (Piece 4, 131-133)	1026.94	4,809	5,088	202.1	32.1	4,789	329.7	44.3	4,549	92.0	28.7
156R-5 (Piece 2B, 53-55)	1030.57	5,461	5,679	50.8	14.4	5,408	141.3	1.9	5,295	238.7	75.5
157R-3 (Piece 3, 89-91)	1038.16	14,906	15,676	246.1	58.2	14,677	351.1	9.1	14,366	86.5	30.2
157R-3 (Piece 3, 92-94)	1038.19	15,260	15,805	261.3	19.9	15,176	147.0	48.7	14,799	5.7	34.4

Table T13 (continued).

Core, section, interval (cm)	L	F	P	T
134R-7 (Piece 1B, 65-67)	1.086	1.022	1.110	–0.576
134R-7 (Piece 1B, 68-70)	1.048	1.059	1.110	0.096
135R-3 (Piece 1, 7-9)	1.056	1.036	1.094	–0.214
135R-3 (Piece 1, 10-12)	1.041	1.066	1.110	0.231
136R-2 (Piece 1B, 56-58)	1.072	1.030	1.104	–0.409
136R-2 (Piece 1B, 59-61)	1.096	1.088	1.193	–0.043
137R-3 (Piece 2A, 40-42)	1.124	1.013	1.139	–0.796
137R-3 (Piece 2A, 43-45)	1.094	1.024	1.120	–0.584
137R-7 (Piece 6, 70-72)	1.092	1.013	1.106	–0.743
138R-3 (Piece 2B, 77-79)	1.053	1.052	1.108	–0.016
138R-3 (Piece 2B, 80-82)	1.050	1.042	1.095	–0.083
139R-1 (Piece 4, 84-86)	1.098	1.009	1.107	–0.831
139R-4 (Piece 4, 110-112)	1.062	1.111	1.179	0.273
139R-4 (Piece 4, 113-115)	1.027	1.050	1.078	0.293
140R-1 (Piece 3A, 29-31)	1.023	1.185	1.213	0.761
140R-1 (Piece 3A, 32-34)	1.037	1.214	1.258	0.686
140R-5 (Piece 2, 40-42)	1.045	1.045	1.093	–0.005
140R-5 (Piece 2, 43-45)	1.035	1.033	1.069	–0.026
141R-1 (Piece 7, 124-126)	1.051	1.042	1.096	–0.098
142R-3 (Piece 4B, 86-88)	1.103	1.037	1.144	–0.465
142R-3 (Piece 4B, 89-91)	1.110	1.025	1.138	–0.623
142R-7 (Piece 1, 9-11)	1.043	1.098	1.145	0.384
142R-7 (Piece 1, 12-14)	1.053	1.071	1.128	0.141
143R-5 (Piece 1, 32-34)	1.070	1.040	1.112	–0.270
143R-5 (Piece 1, 35-37)	1.109	1.041	1.154	–0.437
144R-1 (Piece 1, 13-15)	1.048	1.035	1.085	–0.143
145R-1 (Piece 3, 130-132)	1.028	1.057	1.087	0.336
145R-1 (Piece 3, 134-136)	1.072	1.033	1.107	–0.369
145R-4 (Piece 1, 32-34)	1.082	1.029	1.113	–0.461
145R-4 (Piece 1, 35-37)	1.118	1.056	1.180	–0.345
145R-5 (Piece 6, 83-85)	1.106	1.082	1.197	–0.125
146R-4 (Piece 3, 111-113)	1.048	1.068	1.120	0.166
146R-4 (Piece 3, 114-116)	1.055	1.098	1.159	0.271
146R-6 (Piece 1B, 59-61)	1.040	1.034	1.076	–0.079
147R-6 (Piece 2A, 55-57)	1.027	1.088	1.117	0.514
147R-6 (Piece 2A, 58-60)	1.036	1.100	1.140	0.457
148R-1 (Piece 2G, 101-103)	1.057	1.046	1.105	–0.102
148R-4 (Piece 1A, 7-9)	1.019	1.046	1.067	0.409
148R-7 (Piece 4, 106-108)	1.010	1.023	1.033	0.391
148R-7 (Piece 4, 109-111)	1.023	1.015	1.038	–0.205
149R-2 (Piece 2, 49-51)	1.026	1.108	1.137	0.602
149R-2 (Piece 2, 52-54)	1.041	1.075	1.119	0.290
149R-7 (Piece 2, 115-117)	1.041	1.079	1.123	0.313
149R-7 (Piece 2, 117-119)	1.040	1.082	1.125	0.339
150R-2 (Piece 2A, 42-44)	1.066	1.016	1.082	–0.605
150R-7 (Piece 1, 5-7)	1.044	1.146	1.197	0.517
150R-7 (Piece 1, 8-10)	1.041	1.154	1.202	0.561
151R-1 (Piece 7, 104-106)	1.042	1.050	1.094	0.089
151R-4 (Piece 5, 88-90)	1.016	1.121	1.139	0.753
151R-4 (Piece 5, 91-93)	1.012	1.137	1.150	0.835
151R-5 (Piece 8, 49-51)	1.018	1.194	1.215	0.820
152R-3 (Piece 1, 62-64)	1.048	1.123	1.177	0.420
152R-3 (Piece 1, 65-67)	1.038	1.123	1.165	0.515
152R-6 (Piece 2, 62-64)	1.036	1.075	1.114	0.345
153R-2 (Piece 1, 18-20)	1.018	1.028	1.047	0.208
153R-2 (Piece 1, 21-23)	1.018	1.041	1.060	0.383
153R-7 (Piece 1B, 96-98)	1.019	1.022	1.041	0.077
153R-7 (Piece 1B, 99-101)	1.039	1.050	1.091	0.112
154R-5 (Piece 1, 32-34)	1.036	1.021	1.058	–0.262
155R-1 (Piece 2A, 16-18)	1.015	1.062	1.078	0.599
155R-1 (Piece 2A, 19-21)	1.032	1.052	1.086	0.224
155R-4 (Piece 1, 7-9)	1.041	1.157	1.205	0.570
155R-4 (Piece 1, 10-12)	1.021	1.185	1.210	0.784
156R-2 (Piece 4, 127-129)	1.035	1.075	1.113	0.353
156R-2 (Piece 4, 131-133)	1.063	1.053	1.119	–0.083
156R-5 (Piece 2B, 53-55)	1.050	1.021	1.073	–0.399
157R-3 (Piece 3, 89-91)	1.068	1.022	1.091	–0.508
157R-3 (Piece 3, 92-94)	1.041	1.026	1.068	–0.234

Table T13 (continued).

Core, section, interval (cm)	Curated depth (mbsf)	Volume susceptibility (10^{-6} SI)	γ_1	Declination (°)	Inclination (°)	γ_2	Declination (°)	Inclination (°)	γ_3	Declination (°)	Inclination (°)
157R-5 (Piece 4, 45-47)	1040.72	5,364	5,534	32.4	15.3	5,439	229.7	74.0	5,120	123.6	4.5
158R-4 (Piece 3, 65-67)	1048.63	7,193	7,614	84.1	1.9	7,224	182.7	77.4	6,741	353.7	12.4
158R-4 (Piece 3, 68-70)	1048.66	6,462	6,642	70.6	42.1	6,496	271.6	45.9	6,250	170.4	10.7
159R-4 (Piece 3A, 89-91)	1058.73	5,566	5,726	335.0	33.5	5,547	125.1	52.7	5,426	235.1	14.6
159R-4 (Piece 3A, 92-94)	1058.76	4,499	4,662	70.7	72.5	4,534	340.4	0.1	4,302	250.4	17.5
159R-6 (Piece 4A, 89-91)	1061.70	5,754	5,793	220.0	60.5	5,750	89.0	20.4	5,719	351.1	20.4
160R-2 (Piece 1B, 29-31)	1065.19	4,363	4,526	262.6	50.5	4,403	138.5	24.8	4,161	33.9	28.6
160R-2 (Piece 1B, 32-34)	1065.22	3,604	3,752	263.4	29.0	3,651	99.0	60.1	3,409	357.2	6.7
160R-7 (Piece 1, 16-18)	1072.15	4,719	4,968	197.1	6.5	4,707	106.4	6.0	4,481	334.0	81.1
161R-2 (Piece 2, 20-22)	1074.59	7,737	8,290	98.9	17.4	7,821	211.1	50.3	7,100	356.4	34.4
161R-6 (Piece 3A, 65-67)	1080.59	6,224	6,459	255.0	24.2	6,143	45.5	62.7	6,071	159.6	11.9
161R-6 (Piece 3A, 68-70)	1080.62	7,287	7,364	293.5	46.3	7,308	162.8	32.0	7,188	54.7	26.4
162R-2 (Piece 3, 93-95)	1084.78	14,212	15,087	122.2	11.0	13,991	23.9	36.5	13,558	226.3	51.4
162R-6 (Piece 3, 84-86)	1090.19	4,117	4,286	144.4	14.2	4,118	243.5	32.1	3,947	34.0	54.2
162R-8 (Piece 1, 30-32)	1091.70	3,077	3,225	97.7	1.4	3,118	351.2	85.2	2,889	187.8	4.6
162R-8 (Piece 1, 33-35)	1091.73	4,184	4,404	95.6	8.5	4,214	292.6	81.1	3,933	185.9	2.6
162R-8 (Piece 1, 51-53)	1091.91	6,762	7,166	97.3	13.2	6,788	295.7	76.1	6,332	188.3	4.2
162R-8 (Piece 1, 54-56)	1091.94	7,232	7,787	277.2	3.3	7,212	21.8	77.1	6,696	186.5	12.4
163R-4 (Piece 2A, 85-87)	1096.55	5,572	5,821	153.2	7.8	5,534	301.7	80.8	5,359	62.5	4.7
163R-5 (Piece 3B, 68-70)	1097.64	4,304	4,460	30.0	3.9	4,314	122.4	31.8	4,138	293.8	57.9
164R-3 (Piece 1A, 29-31)	1102.29	2,292	2,443	286.7	9.2	2,252	63.6	77.5	2,182	195.3	8.4
164R-3 (Piece 1A,32-34)	1102.32	3,245	3,443	287.7	7.0	3,191	88.3	82.5	3,100	197.3	2.4
165R-3 (Piece 2A, 104-106)	1108.32	1,039	1,092	232.9	8.9	1,030	140.7	14.0	994	354.2	73.3
165R-4 (Piece 2A, 39-41)	1108.98	975	1,024	240.3	17.2	958	119.8	58.6	944	338.7	25.4
166R-1 (Piece 4A, 21-23)	1111.11	3,341	3,498	115.3	4.9	3,315	209.7	41.7	3,211	19.8	47.8
166R-5 (Piece 3, 77-79)	1116.66	3,060	3,184	136.7	4.2	3,027	233.3	57.4	2,969	44.0	32.3
166R-5 (Piece 3, 81-83)	1116.70	1,583	1,639	146.1	11.2	1,579	257.6	61.8	1,530	50.7	25.6
167R-1 (Piece 3D, 105-107)	1121.55	2,201	2,330	276.6	2.7	2,152	170.8	80.2	2,122	7.1	9.4
167R-6 (Piece 1, 7-9)	1127.32	3,069	3,239	97.2	6.4	3,008	189.1	16.3	2,960	346.6	72.4
167R-6 (Piece 1, 10-12)	1127.35	3,206	3,377	100.6	12.2	3,157	193.6	13.6	3,085	330.3	71.5
168R-2 (Piece 1, 7-9)	1131.46	2,734	2,847	111.9	16.8	2,721	205.6	12.1	2,635	329.6	69.1
168R-2 (Piece 1, 10-12)	1131.49	2,472	2,592	119.8	17.1	2,469	215.2	17.2	2,354	347.6	65.4
168R-7 (Piece 5, 74-76)	1139.39	3,618	3,758	21.8	5.7	3,666	259.2	79.5	3,430	112.7	8.8
169R-2 (Piece 3, 97-99)	1141.88	7,209	7,518	80.3	1.3	7,158	348.9	48.6	6,952	171.4	41.4
169R-4 (Piece 2A, 47-49)	1144.28	2,984	3,065	80.9	14.4	2,963	349.1	6.9	2,923	234.1	73.9
169R-4 (Piece 2A, 50-52)	1144.31	3,310	3,416	87.1	14.0	3,265	348.9	29.7	3,250	199.3	56.6
169R-6 (Piece 3, 79-81)	1147.22	2,774	2,933	86.5	19.2	2,735	196.5	44.5	2,653	339.9	39.3
170R-2 (Piece 3A, 61-63)	1151.14	2,076	2,132	301.9	38.3	2,120	64.0	33.9	1,975	180.4	33.5
170R-5 (Piece 5, 106-108)	1155.70	1,727	1,793	246.7	28.0	1,746	4.2	41.0	1,643	133.8	36.2
171R-2 (Piece 2, 28-30)	1160.73	30,606	38,253	241.1	46.3	27,804	333.9	2.6	25,761	66.4	43.6
171R-5 (Piece 3, 102-104)	1165.93	3,606	3,741	68.0	31.7	3,632	257.1	57.9	3,444	160.5	4.1
171R-5 (Piece 3, 105-107)	1165.96	3,841	3,991	66.7	9.1	3,856	208.0	78.4	3,677	335.6	7.2
172R-1 (Piece 6, 123-125)	1169.93	11,597	12,449	283.5	26.9	11,506	99.1	63.1	10,838	192.6	1.8
173R-1 (Piece 8, 96-98)	1179.36	3,039	3,135	317.4	4.6	3,036	51.5	41.3	2,946	222.2	48.3
173R-1 (Piece 8, 99-101)	1179.39	2,966	3,161	117.4	21.5	2,974	221.8	32.3	2,762	359.7	49.6
173R-3 (Piece 4, 119-121)	1182.45	2,205	2,257	309.6	36.3	2,227	116.9	53.0	2,132	215.1	6.1
173R-5 (Piece 6, 84-86)	1184.87	4,038	4,210	125.2	9.2	4,066	280.7	79.9	3,839	34.5	4.1
175R-1 (Piece 4, 78-80)	1191.88	1,678	1,797	142.7	6.3	1,658	238.6	42.7	1,580	46.0	46.6
175R-1 (Piece 4, 81-83)	1191.91	1,609	1,724	319.3	3.2	1,610	228.0	22.0	1,493	57.2	67.8
176R-3 (Piece 2A, 87-89)	1200.23	3,464	3,711	92.8	20.5	3,417	351.1	28.3	3,264	213.6	53.8
176R-3 (Piece 2A, 90-92)	1200.26	2,554	2,760	95.3	14.8	2,538	357.1	28.2	2,365	209.9	57.5
177R-5 (Piece 2, 57-59)	1207.61	2,013	2,144	76.8	11.8	2,021	172.5	25.3	1,875	323.9	61.7
177R-6 (Piece 4B, 108-110)	1209.62	5,172	5,662	25.8	24.3	5,095	134.9	35.9	4,757	269.7	44.2
177R-6 (Piece 4B, 119-121)	1209.73	6,777	7,272	30.6	16.5	6,671	138.4	46.0	6,389	286.5	39.4
178R-4 (Piece 5B, 113-115)	1216.34	3,528	3,781	317.2	29.3	3,548	59.1	20.2	3,255	178.5	53.2
178R-6 (Piece 5B, 134-136)	1219.40	834	851	252.7	28.6	837	99.9	58.5	814	349.4	12.1
179R-2 (Piece 6C, 130-132)	1223.40	38,383	40,809	114.2	4.0	39,380	207.1	36.1	34,962	18.7	53.7
179R-5 (Piece 3, 107-109)	1227.52	7,103	7,384	260.3	17.8	7057	50.2	69.7	6,867	167.3	9.5
179R-5 (Piece 3, 110-112)	1227.55	4,322	4,481	257.5	24.5	4,344	64.2	64.9	4,141	165.1	5.1
180R-5 (Piece 1, 10-12)	1236.38	10,312	10,645	221.9	20.9	10,276	128.4	8.9	10,014	16.7	67.1
181R-4 (Piece 8, 93-95)	1245.48	2,766	2,819	44.5	9.6	2,771	304.9	44.5	2,710	143.9	43.9
182R-2 (Piece 4, 65-67)	1251.97	1,126	1,201	238.8	41.7	1,174	347.1	19.4	1,004	95.5	42.0
183R-2 (Piece 2A, 75-77)	1261.76	1,875	1,956	149.4	24.5	1,884	19.0	54.9	1,786	250.8	23.5
184R-5 (Piece 3A, 65-67)	1275.55	4,698	4,981	265.3	36.7	4,623	114.0	49.7	4,491	6.4	14.4
184R-5 (Piece 3A, 67-69)	1275.57	4,750	5,032	271.9	37.9	4,709	93.8	52.1	4,508	2.6	0.9
185R-5 (Piece 1, 11-13)	1283.88	2,690	2,789	284.6	2.4	2,651	194.4	4.5	2,630	42.2	84.9
185R-5 (Piece 1, 14-16)	1283.91	3,881	4,068	98.1	11.3	3,954	189.4	6.5	3,620	308.8	76.9
186R-3 (Piece 1A, 21-23)	1291.38	3,195	3,305	78.5	41.3	3,253	299.8	40.5	3,029	189.5	22.2

Table T13 (continued).

Core, section, interval (cm)	L	F	P	T
157R-5 (Piece 4, 45-47)	1.018	1.062	1.081	0.553
158R-4 (Piece 3, 65-67)	1.054	1.072	1.130	0.137
158R-4 (Piece 3, 68-70)	1.022	1.039	1.063	0.271
159R-4 (Piece 3A, 89-91)	1.032	1.022	1.055	–0.182
159R-4 (Piece 3A, 92-94)	1.028	1.054	1.084	0.310
159R-6 (Piece 4A, 89-91)	1.008	1.005	1.013	–0.164
160R-2 (Piece 1B, 29-31)	1.028	1.058	1.088	0.347
160R-2 (Piece 1B, 32-34)	1.028	1.071	1.100	0.431
160R-7 (Piece 1, 16-18)	1.056	1.050	1.109	–0.048
161R-2 (Piece 2, 20-22)	1.060	1.102	1.168	0.248
161R-6 (Piece 3A, 65-67)	1.051	1.012	1.064	–0.620
161R-6 (Piece 3A, 68-70)	1.008	1.017	1.025	0.367
162R-2 (Piece 3, 93-95)	1.078	1.032	1.113	–0.411
162R-6 (Piece 3, 84-86)	1.041	1.043	1.086	0.029
162R-8 (Piece 1, 30-32)	1.034	1.079	1.117	0.387
162R-8 (Piece 1, 33-35)	1.045	1.072	1.120	0.221
162R-8 (Piece 1, 51-53)	1.056	1.072	1.132	0.122
162R-8 (Piece 1, 54-56)	1.080	1.077	1.163	–0.017
163R-4 (Piece 2A, 85-87)	1.052	1.033	1.086	–0.222
163R-5 (Piece 3B, 68-70)	1.034	1.042	1.078	0.108
164R-3 (Piece 1A, 29-31)	1.084	1.032	1.119	–0.440
164R-3 (Piece 1A,32-34)	1.079	1.029	1.111	–0.447
165R-3 (Piece 2A, 104-106)	1.061	1.036	1.099	–0.254
165R-4 (Piece 2A, 39-41)	1.069	1.015	1.085	–0.640
166R-1 (Piece 4A, 21-23)	1.055	1.032	1.090	–0.255
166R-5 (Piece 3, 77-79)	1.052	1.020	1.073	–0.443
166R-5 (Piece 3, 81-83)	1.038	1.032	1.071	–0.078
167R-1 (Piece 3D, 105-107)	1.083	1.014	1.098	–0.704
167R-6 (Piece 1, 7-9)	1.077	1.016	1.094	–0.639
167R-6 (Piece 1, 10-12)	1.070	1.023	1.094	–0.489
168R-2 (Piece 1, 7-9)	1.046	1.033	1.080	–0.167
168R-2 (Piece 1, 10-12)	1.050	1.049	1.101	–0.010
168R-7 (Piece 5, 74-76)	1.025	1.069	1.095	0.456
169R-2 (Piece 3, 97-99)	1.050	1.030	1.081	–0.256
169R-4 (Piece 2A, 47-49)	1.034	1.014	1.049	–0.422
169R-4 (Piece 2A, 50-52)	1.046	1.005	1.051	–0.816
169R-6 (Piece 3, 79-81)	1.073	1.031	1.105	–0.398
170R-2 (Piece 3A, 61-63)	1.006	1.073	1.079	0.853
170R-5 (Piece 5, 106-108)	1.027	1.062	1.091	0.389
171R-2 (Piece 2, 28-30)	1.376	1.079	1.485	–0.614
171R-5 (Piece 3, 102-104)	1.030	1.055	1.086	0.283
171R-5 (Piece 3, 105-107)	1.035	1.049	1.085	0.161
172R-1 (Piece 6, 123-125)	1.082	1.062	1.149	–0.137
173R-1 (Piece 8, 96-98)	1.033	1.031	1.064	–0.030
173R-1 (Piece 8, 99-101)	1.063	1.077	1.144	0.096
173R-3 (Piece 4, 119-121)	1.014	1.044	1.059	0.521
173R-5 (Piece 6, 84-86)	1.035	1.059	1.097	0.247
175R-1 (Piece 4, 78-80)	1.084	1.049	1.137	–0.258
175R-1 (Piece 4, 81-83)	1.071	1.079	1.155	0.051
176R-3 (Piece 2A, 87-89)	1.086	1.047	1.137	–0.285
176R-3 (Piece 2A, 90-92)	1.088	1.073	1.167	–0.087
177R-5 (Piece 2, 57-59)	1.061	1.078	1.143	0.115
177R-6 (Piece 4B, 108-110)	1.111	1.071	1.190	–0.212
177R-6 (Piece 4B, 119-121)	1.090	1.044	1.138	–0.334
178R-4 (Piece 5B, 113-115)	1.066	1.090	1.162	0.151
178R-6 (Piece 5B, 134-136)	1.017	1.029	1.046	0.262
179R-2 (Piece 6C, 130-132)	1.036	1.126	1.167	0.539
179R-5 (Piece 3, 107-109)	1.046	1.028	1.075	–0.248
179R-5 (Piece 3, 110-112)	1.031	1.049	1.082	0.216
180R-5 (Piece 1, 10-12)	1.036	1.026	1.063	–0.156
181R-4 (Piece 8, 93-95)	1.017	1.022	1.040	0.127
182R-2 (Piece 4, 65-67)	1.023	1.169	1.196	0.747
183R-2 (Piece 2A, 75-77)	1.038	1.055	1.095	0.172
184R-5 (Piece 3A, 65-67)	1.078	1.029	1.109	–0.441
184R-5 (Piece 3A, 67-69)	1.068	1.045	1.116	–0.205
185R-5 (Piece 1, 11-13)	1.052	1.008	1.060	–0.730
185R-5 (Piece 1, 14-16)	1.029	1.092	1.124	0.509
186R-3 (Piece 1A, 21-23)	1.016	1.074	1.091	0.641

Table T13 (continued).

Core, section, interval (cm)	Curated depth (mbsf)	Volume susceptibility (10^{-6} SI)	γ_1	Declination (°)	Inclination (°)	γ_2	Declination (°)	Inclination (°)	γ_3	Declination (°)	Inclination (°)
186R-6 (Piece 1, 33-35)	1295.82	2,875	3,017	339.4	24.0	2,903	242.4	15.4	2,705	122.7	60.9
186R-6 (Piece 1, 36-38)	1295.85	2,315	2,392	342.0	21.0	2,317	245.1	17.4	2,236	118.6	62.2
187R-5 (Piece 2B, 60-62)	1302.97	2,133	2,206	43.0	27.9	2,134	313.0	0.0	2,059	222.9	62.1
187R-5 (Piece 2B, 64-66)	1303.01	2,259	2,353	31.8	21.2	2,264	127.1	13.5	2,161	247.4	64.5
188R-3 (Piece 1A, 10-12)	1309.94	2,470	2,582	230.4	28.2	2,467	336.4	27.3	2,360	102.5	48.8
188R-3 (Piece 1D, 127-129)	1311.11	1,315	1,365	206.4	8.5	1,345	297.9	10.0	1,233	76.9	76.8
188R-4 (Piece 2C, 112-114)	1312.33	1,859	1,912	266.8	38.8	1,866	0.5	4.6	1,797	96.1	50.9
188R-4 (Piece 2C, 115-117)	1312.36	1,696	1,739	262.6	32.7	1,714	355.5	4.6	1,634	92.6	56.9
188R-6 (Piece 3, 54-56)	1314.52	3,462	3,585	270.9	22.2	3,493	175.4	13.2	3,307	56.8	63.8
189R-5 (Piece 1A, 7-9)	1322.19	891	933	298.1	10.4	886	207.3	4.2	855	95.7	78.8
189R-5 (Piece 1A, 9-11)	1322.21	916	964	296.3	7.3	908	205.6	5.3	877	79.8	80.9
190R-4 (Piece 3, 64-66)	1330.87	1,625	1,687	232.5	43.5	1,627	135.6	7.2	1,562	38.2	45.6
190R-4 (Piece 3, 67-69)	1330.90	2,149	2,228	245.5	37.5	2,152	136.8	22.7	2,068	23.1	43.9
191R-3 (Piece 3C, 83-85)	1339.40	24,132	25,164	66.9	39.5	24,744	185.3	30.0	22,486	300.1	36.1
191R-8 (Piece 1, 22-24)	1345.13	5,144	5,363	53.6	0.6	5,230	314.6	86.1	4,839	143.6	3.9
191R-8 (Piece 1, 25-27)	1345.16	6,320	6,780	252.8	40.8	6,330	27.2	39.0	5,850	139.2	24.8
192R-2 (Piece 2, 72-74)	1347.52	3,082	3,255	256.7	44.3	3,038	44.8	41.0	2,954	149.8	16.6
192R-4 (Piece 2, 61-63)	1350.02	3,020	3,204	177.8	42.2	3,021	326.5	43.3	2,835	72.5	16.3
192R-4 (Piece 2, 64-66)	1350.05	1,494	1,560	168.1	42.6	1,501	314.1	42.0	1,422	60.9	17.8
193R-1 (Piece 3B, 82-84)	1355.82	1,473	1,520	245.1	44.2	1,457	338.2	3.2	1,443	71.5	45.6
193R-1 (Piece 3B, 85-87)	1355.85	2,552	2,684	262.8	45.6	2,493	60.2	42.1	2,480	160.8	11.5
195R-2 (Piece 1, 2-4)	1365.57	2,760	3,027	243.8	40.4	2,673	82.0	48.1	2,579	341.7	9.1
195R-2 (Piece 1, 5-7)	1365.60	1,778	1,887	266.6	56.0	1,783	73.4	33.3	1,664	167.4	6.2
195R-7 (Piece 3, 38-40)	1372.24	2,720	2,849	212.3	51.2	2,780	64.9	34.1	2,530	323.5	16.2
196R-1 (Piece 3, 27-29)	1373.97	4,779	5,122	294.2	36.4	4,636	131.8	52.3	4,579	30.6	8.5
196R-4 (Piece 7A, 3-95)	1378.09	2,505	2,593	244.8	21.3	2,515	355.9	42.7	2,406	135.9	39.7
196R-4 (Piece 7A, 96-98)	1378.12	1,899	1,934	268.3	30.0	1,916	12.9	23.6	1,847	134.5	50.2
197R-2 (Piece 7, 57-59)	1385.37	1,075	1,099	108.4	26.9	1,066	356.7	36.2	1,060	225.6	42.0
197R-3 (Piece 5A, 87-89)	1387.17	815	838	286.7	39.1	815	149.8	42.0	792	37.1	23.2
198R-1 (Piece 4, 17-19)	1386.57	886	911	70.0	44.0	885	276.8	42.8	861	173.7	13.8
198R-1 (Piece 9B, 117-119)	1387.57	1,195	1,239	238.7	37.5	1,202	69.9	52.0	1,144	332.9	5.4
198R-1 (Piece 9B, 120-122)	1387.60	1,102	1,151	236.1	42.4	1,100	70.7	46.7	1,054	332.9	7.4
198R-4 (Piece 4, 105-107)	1391.69	2,868	2,924	105.5	4.4	2,858	9.1	55.5	2,823	198.5	34.1
199R-2 (Piece 2A, 79-81)	1394.56	2,705	2,876	284.9	27.8	2,666	61.7	54.1	2,572	183.4	20.8
199R-2 (Piece 5, 134-136)	1395.11	2,292	2,371	165.9	19.1	2,299	43.2	57.3	2,208	265.3	25.4
199R-2 (Piece 5, 137-139)	1395.14	2,231	2,353	148.7	16.2	2,188	359.5	71.3	2,152	241.3	9.1
199R-6 (Piece 3, 49-51)	1400.12	8,596	8,866	45.1	35.3	8,623	172.6	40.6	8,299	291.6	29.4
199R-6 (Piece 3, 53-55)	1400.16	9,823	10,204	31.8	16.8	9,759	159.1	63.5	9,506	295.5	19.8
200R-4 (Piece 2B, 58-60)	1406.78	6,377	6,780	103.3	51.7	6,650	243.4	31.2	5,701	346.1	19.9
201R-1 (Piece 1, 11-13)	1411.71	1,069	1,105	285.4	43.2	1,064	140.0	41.3	1,040	33.3	18.1
201R-5 (Piece 2A, 42-44)	1417.08	2,298	2,427	162.2	1.1	2,337	43.0	87.8	2,129	252.2	1.9
201R-7 (Piece 4, 113-115)	1420.72	2,887	2,960	283.7	63.9	2,886	146.6	19.8	2,814	50.5	16.4
201R-7 (Piece 4, 116-118)	1420.75	3,330	3,552	133.0	6.2	3,298	243.3	72.6	3,139	41.1	16.2
202R-1 (Piece 3A, 80-82)	1422.00	2,949	3,023	141.3	24.0	2,988	260.4	47.5	2,836	34.7	32.6
202R-5 (Piece 2C, 109-111)	1427.88	3,023	3,158	66.5	70.5	3,017	310.0	9.0	2,894	217.2	17.2
202R-5 (Piece 2C, 112-114)	1427.91	3,760	3,989	80.8	70.9	3,814	304.3	14.1	3,476	211.1	12.6
202R-8 (Piece 2, 72-74)	1431.27	15,937	16,664	132.5	52.0	16,213	310.2	38.0	14,935	41.0	1.1
203R-2 (Piece 1D, 62-64)	1432.73	4,549	4,793	321.3	3.7	4,590	214.9	77.0	4,262	52.1	12.5
203R-5 (Piece 4, 113-115)	1437.05	6,573	7,089	347.0	18.8	6,510	123.5	64.9	6,119	251.4	16.1
203R-5 (Piece 4, 116-118)	1437.08	3,996	4,359	351.8	7.1	4,095	225.0	78.2	3,533	83.0	9.3
204R-4 (Piece 4, 117-119)	1445.62	4,113	4,475	109.6	47.9	4,195	270.9	40.6	3,668	9.0	9.4
204R-7 (Piece 2, 44-46)	1448.94	4,864	5,062	89.6	50.0	4,956	277.9	39.7	4,575	184.5	4.1
204R-7 (Piece 2, 47-49)	1448.97	3,810	4,151	247.0	7.6	3,951	11.3	76.6	3,329	155.5	10.9
205R-4 (Piece 4A, 115-117)	1455.70	7,553	7,922	141.4	30.5	7,788	301.2	57.9	6,949	46.0	9.1
205R-4 (Piece 4A, 117-119)	1455.72	5,390	5,683	125.1	57.8	5,464	295.1	31.8	5,022	27.9	4.5
206R-2 (Piece 2B, 83-85)	1461.79	4,139	4,439	95.9	32.4	4,339	271.0	57.5	3,639	4.5	2.2
206R-4 (Piece 2, 58-60)	1464.08	2,400	2,562	156.0	35.6	2,416	2.2	51.4	2,222	255.5	12.9
206R-4 (Piece 2, 61-63)	1464.11	3,616	3,836	154.3	25.7	3,681	350.7	63.4	3,330	247.4	6.6
207R-2 (Piece 1, 19-21)	1471.11	1,618	1,726	321.0	14.6	1,630	83.4	64.1	1,499	225.3	20.9
207R-4 (Piece 1B, 60-62)	1473.67	812	841	277.4	18.0	813	159.6	55.2	783	17.6	28.7
207R-7 (Piece 2B, 110-112)	1478.42	1,712	1,817	81.1	34.7	1,779	200.6	35.3	1,541	321.2	35.7
207R-7 (Piece 2B, 113-115)	1478.45	2,960	3,186	74.1	27.9	3,022	193.9	43.2	2,670	323.1	34.0
208R-4 (Piece 1, 9-11)	1482.73	1,027	1,054	292.4	27.4	1,038	68.6	54.3	989	191.0	21.0
208R-4 (Piece 1, 12-14)	1482.76	1,027	1,101	53.2	39.4	1,035	160.2	19.6	947	270.3	44.1
208R-5 (Piece 3C, 106-108)	1485.20	3,860	4,378	269.2	19.4	4,044	177.2	5.5	3,159	72.0	69.8
208R-8 (Piece 2A, 65-67)	1488.72	6,190	6,789	351.8	16.9	6,260	126.9	66.8	5,520	257.0	15.4
209R-2 (Piece 1E, 75-77)	1490.49	854	911	225.8	21.6	837	325.4	22.8	815	97.0	57.6
209R-8 (Piece 4, 103-105)	1498.64	1,950	2,114	66.5	14.8	1,934	170.7	42.9	1,803	322.1	43.3

Table T13 (continued).

Core, section, interval (cm)	L	F	P	T
186R-6 (Piece 1, 33-35)	1.039	1.073	1.115	0.293
186R-6 (Piece 1, 36-38)	1.032	1.036	1.070	0.057
187R-5 (Piece 2B, 60-62)	1.033	1.037	1.071	0.048
187R-5 (Piece 2B, 64-66)	1.039	1.047	1.089	0.092
188R-3 (Piece 1A, 10-12)	1.046	1.045	1.094	–0.012
188R-3 (Piece 1D, 127-129)	1.015	1.091	1.107	0.712
188R-4 (Piece 2C, 112-114)	1.025	1.038	1.064	0.211
188R-4 (Piece 2C, 115-117)	1.015	1.049	1.064	0.531
188R-6 (Piece 3, 54-56)	1.026	1.056	1.084	0.354
189R-5 (Piece 1A, 7-9)	1.053	1.037	1.091	–0.178
189R-5 (Piece 1A, 9-11)	1.062	1.035	1.099	–0.274
190R-4 (Piece 3, 64-66)	1.037	1.042	1.080	0.054
190R-4 (Piece 3, 67-69)	1.035	1.041	1.077	0.075
191R-3 (Piece 3C, 83-85)	1.017	1.100	1.119	0.701
191R-8 (Piece 1, 22-24)	1.025	1.081	1.108	0.510
191R-8 (Piece 1, 25-27)	1.071	1.082	1.159	0.070
192R-2 (Piece 2, 72-74)	1.072	1.028	1.102	–0.426
192R-4 (Piece 2, 61-63)	1.060	1.066	1.130	0.039
192R-4 (Piece 2, 64-66)	1.039	1.055	1.097	0.162
193R-1 (Piece 3B, 82-84)	1.043	1.010	1.053	–0.633
193R-1 (Piece 3B, 85-87)	1.077	1.005	1.083	–0.862
195R-2 (Piece 1, 2-4)	1.132	1.037	1.174	–0.551
195R-2 (Piece 1, 5-7)	1.058	1.072	1.134	0.099
195R-7 (Piece 3, 38-40)	1.025	1.099	1.126	0.591
196R-1 (Piece 3, 27-29)	1.105	1.012	1.119	–0.779
196R-4 (Piece 7A, 3-95)	1.031	1.045	1.078	0.183
196R-4 (Piece 7A, 96-98)	1.010	1.037	1.047	0.578
197R-2 (Piece 7, 57-59)	1.032	1.006	1.038	–0.688
197R-3 (Piece 5A, 87-89)	1.028	1.030	1.058	0.033
198R-1 (Piece 4, 17-19)	1.029	1.028	1.058	–0.013
198R-1 (Piece 9B, 117-119)	1.030	1.051	1.083	0.246
198R-1 (Piece 9B, 120-122)	1.046	1.044	1.092	–0.028
198R-4 (Piece 4, 105-107)	1.023	1.012	1.036	–0.304
199R-2 (Piece 2A, 79-81)	1.079	1.037	1.118	–0.357
199R-2 (Piece 5, 134-136)	1.031	1.041	1.074	0.132
199R-2 (Piece 5, 137-139)	1.076	1.016	1.093	–0.635
199R-6 (Piece 3, 49-51)	1.028	1.039	1.068	0.160
199R-6 (Piece 3, 53-55)	1.046	1.027	1.073	–0.258
200R-4 (Piece 2B, 58-60)	1.019	1.167	1.189	0.778
201R-1 (Piece 1, 11-13)	1.039	1.023	1.063	–0.253
201R-5 (Piece 2A, 42-44)	1.038	1.098	1.140	0.424
201R-7 (Piece 4, 113-115)	1.026	1.026	1.052	–0.001
201R-7 (Piece 4, 116-118)	1.077	1.050	1.131	–0.203
202R-1 (Piece 3A, 80-82)	1.012	1.054	1.066	0.631
202R-5 (Piece 2C, 109-111)	1.047	1.042	1.091	–0.047
202R-5 (Piece 2C, 112-114)	1.046	1.097	1.148	0.345
202R-8 (Piece 2, 72-74)	1.028	1.086	1.116	0.499
203R-2 (Piece 1D, 62-64)	1.044	1.077	1.125	0.261
203R-5 (Piece 4, 113-115)	1.089	1.064	1.158	–0.157
203R-5 (Piece 4, 116-118)	1.065	1.159	1.234	0.403
204R-4 (Piece 4, 117-119)	1.067	1.144	1.220	0.351
204R-7 (Piece 2, 44-46)	1.021	1.083	1.106	0.581
204R-7 (Piece 2, 47-49)	1.051	1.187	1.247	0.552
205R-4 (Piece 4A, 115-117)	1.017	1.121	1.140	0.741
205R-4 (Piece 4A, 117-119)	1.040	1.088	1.132	0.364
206R-2 (Piece 2B, 83-85)	1.023	1.192	1.220	0.769
206R-4 (Piece 2, 58-60)	1.061	1.087	1.153	0.176
206R-4 (Piece 2, 61-63)	1.042	1.105	1.152	0.414
207R-2 (Piece 1, 19-21)	1.059	1.087	1.152	0.186
207R-4 (Piece 1B, 60-62)	1.035	1.038	1.074	0.046
207R-7 (Piece 2B, 110-112)	1.021	1.154	1.179	0.745
207R-7 (Piece 2B, 113-115)	1.054	1.132	1.193	0.402
208R-4 (Piece 1, 9-11)	1.016	1.049	1.065	0.507
208R-4 (Piece 1, 12-14)	1.064	1.093	1.162	0.179
208R-5 (Piece 3C, 106-108)	1.083	1.280	1.386	0.514
208R-8 (Piece 2A, 65-67)	1.085	1.134	1.230	0.215
209R-2 (Piece 1E, 75-77)	1.088	1.027	1.117	–0.520
209R-8 (Piece 4, 103-105)	1.093	1.073	1.173	–0.120

Table T13 (continued).

Core, section, interval (cm)	Curated depth (mbsf)	Volume susceptibility (10^{-6} SI)	γ_1	Declination (°)	Inclination (°)	γ_2	Declination (°)	Inclination (°)	γ_3	Declination (°)	Inclination (°)
209R-8 (Piece 4, 106-108)	1498.67	3,231	3,499	53.6	12.0	3,260	150.1	28.3	2,935	303.0	58.9
210R-4 (Piece 1, 8-10)	1502.46	2,701	2,914	167.4	0.1	2,708	257.6	73.3	2,482	77.4	16.7
210R-4 (Piece 1, 11-13)	1502.49	3,236	3,501	171.7	10.0	3,247	284.6	65.7	2,959	77.7	21.9
210R-4 (Piece 1, 52-54)	1502.90	3,429	3,699	175.1	11.7	3,373	282.8	55.9	3,214	77.8	31.6
210R-4 (Piece 1, 55-57)	1502.93	1,108	1,151	173.5	1.6	1,094	270.0	76.7	1,079	83.1	13.2

Note: γ_1, γ_2, and γ_3 are the maximum, intermediate, and minimum eigenvalues of the susceptibility tensor, respectively, with the declination and inclination of the associated eigenvectors. $L = \gamma_1/\gamma_2$. $F = \gamma_2/\gamma_3$. $P = \gamma_1/\gamma_3$. $T = [2 \times \ln(\gamma_2) - \ln(\gamma_1) - \ln(\gamma_3)]/[\ln(\gamma_1) - \ln(\gamma_3)]$.

Table T13 (continued).

Core, section, interval (cm)	L	F	P	T
209R-8 (Piece 4, 106-108)	1.074	1.111	1.192	0.193
210R-4 (Piece 1, 8-10)	1.076	1.091	1.174	0.086
210R-4 (Piece 1, 11-13)	1.078	1.097	1.183	0.105
210R-4 (Piece 1, 52-54)	1.097	1.050	1.151	–0.312
210R-4 (Piece 1, 55-57)	1.052	1.014	1.067	–0.576

Table T14. Magnetic susceptibility downhole for Hole 735B.

Leg	Site	Hole	Core	Type	Section	Interval (cm)	Depth (mbsf)	Depth (mbsf)	Susceptibility (10^{-5} SI)
176	735	B	89	R	1	4	504.84	504.84	147.4
176	735	B	89	R	1	8	504.88	504.88	77.9
176	735	B	89	R	1	12	504.92	504.92	362.4
176	735	B	89	R	1	16	504.96	504.96	414.7
176	735	B	89	R	1	20	505	505	405.9
176	735	B	89	R	1	24	505.04	505.04	246.4
176	735	B	89	R	1	28	505.08	505.08	265.8
176	735	B	89	R	1	32	505.12	505.12	337
176	735	B	89	R	1	36	505.16	505.16	617.5
176	735	B	89	R	1	40	505.2	505.2	756.9
176	735	B	89	R	1	44	505.24	505.24	621.5
176	735	B	89	R	1	48	505.28	505.28	634.5
176	735	B	89	R	1	52	505.32	505.32	534.1
176	735	B	89	R	1	56	505.36	505.36	519.7
176	735	B	89	R	1	60	505.4	505.4	478.1
176	735	B	89	R	1	64	505.44	505.44	431.8
176	735	B	89	R	1	68	505.48	505.48	203.5
176	735	B	89	R	1	72	505.52	505.52	272.9
176	735	B	89	R	1	76	505.56	505.56	296.8
176	735	B	89	R	1	80	505.6	505.6	349
176	735	B	89	R	1	84	505.64	505.64	216.8
176	735	B	89	R	1	88	505.68	505.68	91.8
176	735	B	89	R	1	92	505.72	505.72	274.1
176	735	B	89	R	1	96	505.76	505.76	356.5
176	735	B	89	R	1	100	505.8	505.8	320.6
176	735	B	89	R	1	104	505.84	505.84	242.9
176	735	B	89	R	1	108	505.88	505.88	286.7
176	735	B	89	R	1	112	505.92	505.92	380.2
176	735	B	89	R	1	116	505.96	505.96	341.6
176	735	B	89	R	1	120	506	506	123.5
176	735	B	89	R	1	124	506.04	506.04	188.2
176	735	B	89	R	2	4	506.11	506.11	258.1
176	735	B	89	R	2	8	506.15	506.15	216.4
176	735	B	89	R	2	12	506.19	506.19	260.5
176	735	B	89	R	2	16	506.23	506.23	281.8
176	735	B	89	R	2	20	506.27	506.27	340.2
176	735	B	89	R	2	24	506.31	506.31	154.4
176	735	B	89	R	2	28	506.35	506.35	79.3
176	735	B	89	R	2	32	506.39	506.39	211.2
176	735	B	89	R	2	36	506.43	506.43	328.6
176	735	B	89	R	2	40	506.47	506.47	305.9
176	735	B	89	R	2	44	506.51	506.51	311.2
176	735	B	89	R	2	48	506.55	506.55	310.9
176	735	B	89	R	2	52	506.59	506.59	304.3
176	735	B	89	R	2	56	506.63	506.63	355.8
176	735	B	89	R	2	60	506.67	506.67	380.7
176	735	B	89	R	2	64	506.71	506.71	439.7
176	735	B	89	R	2	68	506.75	506.75	305.3
176	735	B	89	R	2	72	506.79	506.79	110.5
176	735	B	89	R	2	76	506.83	506.83	147.6
176	735	B	89	R	2	80	506.87	506.87	124.3
176	735	B	89	R	2	84	506.91	506.91	442.3
176	735	B	89	R	2	88	506.95	506.95	464.5
176	735	B	89	R	2	92	506.99	506.99	410.1
176	735	B	89	R	2	96	507.03	507.03	132.8
176	735	B	89	R	2	100	507.07	507.07	41.4
176	735	B	90	R	1	4	507.84	507.84	359.5
176	735	B	90	R	1	8	507.88	507.87	383.6
176	735	B	90	R	1	12	507.92	507.91	411.9
176	735	B	90	R	1	16	507.96	507.95	331.5
176	735	B	90	R	1	20	508	507.98	445.6
176	735	B	90	R	1	24	508.04	508.02	694.6
176	735	B	90	R	1	28	508.08	508.06	777.4
176	735	B	90	R	1	32	508.12	508.09	835.1
176	735	B	90	R	1	36	508.16	508.13	686.5

Note: Only a portion of this table appears here. The complete table is in ASCII format in the **TABLES** directory.

Table T15. Sample bulk and grain densities for Hole 735B.

Leg	Site	Hole	Core	Type	Section	Top (cm)	Bottom (cm)	Piece Number	Depth (mbsf)	Bulk density (g/cm^3)	Grain density (g/cm^3)	Porosity (%)	IUGS rock name
118	735	B	1	D	1	19	21		0.19	2.938			Gabbronorite
118	735	B	1	D	1	141	143		1.41	2.945			Gabbronorite
118	735	B	2	D	1	113	115		7.63	3.103			Oxide gabbronorite
118	735	B	2	D	1	139	141		7.89	2.924			Gabbronorite
118	735	B	2	D	2	99	101		8.99	2.947			Olivine gabbro
118	735	B	4	D	2	7	9		19.07	2.876			Gabbronorite
118	735	B	6	D	1	111	113		25.11	2.900			Gabbronorite
118	735	B	7	D	2	9	11		27.59	3.001			Olivine gabbro
118	735	B	8	D	1	45	48		29.65	2.891			Olivine gabbro
118	735	B	9	D	1	120	122		34.40	2.969			Olivine gabbro
118	735	B	10	D	1	24	26		36.44	3.019			Olivine gabbro
118	735	B	11	D	1	6	8		39.26	3.173			Oxide olivine gabbro
118	735	B	12	R	1	55	62		39.95	2.959			Olivine gabbro
118	735	B	12	R	3	8	10		42.48	2.905			Olivine gabbro
118	735	B	12	R	3	83	85		43.23	2.996			Olivine gabbro
118	735	B	13	R	1	102	105		45.52	2.966			Olivine gabbro
118	735	B	13	R	2	55	58		46.05	2.889			Olivine gabbro
118	735	B	14	R	1	35	38		51.55	3.010			Olivine gabbro
118	735	B	14	R	2	22	25		59.92	3.027			Olivine gabbro
118	735	B	14	R	4	22	25		55.92	2.956			Olivine gabbro
118	735	B	15	R	2	128	130		58.98	2.878			Olivine gabbro
118	735	B	16	R	1	139	141		63.19	2.920			Olivine gabbro
118	735	B	16	R	4	77	79		67.07	2.926			Olivine gabbro
118	735	B	16	R	5	24	26		68.04	2.922			Olivine gabbro
118	735	B	18	R	3	29	31		71.79	2.927			Olivine gabbro
118	735	B	19	R	5	126	128		80.96	2.859			Troctolitic gabbro
118	735	B	20	R	2	54	56		86.24	2.949			Olivine gabbro
118	735	B	21	R	2	49	51		91.19	2.821			Oxide gabbro
118	735	B	22	R	2	41	43		95.91	2.953			Olivine gabbro
118	735	B	22	R	3	118	120		95.18	2.912			Olivine gabbro
118	735	B	23	R	2	34	36		102.34	2.945			Olivine gabbro
118	735	B	23	R	4	120	122		105.20	2.955			Others
118	735	B	24	R	2	95	97		107.95	3.350			Oxide gabbro
118	735	B	24	R	3	50	52		109.00	3.132			Oxide gabbro
118	735	B	24	R	4	26	28		110.26	2.975			Olivine gabbro
118	735	B	25	R	2	5	7		112.05	2.928			Olivine gabbro
118	735	B	25	R	3	137	139		114.87	2.967			Olivine gabbro
118	735	B	26	R	1	62	64		116.12	2.925			Olivine gabbro
118	735	B	27	R	1	84	86		122.34	3.005			Olivine gabbro
118	735	B	27	R	3	32	34		123.82	2.893			Olivine gabbro
118	735	B	28	R	2	12	14		128.12	3.033			Olivine gabbro
118	735	B	28	R	2	114	116		129.14	2.974			Olivine gabbro
118	735	B	29	R	2	46	48		133.46	2.952			Olivine gabbro
118	735	B	29	R	4	19	21		136.19	2.928			Olivine gabbro
118	735	B	30	R	3	137	139		140.87	3.271			Oxide gabbro
118	735	B	30	R	4	14	16		141.14	2.876			Olivine gabbro
118	735	B	30	R	5	91	93		143.41	2.917			Olivine gabbro
118	735	B	31	R	2	120	122		146.20	2.942			Olivine gabbro
118	735	B	31	R	4	118	120		148.18	2.890			Olivine gabbro
118	735	B	32	R	1	64	66		149.14	4.083			Oxide gabbro
118	735	B	32	R	3	14	16		151.64	2.894			Olivine gabbro
118	735	B	33	R	4	27	29		158.27	2.870			Olivine gabbro
118	735	B	33	R	4	129	131		159.29	2.930			Olivine gabbro
118	735	B	34	R	1	103	105		159.53	2.969			Olivine gabbro
118	735	B	34	R	4	30	32		163.30	2.991			Others
118	735	B	35	R	1	39	41		163.79	2.972			Olivine gabbro
118	735	B	35	R	5	131	133		170.31	2.989			Olivine gabbro
118	735	B	36	R	2	11	13		172.61	2.913			Olivine gabbro
118	735	B	36	R	3	36	38		174.36	2.935			Oxide olivine gabbro
118	735	B	37	R	1	11	13		176.11	2.927			Oxide olivine gabbro
118	735	B	37	R	3	80	82		179.80	3.065			Oxide olivine gabbro
118	735	B	38	R	2	15	17		182.65	2.962			Troctolitic gabbro
118	735	B	38	R	4	28	30		184.90	2.981			Oxide olivine gabbro
118	735	B	39	R	1	145	147		187.45	2.958			Oxide olivine gabbro
118	735	B	39	R	3	21	23		189.21	2.871			Oxide olivine gabbro
118	735	B	40	R	2	62	64		193.12	2.895			Oxide olivine gabbro

Note: Only a portion of this table appears here. The complete table is in ASCII format in the **TABLES** directory.

Table T16. Physical properties of principal lithologies for Hole 735B

	Thermal conductivity (W/[m·K])			Density (g/cm^3)			Velocity (m/s)		
	Mean	Standard deviation	Number of points	Mean	Standard deviation	Number of points	Mean	Standard deviation	Number of points
Bulk rock	2.270	0.212	257	2.98	0.12	347	6784	313	367
Troctolite	2.107	0.100	4	2.98	0.11	4	6844	213	4
Troctolitic gabbro	2.394	0.500	6	2.95	0.07	8	6851	233	8
Olivine gabbro	2.284	0.182	166	2.96	0.10	219	6839	316	224
Gabbro	2.231	0.229	37	2.98	0.06	39	6703	214	40
Gabbronorite plus orthopyroxene-bearing gabbro	2.309	0.191	12	2.99	0.12	18	6649	389	19
Oxide gabbronorite	2.268	0.176	4	3.09	0.08	7	6620	353	8
Oxide gabbro	2.462	0.437	5	3.21	0.39	8	6432	313	9
Oxide olivine gabbro	2.176	0.185	20	3.05	0.12	43	6734	272	54
Others	1.941		2	2.96		1	6450		1

Table T17. Thermal conductivities for samples from Hole 735B. (See table note. Continued on next three pages.)

Leg	Site	Hole	Core	Type	Section	Piece Number	Top (cm)	Base (cm)	Midpoint (mbsf)	Thermal conductivity (W/[m·K])	IUGS rock name
118	735	B	12	R	1		36	41	39.8	2.30	Oxide olivine gabbro
118	735	B	12	R	1		55	62	40.0	2.19	Olivine gabbro
118	735	B	14	R	1		20	26	51.4	2.20	Olivine gabbro
118	735	B	14	R	3		122	130	55.2	2.06	Olivine gabbro
118	735	B	16	R	1		80	86	62.6	1.94	Olivine gabbro
118	735	B	19	R	1		138	145	76.1	2.15	Olivine gabbro
118	735	B	19	R	3		126	133	79.0	2.07	Olivine gabbro
118	735	B	23	R	3		33	41	103.8	2.82	Oxide gabbro
118	735	B	25	R	3		42	49	114.0	2.11	Olivine gabbro
118	735	B	27	R	3		21	29	124.8	2.32	Olivine gabbro
118	735	B	28	R	2		105	113	128.1	2.51	Olivine gabbro
118	735	B	33	R	1		93	100	154.5	2.48	Olivine gabbro
118	735	B	37	R	1		77	83	176.8	2.29	Oxide olivine gabbro
118	735	B	42	R	2		123	130	203.8	2.32	Oxide olivine gabbro
118	735	B	44	R	1		102	110	207.1	2.48	Olivine gabbro
118	735	B	47	R	1		34	41	226.4	2.27	Oxide olivine gabbro
118	735	B	49	R	1		53	61	236.6	2.34	Oxide olivine gabbro
118	735	B	51	R	1		52	60	243.6	1.96	Oxide olivine gabbro
118	735	B	53	R	2		81	86	255.3	2.21	Oxide olivine gabbro
118	735	B	55	R	2		45	55	267.0	1.78	Oxide olivine gabbro
118	735	B	56	R	2		76	85	272.3	2.16	Oxide olivine gabbro
118	735	B	57	R	3		23	30	278.3	2.01	Olivine gabbro
118	735	B	59	R	3		126	134	289.8	2.28	Olivine gabbro
118	735	B	62	R	4		32	39	305.4	2.24	Olivine gabbro
118	735	B	64	R	1		18	24	315.2	2.29	Olivine gabbro
118	735	B	65	R	1		34	43	320.4	2.12	Olivine gabbro
118	735	B	67	R	3		79	87	333.8	2.22	Olivine gabbro
118	735	B	71	R	2		50	57	353.0	2.30	Olivine gabbro
118	735	B	72	R	2		90	98	358.4	2.09	Olivine gabbro
118	735	B	75	R	5		31	38	390.9	2.55	Olivine gabbro
118	735	B	76	R	6		21	28	401.7	2.29	Olivine gabbro
118	735	B	77	R	2		37	46	405.4	2.04	Oxide olivine gabbro
118	735	B	79	R	3		127	136	418.8	2.31	Olivine gabbro
118	735	B	80	R	7		56	64	433.6	2.10	Oxide olivine gabbro
118	735	B	81	R	3		142	150	438.0	2.34	Oxide olivine gabbro
118	735	B	85	R	6		134	145	480.4	2.02	Troctolite
118	735	B	86	R	4		24	34	485.8	2.63	Olivine gabbro
118	735	B	87	R	3		72	78	494.2	2.30	Olivine gabbro
176	735	B	89	R	1	2	9	22	504.96	2.240	Olivine gabbro
176	735	B	89	R	2	1	0	24	506.19	2.010	Gabbro
176	735	B	90	R	2	1B	30	40	509.65	2.207	Olivine gabbro
176	735	B	90	R	8	1B	25	46	517.22	2.058	Troctolitic gabbro
176	735	B	91	R	1	2B	29	50	517.80	2.664	Olivine gabbro
176	735	B	91	R	3	1E	103	121	521.07	1.545	Olivine gabbro
176	735	B	92	R	1	2B	75	87	527.81	2.269	Gabbro
176	735	B	92	R	2	7	37	54	528.84	2.426	Olivine gabbro
176	735	B	93	R	3	1C	46	64	534.99	2.342	Olivine gabbro
176	735	B	93	R	5	3	20	41	537.35	2.077	Oxide olivine gabbro
176	735	B	94	R	3	12	50	64	539.76	1.699	Gabbro
176	735	B	94	R	3	5	115	127	540.40	2.626	Gabbro
176	735	B	95	R	1	8	115	135	545.85	2.304	Olivine gabbro
176	735	B	95	R	3	1C	16	29	547.62	2.359	Olivine gabbro
176	735	B	96	R	1	4	22	37	548.60	2.220	Gabbro
176	735	B	96	R	2	4	37	55	550.26	2.376	Oxide gabbronorite
176	735	B	97	R	1	2C	120	130	557.55	2.455	Oxide gabbronorite
176	735	B	97	R	3	1C	21	33	559.09	2.157	Oxide gabbronorite
176	735	B	98	R	1	5B	32	45	561.39	2.292	Olivine gabbro
176	735	B	99	R	4	1C	17	27	570.24	2.285	Gabbronorite
176	735	B	99	R	6	3	23	36	573.04	2.236	Gabbronorite
176	735	B	100	R	1	3D	31	46	575.89	2.205	Oxide gabbro
176	735	B	101	R	3	1D	35	47	588.03	2.345	Olivine gabbro
176	735	B	101	R	4	1B	20	33	589.08	2.231	Oxide olivine gabbro
176	735	B	102	R	1	4A	25	35	590.20	1.873	Oxide olivine gabbro
176	735	B	102	R	3	6	6	55	593.09	2.412	Gabbronorite
176	735	B	103	R	3	4A	45	63	598.19	1.969	Gabbronorite
176	735	B	103	R	4	3D	28	66	599.62	1.921	Gabbro
176	735	B	104	R	2	11	90	112	606.81	2.049	Olivine gabbro

Table T17 (continued).

Leg	Site	Hole	Core	Type	Section	Piece Number	Top (cm)	Base (cm)	Midpoint (mbsf)	Thermal conductivity (W/[m·K])	IUGS rock name
176	735	B	104	R	3	1C	27	39	607.27	2.256	Olivine gabbro
176	735	B	105	R	1	8B	48	63	609.36	2.248	Olivine gabbro
176	735	B	105	R	2	6A	102	118	611.29	2.211	Olivine gabbro
176	735	B	106	R	4	4B	51	63	618.66	2.181	Olivine gabbro
176	735	B	107	R	1	2B	17	30	619.74	2.366	Olivine gabbro
176	735	B	107	R	2	2A	50	70	621.52	2.196	Oxide olivine gabbro
176	735	B	108	R	2	2	44	56	625.47	2.193	Olivine gabbro
176	735	B	108	R	4	4	80	92	628.47	2.084	Olivine gabbro
176	735	B	109	R	1	2A	5	18	628.82	2.036	Olivine gabbro
176	735	B	109	R	2	5B	105	125	631.35	1.735	Gabbro
176	735	B	110	R	1	2D	0	10	633.15	2.309	Olivine gabbro
176	735	B	110	R	3	1	45	55	636.50	2.415	Olivine gabbro
176	735	B	111	R	2	2B	76	97	640.24	2.190	Olivine gabbro
176	735	B	112	R	2	2B	104	116	645.08	2.035	Olivine gabbro
176	735	B	112	R	4	2B	81	95	647.05	2.661	Olivine gabbro
176	735	B	113	R	1	4B	97	112	648.75	2.263	Olivine gabbro
176	735	B	114	R	5	1D	58	75	658.88	2.085	Oxide gabbronorite
176	735	B	115	R	3	1B	18	30	665.14	2.227	Gabbronorite
176	735	B	115	R	4	2	24	38	666.63	2.716	Gabbronorite
176	735	B	115	R	7	4	45	61	671.01	2.530	Gabbronorite
176	735	B	116	R	3	3	38	49	674.71	2.428	Gabbronorite
176	735	B	116	R	5	1A	0	11	677.26	2.285	Gabbronorite
176	735	B	116	R	7	2	10	27	680.22	2.208	Gabbronorite
176	735	B	117	R	5	8	90	105	687.90	2.238	Gabbronorite
176	735	B	118	R	1	7A	92	102	691.77	2.171	Gabbronorite
176	735	B	118	R	7	1	0	15	699.72	2.189	Oxide gabbro
176	735	B	119	R	1	9	90	102	701.36	2.117	Felsic veins
176	735	B	119	R	2	8B	83	92	702.59	2.446	Gabbro
176	735	B	120	R	1	2A	6	24	710.15	2.797	Olivine gabbro
176	735	B	120	R	4	6	51	63	714.95	2.042	Gabbro
176	735	B	120	R	6	1E	83	96	718.12	2.190	Gabbro
176	735	B	121	R	1	4	95	110	720.73	2.895	Gabbro
176	735	B	121	R	2	2D	54	71	721.81	2.481	Olivine gabbro
176	735	B	121	R	4	2B	30	45	724.50	2.486	Gabbro
176	735	B	122	R	2	2	36	52	731.14	2.172	Gabbro
176	735	B	122	R	6	2B	45	55	736.79	2.437	Olivine gabbro
176	735	B	123	R	1	2	37	55	739.46	2.223	Olivine gabbro
176	735	B	123	R	6	4A	70	86	746.49	2.411	Olivine gabbro
176	735	B	123	R	8	5	46	61	748.71	2.035	Olivine gabbro
176	735	B	124	R	1	2A	25	40	749.03	2.418	Olivine gabbro
176	735	B	126	R	2	2B	25	42	757.14	2.231	Olivine gabbro
176	735	B	126	R	5	2C	84	98	761.73	1.765	Felsic Veins
176	735	B	127	R	2	1A	0	22	766.34	2.526	Olivine gabbro
176	735	B	127	R	3	1	0	18	767.71	2.551	Olivine gabbro
176	735	B	128	R	2	4A	45	62	776.45	1.995	Olivine gabbro
176	735	B	128	R	4	2	10	25	779.09	1.951	Gabbro
176	735	B	129	R	2	3A	20	37	785.89	2.321	Olivine gabbro
176	735	B	129	R	3	4B	105	115	788.09	2.309	Olivine gabbro
176	735	B	130	R	4	8B	110	127	799.33	2.215	Olivine gabbro
176	735	B	131	R	1	2A	38	53	803.96	2.048	Oxide olivine gabbro
176	735	B	131	R	2	3	18	30	805.24	2.238	Gabbro
176	735	B	132	R	2	4A	37	59	815.10	2.512	Olivine gabbro
176	735	B	132	R	3	4	75	90	816.85	2.410	Olivine gabbro
176	735	B	132	R	8	7B	103	122	823.30	2.319	Gabbro
176	735	B	133	R	7	1A	0	20	831.36	2.116	Olivine gabbro
176	735	B	134	R	2	2D	97	110	834.99	2.089	Olivine gabbro
176	735	B	135	R	1	1B	25	42	842.54	2.309	Olivine gabbro
176	735	B	135	R	2	3B	95	112	844.71	2.373	Olivine gabbro
176	735	B	137	R	3	2A	33	52	854.55	2.362	Olivine gabbro
176	735	B	137	R	6	5A	103	112	859.40	2.238	Troctolitic gabbro
176	735	B	138	R	2	3	109	128	863.86	2.228	Olivine gabbro
176	735	B	138	R	5	4	120	140	867.95	2.121	Olivine gabbro
176	735	B	139	R	1	4	66	87	871.87	2.366	Gabbro
176	735	B	139	R	6	3B	111	128	879.01	2.336	Gabbro
176	735	B	140	R	2	3A	80	97	882.58	2.094	Gabbro
176	735	B	140	R	6	2	50	71	887.40	2.341	Gabbro
176	735	B	141	R	1	7	123	144	890.64	2.390	Gabbro
176	735	B	142	R	3	4B	85	97	896.52	2.579	Olivine gabbro

Table T17 (continued).

Leg	Site	Hole	Core	Type	Section	Piece Number	Top (cm)	Base (cm)	Midpoint (mbsf)	Thermal conductivity (W/[m·K])	IUGS rock name
176	735	B	142	R	7	1	0	20	900.83	2.327	Olivine gabbro
176	735	B	143	R	2	3	100	118	905.06	2.234	Olivine gabbro
176	735	B	143	R	5	2	40	55	908.36	2.208	Olivine gabbro
176	735	B	144	R	1	1	0	17	912.39	2.148	Olivine gabbro
176	735	B	144	R	1	3E	130	150	913.70	3.038	Oxide gabbro
176	735	B	145	R	2	1B	39	62	923.77	2.306	Olivine gabbro
176	735	B	145	R	5	6	82	94	928.03	2.223	Gabbro
176	735	B	146	R	6	1B	40	65	938.54	1.994	Gabbro
176	735	B	147	R	3	1B	33	42	944.36	2.020	Troctolite
176	735	B	147	R	6	2B	45	65	947.49	2.210	Gabbro
176	735	B	148	R	1	2G	95	102	951.89	2.349	Olivine gabbro
176	735	B	148	R	4	1A	0	15	955.35	2.270	Olivine gabbro
176	735	B	148	R	5	4C	117	127	957.90	2.199	Olivine gabbro
176	735	B	149	R	3	2A	61	84	963.67	2.203	Troctolite
176	735	B	150	R	1	1B	25	40	970.43	2.216	Gabbro
176	735	B	150	R	2	2A	39	57	971.93	2.184	Gabbro
176	735	B	150	R	3	3	77	100	973.45	2.234	Gabbro
176	735	B	151	R	1	7	100	115	980.88	2.122	Gabbro
176	735	B	151	R	5	8	45	55	985.72	2.129	Gabbro
176	735	B	152	R	4	5	130	146	992.69	2.525	Gabbro
176	735	B	152	R	6	2	50	66	994.48	2.381	Gabbro
176	735	B	153	R	6	2	32	55	1002.65	2.334	Olivine gabbro
176	735	B	154	R	3	3B	55	67	1008.36	2.494	Oxide olivine gabbro
176	735	B	154	R	7	1A	0	15	1013.25	2.042	Olivine gabbro
176	735	B	155	R	1	2C	55	77	1015.66	2.333	Olivine gabbro
176	735	B	155	R	6	4	75	87	1022.78	2.358	Olivine gabbro
176	735	B	156	R	4	4	100	120	1029.64	2.510	Olivine gabbro
176	735	B	156	R	5	3	76	99	1030.92	2.185	Olivine gabbro
176	735	B	157	R	2	3A	77	97	1036.64	2.312	Olivine gabbro
176	735	B	157	R	5	4	50	67	1040.86	2.131	Olivine gabbro
176	735	B	158	R	1	5	80	102	1044.91	2.185	Olivine gabbro
176	735	B	158	R	4	3	55	80	1048.66	2.262	Olivine gabbro
176	735	B	158	R	7	4	85	110	1053.14	2.167	Olivine gabbro
176	735	B	159	R	6	4A	81	95	1061.69	2.415	Gabbro
176	735	B	159	R	7	2A	25	45	1062.62	2.059	Oxide gabbro
176	735	B	160	R	2	2B	85	105	1065.85	2.371	Olivine gabbro
176	735	B	160	R	7	1	0	25	1072.12	2.277	Gabbro
176	735	B	161	R	2	2	20	37	1074.68	2.264	Olivine gabbro
176	735	B	161	R	6	3A	59	77	1080.62	2.075	Olivine gabbro
176	735	B	162	R	2	3	87	105	1084.81	2.185	Olivine gabbro
176	735	B	162	R	6	3	81	105	1090.28	2.355	Olivine gabbro
176	735	B	163	R	4	2A	82	93	1096.58	2.252	Olivine gabbro
176	735	B	163	R	5	3B	64	85	1097.71	2.350	Olivine gabbro
176	735	B	164	R	1	4A	32	57	1099.85	2.257	Olivine gabbro
176	735	B	165	R	3	2A	95	110	1108.31	2.305	Olivine gabbro
176	735	B	165	R	4	2A	27	42	1108.94	2.223	Olivine gabbro
176	735	B	166	R	1	4A	20	35	1111.18	2.371	Olivine gabbro
176	735	B	166	R	5	2	46	66	1116.45	2.389	Olivine gabbro
176	735	B	167	R	1	3D	105	121	1121.63	2.176	Olivine gabbro
176	735	B	167	R	6	5	81	101	1128.16	2.147	Olivine gabbro
176	735	B	168	R	3	2A	2	15	1132.98	2.332	Olivine gabbro
176	735	B	168	R	7	5	65	77	1139.36	2.118	Gabbro
176	735	B	169	R	2	3	77	102	1141.81	2.083	Gabbro
176	735	B	169	R	6	3	75	102	1147.32	2.315	Gabbro
176	735	B	170	R	4	6	61	82	1153.94	2.360	Olivine gabbro
176	735	B	170	R	5	5	105	118	1155.76	2.266	Olivine gabbro
176	735	B	171	R	2	2	24	48	1160.81	2.045	Oxide olivine gabbro
176	735	B	171	R	5	1A	0	25	1165.04	2.148	Olivine gabbro
176	735	B	172	R	1	6	120	132	1169.96	2.194	Olivine gabbro
176	735	B	173	R	3	4	115	137	1182.52	2.191	Olivine gabbro
176	735	B	173	R	4	6	120	140	1183.94	1.861	Olivine gabbro
176	735	B	174	R	2	1F	55	70	1190.13	2.143	Olivine gabbro
176	735	B	175	R	1	4	70	91	1191.91	2.602	Olivine gabbro
176	735	B	175	R	4	1B	62	76	1195.43	2.063	Olivine gabbro
176	735	B	176	R	3	1B	35	62	1199.85	2.424	Olivine gabbro
176	735	B	177	R	5	2	51	67	1207.63	2.184	Olivine gabbro
176	735	B	177	R	6	4B	108	125	1209.71	2.456	Olivine gabbro
176	735	B	178	R	4	5B	110	127	1216.40	2.016	Olivine gabbro

Table T17 (continued).

Leg	Site	Hole	Core	Type	Section	Piece Number	Top (cm)	Base (cm)	Midpoint (mbsf)	Thermal conductivity (W/[m·K])	IUGS rock name
176	735	B	178	R	7	1A	0	20	1219.55	2.183	Troctolite
176	735	B	179	R	2	3A	60	72	1222.76	3.403	Troctolitic gabbro
176	735	B	179	R	8	2	25	37	1230.85	2.113	Olivine gabbro
176	735	B	180	R	2	4	77	90	1232.62	2.133	Olivine gabbro
176	735	B	180	R	6	14	110	122	1238.90	2.391	Gabbro
176	735	B	181	R	1	12	71	82	1240.97	2.247	Olivine gabbro
176	735	B	181	R	4	8	94	104	1245.54	2.357	Olivine gabbro
176	735	B	182	R	2	4	58	68	1251.95	2.316	Olivine gabbro
176	735	B	183	R	2	2	94	106	1262.01	2.241	Olivine gabbro
176	735	B	183	R	4	12	115	125	1265.02	2.360	Olivine gabbro
176	735	B	185	R	3	2A	100	120	1282.16	2.360	Olivine gabbro
176	735	B	185	R	5	2B	115	135	1285.02	2.302	Olivine gabbro
176	735	B	186	R	1	4	57	67	1289.02	2.599	Olivine gabbro
176	735	B	187	R	5	2A	41	54	1302.85	2.066	Olivine gabbro
176	735	B	187	R	6	5	72	79	1304.63	2.378	Olivine gabbro
176	735	B	188	R	3	1	42	71	1310.41	2.490	Olivine gabbro
176	735	B	188	R	6	3	52	60	1314.54	2.551	Olivine gabbro
176	735	B	189	R	3	1	0	18	1319.32	2.225	Olivine gabbro
176	735	B	189	R	4	2B	90	97	1321.58	2.337	Olivine gabbro
176	735	B	190	R	1	2D	25	35	1326.40	2.258	Olivine gabbro
176	735	B	190	R	4	4B	80	90	1331.08	2.272	Olivine gabbro
176	735	B	191	R	3	3C	75	87	1339.38	2.186	Troctolitic gabbro
176	735	B	191	R	8	2	30	45	1345.29	2.150	Olivine gabbro
176	735	B	192	R	2	2	52	75	1347.44	2.370	Olivine gabbro
176	735	B	194	R	1	5	113	131	1361.82	2.275	Olivine gabbro
176	735	B	195	R	2	1	0	15	1365.63	2.218	Olivine gabbro
176	735	B	195	R	7	3	30	42	1372.22	2.502	Olivine gabbro
176	735	B	196	R	1	3	20	37	1373.99	2.774	Olivine gabbro
176	735	B	196	R	4	4	43	57	1377.66	2.209	Troctolitic gabbro
176	735	B	197	R	2	7	54	64	1385.39	2.438	Oxide olivine gabbro
176	735	B	198	R	1	4	12	22	1386.57	2.439	Troctolite
176	735	B	198	R	4	4	102	115	1391.73	2.351	Olivine gabbro
176	735	B	198	R	5	4	52	65	1392.38	2.705	Olivine gabbro
176	735	B	199	R	2	2A	70	85	1394.55	2.143	Olivine gabbro
176	735	B	199	R	6	1	0	20	1399.73	2.483	Olivine gabbro
176	735	B	200	R	4	2A	45	57	1406.71	2.089	Olivine gabbro
176	735	B	200	R	7	5A	60	75	1411.29	2.310	Olivine gabbro
176	735	B	201	R	1	1	0	15	1411.68	2.282	Olivine gabbro
176	735	B	201	R	5	2A	35	50	1417.09	2.147	Olivine gabbro
176	735	B	202	R	1	3B	90	105	1422.18	2.408	Olivine gabbro
176	735	B	202	R	8	1A	0	20	1430.65	2.267	Troctolitic gabbro
176	735	B	203	R	2	1D	57	67	1432.73	2.567	Olivine gabbro
176	735	B	203	R	5	4	105	127	1437.08	2.418	Olivine gabbro
176	735	B	204	R	4	3	92	115	1445.49	2.071	Olivine gabbro
176	735	B	205	R	2	1D	34	48	1451.98	2.032	Olivine gabbro
176	735	B	205	R	5	3D	104	122	1457.18	2.615	Olivine gabbro
176	735	B	206	R	2	2B	76	93	1461.81	2.461	Olivine gabbro
176	735	B	206	R	3	1B	38	52	1462.80	2.477	Olivine gabbro
176	735	B	207	R	7	1	105	125	1478.47	1.790	Olivine gabbro
176	735	B	208	R	5	2B	100	117	1485.23	2.685	Olivine gabbro
176	735	B	208	R	8	3C	62	80	1488.78	2.423	Olivine gabbro
176	735	B	209	R	2	4	54	67	1490.35	2.153	Olivine gabbro
176	735	B	209	R	8	2A	85	116	1498.62	2.239	Olivine gabbro
176	735	B	210	R	1	1C	12	21	1498.47	2.229	Olivine gabbro
									Mean	2.270	
									SD	0.212	
									Count	257	

Notes: This table is also available in ASCII format in the **TABLES** directory. SD = standard deviation.

Table T18. Compressional velocity downhole for Hole 735B. (See table note. Continued on next five pages.)

Leg	Site	Hole	Core	Type	Section	Top (cm)	Base (cm)	Depth (mbsf)	Velocity (m/s)	IUGS rock name
118	735	B	1	D	1	19	21	0.19	5530	Gabbronorite
118	735	B	1	D	1	141	143	1.41	6400	Gabbronorite
118	735	B	2	D	1	113	115	7.63	5940	Oxide gabbronorite
118	735	B	2	D	1	139	141	7.89	6380	Gabbronorite
118	735	B	2	D	1	142	145	7.92	6690	Gabbronorite
118	735	B	2	D	2	99	101	8.99	6080	Olivine gabbro
118	735	B	4	D	2	7	9	19.07	6400	Gabbronorite
118	735	B	6	D	1	111	113	25.11	6660	Gabbronorite
118	735	B	7	D	1	74	76	26.74	6900	Olivine gabbro
118	735	B	7	D	2	9	11	27.59	7010	Olivine gabbro
118	735	B	8	D	1	45	48	29.65	6750	Olivine gabbro
118	735	B	9	D	1	120	122	34.40	6820	Olivine gabbro
118	735	B	10	D	1	24	26	36.44	6740	Olivine gabbro
118	735	B	11	D	1	6	8	39.26	6520	Oxide olivine gabbro
118	735	B	12	R	1	36	41	39.76	6740	Oxide olivine gabbro
118	735	B	12	R	1	55	62	39.95	6060	Olivine gabbro
118	735	B	12	R	2	32	34	41.22	6240	Olivine gabbro
118	735	B	12	R	2	36	38	41.26	6730	Olivine gabbro
118	735	B	12	R	3	8	10	42.48	6900	Olivine gabbro
118	735	B	12	R	3	77	84	43.17	6990	Olivine gabbro
118	735	B	12	R	3	83	85	43.23	7190	Olivine gabbro
118	735	B	13	R	1	91	94	45.41	6940	Olivine gabbro
118	735	B	13	R	1	102	105	45.52	7270	Olivine gabbro
118	735	B	13	R	2	55	58	46.05	7190	Olivine gabbro
118	735	B	13	R	2	109	112	47.09	6620	Oxide olivine gabbro
118	735	B	14	R	1	35	38	51.55	7040	Olivine gabbro
118	735	B	14	R	2	22	25	59.92	7190	Olivine gabbro
118	735	B	14	R	4	22	25	55.92	7200	Olivine gabbro
118	735	B	15	R	2	128	130	58.98	6620	Olivine gabbro
118	735	B	16	R	1	139	141	63.19	6690	Olivine gabbro
118	735	B	16	R	4	34	36	66.64	6530	Olivine gabbro
118	735	B	16	R	4	77	79	67.07	6840	Olivine gabbro
118	735	B	16	R	5	24	26	68.04	6700	Olivine gabbro
118	735	B	18	R	3	29	31	71.79	6870	Olivine gabbro
118	735	B	19	R	5	126	128	80.96	7140	Troctolitic gabbro
118	735	B	20	R	1	17	20	84.37	6820	Troctolitic gabbro
118	735	B	20	R	2	54	56	86.24	7220	Olivine gabbro
118	735	B	21	R	2	49	51	91.19	5900	Oxide gabbro
118	735	B	22	R	2	41	43	95.91	7140	Olivine gabbro
118	735	B	22	R	3	118	120	95.18	7150	Olivine gabbro
118	735	B	23	R	2	34	36	102.34	7220	Olivine gabbro
118	735	B	23	R	4	120	122	105.20	6450	Others
118	735	B	24	R	2	95	97	107.95	6780	Oxide gabbro
118	735	B	24	R	3	50	52	109.00	6690	Oxide gabbro
118	735	B	24	R	4	26	28	110.26	6950	Olivine gabbro
118	735	B	25	R	2	5	7	112.05	6610	Olivine gabbro
118	735	B	25	R	3	137	139	114.87	7260	Olivine gabbro
118	735	B	26	R	1	62	64	116.12	6920	Olivine gabbro
118	735	B	26	R	3	64	66	119.14	6910	Olivine gabbro
118	735	B	27	R	1	84	86	122.34	7210	Olivine gabbro
118	735	B	27	R	3	32	34	123.82	7110	Olivine gabbro
118	735	B	28	R	2	12	14	128.12	6960	Olivine gabbro
118	735	B	28	R	2	114	116	129.14	7170	Olivine gabbro
118	735	B	29	R	2	46	48	133.46	7160	Olivine gabbro
118	735	B	29	R	4	19	21	136.19	6851	Olivine gabbro
118	735	B	30	R	3	137	139	140.87	6180	Oxide gabbro
118	735	B	30	R	4	14	16	141.14	6800	Olivine gabbro
118	735	B	30	R	5	91	93	143.41	6720	Olivine gabbro
118	735	B	31	R	2	120	122	146.20	7030	Olivine gabbro
118	735	B	31	R	4	118	120	148.18	6560	Olivine gabbro
118	735	B	32	R	1	64	66	149.14	6710	Oxide gabbro
118	735	B	32	R	3	14	16	151.64	7050	Olivine gabbro
118	735	B	33	R	4	27	29	158.27	6790	Olivine gabbro
118	735	B	33	R	4	129	131	159.29	6570	Olivine gabbro
118	735	B	34	R	1	103	105	159.53	6640	Olivine gabbro
118	735	B	34	R	4	30	32	163.30	6130	Oxide olivine gabbro
118	735	B	35	R	1	39	41	163.79	7210	Olivine gabbro
118	735	B	35	R	2	11	14	165.11	6890	Olivine gabbro

Table T18 (continued).

Leg	Site	Hole	Core	Type	Section	Top (cm)	Base (cm)	Depth (mbsf)	Velocity (m/s)	IUGS rock name
118	735	B	35	R	5	131	133	170.31	7150	Olivine gabbro
118	735	B	35	R	6	71	74	171.71	7050	Oxide olivine gabbro
118	735	B	36	R	2	11	13	172.61	7160	Olivine gabbro
118	735	B	36	R	3	36	38	174.36	7120	Oxide olivine gabbro
118	735	B	37	R	1	11	13	176.11	6860	Oxide olivine gabbro
118	735	B	37	R	3	80	82	179.80	6860	Oxide olivine gabbro
118	735	B	38	R	2	15	17	182.65	7030	Troctolitic gabbro
118	735	B	39	R	1	138	141	187.38	7090	Oxide olivine gabbro
118	735	B	39	R	1	145	147	187.45	6990	Oxide olivine gabbro
118	735	B	39	R	3	21	23	189.21	6110	Oxide olivine gabbro
118	735	B	40	R	2	62	64	193.12	6080	Oxide olivine gabbro
118	735	B	40	R	5	13	15	197.13	6860	Oxide olivine gabbro
118	735	B	41	R	4	68	70	201.18	6900	Oxide olivine gabbro
118	735	B	42	R	2	119	121	203.69	7000	Oxide olivine gabbro
118	735	B	42	R	4	62	65	206.12	6900	Oxide olivine gabbro
118	735	B	43	R	1	126	128	207.26	6750	Oxide olivine gabbro
118	735	B	43	R	4	56	61	211.08	7010	Oxide olivine gabbro
118	735	B	43	R	4	64	66	211.14	6920	Oxide olivine gabbro
118	735	B	44	R	2	131	133	213.81	6710	Oxide olivine gabbro
118	735	B	45	R	2	15	17	217.65	7160	Oxide olivine gabbro
118	735	B	46	R	1	14	17	221.14	6990	Oxide olivine gabbro
118	735	B	46	R	2	21	23	221.71	6900	Oxide olivine gabbro
118	735	B	46	R	2	120	123	223.70	6770	Oxide olivine gabbro
118	735	B	46	R	2	128	130	223.78	6670	Oxide olivine gabbro
118	735	B	47	R	3	50	52	229.50	7010	Oxide olivine gabbro
118	735	B	48	R	4	82	84	235.32	6640	Oxide olivine gabbro
118	735	B	49	R	2	89	91	238.39	6810	Oxide olivine gabbro
118	735	B	50	R	4	87	89	243.37	6620	Oxide olivine gabbro
118	735	B	51	R	1	102	104	244.02	6620	Oxide olivine gabbro
118	735	B	52	R	4	69	71	253.19	6820	Oxide olivine gabbro
118	735	B	53	R	2	15	17	254.65	6740	Oxide olivine gabbro
118	735	B	53	R	2	79	82	255.29	6680	Oxide olivine gabbro
118	735	B	53	R	3	107	110	257.07	6390	Oxide olivine gabbro
118	735	B	54	R	3	125	127	262.25	6750	Oxide olivine gabbro
118	735	B	55	R	3	130	133	270.30	6770	Oxide olivine gabbro
118	735	B	56	R	2	11	14	271.61	6620	Oxide olivine gabbro
118	735	B	56	R	2	22	25	271.72	6750	Oxide olivine gabbro
118	735	B	56	R	2	144	146	272.94	6340	Oxide olivine gabbro
118	735	B	57	R	2	135	137	277.85	6900	Olivine gabbro
118	735	B	58	R	2	33	35	282.33	6950	Olivine gabbro
118	735	B	59	R	3	70	72	289.20	6910	Olivine gabbro
118	735	B	60	R	1	18	20	290.68	7100	Olivine gabbro
118	735	B	61	R	1	81	83	296.31	7100	Olivine gabbro
118	735	B	62	R	3	104	106	304.54	7030	Olivine gabbro
118	735	B	63	R	3	80	82	308.80	7020	Olivine gabbro
118	735	B	63	R	6	28	30	312.78	6990	Olivine gabbro
118	735	B	64	R	2	54	56	317.04	7060	Olivine gabbro
118	735	B	65	R	2	67	69	322.17	7070	Olivine gabbro
118	735	B	66	R	2	86	88	327.36	6790	Olivine gabbro
118	735	B	66	R	3	134	138	329.34	5950	Olivine gabbro
118	735	B	68	R	3	15	17	338.15	6990	Olivine gabbro
118	735	B	69	R	4	138	140	346.88	7150	Olivine gabbro
118	735	B	70	R	1	105	107	347.05	6130	Olivine gabbro
118	735	B	71	R	2	82	84	353.32	7130	Olivine gabbro
118	735	B	72	R	3	36	38	359.36	7250	Olivine gabbro
118	735	B	72	R	6	106	108	364.56	7090	Olivine gabbro
118	735	B	73	R	3	73	75	369.23	7170	Olivine gabbro
118	735	B	74	R	6	41	43	382.91	6470	Oxide gabbronorite
118	735	B	75	R	3	48	50	387.98	7150	Olivine gabbro
118	735	B	75	R	6	75	77	392.75	7200	Olivine gabbro
118	735	B	76	R	3	50	52	397.50	6870	Oxide gabbronorite
118	735	B	77	R	3	52	55	407.05	6830	Oxide olivine gabbro
118	735	B	77	R	4	70	72	408.70	6910	Oxide olivine gabbro
118	735	B	78	R	4	65	67	414.65	7220	Olivine gabbro
118	735	B	79	R	2	64	67	416.64	6970	Oxide olivine gabbro
118	735	B	79	R	7	99	102	423.49	7270	Olivine gabbro
118	735	B	80	R	1	131	133	425.31	6740	Oxide olivine gabbro
118	735	B	80	R	7	23	25	432.23	6790	Oxide olivine gabbro
118	735	B	81	R	2	54	56	435.54	7090	Oxide olivine gabbro

Table T18 (continued).

Leg	Site	Hole	Core	Type	Section	Top (cm)	Base (cm)	Depth (mbsf)	Velocity (m/s)	IUGS rock name
118	735	B	81	R	7	64	66	442.14	7170	Olivine gabbro
118	735	B	82	R	2	13	15	444.63	7070	Troctolitic gabbro
118	735	B	82	R	6	11	13	450.61	6720	Oxide olivine gabbro
118	735	B	83	R	4	95	97	457.95	7090	Olivine gabbro
118	735	B	83	R	7	104	106	461.54	6940	Troctolite
118	735	B	84	R	2	67	69	464.17	5730	Olivine gabbro
118	735	B	84	R	3	14	16	465.14	7060	Olivine gabbro
118	735	B	85	R	4	9	11	476.09	6340	Olivine gabbro
118	735	B	85	R	5	15	17	477.65	6530	Oxide olivine gabbro
118	735	B	85	R	7	17	19	479.67	6850	Troctolite
118	735	B	86	R	6	143	145	489.93	6600	Oxide olivine gabbro
118	735	B	87	R	5	15	17	496.65	6530	Oxide olivine gabbro
118	735	B	87	R	5	20	22	496.70	6340	Oxide olivine gabbro
176	735	B	89	R	1	19	21	505.00	6989	Olivine gabbro
176	735	B	90	R	1	115	117	508.96	7193	Olivine gabbro
176	735	B	90	R	4	35	37	512.35	7145	Olivine gabbro
176	735	B	90	R	6	105	107	515.57	6894	Olivine gabbro
176	735	B	90	R	7	56	58	516.50	7146	Olivine gabbro
176	735	B	90	R	8	27	29	517.14	6651	Olivine gabbro
176	735	B	91	R	1	36	38	517.77	6758	Olivine gabbro
176	735	B	91	R	1	108	110	518.49	6792	Olivine gabbro
176	735	B	91	R	3	113	115	521.09	7163	Olivine gabbro
176	735	B	93	R	1	33	35	532.44	6620	Oxide olivine gabbro
176	735	B	93	R	1	36	38	532.47	6536	Olivine gabbro
176	735	B	93	R	2	94	96	534.16	6877	Oxide olivine gabbro
176	735	B	93	R	3	85	87	535.30	6200	Oxide olivine gabbro
176	735	B	93	R	5	33	35	537.38	6352	Oxide gabbronorite
176	735	B	94	R	1	30	32	536.91	6557	Oxide olivine gabbro
176	735	B	94	R	3	52	54	539.72	6574	Gabbro
176	735	B	94	R	3	55	57	539.75	6592	Gabbro
176	735	B	94	R	3	116	118	540.36	6908	Gabbro
176	735	B	95	R	1	118	120	545.79	6845	Oxide olivine gabbro
176	735	B	95	R	3	19	21	547.59	7021	Oxide olivine gabbro
176	735	B	96	R	1	30	32	548.61	6743	Microgabbro
176	735	B	96	R	2	49	51	550.30	6624	Oxide gabbronorite
176	735	B	97	R	1	128	130	557.59	6451	Oxide gabbronorite
176	735	B	97	R	3	26	28	559.09	6849	Oxide gabbronorite
176	735	B	99	R	3	72	74	569.54	7070	Oxide gabbronorite
176	735	B	99	R	4	23	25	570.26	7220	Oxide gabbronorite
176	735	B	99	R	6	30	32	573.05	6810	Oxide gabbronorite
176	735	B	100	R	1	43	45	575.94	6752	Oxide gabbronorite
176	735	B	101	R	3	31	33	587.94	6868	Olivine gabbro
176	735	B	102	R	1	28	30	590.19	7075	Oxide olivine gabbro
176	735	B	102	R	3	58	60	593.37	6506	Gabbronorite
176	735	B	103	R	2	81	83	597.01	6807	Gabbronorite
176	735	B	103	R	3	48	50	598.14	6320	Oxide gabbronorite
176	735	B	103	R	4	31	33	599.47	6810	Gabbronorite
176	735	B	104	R	2	49	51	606.30	6624	Olivine gabbro
176	735	B	104	R	3	36	38	607.31	6871	Olivine gabbro
176	735	B	105	R	1	52	54	609.33	6819	Olivine gabbro
176	735	B	105	R	3	94	96	612.64	7011	Olivine gabbro
176	735	B	106	R	1	73	75	614.64	6768	Olivine gabbro
176	735	B	106	R	4	54	56	618.64	6999	Olivine gabbro
176	735	B	108	R	2	44	46	625.42	6839	Olivine gabbro
176	735	B	108	R	4	87	89	628.49	6794	Olivine gabbro
176	735	B	110	R	1	46	48	633.57	6505	Olivine gabbro
176	735	B	110	R	4	57	59	638.02	7060	Olivine gabbro
176	735	B	111	R	2	105	107	640.43	6775	Olivine gabbro
176	735	B	112	R	1	54	56	643.25	6735	Olivine gabbro
176	735	B	113	R	1	106	108	648.77	6828	Olivine gabbro
176	735	B	114	R	1	100	102	653.41	7113	Oxide gabbronorite
176	735	B	114	R	5	33	35	658.55	6641	Oxide gabbronorite
176	735	B	115	R	3	70	72	665.61	6683	Gabbronorite
176	735	B	115	R	7	44	46	670.93	6688	Gabbronorite
176	735	B	116	R	4	65	67	676.43	7272	Gabbronorite
176	735	B	116	R	5	7	9	677.28	6591	Gabbronorite
176	735	B	116	R	6	97	99	679.60	6854	Gabbronorite
176	735	B	117	R	2	52	54	683.23	6805	Gabbronorite
176	735	B	117	R	5	91	93	687.84	6183	Gabbronorite

Table T18 (continued).

Leg	Site	Hole	Core	Type	Section	Top (cm)	Base (cm)	Depth (mbsf)	Velocity (m/s)	IUGS rock name
176	735	B	118	R	1	139	141	692.20	6718	Gabbronorite
176	735	B	118	R	3	90	92	694.63	6864	Gabbronorite
176	735	B	118	R	6	112	114	699.29	6205	Oxide gabbro
176	735	B	119	R	2	100	102	702.72	6407	Gabbro
176	735	B	120	R	3	98	100	713.92	6999	Gabbro
176	735	B	120	R	6	41	43	717.64	6980	Olivine gabbro
176	735	B	121	R	2	52	54	721.71	7015	Olivine gabbro
176	735	B	121	R	5	112	114	726.65	6685	Olivine gabbro
176	735	B	121	R	8	65	67	729.93	6653	Olivine gabbro
176	735	B	122	R	7	11	13	737.91	6897	Olivine gabbro
176	735	B	123	R	3	39	41	742.28	6776	Olivine gabbro
176	735	B	123	R	3	46	48	742.35	6715	Olivine gabbro
176	735	B	123	R	4	79	81	743.98	6674	Olivine gabbro
176	735	B	124	R	1	29	31	749.00	6871	Olivine gabbro
176	735	B	126	R	3	77	79	758.91	7051	Olivine gabbro
176	735	B	127	R	3	6	8	767.69	6881	Olivine gabbro
176	735	B	128	R	4	61	63	779.53	6695	Gabbro
176	735	B	129	R	2	35	37	785.96	6825	Olivine gabbro
176	735	B	130	R	2	32	34	795.52	6697	Olivine gabbro
176	735	B	130	R	4	114	116	799.29	6990	Oxide olivine gabbro
176	735	B	131	R	2	22	24	805.23	6516	Oxide olivine gabbro
176	735	B	132	R	3	28	30	816.31	7113	Olivine gabbro
176	735	B	132	R	6	73	75	820.49	6824	Olivine gabbro
176	735	B	132	R	8	120	122	823.38	7125	Oxide gabbro
176	735	B	133	R	2	126	128	825.51	6763	Olivine gabbro
176	735	B	133	R	7	12	14	831.39	7057	Olivine gabbro
176	735	B	134	R	2	102	104	834.98	6754	Olivine gabbro
176	735	B	134	R	7	65	37	841.44	7178	Olivine gabbro
176	735	B	135	R	3	7	9	845.13	6822	Olivine gabbro
176	735	B	136	R	2	56	58	848.70	6960	Olivine gabbro
176	735	B	137	R	3	43	45	854.56	6855	Olivine gabbro
176	735	B	137	R	7	70	72	860.53	6949	Olivine gabbro
176	735	B	138	R	3	77	79	864.76	7167	Olivine gabbro
176	735	B	139	R	1	84	86	871.95	6672	Olivine gabbro
176	735	B	139	R	4	110	112	876.42	6467	Olivine gabbro
176	735	B	140	R	1	32	34	880.63	6694	Olivine gabbro
176	735	B	140	R	5	40	42	886.11	7002	Olivine gabbro
176	735	B	141	R	1	124	126	890.55	7077	Olivine gabbro
176	735	B	142	R	3	86	88	896.48	6686	Olivine gabbro
176	735	B	142	R	7	12	14	900.86	6855	Olivine gabbro
176	735	B	143	R	5	35	37	908.24	6768	Olivine gabbro
176	735	B	144	R	1	13	15	912.44	6739	Olivine gabbro
176	735	B	145	R	1	130	132	923.21	6802	Olivine gabbro
176	735	B	145	R	4	32	34	926.07	6931	Olivine gabbro
176	735	B	145	R	5	83	85	927.99	6581	Gabbro
176	735	B	146	R	4	111	113	936.26	6962	Olivine gabbro
176	735	B	146	R	6	59	61	938.61	6464	Olivine gabbro
176	735	B	147	R	6	55	57	947.50	6268	Gabbro
176	735	B	148	R	1	101	103	951.92	6671	Olivine gabbro
176	735	B	148	R	4	7	9	955.35	6459	Olivine gabbro
176	735	B	148	R	7	109	111	960.58	6557	Olivine gabbro
176	735	B	149	R	2	49	51	962.31	5688	Olivine gabbro
176	735	B	149	R	7	117	119	969.16	6832	Gabbro
176	735	B	150	R	2	42	44	971.88	6190	Gabbro
176	735	B	150	R	7	8	10	978.25	6628	Gabbro
176	735	B	150	R	7	104	106	979.21	6599	Gabbro
176	735	B	151	R	4	88	90	984.61	6564	Gabbro
176	735	B	151	R	5	49	51	985.72	6960	Gabbro
176	735	B	152	R	3	62	64	990.57	6590	Gabbro
176	735	B	152	R	6	62	64	994.53	6459	Gabbro
176	735	B	153	R	2	21	23	997.36	5977	Olivine gabbro
176	735	B	153	R	7	99	101	1004.48	6479	Olivine gabbro
176	735	B	154	R	5	32	34	1010.60	6658	Olivine gabbro
176	735	B	155	R	1	19	21	1015.20	6464	Olivine gabbro
176	735	B	155	R	4	7	9	1019.35	6522	Olivine gabbro
176	735	B	156	R	2	131	133	1026.95	6454	Olivine gabbro
176	735	B	156	R	5	53	55	1030.58	6574	Olivine gabbro
176	735	B	157	R	3	89	91	1038.17	6428	Oxide gabbro
176	735	B	157	R	5	45	47	1040.73	6391	Olivine gabbro

Table T18 (continued).

Leg	Site	Hole	Core	Type	Section	Top (cm)	Base (cm)	Depth (mbsf)	Velocity (m/s)	IUGS rock name
176	735	B	158	R	4	65	67	1048.64	6574	Olivine gabbro
176	735	B	159	R	4	92	94	1058.77	7013	Olivine gabbro
176	735	B	159	R	6	89	91	1061.71	6826	Olivine gabbro
176	735	B	160	R	2	32	34	1065.23	6972	Olivine gabbro
176	735	B	160	R	7	16	18	1072.16	6998	Olivine gabbro
176	735	B	161	R	2	20	22	1074.60	7037	Olivine gabbro
176	735	B	161	R	6	68	70	1080.63	6930	Olivine gabbro
176	735	B	162	R	2	93	95	1084.79	6699	Olivine gabbro
176	735	B	162	R	6	84	86	1090.20	6867	Olivine gabbro
176	735	B	162	R	8	30	32	1091.71	6489	Olivine gabbro
176	735	B	163	R	4	85	87	1096.56	7241	Olivine gabbro
176	735	B	163	R	5	68	70	1097.65	7214	Olivine gabbro
176	735	B	164	R	3	32	34	1102.33	6989	Olivine gabbro
176	735	B	165	R	3	104	106	1108.33	6939	Olivine gabbro
176	735	B	165	R	4	39	41	1108.99	6739	Olivine gabbro
176	735	B	166	R	1	21	23	1111.12	6481	Olivine gabbro
176	735	B	166	R	5	77	79	1116.67	6892	Olivine gabbro
176	735	B	167	R	1	105	107	1121.56	6629	Olivine gabbro
176	735	B	167	R	6	10	12	1127.36	6776	Olivine gabbro
176	735	B	168	R	2	10	12	1131.50	6449	Olivine gabbro
176	735	B	168	R	7	74	76	1139.40	6614	Gabbro
176	735	B	169	R	2	97	99	1141.89	6700	Gabbro
176	735	B	169	R	4	50	52	1144.32	6579	Gabbro
176	735	B	169	R	6	79	81	1147.23	6773	Gabbro
176	735	B	170	R	2	61	63	1151.15	6640	Olivine gabbro
176	735	B	170	R	5	106	108	1155.71	6834	Olivine gabbro
176	735	B	171	R	2	28	30	1160.74	6889	Oxide olivine gabbro
176	735	B	171	R	5	102	104	1165.94	6567	Olivine gabbro
176	735	B	172	R	1	133	135	1170.04	6919	Olivine gabbro
176	735	B	173	R	1	96	98	1179.37	7189	Olivine gabbro
176	735	B	173	R	3	119	121	1182.46	6670	Olivine gabbro
176	735	B	173	R	5	84	86	1184.88	6665	Olivine gabbro
176	735	B	175	R	1	78	80	1191.89	6940	Olivine gabbro
176	735	B	176	R	3	90	92	1200.27	6825	Olivine gabbro
176	735	B	177	R	5	57	59	1207.62	6030	Olivine gabbro
176	735	B	177	R	6	119	121	1209.74	7185	Olivine gabbro
176	735	B	178	R	4	113	115	1216.35	7405	Olivine gabbro
176	735	B	178	R	6	134	136	1219.41	7039	Olivine gabbro
176	735	B	179	R	5	110	112	1227.56	7014	Olivine gabbro
176	735	B	180	R	5	10	12	1236.39	6624	Olivine gabbro
176	735	B	181	R	4	93	95	1245.49	6773	Olivine gabbro
176	735	B	182	R	2	65	67	1251.98	6982	Olivine gabbro
176	735	B	183	R	3	75	77	1263.25	6845	Olivine gabbro
176	735	B	184	R	5	65	67	1275.56	6783	Olivine gabbro
176	735	B	185	R	5	14	16	1283.92	6975	Olivine gabbro
176	735	B	186	R	3	21	23	1291.39	7117	Olivine gabbro
176	735	B	186	R	6	33	35	1295.83	6669	Olivine gabbro
176	735	B	187	R	5	60	62	1302.98	7010	Olivine gabbro
176	735	B	188	R	3	10	12	1309.95	6583	Olivine gabbro
176	735	B	188	R	4	115	117	1312.37	6598	Olivine gabbro
176	735	B	188	R	6	54	56	1314.53	5840	Olivine gabbro
176	735	B	189	R	5	7	9	1322.20	6638	Olivine gabbro
176	735	B	190	R	4	67	68	1330.91	6773	Olivine gabbro
176	735	B	191	R	8	25	27	1345.17	6798	Olivine gabbro
176	735	B	192	R	2	72	74	1347.53	6623	Olivine gabbro
176	735	B	192	R	4	61	63	1350.03	6316	Olivine gabbro
176	735	B	193	R	1	82	84	1355.83	5904	Olivine gabbro
176	735	B	195	R	2	2	4	1365.58	6693	Olivine gabbro
176	735	B	195	R	7	38	40	1372.25	6213	Olivine gabbro
176	735	B	196	R	1	27	29	1373.98	6605	Olivine gabbro
176	735	B	196	R	4	93	95	1378.10	6511	Olivine gabbro
176	735	B	197	R	2	57	59	1385.38	6306	Oxide olivine gabbro
176	735	B	197	R	3	87	89	1387.18	6062	Oxide olivine gabbro
176	735	B	198	R	1	17	19	1386.58	6547	Olivine gabbro
176	735	B	198	R	4	105	107	1391.70	6442	Olivine gabbro
176	735	B	199	R	2	79	81	1394.57	6472	Olivine gabbro
176	735	B	199	R	2	137	139	1395.15	6936	Olivine gabbro
176	735	B	199	R	6	53	55	1400.17	6955	Olivine gabbro
176	735	B	200	R	4	58	60	1406.79	7066	Olivine gabbro

Table T18 (continued).

Leg	Site	Hole	Core	Type	Section	Top (cm)	Base (cm)	Depth (mbsf)	Velocity (m/s)	IUGS rock name
176	735	B	201	R	1	11	13	1411.72	6976	Olivine gabbro
176	735	B	201	R	5	42	44	1417.09	7031	Olivine gabbro
176	735	B	201	R	7	113	115	1420.73	6961	Olivine gabbro
176	735	B	202	R	1	80	82	1422.01	7127	Olivine gabbro
176	735	B	202	R	5	109	111	1427.89	6922	Olivine gabbro
176	735	B	202	R	8	72	74	1431.28	6633	Olivine gabbro
176	735	B	203	R	2	62	64	1432.74	6805	Olivine gabbro
176	735	B	203	R	5	116	118	1437.09	7317	Olivine gabbro
176	735	B	204	R	4	117	119	1445.63	6832	Olivine gabbro
176	735	B	204	R	7	44	46	1448.95	7100	Olivine gabbro
176	735	B	205	R	4	115	117	1455.71	6894	Olivine gabbro
176	735	B	206	R	2	83	85	1461.80	6900	Olivine gabbro
176	735	B	206	R	4	61	63	1464.12	7025	Olivine gabbro
176	735	B	207	R	2	19	21	1471.12	6980	Olivine gabbro
176	735	B	207	R	4	60	62	1473.68	6638	Olivine gabbro
176	735	B	207	R	7	110	112	1478.43	6670	Olivine gabbro
176	735	B	208	R	4	12	14	1482.77	6781	Olivine gabbro
176	735	B	208	R	5	106	108	1485.21	7834	Olivine gabbro
176	735	B	208	R	8	65	67	1488.73	6967	Olivine gabbro
176	735	B	209	R	2	75	77	1490.50	6452	Olivine gabbro
176	735	B	209	R	8	103	105	1498.65	7184	Olivine gabbro
176	735	B	210	R	4	11	13	1502.50	7068	Olivine gabbro
176	735	B	210	R	4	52	54	1502.91	7504	Olivine gabbro
								Mean	6784	
								SD	313	
								Count	367	

Notes: This table is also available in ASCII format in the **TABLES** directory. SD = standard deviation.

Table T19. Resistivity measurements for Hole 735B.

Leg	Hole	Site	Core	Type	Section	Top (cm)	Bottom (cm)	Resistivity (Ωm)
176	735	B	103	R	3	48	50	6.77
176	735	B	95	R	1	118	120	11.3
176	735	B	106	R	4	54	56	7.1
176	735	B	99	R	3	30	32	27.6
176	735	B	94	R	5	30	32	12.8
176	735	B	93	R	3	72	74	5.1
176	735	B	95	R	1	33	35	21.6
176	735	B	100	R	1	19	21	7.4
176	735	B	91	R	1	43	45	79.8
176	735	B	91	R	1	108	110	34
176	735	B	89	R	1	36	38	52.8
176	735	B	90	R	1	19	21	132
176	735	B	90	R	4	115	117	175
176	735	B	90	R	6	35	37	86
176	735	B	90	R	8	105	107	158
176	735	B	90	R	7	27	29	14
176	735	B	105	R	3	56	58	68
176	735	B	91	R	3	94	96	3.8
176	735	B	93	R	1	113	115	7.5
176	735	B	93	R	2	33	35	140
176	735	B	93	R	3	94	96	24
176	735	B	94	R	3	52	54	15.5
176	735	B	94	R	3	116	118	50
176	735	B	96	R	2	49	51	35
176	735	B	97	R	3	26	28	50
176	735	B	99	R	4	23	25	80
176	735	B	101	R	3	31	33	100
176	735	B	102	R	1	28	30	2.2
176	735	B	102	R	3	58	60	20
176	735	B	103	R	2	81	83	35
176	735	B	103	R	4	31	33	40
176	735	B	104	R	2	49	51	50
176	735	B	105	R	1	52	54	17
176	735	B	106	R	1	73	75	54
176	735	B	108	R	2	44	46	54
176	735	B	108	R	4	87	89	50
176	735	B	110	R	1	46	48	60
176	735	B	110	R	4	57	59	68
176	735	B	111	R	2	105	107	66

Notes: This table is also available in ASCII format in the **TABLES** directory.

Table T20. Average and standard deviation of log values calculated for the electrofacies determined by log interpretation.

	Olivine gabbro	Oxide-rich gabbro	Altered zones	Fractured zones
APLC (%):	2.0 ± 1.9	2.3 ± 2.5	**9.0 ± 4.8**	**23.4 ± 17.2**
LLD (Ωm):	3430 ± 4500	**135 ± 395**	**920 ± 2820**	**320 ± 610**
PEF (barn/e$^-$):	3.9 ± 0.6	**5.7 ± 1.5**	3.5 ± 0.6	2.6 ± 0.7
RHOB (g/cm^3):	2.87 ± 0.05	**3.03 ± 0.10**	**2.72 ± 0.08**	**2.41 ± 0.31**
SIGF (c.u.):	17 ± 2	27 ± 6	19 ± 4	24 ± 5
V_p (km/s):	6.6 ± 0.4	6.4 ± 0.3	6.0 ± 0.5	6.0 ± 0.7
V_s (km/s):	3.7 ± 0.2	3.6 ± 0.1	3.5 ± 0.3	3.7 ± 0.6
N:	2325	593	154	108

Note: APLC = neutron porosity; LLD = electrical resistivity deep; PEF = photoelectric factor; RHOB = density; SIGF = capture cross section; V_p = compressional wave velocity; V_s = shear wave velocity; *N* = number of depth points. Bold type indicates significant log values.